MULTI-DISCIPLINARY APPLICATIONS IN MAGNETIC CHRONOSTRATIGRAPHY

EDITED BY: Kenneth Philip Kodama, Luigi Jovane and Linda Hinnov
PUBLISHED IN: Frontiers in Earth Science

frontiers Research Topics

frontiers

ISSN 1664-8714
ISBN 978-2-88966-557-0
DOI 10.3389/978-2-88966-557-0

About Frontiers

Frontiers is more than just an open-access publisher of scholarly articles: it is a pioneering approach to the world of academia, radically improving the way scholarly research is managed. The grand vision of Frontiers is a world where all people have an equal opportunity to seek, share and generate knowledge. Frontiers provides immediate and permanent online open access to all its publications, but this alone is not enough to realize our grand goals.

Frontiers Journal Series

The Frontiers Journal Series is a multi-tier and interdisciplinary set of open-access, online journals, promising a paradigm shift from the current review, selection and dissemination processes in academic publishing. All Frontiers journals are driven by researchers for researchers; therefore, they constitute a service to the scholarly community. At the same time, the Frontiers Journal Series operates on a revolutionary invention, the tiered publishing system, initially addressing specific communities of scholars, and gradually climbing up to broader public understanding, thus serving the interests of the lay society, too.

Dedication to Quality

Each Frontiers article is a landmark of the highest quality, thanks to genuinely collaborative interactions between authors and review editors, who include some of the world's best academicians. Research must be certified by peers before entering a stream of knowledge that may eventually reach the public - and shape society; therefore, Frontiers only applies the most rigorous and unbiased reviews.
Frontiers revolutionizes research publishing by freely delivering the most outstanding research, evaluated with no bias from both the academic and social point of view. By applying the most advanced information technologies, Frontiers is catapulting scholarly publishing into a new generation.

What are Frontiers Research Topics?

Frontiers Research Topics are very popular trademarks of the Frontiers Journals Series: they are collections of at least ten articles, all centered on a particular subject. With their unique mix of varied contributions from Original Research to Review Articles, Frontiers Research Topics unify the most influential researchers, the latest key findings and historical advances in a hot research area! Find out more on how to host your own Frontiers Research Topic or contribute to one as an author by contacting the Frontiers Editorial Office: frontiersin.org/about/contact

MULTI-DISCIPLINARY APPLICATIONS IN MAGNETIC CHRONOSTRATIGRAPHY

Topic Editors:
Kenneth Philip Kodama, Lehigh University, United States
Luigi Jovane, University of São Paulo, Brazil
Linda Hinnov, George Mason University, United States

Citation: Kodama, K. P., Jovane, L., Hinnov, L., eds. (2021). Multi-Disciplinary Applications in Magnetic Chronostratigraphy. Lausanne: Frontiers Media SA. doi: 10.3389/978-2-88966-557-0

Table of Contents

04 ***Editorial: Multi-Disciplinary Applications in Magnetic Chronostratigraphy***
Luigi Jovane, Kenneth P. Kodama and Linda A. Hinnov

06 ***Rock Magnetic Cyclostratigraphy of the Carboniferous Mauch Chunk Formation, Pottsville, PA, United States***
Kenneth P. Kodama

21 ***Magnetic Susceptibility Record in Paleozoic Succession (Rhenohercynian Massif, Northern Europe) – Disentangling Sea Level, Local and Diagenetic Impact on the Magnetic Records***
Damien Pas, Anne-Christine Da Silva, Geoffrey Poulain, Simo Spassov and Frédéric Boulvain

45 ***The Arctic Ocean Manganese Cycle, an Overlooked Mechanism in the Anomalous Palaeomagnetic Sedimentary Record***
Steffen Wiers, Ian Snowball, Matt O'Regan, Christof Pearce and Bjarne Almqvist

62 ***Early Cretaceous Terrestrial Milankovitch Cycles in the Luanping Basin, North China and Time Constraints on Early Stage Jehol Biota Evolution***
Wei Liu, Huaichun Wu, Linda A. Hinnov, Dangpeng Xi, Huaiyu He, Shihong Zhang and Tianshui Yang

77 ***Paleomagnetic Constraint of the Brunhes Age Sedimentary Record From Lake Junín, Peru***
Robert G. Hatfield, Joseph S. Stoner, Katharine E. Solada, Ann E. Morey, Arielle Woods, Christine Y. Chen, David McGee, Mark B. Abbott and Donald T. Rodbell

95 ***Magnetostratigraphy and Paleoenvironments of the Kuntila Lake Sediments, Southern Israel: Implications for Late Cenozoic Climate Variability at the Northern Fringe of the Saharo-Arabian Desert Belt***
Juan Cruz Larrasoaña, Nicolas Waldmann, Steffen Mischke, Yoav Avni and Hanan Ginat

107 ***Rock Magnetic Cyclostratigraphy of Permian Loess in Eastern Equatorial Pangea (Salagou Formation, South-Central France)***
Lily S. Pfeifer, Linda Hinnov, Christian Zeeden, Christian Rolf, Christian Laag and Gerilyn S. Soreghan

120 ***The Birth of a Connected South Atlantic Ocean: A Magnetostratigraphic Perspective***
Dan V. Palcu, Joy R. Muraszko, Plinio F. Jaqueto and Luigi Jovane

139 ***Southward Drift of Eastern Australian Hotspots in the Paleomagnetic Reference Frame is Consistent With Global True Polar Wander Estimates***
Jeroen Hansma and Eric Tohver

155 ***Magnetostratigraphic Chronology of a Cenozoic Sequence From DSDP Site 274, Ross Sea, Antarctica***
Luigi Jovane, Fabio Florindo, Gary Wilson, Stephanie de Almeida Pecchiai Saldanha Leone, Muhammad Bin Hassan, Daniel Rodelli and Giuseppe Cortese

frontiers in Earth Science

EDITORIAL
published: 20 January 2021
doi: 10.3389/feart.2020.634790

Editorial: Multi-Disciplinary Applications in Magnetic Chronostratigraphy

Luigi Jovane[1]*, *Kenneth P. Kodama*[2] *and Linda A. Hinnov*[3]

[1]Instituto Oceanográfico, Universidade de São Paulo, São Paulo, Brazil, [2]Department of Earth and Environmental Sciences, Lehigh University, Bethlehem, PA, United States, [3]Department of Atmospheric, Oceanic, and Earth Sciences, George Mason University, Fairfax, VA, United States

Keywords: magnetostratigraphy, chronostratigraphy, relative paleointensity, paleomagnetism, cyclostratigraphy

Editorial on the Research Article

Multi-Disciplinary Applications in Magnetic Chronostratigraphy

Using magnetic methods, it is possible to assign ages to rocks and sedimentary sequences.

Magnetostratigraphy constitutes a standard dating tool in the Earth Sciences, applicable to a wide variety of rock types formed under different environmental conditions (continental, lacustrine, marine and volcanic). Rock samples are capable of retaining a geologically stable magnetization even if it is very weak because of a relatively low concentration of magnetic minerals (e.g., magnetite or hematite). Sediments and sedimentary rocks acquire a primary natural remanent magnetization (NRM), called a detrital remanent magnetization (DRM) when the sub-micron magnetic grains in the sediments settle through the water column or during post-depositional consolidation and align with the geomagnetic field. In igneous rocks, a primary natural remanent magnetization, called a thermoremanent magnetization (TRM) is acquired when the magnetic minerals in a rock cool below a critical temperature (the Curie temperature for ferrimagnetic minerals, like magnetite and the Neel temperature for antiferromagnetic minerals like hematite). Magnetic minerals can be formed due to changes in post-depositional conditions, i.e., biogenic processes, fluid circulation or oxidation/reduction processes which impart a chemical remanent magnetization (CRM) to the rock. This type of magnetization is secondary and can often mask the primary magnetizations in a rock.

During paleomagnetic studies, geological samples are typically subjected to increasing steps of demagnetization, either temperature steps or alternating magnetic field steps, in order to isolate the primary paleomagnetic directions of the rock. In this way it is possible to determine the geomagnetic polarity intervals in a sedimentary sequence.

Those geomagnetic polarity intervals can be normal (usually depicted by a black zone in a plot) when magnetic polarity is the same as today or reversed (depicted by a white zone) when the polarity is the opposite of today. During the Cenozoic patterns of polarity intervals are grouped together and designated as chrons, based initially on their seafloor magnetic anomaly patterns, and labeled by C. For instance, C1 (Chron 1) includes the normal polarity interval of the past 781 ka (called Bruhnes), and the reversed polarity interval immediately preceding it starting at about 1.8 Ma (called Matuyama), including a short normal polarity interval at about 1 Ma (called Jaramillo). Chrons are not the same as polarity intervals. During the Mesozoic, chrons are designated by an M. Polarity intervals last usually between 1 and 10 Ma but on occasion during Earth history, intervals of one polarity are observed that are tens of millions of years long (superchrons). The time to change from normal to reversed polarity is very short (around 5 ka); consequently, the boundary between polarity intervals is very precise in time.

Edited and reviewed by:
Valerio Acocella,
Roma Tre University, Italy

***Correspondence:**
Luigi Jovane
jovane@usp.br

Specialty section:
This article was submitted to Geomagnetism and Paleomagnetism, a section of the Frontiers in Earth Science

Received: *28 November 2020*
Accepted: *04 December 2020*
Published: *20 January 2021*

Citation:
Jovane L, Kodama KP and Hinnov LA (2021) Editorial: Multi-Disciplinary Applications in Magnetic Chronostratigraphy. Front. Earth Sci. 8:634790. doi: 10.3389/feart.2020.634790

The sequence of geomagnetic polarity intervals is globally calibrated by the seafloor magnetic anomalies, biostratigraphic zonation and numerical radioisotope dating of sedimentary (marine and continental) and volcanic sections from around the globe.

The resulting magnetic polarity sequence can then be correlated to the Geomagnetic Polarity Time Scale (GPTS), thus tying the sedimentary or igneous rock sequence to numerical time. Magnetostratigraphy can produce precise ages for the samples proximal to polarity interval boundaries and allow the interpolation of mean accumulation rates between boundaries.

This Research Topic volume includes a variety of paleomagnetic and rock magnetic studies (10 papers) which use magnetostratigraphy and subsequent correlation to the GPTS to address a series of important geological problems. Paleomagnetic techniques are used to detect and date the initiation of major deep sea currents, such as the initiation of the Antarctic bottom water (DSDP Site 274) during the Miocene/Oligocene transition (Jovane et al.), and the initiation of the Atlantic Ocean circulation in the Paleogene from samples collected from the São Paulo Plateau (Palcu et al.). Larrasoaña et al. investigate the timing of climate variability and early hominid migration out of Africa through the Levantine Corridor from magnetostratigaphic studies of late Cenozoic Lake Kuntila deposits in the Negev Desert of Israel.

Another important magnetic dating tool uses the record of relative paleointensity variations of the geomagnetic field from marine and lacustrine sediments to assign time to the sedimentary sequence. In this case, the intensity of the sediment's magnetization is normalized by the concentration of magnetic minerals by rock magnetic measurements, such as magnetic susceptibility (χ when normalized by mass or κ when normalized by volume), anhysteretic remanent magnetization (ARM) or isothermal remanent magnetization (IRM). The resulting normalized paleointensity curve can be correlated to the global paleointensity curves for the last 2 Ma ($S_{int\text{-}2000}$; Valet et al., 2005). Our Research Topic includes a relative paleointensity study of 88 m of lacustrine sediments measured in u-channels from Lake Junin in Peru. After filtering out the low NRM intensity samples a high-quality relative paleointensity record was obtained that allowed correlation to the master relative paleointensity curves for the Brunhes normal polarity interval (subchron C1n) resulting in a high-resolution age model (Hatfield et al.).

Astronomically-forced climate cycles, i.e., Milankovitch cycles, are encoded by the concentration of magnetic minerals of sediments (Kodama and Hinnov, 2015). Measurements of magnetic susceptibility, ARM and IRM, allow the detection of Milankovitch cycles and hence a high-resolution time calibration of sedimentary sequences from the Precambrian to the present.

Included in our Research Topic are rock magnetic cyclostratigraphy studies of Permian loess in south-central France from equatorial Pangean deposits (Pfeifer et al.) using a portable susceptibility meter, Carboniferous fluvial deposits of red beds from Pennsylvania (Kodama) comparing portable and laboratory susceptibility measurements and Early Cretaceous lacustrine deposits rich in dinosaur/primitive bird fossils of the Jehol Biota (Liu et al.). The magnetic susceptibility cyclostratigraphy in each study was able to identify astronomically-forced global climate change cycles and assign high resolution time to the sequences being studied.

Magnetic chronostratigraphic methods include multidisciplinary approaches to understand the post-depositional changes that occurred to the sediments during climatic changes and sea-level fluctuations. One study in our Research Topic investigates the reliability of magnetic susceptibility for inter-regional correlations in the Ardennes carbonate platform (France) during the Paleozoic (Pas et al.) and another study reports on the link between post-depositional diagenetic changes in magnetic minerals and the manganese cycle in the Arctic Ocean (Wiers et al.).

Finally, the paleomagnetic directions of geochronologically-dated igneous samples from an eastern Australian hotspot track, extending over 34 Ma, delineate the drift of these hotspots with respect to the Earth's spin axis. These results allow an estimate of true polar wander for the last 34 Ma (Hansma and Tohver).

In conclusion, as it is shown by the papers of this Research Topic, magnetic methods, i.e., magnetostratigraphy, rock magnetic cyclostratigraphy, and relative paleointensity records, are currently used to provide high resolution chronostratigraphy for sedimentary sequences and hence the time framework for understanding and correlating ancient paleoclimatic and paleoenvironmental changes both regionally and globally. In the future, these techniques represent robust tools that can be applied to a wide range of stratigraphic sections in order to improve age constraints of past geologic events for better understanding the processes that caused them.

AUTHOR CONTRIBUTIONS

All authors listed have made a substantial, direct, and intellectual contribution to the work and approved it for publication.

REFERENCES

Kodama, K. P., and Hinnov, L. A. (2015). *Rock magnetic cyclostratigraphy*. Oxford, UK: John Wiley and Sons, 176. doi:10.1002/9781118561294

Valet, J. P., Meynadier, L., and Guyodo, Y. (2005). Geomagnetic dipole strength and reversal rate over the past two million years. *Nature* 435, 802. doi:10.1038/nature03674

Conflict of Interest: The authors declare that the research was conducted in the absence of any commercial or financial relationships that could be construed as a potential conflict of interest.

frontiers in Earth Science

ORIGINAL RESEARCH
published: 12 November 2019
doi: 10.3389/feart.2019.00285

Rock Magnetic Cyclostratigraphy of the Carboniferous Mauch Chunk Formation, Pottsville, PA, United States

*Kenneth P. Kodama**

Department of Earth and Environmental Sciences, Lehigh University, Bethlehem, PA, United States

A rock magnetic cyclostratigraphy study was conducted on the Carboniferous Mauch Chunk Formation red beds at Pottsville, Pennsylvania to determine if Milankovitch climate forcing could be detected in these terrestrial, fluvial deposits with hematite as the predominant ferromagnetic mineral. Because fluvial deposits are not deposited continuously it would be important to determine if they could record Milankovitch-scale climate cycles. Furthermore, the hematite magnetic mineral particles in red beds are not always recognized as primary, depositional minerals, so it was unclear whether they could record Milankovitch climate cycles. This locality was chosen because a robust magnetostratigraphy had already been established for it thus giving an estimate of its sediment accumulation rate (SAR). Magnetic susceptibility was measured in the laboratory with a KLY-3s Kappabridge on samples collected every 0.5 m of section for 68 m of section. Magnetic susceptibility measurements were also made in the field using an SM-20 portable susceptibility meter. The time series that resulted were different but yielded very similar power spectra calculated by the multi-taper method (MTM). Significant spectral peaks isolated by robust red noise and harmonic f-tests yielded peaks identified to be short eccentricity (125 and 95 ka), obliquity (35 ka) and precession (21 and 17.5 ka) in the Carboniferous. Average spectral misfit (ASM) analysis of these peaks for both the Kappabridge and SM-20 time series gave the identical SAR of 5.69 cm/ka, somewhat slower than the ∼9 cm/ka average rate for >250 m of section estimated from magnetostratigraphy and biostratigraphic correlation throughout northeastern North America. Analysis of the low temperature magnetic susceptibility versus temperature curves for a 10 m stratigraphic interval of samples indicates that the ferromagnetic content of the bulk susceptibility appears to be driving the precession- and obliquity-scale bulk susceptibility variations. This observation suggests that climate change in the source area causes more or less erosion of ferromagnetic minerals that are then deposited into a background of paramagnetic clays or diamagnetic quartz sand in the depositional basin. Our study clearly shows that fluvial terrestrial sediments can record astronomically forced climate change. Our study also indicates that portable susceptibility measurements are a valid way of collecting reconnaissance rock magnetic time series to determine sampling intervals for more detailed studies.

Keywords: cyclostratigraphy, rock magnetism, Milankovitch cycle, magnetic susceptibility, Mauch Chunk Formation

OPEN ACCESS

Edited by:
Emilio L. Pueyo, Geological and Mining Institute of Spain, Spain

Reviewed by:
Ann Marie Hirt, ETH Zürich, Switzerland
Fatima Martin Hernandez, Complutense University of Madrid, Spain
Juan Cruz Larrasoaña, Geological and Mining Institute of Spain, Spain

***Correspondence:**
Kenneth P. Kodama
kpk0@lehigh.edu

Specialty section:
This article was submitted to Geomagnetism and Paleomagnetism, a section of the journal Frontiers in Earth Science

Received: *06 August 2019*
Accepted: *18 October 2019*
Published: *12 November 2019*

Citation:
Kodama KP (2019) Rock Magnetic Cyclostratigraphy of the Carboniferous Mauch Chunk Formation, Pottsville, PA, United States. Front. Earth Sci. 7:285. doi: 10.3389/feart.2019.00285

INTRODUCTION

Rock magnetic cyclostratigraphy (Kodama and Hinnov, 2015) uses rock magnetic measurements of sedimentary sequences to detect astronomically forced global climate change cycles thus allowing high-resolution chronostratigraphy to be assigned to the sequence. To date most successful rock magnetic cyclostratigraphy studies have been conducted on marine sediments (Kodama et al., 2010; Gunderson et al., 2012; Wu et al., 2012; Hinnov, 2013; Minguez et al., 2015; Gong et al., 2017; Minguez and Kodama, 2017; Pas et al., 2018) which have a greater probability of nearly continuous sedimentation; therefore, ensuring a more complete record of global climate cycles.

The goal of this study of the Carboniferous Mauch Chunk Formation red beds is to determine if rock magnetics can detect astronomically forced global climate cycles in a terrestrial, fluvial depositional environment that doesn't have continuous sedimentation. There have been few cyclostratigraphic studies of terrestrial environments (Abdul Aziz et al., 2000; Abels et al., 2013; Noorbergen et al., 2018; Zhang et al., 2019). There is the additional concern that a red bed, dominated by the anti-ferromagnetic mineral hematite, may not have a depositional remanence, although the Mauch Chunk has demonstrated a robust magnetostratigraphy (DiVenere and Opdyke, 1991) so it either carries a depositional remanence or a very early diagenetic (chemical) remanence. Additional paleomagnetic studies of the Mauch Chunk Formation (Kent and Opdyke, 1985; Stamatakos and Kodama, 1991; Cioppa and Kodama, 2003; Bilardello and Kodama, 2010) strongly suggest, in particular for the anisotropy/inclination shallowing detection and correction work, that the magnetization is a depositional remanence carried by the hematite grains.

Our specific target was the Pottsville, Pennsylvania outcrop of the Mauch Chunk Formation. It is located in east central Pennsylvania and has been described in detail by Levine and Slingerland (1987) (**Figure 1**). The Pottsville outcrop, exposed along Route 61 just south of Pottsville, PA is approximately 600 m thick. We sampled the bottom 68 m of this section which, according to Levine and Slingerland, is comprised of overbank deposits (red calcareous mudstones) and shallow channel deposits (coarse to fine-grained red sandstones). Slingerland and Levine identify upward fining sequences from sandstone to mudstone repeating about every 20 m in this part of the section.

The Pottsville outcrop of the Mauch Chunk also offers a detailed magnetostratigraphy (DiVenere and Opdyke, 1991) which allows constraint of the sediment accumulation rate (SAR) thus allowing more robust identification of any Milankovitch cycles detected by the rock magnetics. The DiVenere and Opdyke (1991) magnetostratigraphy identifies a long (100 m thick) normal polarity event in the bottom part of the section where we have sampled. This normal event (MMCn at the Pottsville section) has been correlated to N5 in the Nova Scotia's Maringouin Peninsula and the Joggins section and the MPN1 at the Broad Cove-Chapel section in Cape Breton Island by Opdyke et al. (2014) based primarily on biostratigraphy (palynology and fossil plants). This correlation suggests that 270.5 m of the Pottsville section represents 2.9 million years (Opdyke et al., 2014) yielding an average SAR of 9.3 cm/ka. The Geologic Time Scale 2012 (Gradstein et al., 2012) indicates that the MMCn normal polarity event is a little less than one million years in duration (SAR∼9–10 cm/ka) and is 330.9 Ma in age.

This paper will demonstrate that Milankovitch cycles (astronomically forced global climate change cycles of periodicities 100, 35, and ∼20 ka) can be detected rock magnetically in a fluvial depositional environment despite the presence of hiatuses in sedimentation typical of this environment. We will also show that measuring the susceptibility in the field with a portable susceptibility meter can yield a time series which records the same Milankovitch cycles.

MATERIALS AND METHODS

To acquire the rock magnetic time series, we collected an un-oriented sample every 0.5 m of stratigraphic thickness, measuring stratigraphic thickness with a Jacob's staff for the nearly vertically dipping strata at the Pottsville section. Based on the time series analysis theory, the shortest cycle detectable is the Nyquist frequency which is determined by the sample spacing.

$$\text{Nyquist frequency} = 1/(2 \times \text{sample spacing})$$

The shortest Milankovitch frequency we hoped to detect is precession which has periodicities of about 17.5 and 21 ka in the Carboniferous (Berger and Loutre, 1994; Waltham, 2015). Based on the SAR estimated from biostratigraphy and magnetostratigraphy (9.3 cm/ka), this would dictate sampling about every 80 cm of stratigraphic thickness to detect precession. Conservatively, we sampled every 50 cm.

In a pilot study, in 2012, a graduate level paleomagnetism class at Lehigh University sampled 40 m of the Pottsville section and measured isothermal remanent magnetization (IRMs) acquired in a 3.5 T field ($IRM_{3.5T}$). The measurements were normalized by sample mass. The magnetic susceptibility (χ) was also measured and the IRMs were alternating field demagnetized at 100 mT to remove the contributions of low coercivity ferromagnetic minerals to the IRM ($IRM_{3.5T-100mT}$).

In 2017, un-oriented samples were collected from 68 m of section, at a 0.5 m spacing. The rock samples were fitted into $2 \times 2 \times 2$ cm^3 plastic sample cubes and their magnetic susceptibility was measured in a KLY-3s Kappabridge. Each sample was measured three times and the measurements were averaged. The average measurements for each sample were normalized by sample mass. In the 2017 study, an SM-20 portable susceptibility meter was used to measure the bulk susceptibility at each place on the outcrop that the un-oriented samples were collected. The *in situ* susceptibility was measured at least three times on the flattest surface available and the results were averaged. The measurement is normalized by the volume that the SM-20 measures, approximately 49 cm^3. The stratigraphic measurements were tied to the bottom of the Mauch Chunk Formation which outcrops at the Pottsville section.

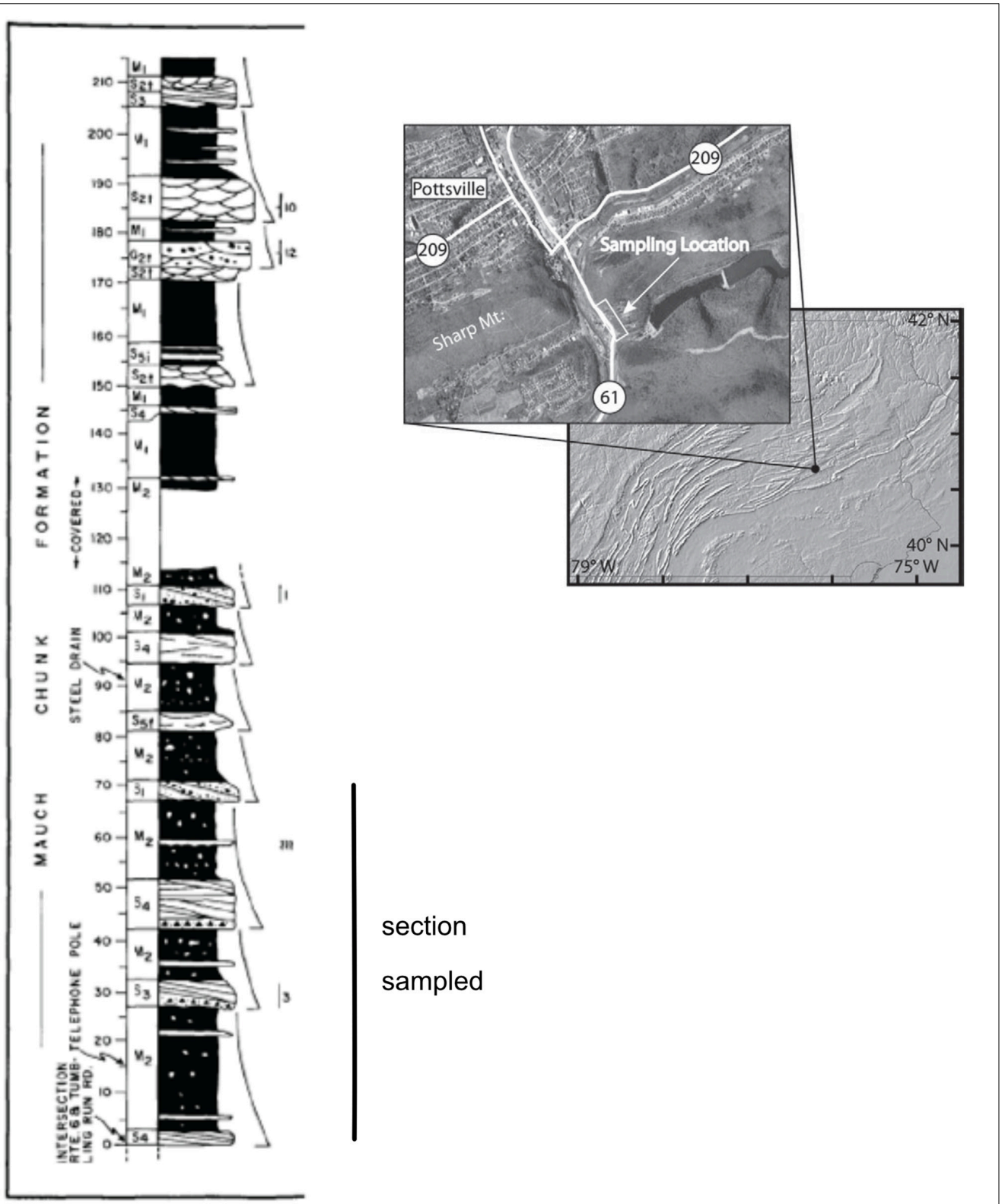

FIGURE 1 | (Left) Stratigraphic column of the Pottsville, PA, Mauch Chunk Formation section from Levine and Slingerland (1987). **(Right)** Location of the Pottsville section of the Mauch Chunk Formation along Route 61 in northeastern Pennsylvania (from Bilardello and Kodama, 2010).

Time series analysis was conducted using the multi-taper method (MTM, Thomson, 1982) with robust (Mann and Lees, 1996) red noise [Gilman et al., 1963; AR-1 autoregressive for both the portable (SM-20) and un-oriented rock samples (Kappabridge)]. Meyers' (2014) and RStudio Team. (2015) was used for the analyses. Evolutionary spectrograms, using Astrochron, were also calculated to monitor how the dominant cycles varied throughout the section.

In the Astrochron time series analysis, outliers were trimmed from the time series using a box and whisker plot to reduce noise, the time series was resampled at an even spacing using linear interpolation, and MTM spectral analysis was conducted. In the

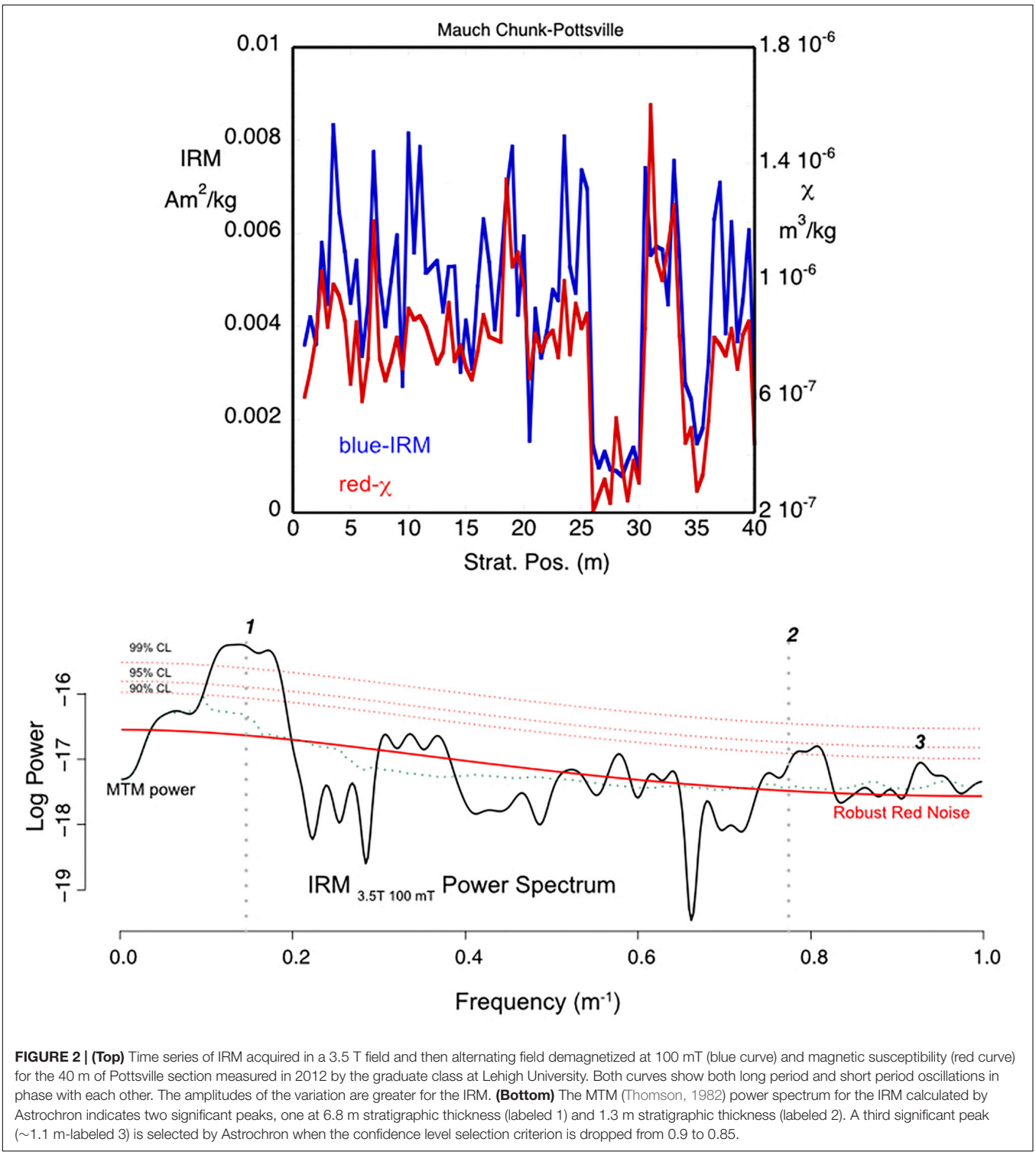

FIGURE 2 | (Top) Time series of IRM acquired in a 3.5 T field and then alternating field demagnetized at 100 mT (blue curve) and magnetic susceptibility (red curve) for the 40 m of Pottsville section measured in 2012 by the graduate class at Lehigh University. Both curves show both long period and short period oscillations in phase with each other. The amplitudes of the variation are greater for the IRM. **(Bottom)** The MTM (Thomson, 1982) power spectrum for the IRM calculated by Astrochron indicates two significant peaks, one at 6.8 m stratigraphic thickness (labeled 1) and 1.3 m stratigraphic thickness (labeled 2). A third significant peak (~1.1 m-labeled 3) is selected by Astrochron when the confidence level selection criterion is dropped from 0.9 to 0.85.

MTM analysis 3 DPSS tapers were used, the mean was subtracted, the data were detrended and zero padded by a factor of 10. AR-1 robust red noise was calculated. Astrochron automatically identifies spectral peaks that are greater than a set value for the confidence level of the robust red noise and the harmonic f-test calculated by the MTM method (Meyers, 2012). The confidence levels were set at the default value (0.9) for the SM-20 time series and 0.85 for the Kappabridge time series.

To check our identification of the Milankovitch cycles, we conducted amplitude modulation (AM) analysis of the cycle we chose to be precession. The time series was filtered at the suspected precession frequency and time series analysis of the amplitude envelope of the filtered series was used to determine if there were cycles at the eccentricity time scale, because eccentricity modulates precession.

Low temperature (liquid N temperature, −195°C, warmed to 0°C) magnetic susceptibility versus temperature (MS vs. T) measurements were made in the KLY-3s Kappabridge to determine the proportion of paramagnetic (clays) and ferromagnetic (hematite and/or magnetite) minerals carrying the magnetic susceptibility. This was done following the constant ferromagnetic susceptibility

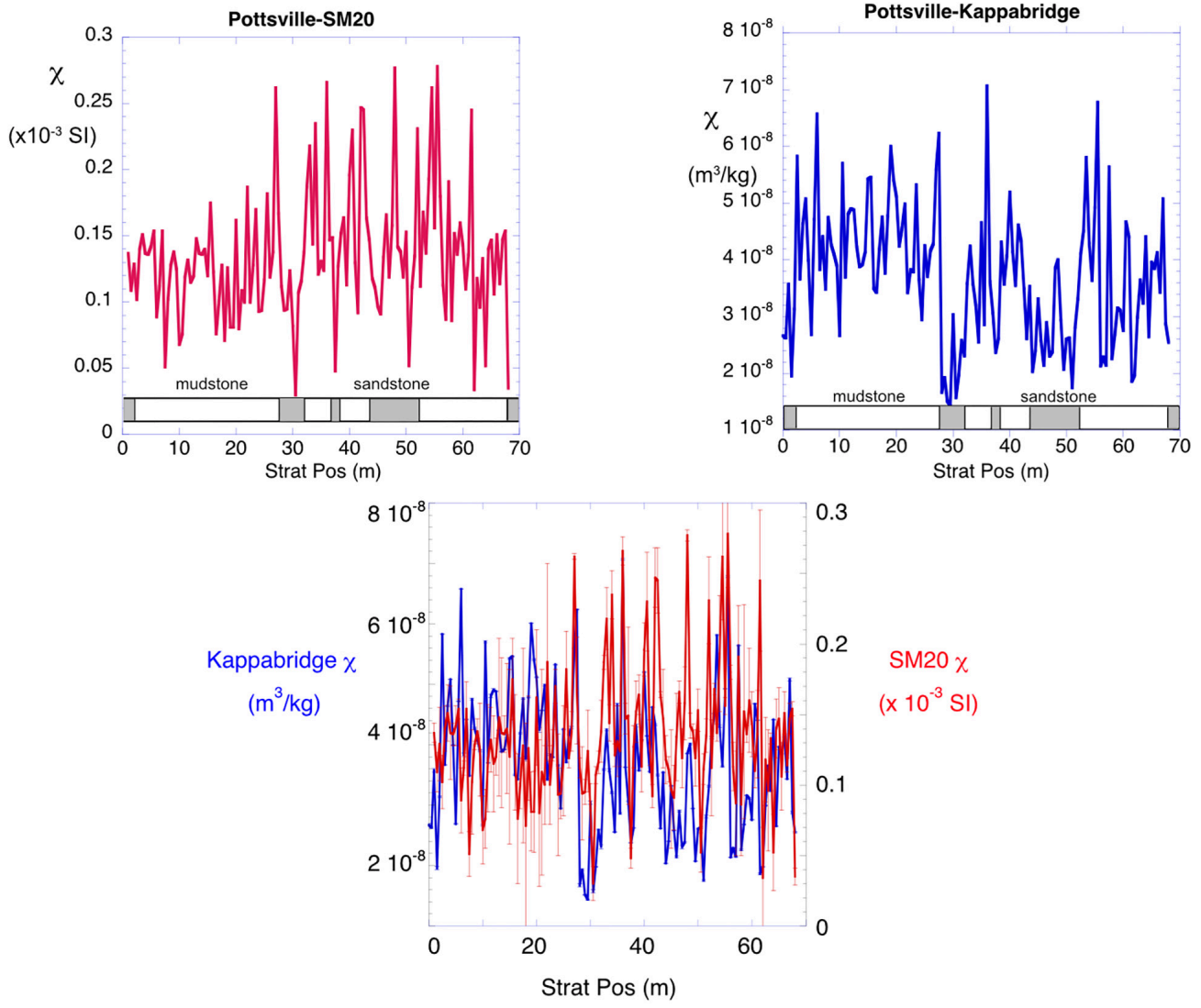

FIGURE 3 | Time series magnetic susceptibility for 68 m of the Pottsville section measured by the SM-20 portable susceptibility meter **(Top left)** and for rock samples collected in the field and measured on the Kappabridge KLY-3s at the Lehigh University **(Top right)**. Below each plot is the stratigraphy for the 68 m samples showing the sandstone channel deposits and the mudstone overbank deposits. Base of the section is to the left. Both time series show both long period and short period variability; however, they do not match. The Kappabridge measured susceptibility shows better correlation to the lithologic variations at long periods, but both time series show short period variations within the different lithologies. A direct comparison of the two time series **(Bottom center)**, with one standard deviation error bars, shows the high uncertainty in the SM-20 measurements compared to the low uncertainty in the Kappabridge measurements (error bars are typically smaller than the symbol for the measurement).

method of Hrouda (1994) in which a hyperbola is fit to the magnetic susceptibility measured as the sample warmed from −195 to 0°C. The goodness of fit determines the percentage of paramagnetic minerals contributing to the bulk susceptibility. High temperature MS vs. T measurements in an argon atmosphere cycled up to 700°C and back down to room temperature were used to identify the ferromagnetic minerals.

Isothermal remanent magnetization acquisition experiments were also conducted to identify the ferromagnetic minerals in the samples. The IRM acquisition data were modeled using the Kruiver et al. (2001) Excel spreadsheet available from the Fort Hoofddijk paleomagnetic laboratory website.

All remanence measurements were conducted in a 2G Enterprises superconducting rock magnetometer (model 755) in a magnetically shielded room with a background magnetic field of ∼350 nT.

RESULTS

Spectral Analysis

The time series constructed from IRM and MS measurements in the 2012 pilot study show a strong correlation between $IRM_{3.5T}$, $IRM_{3.5T-100\ mT}$ and magnetic susceptibility, particularly at stratigraphic thickness wavelengths of 5–10 m, but also at shorter,

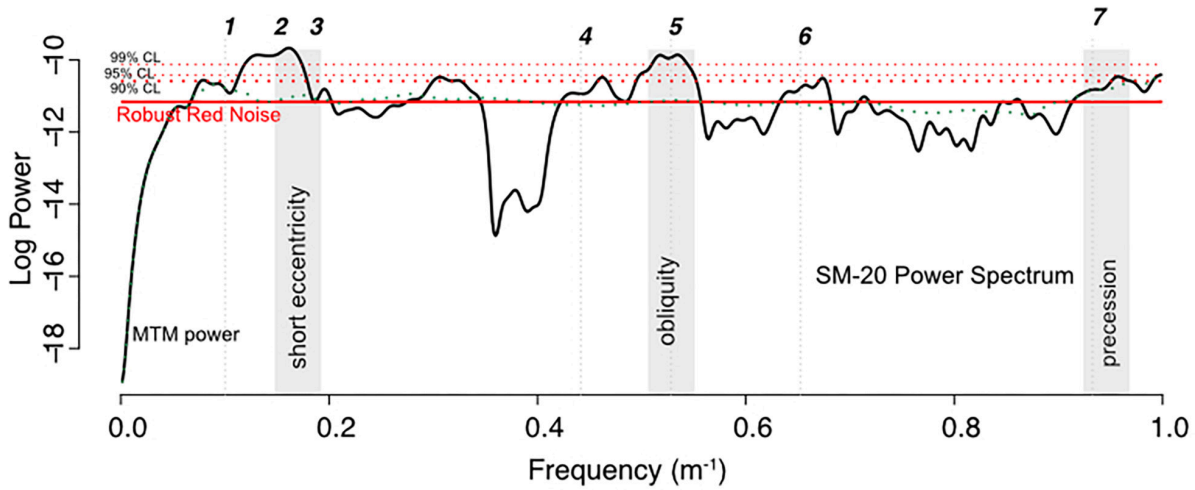

FIGURE 4 | Log power spectrum for the SM-20 portable susceptibility meter magnetic susceptibility time series shown in **Figure 3** showing significant peaks chosen by Astrochron (Meyers, 2014) and numbered (confidence limit set to 0.9). The shaded bands show our choice for the Milankovitch cycles. See **Table 1** for the periods/frequencies of the numbered peaks.

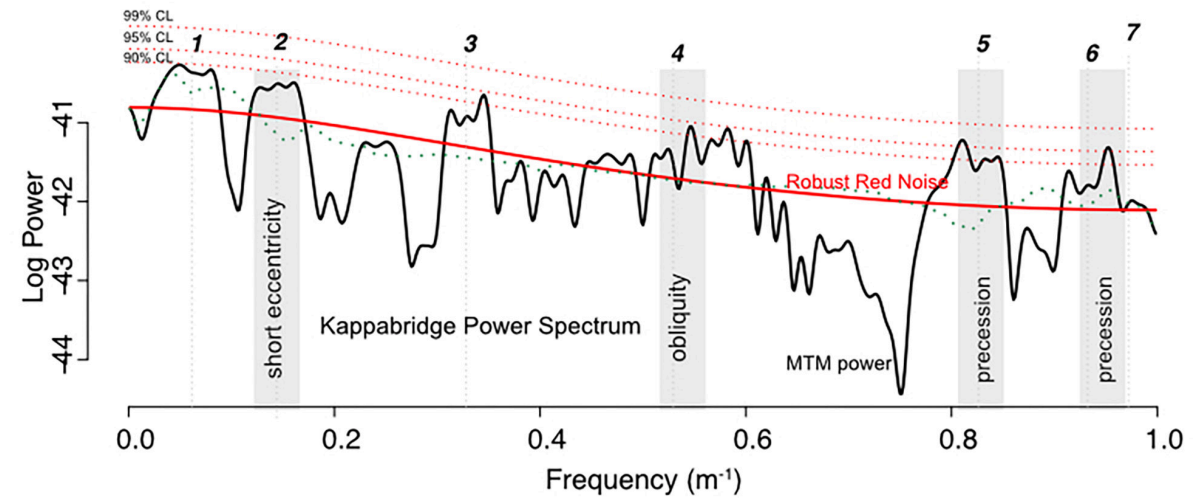

FIGURE 5 | Log power spectrum for the Kappabridge measured magnetic susceptibility time series shown in **Figure 3** showing significant peaks chosen by Astrochron (Meyers, 2014) and numbered (confidence limit set to 0.85). The shaded bands show our choice for the Milankovitch cycles. See **Table 2** for the periods/frequencies of the numbered peaks.

1–2 m scales (**Figure 2** and **Supplementary Table S2**). The $IRM_{3.5T}$ time series shows particularly high amplitude variation at the 1–2 m wavelength stratigraphic thickness scale. The big low in magnetic intensity for all three datasets at 25–30 m along the section correlates with a large sandstone bed indicating lithologic control of the susceptibility at this spatial scale. MTM spectral analysis using Astrochron of the $IRM_{3.5T-100\ mT}$ time series shows significant spectral peaks at 6.8 m stratigraphic thickness (labeled 1) and 1.3 m stratigraphic thickness (labeled 2) (**Figure 2**). A third peak at ∼1.1 m stratigraphic thickness (labeled 3) is selected by Astrochron when the confidence level selection criterion is dropped to 0.85.

For the 2017 dataset, the main study of this paper, the magnetic susceptibility time series for the Kappabridge, laboratory rock sample measurements and the SM-20 portable susceptibility meter measurements both show high amplitude, high frequency (∼1 m stratigraphic thickness periods) content (**Figure 3** and **Supplementary Table S1**). The Kappabridge time series shows a better correlation with the lithologic column with longer wavelength lows associated with sandstone beds. Both time series show high amplitude, high frequency variability within the mudstone overbank deposits exposed between 5 m and about 28 m in the section, indicating that the magnetic susceptibility isn't controlled completely by lithologic variations. Both time series show hierarchical frequency variability, as would be expected for records of different Milankovitch cycles, but the two different time series (SM-20 and Kappabridge) cannot be easily correlated.

A direct comparison of the two time series, including errors bars (one standard deviation), shows that the SM-20 portable susceptibility meter dataset has much higher uncertainty in its measurements. The uncertainty in the SM-20 measurements could be the explanation for the differences in the two time series (**Figure 3**). Given this obvious difference in the two time series, collected by different types of measurement, it is interesting that for the MTM spectral analyses, Astrochron (Meyers, 2014) picks very similar significant peaks using both robust red noise (Mann and Lees, 1996) and harmonic f-test (Thomson, 1982) as selection criteria, for both series (**Figures 4**, **5** and **Tables 1**, **2**).

The most striking similarities between the two time series are spectral peaks at 6.8, 1.9, and 1.1 m. The ratio of these peaks is similar to the ratios of short eccentricity (125 ka), obliquity (35 ka), and short precession (17.5 ka) at 330 Ma (Waltham, 2015). Thus, we have tentatively identified these peaks as the short eccentricity, obliquity and precession Milankovitch cycles in the Carboniferous. Note that the 5.45 m peak in the SM-20 data (**Table 1**) could be 95 ka short eccentricity, and the 1.21 m peak in the Kappabridge data (**Table 2**) could be long precession (21 ka). Note also that the peaks identified from the longer 68 m section are very similar to those observed for the $IRM_{3.5T-100mT}$ measured for the 40 m pilot study. The IRM times series peak at 6.8 m is identified as short eccentricity, the 1.3 and 1.1 m peaks are long and short precession.

We can test these picks using average spectral misfit (ASM) in the Astrochron software package (Meyers and Sageman, 2007; Meyers, 2014). It iteratively tries different SARs to fit the selected spectral peak frequencies to Milankovitch target frequencies.

TABLE 1 | Portable SM-20 spectral peaks.

Peak number	Frequency (1/m)	Period (m)	Harmonic CL (%)	RedNoise CL (%)	Target Milankovitch (ka)
1	0.1	10	97.1	80.2	
2	**0.148**	**6.77**	**94.6**	**99.9**	**125**
3	**0.184**	**5.45**	**97.7**	**63.8**	**95**
4	0.442	2.26	93.9	72.1	
5	**0.528**	**1.89**	**90.2**	**99.8**	**35**
6	0.652	1.53	97.0	81.2	
7	**0.932**	**1.07**	**95.0**	**79.3**	**17.5**

*Bolded peaks used for average spectral misfit (**Figure 6**). CL = confidence limit.*

TABLE 2 | Laboratory sample – Kappabridge spectral peaks.

Peak number	Frequency (1/m)	Period (m)	Harmonic CL (%)	RedNoise CL (%)	Target Milankovitch (ka)
1	0.06	16.2	87.7	85.6	
2	**0.144**	**6.94**	**95.9**	**83.6**	**125**
3	0.328	3.05	96.5	81.4	
4	**0.529**	**1.89**	**99.0**	**70.0**	**35**
5	**0.826**	**1.21**	**91.9**	**86.3**	**21**
6	**0.932**	**1.07**	**97.8**	**77.3**	**17.5**
7	0.972	1.03	98.8	63.4	

*Bolded peaks used for average spectral misfit (**Figure 6**). CL = confidence limit.*

It tests the significance level of the null hypothesis for the best fit SAR (Meyers, 2014). ASM gives statistically significant fits, at greater than 98%, for both the SM-20 series and the Kappabridge time series yielding the identical SAR of 5.69 cm/ka for both time series (**Figure 6**).

Finally, we can test our Milankovitch picks by conducting an AM test of the precession (17.5 ka) cycle we have identified in our spectral analysis. Precession should be modulated by eccentricity, so if we picked precession correctly its amplitude should be modulated by the frequency we have selected as eccentricity. Astrochon (Meyers, 2014) provides a testPrecession routine that could accomplish this test, however, an accurate theoretical model of precession is needed. This exists only as far back in time as the Paleogene, therefore, we conducted our own version of this test. We filtered the Kappabridge rock sample time series at 0.93 m^{-1} (the 1.07 m spectral peak) and the resulting filtered series showed AM with six peaks per pulse (**Figure 7**). We conducted MTM spectral analysis on the amplitude envelope of the filtered series and found a strong peak with a frequency of 0.14 m^{-1}, which is exactly the 125 ka eccentricity peak we targeted with our ASM analysis. The AM test shows that we have correctly selected precession and eccentricity in our spectral analysis.

Evolutionary spectrograms of the portable (SM-20) and laboratory-measured rock samples (Kappabridge) time series (**Figure 8**) show that for the portable susceptibility meter data all three of the Milankovitch cycles are stronger in the upper part of the section, starting at about 30 m for the short eccentricity and obliquity, but only at about 40 m

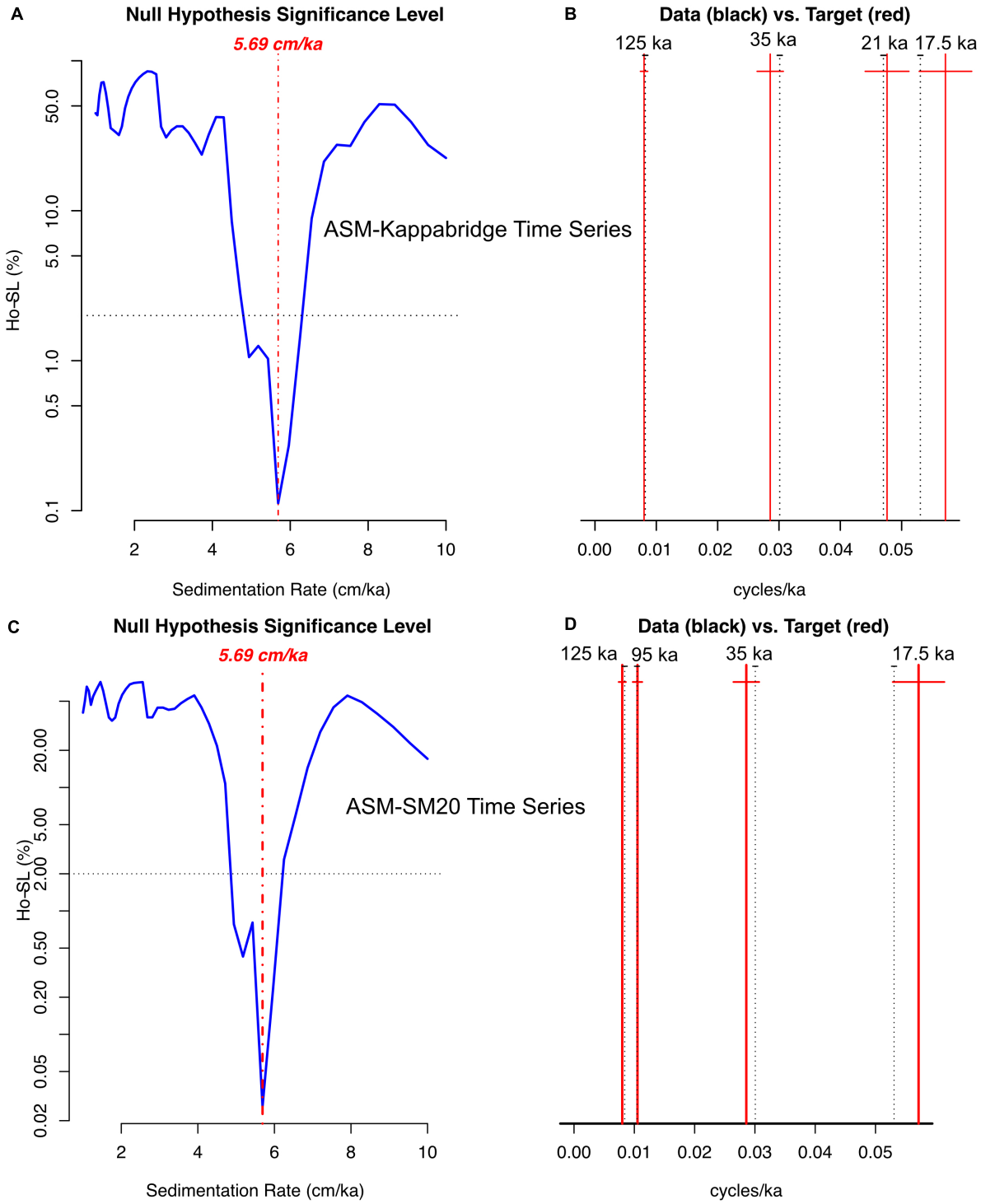

FIGURE 6 | Average spectral misfit (ASM; Meyers and Sageman, 2007) results for the Kappabridge **(A)** and SM-20 **(B)** spectral peaks targeted to eccentricity, obliquity, and precession at 330 Ma. The significant fit for the two different time series indicates an identical sediment accumulation rate of 5.69 cm/ka. In panels **(C)** and **(D)**, the dotted black lines are the data and the red solid lines are the target Milankovitch frequencies.

for the precession cycle. For the Kappabridge-measured rock samples (**Figure 8**) the eccentricity cycles (both long and short eccentricity, 405 and 100 ka) are strong throughout the section while obliquity and precession [both long (21 ka) and short (17.5 ka)] vary in strength throughout the section. The most important observation is that the SAR doesn't

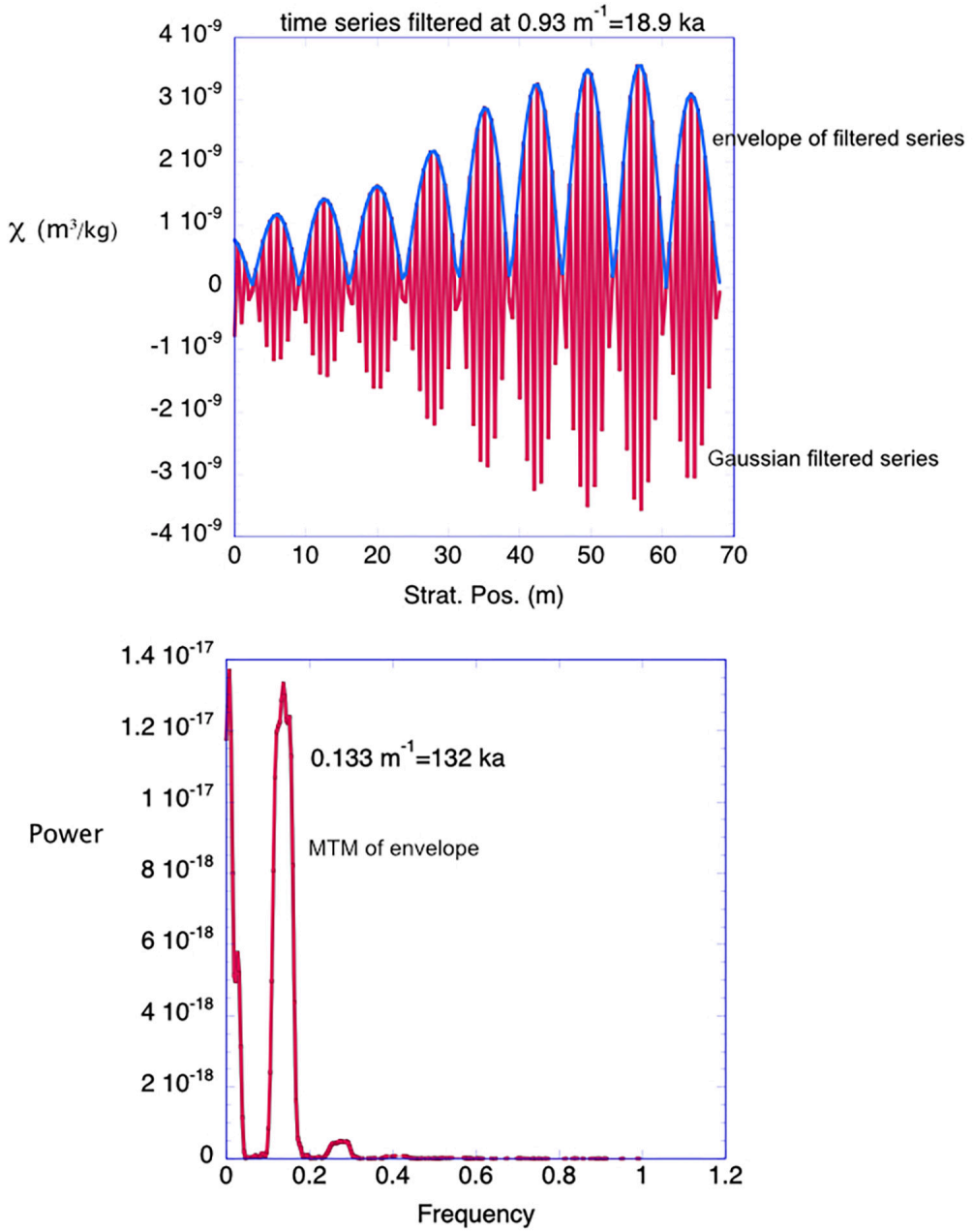

FIGURE 7 | Amplitude modulation (AM) test conducted on the frequency chosen for precession in our results. **(Top)** The Kappabridge time series was filtered at the frequency of the spectral peak chosen to be precession (0.93 m^{-1}) and the envelope of the amplitude variation yields a power spectrum **(Bottom)** with a significant peak at the frequency we have chosen as short eccentricity (0.133 m^{-1}). This result strongly supports our assignment of Milankovitch frequencies to the spectral peaks observed in our data.

appear to change throughout the section. The evolutionary spectrograms are compared to the MTM power spectra for each time series. These spectra were calculated by the SSA-MTM toolkit (Ghil, 1997) with robust red noise (Mann and Lees, 1996) and are identical to the power spectra calculated from Astrochron (**Figure 5**); however, using Astrochron's selection criteria (robust red noise and harmonic f-test) the peak labeled long eccentricity (le) has a wavelength of only 10 m, which would only be 175.7 ka for the 5.69 cm/ka SAR calculated by ASM and would not be consistent with long eccentricity, 405 ka. However, the maximum amplitude of the le peak yields a wavelength of 22.5 m, indicating a period of 395.4 ka for an SAR of 5.69 cm/ka, entirely consistent with long eccentricity. Therefore, the Kappabridge time series also contains a record of long eccentricity which repeats approximately three times in our record. The 40 m

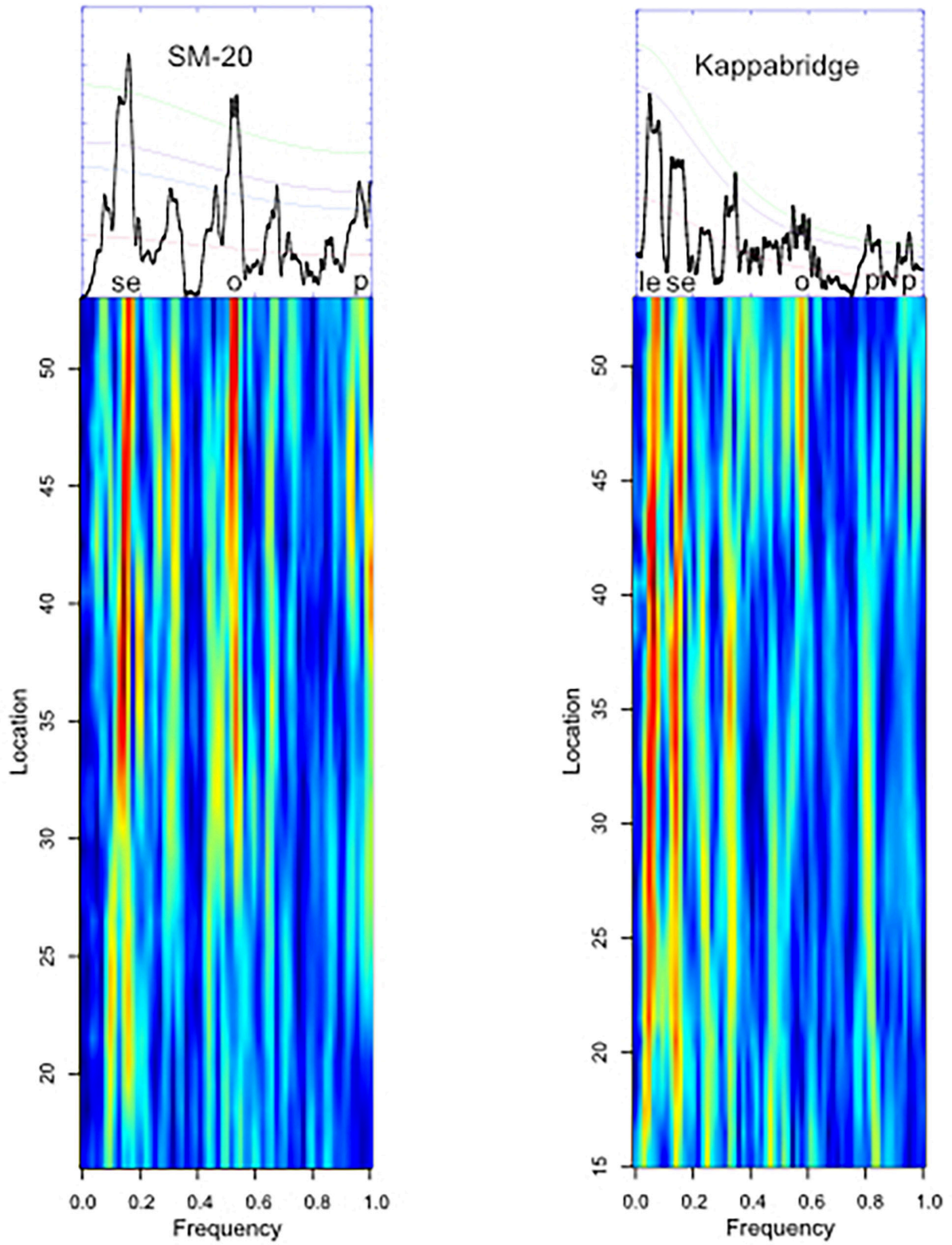

FIGURE 8 | Evolutionary spectrograms calculated using Astrochron (Meyers, 2014) for the SM-20 **(Left)** and the Kappabridge measured samples **(Right)**. The MTM calculated power spectrum for each series (using SSA-MTM) is shown at the top of each evolutionary spectrogram with Milankovitch spectral peaks labeled (le = long eccentricity, se = short eccentricity, o = obliquity, p = precession). The evolutionary spectrograms were calculated with a window of 30 m and a step of 1 m. They show that the sediment accumulation rate does not vary significantly through the section although the power of the different frequencies does vary.

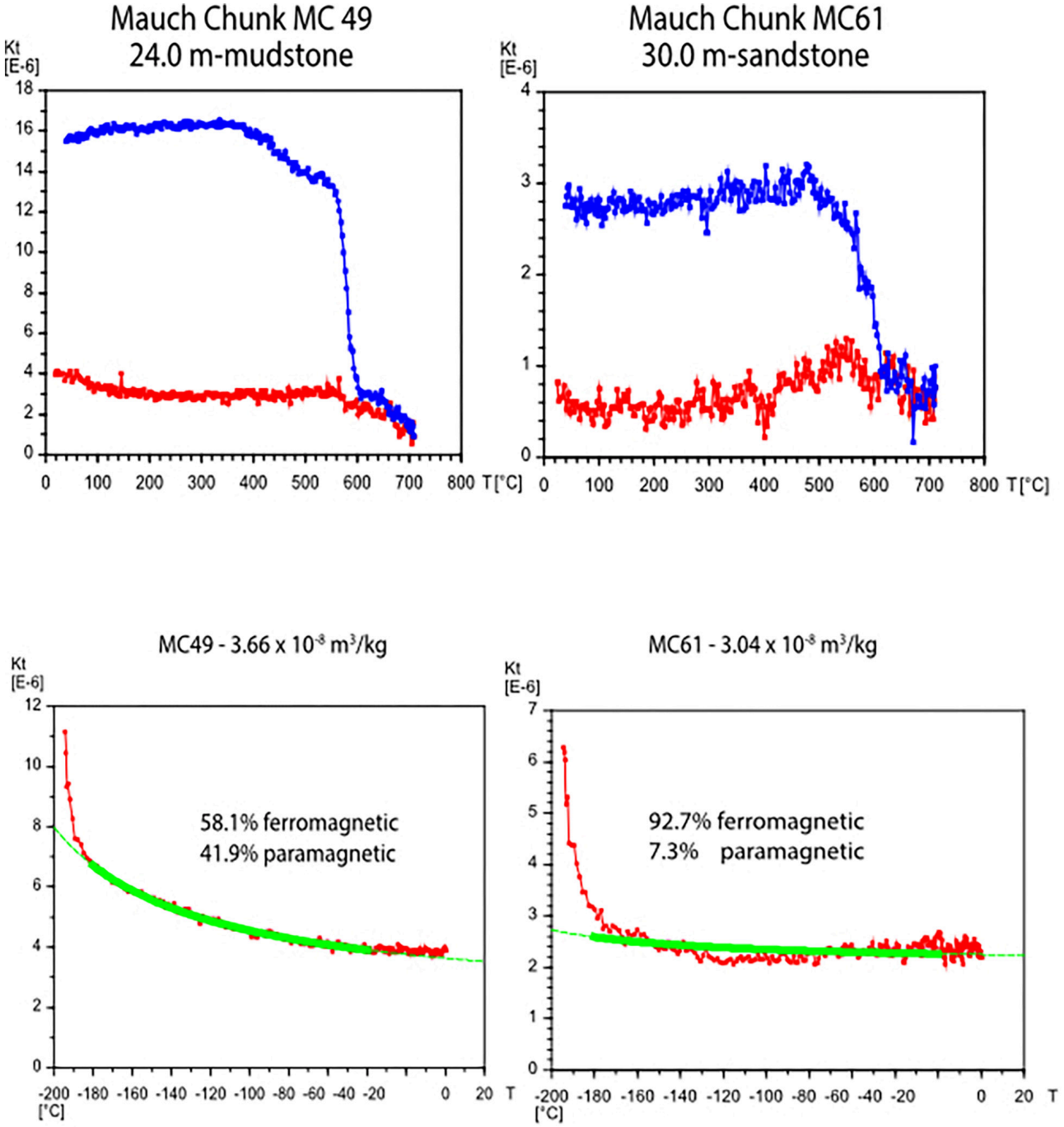

FIGURE 9 | High and low temperature MS vs. T results measured on the Kappabridge for a sample representative of a mudstone lithology and a sandstone lithology. The low temperature results are fit by a paramagnetic hyperbola to determine the relative proportion of ferromagnetic and paramagnetic contributing to the magnetic susceptibility (Hrouda, 1994).

IRM time series collected in 2012 is too short to observe long eccentricity.

Rock Magnetics

The MS vs. T plots measured at temperatures between 20 and 700°C indicate the weak occurrence of magnetite but mainly the presence of hematite in the Mauch Chunk Formation samples (**Figure 9**). On cooling from high temperatures the strong increase in susceptibility at 580°C indicates that magnetite has been created by the heating. This behavior is observed for both a mudstone and a sandstone sample. The low temperature MS vs. T plots measured at temperatures between −195 and 0°C

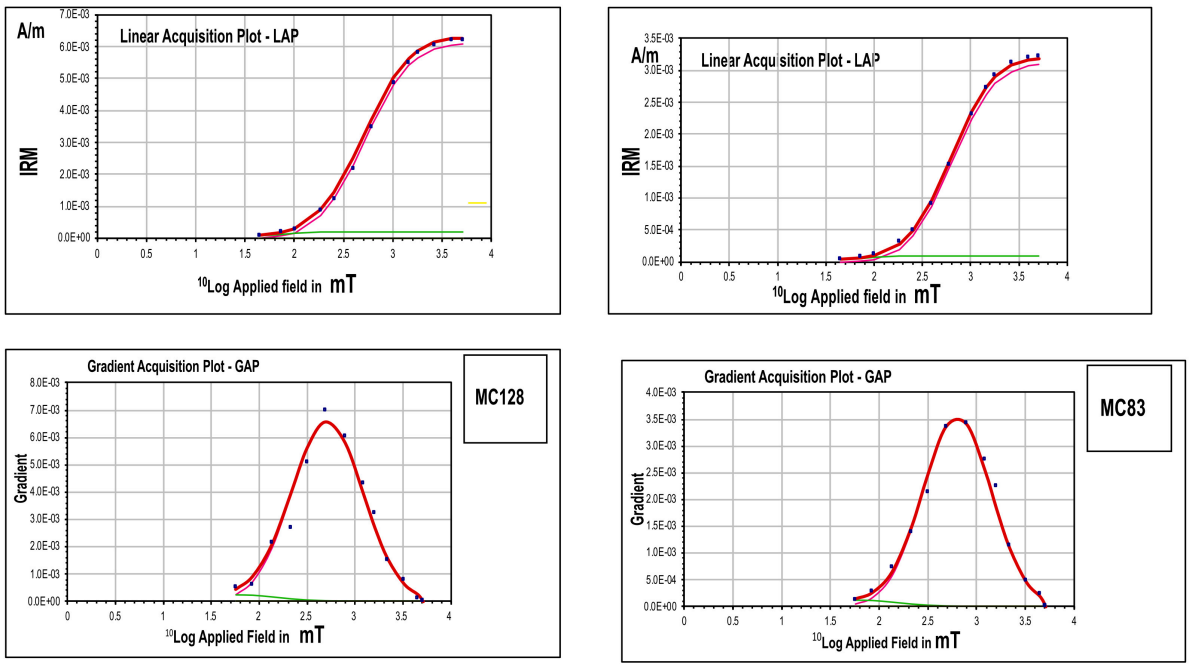

FIGURE 10 | Isothermal remanent magnetization acquisition results showing that the samples are dominated by a high coercivity remanence that saturates by 3.5 T and is probably hematite. There is a minor contribution from a lower coercivity component that is probably magnetite.

show no evidence of a Verwey transition, so magnetite is not present in any great abundance (**Figure 9**). These results are supported by the IRM acquisition experiments (**Figure 10**) which show that the IRM for the Mauch Chunk Formation samples saturates at about 3 T. Modeling of the IRM acquisition data shows that most (97%) of the IRM acquisition data could be fit with a coercivity component of about 0.5–0.6 T indicating a high coercivity mineral, most likely hematite. A very small component (∼3% of the IRM) could be fit with a low coercivity (65 mT) mineral, probably a small amount of magnetite.

The relative proportion of ferromagnetic (hematite) and paramagnetic (clay) contributing to the bulk susceptibility was estimated for 21 samples over a 10 m stratigraphic interval between 20.5 and 30.5 m in the section. The stratigraphic interval included both the red mudstone overbank deposits and the sandstone channel deposits. An example of the hyperbola fit to the low temperature measurements for a mudstone and a sandstone sample to estimate paramagnetic/ferromagnetic content is shown in **Figure 9**. The contribution of paramagnetic and ferromagnetic to the total susceptibility was determined by multiplying the percentage of each by the bulk susceptibility for a sample (**Figure 11**). Two repeated measurements for both a mudstone and a sandstone sample show the percentage estimates are repeatable within about 7% points. The high frequency peaks in bulk susceptibility with a wavelength of 1–2 m are driven mainly by variations in the ferromagnetic minerals. The ferromagnetic minerals are the only contributor to the bulk susceptibility in the sandstone (**Figure 11**). The paramagnetic minerals also drive some of the peaks in the bulk susceptibility. They are sometimes in phase with the ferromagnetic mineral variations and sometimes out of phase. In the 10 m stratigraphic interval measured for this analysis, there are six ferromagnetic peaks which match the six peaks in the bulk susceptibility, suggesting a wavelength of ∼1.5 m, whereas the paramagnetic minerals show two large peaks in phase with the ferromagnetic peaks and possibly an additional two smaller peaks that do not coincide with peaks in the bulk susceptibility. When these estimates of stratigraphic wavelength are compared to the spectral analysis of the Kappabridge time series (**Table 2**), it strongly suggests that ferromagnetic mineral concentration variations are a strong control on the bulk MS variations that record astronomically forced climate change (Milankovitch) cycles at precession (20 ka) and obliquity (35 ka) frequencies. Given the 10 m length of the stratigraphic interval used for this analysis, it is not possible to determine if ferromagnetic or paramagnetic minerals are beating at the eccentricity period of ∼7 m.

DISCUSSION

Recording Milankovitch Cycles

The MS time series collected with the SM-20 portable susceptibility meter and the Kappabridge measurement of rock samples both showed a record of Milankovitch cycles at periods of 100, 35, and 20 ka and the IRM time series showed Milankovitch cycles at 100 and 20 ka. ASM analysis (Meyers, 2014) of both the portable and Kappabridge MS time series indicate a SAR of 5.69 cm/ka showing that the 5–7 m wavelength peaks are short eccentricity at 125 and 95 ka, the 1.9 m peak

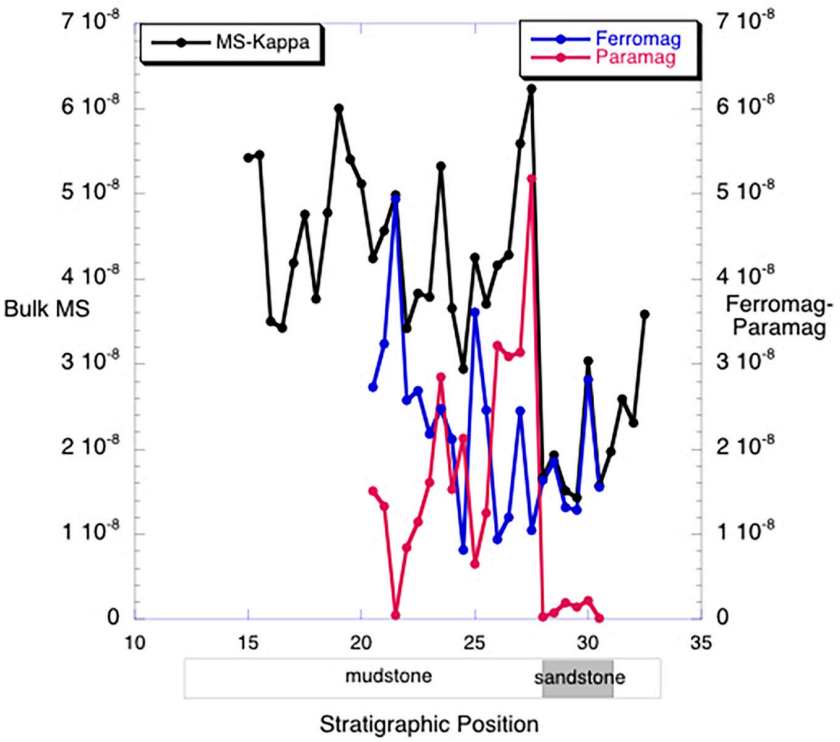

FIGURE 11 | The relative proportion of ferromagnetic minerals (blue curve) and paramagnetic minerals (red curve) contributing to the bulk susceptibility (black curve) for 10 m between 20.5 and 30.5 m in the section. The percentages determined from the low temperature MS vs. T measurements have been multiplied by the bulk susceptibility for a sample to determine the susceptibility for each magnetic mineral type. Note that the blue (ferromagnetic) curve follows all the short period peaks in the bulk susceptibility curve (black curve) indicating that the ferromagnetic mineral variations are the source of the bulk susceptibility variations. The paramagnetic mineral contribution is sometimes in phase with the ferromagnetic variations, sometimes out of phase. The magnetic susceptibility of the sandstone bed is almost all due to ferromagnetic minerals.

is obliquity at 35 ka, and the 1.2–1.1 m wavelength peaks are precession at 21 and 17.5 ka. AM analysis shows that the 1.07 m wavelength peak, picked to be short precession at 17.5 ka, is modulated by a frequency of about 0.14 cycles/m which is our pick for short eccentricity at 125 ka. This result supports our pick for Milankovitch cycles in the data.

Our results indicate that a fluvial, terrigenous depositional environment can record Milankovitch global climate cycles despite the expectation that this type of environment will experience discontinuous sedimentation (i.e., flooding into the overbank environment) and the effects of environmental shredding (Jerolmack and Paola, 2010) due to landscape processes, such as avulsion (channel migration). Our results would suggest, in light of Jerolmack and Paola's analysis, that the shortest Milankovitch cycle recorded (i.e., precession at 17.5 ka) is still a longer period than shredding processes in the depositional basin (e.g., flooding and avulsion).

The SAR derived from these high resolution chronostratigraphy results suggests that the long normal polarity interval of the Earth's geomagnetic field recorded at the Pottsville section and correlated throughout eastern North America (Opdyke et al., 2014) is 1.75 million years in duration and not 1.0 million years as suggested by biostratigraphy (Opdyke et al., 2014) and may help more accurately calibrate this part of the geologic time scale in the Carboniferous (Gradstein et al., 2012).

Encoding the Milankovitch Signal

The strong positive correlation between the percentage of ferromagnetic minerals contributing to the magnetic susceptibility and the bulk susceptibility variations suggests erosion in the source area, driven by climate change, is adding more or less depositional hematite to a background of either clay minerals or quartz sand in the depositional basin at the Milankovitch time scales. Therefore, changes in the source area for the Mauch Chunk sediments are encoding the Milankovitch cycles rather than changes in the depositional basin. This is similar to the record of Milankovitch cycles in marine sediments in which variations in precipitation on the continent changes the supply of clastic sediments into a background of carbonate production in the near-shore marine environment (Kodama et al., 2010; Gong et al., 2017; Minguez and Kodama, 2017). The record of eccentricity and precession by the Mauch Chunk Formation sediments is consistent with its 23°S paleolatitude (Bilardello and Kodama, 2010) where the strength of the monsoon is driven by eccentricity and precession. However, it is interesting that rock magnetics also detect obliquity for this low paleolatitude because obliquity insolation variations are stronger

at high latitudes than low latitudes. In support of our results, Gunderson et al. (2012) did observe a strong obliquity signal in Mediterranean (low latitude) Plio-Pleistocene sediments recorded by magnetic susceptibility. The weak coupling of paramagnetic minerals to the shorter Milankovitch frequencies could be due to variations in chemical weathering in the source area being driven by global climate change.

Portable Susceptibility Meter Measurements

Even though the portable susceptibility meter measurements did not observe exactly the same time series as the more accurate Kappabridge measurements of rock samples, and could not be normalized by sample mass, the spectral analysis of the portable time series was still able to detect the same Milankovitch cycles as the Kappabridge-rock sample measurements. This result indicates that using the portable susceptibility meter for rock magnetic cyclostratigraphy is a valid method for constructing a time series, particularly for clastic, relatively high magnetic mineral content, sedimentary rocks. Conceivably, the portable susceptibility measurements could be used for reconnaissance work to accurately set the sampling interval for more detailed sample collection and rock magnetic measurements in the laboratory.

CONCLUSION

Both measurements in the field using a portable susceptibility meter and magnetic susceptibility and IRM measurement of rock samples in the laboratory could detect Milankovitch cycles in a fluvial depositional environment recorded by depositional hematite grains in red beds deposited during the Carboniferous. This is an important result because it opens up terrestrial, fluvial deposits to the high-resolution dating and correlation afforded by rock magnetic cyclostratigraphy.

A SAR of 5.69 cm/ka derived from both the portable susceptibility meter and the rock sample measurements suggests that the long normal polarity interval in the Pottsville Mauch Chunk Formation section is 1.75 million years in duration, not <1 million years as previously indicated by the biostratigraphy and suggests a slight recalibration of this part of the Carboniferous geologic time scale is needed.

The astronomically forced, Milankovitch-scale climate cycles were probably encoded by variations in erosion of the source area supplying varying amounts of depositional hematite into a background of paramagnetic clay minerals or diamagnetic quartz sand in the depositional basin.

DATA AVAILABILITY STATEMENT

The raw data supporting the conclusion of this manuscript will be made available by the author, without due reservation, to any qualified researcher. The susceptibility measurements are available in the **Supplementary Material**.

AUTHOR CONTRIBUTIONS

KK made susceptibility measurements, helped to collect the samples, analyzed the data, and wrote the manuscript.

FUNDING

This study was partially supported by NSF-EAR 1322002.

ACKNOWLEDGMENTS

Marta Sanchez Anson collected the 68 m section, measured *in situ* susceptibilities with the portable susceptibility meter, prepared the laboratory samples for measurement, and made some of the Kappabridge measurements. Daniel Minguez and Nathan Hopkins collected the 2012 samples for the pilot study and made the laboratory measurements of IRM and susceptibility.

SUPPLEMENTARY MATERIAL

The Supplementary Material for this article can be found online at: https://www.frontiersin.org/articles/10.3389/feart.2019.00285/full#supplementary-material

TABLE S1 | Laboratory Kappabridge and portable SM-20 susceptibility measurements for the Pottstown section of the Mauch Chunk Formation.

TABLE S2 | IRM (3.5 T), IRM (3.5 T demagnetized at 100 mT), and magnetic susceptibility measurements (kappabridge) for the 2012 study of the Mauch Chunk Formation at the Pottsville section.

REFERENCES

Abdul Aziz, H., Hilgen, F., Krijgsman, W., Sanz, E., and Calvo, J. P. (2000). Astronomical forcing of sedimentary cycles in the middle to late miocene continental Calatayud Basin (NE Spain). *Earth Planet. Sci. Lett.* 177, 9–22. doi: 10.1016/s0012-821x(00)00035-2

Abels, H. A., Kraus, M. J., and Gingerich, P. D. (2013). Precession-scale cyclicity in the lower eocene fluvial willwood formation of the bighorn basin. Wyoming (USA). *Sedimentology* 60, 1467–1483.

Berger, A., and Loutre, M. F. (1994). Astronomical forcing through geological time. *Spec. Publs. Int. Assoc. Sediment* 19, 15–24. doi: 10.1002/9781444304039.ch2

Bilardello, D. A., and Kodama, K. P. (2010). A new inclination shallowing correction of the mauch chunk formation of pennsylvania, based on high-field AIR results: implications for the carboniferous north american APW path and pangea reconstructions. *Earth Planet. Sci. Lett.* 299, 218–227. doi: 10.1016/j.epsl.2010.09.002

Cioppa, M. T., and Kodama, K. P. (2003). Evaluation of paleomagnetic and finite strain relationships due to the alleghanian orogeny in the mississippian mauch chunk formation, pennsylvania. *J. Geophys. Res.* 108, 1–16.

DiVenere, V. J., and Opdyke, N. D. (1991). Magnetic polarity stratigraphy in the uppermost mississippian mauch chunk formation pottsville, pennsylvania. *Geology* 19, 127–130.

Ghil, M. (1997). "The SSA-MTM toolkit: applications to analysis and prediction of time series," in *Proceedings of Optical Science, Engineering and Instrumentation*, San Diego, CA.

Gilman, D., Fuglister, R., and Mitchell, J. Jr. (1963). On the power spectrum of "red noise". *J. Atmos. Sci.* 20, 182–184. doi: 10.1175/1520-0469(1963)020<0182:otpson>2.0.co;2

Gong, Z., Kodama, K. P., and Li, Y.-X. (2017). Rock magnetic cyclostratigraphy of the doushantuo formation. *Precambrian Res.* 289, 62–74.

Gradstein, F. M., Ogg, J. G., Schmitz, M. D., and Ogg, G. M. (eds) (2012). *The Geologic Time Scale 2012* (Oxford: Elsevier), 1144.

Gunderson, K. L., Kodama, K. P., Anastasio, D. J., and Pazzaglia, F. J. (2012). Rock magnetic cyclostratigraphy for the late pliocene-early pleistocene strione section. *Geol. Soc. Lond. Spec. Publ.* 373, 309-323. doi: 10.1144/SP373.8

Hinnov, L. A. (2013). Cyclostratigraphy and its revolutionizing applications in the earth and planetary sciences. *Geol. Soc. Am. Bull.* 125, 1703–1734. doi: 10.1130/B30934.1

Hrouda, F. (1994). A technique for the measurement of thermal changes of magnetic susceptibility of weakly magnetic rocks by the CS-2 apparatus and KLY-2 Kappabridge. *Geophys. J. Int.* 118, 604–612. doi: 10.1111/j.1365-246x.1994.tb03987.x

Jerolmack, D. J., and Paola, C. (2010). Shredding of environmental signals by sediment transport. *Geophys. Res. Lett.* 37:L19401.

Kent, D. V., and Opdyke, N. D. (1985). Multicomponent magnetizations from the mississippian mauch chunk formation of the central appalachians and their tectonic implications. *J. Geophys. Res.* 90, 5371–5383. doi: 10.1029/jb090ib07p05371

Kodama, K. P., Anastasio, D. J., Newton, M. L., Pares, J., and Hinnov, L. A. (2010). High resolution rock magnetic cyclostratigraphy in an eocene flysch, spanish pyrenees. *Geochem. Geophys. Geosys.* 11:Q0AA07. doi: 10.1029/2010GC003069

Kodama, K. P., and Hinnov, L. A. (2015). *Rock Magnetic Cyclostratigraphy*. Blackwell: Wiley, 165.

Kruiver, P. P., Dekkers, M. J., and Heslop, D. (2001). Quantification of magnetic coercivity components by the analysis of acquisition curves of isothermal remanent magnetization. *Earth Planet. Sci. Lett.* 189, 269–276. doi: 10.1016/s0012-821x(01)00367-3

Levine, J. R., and Slingerland, R. (1987). Upper mississippian to middle pennsylvanian stratigraphic section. *Geol. Soc. Am. Centen.* 15, 59–63.

Mann, M., and Lees, J. (1996). Robust estimation of background noise and signal detection in climatic time series. *Clim. Chang.* 33, 409–445. doi: 10.1007/BF00142586

Meyers, S. R. (2012). Seeing red in cyclic stratigraphy: spectral noise estimation for astrochronology. *Paleoceanogr. Paleoclimatol.* 27:PA3228. doi: 10.1029/2012PA002307

Meyers, S. R. (2014). *Astrochron: an R Package for Astrochronology*. Available at http://cran.r-project.org/package=astrochron

Meyers, S. R., and Sageman, B. B. (2007). Quantification of deep-time orbital forcing by average spectral misfit. *Am. J. Sci.* 307, 773–792. doi: 10.2475/05.2007.01

Minguez, D., and Kodama, K. P. (2017). Rock magnetic chronostratigraphy of the shuram carbon isotope excursion: wonoka formation. *Aust. Geol.* 45, 567–570. doi: 10.1130/g38572.1

Minguez, D., Kodama, K. P., and Hillhouse, J. W. (2015). Paleomagnetic and cyclostratigraphic constraints on the synchroneity and duration of the shuram carbon isotope excursion, johnnie formation, death valley region, CA. *Precambrian Res.* 266, 395–408. doi: 10.1016/j.precamres.2015.05.033

Noorbergen, L. J., Abels, H. A., Hilgen, F. J., Robson, B. E., Jong, E. D., Dekkers, M. J., et al. (2018). Conceptual models for short-eccentricity climate control on peat formation in a lower Palaeocene fluvial system, northeaster montana (USA). *Sedimentology* 65, 775–808. doi: 10.1111/sed.12405

Opdyke, N. D., Giles, P. S., and Utting, J. (2014). Magnetic polarity stratigraphy and palynostratigraphy of the mississippian-pennsylvanian boundary interval in eastern north america and the age of the beginning of the kiaman. *Geol. Soc. Am. Bull.* 126, 1068–1083. doi: 10.1130/b30953.1

Pas, D., Hinnov, L., Day, J. E., Kodama, K., Sinnesael, M., and Liu, W. (2018). Cyclostratigraphic calibration of the famennian stage (Late Devonian, Illinois Basin, USA), Earth Planet. *Sci. Lett.* 488, 1–13.

RStudio Team. (2015). *Rstudio: Integrated Development for R*. Boston, MA: RStudio, Inc.

Stamatakos, J., and Kodama, K. P. (1991). Flexural flow folding and the paleomagnetic fold test: an example of strain reorientation of remanence in the mauch chunk formation. *Tectonics* 10, 807–819. doi: 10.1029/91tc00366

Thomson, D. J. (1982). Spectrum estimation and harmonic analysis. *Proc. IEEE* 70, 1055–1096. doi: 10.1109/proc.1982.12433

Waltham, D. (2015). Milankovitch period uncertainties and their impact on cyclostratigraphy. *J. Sediment. Res.* 85, 990–998. doi: 10.2110/jsr.2015.66

Wu, H., Zhang, S., Feng, Q., Jiang, G., Li, H., and Yang, T. (2012). Milankovitch and sub-milankovitch cycles of the early triassic daye formation. *Gondwana Res.* 22, 748759. doi: 10.1016/j.gr.2011.12.003

Zhang, R., Li, L., Nai, W., Gu, Y., Huang, C., Ogg, J., et al. (2019). Astronomical forcing of terrestrial climate recorded in the pleistocene of the western tarim basin. *Palaeoclimatol. Palaeoecol.* 530, 78–89. doi: 10.1016/j.palaeo.2019.05.039

Conflict of Interest: The author declares that the research was conducted in the absence of any commercial or financial relationships that could be construed as a potential conflict of interest.

frontiers in Earth Science

ORIGINAL RESEARCH
published: 19 December 2019
doi: 10.3389/feart.2019.00341

Magnetic Susceptibility Record in Paleozoic Succession (Rhenohercynian Massif, Northern Europe) – Disentangling Sea Level, Local and Diagenetic Impact on the Magnetic Records

Damien Pas[1,2], Anne-Christine Da Silva[2], Geoffrey Poulain[3], Simo Spassov[4] and Frédéric Boulvain[2]*

[1] Paleomagnetic Laboratory, Utrecht University, Utrecht, Netherlands, [2] Pétrologie Sédimentaire, Université de Liège, Liège, Belgium, [3] Geolys, Brussels, Belgium, [4] Geophysical Centre, Royal Meteorological Institute of Belgium, Brussels, Belgium

OPEN ACCESS

Edited by:
Kenneth Philip Kodama, Lehigh University, United States

Reviewed by:
Yong-Xiang Li, Nanjing University, China
Belén Oliva-Urcia, Autonomous University of Madrid, Spain

***Correspondence:**
Damien Pas
damienpas@gmail.com

Specialty section:
This article was submitted to Geomagnetism and Paleomagnetism, a section of the journal Frontiers in Earth Science

Received: *18 September 2019*
Accepted: *04 December 2019*
Published: *19 December 2019*

Citation:
Pas D, Da Silva A-C, Poulain G, Spassov S and Boulvain F (2019) Magnetic Susceptibility Record in Paleozoic Succession (Rhenohercynian Massif, Northern Europe) – Disentangling Sea Level, Local and Diagenetic Impact on the Magnetic Records. Front. Earth Sci. 7:341. doi: 10.3389/feart.2019.00341

This study uses an integrated approach, including sedimentology, geochemistry and hysteresis magnetic measurements on a million year Givetian sequence in the southern margin of the Ardennes carbonate platform (France) to test the reliability of magnetic susceptibility (χ) records as inter-regional correlation tools in remagnetized settings. Furthermore, we aim to better understand the N-S depositional variations and sea-level fluctuations in the Ardennes. Sedimentological analyses revealed a complex platform evolution displaying a variety of shallow- and off-reef paleoenvironmental rocks, which ultimately allowed us to improve the sedimentological model of this area and to constrain the main sea-level fluctuations within the southern margin of the Ardennes platform. Comparison of the χ curve of this succession with previously published time-equivalent records in the western margin of the platform indicates a clear correlation between the two areas, despite the distance between the locales, their different sedimentology background and the remagnetization affecting the entire region. In contrast, the comparison of these χ profiles from the Ardennes (SW Rhenohercynian Massif, Belgian and France) with coeval data from the Rheinisches Schiefergebirge (NE Rhenohercynian Massif, Germany) do not show obvious correlations. Therefore, it is inferred that syn-sedimentary autogenic processes (e.g., vicinity to landmasses, wave agitation), which operate at small spatial and temporal scales affected the χ signal and could cause the lack of correlation between χ profiles.

Keywords: Paleozoic, carbonate, remagnetization, paleoenvironment, magnetic minerals, hysteresis, sedimentology

INTRODUCTION

Magnetic susceptibility is a proxy that has been broadly used for paleoenvionmental and correlation purposes in ancient sedimentary records (Ellwood et al., 2001; Bábek et al., 2007; Whalen and Day, 2008; 2010; Hladil et al., 2011; Da Silva et al., 2013; Chadimova et al., 2015). Recent advances in the interpretation of the χ signal have clearly demonstrated the influence of sedimentary settings and post-depositional transformation such as diagenesis and metamorphism (Jackson, 1990; Elmore et al., 1993; Channell and McCabe, 1994; Zegers et al., 2003; Da Silva and Boulvain, 2012; Da Silva et al., 2013). To better understand the effect of these processes on the χ signal, Riquier et al. (2010) and Da Silva et al. (2013) conducted rock magnetic studies on numerous Devonian limestone sections from the NE Rhenohercynian Massif, Ardennes, France and Morocco. Despite the remagnetization highlighted in the NE Rhenohercynian Massif and Ardennes (Molina Garza and Zijderveld, 1996; Zwing et al., 2002, 2005; Zegers et al., 2003), Riquier et al. (2010) and Da Silva et al. (2013) demonstrated that the primary depositionally-induced χ signal was at least partly preserved and that it could be used for paleoenvironmental and paleoclimatic interpretations. Therefore, it is essential to test the origin of the magnetic signal through the combined use of geochemical, facies analyses and hysteresis measurements (Riquier et al., 2010; Da Silva et al., 2015) before applying χ as a paleoclimatic or correlation tool for sections at any scale.

The reconstruction of Paleozoic carbonate platforms is often challenging because of numerous limiting parameters such as complex structural geology, diagenesis, lack of outcrops, differential denudation, ancient reefal communities, etc. In the Ardennes (Northern France, Southern Belgium), major parts of the Givetian platform are buried in the subsurface of major synclines or eroded in the core of anticlines, and relevant outcrops only expose short sections of this extensive platform. For these reasons, the main evolutionary phases of the Givetian Ardennes platform through space and time remain difficult to delineate. In this study, multiple proxies, such as sedimentology, geochemistry and hysteresis magnetic measurements are generated from the million year Fromelennes-Flohimont section in France (southern margin of the Ardennes platform). These data are then integrated with previously published data from the northern margin of the Ardennes platform [La Thure (LT) section] which include facies, geochemistry (Pas et al., 2017) and magnetic susceptibility analyses (De Vleeschouwer et al., 2015). This synthesis sheds new light on the depositional environments, their variations across the platform and the main sea-level fluctuations from the earliest to the latest Givetian time. To test the extent that magnetic susceptibility can be used for inter-regional correlations, we assessed the preservation of the paleoenvironmental information in the magnetic susceptibility records for the Fromelennes-Flohimont section through comparison with facies evolution, geochemical and magnetic hysteresis measurements. To further test the preservation of χ in the LT section (Pas et al., 2017), we also measure hysteresis on selected samples that is compared with published geochemical and magnetic susceptibility results (De Vleeschouwer et al., 2015; Pas et al., 2017). The χ record from the Fromelennes-Flohimont section is then compared with time equivalent published records in the Belgian LT and the German Burgberg sections.

GEOLOGICAL SETTING

This work focuses on the Fromelennes-Flohimont (FF) section, a Givetian (Middle Devonian) carbonate succession from the Ardennes Basin, located in northern France (50°07′04″, N 4°51′26″E, **Figure 1A**). In this study the FF section is compared with the LT section which is located in western Belgium (50°17′11″N, 4°09′40″E, Pas et al., 2017) and to the Burgberg section in Germany (51°24′47″N, 8°42′31″E; Pas et al., 2013). The FF and LT χ datasets were published as part of a Givetian cyclostratigraphic analysis by De Vleeschouwer et al. (2015). Later, the LT section was further investigated for an integrated multi-proxy sedimentological analysis (Pas et al., 2017). In Belgium, Givetian sediments crop out along the border of the Dinant and Vesdre Synclines, in the Philippeville Anticline and along the southern border of the Brabant Massif, within the Brabant Para-Autochthonous area and the Haine-Sambre-Meuse Overturned Thrust sheets (for precise location of these sheets, see Figure 5 in Belanger et al., 2012), which are all large-scale units of the Rhenohercynian fold-and-thrust belt (**Figure 1B**). This major tectonic structure formed during the Carboniferous to Permian as a consequence of the collision between the Laurussia and Gondwana supercontinents during the Variscan orogeny. The tectonic shortening of the pre-Mesozoic sequences in the Rhenohercynian Zone associated with this collision is estimated at ∼40% (Dittmar et al., 1994). Therefore, considering the present day distance of ∼50 km separating the FF from the LT section, we assume a distance of ∼85 km between these two sites at the time of deposition.

Several authors provided evidence that during this orogeny, the rocks belonging to the Rhenohercynian fold-and-thrust belt were affected by remagnetization (e.g., Molina Garza and Zijderveld, 1996; Zegers et al., 2003; Zwing et al., 2005; Da Silva et al., 2012). In the Paleozoic rocks of Ardennes, two remagnetization events were recognized and the Givetian is described in detail by Zegers et al. (2003). The first event corresponds to an early Permian P-component and the second to a Carboniferous C-component. The P-component likely resides in pyrrhotite and is spatially correlated with Mississippi Valley Type (MVT) ore deposits, while the C-component is carried by SP-SD magnetite and is interpreted as formed during the smectite to illite transition. Zegers et al. (2003) recognized two main MVT districts in Belgium, the northern Namur-Verviers district and the southern Dinant district. The FF and the LT sections are not located in these districts.

The Givetian stratigraphy in the study area consists of five stratigraphic units, which are in ascending order the Hannonet (HAN), the Trois-Fontaines (TRF), the Terres d'Haurs (TRH), the Mont d'Haurs (MHR) and the Fromelennes (FRO) formations (Bultynck and Dejonghe, 2001) (**Figure 1C**). In terms of conodont biostratigraphy, the interval covered in

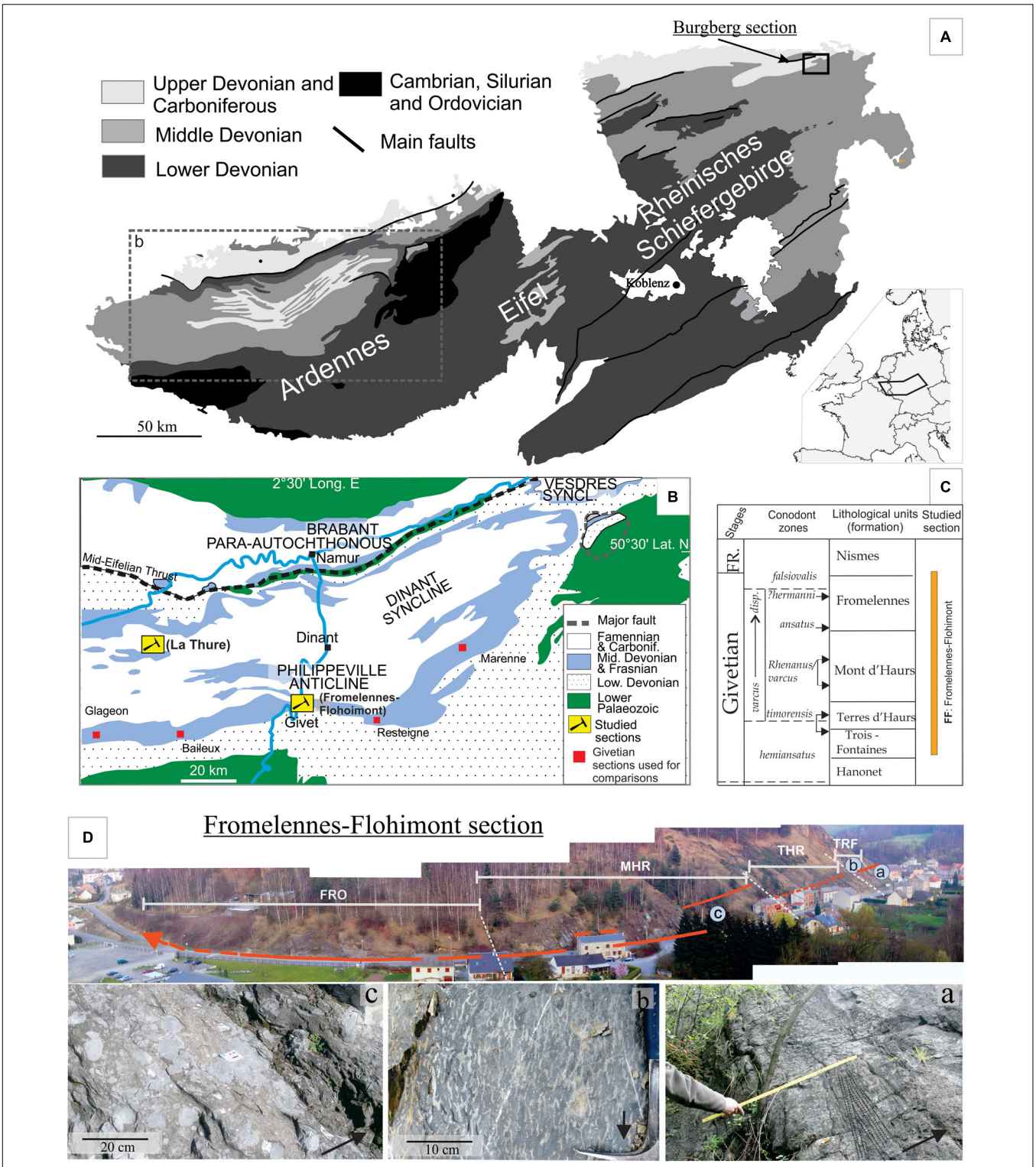

FIGURE 1 | Geological setting. **(A)** Location of the Ardennes, Eifel and Rheinisches Schiefergebirge on a simplified geological map of the Rhenohercynian Massif, modified after Wehrmann et al. (2005). For the location of this Pre-Mesozoic Massif in a present day situation see inset in the western European map in the lower right of **(A)**. The Burgberg section is situated in the upper right of **(A)**. **(B)** Simplified geological map of southern Belgium with location of the Fromelennes-Flohimont (South of the Dinant Syncline) section and La Thure (NW of the Dinant Syncline) section used for comparison in the discussion. For location of the Haine-Sambre-Meuse Overturned Thrust sheets refer to the map of Belanger et al. (2012). **(C)** Givetian lithostratigraphic column established for the southern border of the Dinant Syncline showing lower Givetian to lower Frasnian formations and conodont zones (Bultynck and Dejonghe, 2001). In Column conodont zones:

(Continued)

FIGURE 1 | Continued
timorensis Zone, the upper arrow indicates the base of the zone according to Bultynck (1987), the lower arrow, the base of the zone based on the graphic correlation method (Gouwy and Bultynck, 2003); *rhenanus/varcus* Zone, the upper arrow indicates the base of the zone according to Bultynck (1974), the lower arrow, the base of the zone based on the graphic correlation method (Gouwy and Bultynck, 2003). The interval covered by the Fromelennes-Flohimont sections is showed along the lithostratigraphic column. **(D)** Fromelennes-Flohimont road section showing the four investigated formations (white lines), the sampling track (red lines) and the exact location of pictures below. **(a)** Hummocky-cross stratification within limestone belonging to the lowest part of the Trois-Fontaines Fm. **(b)** Blue-gray limestone showing abundant cm-sized beige vertical burrows belonging to the upper part of the Trois-Fontaines Fm. **(c)** m-thick stromatoporoids-rich limestone beds characteristic of the Mont d'Haurs Fm. For an overview of the La Thure section refers to Pas et al. (2017).

the FF section extends from the lower Givetian *Polygnathus hemiansatus* Zone to the early Frasnian *Palmatolepis falsiovalis* Zone (Bultynck, 1987; Gouwy and Bultynck, 2003; Narkiewicz and Bultynck, 2010). According to Bultynck (1987), the Upper *varcus* and the *hermanni-cristatus* zones are not recognized in the FF section. Additionally, Gouwy and Bultynck (2003) indicated that the *semialternans*, *hermanni-cristatus* and *disparilis* Zones are not recognized in the Ardennes due to lack of guide species, but based on graphic correlation method the latter authors were able to locate the boundary between the *hermani* and the *disparilis* zones (see p. 326 in Gouwy and Bultynck, 2003 for detailed explanations). The portion of the LT section used for comparison herein covers a slightly shorter interval extending from the lower Givetian *Polygnathus varcus* Zone to the early Frasnian *Palmatolepis falsiovalis* Zone (Pas et al., 2015, 2017).

The Burgberg section in the northeastern portion of the Rhenohercynian Massif cut through the southeastern fore-reef fringe of the large atoll-like Brilon Reef Complex and the Hauptgrünsteinzug volcanic complex at the base. It covers a well-constrained stratigraphic interval extending from the Middle Givetian (Middle *varcus* Zone) to the Viséan (*bilineatus* Zone) which is characterized by nine depositional settings organized into off-reef, intermediate fore-reef, and proximal fore-reef main sedimentary domains (Pas et al., 2013). Major sedimentary processes occurring on this portion of the platform are gravity flows (turbidite, debris and grain flows), pelagic sedimentation (settling) and reworking of sediments triggered by storms.

METHODOLOGY

For this study we generated data on microfacies, whole rock geochemistry and hysteresis measurements in the FF section to complement the published magnetic susceptibility dataset (De Vleeschouwer et al., 2015). Hysteresis measurements were also generated for the LT section to further test the preservation of the magnetic susceptibility data reported in De Vleeschouwer et al. (2015) and Pas et al. (2017). Multi-proxy data from the FF section are then compared with new and available datasets in the LT section. The comparison of sedimentological, magnetic susceptibility, whole rock geochemistry and hysteresis measurement from the FF section with the LT datasets will allow better understanding of the origin of the magnetic susceptibility in order to interpret long distance correlations. Our analyses is based on ∼800 magnetic susceptibility samples from FF (De Vleeschouwer et al., 2015) and 31 hysteresis magnetic measurement (11 for the LT and 20 for the FF), 550 thin-sections for the FF and 41 major and trace element analyzes. To be representative of the stratigraphic successions, hysteresis and geochemical samples were taken at regular intervals all along the FF and LT sections.

Sedimentology

A detailed bed by bed description and sampling of Fromelennes-Flohimont section (461 m-thick; **Figure 1C**) was performed with a sampling interval of 25–45 cm, depending on outcrop condition. From the ∼800 samples collected across the section, 550 were used for thin-section analyses. Microfacies description was carried out following the same procedure as in Pas et al. (2017) and are described in full in **Supplementary Text 1**. Because the FF section is a lateral equivalent of the La Thure section, the microfacies described for this section should be similar to those previously described in La Thure (Pas et al., 2017). Therefore, to denote microfacies we used a similar system as in Pas et al. (2017), which relates to both the model type (DS – Drowning shelf, RS – Rimmed shelf, and RP – Ramp) and the studied locality (FF – Fromelennes-Flohimont). When microfacies described in this study were the same than those already published in Pas et al. (2017) (e.g., RS3-LT4) the label "LT" was used to avoid new layers of labeling. Finally, to build a comprehensive sedimentological model for the Givetian Ardennes platform, microfacies labels as in Pas et al. (2017) had to be adjusted. To avoid any confusion we provided an update of the LT microfacies (see table in **Supplementary Text 1**).

Rock Magnetic Analysis

Magnetic susceptibility data for this study are based on De Vleeschouwer et al. (2015). All samples collected along the FF and LT sections had their magnetic susceptibility measured, this included ∼800 samples in FF and ∼400 in the La Thure section. Magnetic susceptibility (χ) measurements (m^3/kg) were performed on a KLY-3S instrument at room temperature on samples weighing between 15 and 45°g (AGICO, noise level 2 $x10^{-8}$ SI) at the University of Liège (Belgium). Each data point is the average of three measurements. Samples were weighed with a precision of 0.01°g, which allowed the determination of the low-field mass-normalized magnetic susceptibility for each sample. χ data for Burgberg section were measured on 340 samples following a similar protocol (Pas, 2015) as the one used for the LT and FF sections.

Hysteresis loop measurements, acquisition of isothermal remanent magnetization (IRM), backfield curves and short-term remanence decay were measured with a J-coercivity rotational magnetometer developed by Kazan University (Burov et al., 1986), located at the Geophysical Centre of the Royal

Meteorological Institute of Dourbes in Belgium. Hysteresis loop measurements were carried out on 20 samples from the FF section and 11 samples from the LT section. All samples were cut into cubes (approximatively 0.9 × 0.7 × 2.5 cm) and weighed with a precision of 0.001 g. Remanent and induced magnetization were measured between +500 and −500 mT with average field increments of 0.5 mT per magnetization step. The magnetization duration at each magnetization step is in the order of tenths of a second. The high field remanence (%) is measured on the remanence backfield curve and corresponds to the difference between the measured field at 300 mT and at 500 mT (e.g., influence of high coercivity minerals). When the backfield curve is finished, the direct current is switched off automatically and the magnetizing field decreases toward a constant residual field of about 0.4 mT within the following 0.4 s. The decay of the remaining remanence (IRM 500 mT, 0.4 s) is monitored over 100 s, and is called the short-term remanence loss. The following parameters were extracted from the hysteresis loops: saturation magnetization M_s (Am^2/kg); remanent saturation magnetization, M_{rs} (Am^2/kg); high-field magnetic susceptibility (χ_{HF}, mł/kg) and coercive force H_c (mT). With the J-coercivity meter high-field susceptibility is measured only between 400 and 500 mT. The slope at high-field corresponding to the high-field magnetic susceptibility (χ_{HF}) is indicative of paramagnetic/diamagnetic contributions to the low-field magnetic susceptibility, if high coercivity minerals such as goethite and hematite are not present. When the IRM_{300}/IRM_{500} ratio is higher than 5%, the high-field slope cannot be used for slope correction and hence the values M_s, H_c, χ_{HF}, M_{rs}/M_s and H_{cr}/H_c are not regarded as reliable for interpretations. M_s, M_{rs}, and χ_{HF} were normalized with respect to sample mass. χ_{HF} thus corresponds to the high-field susceptibility values and represents a direct quantification of the combined diamagnetic/paramagnetic components for rocks that do not contain high-coercivity minerals such as hematite. The normalized decay viscosity coefficient (S_d) is calculated from the remanence decay measured during 100s. S_d represents the slope in the IRM_{500mT} versus Log_{10} (time[s]) diagram. The value χ_{ferro} (mł/kg) corresponds to the ferromagnetic *s.l.* contribution and is calculated by subtracting χ_{HF} from χ (e.g., Walden et al., 1999). Parameters extracted from the hysteresis loop are commonly interpreted using the so-called "Day" plot (Day et al., 1977) which corresponds to linear or logarithmic plot of M_{rs}/M_s and H_{cr}/H_c usually including four grain-size categories, from the coarser to the finest: multidomain (MD), pseudo-single domain (PSD), single domain (SD) and super paramagnetic (SP). Coarser grains (SD or MD) are often interpreted as detrital in origin (Parry, 1982; Königshof et al., 2016), while the smallest grains (SP and PSD) are interpreted as being formed under diagenetic conditions (Channell and McCabe, 1994).

Whole Rock Geochemistry

Major and trace element concentrations in the FF section were generated from 41 samples using X-ray Fluorescence (ARL 9400 XP XRF instrument) at the University of Liège. Precision and accuracy were both shown to be better than 1% for major elements and 5% for trace elements as controlled using 40 international and in-house standards (list available in **Supplementary Table 1**) and analyses of replicate samples, respectively.

RESULTS

Sedimentology

The measured section is ∼460 meters thick with strata oriented N65°E and a dip of 63°S (**Figure 1**). It can be divided into seven lithological units (FFU1-7, described in **Supplementary Text 1**). According to the Belgian lithostratigraphic chart defined by Préat and Bultynck (2006) and the geological map of Mansy et al. (2006), The Trois-Fontaines (TRF), the Terres d'Haurs (THR), Mont d'Haurs (MHR), and Fromelennes (FRO) formations can be identified. FFU1-2 corresponds to the Trois-Fontaines, FFU3-4 to Terre d'Haurs, FFU5 to Mont d'Haurs and FFU6-7 to the Fromelennes formations. Thickness of the above mentioned formations in the Fromelennes-Flohimont section are consistent with their thicknesses defined in the type area (see **Figure 1C**). Description of each formation and lithological units is detailed in **Supplementary Text 1**.

The field observations (e.g., facies geometry and sedimentary structures) and petrographic analyses of thin-sections (e.g., matrix, grain size, fossil content, mineralogy, etc.) allowed to the discrimination of 17 microfacies across the FF section. Specific microfacies for the Givetian in the FF area are presented in **Figure 2** and a full list of microfacies including key features and interpretations is available in **Table 1** (for an extended descriptions and interpretations of individual microfacies see **Supplementary Text 2**). Following the definition of Read (1985) for carbonate platform models, we have organized our microfacies across three main platform profiles: (1) a homoclinal ramp (RP), (2) a rimmed shelf (RS), and (3) a drowning shelf (DS). Vertical microfacies evolution in FF (**Figure 2**) indicates major changes in the depositional record, allowing reconstruction of the main sea-level fluctuations in the southern part of the Ardennes platform (**Figure 2**). These important sedimentological changes are numbered depositional intervals (I) to (VI).

Stratigraphic Evolution of the Magnetic Susceptibility Values

The Fromelennes-Flohimont χ record was first published in De Vleeschouwer et al. (2015) and for the purpose of this study we divided the curve into seven Magnetic Susceptibility Units (MSU-I to MSU-VI, **Figure 2**), based on visual evaluation of the magnetic susceptibility values. MSU-I shows average χ values of $0.08 \pm 0.1 \times 10^{-7}$ m^3/kg (see vertical dotted line in **Figure 2**). MSU-II records the highest average χ value of the entire section ($1.79 \pm 1.1 \times 10^{-7}$ m^3/kg). MSU-III also records high average values of $1 \pm 0.48 \times 10^{-7}$ m^3/kg, with important variations from 0 to 2×10^{-7} m^3/kg. The MSU-IV shows a low and monotonous signal with an average of $0.10 \pm 0.17 \times 10^{-7}$ m^3/kg. MSU-V records an average χ value of 0.48 ± 0.26 10^{-7} m^3/kg. MSU-VI exposes low χ values ($0.14 \pm 0.16 \times 10^{-7}$

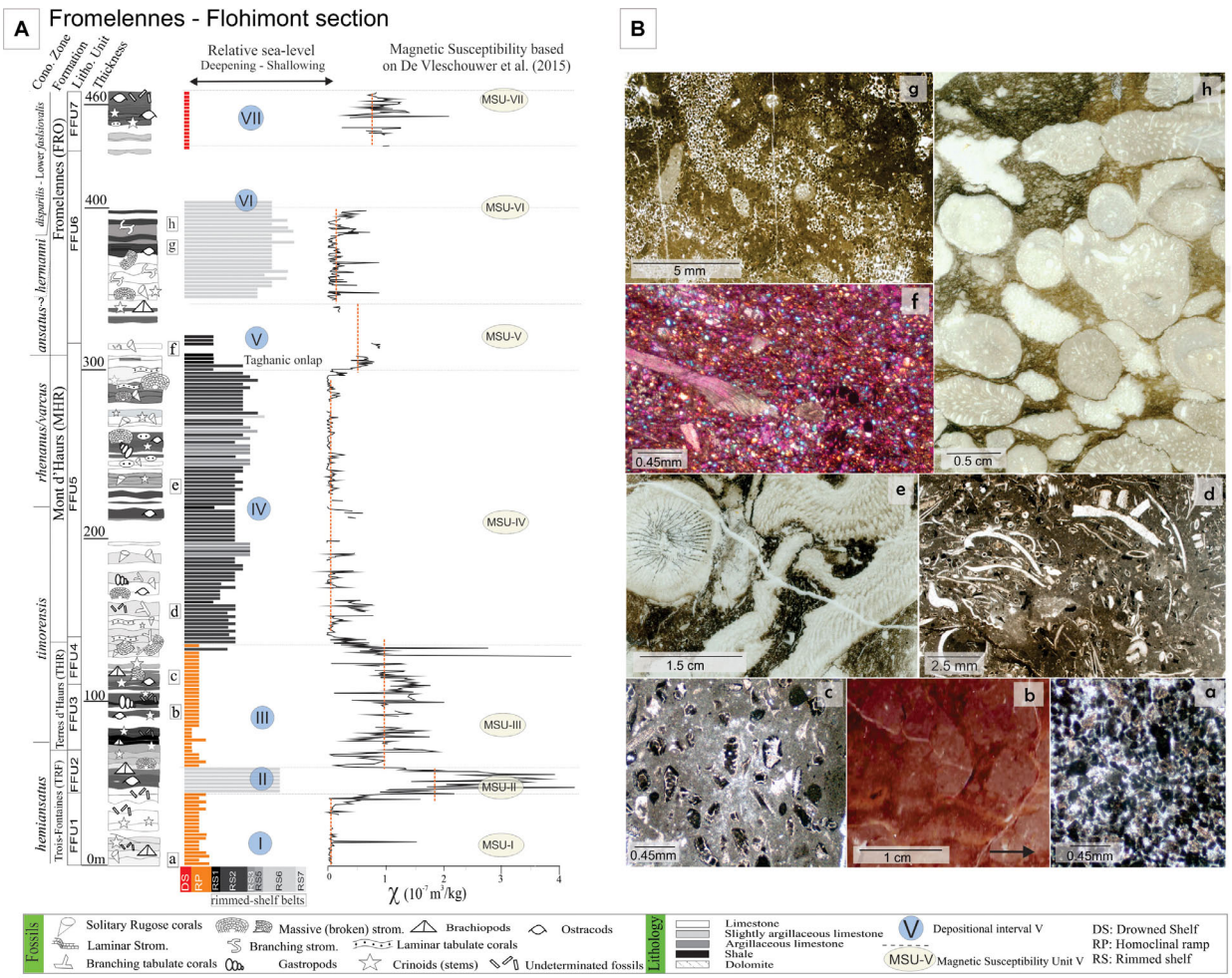

FIGURE 2 | Overview on the Fromelennes-Flohimont sequence. **(A)** Schematic sedimentological log showing formations, main lithological features, microfacies evolution with the depositional intervals (I–VI), magnetic susceptibility curve (De Vleeschouwer et al., 2015) with Magnetic Susceptibility Unit (MSU) and conodont zones (Bultynck and Dejonghe, 2001; Gouwy and Bultynck, 2003; Narkiewicz and Bultynck, 2010). Division of the magnetic susceptibility curve into seven MSU is based on visual evaluation and the symmetry with depositional intervals. **(B)** Overview of the most represented microfacies in the section **(a–h)**. **(a)** RP-FF2a: fine-grained peloidal grainstone (FRO-3, transmitted light). **(b)** PF7-FF7: red clay showing numerous occurrence of mm- to cm-sized intraclast floating in the matrix (FRO39a, transmitted light). **(c)** RP-FF1: thallus of palaeosiphonocladale filled by a darker micrite contrasting with the lighter surrounding micrite (FRO89, transmitted light). **(d)** RP-FF1: shell-rich bioclastic wackestone-packstone (FRO140, transmitted light). **(e)** RS2-LT2: reef-builders rudstone showing tabulate and rugose corals (FRO170, scanned thin-section). **(f)** RS1-FF1 off-reef shelf: brachiopods and rare crinoids in an argillaceous matrix rich in silt-sized quartz grains (FRO219, crossed nicols with gypsum blade). **(g)** PF6-FF6: densely bioturbated mudstone with bioturbations filled by a peloidal grainstone texture (FRO299a, transmitted light). **(h)** PF6-LT12: *Stachyodes* and *Amphipora* rudstone (FRO289a, scanned thin-section).

m^3/kg). MSU-VII shows a relatively high average χ value close to $0.74 \pm 0.26 \times 10^{-7}$ m^3/kg.

Magnetic Measurements and Depositional Proxies

Before χ records can be considered as a tool for stratigraphic correlation, it must be established that the χ signal still contains original paleoenvironmental information (e.g. Da Silva et al., 2013). This is not trivial in the Ardennes, where Late Variscan remagnetization events were recognized by Zegers et al. (2003). To estimate the preservation of the χ records in the FF and LT sections published in De Vleeschouwer et al. (2015), we have performed hysteresis magnetic measurements for both sections and compared the different hysteresis parameters (**Tables 2**, **3**) with the magnetic susceptibility data (e.g., Riquier et al., 2010; Da Silva et al., 2012, 2015).

The FF and LT sections show relatively similar hysteresis loops (mainly wasp-waisted shape with a positive or negative high-field slope and general high level of noise) and magnetic characteristics (**Figures 3**, **4** and **Tables 2**, **3**). After the slope correction, the ferromagnetic contribution is visible and loops appear to be wasp-waisted, and commonly show a high level noise. M_s data are well-correlated with χ for both sections (correlation coefficient r = 0.95 and 0.98 respectively for FF and LT). The correlation is even higher between χ_{ferro} and χ (La

TABLE 1 | Synthesis of microfacies for the Givetian in the Fromelennes-Flohimont road section (N. France).

Microfacies number	Name	Main diagnostic features	Bedding, color and sedimentary structures	Depositional setting
Drowning shelf (DS)				
DS-LT	Brachipod-bivalve shells packstone-rudstone	Limestone with brachiopods, bivalves, gastropods, crinoids. Sediment is poorly- to moderately-sorted and bioturbations are common	Decimetre thick homogeneous dark-gray to black limestone beds	Drowned lagoonal setting above the FWWB
Homoclinal ramp (RP)				
RP2-FF1	Palaeosiphonocladale and shell-rich bioclastic wackestone-packstone	Abundance of palaeosiphonocladales and crinoids. Common occurrence of brachiopods, gastropods, trilobiltes. Abundant bioclastic hash	Cm- to dm-thick fine-grained beds	Mid- to distal-ramp below the FWWB with storm deposits
RP2-FF2a	Fine-grained peloidal grainstone	Coarse-grained crinoids (with micritized rims), gastropods (with common micrite filling internal molds) and bioturbations	Cm- to dm-thick argillaceous black to dark-gray limestone beds	Mid- to distal-ramp below the FWWB with storm deposits
RP2-FF2b	Peloidal bioclastic grainstone with palaeosiphonocladales	Abundance of peloids and palaeosiphonocladaes within a grainstone texture	Cm- to dm-thick fine-grained beds	Mid-ramp within the FWWB
Rimmed shelf (RS)				
Facies belt 1: Fore-reef shelf and off-reef				
RS1-FF1	Argillaceous crinoidal – brachiopods mudstone	Crinoids, brachiopods and trilobites. Slightly argillaceous micrite rich in silt-sized quartz grains and local mica sheets	Strongly weathered argilaceous limestone	Fore-reef to off-reef setting below the FWWB
Facies belt 2: marginal reef and fore-reef shelf				
RS2-LT1	Open-marine bioclastic wackestone-packstone	Crinoids, brachiopods, ostracods, trilobites, bryozoans, tentaculitids and local debris of branching tabulate and rugose corals, and stromatoporoids	Dm thick coarse-grained dark-blue limestone beds	Open-marine setting located below the FWWB and influenced by reefal-construction (barrier-or patch-reef)
RS2-FF2	Fine- to coarse-grained crinoidal bioclastic packstone	Abundant large-sized crinoids, common brachiopods and bioturbations, ostracods, peloids, gastropods, bryozoans, rugose corals, girvanella lumps, trilobites	Dm-thick coarse-gained beds	Crinoidal meadow flanking fore-reef slope below FWWB
RS2-LT2	Coral-stromatoporoid rudstone and flaotstone	Dm-sized stromatoporoids (laminar and buldous), solitary rugose corals, branching tabulate corals, crinoids, brachiopods, trilobites	Coarse-grained dark-blue to dark-gray limestone with large and broken reef-builders in non-living position	Open-marine setting located below the FWWB in the vicinity of reef
RS2-FF3	Dendroid stromatoporoid and bioclast-rich rudstone	*Stachyodes, Amphipora* and open-marine bioclasts such as brachiopods, crinoids. Rugose and tabulate corals, peloids, grivanella and palaeosiphonocladales	Dm-thick coarse-gained beds with visible reef-builder organisms	Fore-reef open-marine setting influenced by internal shelf setting
Facies belt 3: marginal shelf sand shoals				
RS3-LT4	Peloidal – lithoclastic grainstone with gastropods and mud-coated grains	Peloids and micritic lithoclasts, gastropods, brachiopods, crinoids, ostracods and rare tabulate corals and bryozoans	Dm-thick dark blue to dark-gray limestone	Peloid shoal in the FWWB
Facies belt 5: internal restricted shelf				
RS5-LT10	Oolite lithoclastic grainstone – packstone	Type 4 ooids of Strasser (1986)	Cm- to dm-sized light- to dark-gray bed	Lagoonal setting with local higher energy-event
Facies belt 6: Internal evaporitic - brackish shelf				
RS6-LT12	Dendroid stromatoporoid flaotstone to rudstone	*Stachyodes* and *Amphipora*, *Girvanella*, *Renalcis* lumps and stromatoporoids	Pluri-dm-sized beds with local erosive base	Dendroid stromatoporoids patch-reef reworked in lagoonal setting
RS6-FF4	Micritic lithoclast and peloidal grainstone	Abudance of variously-shaped and sized peloids and lithoclasts (micritic or peloidal grainstone. Locally, *Amphipora,* ostracods, calcisphere, allocthtonous ooids	Dm-to pluri dm-sized beds	Tidal channel in the vicinity of intertidal pond and *Amphipora* patch-reefs
RS6-FF5	Mudstone-wackestone with green algae, ostracods and gastropods	*Abundance of kamaena*, *triangulinella and* ostracods. Locally gastropods, *labyrinthoconus*, *Amphipora,* peloids, calcisphere, ortonella and fenestrae	Cm- to dm-thick beds	Brackish lagoonal setting under the FWWB

(Continued)

TABLE 1 | Continued

Microfacies number	Name	Main diagnostic features	Bedding, color and sedimentary structures	Depositional setting
RS6-FF6	Mudstone	Limited flora and fauna, bioturbation filled with peloids and rare ostracods	Dm-thick beds	Evaporitic intertidal ponds
RS6-LT14	Laminated mudstone – peloidal grainstone	Alternation of peloidal grainstone and mudstone layer or light and darker micritic laminae with locally well-spread silt-sized quartz	Dm-thick beds	Tidal-channel and levees bordering channel and intertidal pounds in supratidal setting
Facies belt 7: Supratidal shelf				
RS7-FF7	Palaeosoils	Intraclast in argillaceous matrix. Intraclasts are mudstone in texture and show palaeosiphonocladale, ostracods, calciphere	Dm-thick bed showing brecciated fabric	Palaeosoils in internal supratidal shelf setting

Thure $r = 0.99$; Fromelennes-Flohimont $r = 0.99$; **Figure 4B** and **Table 3**). The nature of ferromagnetic *s.l.* fraction is investigated through the measurement of the coercive force (H_c) and the coercivity of remanence (H_{cr}). H_{cr} and H_c values in our datasets are respectively in the range of 30–70 mT and 0–15 mT and not correlated with χ values (**Figures 4C,D**). Generally, H_{cr} and H_c values are predominantly low regardless of the χ values, which is typical for carbonate platform sediments (Borradaile et al., 1993; Da Silva et al., 2012). As shown in **Figures 4C,D** few samples from the LT and FF section record H_{cr} or H_c values higher or in the range of threshold values for low-coercivity minerals like magnetite (Fe_3O_4). The IRM_{300}/IRM_{500} ratios for FF samples are predominantly lower than 5%, while half of the LT samples record ratios higher than 5%. All samples with IRM_{300}/IRM_{500} ratios higher than 5%, corresponding to non-saturating IRM curves (e.g., **Figure 3**) are shown in **Table 2** and presented along the lithostratigraphic and chemostratigraphic profiles for LT an FF sections in **Figure 5**. When low-coercivity minerals are the main contributor to the χ signal in the dataset (IRM_{300}/IRM_{500} ratios < 5) it allows the use of the high-field magnetic susceptibility (χ_{HF}) results to determine the diamagnetic/paramagnetic contributions in our samples (Sardar Abadi et al., 2015; Königshof et al., 2016). Correlation between χ and χ_{HF} is relatively good for the FF ($r = 0.64$) and the LT ($r = 0.65$) sections (**Figure 4E**) and χ_{HF} values are mostly positive in both sections.

To assess the magnetic grain size distribution in our dataset we plot ratios M_{rs}/M_s and H_{cr}/H_c for samples with IRM_{300}/IRM_{500} ratios $< 5\%$ in the bi-logarithmic "Day" diagram (Day et al., 1977; Dunlop, 2002) (**Figure 6**). Most of our data fall between or along the SD + SP (Dunlop, 2002) and MD + SD (Parry, 1982) mixing lines, which is comparable to the data of for Devonian Pelagic limestone and mudstone from Germany (Riquier et al., 2010) and the Zwing et al.'s (2005) platform carbonates in Germany. The occurrence of superparamagnetic grains, in the analyzed dataset was evaluated by the value of the decay viscosity coefficient S_d. Most samples in the dataset show high S_d values with a median of 26 and 33, respectively, for FF and LT (**Table 3**).

To evaluate the depositional origin of our χ signal we compared the stratigraphic evolution of the χ signal with the corresponding profiles for detrital proxies such as TiO_2, Al_2O_3, K_2O, Zr, and Rb (Calvert and Pedersen, 2007; Śliwiński et al., 2012; see **Table 4** for detailed geochemical datasets). As presented in **Table 3** and in **Figures 4A,B**, the correlation coefficient r between χ values and detrital input proxies for LT and FF sections shows intermediate values (r between 0.51 and 0.61 for LT section and 0.62 to 0.70 for the FF section).

To analyze how χ is facies-dependent in our sediments and even more so in the Givetian Ardennes carbonate platform, we combined published χ data (De Vleeschouwer et al., 2015) with the sedimentological models developed in this study (see section sedimentology).

Homoclinal Ramp

Sediments belonging to this profile are exposed throughout the Lower Givetian Trois-Fontaines and Terres d'Haurs formations. **Figure 5C** shows a general increase of the average χ from the mid- to outer-ramp setting, with the microfacies RP2-FF1 located at the margin between mid- and outer-ramp settings recording an exceptionally high average χ value.

Rimmed Shelf Model

The characteristic sediments in this model correspond to the middle portion of the Trois-Fontaines, the Mont d'Haurs and the Fromelennes formations. In both, the La Thure and the Fromelennes-Flohimont sections, external (RS1 and RS2) and internal shelf belts (RS3, RS4, RS5, RS6, and RS7) deposits are characterized by different χ behavior (see **Figure 5D**). A general decrease of the average χ signal from the off-reef to biostromal belts characterizes the external shelf. In the internal shelf a general increase in the average χ values is observed between the bioclastic shoals and the supratidal setting. The internal shelf oolitic shoal is marked by a decrease of the average χ values and the supratidal setting by a very high average of χ value.

DISCUSSION

Sedimentology

The sedimentological analyses of the FF section allowed the discrimination of 17 microfacies distributed over three carbonate platform types throughout the Early – Late Givetian. Major changes in the platform development can be summarized as

TABLE 2 | Magnetic susceptibility, microfacies (MF) and magnetic hysteresis parameters for each analyzed samples from FF and LT sections with the corresponding interpretations.

Samples	Position	MF	χ (10^{-8})	χ_{HF} (10^{-8})	χ_{ferro} (10^{-8})	M_s (10^{-4})	M_{rs} (10^{-4})	IRM_{300}/IRM_{500}	Mrs/Ms	H_c	H_{cr}	Hcr/Hc	S_d	Interpretation			
	m		m^3/kg	m^3/kg	m^3/kg	Am^2/kg	Am^2/kg	[%]	N/A	mT	mT	N/A	N/A	Dominating non ferro Type	Maghaemite/ Magnetite Presence	Haematite Presence	SP grains Presence
Fromelennes-Flohimont (FF)																	
FRO-10	0.3	RP2-FF2a	0.08	−0.20	0.28	1.00	0.090	4.2	0.09	12.6	50.1	3.98	25.34	Carbonate	−	−	++
FRO22A	**30.5**	**RP2-FF2a**	**0.21**	**−0.07**	**0.28**	**1.78**	**0.050**	**13.0**	**0.03**	**3.9**	**58.3**	**14.95**	**16.68**	**Carbonate**	**−**	**−**	**+**
FRO54	52.2	RS6-FF5	31.38	0.67	30.71	59.56	12.030	2.0	0.20	8.0	49.6	6.20	33.07	Clay	+++	−	++
FRO76A	72.5	RS1-FF1	10.23	0.32	9.91	16.11	3.430	2.5	0.21	8.5	47.8	5.62	26.81	Clay	++	−	++
FRO92A	90.3	RS1-FF1	13.18	0.69	12.50	24.54	5.430	2.5	0.22	9.7	49.1	5.06	27.07	Clay	++	−	++
FRO128	110.1	RS1-FF1	13.49	1.70	11.79	18.84	4.540	3.5	0.24	10.5	53.8	5.12	25.51	Clay	++	−	++
FRO151A	129.8	RS1-FF1	7.51	0.56	6.94	11.35	2.045	3.3	0.18	6.2	45.3	7.31	30.91	Clay	++	−	++
FRO173A	149.1	RS2-LT2	0.87	0.18	0.69	8.18	0.755	4.0	0.09	11.4	37.3	3.27	15.53	Clay/carbonate	+	−	+
FRO195A	**193.6**	**RS2-LT2**	**−0.33**	**−0.35**	**0.02**	**0.56**	**0.039**	**4.4**	**0.07**	**81.2**	**31.8**	**0.39**	**12.84**	**Carbonate**	**No**	**No**	**+**
FRO207C	231.3	RS2-LT2	0.99	−0.28	1.27	2.62	0.219	3.1	0.08	4.2	38.8	9.24	32.00	Carbonate	−	−	++
FRO222A	**245.0**	**RS1-FF1**	**0.94**	**−0.06**	**1.00**	**2.90**	**0.570**	**10.9**	**0.20**	**11.6**	**56.3**	**4.85**	**42.62**	**Carbonate**	**−**	**+**	**+++**
FRO246A	269.8	RS5-LT10	0.39	−0.10	0.49	2.64	0.320	4.4	0.12	7.8	45.4	5.82	19.45	Carbonate	+	−	+
FRO263A	289.9	RS5-LT10	0.24	−0.19	0.43	0.73	0.120	0.5	0.17	8.0	49.4	6.18	19.06	Carbonate	+	−	+
FRO272B	300.0	RS2-LT1	5.51	0.28	5.23	13.22	1.850	2.0	0.14	5.1	42.7	8.37	33.66	Clay	++	−	++
FRO280B	**313.0**	**RS2-LT1**	**8.15**	**0.91**	**7.24**	**9.29**	**1.690**	**5.4**	**0.18**	**7.6**	**48.5**	**6.38**	**28.86**	**Clay**	**++**	**+**	**++**
FRO292B	351.5	RS6-LT12	0.06	0.77	−0.72	14.86	2.310	2.4	0.16	6.5	44.8	6.89	26.72	Clay	++	−	++
FRO317	370.2	RS6-LT12	1.43	−0.24	1.67	1.92	0.212	3.0	0.11	15.4	46.7	3.03	12.14	Carbonate	+	−	−
FRO354B	394.1	DS-LT	1.46	−0.16	1.61	3.60	0.254	1.4	0.07	3.3	34.9	10.58	35.46	Carbonate	+	−	++
FRO362A	440.7	DS-LT	7.37	0.23	7.14	12.49	2.477	3.1	0.20	6.9	44.7	6.48	28.84	Clay	++	−	++
FRO400	461.2	DS-LT	6.60	0.19	6.41	7.76	1.297	2.2	0.17	6.4	43.1	6.69	30.32	Clay	++	−	++
La Thure																	
TUR100	0.1	RS2-LT1	6.37	−0.10	6.47	16.16	1.28	4.0	0.08	3.7	47.9	12.95	40.60	Carbonate	++	+	+++
TUR121	**10.2**	**RS4-LT8**	**2.87**	**0.00**	**2.86**	**4.62**	**1.06**	**5.4**	**0.23**	**7.0**	**49.8**	**7.11**	**33.78**	**Carbonate + clay**	**++**	**+**	**++**
TUR158	**34.9**	**RS5-LT15**	**7.58**	**0.03**	**7.55**	**14.35**	**2.13**	**6.5**	**0.15**	**4.2**	**46.0**	**11.06**	**63.06**	**Carbonate + clay**	**+**	**+**	**+++**
TUR163d	**39.6**	**RS3-LT4**	**2.52**	**0.00**	**2.52**	**4.93**	**0.84**	**5.6**	**0.17**	**7.4**	**51.7**	**7.00**	**32.06**	**Carbonate**	**+**	**+**	**++**
TUR181b	53.8	RS5-LT10b	1.62	0.00	1.62	1.97	0.24	4.2	0.12	5.2	40.9	7.90	29.69	Carbonate	+	+	++
TUR205c	69.1	RS2-LT2	3.10	−0.19	3.30	1.64	0.40	4.6	0.24	8.1	50.0	6.20	26.25	Carbonate	+	+	++
TUR233a	99.8	RS5-LT15	5.20	0.34	4.87	9.46	2.05	3.4	0.22	9.5	48.7	5.13	23.32	Clay	++	+	++
TUR241c	**105.4**	**RS5-LT15**	**1.66**	**0.16**	**1.49**	**0.94**	**0.17**	**12.9**	**0.18**	**11.8**	**60.3**	**5.09**	**22.44**	**Clay**	**−**	**++**	**++**
TUR250b	110.4	RS5-LT15	2.74	0.45	2.30	4.36	0.50	4.1	0.11	4.4	52.4	11.94	29.23	Clay	+	+	++
TUR300b	**145.6**	**RS5-LT15**	**17.09**	**0.68**	**16.42**	**46.00**	**4.85**	**10.4**	**0.11**	**5.0**	**69.8**	**13.95**	**39.74**	**Clay**	**++**	**++**	**++**
TUR306	**149.8**	**RS5-LT15**	**10.24**	**0.18**	**10.06**	**20.00**	**1.69**	**10.4**	**0.08**	**3.0**	**64.7**	**21.56**	**47.07**	**clay**	**+**	**+++**	**+++**

Bold highlights samples that have to be regarded with caution as they record IRM_{300}/IRM_{500} ratio > 5 indicating that a slope correction cannot be calculated. For a definition of each parameter, refer to the main text.

TABLE 3 | Mean value (mean) for each hysteresis parameter showing IRM_{300}/IRM_{500} ratio < 5 and correlation coefficient (*r*) between each hysteresis parameter and the magnetic susceptibility (χ).

		Hysteresis								Geochemistry				
	Number of sample (n)	χ_{HF} ($10^8 m^3/kg$)	χ_{ferro} ($10^8 m^3/kg$)	M_s ($10^4 Am^2/kg$)	M_{rs} ($10^4 Am^2/kg$)	H_c (mT)	H_{cr} (mT)	S_d	Number of sample (n)	SiO_2 % wt.	Al_2O_3 % wt.	TiO_2 % wt.	K_2O % wt.	Zr ppm
LT	**5**								**30**					
r (χ)		0.05	0.99	0.94	0.82	0.05	0.30	0.43		0.51	0.61	0.58	0.48	NM
Mean		0.10	3.71	6.72	0.89	6.17	47.99	29.82		5.00	2.00	0.10	1.01	NM
FF	**16**								**42**					
r (χ)		0.57	1.00	0.95	0.96	0.01	0.45	0.38		0.66	0.70	0.69	0.62	0.64
Mean		0.28	6.22	12.46	2.34	8.16	45.20	26.70		5.49	1.42	0.11	0.18	15.73

Right part of the table shows mean value for each detrital proxy parameters and also correlation coefficient (r) between detrital proxy parameters and χ. Magnetic susceptibility data are from De Vleeschouwer et al. (2015). NM, not measured. For a definition of each parameter, refer to the main text.

follows: (1) development of a homoclinal ramp during the early Givetian, (2) evolving to a rimmed shelf throughout the middle- to late-Givetian and (3) then by the latest Givetian the carbonate factory dramatically collapses and the platform drowns, (4) and was subsequently capped by Frasnian shales. Carbonate platform types observed in this section are similar to those described in the time equivalent LT section in NW part of the Ardennes (Pas et al., 2017). To build a reliable correlation framework between the South and the NW part of the Ardennes platform we compared microfacies defined in the FF section with those published for the in LT section and this allowed the construction of integrated sedimentological models for the ramp (**Figure 7A**) and the rimmed shelf (**Figure 7B**). The integration of both sets of microfacies also enables an insight into the vast array of depositional environments that characterize the Givetian of the Ardennes as well as their proximal – distal distribution. Due to the complexity and diversity of depositional settings defining the rimmed shelf profile, we have divided this model into seven facies belts (RS1-RS7): (RS1) fore-reef to off-reef shelf; (RS2) biostromal and fore-reef shelf; (RS3) bioclastic shoals; (RS4) internal shelf with moderate circulation; (RS5) internal restricted shelf; (RS6) internal evaporitic shelf and (RS7) supratidal shelf setting. Facies belts RS1 and RS7 do not occur in the time-equivalent LT section (Pas et al., 2017) while the facies belt RS4 is not observed in the FF section. The ramp model (RP) shows a homoclinal profile and can be divided into outer- (RP1) and mid-ramp (RP2) settings. This two belts are similarly exposed in the LT section. The drowning shelf model (DS) is also observed in the LT section and characterized by a similar facies.

Origin and Nature of the Ferromagnetic Minerals and Magnetic Susceptibility

Based on the analyses of the hysteresis loops and the comparison of hysteresis parameters with the χ signal (**Figures 3**, **4**) we provide an insight into the origin of the χ signal and the nature of the ferromagnetic susceptibility.

M_s (magnetization at saturation) and χ_{ferro} (ferromagnetic susceptibility) are both proxies for the concentration of ferromagnetic minerals. The very good correlation of χ with M_s and χ_{ferro} indicates that χ values in LT and FF sections is influenced by the ferromagnetic *s.l.* contribution. As noted in Section "Magnetic Measurements and Depositional Proxies," most of our data shows H_{cr} and H_c values that correspond to the domain of remanence coercivity values of low-coercivity minerals like magnetite/maghaemite indicating that these ferromagnetic minerals are the main contributors to the χ signal variation. This observation concurs with results established for sediments found in remagnetized carbonate platforms (Borradaile et al., 1993; Zwing et al., 2005; Riquier et al., 2010; Da Silva et al., 2012, 2013). The LT and FF samples that record H_{cr} and H_c values in the range or higher than threshold values for low-coercivity minerals like magnetite, and a IRM_{300}/IRM_{500} ratios higher than 5% are interpreted as containing a relatively high abundance of hematite grains (e.g., FRO222A, **Figure 3C**). An IRM_{300}/IRM_{500} ratios < 5 is a good indicator of non-saturating IRM curve (e.g., TUR300b, **Figure 3A**) that are characteristic for low-coercivity minerals. The absence of a negative correlation between H_{cr} or H_c and χ indicates that the hematite contribution to the bulk magnetic susceptibility is weak. This can be explained by the fact that the hematite has a remanent saturation much lower than the magnetite/maghaemite, e.g., 2.5 kA/m versus 480 or 380 kA/m.

Correlation between χ and χ_{HF} are relatively good for the FF (r = 0.64) and the LT (r = 0.65) sections (**Figure 4E**), pointing to a paramagnetic/diamagnetic mineral influence to the χ signal. FF and LT sections show both positive and negative χ_{HF} values, which indicate that high-field magnetic susceptibility contribution are either dominated by paramagnetic minerals such as clay and pyrite (positive χ_{HF} values) or diamagnetic minerals such as calcite (negative χ_{HF} values). A summary of our interpretations based on the comparison of χ with hysteresis parameters and on the analysis of hysteresis loops is provided in **Table 2**.

To estimate the main grain-size of ferromagnetic sensu stricto particles in our dataset and to assess whether or not the ferromagnetic signal was overprinted by diagenetic processes we plot ratios M_{rs}/M_s and H_{cr}/H_c obtained for the LT and FF sections in the bi-logarithmic Day diagram (Day et al., 1977) and compare it with previously published data (e.g., Jackson, 1990; Zwing et al., 2005; Devleeschouwer et al., 2010;

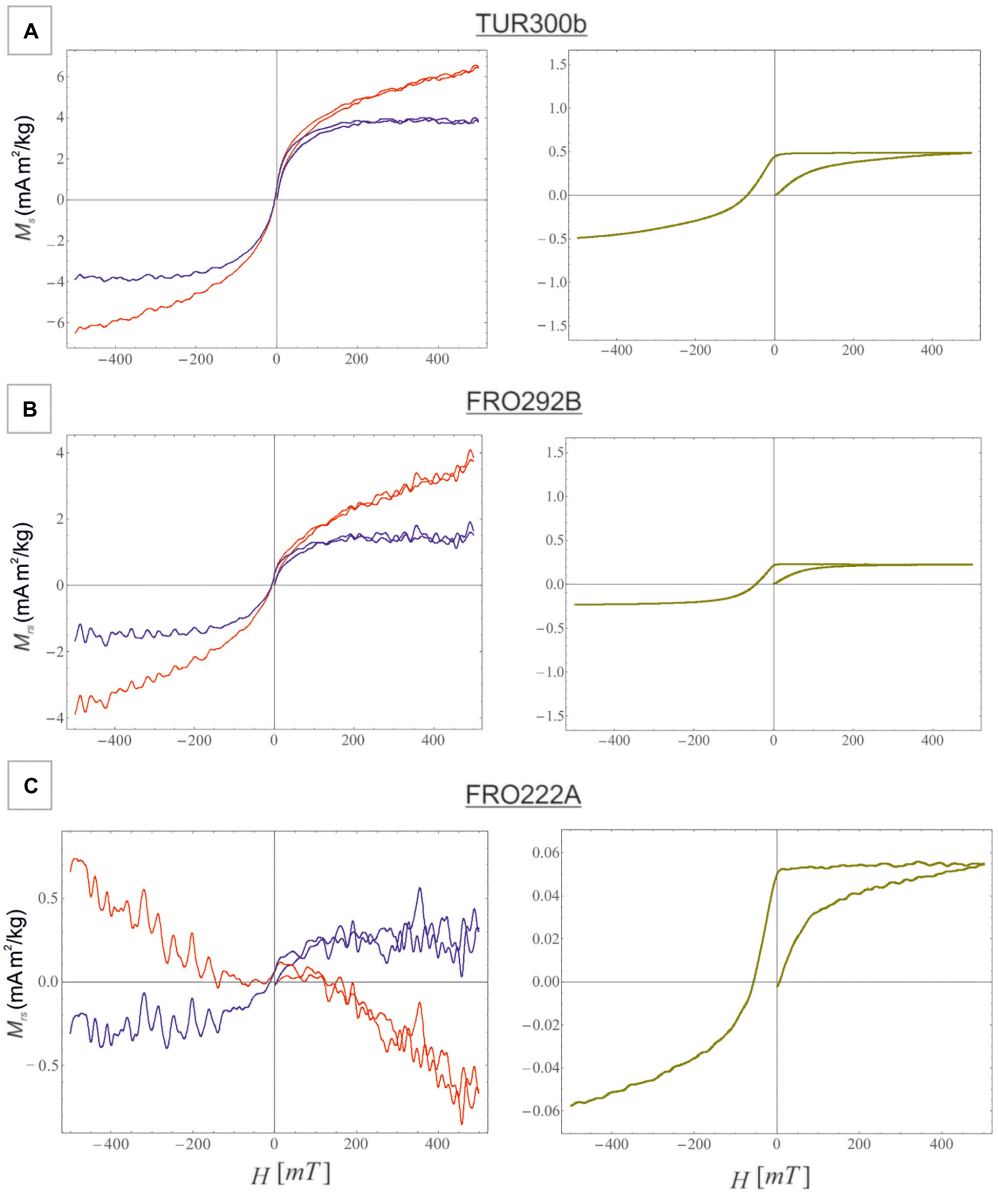

FIGURE 3 | Example of hysteresis curves and corresponding IRM acquisition curves in LT **(A)** and FF **(B,C)** sections. Right column: plots before (red) and after slope correction (blue). Left column: backfield curves.

Riquier et al., 2010; Königshof et al., 2016) and empirical trend lines for different grain-size categories (Parry, 1982; Dunlop, 2002). In this study χ versus T measurements have not been performed which hampers the ability to determine whether a mixture of different ferromagnetic minerals occurs in our dataset. In order to use the Day diagram we have made the assumption that there is no mixture of ferromagnetic minerals in the analyzed data. Indeed, interpretation of the Day diagram is ambiguous for particle size diagnosis and mineralogy when the analyzed data includes different magnetic mineralogy (Tauxe et al., 2002; Roberts et al., 2018). In their paper, Roberts et al. (2018) also discussed several other factors such the stress state, the surface oxidation, the magnetostatic interactions and particle shape that can undermine the use of the Day diagram as a tool for diagnosing domain state, particle size, or mineralogy.

The "Day" diagram in **Figure 6** reveals that our limestone samples are mostly distributed between the SD + SP mixing curve of Dunlop (2002) and the mixing SD + MD curve (Parry, 1982), similar to North America Paleozoic limestones (Jackson, 1990), Paleozoic clastic and carbonate rocks (Zwing et al., 2005) and Frasnian/Famennian limestone/shale (Riquier et al., 2010). Values from Jackson (1990) illustrated in the Day plot were interpreted by Channell and McCabe (1994) as recording a fine-grained fingerprint typical of remagnetized limestone. Data

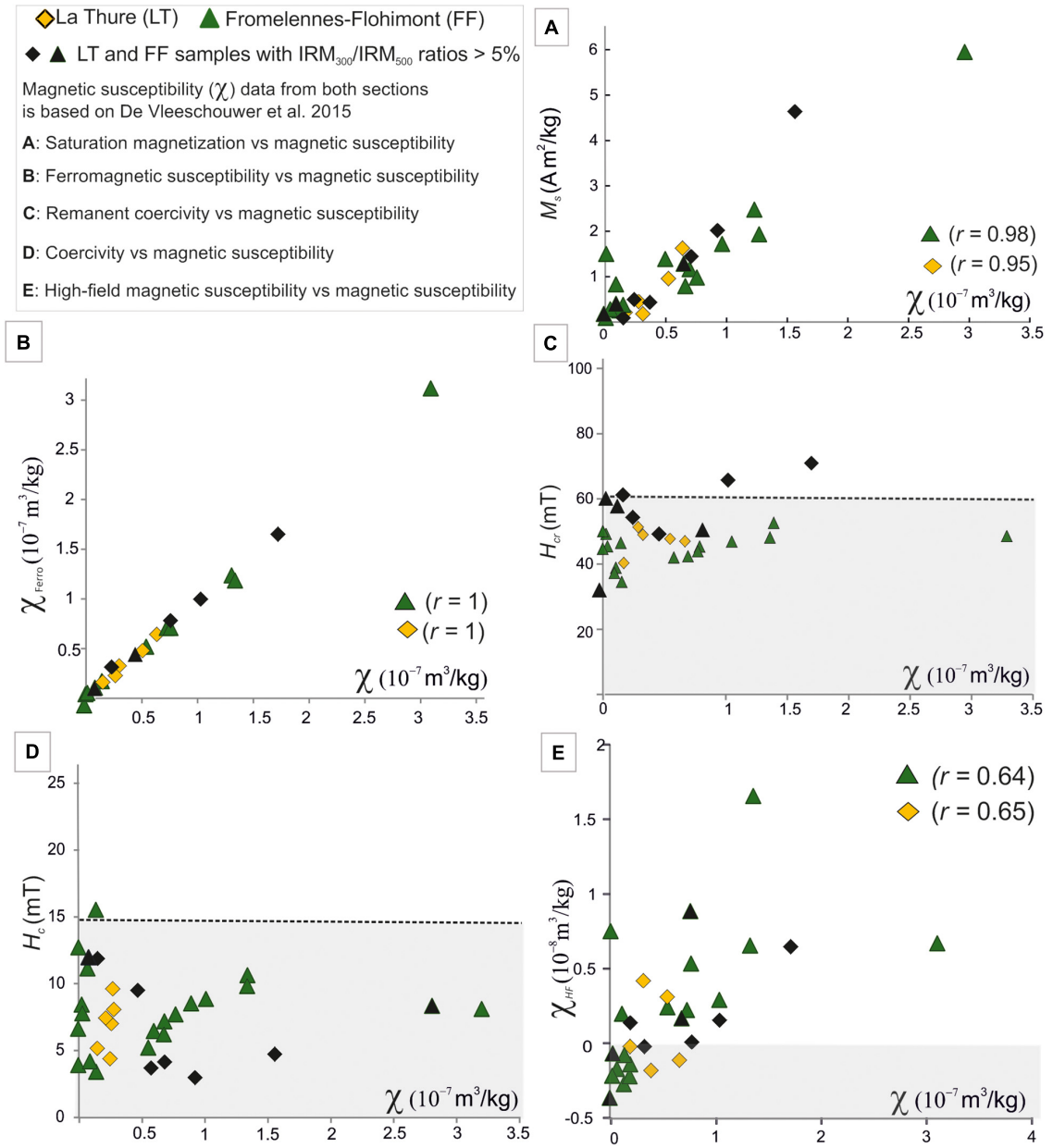

FIGURE 4 | Comparison of initial magnetic susceptibility (χ) published in De Vleeschouwer et al. (2015) with parameters extracted from the hysteresis loops for the Fromelennes-Flohimont and the La Thure sections. **(A)** Magnetization at saturation (M_s, Am^2/kg) versus χ. **(B)** Ferromagnetic susceptibility (χ_{ferro}, m^3/kg) versus χ. **(C)** Comparison of χ with the remanent coercivity (H_{cr}). The shaded band corresponds to the domain of remanence coercivity values of magnetite. **(D)** Comparison of χ with the coercivity (H_c). The Shaded band corresponds to the domain of coercivity values for magnetite. **(E)** High-field magnetic susceptibility (χ_{HF}, m^3/kg) versus χ. Shaded band corresponds to χ_{HF} negative values.

from Riquier et al. (2010) from Devonian sections in the NE Rhenohercynian Massif (Steinbruch Schmidt and Beringhauser Tunnel sections) also show a remagnetized fingerprint. Riquier et al. (2010) interpreted the magnetic signature of their samples as the superposition of a coarse-grained magnetite detrital fraction and a diagenetic fraction showing authigenic SD + SP fine-grained magnetite. Da Silva et al. (2013) studied the Devonian section in Belgium (Tailfer, Villers-le-Gambon, Moulin Bayot, Baileux) and also show a remagnetized fingerprint occurring during the Variscan Orogeny to be a consequence of the Zegers et al.'s (2003) Carboniferous remagnetization event. As described in the geological setting, the FF and LT sections are both located out of the MVT districts, which is related to the P-component of Zegers et al.'s (2003) remagnetization events. The P-component is therefore not considered as affecting the χ signal. The LT and FF samples falling close to data from Zwing et al. (2005)

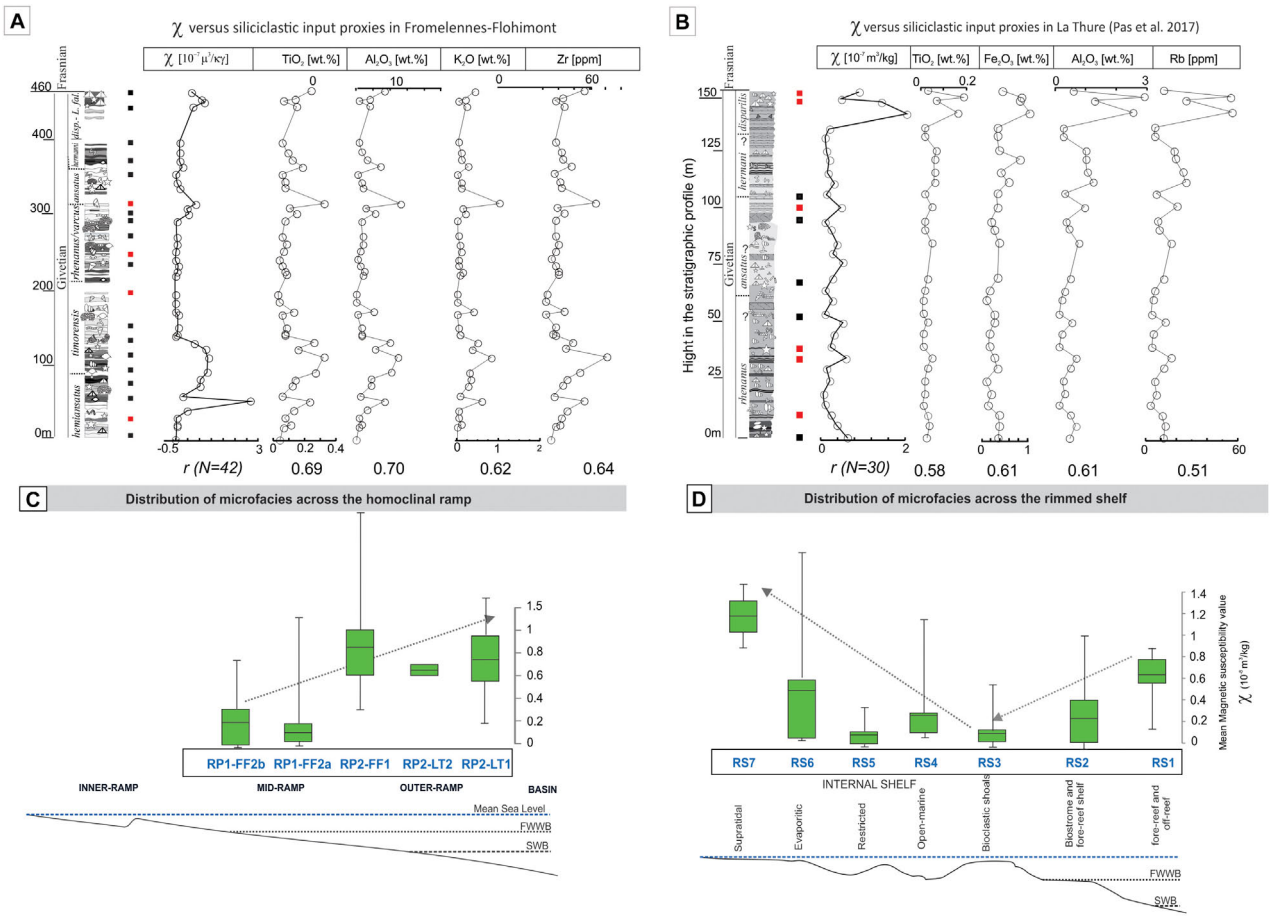

FIGURE 5 | Magnetic susceptibility versus chemostratigraphic profiles and versus sedimentological profiles. Squares along both profiles indicate the position of the samples for magnetic analyses and whether the samples record IRM_{300}/IRM_{500} ratio > 5 (red square). **(A)** Chemostratigraphic profiles of χ, TiO_2, Al_2O_3, K_2O and Zr in the FF section. Concentration of these elements are considered as proxy for detrital inputs and show moderate correlation with χ variations. **(B)** Chemostratigraphic profiles of χ, TiO_2, FeO_2, Al_2O_3, and Rb in the LT section (Pas et al., 2017) for comparison. Concentration of presented elements as proxy for detrital inputs show moderate correlation with χ variations in the LT section. Difference in the selected detrital input proxies between the studied FF section and the published LT section relates to the analytical capability differences between the XRF (used in this study of the FF) and ICP-MS (used in Pas et al., 2017 for the LT section) used for whole rock geochemistry. **(C)** Box-whisker showing median (horizontal line), range of mean 50 percent of results (shaded boxes) and extreme χ values (caps) on relative proximity transect illustrated by the position ramp-related microfacies from proximal to distal location. **(D)** Box-whisker showing median (horizontal line), range of mean 50 percent of results (shaded boxes) and extreme χ values (caps) on relative proximity transect illustrated by the position of the main facies belts (RS1-RS7) defined for the rimmed shelf model.

and Riquier et al. (2010) (**Figure 6**) are therefore interpreted as carrying a secondary signal related to the Late Variscan Carboniferous remagnetization documented by Zegers et al. (2003). For the FF samples falling near to the MD + SD mixing line of Parry (1982), a primary detrital origin could be assumed. However, as a remagnetization overprint is suggested in most of the FF samples (as discussed above), we assume that in these samples the remagnetization fingerprint is masked by the occurrence of coarser-grained (MD) detrital magnetite. Such a hypothesis was also proposed by Zwing et al. (2005) who studied various lithologies from the NE Rhenohercynian Massif extending from siliciclastic rocks to biohermal and platform carbonate.

The sections under investigation were not studied paleomagnetically and in the exception of what is indicated above, we have no direct evidence to prove the Late Carboniferous – Permian remagnetization components outlined in Zegers et al. (2003). However, the Givetian limestones in this study were collected near Givetian samples studied in Zegers et al. (2003), which are characterized by a remagnetized signature as the C-component described above. This outcome strongly supports our interpretation for the origin of the secondary magnetic grains related to the C-component.

The normalized decay viscosity coefficient S_d is another parameter that allows for estimation of fine-grained superparamagnetic (SP) and viscous grain concentration in samples. The relatively high values for the studied samples (**Tables 2**, **3**) is comparable to the S_d coefficient of SP grains contained in Tiva Canyon tuff reference samples TCO4-11M (Sd = 25 × 10-3, containing SP and SSD; Spassov and Valet,

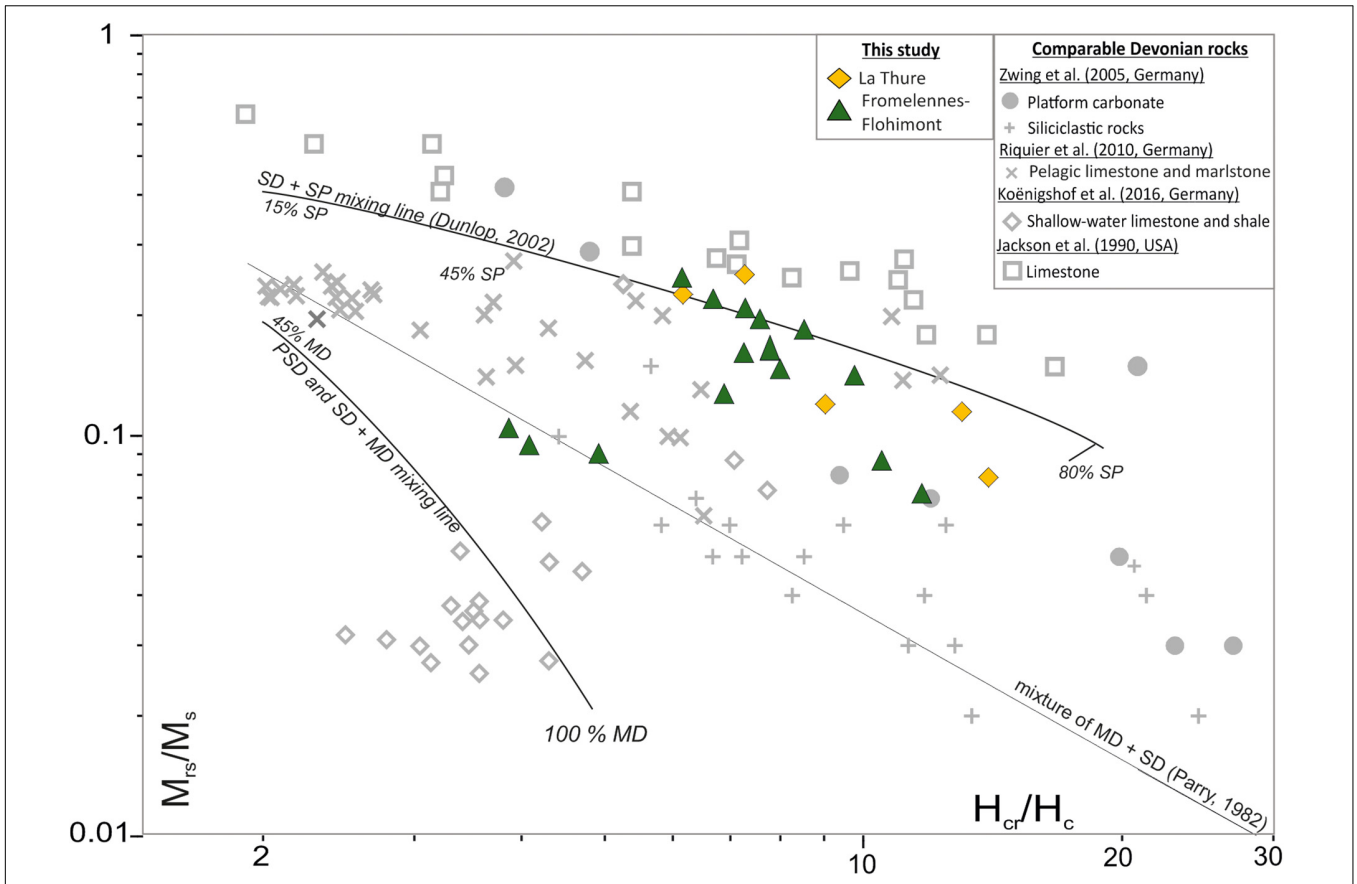

FIGURE 6 | Bi-logarithmic Day plot (Day et al., 1977) for FF and LT datasets compared with reported Paleozoic data for remagnetized siliciclastic and carbonate rocks from Jackson (1990) and Zwing et al. (2005), data from Riquier et al. (2010) and limestone/shale from Königshof et al. (2016). The lines are theoretical SD + SP and PSD and SD + MD curves from Dunlop (2002) that are based on 10 nm SP magnetite grains and coarse-grained magnetite end members, respectively. The dashed line corresponds to a mixture of MD+SD grains according to Parry (1982).

2012). This confirms the occurrence of high viscosity grains such as SP magnetic and hematite minerals in both sections, which is another argument supporting a remagnetization.

Results from Day plot (**Figure 6**), along with normalized magnetic viscosity coefficients point out that the χ signal in the LT and FF sections is triggered by the combined effect of a remagnetization and a primary detrital signature.

Magnetic Susceptibility Versus Detrital and Depositional Proxies

The delivery of detrital materials basinward is considered as the main primary-controlling factor of the χ signal (Vanderaveroet et al., 1999; Ellwood et al., 2000; Tribovillard et al., 2006; Śliwinski et al., 2010; Śliwiński et al., 2012). The ferromagnetic and paramagnetic minerals that have the strongest influence on the χ signal are predominantly derived from continental sources (Crick et al., 1997; Ellwood et al., 2001). Therefore, to interpret the primary character of a χ signal it is worth comparing χ with proxies for detrital input such as TiO_2, Al_2O_3, K_2O, Zr and Rb (Calvert and Pedersen, 2007; Śliwiński et al., 2012) (**Table 4**). To interpret the primary character of the χ signal in the FF section published in De Vleeschouwer et al. (2015), we plot the stratigraphic evolution of the χ signal against the chemostratigraphic profiles of proxy for detrital inputs (**Figure 5A**). This comparison shows similar evolution of both profiles show intermediate *r* value (*r* between 0.62 and 0.70, see also **Table 3**), indicating that the influence of detrital proxies on the χ signal is relatively strong. Pas et al. (2017) showed similar results for the LT section, when comparing the χ profile against detrital input profiles (see Figure 12 in Pas et al., 2017; *r* between 0.51 and 0.61). The relatively good correlation between the χ signal and the chemostratigraphic profiles for both the LT and FF sections indicates that the primary detrital signal is reasonably well preserved in these sections, implying that the primary χ trends could have been retained despite diagenetic or very low grade metamorphic imprints related to burial and remagnetization.

How χ values vary as a function of facies is another technique that provides an insight into the influence of syn-sedimentary parameters (e.g., Mabille et al., 2008b; Da Silva et al., 2009). Da Silva et al. (2013) analyzed a large number of Mid-Upper Belgian Devonian sections and settings (e.g., carbonate ramp, shelf and mud mounds models), and outlined a significant

TABLE 4 | Selected Major and trace element abundances for the Fromelennes-Flohimont section determined by XRF and corresponding χ value from De Vleeschouwer et al. (2015).

Samples	Position	χ	Major elements						Trace elements				
			Al_2O_3	CaO	Fe_2O_3	K_2O	SiO_2	TiO_2	Rb	Sr	Th	U	Zr
	(m)	mł/kg	wt. %	wt. %	wt. %	wt. %	wt. %	wt. %	ppm	ppm	ppm	ppm	ppm
FRO -10	0.32	8.047*E*-10	0.156	96.590	0.309	0.020	1.202	0.044	4.247	321.311	1.683	2.182	5.507
FRO 15	18.23	3.879*E*-09	0.411	98.610	0.648	0.025	0.849	0.062	4.052	277.290	2.502	−0.213	7.736
FRO 18A	20.70	3.395*E*-09	0.749	95.641	0.605	0.112	3.345	0.111	7.079	190.248	2.586	1.921	10.847
FRO 22A	30.51	2.059*E*-09	0.413	97.418	0.685	0.044	1.652	0.073	4.880	205.547	1.616	2.397	12.250
FRO 35B	39.99	4.892*E*-08	1.294	94.763	1.205	0.044	2.697	0.127	9.355	227.890	−0.208	−1.177	15.729
FRO 54	52.19	3.138*E*-07	3.420	78.185	1.218	0.591	12.614	0.235	19.691	236.104	2.840	−0.143	26.279
FRO 61A	58.60	2.673*E*-08	0.522	92.569	0.455	0.078	4.780	0.052	5.640	275.010	4.604	0.747	6.918
FRO 76A	72.52	1.023*E*-07	1.853	88.374	1.008	0.276	6.575	0.123	12.385	247.555	1.626	−1.647	12.722
FRO 88A	80.98	1.035*E*-07	1.822	85.955	1.137	0.338	8.808	0.135	12.761	313.270	2.941	1.172	15.272
FRO 92A	90.27	1.318*E*-07	4.183	77.856	1.528	0.296	13.618	0.272	27.419	326.823	6.865	0.803	23.722
FRO 128	110.10	1.349*E*-07	4.935	69.800	2.367	0.832	16.960	0.320	33.281	287.229	2.424	3.947	40.920
FRO 144	121.01	1.229*E*-07	2.361	84.470	1.781	0.362	8.640	0.152	15.960	405.477	−1.069	1.447	14.495
FRO 151A	129.79	7.506*E*-08	4.026	77.921	1.750	0.492	13.691	0.259	26.415	594.493	1.089	−0.674	19.479
FRO 161A	139.12	−1.354*E*-09	0.795	92.739	0.797	0.088	2.112	0.075	5.616	296.962	−0.480	2.184	7.778
FRO 163B	140.70	5.968*E*-09	0.741	88.026	0.506	0.063	3.107	0.071	6.391	442.167	2.187	0.229	6.031
FRO 173A	149.14	8.678*E*-09	0.665	95.175	0.428	0.047	2.961	0.080	6.050	357.228	−1.826	−1.098	8.482
FRO 180A	166.22	8.238*E*-09	0.242	95.918	0.219	0.020	2.129	0.053	3.457	586.889	−1.290	0.787	1.934
FRO 183B	169.99	−2.271*E*-09	2.094	58.758	1.212	0.417	8.380	0.128	14.724	135.783	4.961	1.176	14.012
FRO 192A	182.86	−2.533*E*-09	0.153	97.768	0.077	0.016	0.867	0.039	2.980	538.076	1.260	1.726	1.665
FRO 195A	193.63	−3.304*E*-09	0.124	97.546	0.041	0.008	0.736	0.032	3.053	440.569	4.538	−0.305	2.339
FRO 199	218.72	−3.304*E*-09	0.901	93.920	0.449	0.075	2.939	0.086	8.129	360.505	5.242	1.653	9.906
FRO 200	222.64	6.912*E*-09	1.004	80.903	0.591	0.139	2.808	0.077	6.721	223.632	1.965	−0.080	10.154
FRO 207C	231.28	9.875*E*-09	0.556	95.542	0.150	0.058	2.748	0.058	4.732	286.864	3.391	−0.154	8.159
FRO 217A	238.91	−2.329*E*-09	0.249	92.947	0.094	0.030	1.385	0.041	3.397	335.239	1.462	1.427	5.362
FRO 222A	245.03	9.352*E*-09	17.755	4.942	7.557	3.648	60.142	0.917	131.980	113.025	12.543	3.266	156.945
FRO 225A	249.79	3.157*E*-10	0.549	90.626	0.320	0.093	3.444	0.065	5.652	226.955	3.694	1.228	8.178
FRO 233A	258.90	7.556*E*-09	0.850	92.770	0.328	0.081	3.705	0.084	6.855	296.343	0.816	3.403	9.996
FRO 246A	269.84	3.863*E*-09	0.854	93.249	0.346	0.031	1.417	0.056	4.684	226.204	−0.167	4.035	7.949
FRO 263A	289.94	2.400*E*-09	0.683	87.552	0.432	0.026	0.985	0.075	5.708	386.930	−0.110	−1.098	7.889
FRO 272B	300.00	5.513*E*-08	2.272	87.271	1.012	0.209	6.941	0.146	13.167	302.134	−0.989	−1.313	13.292
FRO 278C	306.51	4.566*E*-08	1.141	84.937	1.721	0.156	8.757	0.103	7.501	425.737	1.517	3.656	9.520
FRO 280B	312.96	8.152*E*-08	5.214	70.207	2.350	1.030	17.887	0.325	29.347	290.041	4.220	0.513	33.499
FRO 282A	333.89	1.730*E*-08	0.883	56.997	1.030	0.097	6.951	0.076	6.876	123.321	2.686	1.145	12.156
FRO 285A	340.80	5.714*E*-09	0.691	70.755	0.938	0.093	3.356	0.070	6.269	154.306	0.639	−1.002	10.867
FRO 292B	351.51	5.680*E*-10	0.313	93.915	0.211	0.025	3.446	0.056	3.864	333.897	−0.984	−2.120	7.720
FRO 304C	361.44	2.693*E*-08	2.882	76.223	0.897	0.276	9.312	0.186	18.817	210.223	2.726	1.136	17.941
FRO 317	370.24	1.432*E*-08	1.286	92.927	0.619	0.125	4.447	0.123	9.338	303.078	2.802	1.597	12.493
FRO 353	380.48	1.610*E*-08	0.802	94.710	0.253	0.103	3.760	0.088	5.901	241.936	−2.320	−0.833	12.167
FRO 354B	394.12	1.458*E*-08	0.431	96.621	0.375	0.037	2.152	0.058	5.232	265.140	1.778	1.616	7.995
FRO 362A	440.73	7.366*E*-08	1.698	88.726	0.842	0.223	7.935	0.149	12.344	322.654	5.943	0.789	13.399
FRO 368A	447.90	1.210*E*-07	0.419	96.529	0.354	0.043	2.023	0.063	4.621	272.730	3.880	3.175	7.899
FRO 375	450.74	1.095*E*-07	1.673	87.261	1.274	0.191	6.922	0.138	10.958	340.317	2.883	2.578	12.987
FRO 400	461.18	6.602*E*-08	3.394	80.233	1.993	0.440	11.735	0.237	20.078	328.726	0.176	0.901	26.020

difference in χ behavior for each carbonate platform model. In this study, a homoclinal ramp and a rimmed shelf models have been investigated and they both show significant variation of the average χ values with the depositional settings (**Figures 5C,D**).

In the ramp model, χ values decrease toward- the shallowest facies. The χ general behavior coincides with previously published models (Mabille and Boulvain, 2007; Mabille et al., 2008a) for the Devonian ramps in south-western Belgium, corresponding to an increase of the average χ values along a proximal – distal profile. The high value for the RP-FF1 facies is explained by the higher detrital content observed in this facies.

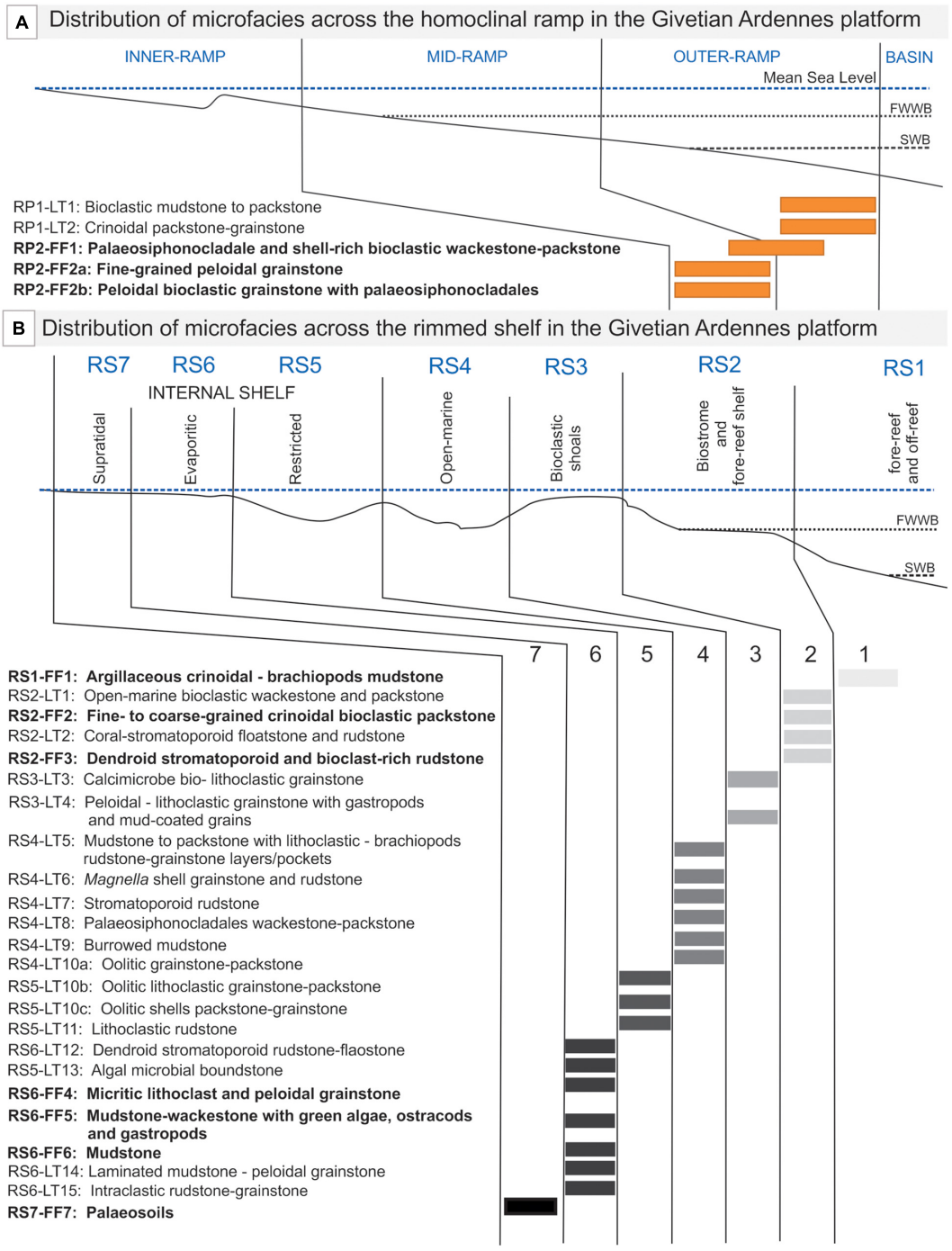

FIGURE 7 | Distribution and name of microfacies across the different sedimentological models based on the combination of this study and published results by Pas et al. (2017). Microfacies in bold are only observed in the FF section. **(A)** Distribution of microfacies along the homoclinal ramp. **(B)** Distribution of microfacies along the rimmed shelf profile. The fair-weather wave base (FWWB) and storm wave base (SWB) are presented for each model.

In the rimmed shelf model, the general decrease of the average χ signal from the off-reef to biostromal belts that characterize the external belt is similar to observations reported in Da Silva et al. (2009) for similar external shelf setting in Belgian Frasnian successions. This decrease is explained by an increase of both carbonate productivity and hydro-energy, which either trigger a dilution of the χ carrying particles and/or prevent them to settle down. The decrease of the average χ value toward the oolitic shoal is assumed to be driven by the high hydro-energy characterizing shoals in shelf interior, preventing

χ carrying minerals from settling down. The higher average χ value for the RS7 is explained by the vicinity of this belt with the emerged landmass and the potential influence of paleosoil development (i.e., ferro-siderite precipitation) and therefore a direct and higher influence of riverine and eolian input. The syn-sedimentary processes and carbonate productivity are commonly involved to explain model of χ variations along a distal proximal transect (Da Silva et al., 2013). The χ varying behavior in the internal and external shelf settings is also clearly visible on the χ curves constructed for the FF section (**Figure 2**), where each deepening upward in microfacies is characterized by increasing χ values. Variation of χ as a function of depositional setting also strongly advocates for preservation of the depositionally-induced trends in the χ signal despite the remagnetization affecting the area. Another example supporting the preservation of the χ signal is the observation of an astronomically-forced imprint in both sections (De Vleeschouwer et al., 2015). These astronomical imprints were used to build an astronomically-tuned time scale for the Givetian Stage.

In summary, the comparison of the χ signal with detrital and depositional proxies has revealed that the recorded χ in the LT and FF sections is still carrying a well-preserved primary signal despite the remagnetized fingerprint established through the analysis of hysteresis parameters. The χ signal in FF and LT sections thus corresponds to the superposition of a primary depositional χ signal overprinted by the χ carried by the secondary diagenetic magnetic minerals likely related to the C-component of Zegers et al.'s (2003) remagnetization event. The preservation of the χ signal in LT and FF sections indicates that the C-component with formation of fine-grained ferromagnetic minerals did not strongly affect or distort the primary χ trends. The C-component is interpreted as formed during the smectite to illite transition, a process that does not require external fluids in the system to be important (Zegers et al., 2003). As suggested by Da Silva et al. (2012) for Devonian carbonate in Belgium, we propose that during the formation of the secondary diagenetic fine-grained magnetic fingerprint in LT and FF sediments the system remained in situ or isochemical, so the authigenic-related susceptibility minerals did not strongly affect the primary signal and even enhanced it.

Early-Late Givetian Sea-Level Fluctuations and Carbonate Platform Development

When we compare the microfacies and magnetic susceptibility evolution for the Givetian sequences in Belgium and France, parallel trends occur in time-equivalent deposits (**Figure 8**) although both areas are separated by nearly a 100 km. The similarities in χ and microfacies patterns agree with published data (Boulvain and Préat, 1986; Préat et al., 1987; Préat and Boulvain, 1988; Bultynck et al., 1991; Boulvain et al., 1995; Préat, 2006; Préat and Bultynck, 2006; Boulvain et al., 2009; Maillet et al., 2011; Maillet et al., 2013) and allowed us to correlate a series of sedimentological events between the southern and the western margin of the Ardennes Givetian platform. In addition, the correlation of shallowing and deepening trends confirmed the occurrence of barrier-reefs through the Middle-Late Givetian within the intermediate buried part of the platform and completed the stratigraphic and paleogeographic model proposed in Figure 23 in Boulvain et al. (2009) (**Figure 9**). It is important to note that labels referred in Pas et al. (2017) that defined the main sedimentary interval and MSU (e.g., I to V, MSUI-V) had to be modified to create a comprehensive correlation chart included both stratigraphic records. Interval I (MSU-I) in Pas et al. (2017) became interval III (MSU-II) in this study and the same modification applies for all the sedimentary intervals.

Figure 8 shows the correlation between the main depositional changes (intervals I to VII) and the associated shallowing – deepening trends interpreted for the Givetian in the Ardennes.

The first depositional interval (I) within the Lower Givetian was deposited within the storm wave base (SWB) on a homoclinal ramp. Deposition on a ramp is unusual for this time in the southern margin of the Ardennes area. Indeed, classical sections (i.e., Glageon, Resteigne, Baileux; see location on **Figure 1B**) expose meter thick accumulations of reefal carbonate rich in stromatoporoids, corals, and algae, corresponding to the so-called "premier biostrome" (Préat et al., 1984). This "premier biostrome" is interpreted as the result of a reef that extends over 150 km, from Glageon in the west to Ferrieres in the east (Boulvain et al., 2009). The absence of reef-building organisms within the FF section suggests local changes in the environmental conditions, hampering reef-related deposition and creating a discontinuity in the reef. Time-equivalent shallow-water carbonate deposits located in the "Marenne Est" quarry section (Mabille et al., 2008a) (south-eastern part of the DS; located in **Figure 1B**) expose limestone with high concentration of sandy and silt materials. According to De Wilde (2005), the siliciclastic materials in the limestone are related to the Caledonian Stavelot Massif, which prompted increasing detrital inputs seaward, and thus inhibited the development of shallow-water communities. Another hypothesis explaining the absence of the "premier biostrome" in Fromelennes-Flohimont depositional area is that it was located in a fore-reef setting, south of the barrier-reef that had formed the "premier biostrome" (see Figure 16 in Boulvain et al., 2009).

The transition from the first (I) to the second (II) interval is characterized by an important change in microfacies, corresponding to the first occurrence of sediments interpreted as deposited in restricted lagoonal and supratidal settings (RS6 and RS7). This abrupt change in the sedimentary record is interpreted as a major sea-level fall, likely corresponding to the upper part of cycle If of Johnson et al. (1985). This event triggered basinward drift of adjacent reef-building communities, enabling the formation of a continuous "barrier" or paleo-high structures within the early Givetian. Indeed, we assume that during the sea-level fall reef-building communities, observed in interval (I) in adjacent areas, migrated basinward to accommodate the drop in the sea-level and rebuilt new reefal structures. As stated in Boulvain et al. (2009), the development of a reefal structure basinward (e.g., southward) is likely responsible for the lagoonal deposits occurring in the interval (II). Shoals structure could also be responsible for the development of landward lagoonal

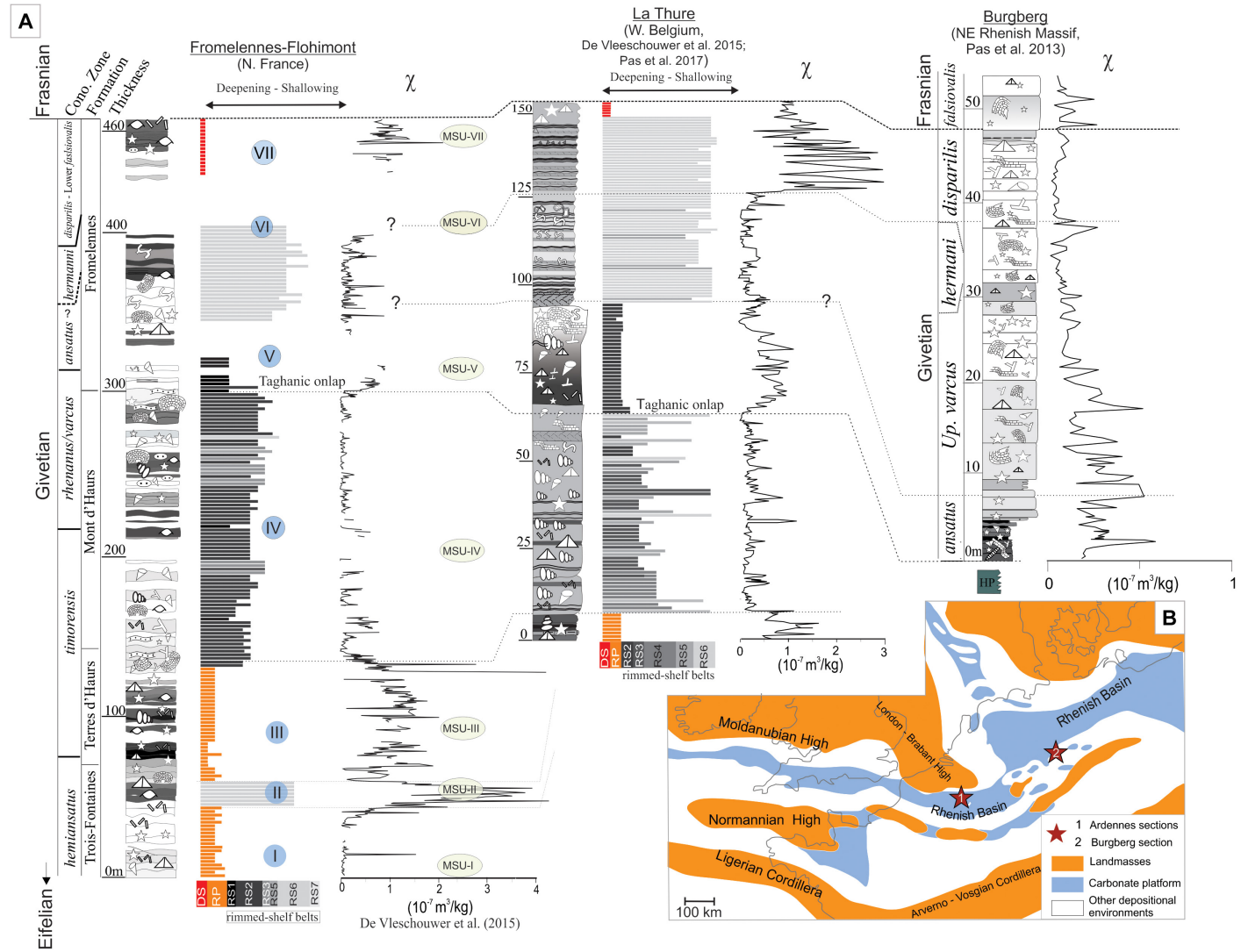

FIGURE 8 | Comparison and correlation of vertical microfacies evolution and associated magnetic susceptibility curves for the studied sections (Pas et al., 2013; De Vleeschouwer et al., 2015; Pas et al., 2017). Note that sedimentary intervals and MSU (e.g., I to V, MSUI-V) labels, as referred in Pas et al. (2017), had to be modified in order to build this correlation chart. For instance, interval I (MSU-I) in Pas et al. (2017) became interval III (MSU-II) in this study and the same modification applies for all defined sedimentary intervals. **(A)** Correlation chart showing the Ardennes and the Burgberg sections. Note that the scale of the χ values for the Burgberg section is not similar to those of the FF and LT sections in order to overcome the very low χ values in this section. **(B)** Middle Devonian paleogeographic setting showing the large carbonate platform developed in northern Europe and the relative location of the three sections, modified after Ziegler (1982) and McKerrow and Scotese (1990).

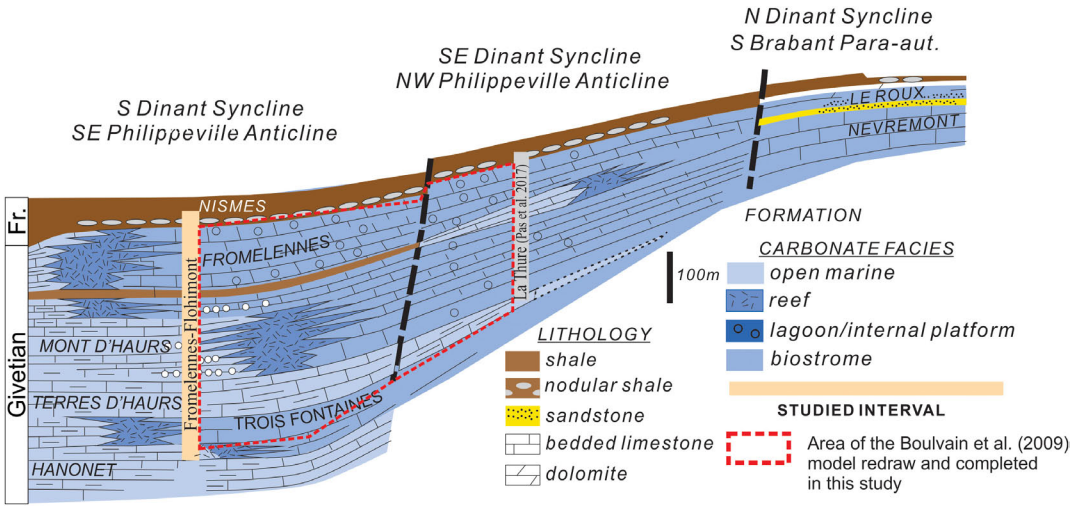

FIGURE 9 | Redraw and completed (red dotted line area) lithostratigrahic and paleogeographic framework for the Givetian in Belgium and France from Boulvain et al. (2009) showing the location of the new data collected in this study.

environments as they could produce wave attenuation. Assuming the thickness of carbonate (several tens of meters) characterizing this specific environment in the FF section, and in other locations in the south of the Ardennes (i.e., Resteigne, Marenne, Glageon), the reefal or paleo-high like shoal structures separating internal and external shelf should have been continuous and stable for a relatively long period of time. Given the lack of outcrops, the "barrier" or paleo-high controlling the lagoon development has never been observed. Although, we might assume that this "barrier" or paleo-high was located a few kilometers south of the Dinant Syncline southern margin. The E-W lateral extension of the "barrier" controlling the deposition of lagoonal sedimentation in the upper part of the Trois-Fontaine Fm. is illustrated in Figure 16 in Boulvain et al. (2009).

The transition to the third (III) Interval (e.g., Trois-Fontaine Fm. to Terre d'Haurs Fm., transition *hemiansatus* to *timorensis* conodont Zones), records a deepening trend and the return to a ramp model (RP). The homogenous deposits occurring throughout this third interval (III) are assumed to reflect a mid- to distal ramp environment influenced by storms, showing the local development of patch-reefs seen in outcrop. The similar evolution of microfacies and magnetic susceptibility in the uppermost part of the third interval (III) in FF section and the lowermost part of the LT section allowed us to match both sequences.

A principal turning point in facies and magnetic susceptibility occurs at the transition to the fourth (IV) interval, corresponding to a major sedimentological shift in the Ardennes. This transition from Interval (III) to (IV) is characterized in the south (Fromelennes-Flohimont), by a transition from mid- and outer-ramp settings (RP2-FF1) to biostromal and fore-reef shelf facies (RS2, open-marine deposits rich in reefal debris) with meters thick accumulation of reefal limestone while in the west (La Thure), the coeval transition consists of a change from mid-ramp (RP1-LT2) to well-bedded internal shelf deposits (RS3, RS4 and RS5). Such a contrast in facies must involve an important difference in paleo-depth and likely the existence of a reefal structures between both localities, supplying reefal debris basinward (e.g., biostromal and fore-reef shelf facies, RS2, see **Figure 2B** (pictures e-d)) and allowing an internal-shelf sedimentation landward (RS2, RS3, and RS5). Paleo-high structure such as shoals have not been proposed here because biostromal and fore-reef shelf facies observed in FF could not be derived from it. As a result of the Variscan folding in the area, this structure does not outcrop but must be located somewhere in the subsurface near the Dinant Syncline axis.

The transition to the fifth (V) interval is characterized by a major rise in sea-level, leading to the accumulation of off-reef and fore-reef deposits (RS1-FF1) in the FF section and biostromal and fore-reef facies (RS2-LT2-3) in the LT section. As discussed in Pas et al. (2017), this sea-level increase was associated with the so-called Taghanic Onlap (Johnson, 1970) (event IIa in Johnson et al., 1985) which led to major extinctions within a number of groups in both the marine and terrestrial realm (Aboussalam and Becker, 2011; Marshall et al., 2011).

Shortly after this major sea-level rise, both sections record a shallowing-upward shift defining the intervals (V) and (VI) transition. This sea-level drop corresponds to a similar shift of facies from fore-reef (RS1 and RS2) to internal shelf (RS5, RS4) in both sections. The causes of this particular transition to very shallow settings is explained in Pas et al. (2017).

The transition to Interval (VII) is marked by the drowning of the lagoonal deposits (e.g., RP-LT1) in both areas. Densely-packed brachiopod-bivalves shell levels forming these drowning deposits are several tens of meters thick in FF but only several meters thick in the LT section (see Figure 3 in Pas et al., 2017). As summarized in Pas et al. (2017), the drowning of the Ardennes Givetian platform could be triggered by the combination of the

global late Devonian sea-level rise, the increasing terrestrial influx and the active syn-sedimentary faulting.

Reliability of χ Records for Long-Distance Correlation of Million-Year Trends in Devonian Carbonate: Implication for the Devonian Stratigraphy

Belgian and France long-term χ curves and sedimentological patterns can be easily correlated (**Figure 8**) despite (1) the Late Variscan remagnetization event recognized by Zegers et al. (2003), (2) the hundred kilometers separating both localities and (3) the different depositional background. In the Ardennes, the similarity in the χ evolution model through a proximal – distal transect ranging from south to north can be partly attributed to a similar response of the environment to external environmental forcing (e.g., relative sea-level variations and siliciclastic influx change). On an intra-basinal/regional scale, the magnetic susceptibility tool has already been successfully used for the correlation of sections (Whalen and Day, 2010; Da Silva and Boulvain, 2012). An important question that arises from these results is if the million year scale correlations of χ records are reliable on a larger inter-regional scale. The χ signal as a tool for inter-regional correlation of stratigraphic records has already been assessed by different authors (e.g.,Ellwood et al., 1999; Ellwood et al., 2001, 2008; Boulvain et al., 2010). Their results suggested the high potential of χ signal for global correlation in ancient sedimentary sequences. Whereas promising, these results lack the geochemical and magnetic basis that are now regarded as crucial prior to any interpretation or use of the χ signal (e.g., Da Silva et al., 2015).

Using available conodont data, marker beds (e.g., Taghanic onlap) and the sedimentological patterns, we have developed a correlation chart (**Figure 8A**) comparing Givetian datasets from the Ardennes with the time-equivalent data from the Burgberg section in Germany (Pas et al., 2013). These sites bordered the Old Red continent in the north (see **Figure 8B**) and were located at the same paleolatitude, near the equator (see Figure 7 in Eckelmann et al., 2014). At present, the Burgberg area is situated ∼280 km away from the FF section and ∼340 km from the LT section (see **Figure 1A**). Assuming a Variscan compression with a NE-SW direction and the fact that the Burgberg section is located in the northeast of the Ardennes, we made the assumption that the distance between LT and Burgberg, and FF and Burgberg should not be that much different than today. Finally, the Burgberg section corresponds to a fore-reef related deposition providing a good biostratigraphic constraint. In addition, the results from the magnetic susceptibility, the sedimentological observations, the geochemistry and magnetic hysteresis measurements indicated a well-preserved χ signal (Pas et al., 2013; Pas, 2015).

Published χ records from time-equivalent sections in United States, Czech Republic, and Morocco (Ellwood et al., 1999, 2011; Hladil et al., 2006) have not been used for comparison in the following discussion because the preservation of χ signal was not established through geochemistry or hysteresis measurements. Indeed, an important aspect of this assessment is to compare datasets which show a preserved χ signal.

Visual evaluation of the long-term χ trends recorded from the Ardennes and the Burgberg sections highlight a lack of correlation, e.g., the χ signal increase just prior the Givetian-Frasnian boundary in Belgium and France but a reverse trend is observed in Germany. Another well-visible example occurs in the *disparilis* – Lower *falsiovalis* zone where χ signal shows high and strongly fluctuating values in Belgium but very stable low values in Germany.

The first element that might have influenced the lack of correlation between the Ardennes and the Burgberg sections is the sampling resolution of our χ records, as well as the resolution of the conodont zonation. Indeed, in thick shallow-water successions such as the FF and LT sections, the biostratigraphic constraint is relatively weak compared to the Burgberg section, which is well-constrained by conodonts. Moreover the average sampling interval for all the sections is the same, whereas the sections have different sedimentation rates. For instance, for the Givetian interval in the relatively condensed Burgberg section, we collected around 200 samples while in the FF section for slightly shorter time-scale we count nearly 600 samples. This difference in the relative sampling interval has a direct impact on the χ signal resolution and may reduce the visibility of the expected long-term trends but it should not modify the main trends observed throughout the sections.

Another major element that should be considered in understanding the different pattern in χ trends between the LT, FF and Burgberg sections is the impact of the various depositional parameters on the χ signal recorded over short- and long-time scales in marine sedimentary rocks. They are depositional variations that arise due to factors inherent to the sedimentary system (i.e., autogenic; wave agitation, lateral migration of sediment body, tidal current, channel migration, paleosoil development) and to externally controlled forcing such as climate, tectonic, source rocks and sea-level/accommodation (i.e., allogenic).

Allogenic parameters are acting over both, long- and short-time scales and are the primary causes of changes in detrital supply basinward, which is itself the strongest χ primary-controlling factor (e.g., Crick et al., 1997; Vanderaveroet et al., 1999; Ellwood et al., 2000; Śliwiński et al., 2012). Autogenic processes play a role over small spatial and temporal scales and they have the potential to remove all evidence from sedimentary archives that originated from low-magnitude or high-frequency climate or tectonic changes (Jerolmack and Paola, 2010). Shallow carbonate platforms such as the one under investigation here commonly exhibit a pronounced lateral heterogeneity where coral reefs, oolitic or bioclastic shoals, lagoons, and tidal flats are juxtaposed (facies mosaic; Wright and Burgess, 2005) and therefore such context is particularly influenced by autogenic processes.

For each section investigated in this study we explored the link between average χ signal and syn-sedimentary parameters such as wave agitation, carbonate productivity/sedimentation rate and the vicinity to landmasses through the qualitative

comparison with facies belts/microfacies (see section Magnetic Susceptibility versus Detrital and Depositional Proxies and **Figures 5C,D**). Across different platform profiles, the impact of syn-sedimentary processes were proven to exert a significant role in the χ signature (e.g., Bábek et al., 2007; Mabille et al., 2008b; Da Silva et al., 2009). Concerning the Givetian sections in Ardennes two models of magnetic susceptibility evolution were considered (e.g., homoclinal ramp and rimmed shelf; **Figures 5C,D**). For the Burgberg section, deposited in a fore-reef setting, the model shows χ values decreasing through shallowing upward facies (Pas, 2015; p. 57), which is hence a completely different χ evolutionary model than those highlighted in Ardennes sections. For instance, weak current and wave agitation (e.g., off-reef setting) will allow magnetic particles to settle down and concentrate in the sediment, while substantial wave agitation (e.g., barrier or shoals settings) will prevent the settlement of small particles carrying the magnetic susceptibility (see Da Silva et al., 2009 for an overview of the influence of local environmental parameters on the magnetic susceptibility). In other words, we suggest that autogenic processes, which operate at small spatial and temporal scales and modulate the externally-forced χ signal have a strong influence over the final magnetic susceptibility signal. This influence varies from one depositional locality to another due to the various sedimentary processes, and can result in the absence of correlation in the long-term χ signal. On a regional scale and for a shorter time-interval (e.g., three to four conodont Zones), Da Silva et al. (2009) observed a similar pattern when trying to correlate time-equivalent χ curves obtained in the distal and the intermediate part of the Belgian Frasnian platform; distal and intermediate (internal) part are ruled by different χ evolutionary models.

Long-distance χ based correlations in remagnetized settings must be considered carefully because the situation is more complex, and time-equivalent long-term χ curves from other paleogeographic settings and platforms are still highly necessary. Magnetic susceptibility-based correlation from modern deep-sea and other deep marine repositories (Ridgwell, 2002; Irino and Tada, 2003; Larrasoaña et al., 2008; Weber et al., 2012) showed spectacular results which are recommended for performing long-distance correlation. Deep-marine records are much less affected by syn-sedimentary processes and have proven to carry a more complete signal. This because they are less subject to severe alteration by chemical and physical processes as well as erosion/redeposition, as observed in continental or shallow-marine deposits.

CONCLUSION

The Fromelennes-Flohimont section is composed of a large number of microfacies organized in three sedimentological models, a rimmed shelf, a homoclinal ramp and a drowning shelf. The early Givetian homoclinal ramp evolved to a rimmed shelf throughout middle- to late-Givetian, and by the latest Givetian the platform drowned, and was subsequently capped by Frasnian shales.

Hysteresis measurements on our sample sets indicate a χ signal predominantly controlled by ferromagnetic (s.l.) minerals although paramagnetic and diamagnetic minerals such as clay, pyrite and calcite, also contributed to χ. Low-coercivity ferromagnetic component ($H_{cr} < 60$ mT), such as magnetite have the strongest influence on χ variations within the sampled sections. Even though the high-coercivity minerals, such as hematite, are clearly indicated in both sections, their influence on the χ is weak. The analysis of H_{cr}/H_c and M_{rs}/M_s ratios on samples with an $IRM_{300}/IRM_{500} < 5\%$ indicates a χ signal distinctly influenced by fine-grained SP magnetic particles, which are also shown through the analysis of S_d values. These SP grains have probably been formed during the Carboniferous remagnetization in the Ardennes. Nevertheless, the comparison of χ with facies evolution and terrestrial proxies clearly shows that the χ in both datasets is carrying primary depositional signal. The χ signal in FF and LT sections result from a primary depositional χ signal overprinted by the susceptibility carried by the secondary diagenetic magnetic minerals. The secondary diagenetic overprint did not obliterated the primary signal, hence, it can potentially be used as for correlation and paleoenvironmental interpretation.

Comparison of long-time scale sedimentological and χ profiles of time-equivalent sequences from Belgium and France emphasized similarities despite the different sedimentological background, the remagnetization affecting the region and the relatively long-distance separating the sections. This regional correlation provided new information allowing us to recognize important sedimentary changes during the Givetian in the Ardennes, some of them correlated with major Devonian T-R events (e.g., T-R IIa or Taghanic Event).

The correlation of depositional trends between the southern and the western margin of the platform confirmed the occurrence of barrier-reefs through the Middle-Late Givetian within the intermediate buried part of the platform and to complete the previously published stratigraphic and paleogeographic model.

The Belgian/French sections were compared with the Burgberg section in Germany using the magnetic susceptibility signal, but the correlations are not successful.

Our analyses show that similar facies development along a carbonate platform profile, in response to changes caused by sea-level fluctuations, might result in a similar model of χ profiles that can be used for correlation. We also suggested that the different modulation of the long-term changes in the allogenic χ signal by autogenic processes could be responsible for the absence of correlation between the long-term χ curves in Ardennes and the Rheinisches Schiefergebirge.

DATA AVAILABILITY STATEMENT

Publicly available datasets were analyzed in this study. This data can be found here: https://doi.org/10.1594/PANGAEA.855764. All additional raw data supporting the conclusion of this article will be made available by the author, without due reservation, to any qualified researcher.

AUTHOR CONTRIBUTIONS

DP conceived the study, carried out the research, and wrote the manuscript. A-CD and FB contributed to the interpretation and discussion. GP collected the rock samples. SS provided access to the hysteresis measurement device and helped at interpreting the dataset.

ACKNOWLEDGMENTS

This work was partly written during a post-doctoral fellowship awarded by a BeIPD Marie-Curie COFUND Program (University of Liège, Belgium) assigned to DP (Grant N° 600405). A-CD and DP acknowledge the Netherlands Organization for Scientific Research (NWO, grant WE.210012.1). We are very grateful to Sean Karoly of George Mason University (United States) for his thorough review of the English. We would like to thank the editor KK and the two reviewers for their constructive comments that helps at improving the quality of this manuscript. We would also like to express our thanks to Michael Whalen, John. J. G. Reijmer, Peir Pufahl, Erika Kido, and Marco Maffione who contributed to improve previous versions of this manuscript. This paper is a contribution of the IGCP-652 project "Reading geologic time in Paleozoic sedimentary rocks: the need for an integrated stratigraphy."

SUPPLEMENTARY MATERIAL

The Supplementary Material for this article can be found online at: https://www.frontiersin.org/articles/10.3389/feart.2019.00341/full#supplementary-material

REFERENCES

Aboussalam, Z. S., and Becker, R. T. (2011). The global Taghanic Biocrisis (Givetian) in the eastern Anti-Atlas, Morocco. *Palaeogeogr. Palaeoclimatol. Palaeoecol.* 304, 136–164. doi: 10.1016/j.palaeo.2010.10.015

Bábek, O., Pøikryl, T., and Hladil, J. (2007). Progressive drowning of carbonate platform in the Moravo-Silesian Basin (Czech Republic) before the Frasnian/Famennian event: facies, compositional variations and gamma-ray spectrometry. *Facies* 53, 293–316. doi: 10.1007/s10347-006-0095-8

Belanger, I., Delaby, S., Delcambre, B., Ghysel, P., Hennebert, M., Laloux, M., et al. (2012). Redéfinition des unités structurales du front varisque utilisées dans le cadre de la nouvelle Carte géologique de Wallonie (Belgique). *Geol. Belg.* 15, 169–175.

Borradaile, G. J., Chow, N., and Werner, T. (1993). Magnetic hysteresis of limestones: facies control? *Phys. Earth Planet. Inter.* 76, 241–252. doi: 10.1016/0031-9201(93)90016-3

Boulvain, F., Coen-Aubert, M., Mansy, J. L., Proust, J. N., and Tourneur, F. (1995). Le Givetien en Avesnois (Nord de la France): paléoenvironnements et implications paléogéographiques. *Bull. de la Société belge de Géol.* 103, 171–203.

Boulvain, F., Da Silva, A. C., Mabille, C., Hladil, J., Gersl, M., Koptikova, L., et al. (2010). Magnetic susceptibility correlation of km-thick Eifelian-Frasnian sections (Ardennes and Moravia). *Geol. Belg.* 13, 309–318.

Boulvain, F., Mabille, C., Poulain, G., and Da Silva, A. C. (2009). Towards a palaeogeographical and sequential framework for the givetian of Belgium. *Geol. Belg.* 12, 161–178.

Boulvain, F., and Préat, A. (1986). Les calcaires laminaires du Givétien Supérieur du bord sud du Bassin de Dinant (Belgique, France): témoins d'une évolution paléoclimatique. *Annales de la Societé Géologique de Belgique* 109, 609–619.

Bultynck, P. (1974). Conodontes de la formation de Fromelennes du Givetien de l'Ardenne franco-belge. *Bulletin de l'Institut Royal des Sciences Naturelles de Belgique Sciences de la Terre* 50, 1–30.

Bultynck, P. (1987). Pelagic and neritic conodont successions from the Givetian of pre-Sahara Morocco and the Ardennes. *Bulletin de l'Institut Royal des Sciences Naturelles de Belgique Sciences de la Terre* 57, 149–181.

Bultynck, P., Coen-Aubert, M., Dejonghe, L., Godefroid, J., Hance, L., Lacroix, D., et al. (1991). Les formations du Dévonien moyen de la Belgique. *Mémoires pour servir à l'explication des cartes géologiques et minières de la Belgique* 30, 1–105.

Bultynck, P., and Dejonghe, L. (2001). "Devonian lithostratigraphic units (Belgium)," in *Guide to a Revised Lithostratigraphic Scale of Belgium*, eds P. Bultynck, and L. Dejonghe, (Brussels: Geologica Belgica), 39–69.

Burov, B., Nurgaliev, D. K., and Jasonov, P. G. (1986). *Paleomagnetic Analysis Kazan*. Kazan: University Press.

Calvert, S. E., and Pedersen, T. F. (2007). "Chapter Fourteen Elemental Proxies for Palaeoclimatic and Palaeoceanographic Variability in Marine Sediments: Interpretation and Application," in *Developments in Marine Geology*, eds H. M. Claude, and D. V. Anne, (Amsterdam: Elsevier), 567–644. doi: 10.1016/s1572-5480(07)01019-6

Chadimova, L., Vacek, F., Sobien, K., Slavik, L., and Hladil, J. (2015). Petrophysical record of the Late Silurian shallow-water carbonate facies across the Lau Event (Prague Synform, Czech Republic) and dynamic time warping alignment of the magnetic susceptibility logs. *Geol. Soc. Spec. Publ.* 414, 133–155. doi: 10.1144/SP414.14

Channell, J. E. T., and McCabe, C. (1994). Comparison of magnetic hysteresis parameters of unremagnetized and remagnetized limestones. *J. Geophys. Res.* 99, 4613–4623. doi: 10.1029/93jb02578

Crick, R. E., Ellwood, B. B., El Hassani, A., Feist, R., and Hladil, J. (1997). Magnetosusceptibility event and cyclostratigraphy (MSEC) of Eifelian-Givetian GSSP and associated boundary sequences in North Africa and Europe. *Episodes* 20, 167–175. doi: 10.18814/epiiugs/1997/v20i3/004

Da Silva, A. C., and Boulvain, F. (2012). Analysis of the Devonian (Frasnian) platform from Belgium: a multi-faceted approach for basin evolution reconstruction. *Basin Res.* 24, 338–356. doi: 10.1111/j.1365-2117.2011.00526.x

Da Silva, A. C., De Vleeschouwer, D., Boulvain, F., Claeys, P., Fagel, N., Humblet, M., et al. (2013). Magnetic susceptibility as a high-resolution correlation tool and as a climatic proxy in Paleozoic rocks - Merits and pitfalls: examples from the Devonian in Belgium. *Mar. Pet. Geol.* 46, 173–189. doi: 10.1016/j.marpetgeo.2013.06.012

Da Silva, A. C., Dekkers, M. J., Mabille, C., and Boulvain, F. (2012). Magnetic susceptibility and its relationship with paleoenvironments, diagenesis and remagnetization: examples from the Devonian carbonates of Belgium. *Stud. Geophys. Geod.* 56, 677–704. doi: 10.1007/s11200-011-9005-9

Da Silva, A. C., Mabille, C., and Boulvain, F. (2009). Influence of sedimentary setting on the use of magnetic susceptibility: examples from the Devonian of Belgium. *Sedimentology* 56, 1292–1306. doi: 10.1111/j.1365-3091.2008.01034.x

Da Silva, A. C., Whalen, M. T., Hladil, J., Chadimova, L., Chen, D., Spassov, S., et al. (2015). Magnetic susceptibility application: a window onto ancient environments and climatic variations. *Geol. Soc. Lond. Spec. Pub.* 414:283. doi: 10.1144/sp414.12

Day, R., Fuller, M., and Schmidt, V. A. (1977). Hysteresis properties of titanomagnetites: grain-size and compositional dependence. *Phys. Earth Planet. Inter.* 13, 260–267. doi: 10.1016/0031-9201(77)90108-X

De Vleeschouwer, D., Boulvain, F., Da Silva, A.-C., Pas, D., Labaye, C., and Claeys, P. (2015). The astronomical calibration of the Givetian (Middle Devonian) timescale (Dinant Synclinorium, Belgium). *Geol. Soc. Lond. Spec. Pub.* 414, 245–256. doi: 10.1144/sp414.3

De Wilde, C. (2005). *Sédimentologie de la Formation de Trois-Fontaines à Marenne*. Msc thesis, Université de Liège, Liège

Devleeschouwer, X., Petitclerc, E., Spassov, S., and Préat, A. (2010). The Givetian-Frasnian boundary at nismes parastratotype (Belgium): the magnetic susceptibility signal controlled by ferromagnetic minerals. *Geol. Belg.* 13, 351–366.

Dittmar, D., Meyer, W., Oncken, O., Schievenbusch, T., and Von Winterfeld, C. (1994). Strain partitioning across a fold and thrust belt, the Rhenish Massif, Mid)European Variscides. *J. Struct. Geol.* 16, 1335–1352. doi: 10.1016/0191-8141(94)90001-9

Dunlop, D. J. (2002). Theory and application of the Day plot (Mrs/Ms versus Hcr/Hc) 1. Theoretical curves and tests using titanomagnetite data. *J. Geophys. Res. Atmos.* 107, 260–267.

Eckelmann, K., Nesbor, H. D., Königshof, P., Linnemann, U., Hofmann, M., Lange, J. M., et al. (2014). Plate interactions of Laurussia and Gondwana during the formation of Pangaea - Constraints from U-Pb LA-SF-ICP-MS detrital zircon ages of Devonian and Early Carboniferous siliciclastics of the Rhenohercynian zone, Central European Variscides. *Gondwana Res.* 25, 1484–1500. doi: 10.1016/j.gr.2013.05.018

Ellwood, B. B., Crick, R. E., and El Hassani, A. (1999). Magnetosusceptibility event and cyclostratigraphy (MSEC) method used in geological correlation of Devonian rocks from Anti-Atlas Morocco. *Am. Assoc. Pet. Geol. Bull.* 83, 1119–1134.

Ellwood, B. B., Crick, R. E., Garcia-Alcalde Fernandez, J. L., Soto, F. M., Truyols-Massoni, M., El Hassani, A., et al. (2001). Global correlation using magnetic susceptibility data from Lower Devonian rocks. *Geology* 29, 583–586.

Ellwood, B. B., Crick, R. E., Hassani, A. E., Benoist, S. L., and Young, R. H. (2000). Magnetosusceptibility event and cyclostratigraphy method applied to marine rocks: detrital input versus carbonate productivity. *Geology* 28, 1135–1138. doi: 10.1130/0091-7613200028<1135:meacma<2.0.co;2

Ellwood, B. B., Tomkin, J. H., El Hassani, A., Bultynck, P., Brett, C. E., Schindler, E., et al. (2011). A climate-driven model and development of a floating point time scale for the entire Middle Devonian Givetian Stage: a test using magnetostratigraphy susceptibility as a climate proxy. *Palaeogeogr. Palaeoclimatol. Palaeoecol.* 304, 85–95. doi: 10.1016/j.palaeo.2010.10.014

Ellwood, B. B., Tomkin, J. H., Ratcliffe, K. T., Wright, M., and Kafafy, A. M. (2008). High-resolution magnetic susceptibility and geochemistry for the Cenomanian/Turonian boundary GSSP with correlation to time equivalent core. *Palaeogeogr. Palaeoclimatol. Palaeoecol.* 261, 105–126. doi: 10.1016/j.palaeo.2008.01.005

Elmore, R. D., London, D., Bagley, D., Fruit, D., and Gao, G. (1993). Remagnetization by basinal fluids: testing the hypothesis in the Viola Limestone, southern Oklahoma. *J. Geophys. Res.* 98, 6237–6254. doi: 10.1029/92jb02577

Gouwy, S., and Bultynck, P. (2003). Conodont based graphic correlation of the Middle Devonian formations of the Ardenne (Belgium): implications for stratigraphy and construction of a regional composite. *Rev. Española de Micropaleontol.* 35, 315–344.

Hladil, J., Gersl, M., Strnad, L., Frana, J., Langrova, A., and Spisiak, J. (2006). Stratigraphic variation of complex impurities in platform limestones and possible significance of atmospheric dust: a study with emphasis on gamma-ray spectrometry and magnetic susceptibility outcrop logging (Eifelian-Frasnian, Moravia, Czech Republic). *Int. J. Earth Sci.* 95, 703–723. doi: 10.1007/s00531-005-0052-8

Hladil, J., Slavik, L., Vondra, M., Koptikova, L., Cejchan, P., Schnabl, P., et al. (2011). Pragian-Emsian successions in Uzbekistan and Bohemia: magnetic susceptibility logs and their dynamic time warping alignment. *Stratigraphy* 8, 217–235.

Irino, T., and Tada, R. (2003). High-resolution reconstruction of variation in aeolian dust (Kosa) deposition at ODP site 797, the Japan Sea, during the last 200 ka. *Glob. Planet. Change* 35, 143–156. doi: 10.1016/S0921-8181(02)00135-2

Jackson, M. (1990). Diagenetic sources of stable remanence in remagnetized Paleozoic cratonic carbonates: a rock magnetic study. *J. Geophys. Res.* 95, 2753–2761.

Jerolmack, D. J., and Paola, C. (2010). Shredding of environmental signals by sediment transport. *Geophys. Res. Lett.* 37:L19401. doi: 10.1029/2010GL044638

Johnson, J. G. (1970). Taghanic onlap and the end of north american devonian provinciality. *Bull. Geol. Soc. Am.* 81, 2077–2106.

Johnson, J. G., Klapper, G., and Sandberg, C. A. (1985). Devonian eustatic fluctuations in Euramerica. *Geol. Soc. Am. Bull.* 96, 567–587.

Königshof, P., Da Silva, A. C., Suttner, T. J., Kido, E., Waters, J., Carmichael, S. K., et al. (2016). Shallow-water facies setting around the Kaèák event: a multidisciplinary approach. *Geol. Soc. Lond. Spec. Pub.* 423, 171–199. doi: 10.1144/sp423.4

Larrasoaña, J. C., Roberts, A. P., and Rohling, E. J. (2008). Magnetic susceptibility of eastern mediterranean marine sediments as a proxy for Saharan dust supply? *Mar. Geol.* 254, 224–229. doi: 10.1016/j.margeo.2008.06.003

Mabille, C., and Boulvain, F. (2007). Sedimentology and magnetic susceptibility of the Upper Eifelian-Lower Givetian (Middle Devonian) in SW Belgium: insights into carbonate platform initiation. *Geol. Soc. Spec. Publ.* 275, 109–123. doi: 10.1144/gsl.sp.2007.275.01.08

Mabille, C., De Wilde, C., Hubert, B., Boulvain, F., and Da Silva, A. C. (2008a). Detailed sedimentological study of a non-classical succession for Trois-Fontaines and Terres d'Haurs formations (Lower Givetian, Marenne, Belgium) - Introduction to the Marenne Member. *Geol. Belg.* 11, 217–238.

Mabille, C., Pas, D., Aretz, M., Boulvain, F., Schröder, S., and Silva, A. C. (2008b). Deposition within the vicinity of the Mid-Eifelian High: detailed sedimentological study and magnetic susceptibility of a mixed ramp-related system from the eifelian lauch and nohn formations (Devonian. Ohlesberg, Eifel, Germany). *Facies* 54, 597–612. doi: 10.1007/s10347-008-0145-5

Maillet, S., Milhau, B., and Dojen, C. (2013). Stratigraphical distribution of Givetian ostracods in the type-area of the Fromelennes Formation (Fromelennes, Ardennes, France) and their relationship to global event. *Bull. Geosci.* 88, 865–892. doi: 10.3140/bull.geosci.1424

Maillet, S., Milhau, B., and Pinte, E. (2011). The fromelennes formation in the type-area (Fromelennes, Ardennes, France). *Ann. de la Soc. Géol. du Nord* 18, 9–34.

Mansy, J. L., Lacquement, F., Meilliez, F., and Van Vliet-Lanoë, B. (2006). *Carte géologique de France (1/50000), feuille Givet (40),* 2nd Edn. Orléans: BRGM.

Marshall, J. E. A., Brown, J. F., and Astin, T. R. (2011). Recognising the Taghanic Crisis in the Devonian terrestrial environment and its implications for understanding land-sea interactions. *Palaeogeogr. Palaeoclimatol. Palaeoecol.* 304, 165–183. doi: 10.1016/j.palaeo.2010.10.016

McKerrow, W. S., and Scotese, C. R. (1990). *Paleozoic Palaeogeography and Biogeography*. London: The Geological Society.

Molina Garza, R. S., and Zijderveld, J. D. A. (1996). Paleomagnetism of Paleozoic strata, Brabant and Ardennes Massifs, Belgium: implications of prefolding and postfolding Late Carboniferous secondary magnetizations for European apparent polar wander. *J. Geophys. Res. B Solid Earth* 101, 15799–15818. doi: 10.1029/96jb00325

Narkiewicz, K., and Bultynck, P. (2010). The upper Givetian (Middle Devonian) Subterminus conodont zone in North America, Europe and North Africa. *J. Paleontol.* 84, 588–625. doi: 10.1666/10-029.1

Parry, L. G. (1982). Magnetization of immobilized particle dispersions with two distinct particle sizes. *Phys. Earth Planet. Inter.* 28, 230–241. doi: 10.1016/0031-9201(82)90004-8

Pas, D. (2015). *Sedimentary Development and Correlation of Long-Term Off-Reef to Shallow-Water Devonian Carbonate Records in Europe*. Ph.D. thesis, University of Liège, Liège.

Pas, D., Da Silva, A. C., Cornet, P., Bultynck, P., Königshof, P., and Boulvain, F. (2013). Sedimentary development of a continuous Middle Devonian to Mississippian section from the fore-reef fringe of the Brilon Reef Complex (Rheinisches Schiefergebirge, Germany). *Facies* 59, 969–990. doi: 10.1007/s10347-012-0351-z

Pas, D., Da Silva, A. C., Devleeschouwer, X., De Vleeschouwer, D., Cornet, P., Labaye, C., et al. (2017). Insights into a million-year-scale Rhenohercynian carbonate platform evolution through a multi-disciplinary approach: example of a Givetian carbonate record from Belgium. *Geol. Mag.* 154, 707–739. doi: 10.1017/S0016756816000261

Pas, D., Da Silva, A. C., Devleeschouwer, X., De Vleeschouwer, D., Labaye, C., Cornet, P., et al. (2015). Sedimentary development and magnetic susceptibility evolution of the Frasnian in Western Belgium (Dinant Synclinorium, La Thure section). *Geol. Soc. Lond. Spec. Pub.* 414, 15–36. doi: 10.1144/sp414.7

Préat, A. (2006). Le Givétien franco-belge: moteur de la sédimentation eustatisme vs subsidence? *Géologie de la France* 1-2, 45–51.

Préat, A., and Boulvain, F. (1988). "Middle and upper Devonian carbonate platform evolution in Dinant and Namur Basins (Belgium, France)," in *Proceedings of the Excursion A-1, IAS 9th European Regional Meeting: Excursion Guidebook*, Leuven, 1–25.

Préat, A., and Bultynck, P. (2006). "Givetian," in *Chronostratigraphic Units Named from Belgium*, eds P. Bultynck, and L. Dejonghe, (Brussels: Geologica Belgica), 9–18.

Préat, A., Ceuleneer, G., and Boulvain, F. (1987). Etude sédimentologique des calcaires du Givétien Inférieur d'Olloy-sur-Viroin (bord Sud du Bassin de Dinant, Belgique). *Ann. de la Soc. Géol. du Nord* 106, 251–265.

Préat, A., Coen-Aubert, M., Mamet, B., and Tourneur, F. (1984). Sédimentologie et paléoécologie de trois niveaux récifaux du Givetien inférieur de Resteigne (bord sud du Bassin de Dinant, Belgique). *Bull. de la Soc. belge de Géol.* 93, 227–240.

Read, J. F. (1985). Carbonate platform facies models. *Am. Assoc. Pet. Geol. Bull.* 69, 1–21. doi: 10.1126/sciadv.1602158

Ridgwell, A. J. (2002). Dust in the earth system: the biogeochemical linking of land, air and sea. *Philos. Trans. R. Soc. A Math. Phys. Eng. Sci.* 360, 2905–2924. doi: 10.1098/rsta.2002.1096

Riquier, L., Averbuch, O., Devleeschouwer, X., and Tribovillard, N. (2010). Diagenetic versus detrital origin of the magnetic susceptibility variations in some carbonate Frasnian-Famennian boundary sections from Northern Africa and Western Europe: Implications for paleoenvironmental reconstructions. *Int. J. Earth Sci.* 99, 57–73. doi: 10.1016/j.palaeo.2014.09.030

Roberts, A. P., Tauxe, L., Heslop, D., Zhao, X., and Jiang, Z. (2018). A critical appraisal of the "Day" diagram. *J. Geophys. Res. Solid Earth* 123, 2618–2644. doi: 10.1002/2017jb015247

Sardar Abadi, M., Da Silva, A.-C., Mossadegh, H., Spassov, S., and Boulvain, F. (2015). Lower carboniferous ramp sedimentation of the Central Alborz Basin, northern Iran: integrated sedimentological and rock–magnetic studies. *Geol. Soc. Lond. Spec. Pub.* 414, 73–91. doi: 10.1144/sp414.13

Śliwinski, M. G., Whalen, M. T., and Day, J. (2010). Comparison of magnetic susceptibility (MS) and other geochemical proxies from the Middle-Late Frasnian of the Canadian Rocky Mountains: implications for paleoenvironmental and paleoclimatic analyses and interpretations of the punctata Event. *Przeglad Geol.* 58, 1152–1160.

Śliwiński, M. G., Whalen, M. T., Meyer, F. J., and Majs, F. (2012). Constraining clastic input controls on magnetic susceptibility and trace element anomalies during the Late Devonian punctata Event in the Western Canada Sedimentary Basin. *Terra Nova* 24, 301–309. doi: 10.1111/j.1365-3121.2012.01063.x

Spassov, S., and Valet, J. P. (2012). Detrital magnetizations from redeposition experiments of different natural sediments. *Earth Planet. Sci. Lett.* 351-352, 147–157. doi: 10.1016/j.epsl.2012.07.016

Tauxe, L., Bertram, H. N., and Seberino, C. (2002). Physical interpretation of hysteresis loops: micromagnetic modeling of fine particle magnetite. *Geochem. Geophys. Geosyst.* 3:1055. doi: 10.1029/2001GC000241

Tribovillard, N., Algeo, T. J., Lyons, T., and Riboulleau, A. (2006). Trace metals as paleoredox and paleoproductivity proxies: an update. *Chem. Geol.* 232, 12–32. doi: 10.1016/j.chemgeo.2006.02.012

Vanderaveroet, P., Averbuch, O., Deconinck, J. F., and Chamley, H. (1999). A record of glacial/interglacial alternations in Pleistocene sediments off New Jersey expressed by clay mineral, grain-size and magnetic susceptibility data. *Mar. Geol.* 159, 79–92. doi: 10.1016/S0025-3227(98)00203-5

Walden, J., Oldfield, F., and Smith, J. (1999). *Environmental Magnetism: A Practical Guide*. London: Quaternary Research Association.

Weber, M. E., Kuhn, G., Sprenk, D., Rolf, C., Ohlwein, C., and Ricken, W. (2012). Dust transport from Patagonia to Antarctica - A new stratigraphic approach from the Scotia Sea and its implications for the last glacial cycle. *Quat. Sci. Rev.* 36, 177–188. doi: 10.1016/j.quascirev.2012.01.016

Wehrmann, A., Hertweck, G., Brocke, R., Jansen, U., Königshof, P., Plodowski, G., et al. (2005). Paleoenvironment of an Early Devonian land-sea transition: a case study from the southern margin of the old red continent (Mosel Valley, Germany). *Palaios* 20, 101–120. doi: 10.2110/palo.2003.p03-33

Whalen, M. T., and Day, J. E. (2008). Magnetic susceptibility, biostratigraphy, and sequence stratigraphy: insights into Devonian carbonate platform development and basin infilling, western Alberta, Canada. *Soc. Sediment. Geol.* 89, 291–314. doi: 10.2110/pec.08.89.0291

Whalen, M. T., and Day, J. E. (2010). Cross-basin variations in magnetic susceptibility influenced by changing sea level, paleogeography, and paleoclimate: upper Devonian, western Canada sedimentary basin. *J. Sediment. Res.* 80, 1109–1127. doi: 10.2110/jsr.2010.093

Wright, V. P., and Burgess, P. M. (2005). The carbonate factory continuum, facies mosaics and microfacies: an appraisal of some of the key concepts underpinning carbonate sedimentology. *Facies* 51, 17–23. doi: 10.1007/s10347-005-0049-6

Zegers, T. E., Dekkers, M. J., and Baily, S. (2003). Late carboniferous to Permian remagnetization of Devonian limestones in the Ardennes: Role of temperature, fluids, and deformation. *J. Geophys. Res.* 108, 5/1–5/19.

Ziegler, A. P. (1982). *Geological Atlas of Western and Central Europe*. Brussels: Shell Internationale Petroleum Maatschappij B.V, 130.

Zwing, A., Bachtadse, V., and Soffel, H. C. (2002). Late Carboniferous remagnetisation of Palaeozoic rocks in the NE Rhenish Massif, Germany. *Phys. Chem. Earth A* 27, 1179–1188. doi: 10.1016/S1474-7065(02)00128-6

Zwing, A., Matzka, J., Bachtadse, V., and Soffel, H. C. (2005). Rock magnetic properties of remagnetized Palaeozoic clastic and carbonate rocks from the NE Rhenish massif, Germany. *Geophys. J. Int.* 160, 477–486. doi: 10.1111/j.1365-246X.2004.02493.x

Conflict of Interest: GP is now employed by the company Geolys.

The remaining authors declare that the research was conducted in the absence of any commercial or financial relationships that could be construed as a potential conflict of interest.

The handling Editor declared a past co-authorship with one of the authors DP.

frontiers in Earth Science

ORIGINAL RESEARCH
published: 20 March 2020
doi: 10.3389/feart.2020.00075

The Arctic Ocean Manganese Cycle, an Overlooked Mechanism in the Anomalous Palaeomagnetic Sedimentary Record

Steffen Wiers[1], Ian Snowball[1], Matt O'Regan[2], Christof Pearce[3] and Bjarne Almqvist[1]*

[1] Department of Earth Sciences, Uppsala University, Uppsala, Sweden, [2] Department of Geological Sciences, Stockholm University, Stockholm, Sweden, [3] Department of Geoscience and Arctic Research Centre, Aarhus University, Aarhus, Denmark

Palaeomagnetic records obtained from Arctic Ocean sediments are controversial because they include numerous and anomalous geomagnetic excursions. Age models that do not rely on palaeomagnetic interpretations reveal that the majority of the changes in inclination do not concur with the established global magnetostratigraphy. Seafloor oxidation of (titano)magnetite to (titano)maghemite with self-reversal of the (titano)maghemite coatings has been proposed as an explanation. However, no existing model can explain when the self-reversed components formed and how they are linked to litho-stratigraphic changes in Arctic Ocean sediments. In this study, we present new palaeo- and rock magnetic measurements of a sediment core recovered from the Arlis Plateau, close to the East Siberian Shelf. The magnetic data set is evaluated in the context of the regional stratigraphy and downcore changes in physical and chemical properties. By cross-core correlation, we show that magnetic inclination changes in the region do not stratigraphically align, similar to results of studies of sediments from the Lomonosov Ridge and Yermak Plateau. Rock magnetic and chemical parameters indicate post-depositional diagenetic changes in the magnetic mineral assemblage that can be linked to manganese cycling in the Arctic Ocean. The potential presence of a magnetic remanence bearing manganese-iron oxide phase, which can undergo self-reversal, leads to an alternative hypothesis to primary seafloor oxidation of (titano)magnetite. This phase may form by precipitation from seawater or by changing redox conditions in the sediment column by mineral precipitation from ions dissolved in pore water. These findings highlight the need for further investigation into the magnetic mineral assemblage, its link to manganese cycling and pore water geochemistry in Arctic Ocean sediments.

Keywords: Arctic Ocean, lithostratigraphy, palaeomagnetism, mineral magnetism, diagenesis

OPEN ACCESS

Edited by:
Juan Cruz Larrasoaña, Geological and Mining Institute of Spain, Spain

Reviewed by:
Luigi Jovane, University of São Paulo, Brazil
Christian Ohneiser, University of Otago, New Zealand

****Correspondence:***
Steffen Wiers
steffen.wiers@geo.uu.se

Specialty section:
This article was submitted to Geomagnetism and Paleomagnetism, a section of the journal Frontiers in Earth Science

Received: *03 December 2019*
Accepted: *28 February 2020*
Published: *20 March 2020*

Citation:
Wiers S, Snowball I, O'Regan M, Pearce C and Almqvist B (2020) The Arctic Ocean Manganese Cycle, an Overlooked Mechanism in the Anomalous Palaeomagnetic Sedimentary Record. Front. Earth Sci. 8:75. doi: 10.3389/feart.2020.00075

INTRODUCTION

The magnetostratigraphy of Arctic Ocean sediments has bewildered geologists because palaeomagnetic studies yield high frequency changes in polarity (e.g., Backman et al., 2004) that do not match the established Geomagnetic Polarity Time Scale (GPTS; Cande and Kent, 1995). Early works in the Arctic Ocean interpreted the observed polarity changes

as geomagnetic reversals, with the uppermost change in inclination assigned to the Matuyama-Brunhes polarity transition (e.g., Steuerwald et al., 1968; Clark, 1970), which resulted in low sedimentation rate estimates. These low rates were later challenged by alternative dating approaches, with the conclusion that the most extreme palaeomagnetic directional changes (in inclination) were records of geomagnetic excursions during the Brunhes chron (e.g., Nowaczyk et al., 1994, 2001; Jakobsson et al., 2000; Nowaczyk and Knies, 2000; Backman et al., 2004). Sedimentation rates based on the alternative dating approaches are, however, still lower than the critical rate of ca. 10 cm/ka that models of natural remanent magnetisation (NRM) acquisition by sediments predict is necessary to record short-term polarity changes, such as geomagnetic excursions (Roberts and Winklhofer, 2004).

These difficulties in interpreting palaeomagnetic data in the Arctic led to the exclusion of magnetostratigraphy in the construction of the Arctic Coring Expedition (ACEX, IODP Expedition 302) age model for the Neogene (Backman et al., 2008). Some recent studies challenge the ACEX-based age model through U-Th ages (Hillaire-Marcel et al., 2017) and palaeomagnetic interpretations (Liu et al., 2019) that support the low-sedimentation rate scenario of Clark (1970). While some studies (e.g., Spielhagen et al., 2004) of Arctic Ocean sediments assumed inclination changes to be coeval and used them for stratigraphic correlation, more recent studies that placed inclination changes into the lithostratigraphic context of the Arctic Ocean (e.g., O'Regan et al., 2008; Wiers et al., 2019) have confirmed the abnormal nature of the palaeomagnetic record by showing that inclination changes are not stratigraphically coeval.

While the entire Arctic Ocean falls into the region of the tangent cylinder (e.g., Kono and Roberts, 2002), which could hypothetically create a very different surface expression of the geomagnetic field from the rest of the world, palaeomagnetic studies from Antarctic sediments have not uncovered evidence of unregular field behaviour within the region of the tangent cylinder (Jovane et al., 2008; Lawrence et al., 2009). Most work on post-depositional transformations of magnetic minerals in marine and lacustrine sediments has focussed on sulphide-driven iron-oxide dissolution and the authigenesis of ferrimagnetic iron sulphides (reviewed by Roberts, 2015). However, Channell and Xuan (2009) proposed that the observed changes in palaeomagnetic direction in Arctic sediments are the result of post-depositional seafloor oxidation of (titano)magnetite to (titano)maghemite. This oxidation is accompanied by the acquisition of a reversed chemical remanent magnetisation (CRM) in the (titano)maghemite phase. The process would therefore, be similar to that already proposed to explain anomalous palaeomagnetic records from the North Pacific (Kent and Lowrie, 1974; Johnson et al., 1975). Although Xuan and Channell (2010) further developed the model and showed that Arctic Ocean sediments contain a population of high-Ti magnetite with high oxidation states, which are necessary to form reversed CRM's (O'Reilly and Banerjee, 1966), a clear mechanism that differentiates normal from reversed zones is still missing. Particularly troublesome is that the observed mean Ti content (x) is less than 0.5 (Xuan and Channell, 2010), which is too low for a reversed CRM to form (O'Reilly and Banerjee, 1966). Henshaw and Merrill (1980) proposed that a magnetic ferromanganese phase is responsible for the anomalous palaeomagnetic records from the North Pacific, which is also a conceivable scenario for Arctic sediments, amongst others.

Modern, interglacial and interstadial sediments from the central Arctic Ocean tend to be relatively fine-grained, bioturbated brown clays and silty-clays that contain, at least in near surface sediments, calcareous microfossils. The brown colour comes from a notable enrichment in the manganese (Mn) content of interglacial and interstadial sediments (Jakobsson et al., 2000). Although Mn can undergo post-burial remobilisation, bioturbated, brown (Mn-enriched) layers are widely used for the lithostratigraphic correlation and dating of Arctic marine sediments (e.g., Jakobsson et al., 2000; März et al., 2011; Löwemark et al., 2014; Schreck et al., 2018; Ye et al., 2019). Mn and Fe cycling in the sediments has received little to no attention with respect to palaeo- and rock magnetic data, even though ferromagnetic manganese minerals exist, such as jacobsite ($MnFe_2O_4$). Fe/Mn ratios in Arctic ferromanganese nodules are considerably higher than deposits in other ocean basins (Hein et al., 2017; Konstantinova et al., 2017, 2018) and there is a known connection between Mn and Fe redox reactions (e.g., Schulz and Zabel, 2006).

In this study we present new palaeo- and rock magnetic data in combination with physical and chemical properties of sediments from the Arlis Plateau close to the East Siberian Shelf, Arctic Ocean. These data are evaluated in the context of the regional litho- and chronostratigraphy (Schreck et al., 2018) with a focus on diagenetic changes associated with Mn cycling (März et al., 2011; Löwemark et al., 2014).

MATERIALS AND METHODS

Coring Site and Sampling

The studied piston core SWERUS-L2-13-PC1 (hereafter referred to as 13PC; **Figure 1**) was collected from the Arlis Plateau (76.18° N, 179.29° E) during the Swedish-Russian-US expedition on the Swedish icebreaker Oden in 2014, from a water depth of 1119 m. The core length was 7.68 m. Samples for organic carbon and sterols were taken onboard after splitting, with 10 cm^3 scoops and frozen at −20°C. The core was stored at 4°C before the archive halves were subsampled with standard palaeomagnetic cubes (7 cm^3) at Stockholm University in 2016.

Physical Properties

Bulk density (BD, ρ) and magnetic susceptibility (κ) were measured shipboard at 1 cm downcore resolution on whole core sections approximately 24 h after the core was recovered. Measurements were performed using a GeoTek multi-sensor core logger (MSCL). Line scan images were taken from the archive halves after splitting. A fall cone was used to measure the undrained shear strength of the sediment on the working halves. Sediment colour is often used in the western Arctic Ocean as an indicator for glacial-interglacial cycles and cross-core correlation (Jakobsson et al., 2000). We measured sediment colour of

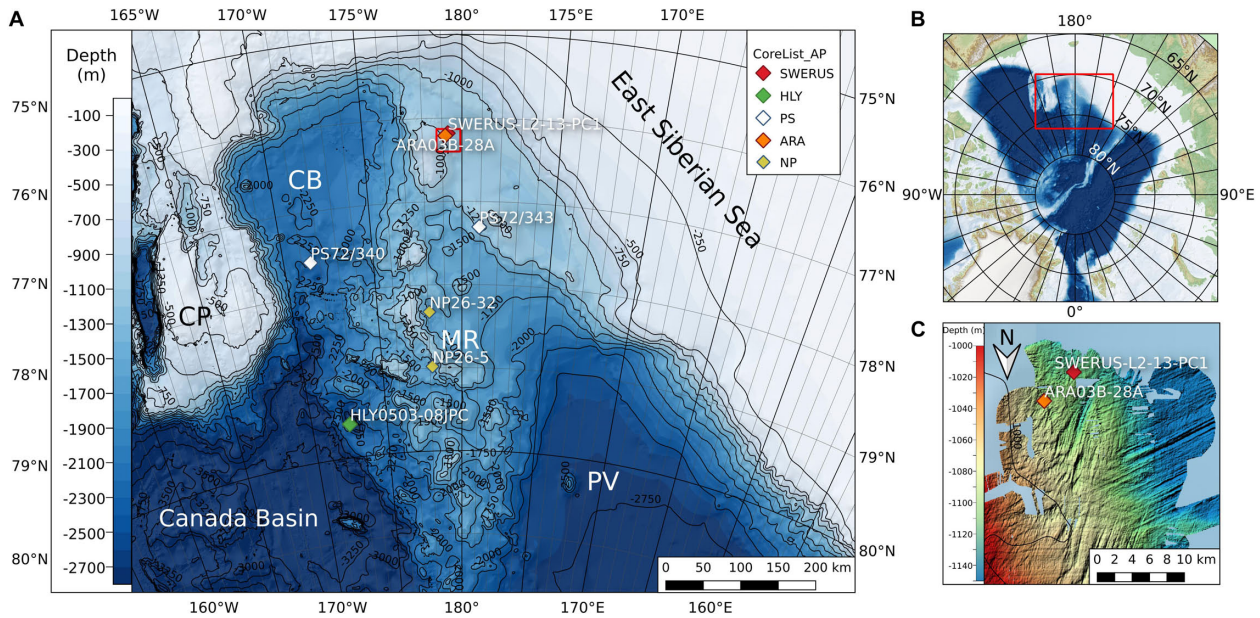

FIGURE 1 | Overview maps of Arlis Plateau and the Chukchi Sea, showing topography and bathymetry (data from IBCAO; Jakobsson et al., 2012). **(A)** Overview map displaying cores used in this study and reference cores mentioned in the text. **(B)** Overview map of the Arctic Ocean. **(C)** Detailed bathymetry around the core location of SWERUS-L2-13PC1. CB, Chukchi Basin; MR, Mendelev Ridge; CP, Chukchi Plateau; PV, Podvodnikov Basin.

the archive halves with a handheld Minolta spectrophotometer (model CM-700d) at 2 cm intervals at Stockholm University. Colours are expressed as components of lightness (L), green-red (a*) and blue-yellow (b*). Radiographic images were obtained from the archive halves using an ITRAX core scanner (Stockholm University) with a Mo tube at 30 kV, 45 mA and 200 μm increments.

(Organic)Geochemical Properties

Relative elemental composition was measured by means of X-Ray Fluorescence (XRF) with the ITRAX core scanner on the archive halves of the core. Measurements were made with a Mo tube (30 kV, 45 mA and 20 s dwell time) at 2 mm increments. Elements with low average counts and/or noisy signals (Al, P, S, Ga, Y, Ba, Ta, W) and elements that exhibited large concentration changes at section breaks (Ar, Ni, Pb), were disregarded. The remaining elemental counts (Si, Cl, K, Ca, Ti, V, Cr, Mn, Fe, Cu, Zn, Br, Rb, Sr, Zr) were normalised to the ratio of incoherent to coherent scattering and log normalised (base e).

Total organic carbon (TOC), the stable isotopic composition of organic carbon ($\delta^{13}C_{org}$) and sterol concentrations were measured at 10 cm resolution at the Department of Geological Sciences, Stockholm University. Samples were freeze-dried and homogenised in the laboratory before subsequent analyses. For TOC and $\delta^{13}C_{org}$, the homogenised samples were first treated with a 1M HCl-solution to remove any carbonates, and then measured using a Carlo Erba NC2500 elemental analyser coupled to a Finnigan Delta V Advantage mass spectrometer. For the sterols, Androstanol was added as an internal standard before extraction to allow quantification of the concentration of sterols in the sediments. The homogenised samples were subjected to three cycles of 15 min sonication with dichloromethane and methanol (DCM/MeOH; 2:1 v/v), followed by centrifugation and decanting to obtain the total organic extracts. The polar fraction containing the sterols was eluted with DCM:MeOH (1:1) using glass pipette columns packed with pre-combusted silica gel and cotton wool. The fraction was silylated in BSTFA and pyridine (1:1) at 60°C for 20 min. The samples were then further separated using a Shimadzu QP2010 Ultra Gas Chromatography-Mass Spectrometry (GC-MS) with a ZB-5-HT column using a temperature increase of 10°C/minute from 40 to 300°C. The abundances of brassicasterol and ß-sitosterol were quantified as trimethylsilyl ethers (TMS) in selected ion mode (SIM) at m/z 470 and m/z 486, respectively.

Magnetic Properties

Anisotropy of magnetic susceptibility (AMS) and frequency dependent magnetic susceptibility were measured with an AGICO MFK1-FA Kappabridge equipped with a sample rotator for spinning specimen measurements in three positions (Pokorný et al., 2011) at the Department of Earth Sciences, Uppsala University, Sweden. AMS was measured to assess potential sampling induced fabric deformation and identify resulting unreliable palaeomagnetic records (Marino and Ellwood, 1978). The degree of anisotropy (P_j) and the shape parameter (T; both after Jelinek, 1981) describe the fabric. We further utilise the parameter $90\text{-}K3_{Inclination}$, where K_3 is the axis of minimum susceptibility, to identify disturbed/unreliable portions of the core (Hrouda and Kahan, 1991). Where this parameter is >15° the palaeomagnetic directional data are considered unreliable (Snowball et al., 2019). To quantify the proportion of superparamagnetic (SP) particles we calculated $\chi_{fd1,16}$ (after

Hrouda, 2011) using bulk magnetic susceptibility measurements at 976 Hz and 15616 Hz.

NRM, anhysteretic remanent magnetisation (ARM) and isothermal remanent magnetisation (IRM) were measured with a 2G Enterprises 760 superconducting rock magnetometer (SRM) at the University of Bremen, Germany. NRM was measured and subsequently demagnetised with 15 incremental alternating field (AF) demagnetisation steps from 5 to 100 mT. Characteristic remanence magnetisation (ChRM) inclination and prolate maximum angular deviation (MAD_p; Love, 2007) were calculated by principal component analysis (PCA) in the 20 to 60 mT demagnetisation range (Kirschvink, 1980).

ARM was imparted using an AF of 100 mT and a 0.05 mT DC bias field and subsequently measured and demagnetised using the same steps as for the NRM. Susceptibility of ARM (χ_{ARM}) was calculated by normalising ARM to the bias field. IRM was first imparted with a 2.5 T field and measured as the saturation IRM (SIRM). Afterward, 20 increasing fields from 10 to 300 mT were imparted in the opposite direction as the SIRM. Based on the IRM data we calculated the average coercivity of remanence (B_{cr}) for each sample by interpolation of IRM values to a resolution of 0.1 mT, as well as the S-Ratio and Hard IRM (HIRM) at 100 and 300 mT backfields to characterise the magnetic mineralogy. The S-Ratio gives the relative concentrations of minerals with B_{cr} higher than 100 and 300 mT, whereas HIRM is the absolute magnetisation of minerals with B_{cr} higher than 100 and 300 mT (e.g., Liu et al., 2007). ARM, SIRM and HIRM were mass normalised using the cube weights, corrected for the weight of an empty cube.

To identify magnetic domain states, hysteresis properties (Coercive force, B_c; Saturation magnetisation M_s; Remanent magnetisation, M_{rs}) were measured on 20 selected samples by subsampling bulk material from the palaeomagnetic cubes. Measurements were made with a Lakeshore VSM at the Ångström Laboratory, Uppsala University, Sweden. A maximum field of 1 T was used to magnetise the samples. Measurement results were processed using HystLab (Paterson et al., 2018).

Statistical Analysis

To find relationships between different parameter types that relate to (1) sediment input or (2) diagenetic changes, we calculated Pearson correlation coefficients using the pandas python library (McKinney, 2010). To correlate values that were measured at different sampling intervals, data were resampled to match the resolution of the palaeomagnetic samples using NumPy (van der Walt et al., 2011). Corresponding values for organic carbon content and sterol concentrations were linearly interpolated. XRF values were averaged across the length (2.2 cm) of palaeomagnetic cubes.

In order to differentiate sediments based on their physical, chemical, biological and magnetic properties, we employed fuzzy c-means clustering (FCM) on data matrices with the SciKit fuzzy logic toolbox for python (Warner et al., 2017). Before clustering, data were standardised using

$$z_i = \frac{x_i - \bar{X}}{s}$$

where z_i is the standardised value, x_i the original value and s the standard deviation. Data were transformed into standard normal form to eliminate different measurement units across parameters. Clustering was performed based on Euclidean distances with a fuzzy exponent chosen according to the data matrix dimensions (after Schwämmle and Jensen, 2010). The optimal number of clusters was determined based on a combination of different validation indices (Schwämmle and Jensen, 2010).

FCM was run on a combined data set of physical (ρ, κ, L, a*, b*), chemical (Ca, Fe, Mn) and biological (TOC, $\delta^{13}C_{org}$, brassicasterol, β-sitosterol) data (denoted SC) and rock magnetic data (denoted MC). In the following text and figures, clusters are referred to by their denomination (SC or MC), a subscript that identifies the cluster in question (1, 2, 3, etc.) and the downcore occurrence of aforementioned cluster (a, b, c, etc.).

RESULTS

Sediment Stratigraphy

The sediments of 13PC consist of alternating dark greyish brown to olive brown (2.5Y 4/2 – 4/3) and dark grey to dark greenish grey (GLEY1 4/- 4/1) layers. Density (1.5 to 1.7 g/cm^3) and shear strength (∼2 to 10 kPa) show a downcore trend to higher values (**Figure 2**), characteristic of compaction associated with dewatering as burial depth increases.

Brown layers comprise dark brown to greyish brown mud with slightly darker layers/mottles and signs of bioturbation that extend into underlying grey layers. The brown layers are characterised by red (a*) and yellow (b*) colour components, minimum organic carbon and sterol content, high $\delta^{13}C_{org}$ values, and high Ca and Mn. In 13PC, two distinct brown layers are found at 0 to 0.72 m and 2.5 to 3.5 m. A third layer that exhibits similar characteristics is found between 6.3 and 7.3 m. However, this third brown layer lacks high Ca concentrations, displays a larger density and lightness (L) and is a different shade of brown compared to the two other brown layers (cf., **Figure 2**).

Grey layers comprise olive grey to greenish grey mud with yellowish-brown layering and mottles. They display low density, low magnetic susceptibility and elevated β-sitosterol and brassicasterol concentrations. Additionally, grey layers exhibit low $\delta^{13}C_{org}$ values and low Mn and Ca concentrations.

Stability of the Natural Remanent Magnetisation

Analysis of vector end-point diagrams (Zijderveld, 1967) reveals multi component demagnetisation behaviour (**Figure 3**). One set of samples is characterised by the removal of a low coercivity (viscous) magnetisation between 0 and 15 mT and a more stable component of magnetisation above 15 mT. A second set of samples is characterised by a curved demagnetisation behaviour indicative of at least two components with overlapping coercivity spectra. Both sets contain normal and reversed directions. NRM averages $4.92 \times 10^{-3} \pm 3.31 \times 10^{-3}$ A/m, with slightly higher values and variability in the brown layers ($6.31 \times 10^{-3} \pm 4.12 \times 10^{-3}$ A/m) compared to the grey layers ($4.08 \times 10^{-3} \pm 2.35 \times 10^{-3}$ A/m). We attribute the shallow

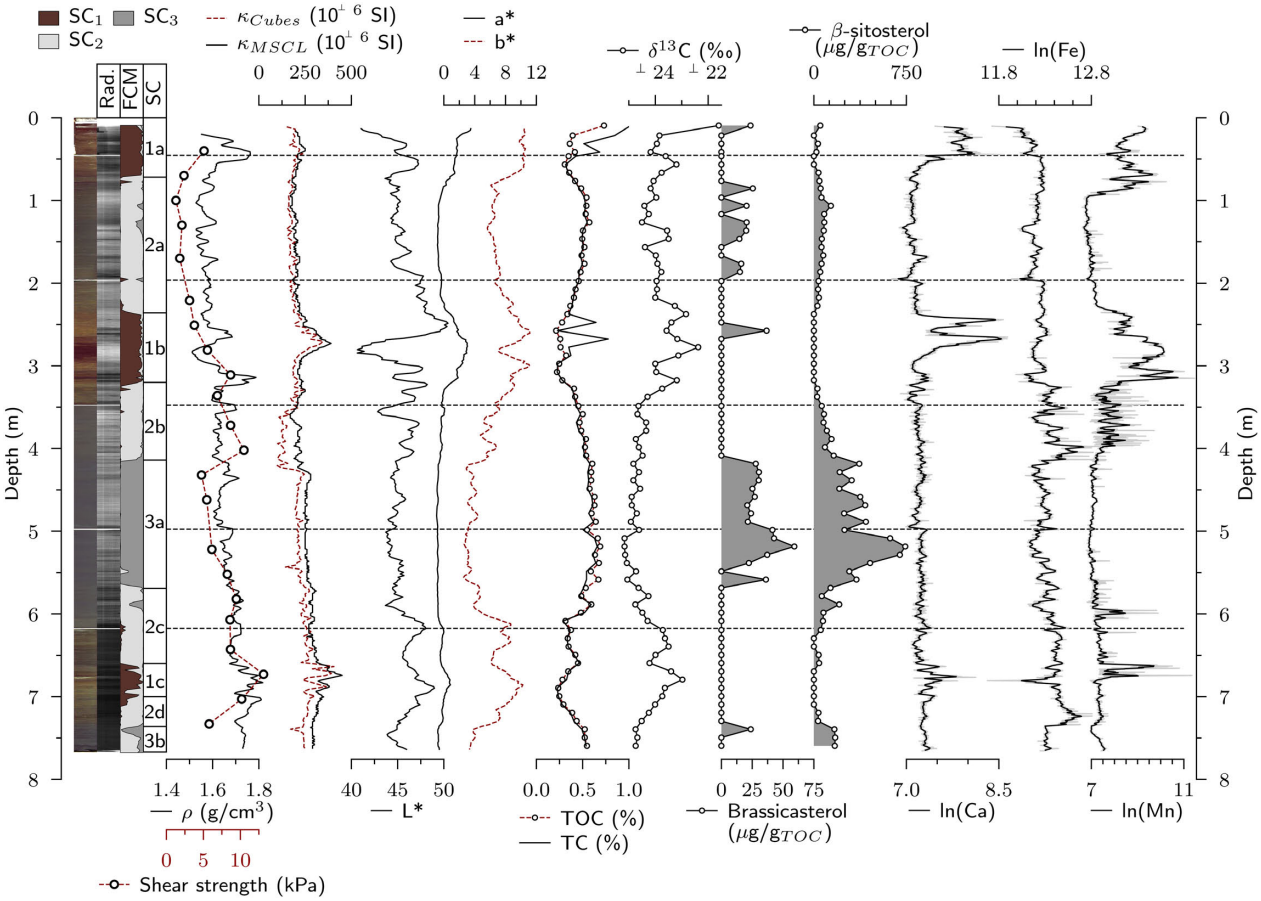

FIGURE 2 | Line-scan image, radiographs, FCM results and downcore variations of physical, chemical, carbon and biomarker data of core SWERUS-L2-13-PC1. From left to right: density (ρ; solid black line) and shear strength (red dashed line), volume magnetic susceptibility from multi sensor core logger loop sensor (solid black line) and palaeomagnetic cubes (red dashed line), colour lightness (L), green-red (a*; solid black line) and blue-yellow (b*; red dashed line) colour components, total carbon (TC; solid black line) and total organic carbon (TOC; red dashed line), stable carbon isotopes ($\delta^{13}C$), (marine) organic sterol concentration (brassicasterol), (terrigenous) organic sterol concentration (β-sitosterol), relative calcium (Ca) content, relative iron (Fe) content and relative manganese (Mn) content. FCM is based on all displayed parameters except shear strength, κ_{MSCL} and TC. Elemental data are scatter and log normalised.

inclination component found in most samples (c.f., **Figure 3**) to a viscous component acquired during horizontal storage in Stockholm between sample retrieving and sub-sampling.

The MDF_{NRM} (**Figure 4**) displays a high variability within the uppermost 2 m of the core. Below 2 m, MDF_{NRM} drops to less than 10 mT on average with high variability between 4 and 6 m. The very high values of MDF_{NRM} around 3 m are associated with low NRM intensity, which we attribute to the presence of anti-parallel directional components that have overlapping coercivities. Additionally, samples from the uppermost 2 m of the core exhibit a predominantly inverted AMS fabric as identified by the 90-K_3 parameter.

PCA isolated ChRM inclinations in the range of 20 to 60 mT show average MAD_p values of approximately 8° with 28% being steeper than 10° (**Figure 4**). Almost 20% of the samples show an inclination below 0° that is prevalent in, but not restricted to, brown layers. Using rejection criteria to filter ChRM inclination based on high MAD_p values (>10°) and the detection of potentially disturbed sediment (90-K_3 > 15°) discards about half (149 out of 283) of the data set.

Rock Magnetic Properties

Values of χ, χ_{ARM} and SIRM suggest high concentrations of magnetic minerals in brown layers (**Figure 5**) although the most prominent peak in concentration, between 2.5 and 3.0 m, is slightly offset across the parameters. The peak in χ_{ARM} is approximately 0.1 m deeper than in χ and SIRM, although the peak in χ_{ARM} coincides with a peak in χ_{fd}. The HIRM reveals that magnetic minerals with coercivities > 100 mT but lower than 300 mT are more prominent in the uppermost 4.25 m of the core. Accordingly, magnetic mineralogical dependent parameters (S-Ratio, B_{cr}) indicate a distinct change to a lower average coercivity at 4.25 m. This change is accompanied by an increase in degree of anisotropy (P_j) and shape (T) of the magnetic susceptibility ellipsoid below 4.25 m.

The ratios of ARM/SIRM, χ_{ARM}/χ and SIRM/κ, which are commonly interpreted as proxies for magnetic domain

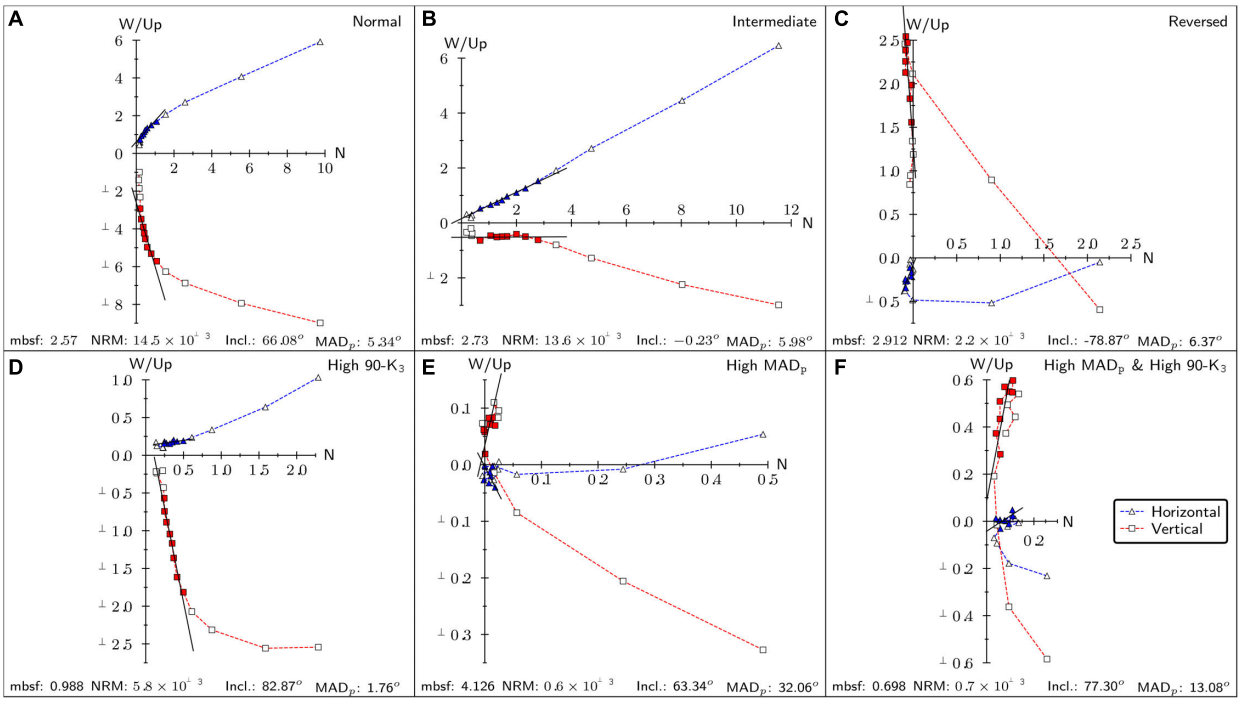

FIGURE 3 | Orthogonal projections of alternating field demagnetisation data for six selected samples from 13PC. Axis units are in mA/m, NRM values are in A/m. All samples show the removal of a potential viscous component followed by the demagnetisation of one component toward the origin. Samples **(A,D)** show curved demagnetisation behaviour, indicative of 2 (or more) directional components. Sample **(B)** shows a strong horizontal magnetisation. Sample **(C)** shows a low coercivity horizontal component and a steep negative component. Samples **(E,F)** display rapid demagnetisation within the first few steps (15–20 mT) followed by erratic demagnetisation.

state or magnetic mineralogy (Peters and Dekkers, 2003) are dominated by magnetic mineralogy changes in 13PC (**Figure 6A**). The peaks at 0.15 and 2.8 m in ARM/SIRM and χ_{ARM}/χ coincide with peaks in χ_{ARM} and SIRM and lows in B_{cr} and S-Ratio$_{100}$ (**Figure 5**), which indicates a higher concentration of low coercivity magnetic minerals rather than changes in magnetic domain state of a single mineral. Accordingly, SIRM/χ follows trends in SIRM, S-Ratio$_{100}$ and HIRM$_{100}$, which indicates a strong influence of compositional changes in the magnetic mineral assemblage. Results from hysteresis measurements (**Figure 6B**) confirm this influence by showing a low correlation of B_{cr}/B_c vs. M_{rs}/M_s values with χ_{ARM}/χ. The interpretation of the Day plot (**Figure 6**; Day et al., 1977) is, however, complex because the magnetic hysteresis parameters are influenced by a large number of factors, such as mineralogy, magnetocrystalline anisotropy and particle interactions to name just three (Roberts et al., 2018).

Statistics

The optimal number of clusters was determined to be 3 for both FCM runs (SC and MC) with a fuzzy exponent of ∼1.3. Results from SC confirm our initial division into brown and grey layers with SC_1 correlating with brown layers while SC_2 and SC_3 correlate with grey layers (**Figure 2**). The subdivision of the grey layers in the FCM results is mainly based on differences in β-sitosterol, brassicasterol and Mn concentrations.

MC results indicate that there is no simple connection between magnetic properties of 13PC and its other physical and chemical properties (**Figure 5**). Based on its magnetic properties, the core can clearly be divided into an upper part (0–4.25 m, MC_1 and MC_2) and a lower part (4.25 m and below, MC_3) that display different magnetic properties. The division is mainly based on the difference in high coercivity minerals (i.e., >100 mT, based on S-Ratio$_{100}$) because a clear separation is not apparent in FCM results from physical and chemical properties (i.e., the SC clusters). MC_1 is characterised by high values in χ, χ_{fd}, χ_{ARM}, SIRM and HIRM$_{100}$ while MC_2 and MC_3 are characterised by lower values in χ_{fd} and χ_{ARM}. MC_2 and MC_3 are distinctly different in their χ, SIRM, HIRM$_{100}$, S-Ratio$_{100}$ and B_{CR} values. SC and MC correlate within the first 4 m of 13PC, but with offsets in the location of boundaries. MC_1 correlates with SC_1 but is thinner, whereas MC_2 and MC_3 are not uniquely bound to SC_2 and SC_3 but merely separate the core into an upper and lower part.

DISCUSSION

Stratigraphy and Age Constraints

The lithostratigraphy of core 13PC is similar to other cores from the region, specifically nearby cores ARA03-28A and HLY0503-8JPC (hereafter 8JPC; Adler et al., 2009; Schreck et al., 2018;

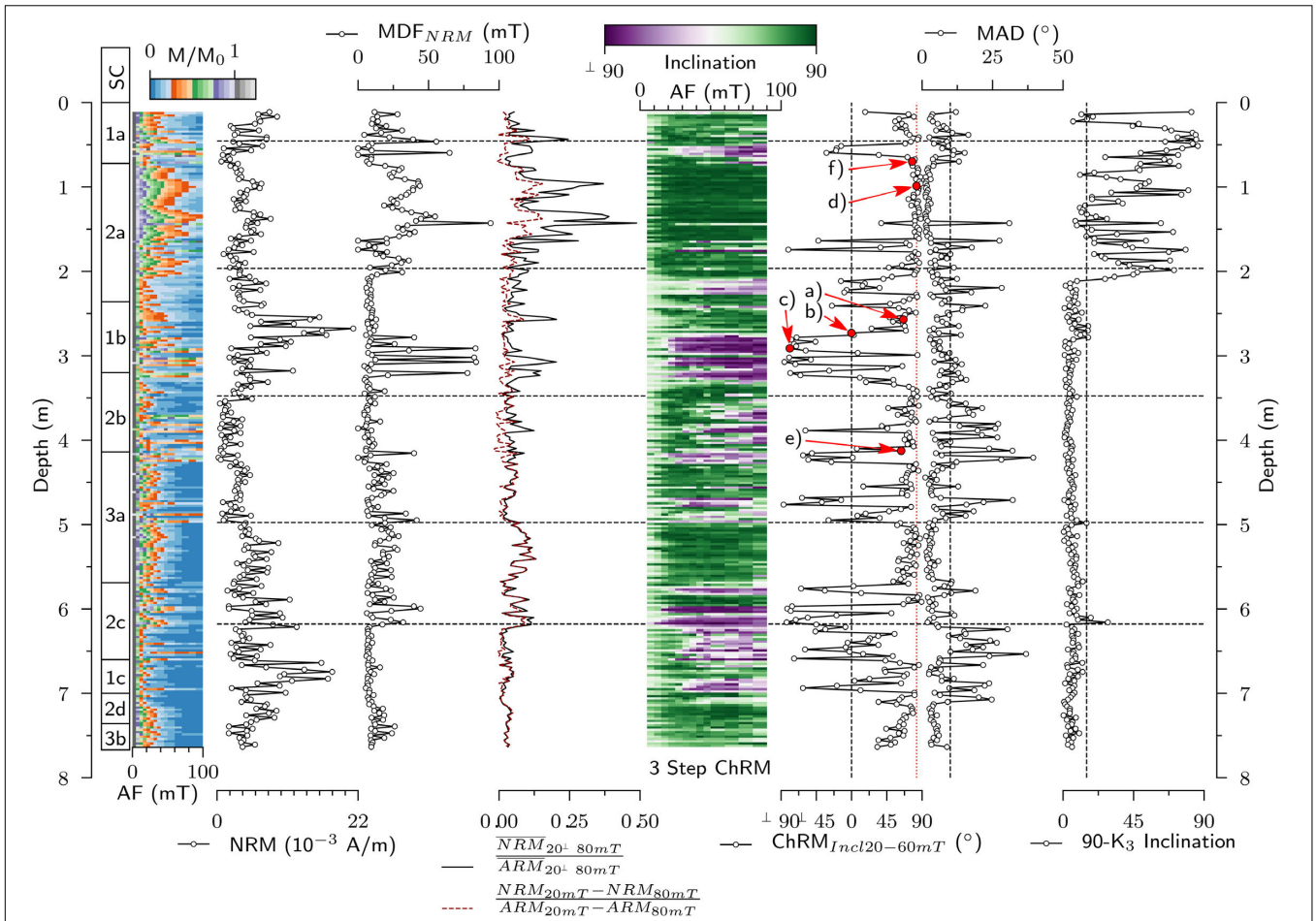

FIGURE 4 | Natural remanent magnetisation (NRM) and related parameters. From left to right: remaining intensity of NRM after each demagnetisation step normalised to NRM intensity, NRM intensity, median destructive field of the NRM, palaeomagnetic "stability" parameters, characteristic remanent magnetisation (ChRM) inclination based on 3-step principal component analysis (PCA), ChRM inclination (based on 20–60 mT PCA), median angular deviation (MAD) of PCA and 90 - K_3 inclination (inclination of axis of minimum magnetic susceptibility). Red dots in ChRM inclination mark positions of orthogonal projections in **Figure 3**.

Figures 7, **8**). The lithostratigraphic framework presented by Schreck et al. (2018) follows the nomenclature used in the western Arctic with dark brown layers labelled as Bx and yellowish to greyish layers labelled Gx, where *x* is a downcore increasing number that indexes the occurrence of successive layers. The dark brown layers are interpreted to represent interglacial intervals while the grey layers represent glacial intervals. We find a good correlation of brown layers B1 and B2 in 13PC and ARA03-28A, with the characteristic double peak in Ca in layer B2 (**Figure 7**). Three radiocarbon ages from core 13PC (**Table 1**; Jakobsson et al., 2016) confirm a Holocene age for layer B1 and a minimum MIS 3 age for B2. Jakobsson et al. (2016) further suggest an MIS 5 age for B2 based on the rare occurrences of *E. huxleyi* and *Gephyrocapsa* spp. at 2.86 m. However, based on the stratigraphic correlation an MIS 3 age of B2 would be more consistent with reported basal ages of 40 to 45 ka for this layer (Schreck et al., 2018). The much older ^{14}C ages we obtain from our two samples from B2 (>43 and >48 ka) may be a result of reworking of older material and a small sample size, which can bias the results toward older ages (Lougheed et al., 2018). There still remains considerable uncertainty in age-depth models for Arctic Ocean sediments, and beyond the limit of radiocarbon dating it becomes difficult to differentiate between substages in glacial cycles, or define the boundaries between glacial and interglacial marine isotope stages. Here we simply acknowledge the difference in the age models reported by Jakobsson et al. (2016) and Schreck et al. (2018), and do not present any new data to support or refute either one.

FCM results confirm the general division in brown and grey layers but they do allow for a more detailed distinction of the sediment sequence. While cluster SC_1 is closely associated with the interglacial brown layers (B1 and B2), SC_2 and SC_3 differentiate the glacial layers (G1 and G2). The differences between SC_2 and SC_3 can indicate changing depositional environments and different (glacial) conditions or they may be the result of diagenetic alterations and dewatering due to compaction. SC_{1c} shows a distinctly different colour compared

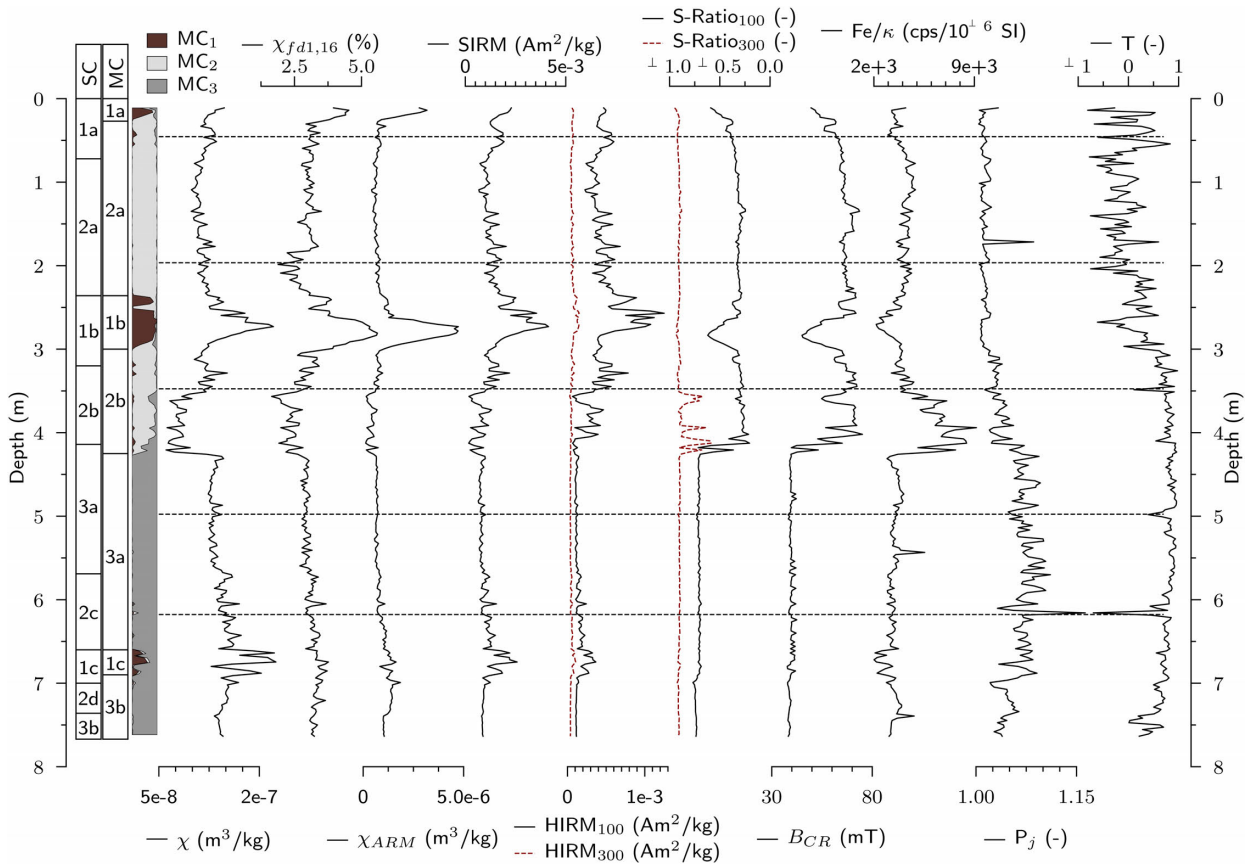

FIGURE 5 | Rock magnetic parameters and results from fuzzy c-means cluster analysis (FCM) based on displayed parameters. From left to right: mass normalised magnetic susceptibility (χ), frequency dependent magnetic susceptibility ($\chi_{fd1,16}$), mass normalised susceptibility of anhysteretic remanent magnetisation (χ_{ARM}), saturation remanent magnetisation (SIRM, acquired in 2.5 T), hard isothermal remanent magnetisation from 100 mT ($HIRM_{100}$, solid black line) and 300 mT ($HIRM_{300}$, red dashed line) backfields, S-Ratio from 100 mT ($S\text{-}Ratio_{100}$, solid black line) and 300 mT ($S\text{-}Ratio_{300}$, red dashed line) backfields, coercivity of remanence (B_{cr}), ratio of iron over volume magnetic susceptibility (Fe/κ), degree of anisotropy (P_j) and shape parameter (T).

to the rest of layer G2 and may represent glacially reworked (brown) sediments as suggested by Schreck et al. (2018) for core PS72/342-1. Alternatively, SC_{1c} could represent diagenetically altered sediments as proposed by März et al. (2012) which would open the possibility that it is layer B3.

(Organic)Geochemistry

The higher (organic) carbon concentrations in the glacial or stadial grey layers in 13PC contrast with Polyak et al.'s (2004) results for cores from the Mendeleev Ridge, where more organic carbon is found in interglacial sediments (NP26 cores; **Figure 1**). Increased erosion and remobilisation of sediments and permafrost carbon from the Siberian Shelf during glacial or deglacial periods can explain the high values in the glacial and stadial sediments in 13PC (Martens et al., 2018). The proximity of 13PC to the shelf and the stable carbon isotope signature support this interpretation. The intervals of increased TOC and sterol concentrations are characterised by more depleted stable isotopic composition of the organic carbon, which suggests a terrestrial source (Goñi et al., 2005). While brassicasterol and β-sitosterol can have both terrigenous or marine origins, brassicasterol is more often considered to be of marine origin whereas β-sitosterol is considered to be of terrigenous origin (Fahl and Stein, 2012). Further support for our interpretation is the $\delta^{13}C$ composition of the organic matter, where lower values (−24 to −25‰) are typically indicative of land-derived carbon, while pure marine organic carbon displays higher values (−21 to −22‰). The low concentrations of organic carbon in the brown layers can also be the result of immediate seafloor consumption of dominantly marine organic matter and release of carbon (as carbon dioxide) due to high microbial activity, which can be linked to increased Mn input (Löwemark et al., 2014).

High Mn concentrations in brown layers in 13PC indicate oxic bottom water conditions (Calvert and Pedersen, 1993, 1996), but we can not infer anoxic or suboxic conditions during the deposition of grey layers. It has been shown that sediment Mn content in the Arctic Ocean is controlled by variable input of Mn that correlates with glacial/interglacial cycles and that bottom waters remained oxic during glacial times (e.g., Löwemark et al., 2014). Elevated concentrations of Mn in pore waters in Arctic Ocean cores show that buried Mn rich layers undergo diagenesis (Meinhardt et al., 2016). Mn (oxyhydr)oxides are

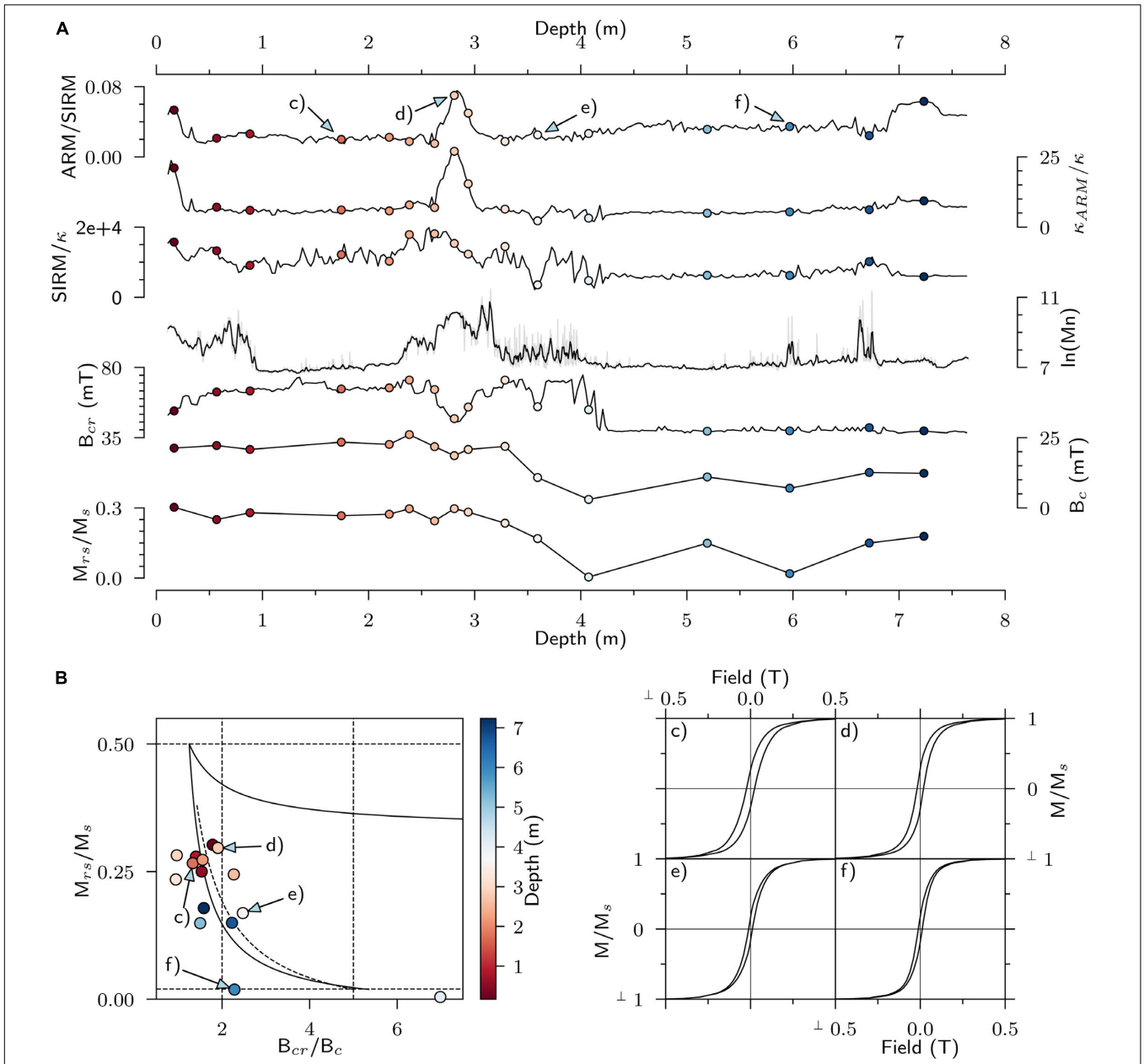

FIGURE 6 | Parameters related to magnetic domain state and mineralogy alongside manganese (Mn) content. **(A)** Downcore variations of, from top to bottom: ratio of anhysteretic remanent magnetisation (ARM) to saturation isothermal remanent magnetisation (SIRM), ratio of ARM susceptibility (κ_{ARM}) to bulk magnetic susceptibility (κ), ratio of SIRM to κ, log normalised Mn content (original: grey line; 10-point moving average: black line), coercivity of remanence (B_{cr}), coercivity (B_c), ratio of saturation remanence (M_{rs}) to saturation magnetisation (M_s). Points show positions of samples that were subjected to hysteresis measurements, coloured by depth (see colour bar in **B**); **(B)** results from hysteresis measurements, coloured by depth; (c–f) hysteresis loops from 4 selected samples [positions are marked in **(A,B)**], slope corrected and cropped to between −0.5 and 0.5 T.

dissolved under suboxic conditions and dissolved Mn migrates upwards to reprecipitate in oxic pore waters. The effect of this process is clearly seen within some of the late Quaternary diamicts identified in sediment cores on the central Lomonosov Ridge. Decimeter scale intervals within these diamicts are dark grey, contain higher concentrations of TOC than surrounding interglacial sediments, with unusual spikes in Mn concentration found at the top and/or base of these intervals (see **Figure 4** in Löwemark et al., 2014). The lowermost brown layer in 13PC, classified as SC_{1c}, may thus be layer B3 that underwent extensive Mn reduction. Mn variations have been used in the Arctic Ocean for cross-core correlation and cyclostratigraphy (Jakobsson et al., 2000; Ye et al., 2019; Park et al., 2020), however, the possibility of asynchronous Mn diagenesis in some areas and downcore

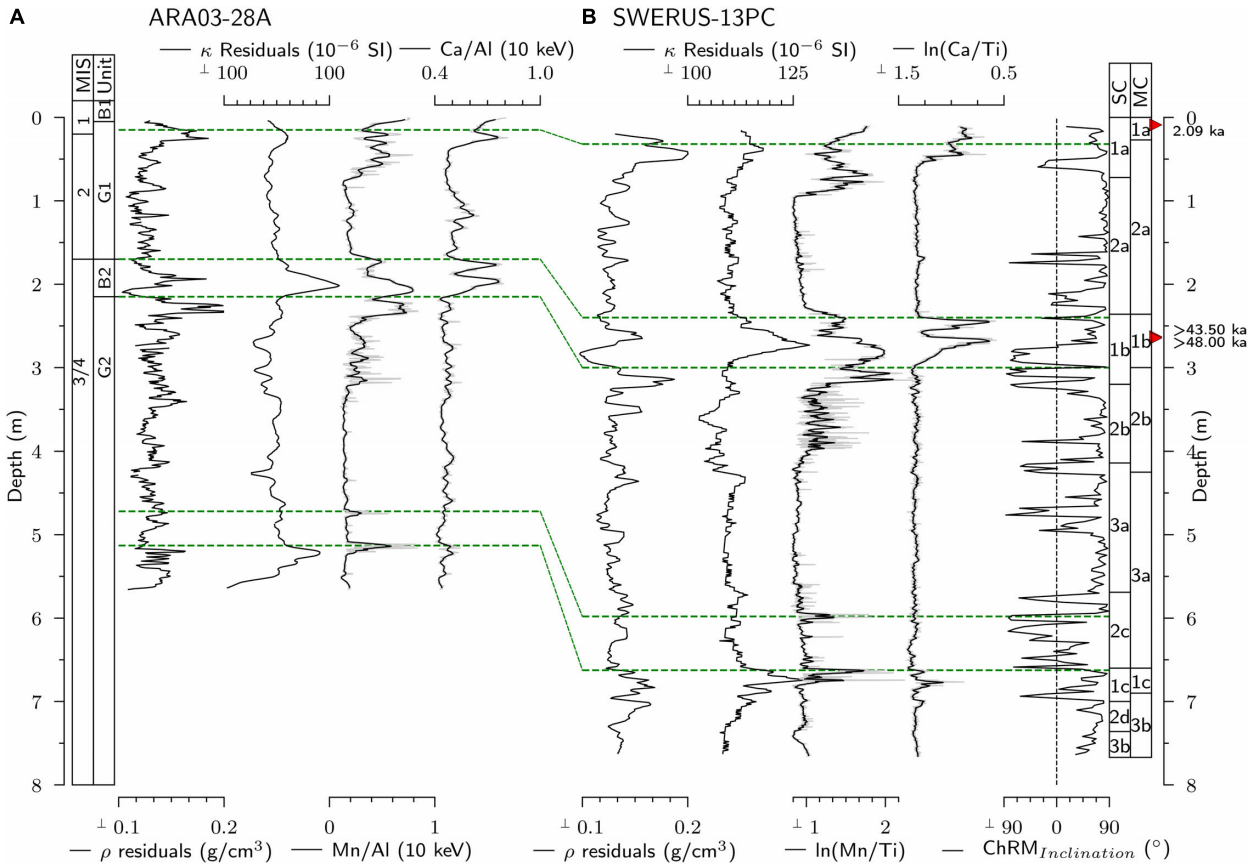

FIGURE 7 | Correlation of sediment cores ARA03-28A (28A) and SWERUS-13PC (13PC; c.f., **Figure 1** for core locations) based on bulk density (ρ) residuals, volume magnetic susceptibility (κ) residuals, manganese (Mn) content and calcium (Ca) content. **(A)** parameters of 28A with the location of marine isotope stage (MIS) boundaries and locations of brown and grey layers as presented by Schreck et al. (2018). **(B)** parameters for SWERUS-13PC with characteristic remanent magnetisation (ChRM) inclination and fuzzy c-means cluster (FCM) results from physical (SC) and magnetic (MC) properties. Position and age of three radiocarbon ages (uncorrected ages; ^{14}C yrs BP) are shown as red triangles.

intervals necessitates considerable scrutiny before using the approach (März et al., 2011; Meinhardt et al., 2016).

Palaeomagnetism

Correlative patterns in downcore inclination changes in Arctic Ocean sediments, whether they are a genuine palaeomagnetic field recording or a diagenetic chemical remanence, are often assumed as evidence of synchronicity (e.g., Frederichs, 1995; Jakobsson et al., 2001; Adler et al., 2009; Polyak et al., 2009). However, when cores are aligned using independent lithological parameters it becomes clear that inclination changes fall within different intervals (O'Regan et al., 2008; Wiers et al., 2019).

The changes in inclination (based on ChRM, 20–60 mT) in core 13PC are difficult to correlate to known geomagnetic field changes in the time frame provided by our (litho)stratigraphic correlation. Some excursional features coincide with globally accepted geomagnetic excursions, e.g., the negative inclination interval at approximately 3 m which dates at around 40 ka (i.e., the age of the Laschamps excursion). On the other hand, given the frequent occurrence of anomalous palaeomagnetic directions in sediments that were probably deposited during periods when no accepted excursions took place, we cannot rule out that apparently genuine features simply coincide with accepted excursions.

Channell and Xuan (2009) and Xuan and Channell (2010) proposed that negative inclinations are carried by a reversed CRM caused by seafloor oxidation of (titano)magnetite to (titano)maghemite, similar to the explanation proposed for organic-poor pelagic sediments in the north Pacific (Kent and Lowrie, 1974; Johnson et al., 1975). However, according to O'Reilly and Banerjee (1966) Ti-content and oxidation state in titanomaghemite need to be large (e.g., for $x = 0.7$, $z > 0.8$) to generate reversed CRM's.

By placing 13PC into the stratigraphic framework of Schreck et al. (2018) (cf., **Figure 7**) we can compare it with core 8JPC (**Figure 8**; Adler et al., 2009; Schreck et al., 2018), one of the cores studied by Xuan and Channell (2010). Here we base core-to-core correlation on sediment physical and geochemical properties, not on the palaeomagnetic inclination records. In comparing 13PC and 8JPC it is evident that 13PC contains many inclination changes in a depth interval that exhibits mostly normal inclinations in the corresponding interval in 8JPC. This

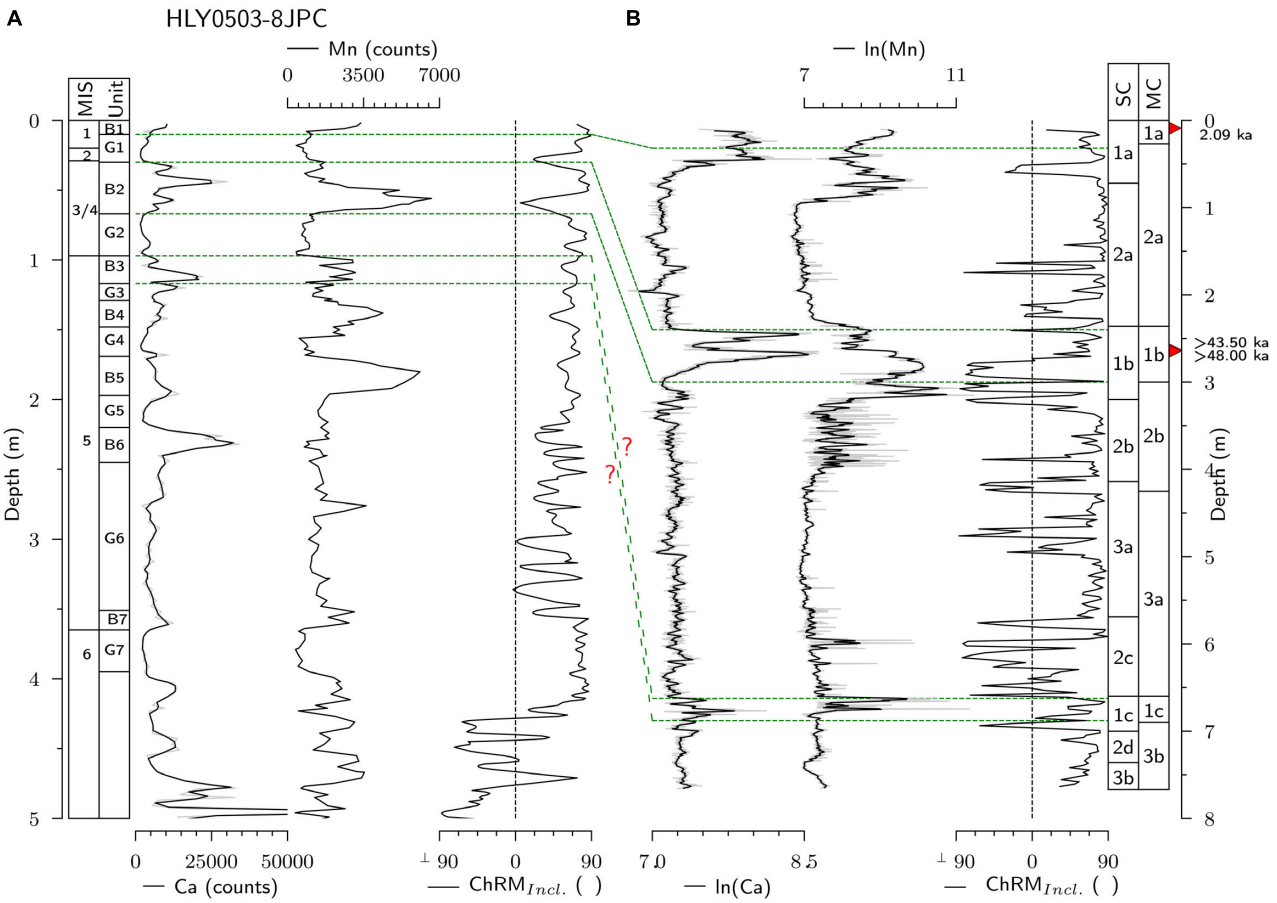

FIGURE 8 | Correlation of sediment cores HLY0503-8JPC (8JPC) and SWERUS-13PC (13PC; c.f., **Figure 1** for core locations) based in the positions of brown layers B1 and B2. Locations of brown layers in 8JPC is based on Schreck et al. (2018) and the correlation presented in **Figure 7** for 13PC. Parameters shown are calcium (Ca), manganese (Mn) and characteristic remanent magnetisation (ChRM) inclination. **(A)** Parameters for 8JPC with the location of marine isotope stage (MIS) boundaries and locations of brown and grey layers. **(B)** Parameters for 13PC with characteristic remanent magnetisation (ChRM) inclination and fuzzy c-means cluster (FCM) results from physical (SC) and magnetic (MC) properties. Position and age of three radiocarbon ages (uncorrected ages; ^{14}C yrs BP) are shown as red triangles.

TABLE 1 | Radiocarbon ages for 13PC.

Depth (m)	Cal. Curve	Uncorrected age (14C years BP)	Calibrated age (years BP)	Source
0.09		2090 ± 30		N. pachyderma
	Marine13		1175 ± 109	
	IntCal13		1512.5 ± 112.5	
2.63		>43500		N. pachyderma
2.645		>48000		N. pachyderma

is an important observation, as the two cores should show a more coherent pattern if widespread seafloor oxidation, caused by low (organic) carbon influx and low sedimentation rates, is the common cause of the inclination changes. Based on the available age estimates, 13PC exhibits higher sedimentation rates than 8JPC but more intervals of negative inclination. The differences in the Ti content and oxidation state of (titano)maghemite between the two cores may explain the incoherency. However, high sedimentation rates in 13PC should reduce the exposure time of (titano)magnetite to oxic bottom waters and hence should lead to a lower degree of oxidation. Additional complications arise from the fact that 8JPC's record was generated using measurements of u-channels, which smooths the signal.

Rock Magnetism

Based on FCM results on rock magnetic parameters (MC), the magnetic properties of 13PC seem to deviate somewhat from lithological changes (SC), especially below 4.15 m, which is due to the lower concentration of minerals with B_{cr} of 100–300 mT. The shift in magnetic properties may reflect a subtle diagenetic

process, since there is no comparable prominent feature in the lithostratigraphy (**Figure 2**). The sharp increase in Fe/κ just above 4.15 m (**Figure 5**) is indicative of (titano)magnetite dissolution (Funk et al., 2003; Korff et al., 2016) and may mark the current or a former Fe-Redox boundary. Changes in Fe/κ between 4.15 and 3.0 m are concurrent with minima in χ, χ_{ARM} and a downcore decrease in high coercivity magnetic minerals ($HIRM_{100}$). Above the indicated dissolution front, we find a correlation of $\chi_{fd1,16}$ (r = 0.54; **Figure 9**) and χ_{ARM} (r = 0.59; **Figure 9**) with Mn that may be the result of iron (oxyhydr)oxide enrichment within a narrow band in brown layers SC_{1a} and SC_{1b} (MC_{1b}) and potentially to a lesser extent in layer SC_{1c} (MC_{1c}).

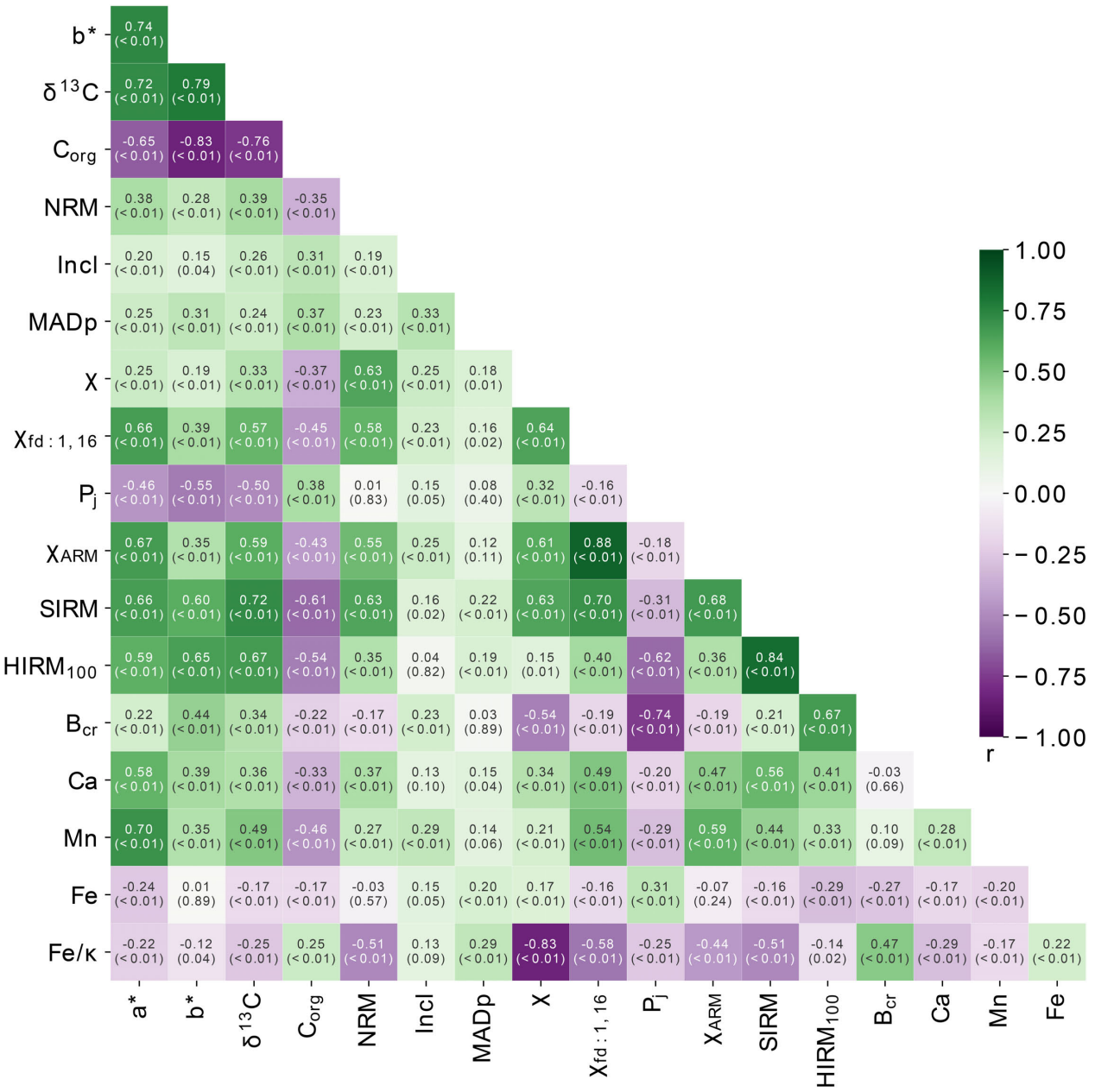

FIGURE 9 | Correlation matrix of physical, chemical, palaeomagnetic and rock magnetic properties of SWERUS-13PC (13PC). Pearson correlation coefficients (r) are displayed as numbers and colour by value, numbers in brackets are p-values for each correlation. Parameters are: green-red (a*) and blue-yellow (b*) colour components, total organic carbon (C_{org}), stable carbon isotopes ($\delta^{13}C$), natural remanent magnetisation (NRM), characteristic remanent magnetisation inclination (Incl), median angular deviation (MAD_p; prolate), mass normalised magnetic susceptibility (χ), frequency dependent magnetic susceptibility ($\chi_{fd:1,16}$), degree of anisotropy (P_j; magnetic fabric), susceptibility of anhysteretic remanent magnetisation (χ_{ARM}), saturation isothermal remanent magnetisation (SIRM), hard isothermal remanent magnetisation ($HIRM_{100}$; from 100 mT backfield), coercivity of remanence (B_{cr}), calcium (Ca), manganese (Mn), iron (Fe) and the ratio of iron to volume magnetic susceptibility (Fe/κ).

This enrichment may be facilitated by the upward migration of released iron from the underlying dissolution front (Myers and Nealson, 1988; **Figure 6**). The strong correlation of $\chi_{fd1,16}$ and χ_{ARM} ($r = 0.88$; **Figure 9**) supports the interpretation of mineral authigenesis within the sediment column.

The low concentration of high coercivity minerals below 4.15 m may be due to dissolution of one or more diagenetic-authigenic magnetic phases. Given previous work on Arctic Ocean sediments (Channell and Xuan, 2009; Xuan and Channell, 2010), a potential candidate for this phase may be coatings of (titano)maghemite that formed during seafloor oxidation. Smirnov and Tarduno (2000) show that pelagic sediments from the western equatorial Pacific contain (titano)magnetite coated in (titano)maghemite, and the coating is dissolved below the Fe-Redox boundary. The changes in hysteresis parameters Smirnov and Tarduno (2000) show are comparable to the ones in 13PC (**Figure 6**). The migration of redox fronts due to changing organic matter and Mn input across glacial-interglacial cycles (März et al., 2012) may facilitate dissolution of previously precipitated or deposited iron minerals and upward migration of released iron. To test this hypothesis, pore water ion concentration of Mn and Fe are necessary, which do not exist for 13PC. Mn pore water concentrations from nearby core PS72/343-1 (**Figure 1**) rise below B3 or approximately 3 m, and display the reduction of Mn (oxyhydr)oxides below this depth (März et al., 2011).

Integrating Magnetic and Chemical Changes

Henshaw and Merrill (1980) showed that the anomalous palaeomagnetic record in the north Pacific is more likely due to the formation of an authigenic ferromanganese phase than to maghemitisation. Substitution of Mn into the spinel lattice of (titano)magnetite can lead to self-reversals (Henshaw and Merrill, 1980), although this mechanism has not received much attention. In the Arctic Ocean, the enhanced deposition of Mn-oxides and enrichment of trace metals during interglacials shifts the Mn-Redox boundary upwards, close to the sediment/water interface. This shift triggers Mn cycling (März et al., 2011) and associated enrichment of iron (oxyhydr)oxides (Fe_{ox1} and Fe_{ox2} in März et al., 2012). Reduced Mn input during glacials results in potential diagenetic Mn redistribution in deeper sediment layers

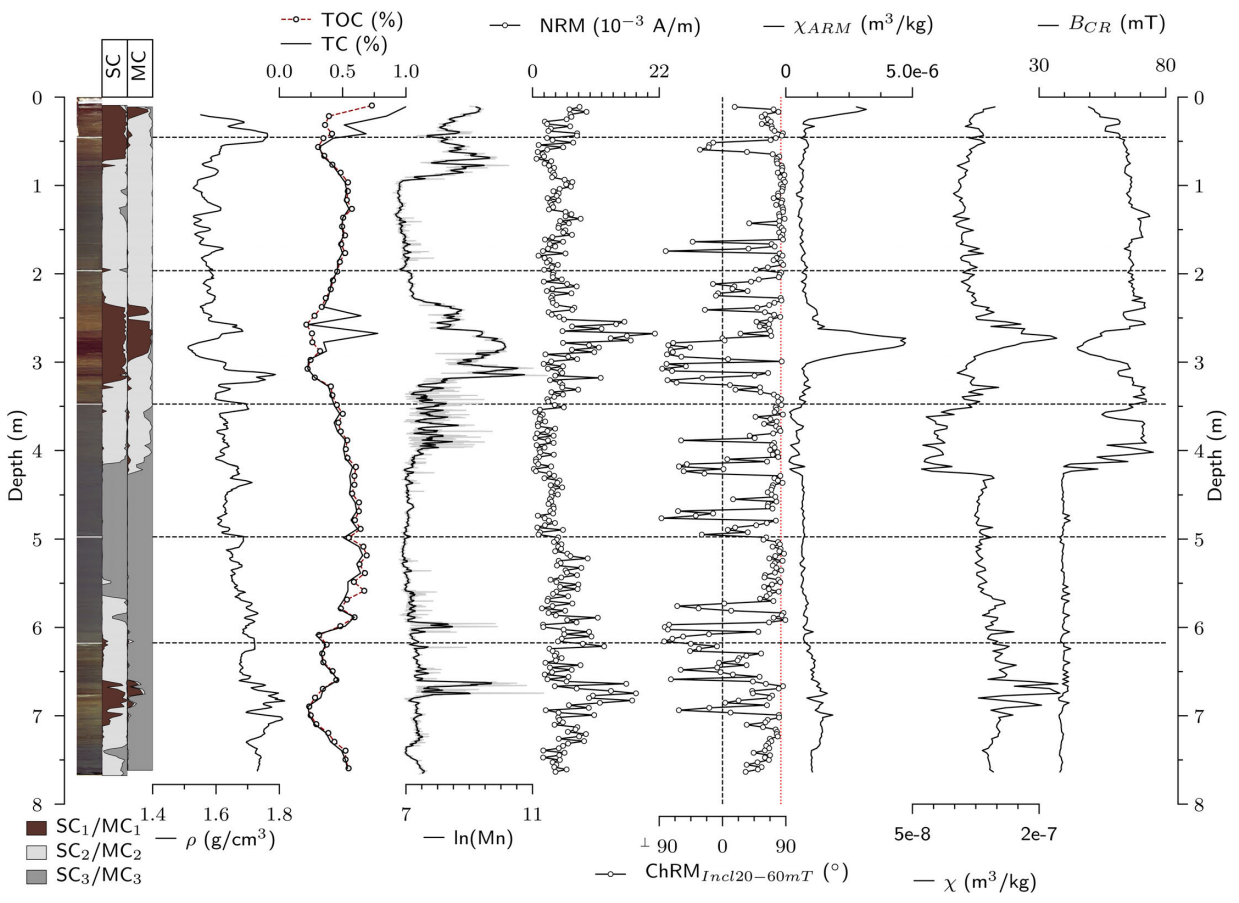

FIGURE 10 | Summary figure that displays the most important parameters of 13PC for comparison. From left to right: line-scan images, fuzzy c-means cluster (FCM) results from physical (SC) and magnetic (MC) properties, density (ρ), total carbon (TC) and total organic carbon (TOC), relative manganese (Mn) content, natural remanent magnetisation (NRM) intensity, inclination of characteristic remanent magnetisation based on principal component analysis between 20 and 60 mT, mass normalised susceptibility of anhysteretic remanent magnetisation (χ_{ARM}), mass normalised magnetic susceptibility (χ) and coercivity of remanence (B_{CR}).

that may lead to post-depositional biogeochemical Fe cycling and (titano)magnetite/maghemite formation (März et al., 2012).

März et al. (2012) did not find a direct relationship between Fe_{mag} [(titano)magnetite, (titano)maghemite] and χ, hinting at a different magnetic carrier in the Mn-rich (brown) layers. Similarly, in 13PC Mn shows weak to zero correlation with magnetic susceptibility (r = 0.21; **Figure 9**) even though Mn has been shown to be linked to iron reduction (Myers and Nealson, 1988; Smirnov and Tarduno, 2000). The precipitation of ferromanganese oxides, congruent to what was proposed for north Pacific sediments (Henshaw and Merrill, 1980), is conceivable in the Arctic Ocean. The formation of these oxides would be linked to Mn influx and changing redox conditions (**Figure 6**) and may present an alternative hypothesis to seafloor oxidation or genuine recordings of the palaeomagnetic field, and would explain the unusual palaeomagnetic record in 13PC. März et al. (2012) used the same extraction method for the Fe_{ox1} phase as Henshaw and Merrill (1980) used to dissolve a magnetic manganese-iron phase. The Fe_{ox1} phase could, therefore, contain an unidentified magnetic ferromanganese phase and the correlation of Fe_{ox1} to Mn content found by März et al. (2012) supports our hypothesis of a link between the anomalous palaeomagnetic records and the presence of ferromanganese oxides.

Neither lithology nor magnetic mineral composition show a strong correlation to the ChRM inclination. On the other hand, there is a weak correlation between ChRM inclination and Mn (r = −0.29; **Figure 9**). As expected, NRM intensity is more strongly affected by changes in the composition of the magnetic mineral assemblage (SIRM – NRM, r = 0.64; χ – NRM, r = 0.61; χ_{ARM} – NRM, r = 0.58; **Figure 9**). The low correlation coefficient between Mn and ChRM inclination may be a result of the dominantly bimodal nature of the inclination data and ongoing processes driving Mn redistribution within the sediments. A more robust approach to test the correlation was applied by calculating the circular-linear correlation coefficient (e.g., Mardia and Jupp, 2009), however, this results in the same coefficient (r = −0.29) for Mn and ChRM inclination. Yet, correlation of the filtered ChRM inclination with Mn yields a larger coefficient (r = −0.47). On the other hand, visual inspection of Mn and ChRM inclination reveals some coherence between negative inclinations and increased Mn values (**Figure 10**).

Non-steady-state diagenesis (Kasten et al., 2004), driven by changes in sediment input and bottom water ventilation, may facilitate upward migration of released ions that further distort the magnetic record. Changes in sea level across interglacial/glacial cycles that move the position of (Arctic) Atlantic water may also impact the position of redox boundaries, especially in water depths of <1500 m where the lower boundary of the Atlantic water layer generally resides today (Rudels, 2009).

CONCLUSION

Sediment core 13PC from the Arlis Plateau, western Arctic Ocean, displays a perplexing palaeomagnetic record that is common to many Arctic Ocean sediment cores. By integrating 13PC into the regional lithostratigraphy, we are able to show that magnetic inclination changes were not recorded synchronously across the region. This finding means that one should not use inclination changes in Arctic Ocean sediments as magnetostratigraphic tie points because there is no common primary, regional lithological control over the palaeomagnetic record. Our combined magnetic and chemical approach suggest that seafloor oxidation of (titano)magnetite to (titano)maghemite takes place as proposed for other cores from the western Arctic Ocean (Channell and Xuan, 2009; Xuan and Channell, 2010). However, deeper diagenetic changes that are linked to Mn-oxide and Fe-oxide reduction may completely or partially remove (titano)maghemite coatings formed by seafloor oxidation. This challenges the ubiquitous role of seafloor oxidation as a mechanism for reversed palaeomagnetic inclinations in Arctic Ocean sediments. Our study suggests that the palaeomagnetically important diagenetic changes take place between 3 and 4 meters below the seafloor. The main lines of evidence are (1) changes in the magnetic mineral assemblage in the form of the absence of a > 100 mT (but <300 mT) magnetic mineral component, (2) changes in the magnetic fabric and (3) the identification of a (titano)magnetite/(titano)maghemite dissolution zone by Fe/κ. Peaks in magnetic parameters (χ, χ_{ARM}, SIRM) display an increased concentration of a fine-grained (high $\chi_{fd1,16}$) magnetic phase within Mn-rich brown layers in 13PC. These measurements point to the precipitation of authigenic magnetic ferromanganese minerals and hence the acquisition of a secondary CRM that may be superimposed upon (and partially replace) a primary NRM. This process potentially occurs in addition to seafloor oxidation of (titano)magnetite to (titano)maghemite or may even be facilitated by initial oxidation. The position of high χ_{ARM}, high Mn layers suggests a link between magnetic mineral diagenesis and glacial/interglacial cycles as expressed by enhanced Mn precipitation during interglacials.

To summarise, our study of Arctic Ocean sediments leads us to hypothesise that there is a connection between the Arctic Mn-cycle and magnetic mineral diagenesis, which leads to the perplexing palaeomagnetic record. The hypothesis can be tested through a thorough investigation of (1) chemical changes related to diagenetic redox horizons, solid phase (mineralogy of magnetic minerals) and pore water measurements, combined with (2) palaeomagnetic and rock magnetic investigations.

DATA AVAILABILITY STATEMENT

The data are available on PANGAEA (https://www.pangaea.de/, keyword: SWERUS-C3).

AUTHOR CONTRIBUTIONS

SW, IS, MO'R, and BA developed the concept for the manuscript. MO'R was involved in the organisation and implementation of the icebreaker led expedition that

recovered the sediment core presented in this manuscript, including the generation of shipboard data. SW performed all presented palaeo- and rock magnetic measurements and colour measurements. CP contributed sterol analyses. All authors contributed to the writing and editing of the manuscript.

FUNDING

Funding for this project was provided by the Swedish Research Council (VR), Grant 2014-4108.

ACKNOWLEDGMENTS

We would like to thank the captain and crew of I/B Oden for their valuable work during the SWERUS-C3 expedition in 2014. Further, thanks to Thomas Frederichs of the University of Bremen for his support during laboratory measurements at the Laboratory for Palaeomagnetic, Rock and Environmental Magnetics. Thanks to Daniel Hedlund of the Ångström Laboratory, Uppsala University, Sweden, for his help with the magnetic hysteresis measurements. We also thank Michael Schreck and Seung-Il Nam for providing the data for sediment core ARA03B-28A.

REFERENCES

Adler, R. E., Polyak, L., Ortiz, J. D., Kaufman, D. S., Channell, J. E. T., Xuan, C., et al. (2009). Sediment record from the western arctic ocean with an improved late quaternary age resolution: HOTRAX core HLY0503-8JPC, Mendeleev Ridge. *Global Planet. Change* 68, 18–29. doi: 10.1016/j.gloplacha.2009.03.026

Backman, J., Jakobsson, M., Frank, M., Sangiorgi, F., Brinkhuis, H., Stickley, C., et al. (2008). Age model and core-seismic integration for the cenozoic arctic coring expedition sediments from the lomonosov ridge. *Paleoceanography* 23:A1S03. doi: 10.1029/2007pa001476

Backman, J., Jakobsson, M., Lovlie, R., Polyak, L., and Febo, L. A. (2004). Is the central Arctic Ocean a sediment starved basin? *Quat. Sci. Rev.* 23, 1435–1454. doi: 10.1016/j.quascirev.2003.12.005

Calvert, S. E., and Pedersen, T. F. (1993). Geochemistry of Recent oxic and anoxic marine sediments: implications for the geological record. *Mar. Geol.* 113, 67–88. doi: 10.1016/0025-3227(93)90150-T

Calvert, S. E., and Pedersen, T. F. (1996). Sedimentary geochemistry of manganese; implications for the environment of formation of manganiferous black shales. *Econ. Geol.* 91, 36–47. doi: 10.2113/gsecongeo.91.1.36

Cande, S. C., and Kent, D. V. (1995). Revised calibration of the geomagnetic polarity timescale for the Late Cretaceous and Cenozoic. *J. Geophys. Res.* 100:6093. doi: 10.1029/94jb03098

Channell, J. E. T., and Xuan, C. (2009). Self-reversal and apparent magnetic excursions in arctic sediments. *Earth Planet. Sci. Lett.* 284, 124–131. doi: 10.1016/j.epsl.2009.04.020

Clark, D. L. (1970). Magnetic reversals and sedimentation rates in the arctic ocean. *Geol. Soc. Am. Bull.* 81, 3129–3134.

Day, R., Fuller, M., and Schmidt, V. A. (1977). Hysteresis properties of titanomagnetites: grain-size and compositional dependence. *Phys. Earth Planet. Inter.* 13, 260–267. doi: 10.1016/0031-9201(77)90108-x

Fahl, K., and Stein, R. (2012). Modern seasonal variability and deglacial/holocene change of central Arctic Ocean sea-ice cover: new insights from biomarker proxy records. *Earth Planet. Sci. Lett.* 35, 123–133. doi: 10.1016/j.epsl.2012.07.009

Frederichs, T. (1995). Regional and temporal variations of rock magnetic parameters in Arctic marine sediments. *Ber. Polarforschung* 164, 1–212.

Funk, J. A., Dobeneck, T., von, Wagner, T., and Kasten, S. (2003). "Late quaternary sedimentation and early diagenesis in the equatorial atlantic ocean: patterns, trends and processes deduced from rock magnetic and geochemical records," in *The South Atlantic in the Late Quaternary*, eds G. Wefer, S. Mulitza, and V. Ratmeyer (Berlin: Springer), 461–497. doi: 10.1007/978-3-642-18917-3_21

Goñi, M. A., Yunker, M. B., Macdonald, R. W., and Eglinton, T. I. (2005). The supply and preservation of ancient and modern components of organic carbon in the Canadian Beaufort Shelf of the Arctic Ocean. *Mar. Chem.* 93, 53–73. doi: 10.1016/j.marchem.2004.08.001

Hein, J. R., Konstantinova, N., Mikesell, M., Mizell, K., Fitzsimmons, J. N., Lam, P. J., et al. (2017). Arctic deep water ferromanganese-oxide deposits reflect the unique characteristics of the arctic ocean. *Geochem. Geophys. Geosyst.* 18, 3771–3800. doi: 10.1002/2017GC007186

Henshaw, P. C., and Merrill, R. T. (1980). Magnetic and chemical changes in marine sediments. *Rev. Geophys.* 18, 483–504. doi: 10.1029/RG018i002p00483

Hillaire-Marcel, C., Ghaleb, B., Vernal, A. D., Maccali, J., Cuny, K., Jacobel, A., et al. (2017). A new chronology of late quaternary sequences from the central arctic ocean based on "extinction ages" of their excesses in 231 Pa and 230 Th. *Geochem. Geophys. Geosyst.* 18, 4573–4585. doi: 10.1002/2017gc007050

Hrouda, F. (2011). Models of frequency-dependent susceptibility of rocks and soils revisited and broadened. *Geophys. J. Int.* 187, 1259–1269. doi: 10.1111/j.1365-246x.2011.05227.x

Hrouda, F., and Kahan, S. (1991). The magnetic fabric relationship between sedimentary and basement nappes in the High Tatra Mountains, N. Slovakia. *J. Struct. Geol.* 13, 431–442. doi: 10.1016/0191-8141(91)90016-C

Jakobsson, M., Lovlie, R., Al-Hanbali, H., Arnold, E., Backman, J., and Mörth, M. (2000). Manganese and color cycles in Arctic Ocean sediments constrain Pleistocene chronology. *Geology* 28, 23–26. doi: 10.1130/0091-76132000

Jakobsson, M., Løvlie, R., Arnold, E. M., Backman, J., Polyak, L., Knutsen, J.-O., et al. (2001). Pleistocene stratigraphy and paleoenvironmental variation from Lomonosov Ridge sediments, central Arctic Ocean. *Global Planet. Change* 31, 1–22. doi: 10.1016/s0921-8181(01)00110-2

Jakobsson, M., Mayer, L., Coakley, B., Dowdeswell, J. A., Forbes, S., Fridman, B., et al. (2012). The international bathymetric chart of the arctic ocean (IBCAO) version 3.0. *Geophys. Res. Lett.* 39:L12609. doi: 10.1029/2012gl052219

Jakobsson, M., Nilsson, J., Anderson, L., Backman, J., Björk, G., Cronin, T. M., et al. (2016). Evidence for an ice shelf covering the central arctic ocean during the penultimate glaciation. *Nat. Commun.* 7:10365. doi: 10.1038/ncomms10365

Jelinek, V. (1981). Characterization of the magnetic fabric of rocks. *Tectonophysics* 79, T63–T67. doi: 10.1016/0040-1951(81)90110-4

Johnson, H. P., Kinoshita, H., and Merrill, R. T. (1975). Rock magnetism and paleomagnetism of some north pacific deep-sea sediments. *GSA Bull.* 86, 412–420.

Jovane, L., Acton, G., Florindo, F., and Verosub, K. L. (2008). Geomagnetic field behavior at high latitudes from a paleomagnetic record from Eltanin core 27–21 in the Ross Sea sector, Antarctica. *Earth Planet. Sci. Lett.* 267, 435–443. doi: 10.1016/j.epsl.2007.12.006

Kasten, S., Zabel, M., Heuer, V., and Hensen, C. (2004). "Processes and signals of nonsteady-state diagenesis in deep-sea sediments and their pore waters," in *The South Atlantic in the Late Quaternary: Reconstruction of Material Budgets and Current Systems*, eds G. Wefer, S. Mulitza, and V. Ratmeyer (Berlin: Springer), 431–459. doi: 10.1007/978-3-642-18917-3_20

Kent, D. V., and Lowrie, W. (1974). Origin of magnetic instability in sediment cores from the central North Pacific. *J. Geophys. Res. (1896-1977)* 79, 2987–3000. doi: 10.1029/JB079i020p02987

Kirschvink, J. L. (1980). The least-squares line and plane and the analysis of palaeomagnetic data. *Geophys. J. Int.* 62, 699–718. doi: 10.1111/j.1365-246x.1980.tb02601.x

Kono, M., and Roberts, P. H. (2002). Recent geodynamo simulations and observations of the geomagnetic field. *Rev. Geophys.* 40, 4-1-4-53. doi: 10.1029/2000RG000102

Konstantinova, N., Cherkashov, G., Hein, J. R., Mirão, J., Dias, L., Madureira, P., et al. (2017). Composition and characteristics of the ferromanganese crusts from the western Arctic Ocean. *Ore Geol. Rev.* 87, 88–99. doi: 10.1016/j.oregeorev.2016.09.011

Konstantinova, N., Hein, J. R., Gartman, A., Mizell, K., Barrulas, P., Cherkashov, G., et al. (2018). Mineral phase-element associations based on sequential leaching of ferromanganese crusts, amerasia basin arctic ocean. *Minerals* 8:460. doi: 10.3390/min8100460

Korff, L., Dobeneck, T. V., Frederichs, T., Kasten, S., Kuhn, G., Gersonde, R., et al. (2016). Cyclic magnetite dissolution in Pleistocene sediments of the abyssal Northwest Pacific Ocean: evidence for glacial oxygen depletion and carbon trapping. *Paleoceanography* 31, 600–624. doi: 10.1002/2015pa002882

Lawrence, K. P., Tauxe, L., Staudigel, H., Constable, C. G., Koppers, A., McIntosh, W., et al. (2009). Paleomagnetic field properties at high southern latitude. *Geochem. Geophys. Geosystems* 10, 1–27. doi: 10.1029/2008gc002072

Liu, J., Shi, X., Liu, Y., Liu, Q., Liu, Y., Zhang, Q., et al. (2019). A thick negative polarity anomaly in a sediment core from the central arctic ocean: geomagnetic excursion versus reversal. *J. Geophys. Res. Solid Earth* 124, 10687–10703. doi: 10.1029/2019JB018073

Liu, Q., Roberts, A. P., Torrent, J., Horng, C.-S., and Larrasoaña, J. C. (2007). What do the HIRM and S-ratio really measure in environmental magnetism? *Geochem. Geophys. Geosyst.* 8, 1–10. doi: 10.1029/2007gc001717

Lougheed, B. C., Metcalfe, B., Ninnemann, U. S., and Wacker, L. (2018). Moving beyond the age–depth model paradigm in deep-sea palaeoclimate archives: dual radiocarbon and stable isotope analysis on single foraminifera. *Climate Past* 14, 515–526. doi: 10.5194/cp-14-515-2018

Love, J. J. (2007). "Principal component analysis in paleomagnetism," in *Encyclopedia of Geomagnetism and Paleomagnetism*, eds D. Gubbins and E. Herrero-Bervera (Dordrecht: Springer), 845–850. doi: 10.1007/978-1-4020-4423-6_271

Löwemark, L., März, C., O'Regan, M., and Gyllencreutz, R. (2014). Arctic ocean mn-stratigraphy: genesis, synthesis and inter-basin correlation. *Quat. Sci. Rev.* 92, 97–111. doi: 10.1016/j.quascirev.2013.11.018

Mardia, K. V., and Jupp, P. E. (2009). *Directional Statistics*. Hoboken, NJ: John Wiley & Sons.

Marino, R. J., and Ellwood, B. B. (1978). Anomalous magnetic fabric in sediments which record an apparent geomagnetic field excursion. *Nature* 274, 581–582. doi: 10.1038/274581a0

Martens, J., Wild, B., Pearce, C., Tesi, T., Andersson, A., Bröder, L., et al. (2018). Remobilization of old permafrost carbon to chukchi sea sediments during the end of the last deglaciation. *Global Biogeochem. Cycles* 33, 2–14. doi: 10.1029/2018GB005969

März, C., Poulton, S. W., Brumsack, H.-J., and Wagner, T. (2012). Climate-controlled variability of iron deposition in the Central Arctic Ocean (southern Mendeleev Ridge) over the last 130,000years. *Chem. Geol.* 33, 116–126. doi: 10.1016/j.chemgeo.2012.08.015

März, C., Stratmann, A., Matthiessen, J., Meinhardt, A.-K., Eckert, S., Schnetger, B., et al. (2011). Manganese-rich brown layers in arctic ocean sediments: composition, formation mechanisms, and diagenetic overprint. *Geochim. Cosmochim. Acta* 75, 7668–7687. doi: 10.1016/j.gca.2011.09.046

McKinney, W. (2010). "Data structures for statistical computing in python," in *Proceedings of the 9th Python in Science Conference*, eds S. van der Walt and J. Millman (Austin: SciPy Society), 51–56.

Meinhardt, A.-K., März, C., Schuth, S., Lettmann, K. A., Schnetger, B., Wolff, J.-O., et al. (2016). Diagenetic regimes in arctic ocean sediments: implications for sediment geochemistry and core correlation. *Geochim. Cosmochim. Acta* 188, 125–146. doi: 10.1016/j.gca.2016.05.032

Myers, C. R., and Nealson, K. H. (1988). Microbial reduction of manganese oxides: interactions with iron and sulfur. *Geochim. Cosmochim. Acta* 52, 2727–2732. doi: 10.1016/0016-7037(88)90041-5

Nowaczyk, N. R., Frederichs, T. W., Eisenhauer, A., and Gard, G. (1994). Magnetostratigraphic data from late quaternary sediments from the yermak plateau, arctic ocean: evidence for four geomagnetic polarity events within the last 170 Ka of the brunhes chron. *Geophys. J. Int.* 117, 453–471. doi: 10.1111/j.1365-246x.1994.tb03944.x

Nowaczyk, N. R., Frederichs, T. W., Kassens, H., Nørgaard-Pedersen, N., Spielhagen, R. F., Stein, R., et al. (2001). Sedimentation rates in the makarov basin, central arctic ocean: a paleomagnetic and rock magnetic approach. *Paleoceanography* 16, 368–389. doi: 10.1029/2000pa000521

Nowaczyk, N. R., and Knies, J. (2000). Magnetostratigraphic results from the eastern Arctic Ocean: AMS 14 C ages and relative palaeointensity data of the Mono Lake and Laschamp geomagnetic reversal excursions. *Geophys. J. Int.* 140, 185–197. doi: 10.1046/j.1365-246x.2000.00001.x

O'Regan, M., King, J., Backman, J., Jakobsson, M., Pälike, H., Moran, K., et al. (2008). Constraints on the pleistocene chronology of sediments from the lomonosov ridge. *Paleoceanography* 23:A1S19. doi: 10.1029/2007pa001551

O'Reilly, W., and Banerjee, S. K. (1966). Oxidation of titanomagnetites and self-reversal. *Nature* 211:26. doi: 10.1038/211026a0

Park, K., Kim, J.-H., Asahi, H., Polyak, L., Khim, B.-K., Schreck, M., et al. (2020). Cyclostratigraphic age constraining for quaternary sediments in the makarov basin of the western arctic ocean using manganese variability. *Quat. Geochronol.* 55:101021. doi: 10.1016/j.quageo.2019.101021

Paterson, G. A., Zhao, X., Jackson, M., and Heslop, D. (2018). Measuring, processing, and analyzing hysteresis data. *Geochem. Geophys. Geosyst.* 19, 1925–1945. doi: 10.1029/2018GC007620

Peters, C., and Dekkers, M. J. (2003). Selected room temperature magnetic parameters as a function of mineralogy, concentration and grain size. *Phys. Chem. Earth Parts A/B/C* 28, 659–667. doi: 10.1016/s1474-7065(03)00120-7

Pokorný, J., Pokorný, P., Suza, P., and Hrouda, F. (2011). "A multi-function kappabridge for high precision measurement of the AMS and the variations of magnetic susceptibility with field, temperature and frequency," in *The Earth\textquotesingles Magnetic Interior*, eds E. Petrovský, E. Herrero-Bervera, T. Harinarayana, and D. Ivers (Berlin: Springer), 293–301. doi: 10.1007/978-94-007-0323-0_20

Polyak, L., Bischof, J., Ortiz, J. D., Darby, D. A., Channell, J. E. T., Xuan, C., et al. (2009). Late quaternary stratigraphy and sedimentation patterns in the western arctic ocean. *Global Planet. Change* 68, 5–17. doi: 10.1016/j.gloplacha.2009.03.014

Polyak, L., Curry, W. B., Darby, D. A., Bischof, J., and Cronin, T. M. (2004). Contrasting glacial/interglacial regimes in the western Arctic Ocean as exemplified by a sedimentary record from the Mendeleev Ridge. *Palaeogeogr. Palaeoclimatol. Palaeoecol.* 203, 73–93. doi: 10.1016/s0031-0182(03)00661-8

Roberts, A. P. (2015). Magnetic mineral diagenesis. *Earth-Sci. Rev.* 151, 1–47. doi: 10.1016/j.earscirev.2015.09.010

Roberts, A. P., Tauxe, L., Heslop, D., Zhao, X., and Jiang, Z. (2018). A critical appraisal of the "day" diagram. *J. Geophys. Res. Solid Earth* 123, 2618–2644. doi: 10.1002/2017JB015247

Roberts, A. P., and Winklhofer, M. (2004). Why are geomagnetic excursions not always recorded in sediments? Constraints from post-depositional remanent magnetization lock-in modelling. *Earth Planet. Sci. Lett.* 227, 345–359. doi: 10.1016/j.epsl.2004.07.040

Rudels, B. (2009). *Arctic Ocean Circulation. In Encyclopedia of Ocean Sciences*. Amsterdam: Elsevier, 211–225. doi: 10.1016/b978-012374473-9.00601-9

Schreck, M., Nam, S.-I., Polyak, L., Vogt, C., Kong, G.-S., Stein, R., et al. (2018). Improved pleistocene sediment stratigraphy and paleoenvironmental implications for the western Arctic Ocean off the East Siberian and Chukchi margins. *Arktos* 4:21. doi: 10.1007/s41063-018-0057-8

Schulz, H. D., and Zabel, M. (eds). (2006). *Marine Geochemistry*, 2nd ed. Berlin: Springer-Verlag, doi: 10.1007/3-540-32144-6

Schwämmle, V., and Jensen, O. N. (2010). A simple and fast method to determine the parameters for fuzzy c–means cluster analysis. *Bioinformatics* 26, 2841–2848. doi: 10.1093/bioinformatics/btq534

Smirnov, A. V., and Tarduno, J. A. (2000). Low-temperature magnetic properties of pelagic sediments (Ocean Drilling Program Site 805C): tracers of maghemitization and magnetic mineral reduction. *J. Geophys. Res.* 105, 16457–16471. doi: 10.1029/2000jb900140

Snowball, I., Almqvist, B., Lougheed, B. C., Wiers, S., Obrochta, S., and Herrero-Bervera, E. (2019). Coring induced sediment fabrics at IODP Expedition 347 Sites M0061 and M0062 identified by anisotropy of magnetic susceptibility (AMS): criteria for accepting palaeomagnetic data. *Geophys. J. Int.* 217, 1089–1107. doi: 10.1093/gji/ggz075

Spielhagen, R. F., Baumann, K.-H., Erlenkeuser, H., Nowaczyk, N. R., Norgaard-Pedersen, N., Vogt, C., et al. (2004). Arctic ocean deep-sea record of northern eurasian ice sheet history. *Quat. Sci. Rev.* 23, 1455–1483. doi: 10.1016/j.quascirev.2003.12.015

Steuerwald, B. A., Clark, D. L., and Andrew, J. A. (1968). Magnetic stratigraphy and faunal patterns in Arctic ocean sediments. *Earth Planet. Sci. Lett.* 5, 79–85. doi: 10.1016/s0012-821x(68)80018-4

van der Walt, S., Colbert, S. C., and Varoquaux, G. (2011). The NumPy array: a structure for efficient numerical computation. *Comput. Sci. Eng.* 13, 22–30. doi: 10.1109/MCSE.2011.37

Warner, J., Sexauer, J., scikit-fuzzy, twmeggs, Alexander, M. S., Unnikrishnan, A., et al. (2017). JDWarner/scikit-fuzzy: scikit-Fuzzy 0.3.1 (Version 0.3.1). *Zenodo* . doi: 10.5281/zenodo.1002946

Wiers, S., Snowball, I., O'Regan, M., and Almqvist, B. (2019). Late pleistocene chronology of sediments from the yermak plateau and uncertainty in dating based on geomagnetic excursions. *Geochem. Geophys. Geosyst.* 20, 3289–3310. doi: 10.1029/2018GC007920

Xuan, C., and Channell, J. E. T. (2010). Origin of apparent magnetic excursions in deep-sea sediments from Mendeleev-Alpha Ridge, Arctic Ocean. *Geochem. Geophys. Geosyst.* 11, 1–17. doi: 10.1029/2009gc002879

Ye, L., März, C., Polyak, L., Yu, X., and Zhang, W. (2019). Dynamics of manganese and cerium enrichments in arctic ocean sediments: a case study from the alpha ridge. *Front. Earth Sci.* 6:236. doi: 10.3389/feart.2018.00236

Zijderveld, J. D. A. (1967). "AC demagnetization of rocks: analysis of results," in *Methods in Palaeomagnetism*, eds S. K. Runcorn, K. M. Creer, and D. W. Collinson (Amsterdam: Elsevier), 254–286. doi: 10.1016/b978-1-4832-2894-5.50049-5

Conflict of Interest: The authors declare that the research was conducted in the absence of any commercial or financial relationships that could be construed as a potential conflict of interest.

frontiers in Earth Science

ORIGINAL RESEARCH
published: 02 June 2020
doi: 10.3389/feart.2020.00178

Early Cretaceous Terrestrial Milankovitch Cycles in the Luanping Basin, North China and Time Constraints on Early Stage Jehol Biota Evolution

Wei Liu[1,2], Huaichun Wu[1,2], Linda A. Hinnov[3], Dangpeng Xi[1], Huaiyu He[4], Shihong Zhang[1] and Tianshui Yang[1]*

[1] State Key Laboratory of Biogeology and Environmental Geology, China University of Geosciences (Beijing), Beijing, China, [2] School of Ocean Sciences, China University of Geosciences, Beijing, China, [3] Department of Atmospheric, Oceanic, and Earth Sciences, George Mason University, Fairfax, VA, United States, [4] Institute of Geology and Geophysics, Chinese Academy of Sciences, Beijing, China

This research analyzes the cyclostratigraphy of the lacustrine Dabeigou Formation (DBG) of early Jehol Biota age (~130–135 Ma) in the Luanping Basin, northern China. A high-resolution (2 cm interval), 117.82-m-long magnetic susceptibility (MS) stratigraphic series was measured along the Yushuxia section. MS is positively correlated with thorium, potassium and uranium concentrations associated with gamma ray intensity, and represents a proxy for detrital influx to the Luanping Basin. Power spectral analysis identifies a hierarchy of sedimentary cycles with wavelengths of 16.38 m, 5.85–3.28 m, 1.88–1.33 m, and 0.98–0.7 m, which are interpreted to represent Earth's orbital eccentricity, obliquity and precession index cycles. Objective testing of the MS series supports the interpretation of Milankovitch cycles, indicating an average sedimentation rate of 4.642–4.723 cm/kyr. A floating astronomical time scale with a duration of 2478 kyr is established from interpreted 405 kyr long orbital eccentricity cycles along the MS series. The 405-kyr tuned DBG MS time series closely matches the predicted orbital eccentricity of the La2004 astronomical solution from 130.787 to 133.265 Ma, providing independent temporal constraints on early stage Jehol Biota evolution. Finally, this estimated time interval for the DBG MS time series indicates that it occurred entirely within the Weissert Event.

Keywords: Early Cretaceous, Dabeigou Formation, magnetic susceptibility, astrochronology, Jehol Biota, Weissert Event

OPEN ACCESS

Edited by:
Juan Cruz Larrasoaña, Instituto Geológico y Minero de España, Spain

Reviewed by:
Hong Ao, Institute of Earth Environment, Chinese Academy of Sciences, China
Maodu Yan, Institute of Tibetan Plateau Research, Chinese Academy of Sciences, China

***Correspondence:**
Huaichun Wu
whcgeo@cugb.edu.cn

Specialty section:
This article was submitted to Geomagnetism and Paleomagnetism, a section of the journal Frontiers in Earth Science

Received: *05 January 2020*
Accepted: *06 May 2020*
Published: *02 June 2020*

Citation:
Liu W, Wu H, Hinnov LA, Xi D, He H, Zhang S and Yang T (2020) Early Cretaceous Terrestrial Milankovitch Cycles in the Luanping Basin, North China and Time Constraints on Early Stage Jehol Biota Evolution. Front. Earth Sci. 8:178. doi: 10.3389/feart.2020.00178

INTRODUCTION

The Early Cretaceous terrestrial Jehol Biota in East Asia is well-known for its exceptionally well-preserved feathered dinosaurs, early birds, mammals, pterosaurs, amphibians, insects and early flowering plants, and provides a unique window for understanding the evolution of Early Cretaceous terrestrial ecosystems (Zhou et al., 2003; Zhou, 2014). Geographically, the Jehol Biota is found in the Liaoning Province and adjacent areas in northeastern China. Stratigraphically, it is preserved mainly in the Dabeigou/Huajiying, Dadianzi, Yixian, and Jiufotang formations in ascending order in the Liaoning and Hebei

provinces (**Figure 1**; Xu et al., 2019), with an age range of ∼135–120 Ma (Swisher et al., 1999, 2002; He et al., 2006; Yang et al., 2007; Chang et al., 2009).

It has been increasingly recognized that the biota preserved in the Dabeigou Formation (DBG) reflect the origin and early stage Jehol Biota evolution (e.g., Tian et al., 2004; Ji et al., 2006; Wang and Ji, 2009; Zhou et al., 2009; Huang et al., 2015; Niu et al., 2015; Wang et al., 2015). The discovery of the earliest occurrence of the insect *Ephemeropsis trisetalis* and ostracods in the DBG, together with other fossils, suggests that the earliest Jehol Biota might already have appeared at the time when the lowermost part of Member 2 of the DBG was deposited (Zhou, 2014; Xu et al., 2019). The geochronology of the DBG indicates a range from ∼135 to ∼130 Ma (Liu et al., 2003; Zhang et al., 2005; He et al., 2006; Gao et al., 2018), but has large uncertainties, which impedes further progress in understanding early stage Jehol Biota evolution.

Cyclostratigraphy has been instrumental in establishing a 405-kyr-scale astronomical time scale (ATS) for the Cretaceous Period from well-preserved marine and continental successions (Hinnov, 2018; Huang, 2018). This has been possible due to the stability of the 405-kyr orbital eccentricity cycle over hundreds of millions of years (Laskar et al., 2004, 2011a; Kent et al., 2018). Cyclostratigraphy of the Cretaceous terrestrial strata from the Songliao Basin in northeastern China was interpreted with Milankovitch cycles, and established a ∼28 Myr-long ATS for the upper Turonian-Maastrichtian stages (Wu et al., 2009, 2013a, 2014). Subsequently, Wu et al. (2013b) analyzed cyclostratigraphy of the Lower Cretaceous Yixian Formation in the Sihetun Basin, northeastern China, estimating an average sedimentation rate of ∼1.70 cm/kyr for the Jianshangou Beds that host "feathered" dinosaur/primitive bird fossils of the Jehol Biota. Most recently, Liu et al. (2020) found that the cyclic alluvial-fluvial synrift deposits of the Lower Cretaceous (Valanginian-Hauterivian) Shahezi Formation in Songliao Basin were controlled by astronomical forcing, and reconstructed an ∼11.14 Myr-long floating astrochronology based on interpreted 405-kyr cycles.

The Lower Cretaceous DBG in the Yushuxia section, Luanping Basin (LPB), Hebei Province, the focus of this study, consists of 213 m of dominantly cyclic continental strata in well-exposed outcrops with abundant fossils (Liu et al., 2002; Tian et al., 2004; Wu et al., 2004; Zhang et al., 2007; Zhou et al., 2009; Niu et al., 2010). It provides a unique opportunity to develop an astrochronology to enable characterization of terrestrial climate change and environmental evolution of the Early Cretaceous Period. In this study, we conducted detailed time series analysis and modeling of the high-resolution (2 cm interval) magnetic susceptibility (MS) series of the DBG. The objectives were to search for and identify astronomical signals in the DBG, to develop an astrochronology for the early stage Jehol Biota, and to test the reliability of the astronomical solutions for early Cretaceous time.

GEOLOGICAL SETTING

The Luanping Basin (LPB) is located in northeastern Hebei Province, northern China, near the northern margin of the Yanshan orogenic belt (**Figure 1**). The paleo-latitude of LPB was ∼40° N during the Cretaceous Period, i.e., approximately the same as today (Wang, 2013; Wang C. S. et al., 2013). Here, the Volcanic Sedimentary Basin Group was formed by the active tectonics and frequent volcanic eruptions during the Late Jurassic to Early Cretaceous (Tian et al., 2004). The LPB is one of the small, terrestrial extensional basins in the Yanshan structural belt with a complete sedimentary sequence (Wu et al., 2004; Zhang et al., 2007). Its sedimentary evolution involved three successive stages: (1) "vigorous volcanic eruptions," (2) "extensional subsidence," and (3) "sedimentary infilling" (Zhang et al., 2007). The Jurassic and Cretaceous terrestrial strata in LPB are divided into six lithologic formations (in descending order): Jiufotang, Xiguayuan, Dadianzi, DBG, Zhangjiakou and Houcheng formations (Tian et al., 2008; Wang and Ji, 2009; Wang S. E. et al., 2013).

The DBG of the 213 meter-thick Yushuxia section (**Figure 1**) is well-known for its continuous non-marine Lower Cretaceous deposits and preservation of early stage Jehol Biota, including plants, pollen, spores, spinicaudatans, gastropods, bivalves, ostracods, insects, and fishes (Liu et al., 2002; Tian et al., 2004; Li et al., 2004; Zhou et al., 2009; Wang et al., 2015). The stratigraphy is characterized by alternating deposition of mudstones, shales, and siltstones, interbedded with sandstones and conglomerates of semi-deep lake facies in the lower part and deep lake facies in front of fan deltas in the upper part (**Figure 2**; Liu et al., 2001; Wang and Ji, 2009).

The DBG is divided into 3 members and 46 layers according to a detailed description of sedimentology and stratigraphy (Li et al., 2004; Qin et al., 2018). Member 1 (49.39 m) consists of tuffaceous, pebbly and coarse-grained sandstones, and medium to fine-grained sandstones intercalated with tuffaceous siltstone, sedimentary tuff and thin volcanic ashes. Member 2 (98.44 m) consists of siliceous mudstones and shales, interlayered with siltstones, fine to medium-grained sandstones; abundant fossils occur in this member. Member 3 (76.68 m) consists of mudstones, silty mudstones, calcareous mudstones and pelitic siltstones, and abundant fossils. The DBG represents shoreline-shallow lake to fan delta front-semi-deep lake facies in the lower part, and deep lake to fan delta front facies in the upper part (Liu et al., 2001).

The age of the DBG has been disputed for a long time. The paleontological data, including ostracods, spinicaudatans, palynotaxa, and plant macrofossils indicate that the DBG ranges from Late Jurassic to Early Cretaceous (e.g., Wan et al., 2016; Qin et al., 2018; Xi et al., 2019). Radioisotopic dating provides further constraints: in the Yushuxia section, SHRIMP zircon U-Pb dating of the tuffs in Layers 34 and 21, and the volcanic rocks of the underlying Zhangjiakou Formation indicates ages of 133.9 ± 2.5 Ma, 129.9 ± 1.2 Ma, and 135.4 ± 1.6 Ma, respectively (**Figure 2**; Liu et al., 2003; Gao et al., 2018). Zhang et al. (2005) obtained a LA-ICP-MS zircon U-Pb age of 135.2 ± 2.3 Ma from the Zhangjiakou Formation in the same section (**Figure 2**). $^{39}Ar/^{40}Ar$ dating of a tuff layer in the upper DBG of the Jiecaigou section, near LPB, yielded an age of 130.7 ± 1.2 Ma (He et al., 2006). Thus, the DBG can be constrained roughly from ∼135 to ∼130 Ma. The most recent constraints for Valanginian-Hauterivian time

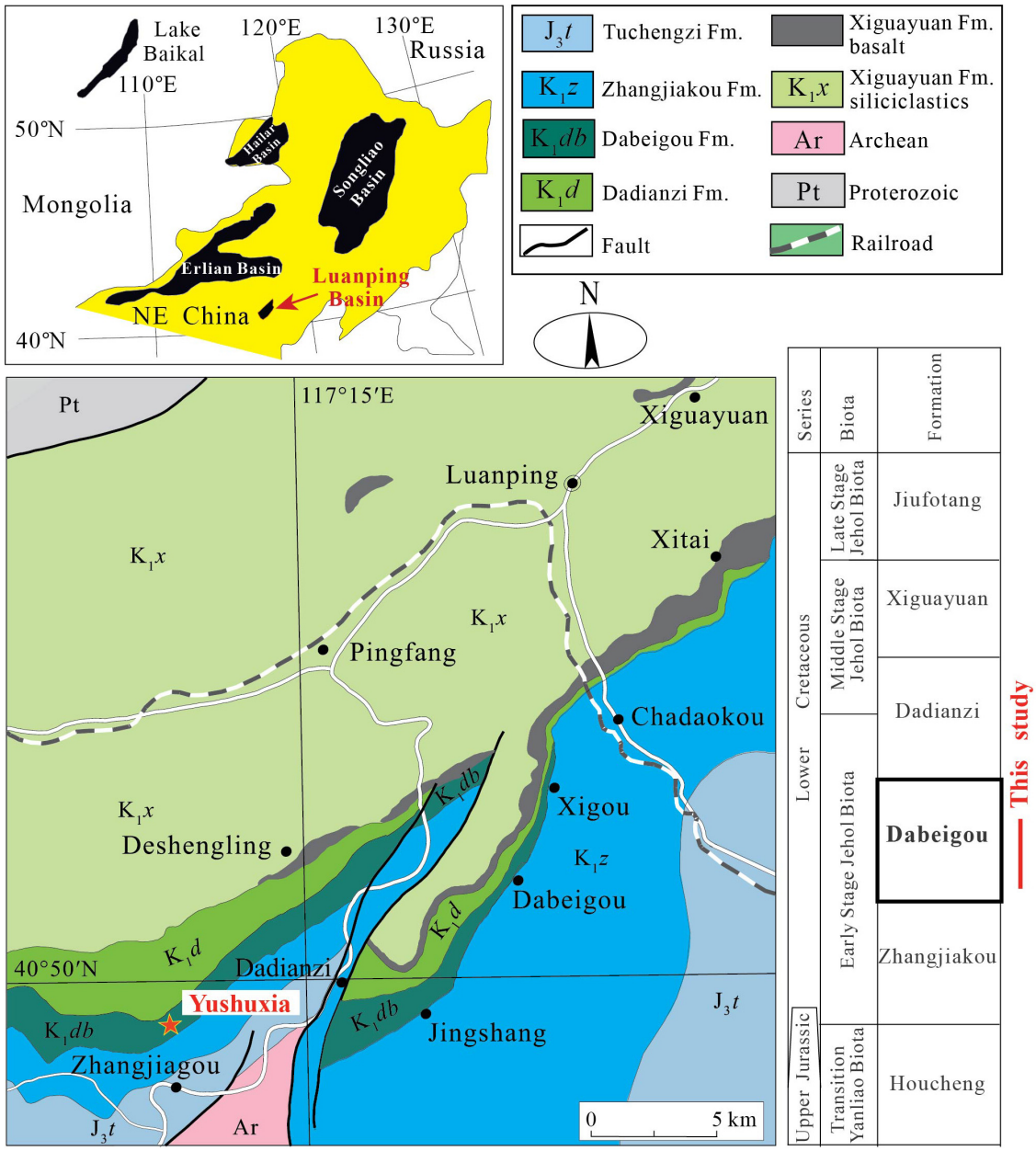

FIGURE 1 | Left: Map of northeastern China, Songliao Basin (SLB), and Luanping Basin (LPB), modified from Qin et al. (2018). The location of the Yushuxia section is indicated with the red star, at GPS coordinates 40°47′ N, 117°12′ E. Right: Lower Cretaceous stratigraphic column of northern China indicating the evolution stages of the Jehol Biota. The Dabeigou Formation is highlighted with bold lines; the stratigraphic coverage of this study is shown by the vertical red line at the far right.

are: 126.08 ± 0.19 Ma (top Hauterivian) 131.29 ± 0.19 Ma (top Valanginian); and 137.05 ± 1.0 Ma (top Berriasian) (Martinez et al., 2015; Aguirre-Urreta et al., 2019), which indicates that the DBG corresponds to late Valanginian to early Hauterivian time.

DATA

Magnetic susceptibility (MS) is a measure of the degree of magnetization of a material when subject to an external magnetic field. In sediments and sedimentary rocks, MS is affected by the concentration, grain size and shape of magnetic minerals (Kodama, 2012). Many studies have shown that MS is an effective indicator for Milankovitch-scale signals in stratigraphy, and it has been extensively used to characterize both marine and terrestrial sediments (e.g., Wu et al., 2013b; Zhong et al., 2018; Kodama, 2019).

MS was measured at 0.02 m intervals (on average) along the recently exposed Yushuxia section using a portable SM-30 MS detector. A total of 117.82 meters was measured, for a total of

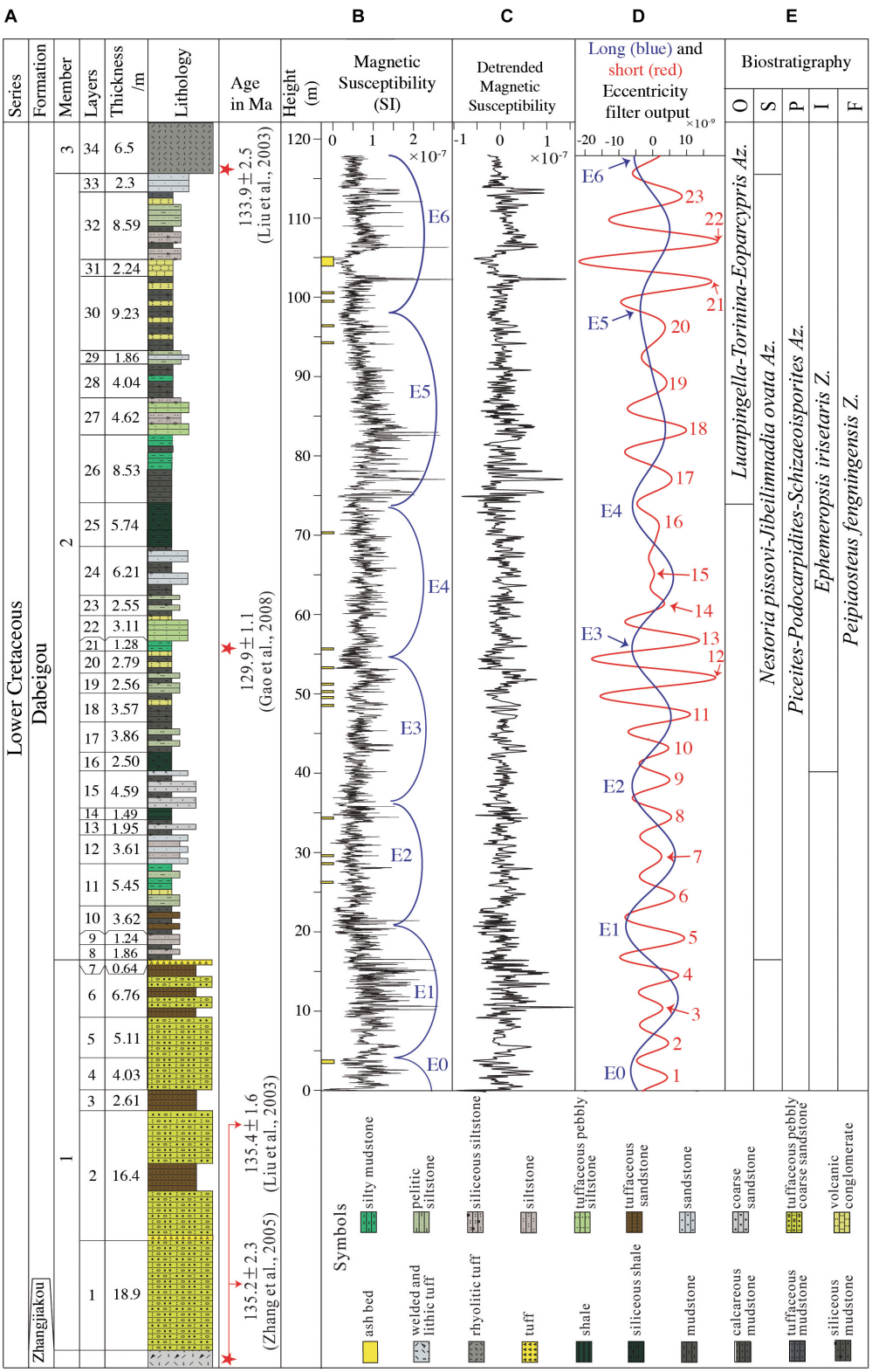

FIGURE 2 | MS series of the DBG section. **(A)** The detailed measured section with numbered beds and U-Pb ages (modified from Qin et al., 2018). **(B)** The MS series with interpreted long orbital eccentricity (E0-E6) cycles. **(C)** Detrended MS series. **(D)** Long (blue) and short (red) orbital eccentricity Gaussian filter outputs with passbands of 0.053 ± 0.01 and 0.2 ± 0.05 cycles/m, respectively. **(E)** Biostratigraphy from Qin et al. (2018). O, ostracods; S, spinacaudatans; P, palynotaxa; B, bivalves; I, insects; F, fishes.

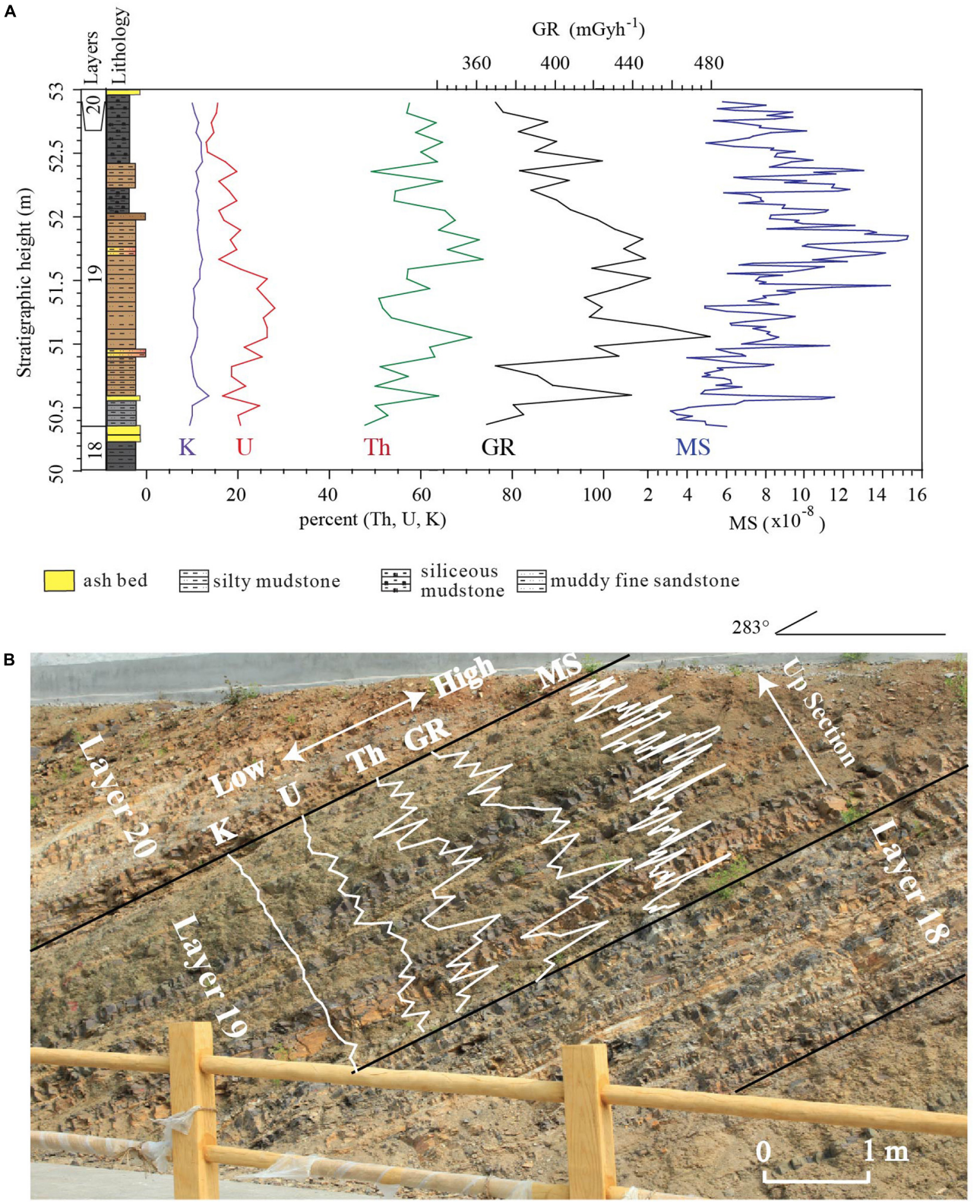

FIGURE 3 | (A) Comparison of lithology, MS, gamma ray (GR) intensity, and percent (%) of Th, K and U contributions in Layer 19. **(B)** Outcrop photo of Layers 17–20 with *in situ* measured data from Layer 19.

TABLE 1 | Orbital eccentricity, obliquity, and precession index periodicities from the periodogram of the La2004 astronomical solution (Laskar et al., 2004), between 129.55 and 134.55 Ma, i.e., a 5 Myr-long interval with a median age 132.05 Ma, calculated by Acycle for the TimeOpt astronomical target (orbital eccentricity and precession index) and for the ASM and COCO astronomical frequency targets (all three astronomical parameters).

Astronomical parameter	Periodicity (kyr)
Orbital eccentricity	409.6000
	132.1290
	124.1212
	99.9024
	94.1609
Obliquity	36.6000
Precession index	21.1405
	20.9514
	18.0839
	17.9256

Frequency in cycles/kyr is obtained by 1/periodicity.

5892 data points. This MS stratigraphic series covers from the top part of Member 1 (Layers 4–7; 16.54 m), Member 2 (Layers 8–33; 99.39 m) and the lower part of Member 3 (Layer 34; 1.89 m) (**Figure 2B**). Gamma ray intensity was measured at 0.1 m intervals along the section using a portable RS-230 GR detector; in this study measurements are presented for Layer 19 only for comparison (**Figure 3**).

MATERIALS AND METHODS

Pre-processing

The Prior to analysis, the data of 16 ash beds was removed, and MS series was interpolated to the average sample rate of 0.02 m. A low-pass filter was applied to the MS stratigraphic series using *tanerfilter.m* to retain astronomical frequencies while removing the very high frequencies. A cut-off frequency of 5 cycles/m and roll-off rate of 10^{12} were defined to reject wavelengths shorter than 0.2 m. The low-pass filtered MS series was then smoothed with a 40-meter-long window with the Matlab function *smooth.m* with the "lowess" option to estimate irregular long-term trends that could interfere with the detection of low frequency orbital eccentricity cycles. This smoothed curve was then subtracted from the MS series (**Figure 2C**).

Spectral Analysis

Multi-taper method (MTM) power spectral analysis (Thomson, 1982) with *pmtm.m*, and the evolutionary Fast Fourier Transform (FFT) spectrogram with *evofft.m* (Kodama and Hinnov, 2015) were used to characterize the frequency content of the processed MS series. The MTM F-ratio test was used to determine significant harmonic lines. The MTM harmonic *F*-test used in the average spectral misfit analysis (see below) was performed using the "eha" function of the Astrochron package in R (Meyers, 2014); otherwise *F*-test significance values were computed with Acycle (Li et al., 2019). The application of frequency ratios, e.g., 20:5:2:1 for long orbital eccentricity (405 kyr), short orbital eccentricity (100 kyr), obliquity (36.6 kyr), and precession (20 kyr) served as a preliminary test for astronomical frequencies in the MS stratigraphic series (Huang et al., 1992; Mayer and Appel, 1999; Laskar et al., 2004).

Sedimentation Rate Modeling

Three objective methods were used to test jointly for the presence of astronomical frequencies and the most probable sedimentation rate for the DBG MS stratigraphic series:

1. Average spectral misfit (ASM) analysis (Meyers and Sageman, 2007) estimates an optimal sedimentation rate given a set of astronomical target frequencies that is compared with the set of statistically significant frequencies of the stratigraphic data series for a specified range of sedimentation rates. The sedimentation rate with the lowest misfit between data and target frequencies is the "optimal sedimentation rate" (**Supplementary Material**).
2. Time Optimization (TimeOpt) analysis evaluates orbital eccentricity-like variations in the data, together with supporting evidence from amplitude modulations of the precession index band, across a test range of sedimentation rates (Meyers, 2015, 2019). TimeOptSim performs Monte Carlo AR1 model simulations to evaluate significance of TimeOpt results (Meyers and Malinverno, 2018; **Supplementary Material**).
3. Correlation coefficient (COCO) analysis (Li et al., 2018) estimates the correlation coefficient between power spectra of a stratigraphic proxy series and an astronomical solution in the time domain for a range of sedimentation rates. The evolutionary correlation coefficient (eCOCO) procedure was used to investigate changes in sedimentation rate along the stratigraphic series (Li et al., 2018). COCO and eCOCO analysis with 5000 Monte Carlo simulations was performed on test sedimentation rates ranging from 1 to 10 cm/kyr (**Supplementary Material**).

The ASM procedure was carried out using the Astrochron package in R (Meyers, 2014); TimeOpt, TimeOptSim, COCO, and eCOCO procedures were performed using the software ACycle v 2.1 (Li et al., 2019). The astronomical target frequencies used in these three procedures are based the La2004 astronomical solution periodogram for the 5-myr-long interval 129.55–34.55 Ma (median age of 132.05 Ma) (**Table 1**; Laskar et al., 2004).

The La2004 Astronomical Solution

The accuracy of astronomical solutions declines rapidly prior to 50 Ma, and solutions other than the well-known La2004, e.g., La2010 and La2011, are thought to incorporate parameterizations and initial conditions that are superior to those used in La2004 (Laskar et al., 2011a,b), and more closely fit geological data around and prior to 50 Ma, e.g., La2010c and ZB18a (Zeebe and Lourens, 2019). The main issue centers on modeling the fundamental frequencies that involve the orbits of Earth (g_3, s_3) and Mars (g_4, s_4), and the expectation for chaotic interactions

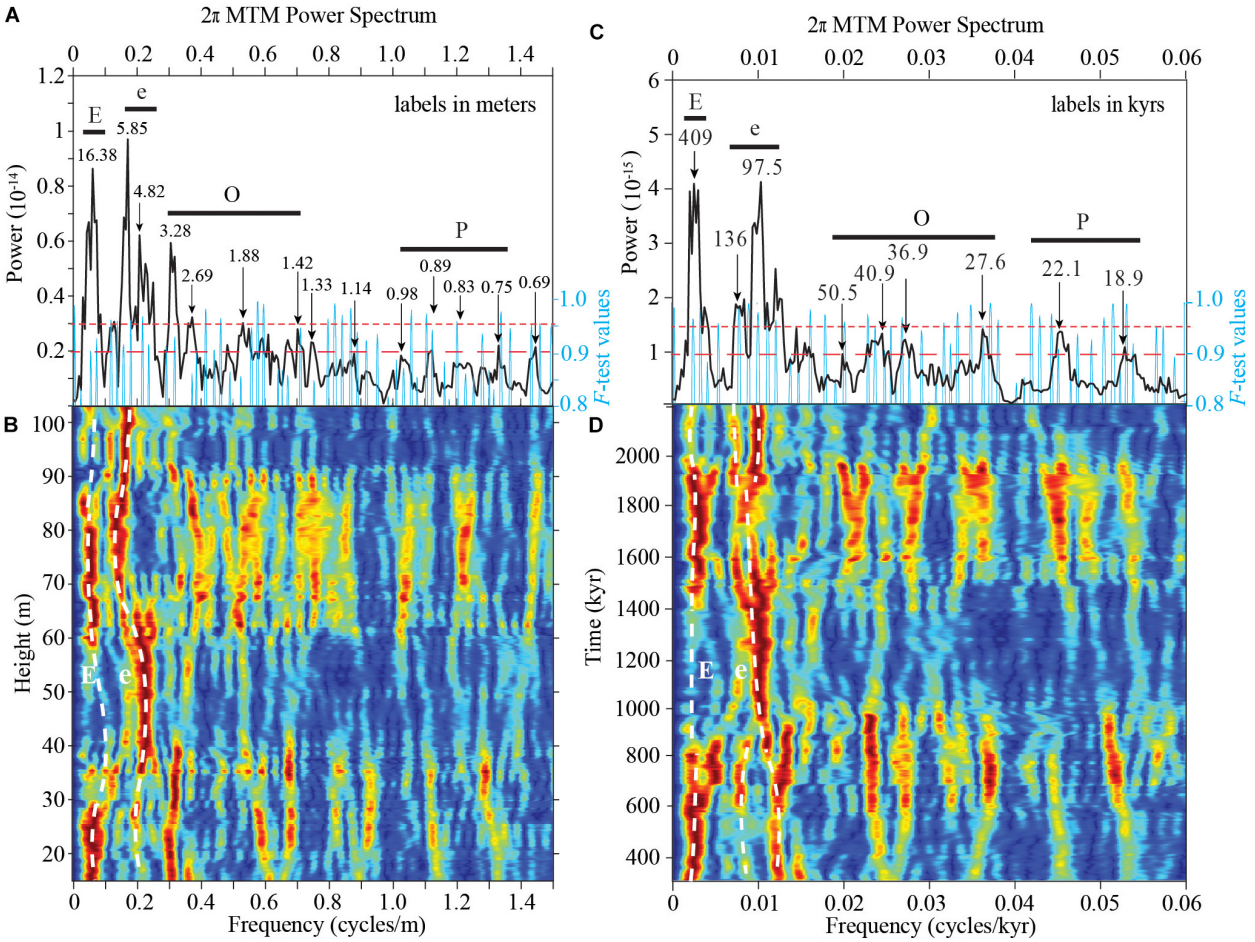

FIGURE 4 | Spectral analysis of the DBG MS stratigraphic series and 405-kyr-tuned series, frequency range: f = (0, 1.5 cycles/m) and f = (0, 0.06 cycles/kyr). **(A)** 2π MTM power spectrum of MS stratigraphic series with F-test values for significant harmonic lines. **(B)** Evolutionary FFT spectrogram of MS stratigraphic series with a 30 m sliding window. **(C)** 2π MTM power spectrum of 405-kyr-tuned MS series with F-test significance values for harmonic lines. **(D)** Evolutionary FFT spectrogram of 405-kyr-tuned MS series with a 600 kyr sliding window. E, long orbital eccentricity; e, short orbital eccentricity; O, obliquity; P, precession index.

between these two planetary orbits through deep time. For example, La2004 from 92 to 90 Ma and 87 to 85 Ma, predicts chaotic transitions between the Earth and Mars orbits. Recently, it was discovered that these two transitions closely fit Late Cretaceous cyclostratigraphic patterns from the Western Interior Seaway (Ma et al., 2017, 2019). Here we will test whether the La2004 solution also fits cyclostratigraphic patterns of the Early Cretaceous time represented by the DBG.

RESULTS

MS Variations

MS values range from -2.4×10^{-8} SI to 4.2×10^{-7} SI, with an average of 7.02×10^{-8} SI (**Figure 2B**). The MS stratigraphic series shows a sustained cyclic pattern that is consistent with the decimeter- to meter-scale lithological cycles (**Figures 2**, **3**). MS is positively correlated with gamma ray intensity and elevated ^{232}Th, ^{40}K, and ^{238}U (**Figure 3**). Th contributes ~60% of the GR signal, which identifies GR as a primarily clay proxy ("shale log") (Crain, 2019) that tracks the detrital influx from surrounding terrestrial source areas (Ohta et al., 2011). Recently, Pei et al. (2019) identified primary magnetic remanence and constructed a magnetostratigraphic framework for the upper DBG in LPB, further supporting the validity of the MS series as an important paleoenvironmental and paleoclimatic proxy. We propose that DBG MS is a proxy for the terrestrial hydrologic cycle, weathering and fluvial intensity, and if these processes were forced by insolation, represent Milankovitch cycles.

The DBG Stratigraphic Spectrum

2π MTM power spectral analysis of the MS stratigraphic series indicates spectral peaks at wavelengths of 16.38 m, 5.85–4.82 m, 3.28–1.42 m, and 0.98–0.7 m above the 90% F-test value (**Figures 4A,B**). The ratio of the major cycle bands of 20.5–16.4 m: 5.85–4.82 m: 3.28–1.42 m: 0.98–0.7 m is similar to the ratio of the Early Cretaceous astronomical periodicities of long orbital eccentricity (405 kyr) : short orbital eccentricity (132, 124, 99, and

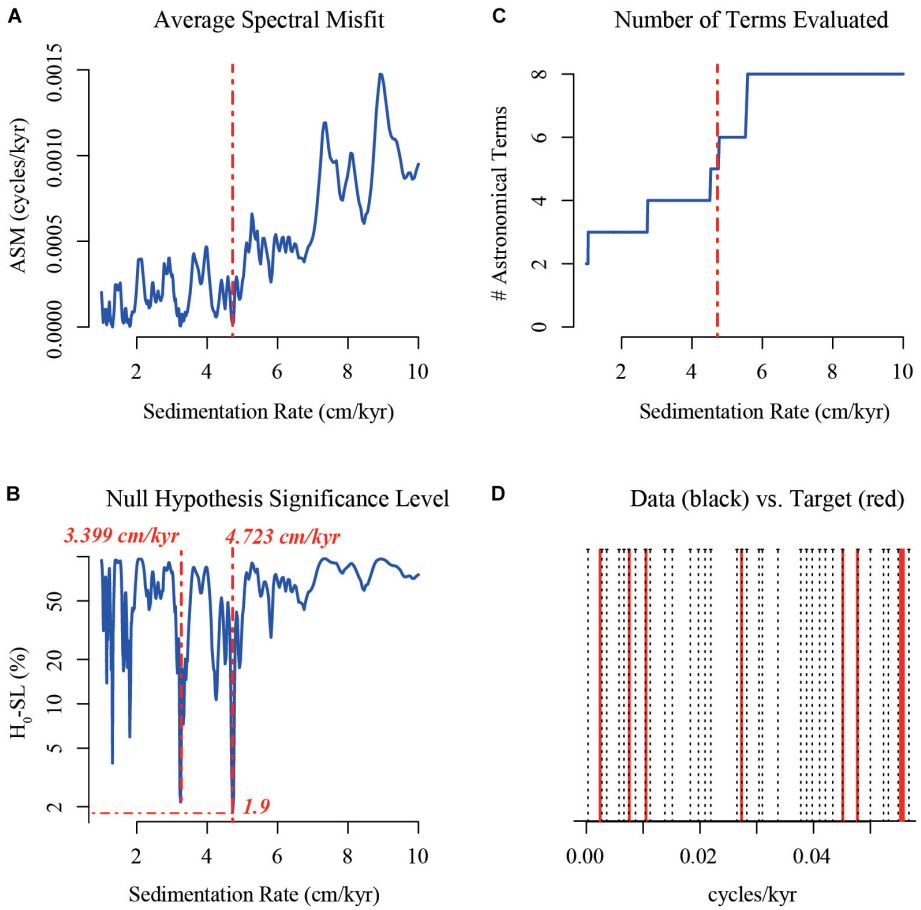

FIGURE 5 | ASM analysis of the DBG MS series, applied over a range of sedimentation rates from 1 to 10 cm/kyr by 0.0225 cm/kyr steps, using the La2004 astronomical target frequencies for 129.55–134.55 Ma (**Table 1**). All harmonics in the MS series exceeding 85% significance level, a total of 42, are evaluated. The astronomical target used is based on the list in **Table 1**, but has reduced the number of short eccentricity terms from four (1/132.129, 1/124.1212, 1/99.9024, 1/94.1609) to two (1/132.129, 1/95.25), which was found to yield a significantly lower H_0 (see **Supplementary Material** for ASM analysis with all 10 terms). **(A)** The ASM statistic between data and target spectrum. **(B)** The results of null hypothesis testing: H_0 is the probability of no target astronomical frequencies in the data. The optimal sedimentation rate occurs at the first joint lowest value ASM statistic and statistically significant H_0 minimum in the tested sedimentation rate range. **(C)** The number of astronomical terms used in the statistic; a total of 8 terms (frequencies) are included in the target (see above). **(D)** Comparison of significant spectral lines (dotted black lines) evaluated at the optimal sedimentation rate identified in **(C)** and the astronomical target lines (solid red lines). Vertical dash-dot red lines indicate solutions for optimal sedimentation rates.

95 kyr) : obliquity (37 kyr) : precession (23.0, 22.5, 21.8, 18.7, and 18.5 kyr) (Laskar et al., 2004). These cycles may be correlated with Milankovitch cycles of short orbital eccentricity, obliquity and precession according to the cycle length ratios. The evolutionary FFT spectrogram of the MS stratigraphic series (**Figure 4A**) indicates a sudden shift of power to higher frequencies in the 35–65 m interval, followed at ∼65 m by an equally sudden shift back to the lower frequencies that is then maintained to the base of the series. The question is whether these shifts indicate sudden changes in sedimentation rate, or evolution of the astronomical frequencies.

Sedimentation Rate Optimization

ASM Analysis

ASM analysis indicates a statistically significant (H0∼1%) solution at 4.723 cm/kyr (**Figure 5**). However, only five of the total of eight astronomical target frequencies were evaluated for this result, with the long orbital eccentricity at 409.6 kyr, and short precession index terms at 18.08 and 17.9256 kyr not successfully fitted to within the half-Rayleigh spacing required by the ASM statistic (Equation 1 in Meyers and Sageman, 2007), as indicated by three vertical red lines that do not coincide with any of the black vertical dashed lines in **Figure 5D**.

TimeOpt/TimeOptSim Analysis

TimeOpt analysis (**Figure 6**) indicates a r^2_{opt} maximum at a sedimentation rate of 4.642 cm/kyr, for which TimeOptSim analysis estimates a *p*-value of 0.119 (**Figure 6I**). This is close to the 4.723 cm/kyr sedimentation rate solution obtained by ASM (see above). The $r^2_{envelope}$ assessment (**Figure 6A**) indicates a much faster 9.224 cm/kyr with a very low *p*-value of 0.05348 (**Figure 6G**); r^2_{power} (**Figure 6A**) indicates 6.339 cm/kyr, and

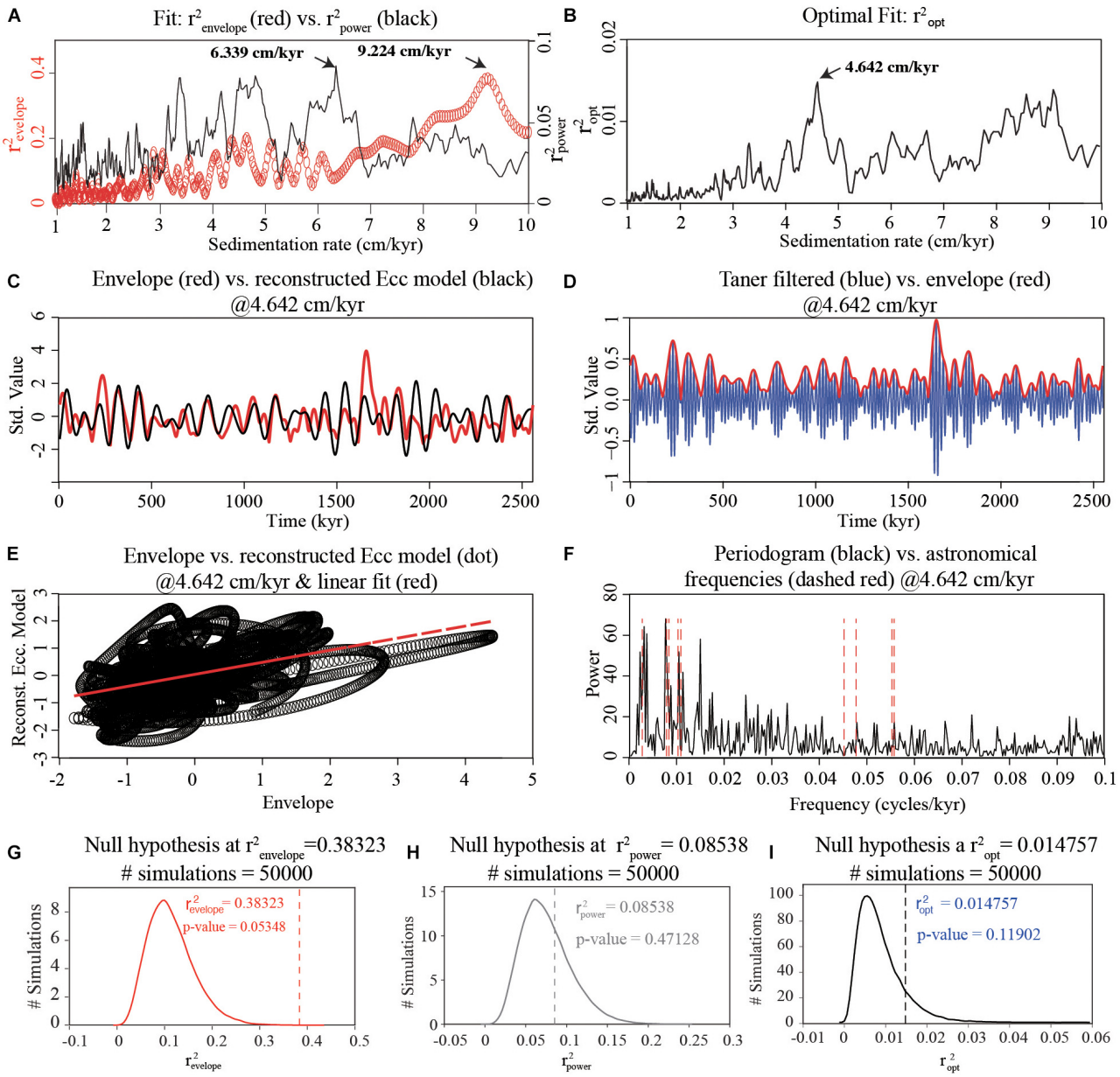

FIGURE 6 | TimeOpt **(A–F)** analysis and Monte Carlo simulation **(G–I)** results for the DBG MS series for 400 test sedimentation rates from 1 to 10 cm/kyr. The Taner filter passband was set to f_{low} = 0.045 cycles/kyr and f_{high} = 0.069 cycles/kyr; the roll-off was set to 10^{12}. The input orbital eccentricity model frequencies and precession index frequencies are from the La2004 solution (**Table 1**). **(A)** Pearson correlation coefficient vs. test sedimentation rate for the amplitude envelope of the precession index band ($r^2_{envelope}$) and eccentricity model (r^2_{power}). **(B)** The combined Pearson correlation coefficient $r^2_{opt} = r^2_{envelope} \cdot r^2_{power}$ indicating an optimal sedimentation rate of 4.642 cm/kyr. **(C)**. Comparison of the precession band amplitude envelope (red) and eccentricity model (black) for the optimal sedimentation rate of 4.6416 cm/kyr. **(D)** Taner-filtered precession band and amplitude envelope. **(E)** Paired amplitude envelope and eccentricity model points illustrating the correlation at the optimal sedimentation rate of 4.642 cm/kyr. **(F)**. Unsmoothed power spectrum of the MS series evaluated as a time series at the optimal sedimentation rate of 4.642 cm/kyr. **(G)** 50000 Monte Carlo simulations of AR1 red noise at the sedimentation rate indicated by the amplitude envelope of the precession index band (9.224 cm/kyr; $r^2_{envelope}$ = 0.38323; p = 0.05348). **(H)** 50000 Monte Carlo simulations of AR1 red noise at the sedimentation rate indicated by the orbital eccentricity model (6.339 cm/kyr; r^2_{power} = 0.08538; p = 0.47128). **(I)** 50000 Monte Carlo simulations of AR1 red noise at the optimal sedimentation rate (4.6416 cm/kyr; r^2_{opt} = 0.014757, p = 0.11902).

a much higher p-value of 0.47128 (**Figure 6H**). Adopting 4.642 cm/kyr as the optimal sedimentation rate, the MS series has a periodogram with a strong orbital eccentricity signature (**Figure 6F**).

COCO/eCOCO Analysis

COCO analysis indicates three maxima at 3.32, 4.72, and 6.34 cm/kyr, the largest at 4.72 cm/kyr with a correlation coefficient value exceeding 0.4 (**Figure 7A**). All three

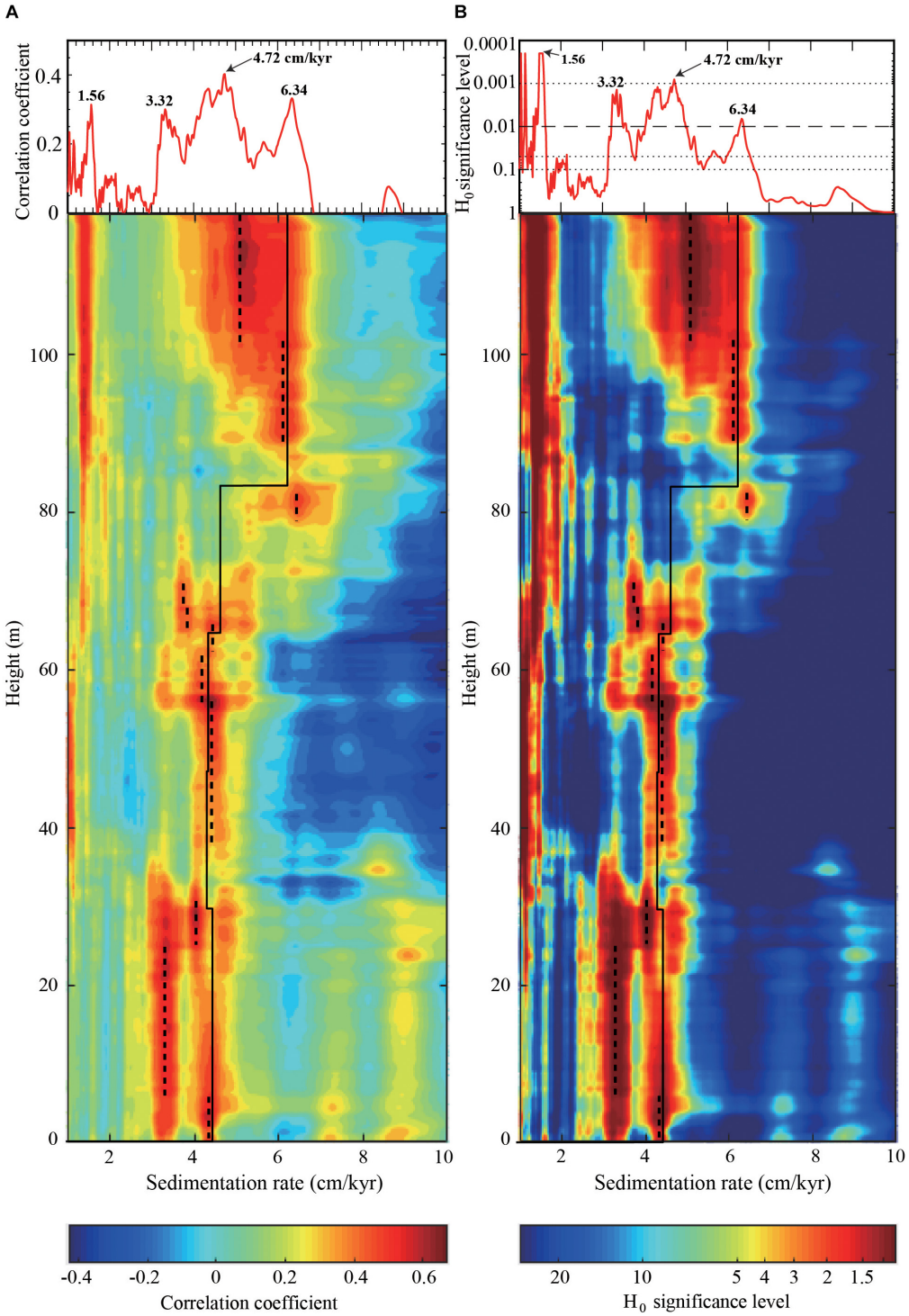

FIGURE 7 | Correlation coefficient (COCO) and evolutionary correlation coefficient (eCOCO) analysis of the DBG MS stratigraphic series. **(A)** Correlation coefficient vs. test sedimentation rate estimation of the correlation coefficient between the power spectra of astronomical solutions and the DBG MS series indicating an optimal sedimentation rate of 4.72 cm/kyr (top), and a sliding stratigraphic window to track variable sedimentation rates through the MS series (bottom). The vertical black lines indicate sedimentation rates according to the 405-kyr tuning (**Table 2**); the vertical dashed lines highlight the higher COCO values along the section. **(B)** The null hypothesis (H_0) significance level test (top) and evolutionary null hypothesis (H_0) significance level (bottom). For both the COCO and eCOCO, tested sedimentation rates range from 1 to 10 cm/kyr with a step of 0.02 cm/kyr, and the number of Monte Carlo simulations is 5000. For eCOCO analysis, the sliding window size is 38 m; the sliding window step is 0.02 m. In the top graph: the dashed horizontal line indicates H_0 = 0.01; the horizontal dotted lines, from top to bottom, indicate H_0 = 0.001, 0.05, and 0.1.

sedimentation rates have H_0 significance levels lower than 0.01 (**Figure 7B**). The results of eCOCO analysis shows that the sedimentation rates vary from 4.72 to 6.3 cm/kyr (**Figure 7A**).

DISCUSSION

Sedimentation Rate Variations in the DBG MS Series

The optimal sedimentation rates indicated by the ASM, TimeOpt and COCO methods are summarized in **Table 3**. Only one sedimentation rate is shared by all three methods: 4.642 cm/kyr (TimeOpt) to 4.72 cm/kyr (ASM, COCO). Other sedimentation rates arising at 3.4 and 6.34 cm/kyr can be explained as the result of sedimentation rate variations, as revealed by eCOCO (**Figure 7**). The TimeOpt precession index amplitude envelope model result indicating 9.224 cm/kyr (red circles, **Figure 6A**) with an extremely low *P*-value of 0.05348 (**Figure 6G**), is twice the joint optimal sedimentation rate of 4.642 cm/kyr that has a higher *P*-value of 0.11902, but shows an excellent fit of orbital eccentricity model frequencies in the periodogram (from 0 to 0.12 cycles/kyr) (**Figure 6F**). It is worth further considering this periodogram, and rescaling the frequencies by a factor of 2 (for 9.224 cm/kyr). This would shift the data spectral peaks that are currently at ∼100 kyr (0.01 cycles/kyr) to ∼50 kyr, and ∼400 kyr (0.0025 cycles/kyr) to ∼200 kyr, which do not coincide with the orbital eccentricity terms. Indeed, r^2_{power}, which compares the orbital eccentricity model and sedimentation rate-calibrated data, records a low value at 9.224 cm/kyr (**Figure 6A**). The joint modeling by r^2_{opt} steers the TimeOpt solution toward the sedimentation rate (4.642 cm/kyr) that produces a data periodogram with credible orbital eccentricity frequencies, and it is comparable to the sedimentation rate (4.72 cm/kyr) estimated by the other methods.

TABLE 2 | 405-kyr cycle and 100-kyr cycle picks (in bold and italic) based on MS minima in the MS stratigraphic series (see **Figure 2B**) that were identified with elevated statistical significance by the MTM harmonic F-ratio test (**Figure 4A**) and bandpass filters (**Figure 2D**).

Stratigraphic position (m)	Time (kyr)
0.0	***0***
3.92	98
20.06	503
36.18	908
54.44	1313
72.88	1718
97.84	2123
115.20	***2428***
117.82	***2478***

100-kyr cycle picks (in bold and italic) based on MS minima in the MS stratigraphic series.

TABLE 3 | Summary of sedimentation rates indicated by the ASM, TimeOpt, and COCO methods.

Method	Sedimentation rate (cm/kyr)			
ASM	3.339	4.723	–	–
TimeOpt/TimeOptSim	–	4.642	6.339	9.224
COCO	3.4	4.72	6.34	–

Astrochronology of the DBG MS Series

The astronomical frequencies identified in the DBG are supported by coeval evidence for astronomical forcing in the Valanginian–Hauterivian marine systems (e.g., Fiet et al., 2006; Martinez et al., 2015; Aguirre-Urreta et al., 2019). The optimization procedures reveal that the 20.5–16.4 m, 5.85–4.82 m, 3.28–1.42 m, and 0.98–0.75 m wavelengths in the MS stratigraphic series are associated with the periodicities of the long and short orbital eccentricity, obliquity and precession index, respectively.

Notably, assuming that the 16–20 m thick MS cycles along the section are 405 kyr cycles indicates sedimentation rates that are closely aligned with the objective testing (**Figure 7**: vertical dashed and solid black lines in the eCOCO color maps). The recognition of 405-kyr cycles is important for the ongoing initiative to define cyclostratigraphy in terms of the 405-kyr g_2-g_5 orbital eccentricity metronome for the geologic time scale (Kent et al., 2018; Hinnov, 2018). Applying the 405-kyr-based chronology model (**Table 2**) to convert the DBG MS stratigraphic series to a time series results in a spectrum with power concentrated in the short orbital eccentricity (influenced in part by three 100-kyr scale time points in **Table 2**), obliquity [1/(40.9 kyr), 1/(36.9 kyr) and 1/(27.6 kyr)] and precession index [1/(22.1 kyr) and 1/(18.9 kyr)] bands (**Figure 4C**). The spectrogram of the 405-kyr tuned MS series also indicates that the long and short orbital eccentricity trade positions in dominance at ∼400–500 kyr intervals along the section (**Figure 4D**).

The DBG MS cyclostratigraphy and the La2004 astronomical solution from 135 to 130 Ma are shown together in **Figure 8**. The yellow shading indicates a proposed correlation interval between data and model, from 133.265 to 130.787 Ma. This specific correlation was selected according to the singular coincidence at 131.538 Ma of an obliquity maximum and an orbital eccentricity minimum in both the La2004 astronomical solution and the 405-kyr tuned DBG time series (green vertical line in **Figure 8**). The obliquity-filtered DBG series (**Figure 8D**) also shows a pronounced amplitude modulation cycle that repeats every 6–7 cycles, which could be evidence for the recently described 173-kyr s_3–s_6 metronome, that is also present in the La2004 obliquity (**Figure 8B**; Boulila et al., 2018; Hinnov, 2018).

Paleoclimate Implications: The Weissert Event

The Weissert Event, characterized by a positive marine $d^{13}C$ excursion and global cooling, is the first major Early Cretaceous Earth system perturbation in the geologic record (Erba et al., 2004; Gröcke et al., 2005; Gréselle et al., 2011; Föllmi, 2012; Bajnai et al., 2017; Price et al., 2018). It is thought to span as much as 5.85 Myr (135.22–129.37 Ma) from the start of the Late Valanginian to the end of the Early Hauterivian (Martinez et al., 2015).

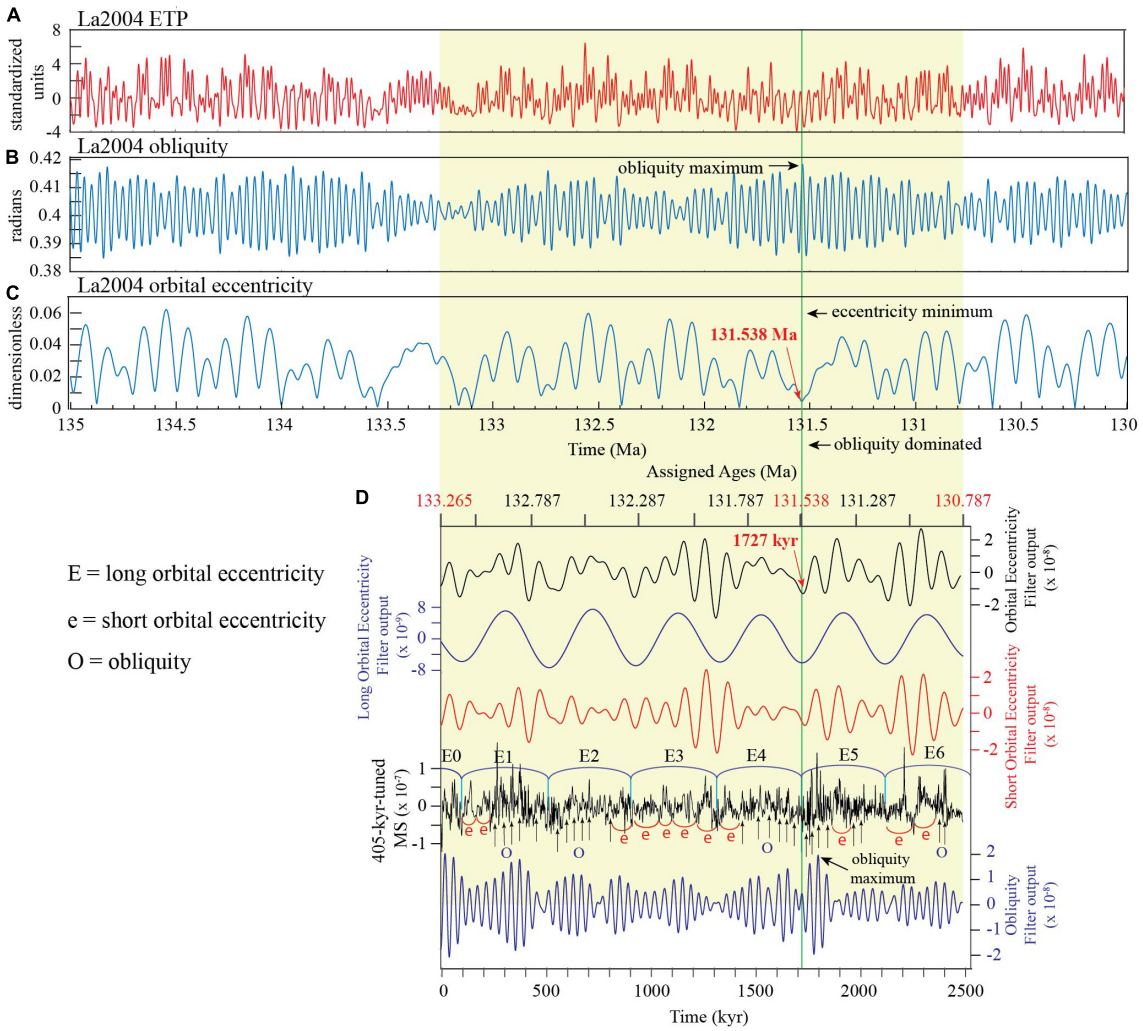

FIGURE 8 | Proposed correlation between DBG MS cyclostratigraphy and the La2004 astronomical solution from 135 to 130 Ma. The yellow shading indicates the proposed correlation interval, from 133.265 to 130.787 Ma; the green vertical line indicates a confluence of minimum orbital eccentricity and maximum obliquity in the La2004 solution. **(A)** La2004 ETP computed by standardizing and adding together the orbital eccentricity, obliquity and precession index solutions, producing a model with equal variance contributions from all three astronomical parameters. **(B)** The La2004 obliquity variation. **(C)** The La2004 orbital eccentricity solution. **(D)** The 405-kyr-tuned DBG MS time series, from the top: orbital eccentricity bandpass-filtered time series; 405-kyr (long orbital eccentricity) bandpass-filtered time series (E0-E6 are as in **Figure 2**); ∼100 kyr (short orbital eccentricity) bandpass-filtered time series; the Taner-highpass-filtered time series (see Preprocessing); and ∼37-kyr (obliquity) bandpass-filtered time series.

By this measure, the DBG, from 133.265 to 130.787 Ma (**Figure 8**), falls entirely within the Weissert Event. Geochemical analysis of the DBG indicates that the formation was deposited under relatively low-intensity hinterland weathering related to the boreal or semiarid regions; the upper unit of the DBG records hinterland weathering that is comparable to that in temperate and humid mid-latitude regions (Ohta et al., 2011). Palynoflora data also indicate that the paleoclimate changed from semi-humid to relatively temperate and humid conditions during DBG time (Wang et al., 2016).

The change toward more humid conditions during the late Berriasian and intensification during the Valanginian Weissert Event evidently influenced terrestrial biota, and especially the evolution of herbivore vertebrates. A study of oxygen isotope composition of vertebrate apatite in Liaoning Province, China, indicates global cooling during Jehol Biota time, demonstrated by an estimated air temperature of 10 ± 4°C (Amiot et al., 2011). Zhou (2014) also found temperate-to-cool-temperate fossil wood genus *Xenoxylon* in the Jehol Lagerstätte and an absence of crocodilians in northeastern China.

CONCLUSION

The DBG in the LPB, Hebei Province, northeastern China represents the prelude to the Jehol Biota, the spectacular Lagerstätte in the Lower Cretaceous. However, the DBG also occurs in a geologic interval that is chronostratigraphically very

poorly constrained. This state of affairs motivated measuring the DBG for MS to search for astronomical signals during DBG time, with the larger goal of developing an astrochronology for the formation. The results are as followings:

- A high-resolution (2 cm measuring interval) MS stratigraphic series was collected from the predominantly cyclic continental (lacustrine) DBG of the Yushuxia section in Luanping Basin, NE China.
- Gamma ray (GR) data indicate that MS increases with detrital content of the sediment, linking MS to fluvial delivery of sediment to the LPB, the hydrologic cycle, and climate forcing.
- Spectral analysis of the DBG MS stratigraphic series indicates that cyclicity occurs at wavelengths of 16.38 m, 5.85–4.82 m, 3.28–1.42 m, and 0.98–0.75 m. These are proposed to represent long orbital eccentricity, short orbital eccentricity, obliquity and precession index cycles.
- Objective testing using ASM, TimeOpt/TimeOptSim and COCO/eCOCO indicates the presence of Early Cretaceous (∼132.05 Ma) astronomical frequencies predicted by the La2004 astronomical solution. The testing identifies common optimal sedimentation rates of 4.642–4.72 cm/kyr measured by all three methods.
- Correlation between the 405-kyr-tuned DBG MS time series and the La2004 astronomical solution, generally constrained by radioisotope dating, suggests that the DBG was deposited from 133.265 to 130.787 Ma with a duration of 2478 kyr.
- Strong correlation between the DBG MS-La2004 astronomical solution raises the possibility that the La2004 solution is valid much further back in time than is currently recognized.
- The global cooling Weissert Event lasted from 135.22 to 129.37 Ma, indicating that DBG deposition, and hence, early stage Jehol Biota, occurred entirely within the Weissert Event.

DATA AVAILABILITY STATEMENT

The raw data supporting the conclusions of this article will be made available by the authors, without undue reservation, to any qualified researcher.

AUTHOR CONTRIBUTIONS

HW designed the study. WL measured the data and performed the analysis and modeling. WL, LH, and HW wrote the manuscript. All authors contributed to data interpretation and provided significant input to the final manuscript.

FUNDING

This work was supported by the National Natural Science Foundation of China (41790451, 41925010, and 41688103), the National Key R&D Program of China (2019YFC0605403), and the Chinese "111" project (B20011).

ACKNOWLEDGMENTS

We express our sincere thanks to associate editor Prof. Juan C. Larrasoaña, guest editors Profs. Kenneth Philip Kodama and Luigi Jovane. We thank two reviewers for their careful review and constructive suggestions that significantly improved the manuscript. We also thank Zuohuan Qin, Jichuang Fang, Wenjun Cai, and Chengke He for their help in the field.

SUPPLEMENTARY MATERIAL

The Supplementary Material for this article can be found online at: https://www.frontiersin.org/articles/10.3389/feart.2020.00178/full#supplementary-material

REFERENCES

Aguirre-Urreta, B., Martinez, M., Schmitz, M., Lescano, M., Omarini, J., Tunik, M., et al. (2019). Interhemispheric radio-astrochronological calibration of the time scales from the andean and the tethyan areas in the valanginian-hauterivian (Early Cretaceous). *Gondwana Res.* 70, 104–132. doi: 10.1016/j.gr.2019.01.006

Amiot, R., Wang, X., Zhou, Z. H., Wang, X. L., Buffetaut, E., Lécuyer, C., et al. (2011). Oxygen isotopes of East Asian dinosaurs reveal exceptionally cold Early Cretaceous climates. *Proc. Natl. Acad. Sci. U.S.A.* 108, 5179–5183. doi: 10.1073/pnas.1011369108

Bajnai, D., Pálfy, J., Martinez, M., Price, G. D., Nyerges, A., and Fõzy, I. (2017). Multi-proxy record of orbital-scale changes in climate and sedimentation during the weissert event in the valanginian bersek marl formation (Gerecse Mts., Hungary). *Cretaceous Res* 75, 45–60. doi: 10.1016/j.cretres.2017.02.021

Boulila, S., Vahlenkamp, M., De Vleeschouwer, D., Laskar, J., Yamamoto, Y., Pälike, H., et al. (2018). Towards a robust and consistent middle Eocene astronomical timescale. *Earth Planet. Sci. Lett.* 486, 94–107. doi: 10.1016/j.epsl.2018.01.003

Chang, S. C., Zhang, H. C., Renne, P. R., and Fang, Y. (2009). High-precision 40Ar/39Ar age for Jehol Biota. *Palaeogeogr. Palaeoclimatol. Palaeoecol.* 280, 94–104. doi: 10.1016/j.palaeo.2009.06.021

Crain, E. R. (2019). Avaliable at: www.spec2000.net. (accessed December 31, 2019).

Erba, E., Bartolini, A., and Larson, R. (2004). Valanginian Weissert oceanic anoxic event. *Geology* 32, 149–152. doi: 10.1130/G20008.1

Fiet, N., Quidelleur, X., Parize, O., Bulot, L. G., and Gillot, P. Y. (2006). Lower Cretaceous stage durations combining radiometric data and orbital chronology: towards a more stable relative time scale? *Earth Planet. Sci. Lett.* 246, 407–417. doi: 10.1016/j.epsl.2006.04.014

Föllmi, K. B. (2012). Early Cretaceous life, climate and anoxia. *Cretaceous Res.* 35, 230–257. doi: 10.1016/j.cretres.2011.12.005

Gao, L. Z., Wang, Y. S., and Zhang, H. (2018). A discussion on Jurassic and Cretaceous boundary based on the SHRIMP zircon U-Pb dating of Mesozoic holitype section in Luanping basin. *Geol. Bull. China* 37, 1186–1192.

Gréselle, B., Pittet, B., Mattioli, E., Joachimski, M., Barbarin, N., Riquier, L., et al. (2011). The Valanginian isotope event: a complex suite of palaeoenvironmental perturbations. *Palaeogeogr. Palaeoclimatol. Palaeoecol.* 306, 41–57. doi: 10.1016/j.palaeo.2011.03.027

Gröcke, D. R., Price, G. D., Robinson, S. A., Baraboshkin, E. Y., Mutterlose, J., and Ruffell, A. H. (2005). The upper valanginian (Early Cretaceous) positive carbon-isotope event recorded in terrestrial plants. *Earth Planet. Sci. Lett.* 240, 495–509. doi: 10.1016/j.epsl.2005.09.001

He, H. Y., Wang, X. L., Zhou, Z. H., Jin, F., Wang, F., Yang, K. L., et al. (2006). The 40Ar/39Ar dating of the early jehol biota from fengning, hebei province, northern China. *Geochem. Geophys. Geosyst.* 7:Q04001. doi: 10.1029/2005GC001083

Hinnov, L. A. (2018). "Chapter 1: cyclostratigraphy and Astrochronology in 2018," in *Stratigraphy and Timescales*, Vol. 3, ed. M. Montenari (Cambridge, MA: Academic Press), 1–80. doi: 10.1016/bs.sats.2018.08.004

Huang, C. J. (2018). "Chapter two: astronomical time scale for the mesozoic," in *Stratigraphy and Timescales* ed M. Montenari. (Cambridge, MA: Academic Press)3, 81–150. doi: 10.1016/bs.sats.2018.08.005

Huang, D. Y., Cai, C. Y., Jiang, J. Q., Su, Y. T., and Liao, H. Y. (2015). Daohugou bed and fossil of its basal conglomerate section. *Acta Palaeontol. Sin.* 54, 351–357.

Huang, Z. H., Boyd, R., and O'Connell, S. B. (1992). "Upper Cretaceous cyclic sediments from hole 762C, exmouth plateau, Northwest Australia," in *Proceedings of the Ocean Drilling Program, Scientific Results*, Vol. 122, eds U. Van Rad, B. U. Haq, (College Station, TX: Ocean Drilling Program), 259–277.

Kent, D. V., Olsen, P. E., Rasmussen, C., Lepre, C., Mundil, R., Irmis, R. B., et al. (2018). Empirical evidence for stability of the 405 kyr Jupiter-Venus eccentricity cycle over hundreds of millions of years. *Proc. Natl. Acad. Sci. U.S.A.* 115, 6153–6158. doi: 10.1073/pnas.1800891115

Ji, Q., Liu, Y. Q., Ji, S. A., Chen, W., Lv, J. C., You, H. L., et al. (2006). On the terrestrial Jurassice-Cretaceous Boundary in China. *Geol. Bull. China* 25, 336–339. doi: 10.3969/j.issn.1671-2552.2006.03.003

Kodama, K. P. (2012). *Paleomagnetism of Sedimentary Rocks: Process and Interpretation*. Chichester: John Wiley and Sons, 157.

Kodama, K. P. (2019). Rock magnetic cyclostratigraphy of the carboniferous mauch chunk formation, Pottsville, PA, United States. *Front. Earth Sci.* 7:285. doi: 10.3389/feart.2019.00285

Kodama, K. P., and Hinnov, L. A. (2015). *Rock Magnetic Cyclostratigraphy*. Chichester: Wiley Blackwell, 165.

Laskar, J., Fienga, A., Gastineau, M., and Manche, H. (2011a). La2010: a new orbital solution for the long-term motion of the earth. *Astron. Astrophys* 532:A89. doi: 10.1051/0004-6361/201116836

Laskar, J., Gastineau, M., Delisle, J. B., Farrés, A., and Fienga, A. (2011b). Strong chaos induced by close encounters with Ceres and Vesta. *Astron. Astrophys.* 532:L4. doi: 10.1051/0004-6361/201117504

Laskar, J., Robutel, P., Joutel, F., Gastineau, M., Correia, A. C. M., and Levrard, B. (2004). A long-term numerical solution for the insolation quantities of the Earth. *Astron. Astrophys* 428, 261–285. doi: 10.1051/0004-6361:20041335

Li, M. S., Hinnov, L. A., and Kump, L. R. (2019). Acycle: time-series analysis software for paleoclimate research and education. *Comput. Geosci.* 127, 12–22. doi: 10.1016/j.cageo.2019.02.011

Li, M. S., Kump, L. R., Hinnov, L. A., and Mann, M. E. (2018). Tracking variable sedimentation rates and astronomical forcing in Phanerozoic paleoclimate proxy series with evolutionary correlation coefficients and hypothesis testing. *Earth Planet. Sci. Lett.* 501, 165–179. doi: 10.1016/j.epsl.2018.08.041

Li, P. X., Liu, Y. Q., and Tian, S. G. (2004). Advances in the study of the Jurassic–Cretaceous lithostratigraphy in the Luanping basin, northern Hebei. *Geol. Bull. China* 23, 757–765. doi: 10.3969/j.issn.1671-2552.2004.08.006

Liu, W., Wu, H. C., Hinnov, L. A., Baddouh, M., Wang, P. J., Gao, Y. F., et al. (2020). An 11 million-year-long record of astronomically forced fluvial-alluvial deposition and paleoclimate change in the Early Cretaceous songliao synrift basin, China. *Palaeogeogr. Palaeoclimatol. Palaeoecol.* 541:109555. doi: 10.1016/j.palaeo.2019.109555

Liu, Y. Q., Li, P. X., and Tian, S. G. (2003). SHRIMP U-Pb zircon age of Late Mesozoic tuffs (lava) in Luanping basin, northern Hebei, and its implications. *Acta Petrologica Mineralogical.* 22, 237–244. doi: 10.3969/j.issn.1000-6524.2003.03.005

Liu, Y. Q., Pang, Q. Q., Li, P. X., Tian, S. G., and Niu, S. W. (2002). Advances in the study of non-marine jurassic Cretaceous biostratigraphical boundary and candidate stratotype in Luanping basin, northern Hebei. *Geol. Bull. China* 21, 176–180. doi: 10.3969/j.issn.1671-2552.2002.03.015

Liu, Y. Q., Tian, S. G., Li, P. X., Pang, Q. Q., and Li, Y. (2001). The stratigraphic framework of the dabeigou-dadianzi formations in luanping basin, Northern Hebei and its stratotype significance. *Acta Geosci. Sin.* 22, 391–396.

Ma, C., Meyers, S. R., and Sageman, B. B. (2017). Theory of chaotic orbital variations confirmed by Cretaceous geological evidence. *Nature* 542, 468–470. doi: 10.1038/nature21402

Ma, C., Meyers, S. R., and Sageman, B. B. (2019). Testing late cretaceous astronomical solutions in a 15 million year astrochronologic record from North America. *Earth Planet. Sci. Lett.* 513, 1–11. doi: 10.1016/j.epsl.2019.01.053

Martinez, M., Deconinck, J. F., Pellenard, P., Riquier, L., Company, M., Reboulet, S., et al. (2015). Astrochronology of the valanginian-hauterivian stages (Early Cretaceous): chronological relationships between the Paraná-Etendeka large igneous province and the Weissert and the Faraoni events. *Global Planet. Change* 131, 158–173. doi: 10.1016/j.gloplacha.2015.06.001

Mayer, H., and Appel, E. (1999). Milankovitch cyclicity and rock-magnetic signatures of paleoclimatic changes in the Early Cretaceous Biancone Formation of the Southern Alps. Italy. *Cretaceous Res.* 20, 189–214. doi: 10.1006/cres.1999.0145

Meyers, S. R. (2014). *Astrochron: An R Package for Astrochronology*. Avaliable at: https://cran.r-project.org/package=astrochron

Meyers, S. R. (2015). The evaluation of eccentricity-related amplitude modulation and bundling in paleoclimate data: an inverse approach for astrochronologic testing and time scale optimization. *Paleoceanography* 30, 1625–1640. doi: 10.1002/2015PA002850

Meyers, S. R. (2019). Cyclostratigraphy and the problem of astrochronologic testing. *Earth Sci. Rev.* 190, 190–223. doi: 10.1016/j.earscirev.2018.11.015

Meyers, S. R., and Malinverno, A. (2018). Proterozoic milankovitch cycles and the history of the solar system. *Proc. Natl. Acad. Sci. U.S.A.* 115, 6363–6368. doi: 10.1073/pnas.1717689115

Meyers, S. R., and Sageman, B. B. (2007). Quantification of deep-time orbital forcing by average spectral misfit. *Am. J. Sci.* 307, 773–792. doi: 10.2475/05.2007.01

Niu, S. W., Sun, C. L., Zhang, F. C., Li, W. G., Xu, F., Li, H., et al. (2015). Local fossil assemblage of the Jehol biota and its geological significance in Chengde area. Hebei Province, China. *Geol. Surv. Res.* 38, 241–247.

Niu, S. W., Tian, S. G., and Pang, Q. Q. (2010). Conchostracan biostratigraphy of the dadianzi formation in the luanping basin, northern Hebei, China and the boundary of continental Jurassic and Cretaceous strata. *Geol. Bull. China* 29, 961–979.

Ohta, T., Li, G., Hirano, H., Sakai, T., Kozai, T., Yoshikawa, T., et al. (2011). Early Cretaceous terrestrial weathering in Northern China: relationship between paleoclimate change and the phased evolution of the jehol biota. *J. Geol.* 119, 81–96. doi: 10.1086/657341

Pei, J. L., Yang, Z. Y., Sun, Z. M., Tong, Y. B., Cai, Y. H., Wang, X. R., et al. (2019). Magnetostratigraphic dating of the early jehol biota. *Acta Geosci. Sin.* 40, 393–404.

Price, G. D., Janssen, N. M. M., Martinez, M., Company, M., Vandevelde, J. H., and Grimes, S. T. (2018). A High-Resolution belemnite geochemical analysis of early Cretaceous (Valanginian-Hauterivian) environmental and climatic perturbations. *Geochem. Geophys. Geosyst.* 19, 3832–3843. doi: 10.1029/2018GC007676

Qin, Z. H., Xi, D. P., Sames, B., Do Carmo, D. A., Wang, X. R., Xu, K. K., et al. (2018). Ostracods of the non-marine lower Cretaceous dabeigou formation at yushuxia (Luanping basin, North China): implications for the early Jehol Biota age. *Cretaceous Res.* 86, 199–218. doi: 10.1016/j.cretres.2018.03.010

Swisher, C. C., Wang, X. L., Zhou, Z. H., Wang, Y. Q., Jing, F., Zhang, J. Y., et al. (2002). Further support for a Cretaceous age for featured dinosaur beds of liaoning province, China: new 40Ar/39Ar dating of the Yixian and Tuchengzi formations. *Chin. Sci. Bull.* 47, 135–138.

Swisher, C. C., Wang, Y. Q., Wang, X. L., Xu, X., and Wang, Y. (1999). Cretaceous age for the feathered dinosaurs of Liaoning. China. *Nature* 400, 59–61. doi: 10.1038/21872

Thomson, D. (1982). Spectrum estimation and harmonic analysis. *Proc. IEEE* 70, 1055–1096. doi: 10.1109/PROC.1982.12433

Tian, S. G., Niu, S. W., and Pang, Q. Q. (2008). Redefinition of the lower Cretaceous terrestrial Yixianian Stage and its stratotype candidate in the Luanping basin, northern Hebei. *Geol. Bull. China* 27, 739–752. doi: 10.3969/j.issn.1671-2552.2008.06.003

Tian, S. G., Pang, Q. Q., Niu, S. W., Li, P. X., and Liu, Y. Q. (2004). Terrestrial Jurassic-Cretaceous stratotype candidate in Luanping basin, northern Hebei. *Geol. Bull. China* 23, 1170–1179. doi: 10.3969/j.issn.1671-2552.2004.12.002

Wan, X. Q., Gao, F. L., Qin, Z. H., Cui, C., and Xi, D. P. (2016). The Jurassic-Cretaceous boundary problem and the discussion on continental boundary of northern China. *Geosci. Front.* 23, 1–6.

Wang, C. S. (2013). Environmental/climate change in the Cretaceous greenhouse world: records from Terrestrial scientific drilling of songliao basin and adjacent areas of China. *Palaeogeogr. Palaeoclimatol. Palaeoecol.* 385, 1–5. doi: 10.1016/j.palaeo.2013.05.006

Wang, C. S., Feng, Z. Q., Zhang, L. M., Huang, Y. J., Cao, K., Wang, P. J., et al. (2013). Cretaceous paleogeography and paleoclimate and the setting of SKI borehole sites in Songliao Basin, northeast China. *Palaeogeogr. Palaeoclimatol. Palaeoecol* 385, 17–30. doi: 10.1016/j.palaeo.2012.01.030

Wang, S. E., Gao, L. Z., Wan, X. Q., and Song, B. (2013). Ages of Tuchengzi Formation in western Liaoning-northern Hebei area in correlation with those of international strata. *Geol. Bull. China* 32, 1673–1690. doi: 10.3969/j.issn.1671-2552.2013.11.001

Wang, D. N., Wang, X. R., and Ji, Q. (2016). The Palynoflora alternation and the paleoclimate change at the turning time between Late Jurassic and Early Cretaceous in Northern Hebei and Western Liaoning. *Acta Geosci. Sin.* 37, 449–459. doi: 10.3975/cagsb.2016.04.07

Wang, S. E., and Ji, Q. (2009). Lithostratigraphy and biostratigraphy features of zhangjiakou formation and dabeigou formation and its significance for stratigraphic subdivision and correlation in the Northeast Asia. *Geol. Bull. China* 28, 821–828.

Wang, Y. Q., Sha, J. G., Pan, Y. H., and Zhang, X. L. (2015). Early Cretaceous nonmarine ostracod biostratigraphy of western Liaoning area. NE China. *Micropaleontology* 61, 135–145. doi: 10.1002/rcm.2049

Wu, F. D., Chen, Y. J., Hou, Y. A., Zhang, F., and Li, U. (2004). Characteristics of sedimentary tectonic evolution and high-resolution sequence stratigraphy in luanping basin. *Earth Sci. J. China Unive. Geosci.* 29, 625–630.

Wu, H. C., Zhang, S. H., Hinnov, L. A., Jiang, G. Q., Yang, T. S., Li, H. Y., et al. (2014). Cyclostratigraphy and orbital tuning of the terrestrial upper Santonian-Lower Danian in Songliao Basin, northeastern China. *Earth Planet. Sci. Lett.* 407, 82–95. doi: 10.1016/j.epsl.2014.09.038

Wu, H. C., Zhang, S. H., Jiang, G. Q., Hinnov, L. A., Yang, T. S., Li, H. Y., et al. (2013a). Astrochronology of the early turonian-early campanian terrestrial succession in the songliao basin, northeastern China and its implication for long-period behavior of the Solar System. *Palaeogeogr. Palaeoclimatol. Palaeoecol.* 385, 55–70. doi: 10.1016/j.palaeo.2012.09.004

Wu, H. C., Zhang, S. H., Jiang, G. Q., Yang, T. S., Guo, J. H., and Li, H. Y. (2013b). Astrochronology for the Early Cretaceous Jehol Biota in Northeastern China. *Palaeogeogr. Palaeoclimatol. Palaeoecol.* 385, 221–228. doi: 10.1016/j.palaeo.2013.05.017

Wu, H. C., Zhang, S. H., Jiang, G. Q., and Huang, Q. H. (2009). The floating astronomical time scale for the terrestrial late Cretaceous Qingshankou formation from the Songliao Basin of Northeast China and its stratigraphic and paleoclimate implications. *Earth Planet. Sci. Lett.* 278, 308–323. doi: 10.1016/j.epsl.2008.12.016

Xi, D. P., Wan, X. Q., Li, G. B., and Li, G. (2019). Cretaceous integrative stratigraphy and timescale of China. *Sci. China: Earth Sci.* 62, 256–286. doi: 10.1007/s11430-017-9262-y

Xu, X., Zhou, Z., Wang, Y., and Wang, M. (2019). Study on Jehol Biota: recent advances and future prospects. *Sci. China: Earth Sci.* 49, 1491–1511. doi: 10.1360/SSTe-2019-0121

Yang, W., Li, S. G., and Jiang, B. Y. (2007). New evidence for Cretaceous age of the feathered dinosaurs of Liaoning: zircon U-Pb SHRIMP dating of the Yixian Formation in Sihetun, northeast China. *Cretaceous Res.* 28, 177–182. doi: 10.1016/j.cretres.2006.05.011

Zeebe, R. E., and Lourens, L. (2019). Solar System chaos and the Paleocene-Eocene boundary age constrained by geology and astronomy. *Nature* 365, 926–929. doi: 10.1126/science.aax0612

Zhang, H., Liu, X. M., Zhang, Y. Q., Yuan, H. L., and Hu, Z. C. (2005). Zircon U-Pb ages and significance of bottom and top beds of Zhangjiakou Formation in Liaoning and Hebei Provinces. *Earth Science-Journal of China University of Geosciences* 30, 387–401.

Zhang, Y. L., Qu, H. J., and Meng, Q. R. (2007). Depositional process and evolution of Luanping Early Cretaceous basin in the Yanshan structural belt. *Acta Petrol. Sin.* 23, 667–678. doi: 10.3321/j.issn:1000-0569.2007.03.013

Zhong, Y. Y., Wu, H. C., Zhang, Y. D., Zhang, S. H., Yang, T. S., Li, H. Y., et al. (2018). Astronomical calibration of the middle ordovician of the yangtze block, South China. *Palaeogeogr. Palaeoclimatol. Palaeoecol.* 505, 86–99. doi: 10.1016/j.palaeo.2018.05.030

Zhou, Z. H. (2014). The Jehol biota, an early Cretaceous terrestrial Lagerstätte: new discoveries and implications. *Natl. Sci. Rev.* 1, 543–559. doi: 10.1093/nsr/nwu055

Zhou, Z. H., Barrett, P. M., and Hilton, J. (2003). An exceptionally preserved lower Cretaceous ecosystem. *Nature* 421, 807–814. doi: 10.1038/nature01420

Zhou, Z. H., He, H. Y., and Jiang, X. L. (2009). The continental Jurassic-Cretaceous boundary in China. *Acta Palaeontol. Sin.* 48, 541–555.

Conflict of Interest: The authors declare that the research was conducted in the absence of any commercial or financial relationships that could be construed as a potential conflict of interest.

frontiers in Earth Science

ORIGINAL RESEARCH
published: 02 June 2020
doi: 10.3389/feart.2020.00147

Paleomagnetic Constraint of the Brunhes Age Sedimentary Record From Lake Junín, Peru

Robert G. Hatfield[1,2], Joseph S. Stoner[2], Katharine E. Solada[2], Ann E. Morey[2], Arielle Woods[3], Christine Y. Chen[4], David McGee[4], Mark B. Abbott[3] and Donald T. Rodbell[5]*

[1] Department of Geological Sciences, University of Florida, Gainesville, FL, United States, [2] College of Earth, Ocean, and Atmospheric Sciences, Oregon State University, Corvallis, OR, United States, [3] Department of Geology and Environmental Science, University of Pittsburgh, Pittsburgh, PA, United States, [4] Department of Earth, Atmospheric and Planetary Sciences, Massachusetts Institute of Technology, Cambridge, MA, United States, [5] Department of Geology, Union College, Schenectady, NY, United States

OPEN ACCESS

Edited by:
Luigi Jovane, University of São Paulo, Brazil

Reviewed by:
Quentin Simon, UMR7330 Centre de Recherche et d'Enseignement de Géosciences de l'Environnement (CEREGE), France
Christian Ohneiser, University of Otago, New Zealand
Agathe Lise-Pronovost, The University of Melbourne, Australia

***Correspondence:**
Robert G. Hatfield
rhatfield1@ufl.edu

Specialty section:
This article was submitted to Geomagnetism and Paleomagnetism, a section of the journal Frontiers in Earth Science

Received: *23 January 2020*
Accepted: *20 April 2020*
Published: *02 June 2020*

Citation:
Hatfield RG, Stoner JS, Solada KE, Morey AE, Woods A, Chen CY, McGee D, Abbott MB and Rodbell DT (2020) Paleomagnetic Constraint of the Brunhes Age Sedimentary Record From Lake Junín, Peru. Front. Earth Sci. 8:147. doi: 10.3389/feart.2020.00147

Normalized remanence, a proxy for relative geomagnetic paleointensity, along with radiocarbon and U-Th age constraints, facilitates the generation of a well-constrained chronology for sediments recovered during International Continental Scientific Drilling Program (ICDP) coring of Lake Junín, Peru. The paleomagnetic record of the ∼88 m stratigraphic section from Lake Junín was studied, and rock magnetic variability constrained, through analysis of 109 u-channel samples and 56 discrete samples. Downcore variations in sediment lithology reflect climate and hydrological processes over glacial-interglacial time frames and these changes are strongly reflected in the bulk magnetic properties. Glacial sediments are characterized by higher detrital silt content, higher magnetic susceptibility and magnetic remanence values, and a magnetic coercivity that is characteristic of ferrimagnetic (titano)magnetite and/or maghemite. Interglacial sediments and low lake-level facies are dominated by carbonate lithologies and/or peat horizons that result in lower magnetic concentration values. Sediments with moderately high Natural Remanent Magnetization (NRM) intensity ($>1 \times 10^{-3}$ A/m) have well resolved component directions and inclination values that vary around geocentric axial dipole expectations. This remanence value can be used as a threshold to filter the lowest quality paleomagnetic data from the record. Normalized NRM intensity values are also sensitive to lithologic variability, but following NRM remanence filtering, only the highest quality ferrimagnetic dominated data are retained which then show no coherence with bulk magnetic properties. Constrained by the existing radiocarbon based chronology over the last 50 kyrs and 18 U-Th age constraints that are restricted to five interglacial sediment packages, filtered normalized remanence parameters compare well with global relative paleointensity stacks, suggesting relative variations in geomagnetic intensity are preserved. By adjusting the existing age-depth model we improve the correlation between the Junín normalized intensity record and a well-dated RPI stack and RPI model. We then incorporate these paleomagnetic tie points with the existing radiometric dates using a modeling approach to assess uncertainty and refine

the age-depth model for Lake Junín. In combining relative and radiometric dating, the new age-depth model captures glacial-interglacial variations in sedimentation rate and improves the orbital-scale age model for the sediments accumulated in Lake Junín basin over most of the Brunhes.

Keywords: lake sediments, paleomagnetism, RPI, age models, stratigraphy, chronology

INTRODUCTION

To derive meaningful information about earth systems from marine and lacustrine sediment records relies on the development of a robust chronological framework. A number of chronological tools have been developed to address this need that include, but are not restricted to; radiometric dating (e.g., radiocarbon, U-Th, and Ar-Ar), paleomagnetism [e.g., reversal stratigraphy, paleosecular variation (PSV), relative paleointensity (RPI)], exposure dating (e.g., *in situ* cosmogenic nuclides (^{10}Be, ^{26}Al), optically stimulated luminescence (OSL)], layer counting (e.g., varves, ice cores), and tuning of some physical or geochemical property [e.g., magnetic susceptibility, color reflectance, and X-Ray Fluorescence (XRF)] to well-dated reference records (e.g., δ^{18}O, Earth's orbital parameters). Each approach often has unique advantages or applications over other techniques, but all methods are constrained to a specific or optimal time window, have a set of underlying assumptions that need to be adhered to, and often require a specific set of environmental conditions to be met (e.g., sediment composition, lack of post depositional alteration). In an ideal setting, an abundance of available datable material is accompanied by steady-state environmental conditions, over a period of time that is contained within, and optimal for, that specific chronological application. In these situations, quasi-continuous application of a single method can lead to generation of a high-quality age-depth relationship that can be used to generate an age model. In practice, the environmental changes that are often the object of study frequently dictate that this idealized setting rarely occurs in the natural environment and compromises are often required.

These compromises most often take the form of relatively large spacing between datable horizons and can result in the sub-optimal application of specific techniques and/or unconstrained age-model projections that go beyond the window of application. As a result, variations in sedimentation rate and/or hiatuses can go unnoticed and large uncertainties can be introduced, or more importantly, can go unrecognized in the resulting age-depth model. Lacustrine settings are often more dynamic depositional settings than deep-sea marine environments, heightening the potential for environmental change and non-steady state conditions. Therefore, in these settings, chronologies are most secure when multiple lines of independent chronostratigraphic evidence are integrated and uncertainties are accurately characterized. This approach builds confidence in any resulting age model by increasing the viable number of datable horizons, optimizing chronometer application to specific lithofacies, and independent multi-method dating of the same intervals. However, application of this approach beyond the radiocarbon window (>50 kyrs) can be difficult, making the study of long lacustrine records such as those recovered on International Continental Scientific Drilling Program (ICDP) projects particularly problematic.

The majority of long lake-sediment age-models rely on the aggregation of discretely dated horizons using a variety of "one sample, one date" methods (e.g., radiocarbon, U-Th, OSL, and paleomagnetic reversals) with varying degrees of success and attempts to constrain measurement and geological uncertainty (Fritz et al., 2007; Melles et al., 2011; Scholz et al., 2011; Shanahan et al., 2013). In contrast, paleomagnetic techniques can provide quasi-continuous measurements of geomagnetic paleosecular variation (PSV; e.g., Turner and Thompson, 1981; Thouveny et al., 1990; Peng and King, 1992; Lund, 1996; Lougheed et al., 2012; Reilly et al., 2018) and relative paleointensity (RPI; Peck et al., 1996; Stoner et al., 1998, 2002, 2003; Williams et al., 1998; Channell et al., 2002, 2019) that can be correlated in a wider chronological context to well-dated reference templates. These approaches that exploit regional directional variability (PSV) or regional to global intensity changes (RPI) in the earth's magnetic field have demonstrated the potential to generate accurate chronologies either as stand-alone techniques (Lougheed et al., 2012; Ólafsdóttir et al., 2013; Blake-Mizen et al., 2019) or in concert with other approaches to bridge gaps between dated horizons (Stott et al., 2002; Channell et al., 2014; Hatfield et al., 2016). However, these approaches are more frequently employed in marine settings than in sedimentologically complex lacustrine environments. Here, we make continuous u-channel based paleomagnetic measurements on sediments recovered during ICDP Drilling of Lake Junín, Peru to augment and refine the existing ^{14}C and U-Th radiometric-based age model (Woods et al., 2019; Chen et al., 2020). We then integrate all new and existing age-depth constraints and use the age-depth modeling software "*Undatable*" (Lougheed and Obrochta, 2019) to provide estimates of uncertainty alongside the new higher-density age-model for the Lake Junín sediment record.

BACKGROUND, MATERIALS, AND METHODS

Proyecto Lago Junín (The Lake Junín Project)

Lake Junín (11.03° S, 76.11°W) is a large (300 km^2), but shallow (<15 m water depth), semi-closed basin lake located 4,085 m above sea level in the Peruvian Andes (Seltzer et al., 2000; Rodbell et al., 2014) (**Figure 1A**). Regional moraine mapping and cosmogenic radionuclide dating indicate that paleoglaciers reached the lake edge, but have not overridden the lake in

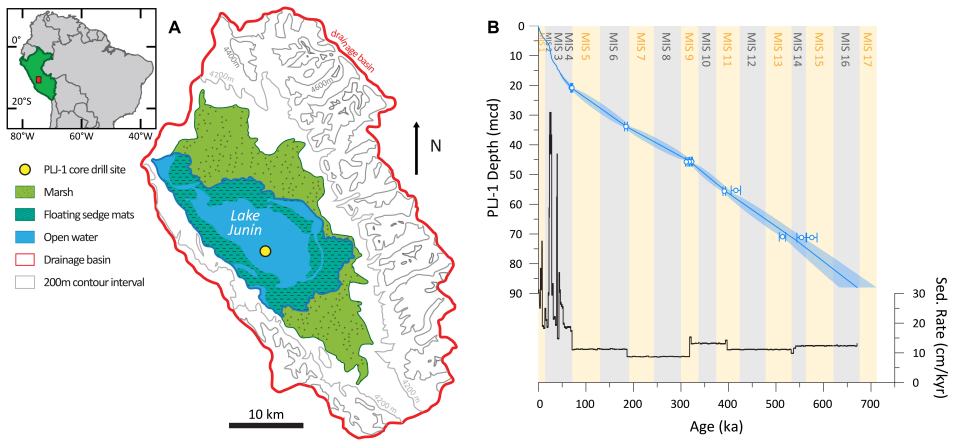

FIGURE 1 | (A) Location of the Lake Junín drainage basin and the position of the PLJ-1 ICDP drill site (yellow circle), and **(B)** existing *Bacon*-derived radiometric-based age-depth model (blue line) based on 79 radiocarbon dates and 18 U-Th age constraints for the Lake Junin splice (Woods et al., 2019; Chen et al., 2020) with 2-sigma uncertainty (blue shading) and calculated mean sedimentation rate (black line). The 79 radiocarbon and 6 U-Th age constraints from the last 50 kyrs are not shown on the age-depth plot for clarity. Marine Isotope Stages (MIS) are indicated with glaciations shaded gray and interglaciations shaded yellow as defined in LR04 (Lisiecki and Raymo, 2005).

the last million years (Wright, 1983; Smith et al., 2005a,b). Previous shallow coring efforts revealed that Lake Junín is strongly sensitive to tropical hydroclimate and that $\delta^{18}O$ records from Junin sediments are comparable to stable isotope records from regional ice cores and speleothems (Thompson et al., 1985, 2000; Seltzer et al., 2000; Kanner et al., 2012; Burns et al., 2019). A 2012 geophysical site survey revealed that the Lake Junín basin contained a thick (>125 m) sediment package that spanned several hundred thousand years if extrapolated using shallow coring sedimentation rates. The aim of the Lake Junín ICDP project was to develop continuous high-resolution records to study phenomena such as the El Nino-Southern Oscillation, the South America Summer Monsoon, and the Intertropical Convergence Zone, and their influence on tropical glaciation over multiple glacial-interglacial cycles. The first step of this, and of any paleo-study, is to establish a robust age model within which to seat the observed environmental changes.

Sediment Coring

Five holes were drilled in the deep central part of Lake Junín in 2015. The uppermost sediments were resampled with a Livingstone push corer that better preserves softer, less-consolidated materials, and a quasi-continuous stratigraphic splice (PLJ-1) was constructed for the upper ∼95 m composite depth (mcd) (Hatfield et al., 2020). Sediment composition alternates between the influx of detrital clastic sediments during glacial periods, accumulation of authigenic calcite during interstadial periods, and organic matter rich peat horizons during lake-level low stands that results in a heterogenous lithostratigraphy that reflects sensitivity to climatic and hydrological variations (Seltzer et al., 2000; Woods et al., 2019; Chen et al., 2020; Hatfield et al., 2020). Following completion of the field season all cores were shipped to the National Lacustrine Core Facility (LacCore) at the University of Minnesota for acquisition of physical property measurements, splitting, imaging, and long term curation. A color profile and color indexes (L*a*b*) were generated for the PJL-1 splice during this process by scanning the split cores at 0.5 cm intervals using a color spectrophotometer (absorption bands ranged between 360 and 740 nm at 10 nm spacing) mounted on a multi-sensor track.

Existing Age Models and Dating Strategy

The sediment splice from Lake Junín has been dated using 79 radiocarbon dates that tightly constrain the upper ∼17 mcd to the last ∼50 kyrs (Woods et al., 2019) and 18 U-Th age constraints located between 1 and 71 mcd that project a mean age of ∼671 ka at 88 mcd (**Figure 1B**). The 18 U-Th age constraints are error-weighted means of 55 U-Th dates from 18 unique samples. Six of the U-Th age constraints are within the radiocarbon window validating the upper 17 mcd of the U-Th age model (Chen et al., 2020), while the remaining 12 U-Th age constraints group around five carbonate-rich horizons with ages consistent with the Marine Isotope Stage (MIS) 4/5 and 7/6 boundaries, and MIS 9, 11, and 13–15 interglaciations (**Figure 1B**). Because the U-Th dates are largely limited to intervals with authigenic carbonate facies that formed during warmer, likely interglacial, periods, the resulting age-depth model is forced to bridge up to 140 kyrs between adjacent U-Th constraints (Chen et al., 2020; **Figure 1B**). The linear sedimentation rates implied by the U-Th constraints fails to capture glacial-interglacial changes in sediment accumulation observed in the radiocarbon interval (Woods et al., 2019) and might be expected in the earlier part of the record (**Figure 1B**).

In contrast to U-Th dating approaches, which perform best with carbonate samples that are free from detrital material (Edwards et al., 2003 and references therein), paleomagnetic records are often best resolved in sediments with high lithogenic content. Therefore, the occurrence of silt-rich detrital lithofacies between the carbonate-rich U-Th dated horizons in Lake Junín sediments presents an opportunity to use the paleomagnetic normalized intensity record in conjunction with reference RPI

templates to examine the existing U-Th based chronology and to bridge the relatively large gaps between U-Th age constraints. The RPI reference records we use for comparison are PISO-1500 (Channell et al., 2009) and PADM-2M (Ziegler et al., 2011). PISO-1500 is a stack of 13 globally distributed RPI records, many with sedimentation rates of 10–15 cm/kyr which are similar to those of deeper Lake Junín record (**Figure 1B**). The PISO-1500 record was constructed by tuning paired RPI and $\delta^{18}O$ records to the RPI and $\delta^{18}O$ record of Integrated Ocean Drilling Program (IODP) Site U1308; the chronology of IODP Site U1308 results from the tuning of its benthic $\delta^{18}O$ record to the LR04 benthic $\delta^{18}O$ stack (Lisiecki and Raymo, 2005; Channell et al., 2008). PADM-2M is a lower resolution global paleointensity model developed using both relative and absolute paleointensity data constrained by more lower-latitude paleointensity data than used in the PISO-1500 stack. Each of the 76 RPI records remains on its own chronology in PADM-2M, but minor age recalibrations are applied to fix the Matuyama–Brunhes boundary at 780 ka, compared to 775 ka in PISO-1500. These two different approaches yield slight differences for apparently coeval geomagnetic features, for example, the RPI-low associated with the Iceland Basin excursion is given an age of 189 ka in PADM-2M and 194 ka in PISO-1500. Notwithstanding these slight offsets, through the integration of the radiometric and paleomagnetic chronologies, we can then generate a new, higher-density, age-depth model for the Lake Junín sediment record and, using age-depth modeling approaches, generate uncertainty estimates.

Laboratory Methods

The PLJ-1 splice was sampled continuously between 6.67 and 88 mcd using 109 u-channels (2 × 2 × 150 cm samples encased in plastic); the lowest part of the PLJ-1 splice (88–95 mcd) was not sampled as the splice at these depths is discontinuous and relies on recovery from a single hole (Hatfield et al., 2020). In addition, discrete 1–2 cc samples were taken from the end of every 1–2 u-channels (every 1.5–3 m) for the measurement of rock magnetic properties. Measurements of the Natural Remanent Magnetization (NRM) were made on each u-channel at 1 cm intervals on a 2G Enterprises superconducting rock magnetometer (SRM) optimized for the measurement of u-channel samples at Oregon State University (OSU). NRM directions (inclination and declination) and intensity were measured before and following stepwise alternating field (AF) demagnetization over a 10–80 mT range. The characteristic remanent magnetization (ChRM) directions were determined, and maximum angular deviation (MAD) values calculated, using principal component analysis (PCA) (Kirschvink, 1980) over a 20–60 mT range without anchoring to the origin. Cores were not oriented during drilling so declination for each core in the splice was rotated to a mean of 0°. Maximum angular deviation (MAD) values are used to monitor the stability of demagnetization and are converted to an alpha 95 confidence interval (Khokhlov and Hulot, 2016) to provide uncertainty estimates on the directional data.

Anhysteretic Remanent Magnetization (ARM) was imparted in a peak AF demagnetization of 100 mT and a 50 μT direct current (DC) bias field. ARM was measured at 1 cm intervals before and following stepwise (5–10 mT increments) AF demagnetization over a 10–100 mT range. U-channel magnetic susceptibility (MS) was measured at 1 cm interval spacing using a 38 mm Bartington MS2C loop sensor connected to a MS3 susceptometer mounted on a computer motion-controlled track at OSU. Each u-channel was measured three times and the average and standard deviation of the three runs calculated. Although MS, NRM, and ARM are measured every centimeter, the response functions of the SRM and MS2C integrate data over a larger window, smooth the data downcore, and introduce volumetric edge effects at the end of u-channels. The first and last three datapoints are removed from each u-channel dataset to reduce this effect. κarm/κ was calculated for the u-channel data by first normalizing the ARM for the DC bias field (κarm) and then by MS (κ) to generate a proxy for ferrimagnetic grain size (Banerjee et al., 1981; King et al., 1982). The median destructive field (MDF) of the ARM (MDF_{ARM}) provides an estimate of magnetic coercivity, which is sensitive to magnetic mineralogy and grain size variations, and is calculated as the AF field size at which the imparted ARM is demagnetized by 50% (Johnson et al., 1975; Dankers, 1981). The NRM intensity following 20 mT AF demagnetization was normalized by MS (NRM_{20mT}/MS) and the NRM intensity was also normalized by ARM using the slope method over the 20–60 mT demagnetization range (NRM/ARM_{slope}) (Tauxe et al., 1995; Channell et al., 2002). The linear correlation coefficient (r-value) of the NRM/ARM_{slope} normalization monitors the quality of the fit to the slope and can be used as an estimate of data quality and RPI reliability (Xuan and Channell, 2009).

Saturation magnetization (M_s), saturation remanence (M_{rs}), and coercivity (H_c) data were derived from hysteresis loops measured to a saturating field of 1,000 mT in 5 mT steps and are presented after correction of paramagnetic contributions using the high field slope above 800 mT unless otherwise stated. The coercivity of remanence (H_{cr}) was determined by demagnetization of the 1,000 mT Isothermal Remanent Magnetization (IRM) in 2.5 mT steps. All hysteresis measurements were made on a Princeton Measurements Corporation Micromag model 3900 vibrating sample magnetometer at Western Washington University. High temperature magnetic susceptibility (HTMS) was measured for 16 discrete samples on a Kappabridge KLY-3 at a frequency of 920 Hz in a 300 A/m field at the University of Florida. Samples were measured in air every 3–4°C on heating from room temperature to 700°C and during cooling to 50°C. Data are presented as normalized values using their initial room temperature MS value for normalization ($\kappa(T)/\kappa_0$). U-channel, hysteresis, and HTMS measurements are available in **Supplementary Data Sheet S1**.

RESULTS

Sediment and Rock Magnetic Properties

Sediments in the Lake Junín PLJ-1 splice vary between intervals of authigenic carbonate, glacially derived clastic silts, and

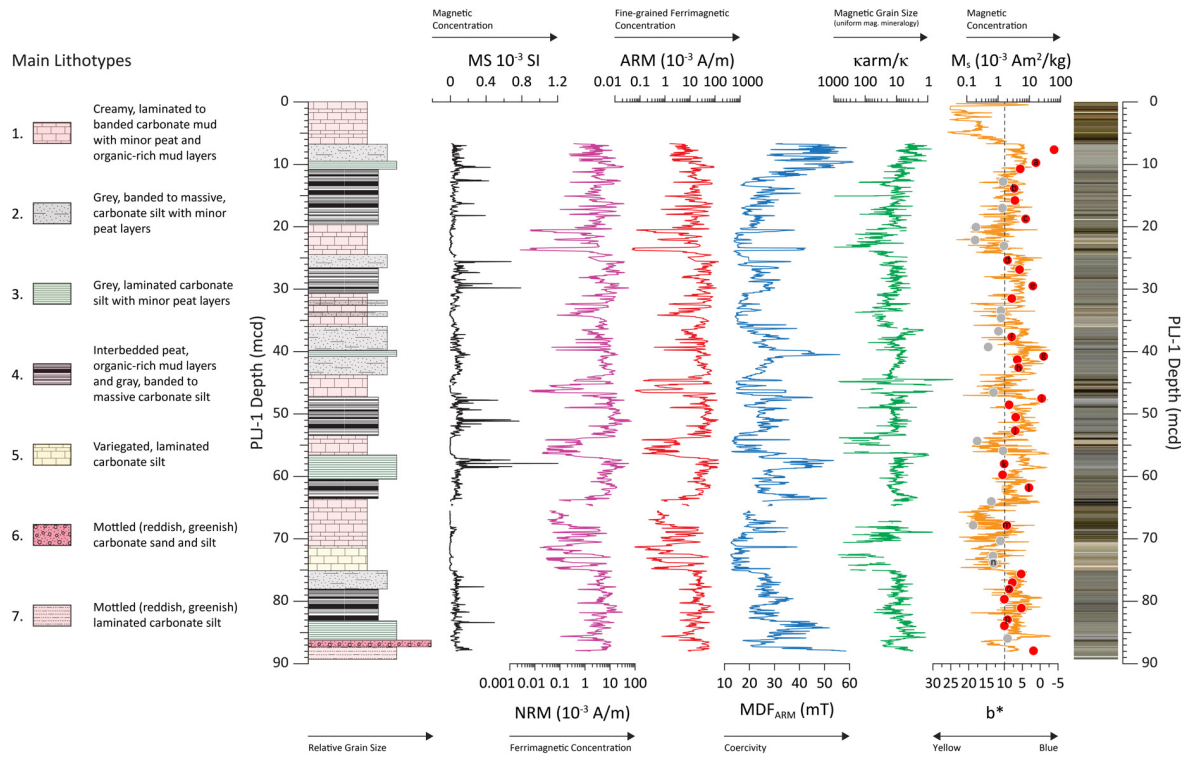

FIGURE 2 | From left to right. Stratigraphic column of the Lake Junín splice from Chen et al. (2020). Downcore u-channel derived magnetic properties; magnetic susceptibility (black line), natural remanent magnetization (NRM) (purple line), anhysteretic remanent magnetization (ARM) (red line), median destructive field of the ARM (blue line), and κarm/κ (green line). Downcore physical properties; b^* color index (orange line) and the synthetic color profile generated from the spectrophotometer. Discrete sample, paramagnetic slope corrected, M_S values [red ($>1.5 \times 10^{-3}$ Am^2/kg) and gray ($<1.5 \times 10^{-3}$ Am^2/kg) symbols] overlie the b^* color index. Gaps in the κarm/κ record relate to negative κarm/κ values that cannot be plotted on the x-axis logarithmic scale, letter annotations on the M_S data are used as sample identifiers across **Figures 3**, **4**. Note the prominent shifts across, and sensitivity of, all five magnetic property datasets associated with visible changes in sediment color and generalized lithology.

discrete horizons of organic-rich peats. This lithologic variability results in pronounced changes in sediment color and magnetic properties (Seltzer et al., 2000; Woods et al., 2019; Chen et al., 2020; Hatfield et al., 2020) (**Figure 2**). Carbonate dominated intervals (lithotypes 1 and 5 in **Figure 2**) have lower median MS [3.1×10^{-6} SI; Inter-Quartile Range (IQR) = -2.9–23×10^{-6} SI], NRM (0.5×10^{-3} A/m; IQR = 0.1–2.7×10^{-3} A/m), and ARM (4.1×10^{-3} A/m; IQR = 0.8–19×10^{-3} A/m) values than the median values of the other 5 lithofacies [MS = 66 (IQR = 45–92) $\times 10^{-6}$ SI; NRM = 6.1 (IQR = 3.4–11) $\times 10^{-3}$ A/m; ARM = 25 (IQR = 14–40) $\times 10^{-3}$ A/m] suggesting that lithology drives magnetic concentration variations. This relationship is again illustrated when the magnetic datasets are compared to the color profile output from the spectrophotometer and the sediment b^* values that monitor yellow ($+b^*$) and blue ($-b^*$) sediment coloration (**Figure 2**). Creamy colored carbonates and browner colored organic rich sediments are associated with more positive b^* values and the lowest values of MS, NRM, and ARM whereas the grayer sediments that suggest higher detrital input have more negative b^* values, higher MS, NRM, and ARM values (**Figure 2**).

Bulk magnetic coercivity, as estimated by MDF_{ARM}, is also influenced by lithology with lithotypes 1 and 5 possessing lower median MDF_{ARM} values (17.4 mT) than those lithotypes with higher bulk magnetic concentration values (26.9 mT). Gray laminated carbonate silts (lithotype 3) have relatively high MS and ARM values and also possess the highest MDF_{ARM} values, often in excess of 40 mT (**Figure 2**). In addition, several discrete peat rich layers with low magnetic concentration values (e.g., at 20.5 and 23.5 mcd) also appear to have relatively high values of MDF_{ARM} (**Figure 2**) that indicates a similar fine-grained ferrimagnetic mineral assemblage. κarm/κ shows a similar strong dependence on lithology with highest κarm/κ values associated with creamy carbonate muds and silts (lithotypes 1 and 5) (**Figure 2**). For a uniform magnetic mineral assemblage dominated solely by magnetite, we would expect higher MDF_{ARM} values to correspond to higher κarm/κ values (Maher, 1988). The observed inverse relationship in the Lake Junín sediments, where low values of MDF_{ARM} are associated with high κarm/κ values, suggests a more heterogeneous magnetic mineralogy that varies with lithotype.

High temperature magnetic susceptibility (HTMS) values of cooling curves are consistently higher than heating curves suggesting alteration of the magnetic mineral assemblage at high temperature (**Figure 3**). Although some variability is observed between samples, no samples show strong evidence for a

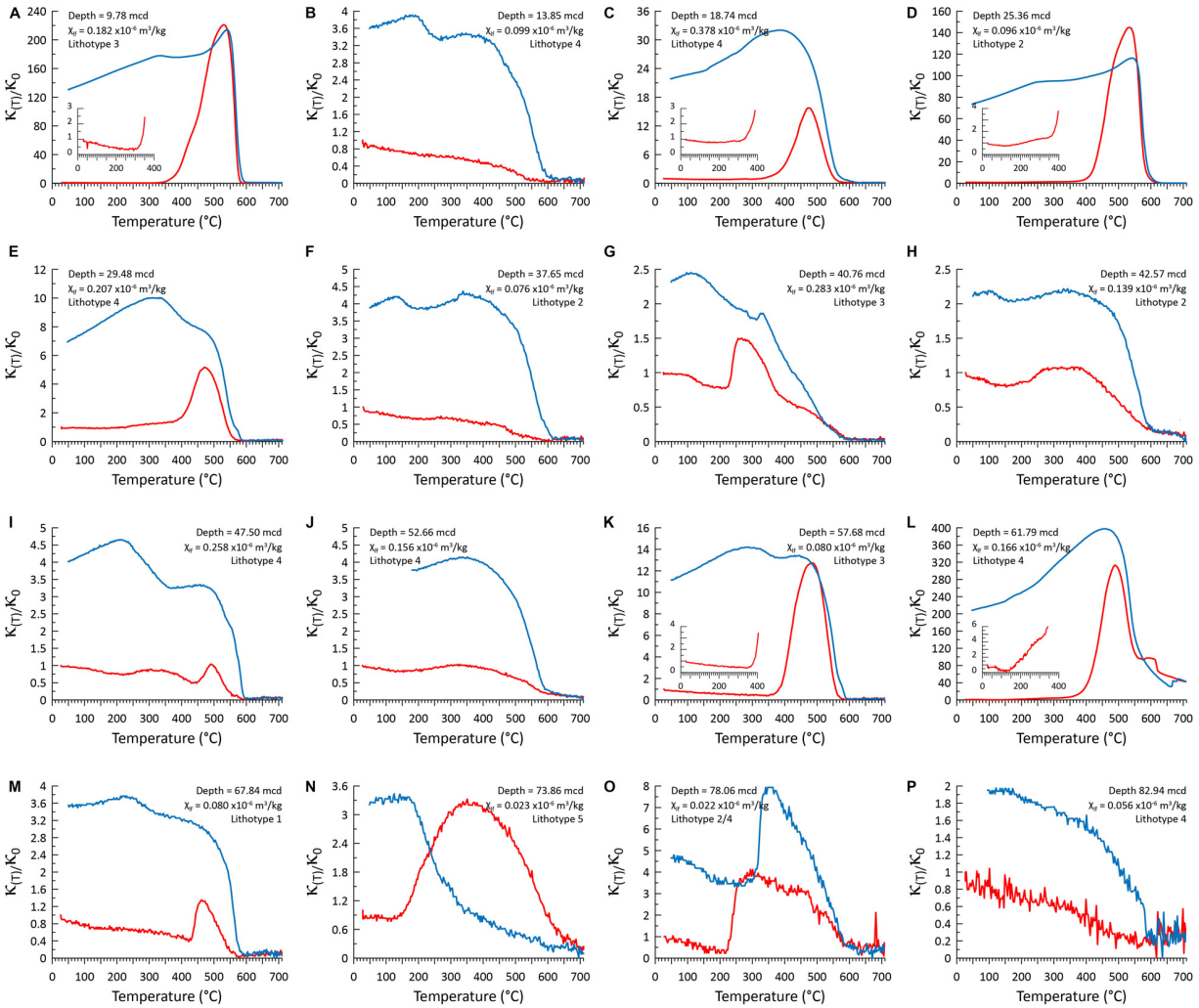

FIGURE 3 | High temperature magnetic susceptibility (HTMS) of 16 select discrete samples. MS was measured during heating from room temperature to 700°C (red curves) and on cooling to 50°C (blue curves). Data at each temperature [$\kappa_{(T)}$] are presented normalized to the MS value at the beginning of the experiment κ_0 and are shown alongside the sample depth, room temperature mass normalized MS (χ_{lf}) and the lithotype from which it was sampled (**Figure 2**). Where variations in the normalized MS data on heating between ∼25 and 400°C are obscured by higher values on cooling **(A,C,D,K,L)** the ∼25 – 400°C heating curve is provided as an inset. Panel letter identifiers are used consistently across **Figures 2**, **4** to aid comparison of samples. Note the general lack of Curie temperatures associated with ferrimagnetic pyrrhotite (∼320°C) and/or greigite (∼350°C) and the dominance of weakly paramagnetic mineral phases that alter above ∼400°C to produce ferrimagnetic magnetite.

Curie temperature associated with either ferrimagnetic pyrrhotite (∼320°C; Dekkers, 1989) or greigite (∼350°C; Dekkers et al., 2000; Chang et al., 2008) on heating. The only sample that shows a significant decrease in MS on heating between 300 and 350°C (**Figure 3G**) is preceded by a large increase in MS between 225–260°C. This change is consistent with the lambda-transition (Schwarz, 1975) in hexagonal pyrrhotite (e.g., Fe_9S_{10} or $Fe_{11}S_{12}$) as it alters into ferrimagnetic monoclinic pyrrhotite (Fe_7S_8), suggesting that at room temperature any sedimentary pyrrhotite exists in an antiferromagnetic form. A subset of samples (**Figures 3A,C–E,K–M**) show relatively weak MS on heating to ∼400°C, strong increases between ∼400 and 500°C, followed by strong decreases to zero values between ∼500 and 600°C. Slight increases in MS in some of these samples on heating between ∼300 and 400°C could be indicative ferrimagnetic greigite as it oxidizes to magnetite (Roberts and Turner, 1993; Roberts et al., 2011). However, the lack of minimum magnetizations in this temperature range suggests an admixture of magnetic minerals (Roberts et al., 2011) of which greigite is likely only a minor constituent. Large MS increases on cooling at ∼580°C is consistent with magnetite being the primary product of the high temperature alteration of paramagnetic and/or clay minerals in these samples. The remainder of the samples (**Figures 3B,F,H–J,P**) generally show decreasing MS values with increasing temperature and Curie temperatures consistent with titanomagnetite and magnetite. Cooling curves are also higher than heating curves, but MS increases are not as high as in the first subset of samples

indicating a lower intensity of paramagnetic alteration. One weakly magnetic sample ($\chi = 0.023 \times 10^{-6}$ m^3/kg; **Figure 3N**) from lithotype 5 shows more complex behavior associated with the carbonate rich sediment intervals.

Uncorrected hysteresis loops also reveal strong paramagnetic contributions, consistent with the HTMS data (**Figure 4A**). Samples with higher M_s values (red symbols in **Figure 2**) are associated with lower values of b^* and possess identifiable ferrimagnetic hysteresis behavior, while weaker samples that have higher b^* values and are more commonly dominated by paramagnetic contributions (**Figures 2, 4A**). For the samples with higher M_s values, saturation (following paramagnetic high field slope correction) is achieved in a field < 300 mT and when hysteresis and other magnetic and ratio data are compared with the data of Peters and Thompson (1998) (**Figures 4C,D**) the Lake Junín samples are consistent with ferrimagnetic mineralogies e.g., titanomagnetite, magnetite, maghemite, and/or greigite. Several Lake Junín samples span the (titano)magnetite – greigite space in **Figure 4C** and three of these samples showed alteration during heating to 400°C (**Figure 3**). While greigite can overprint the primary depositional remanent magnetization (DRM) with a secondary CRM, potentially complicating paleomagnetic interpretations (Roberts and Weaver, 2005; Rowan et al., 2009), it also may grow rapidly soon after deposition so that it would be considered equivalent to a DRM (Vasiliev et al., 2007; Chang et al., 2014). Examination of the demagnetization behavior of the NRM can assist in discriminating these contributions. When M_{rs}/M_s and H_{cr}/H_c values for these paramagnetic slope corrected samples are combined and viewed on a Day Plot (Day et al., 1977) they suggest a relatively fine average magnetic mineral assemblage which follows a magnetite trend that spans the mixing space from ultra-fine superparamagnetic (SP) grains through psuedo-single domain (PSD) space (**Figure 4B**) that generally have proven suitable for paleomagnetic reconstruction (King et al., 1983; Tauxe, 1993).

Because lithology has a strong influence on the down core variability in magnetic concentration, the magnetically weaker, non-ferrimagnetic intervals that are likely inferior for paleomagnetic reconstructions (e.g., **Figure 3N**) can be effectively filtered from the magnetic record using magnetic concentration parameters. Organic-rich layers that could potentially fuel early sediment diagenesis and alteration of the primary detrital magnetic signal (Roberts and Turner, 1993; Liu, 2004; Rowan et al., 2009) are also characterized by low magnetic concentration values and would also be filtered out via this process. From the hysteresis data, it appears that an approximate M_s value > 1.5×10^{-3} Am^2/kg appears suitable to discriminate the ferrimagnetic and paramagnetic dominated discrete samples (**Figure 2**). Although limited in number, these discrete data can be compared to the u-channel results to suggest equivalent filtering thresholds that can be applied to the MS ($\sim 4 \times 10^{-5}$ SI), NRM intensity ($\sim 1 \times 10^{-3}$ A/m), and/or ARM intensity ($\sim 5 \times 10^{-3}$ A/m) values (**Figure 2**).

Paleomagnetic Record

Stepwise AF demagnetization progressively reduces the NRM intensity and reveals a soft viscous component to the magnetization that is removed following peak AF of 15–20 mT (**Figure 5**). Following demagnetization in a peak AF of 60 mT a median of ∼9% of the NRM remains, and after increasingly higher AF demagnetization NRM directions often become increasingly scattered, justifying our use of the 20–60 mT component demagnetization range for estimation of ChRM directions (**Figure 5**). Like the environmental magnetic record, NRM intensity and paleomagnetic data quality appears to be strongly influenced by sediment lithology. For sediments with $NRM_{0\ mT}$ intensity values > 1×10^{-3} A/m the median MAD value is 1.7° (IQR = 1.0–2.7°) and ∼95% of MAD values are <5° (**Figure 6**). Relatively low MAD values indicate that the remanent vector is stable, well-defined, and possesses a single component that trends linearly toward the origin during AF demagnetization; criteria that are optimal for paleomagnetic reconstructions (Tauxe, 1993; Stoner and St-Onge, 2007). Low MAD values and single component, linearly demagnetizing vectors (**Figure 5**), also suggest that the magnetization is likely controlled by a (post)depositional remanent magnetization pDRM process, free of complications and overprints that would arise from a greigite induced gyroremanence and/or secondary CRM (e.g., Roberts et al., 2011). In contrast, sediments with $NRM_{0\ mT}$ intensity values < 1×10^{-3} A/m have higher MAD values (median = 8°; IQR = 4.3–18.9°) that result in less well-defined remanent vectors (**Figure 5**) and greater uncertainty in ChRM directions (**Figure 6**) that should be treated with caution (Stoner and St-Onge, 2007). Building on the observations provided by rock magnetic parameters we adopt a NRM intensity value of 1×10^{-3} A/m as a threshold to discriminate higher quality and higher intensity paleomagnetic data (H-NRMint), from lower quality and lower intensity (L-NRMint) paleomagnetic data.

Inclination values of the H-NRMint intervals cluster around the expected value of −21° (median = −23.8°; IQR = −20.1 – −27°) during periods of normal polarity for the site latitude assuming a Geocentric Axial Dipole (GAD) field. VGP latitude of the H-NRMint intervals cluster between +80° and +90° further suggesting that paleomagnetic directions reflect geomagnetic behavior and that the entire record was deposited during the Brunhes chron and is younger than ∼773 ka (Channell et al., 2010; Simon et al., 2019; Singer et al., 2019) (**Figure 6**), consistent with the U-Th age constraints by Chen et al. (2020). Variability in both inclination and declination of a few tens of degrees throughout the H-NRMint record is consistent with normal secular variation suggesting that the Junín sediments may also preserve non-axial dipole features of the field. During the L-NRMint intervals paleomagnetic directions deviate more widely from expected values (median inclination = −19.47°; IQR = −6.8 – −27.4°), with higher MAD values resulting in greater directional uncertainty. Filtering out the L-NRMint data effectively cleans the lowest quality directional data that are dominantly associated with carbonate rich lithologies, while still retaining 78% of the record. We should note that this threshold filtering process does not discriminate between low NRM intensity data associated with lithologic variations and low intensity data associated with true geomagnetic variability. Therefore, for examination of potential geomagnetic excursion

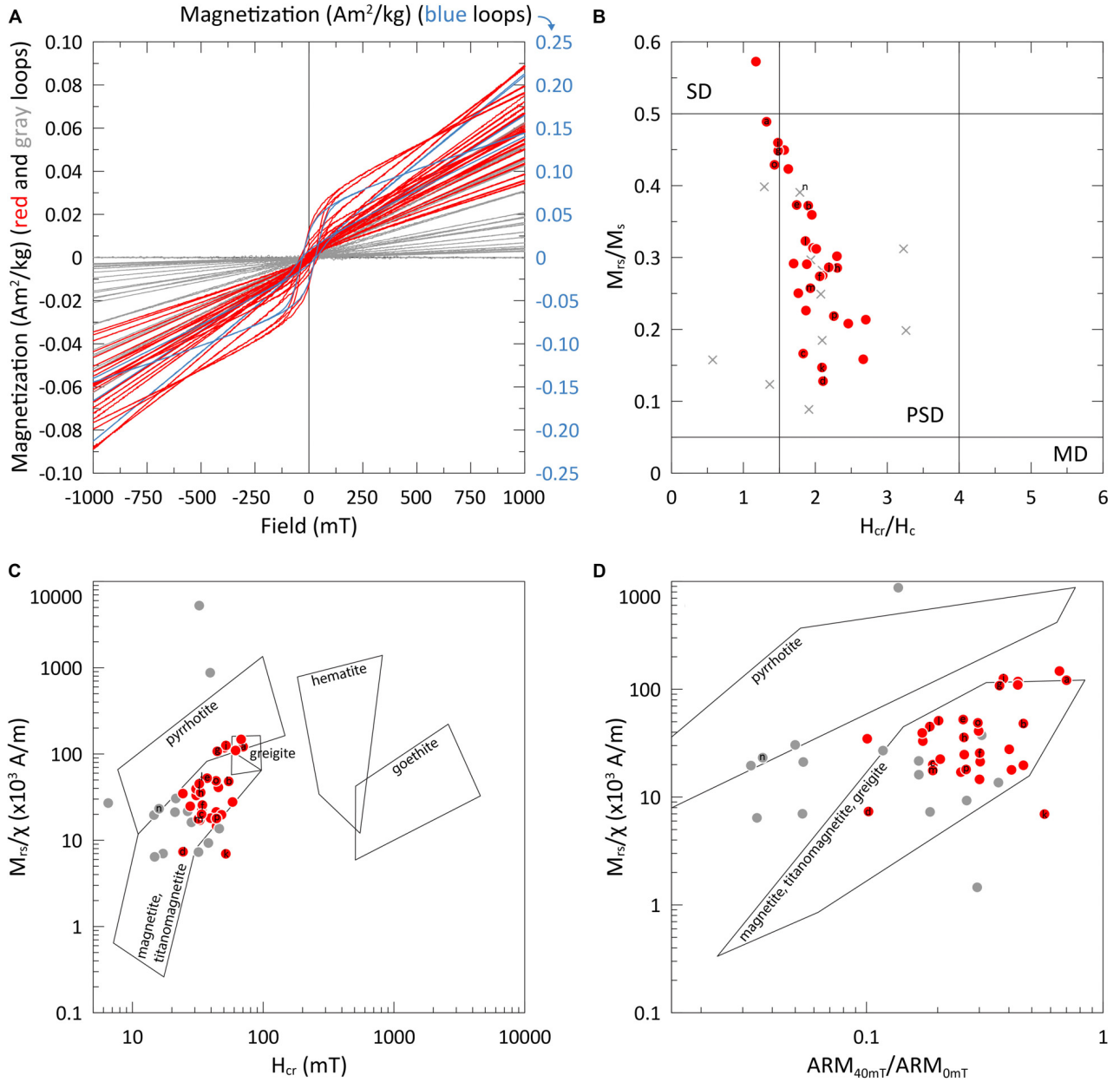

FIGURE 4 | (A) Uncorrected hysteresis loops of discrete samples from the Lake Junín Splice. Red loops and blue loops (slope corrected $M_s > 1.5 \times 10^{-3}$ Am^2/kg) have an identifiable ferrimagnetic component in addition to paramagnetic behavior, gray loops (slope corrected $M_s < 1.5 \times 10^{-3}$ Am^2/kg) have weaker magnetizations and are dominated by paramagnetic behavior. The four blue loop samples have M_s values > 0.1 Am^2/kg and are plotted on a separate *y*-axis with a different color for clarity purposes only. **(B)** Discrete samples following paramagnetic correction plotted within Day Plot space [H_{cr}/H_c 0–6; M_{rs}/M_s 0–0.6; (Day et al., 1977)]; magnetically weaker gray loop data are denoted as crosses. **(C)** H_{cr} vs. M_{rs}/χ biplot and **(D)** ARM intensity following 40 mT AF demagnetization normalized by the acquired ARM intensity prior to AF demagnetization ($ARM_{40\ mT}/ARM_{0\ mT}$) vs. M_{rs}/χ biplot. Data in **(C,D)** are compared to measured data from individual mineral species by Peters and Thompson (1998) and show that titanomagnetite and/or magnetite are important ferrimagnetic components of the Lake Junín sediments. Letter annotations for individual samples are consistent across **Figures 2–4**.

candidates in this, or any other record that follows this approach, the original unfiltered dataset would need to be examined. For Lake Junín, if we exclude the extended L-NRMint interval between 64 and 75 mcd, then eight L-NRMint intervals have VGP latitude values shallower than 45° (**Figure 6**). However, detailed investigation of each of these intervals revealed that the L-NRMint values resulted from lithogenic and rock magnetic, rather than paleomagnetic, variability and therefore cannot be used as additional chronostratigraphic constraints.

Natural Remanent Magnetization intensity was normalized to generate a proxy for RPI using two methods. First, the NRM intensity following 20 mT AF demagnetization ($NRM_{20\ mT}$) was

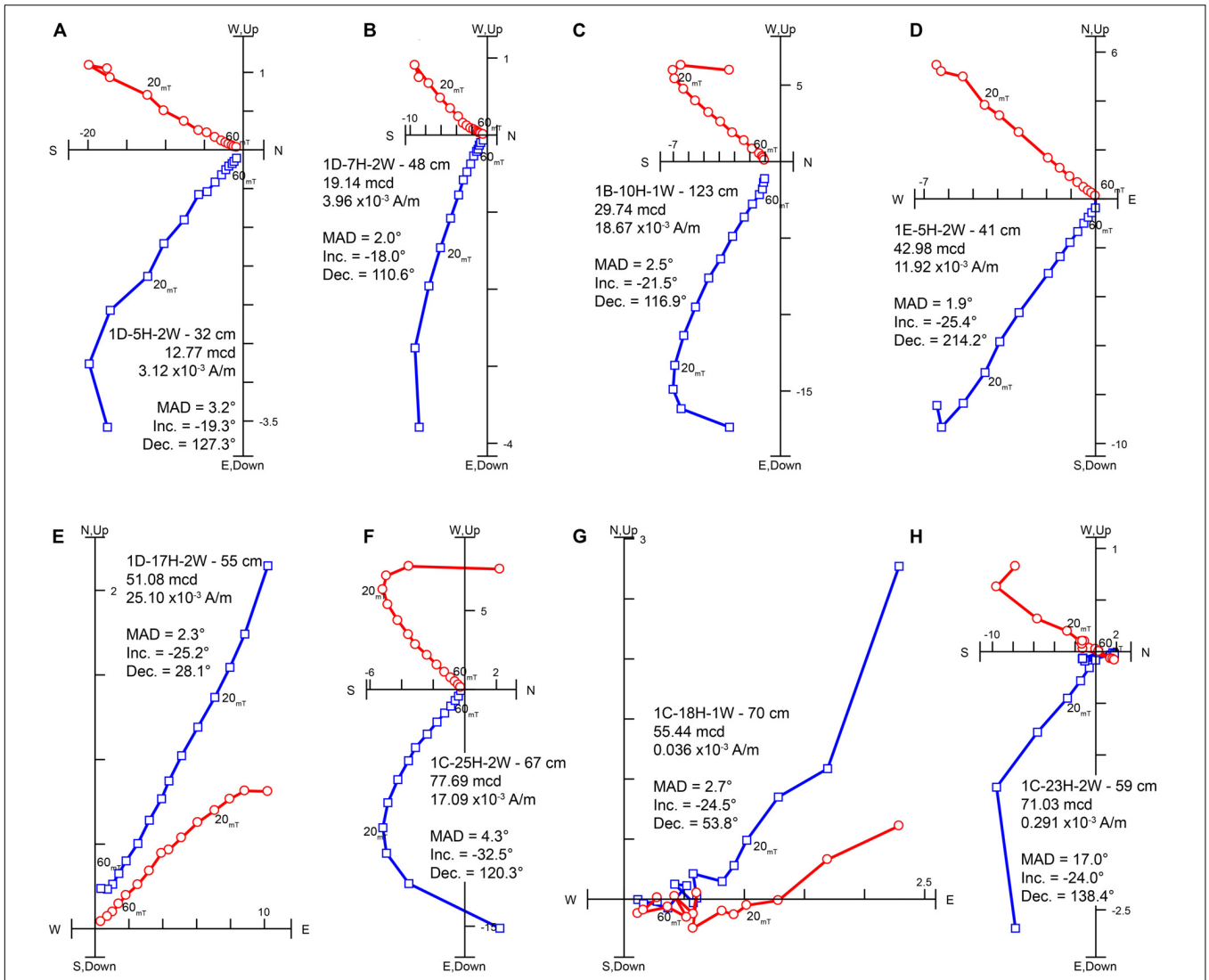

FIGURE 5 | Examples of orthogonal projections of AF demagnetization from u-channel samples. Red data and blue data represent the vertical and horizontal components of the field, respectively. The core section depth, meters composite depth, $NRM_{0\ mT}$ intensity value, MAD value, ChRM inclination, and ChRM declination are given. Note the stable and well-defined AF demagnetization structure and relatively low MAD values of samples with $NRM_{0\ mT}$ intensity values $> 1 \times 10^{-3}$ A/m **(A–F)** that contrasts with the more scattered AF demagnetization and higher MAD values of samples with $NRM_{0\ mT}$ intensity values $< 1 \times 10^{-3}$ A/m **(G,H)**.

normalized using MS ($NRM_{20\ mT}$/MS) (**Figure 7A**). Second, NRM intensity was normalized by ARM intensity over the 20–60 mT AF demagnetization range using the slope method [NRM/ARM_{slope})] with the fit of the two datasets monitored using the *R*-value (**Figure 7A**). L-NRMint intervals have lower NRM/ARM_{slope} values (median = 0.09; IQR = 0.06–0.14) and lower average *R*-values ($r = 0.83$) than the H-NRMint intervals (median = 0.23; IQR = 0.17 – 0.28; *R*-value > 0.99). A similar relationship is observed in the $NRM_{20\ mT}$/MS dataset with many of the L-NRMint intervals possessing negative values of $NRM_{20\ mT}$/MS that originate from the weakly negative MS values of the diamagnetic carbonate dominated sediments (**Figure 7A**). Distributions of normalized ratios reveal the bias that L-NRMint values have for lower ratio values, that lithological variation strongly affects the normalized NRM ratios and the quality of the normalization, and that these poorly defined values can be effectively filtered out by restricting our analysis to the H-NRMint dataset (**Figures 7B,C**). Neither filtered ratio dataset shows affinity to its normalizer suggesting little to no magnetic concentration influence on the H-NRMint normalized ratios (**Figures 7D,E**). Long period changes in the H-NRMint NRM/ARM_{slope} and H-NRMint $NRM_{20\ mT}$/MS values largely track each other suggesting a common driver of variability, however, the $NRM_{20\ mT}$/MS data appears more afflicted by higher frequency spike noise and negative values (**Figure 7A**). This increased variability likely relates to discrete intervals of lithologic variability that are likely inefficiently normalized using MS compared to ARM and NRM that are only sensitive to remanence

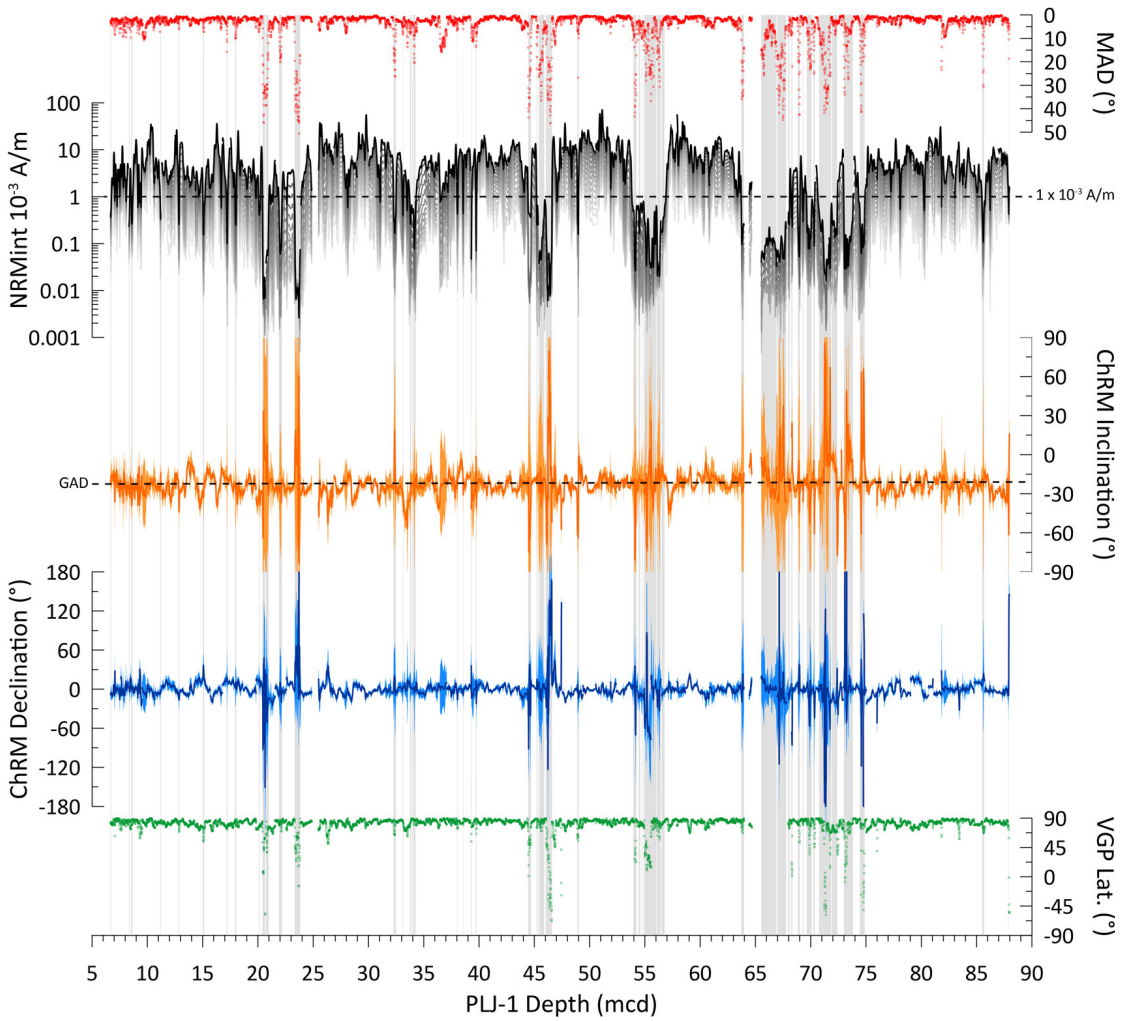

FIGURE 6 | Maximum angular deviation (MAD) values (red points), NRM intensity before (black data) and through progressive AF demagnetization (gray data), component inclination (orange) compared against a predicted value assuming a GAD and corrected (rotated to core mean of zero) component declination (blue), and virtual geomagnetic pole latitude (green points). a95 directional uncertainties (colored shading around the inclination and declination values) are calculated from MAD values using the method of Khokhlov and Hulot (2016). Gray vertical shading denotes $NRM_{0\ mT}$ intensity values below a 1×10^{-3} A/m threshold. Note the higher MAD values, greater directional variability, uncertainty, and VGP latitude scatter with lower than threshold $NRM_{0\ mT}$ intensity values.

carrying minerals and to the different response functions of the measurements. As a result we restrict the following discussion to the H-NRMint NRM/ARM_{slope} dataset, which coupled with R-values > 0.99, implies a well-defined and stable ratio.

Together, the demagnetization behavior, coherent directions, and well-defined and behaved normalized remanence ratios yield attributes that often result in the generation of reliable paleomagnetic records. Tauxe (1993) proposed a set of criteria to evaluate the reliability of sediment paleomagnetic and paleointensity records which we briefly summarize here: (1) the NRM must be carried by stable magnetite with a single well-defined component to the magnetization; (2) the detrital remanence must exhibit no inclination error; (3) concentration variations of more than about an order of magnitude should be avoided; (4) normalization by multiple methods should yield consistent results; (5) normalized intensity records should not be coherent with bulk rock magnetic parameters and; (6) records from a given region should agree within limits of a common timescale. Rock magnetic and paleomagnetic properties showed that samples are dominated by ferrimagnetic mineralogies (e.g., magnetite, titanomagnetite, and/or maghemite), and that by filtering the L-NRMint values from the dataset preferentially removes intervals dominated by non-ferrimagnetic components (**Figures 2–4**). In turn, this retains the most well-defined single-component ChRM's (**Figure 5**), reduces median MAD values to 1.7° and removes the more highly scattered directional variability (**Figure 6**), reduces the variance in MS and ARM values (90% of H-NRMint ARM intensity values are within one order of magnitude) (**Figure 2**), and results in normalized ratios that have little to no dependence on their normalizer (**Figure 7D**). As a result the H-NRMint dataset predominantly satisfies the first five criteria of Tauxe (1993) suggesting that the NRM/ARM_{slope}

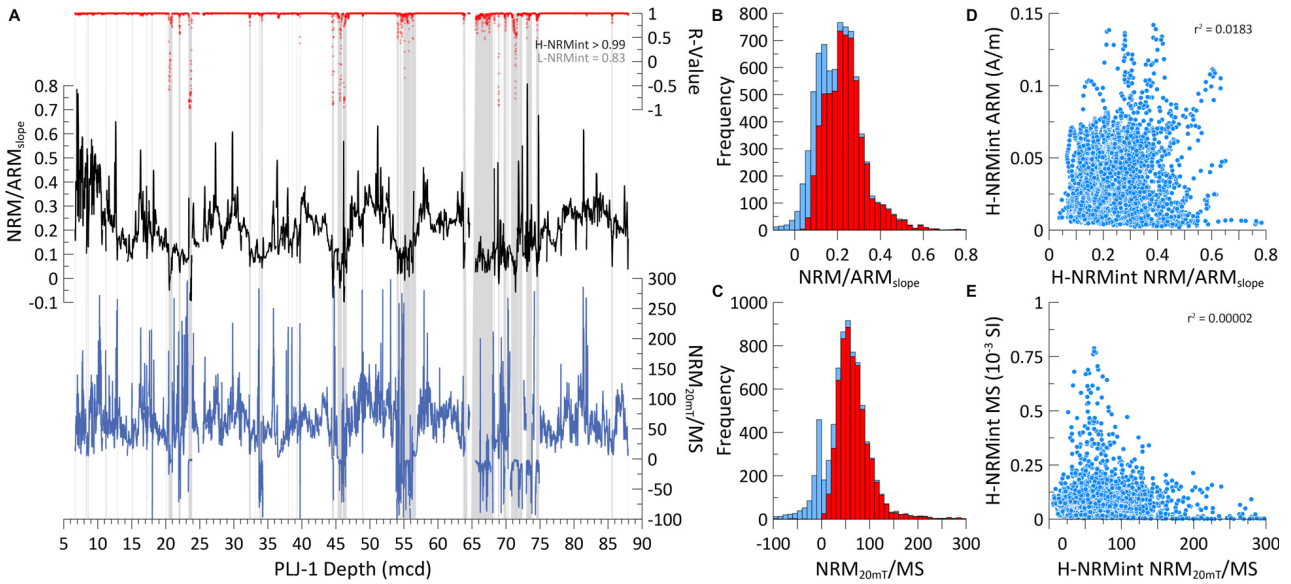

FIGURE 7 | (A) Normalized remanence ratios $NRM_{20\ mT}$/MS (blue) and NRM/ARM_{slope} (black) values and the associated *R*-value (red). Gray vertical shading highlights $NRM_{0\ mT}$ intensity values below a threshold of 1×10^{-3} A/m as in **Figure 6**. Median *R*-values of data with NRM intensity higher than the threshold (H-NRMint) exceed 0.99 while *R*-values of data with NRM intensity lower than the threshold (L-NRMint) are much lower; median values of these two populations are annotated. **(B)** Distribution of all NRM/ARM_{slope} data (blue) and the H-NRMint NRM/ARM_{slope} data (red). **(C)** Distribution of all $NRM_{20\ mT}$/MS data (blue) and the H-NRMint $NRM_{20\ mT}$/MS data (red). Note the L-NRMint data are biased toward lower, and in the case of $NRM_{20\ mT}$/MS negative, values. **(D)** NRM/ARM_{slope} values plotted against ARM intensity values for the H-NRMint dataset. **(E)** $NRM_{20\ mT}$/MS values plotted against MS values for the H-NRMint dataset. Note the lack of correlation between the normalized ratio and its normalizer for the H-NRMint datasets suggesting little influence of bulk magnetic concentration parameters on the normalized ratios.

record is likely capable of recording and preserving variability in geomagnetic field intensity.

To determine if Lake Junín sediments preserve a record of geomagnetic field intensity changes, we would expect it to reproduce the variability in independently dated reference records (Tauxe, 1993; Stoner and St-Onge, 2007). The H-NRMint filtered NRM/ARM_{slope} record is shown on the Chen et al. (2020) age model alongside the PISO-1500 global relative paleointensity stack (Channell et al., 2009) and the PADM-2M (Ziegler et al., 2011) axial dipole moment model in **Figure 8**. Similar features are identifiable and appear to be correlatable across the records (**Figure 8**). Low NRM/ARM_{slope} values appear associated with the low geomagnetic intensity values associated with the Laschamp excursion (∼41 ka), but between ∼60 and ∼110 ka on the Chen et al. (2020) age model NRM/ARM_{slope} values are relatively low and invariant making it difficult to correlate to PISO-1500 or PADM-2M. This carbonate dominated interval (lithotype 1) between 20–24 mcd has some of the weakest H-NRMint values (**Figure 2**), possibly explaining the reduced quality of this interval. As the upper ∼50 ka is well constrained by radiocarbon and two U-Th age constraints exist around ∼70 ka we focus our paleomagnetic investigations on the record prior to 120 ka.

In detail, the similarity of the three records varies through time with variability in the Lake Junín NRM/ARM_{slope} record appearing to both lead and lag changes in the global intensity estimate reference records. Although magnetic acquisition may play a role, any lock-in depth effect would only be expected to cause hundreds to a few thousand years of delay given sedimentation rates in excess of 10 cm/kyr (Roberts and Winklhofer, 2004; Suganuma et al., 2011). Instead, it is more likely that these longer-period offsets result from variations in sedimentation rate linked to changes in the regional environment, including lake level and glacial extent. Clearly sediment lithology is not adequately captured in the underconstrained radiometric-based age-model. By adopting 17 tie points (**Table 1**) based on the visual correlations in **Figure 8** the correlation coefficient (r) between the NRM/ARM_{slope} record from Lake Junín and PISO-1500 improves from 0.15 to 0.51 and 0.62 to PADM-2M (**Figure 8e**), approaching the $r = 0.69$ correlation between PISO-1500 and PADM-2M over the same time period. The improved correlation argues for viability of a paleointensity assisted chronology for the Lake Junín record.

DISCUSSION

Normalized remanence ratios such as NRM/ARM_{slope} are frequently generated to address two main questions: (1) to provide an estimation of geomagnetic relative paleointensity (RPI) that can be used to comment on some behavioral aspect of the geodynamo (e.g., reversals, excursions, and/or non-dipolar PSV behavior) (Stoner et al., 2002, 2013; Valet et al., 2005; Channell et al., 2009; Channell, 2017); and/or (2) to provide a continuous record of paleomagnetic field intensity variability

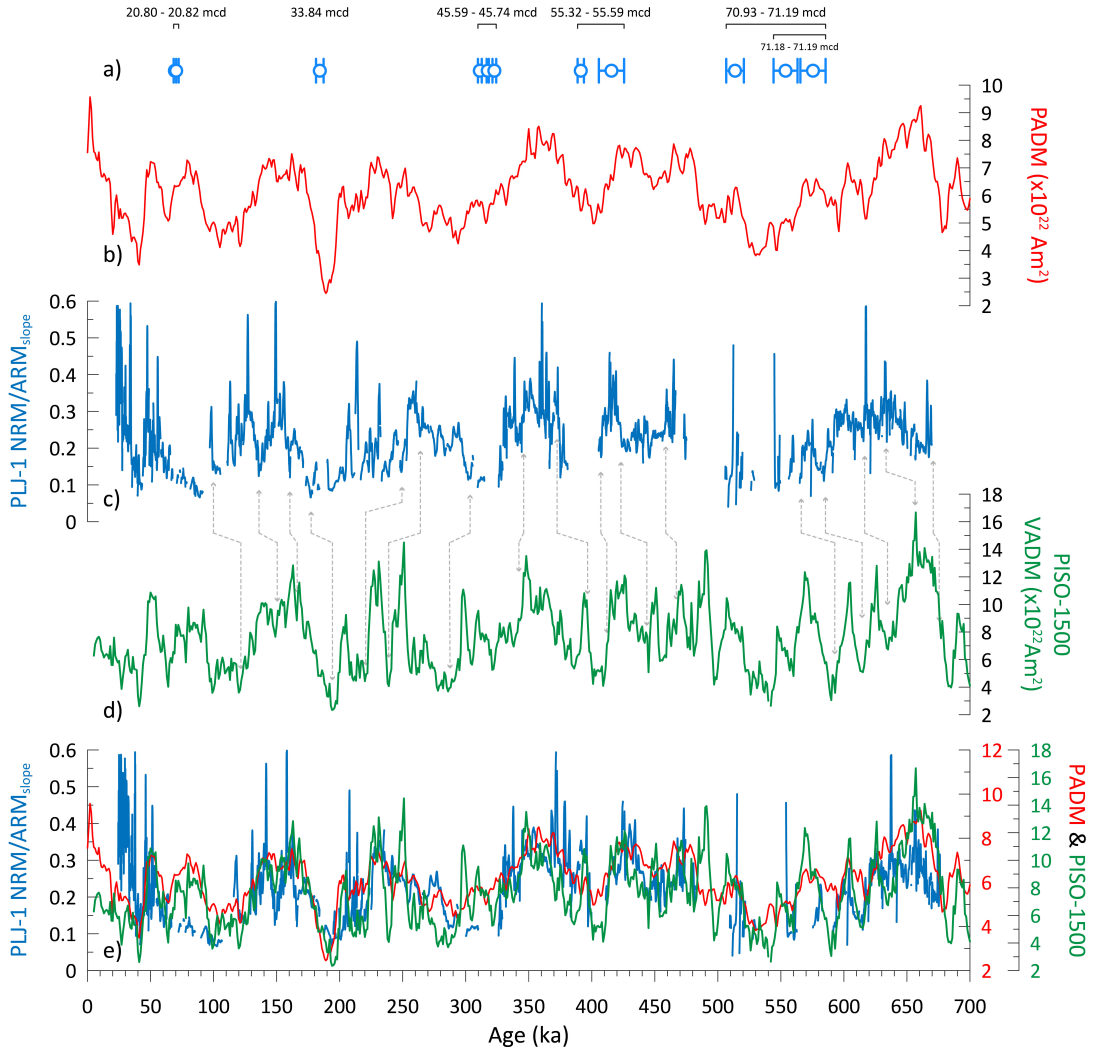

FIGURE 8 | (a) The 12 U-Th age constraints and 1-sigma uncertainty from the five horizons used to construct the age-depth model of Chen et al. (2020); the depth ranges of the dated samples are also given. **(b)** PADM-2M (red) dipole moment model of Ziegler et al. (2011). **(c)** The filtered Lake Junín H-NRMint NRM/ARM_{slope} RPI estimate (blue) using the age model of Chen et al. (2020). **(d)** PISO-1500 (green) RPI stack of Channell et al. (2009). Gray dashed lines between the Junín record and the PISO-1500 RPI stack is used to improve the correlation between the two from $r = 0.15$ to $r = 0.51$. **(e)** Comparison of PADM-2M, PISO-1500, and Junín RPI estimate after age adjustment using the gray tie-points. Correlation is restricted to the period prior to 120 ka (see text for further details).

that can be compared to well-dated stacks for the purpose of chronostratigraphy (Evans et al., 2007; Hatfield et al., 2016; Blake-Mizen et al., 2019; Channell et al., 2019). Although the differences between these two aims may seem subtle, the distinction can be important. RPI records used to define and study some aspect of the geodynamo should be of the utmost quality, ideally homogenous in composition, and be unambiguously clean of environmental influences or geochemical effects (Stoner and St-Onge, 2007). Natural variations in lithology can often complicate remanence normalization, but if these effects are not too severe, then RPI proxies (i.e., NRM/ARM_{slope}) can be adequately matched to RPI reference templates to provide chronological control (Stoner et al., 2000, 2003; Evans et al., 2007; Blake-Mizen et al., 2019; Channell et al., 2019). By these criteria, the sedimentological and rock magnetic variability outlined in **Figures 2–4** precludes the use of the Lake Junín record for detailed study of geomagnetic variability. However, the filtering process outlined in **Figure 7** to retain the highest quality data and the improved RPI correlations outlined in **Figure 8** suggest that we can potentially use the NRM/ARM_{slope} values of the Lake Junín sediments to provide additional age model constraints to refine the existing chronology.

Age Model Construction

To integrate the paleomagnetic data with the existing age-depth points we use the MatLab-based age-depth modeling program *Undatable* (Lougheed and Obrochta, 2019). The advantage of using *Undatable* over other available age-depth modeling programs is that it allows for uncertainties in both age and depth, for a series of different types of age control points to be

incorporated (e.g., absolute ages and tie-points), and for selective bootstrapping of the included ages (Lougheed and Obrochta, 2019). The age-depth tie points we use take three forms: (1) the 79 radiocarbon dates for the upper 17 mcd (Woods et al., 2019); (2) the 12 U-Th ages grouped around the 5 interglacial horizons (Chen et al., 2020); and (3) the 17 tie points made between the Junín NRM/ARM_{slope} record and PISO-1500 (**Figure 8**). The 29 combined U-Th and RPI tie points are listed in **Table 1**. For the radiocarbon dates, we assumed uniform depth uncertainty based on the sampling interval (often 2 cm). When running *Undatable*, radiocarbon calibration to calendar years using IntCal13 (Reimer et al., 2013) is automatically performed with MatCal (Lougheed and Obrochta, 2016), which uses highest posterior density to calculate the discrete one- and two-sigma ranges. Where U-Th age constraints occur within a few tens of centimeters of each other, we group the dated horizons within a uniform depth window using the maximum range for the grouped samples. This approach is used for the two U-Th age constraints at 20.80 and 20.82 mcd, the four constraints between 45.59 and 45.74 mcd, the two constraints at 55.32 and 55.58 mcd, and the three deepest constraints between 70.94 and 71.19 mcd (see **Figure 8**). By grouping the age constraints in this manner we combine their age probability density functions (PDFs) in *Undatable* and sample the entire interval using the information from the cumulative, multi-modal pdf's over the grouped depth range [see Fujiwara et al. (2019) for an explanation and practical example]. Age uncertainties for the individual U-Th age constraints uses the 1-sigma age uncertainty reported by Chen et al. (2020) (**Table 1**). For the paleomagnetic tie points, we used a Gaussian depth uncertainty (in most cases the range used was ±5 cm) which is more appropriate than uniform uncertainty when aligning reference series using tie points in *Undatable* (Lougheed and Obrochta, 2019). We adopt a conservative 1-sigma age uncertainty of ±5,000 years for the majority of paleomagnetic tie-points to account for "fuzziness" in paleomagnetic acquisition processes between records (e.g., sediment lock-in), potential aliasing of the paleomagnetic signal, and age model differences in different reference curves; e.g., the age of the RPI-low associated with the Iceland basin excursion varies between PISO-1500 (194 ka), SINT-2000 (190 ka), HINAPIS (187.5 ka), and PADM-2M (189 ka) (Valet et al., 2005; Channell et al., 2009; Ziegler et al., 2011; Xuan et al., 2016). The tie-point uncertainties are much greater than the depth uncertainties, but are similar in duration to the 1-sigma uncertainties reported for the U-Th age constraints by Chen et al. (2020) and are of the same order of magnitude as age-model uncertainties for the same features in different RPI stacks. The lowermost age-depth constraint provides an end point for the age-depth simulation in *Undatable*, cannot be included in the bootstrapping routine, and therefore has greater weight in the resulting age model (Lougheed and Obrochta, 2019). As a result we adopt a larger depth uncertainty of ±10 cm and a 1-sigma age uncertainty of 10,000 years for the basal paleomagnetic tie point, to provide a less rigid constraint to facilitate more reliable uncertainty estimates.

TABLE 1 | Tie points, sample depths, age, and age uncertainty for the U-Th and RPI age-depth constraints used for the *Undatable* Lake Junín age model.

Tie point	U-Th: Sample top (cm) RPI: Sample mid-point (cm)	U-Th Sample base (cm) RPI: Sample uncertainty (cm)	Age (yrs)	1-sigma age uncertainty (yrs)
UTh-K16	2080.4	2082.4	69109	1209
UTh-L1	2080.4	2082.4	70499	1757
RPI #1	2420	5	120000	5000
RPI #2	2850	5	150000	5000
RPI #3	3108	5	166000	5000
RPI #4	3291	5	194000	5000
UTh-D6	3383.7	3384	184267	2910
RPI #5	3945	5	220000	5000
RPI #6	4072	5	239000	5000
RPI #7	4407	5	287000	5000
UTh-M1	4559.4	4574.2	322714	1539
UTh-M3	4559.4	4574.2	322595	1020
UTh-J8	4559.4	4574.2	317456	867
UTh-J9	4559.4	4574.2	311209	1659
RPI #8	4931	5	345000	5000
RPI #9	5279	5	396000	5000
UTh-E12	5531.7	5558.8	415608	9928
UTh-F4	5531.7	5558.8	391269	2738
RPI #10	5715	5	412000	5000
RPI #11	5890	5	442000	5000
RPI #12	6292	5	468000	5000
UTh-B5	7093.9	7119.1	513645	6781
UTh-B11	7093.9	7119.1	553699	9685
UTh-B13	7093.9	7119.1	575476	10938
RPI #13	7500	5	593000	5000
RPI #14	7728	5	615000	5000
RPI #15	8117	5	635000	5000
RPI #16	8335	5	657000	5000
RPI #17	8800	10	677000	10000

For the U-Th constraints the sample top and sample base depths are given, for the RPI tie points the same mid-point and 1-sigma uncertainty on that depth point is given. U-Th sample nomenclature follows (Chen et al., 2020).

Undatable was run using 100,000 simulations, an xfactor of 0.1, and a bootpc of 30. The xfactor controls the sediment accumulation rate assumptions between pairs of age-depth constraints with larger values leading to greater freedom and therefore greater "uncertainty bubbles" (Lougheed and Obrochta, 2019). Published age models using *Undatable* have typically adopted an xfactor value of 0.1 (Lougheed and Obrochta, 2019). Bootpc controls the percentage of age-depth constraints that are bootstrapped (i.e., randomly removed) during each simulation, with a higher bootpc value allowing the age-model to explore a larger number of routing possibilities that produces a smoother result with larger uncertainty (Lougheed and Obrochta, 2019). As the radiocarbon interval is well-defined (Woods et al., 2019) and the major focus of the age-model refinement is the period >120 ka we only bootstrap the U-Th and paleomagnetic tie-points to prevent their under-sampling in the bootstrapping routine if all available dates had been used. Experiments were run varying the xfactor (0.05, 0.1, and 0.2) and bootpc (10, 20, 30, 40, and 50%) values, but these had little impact on the mean age

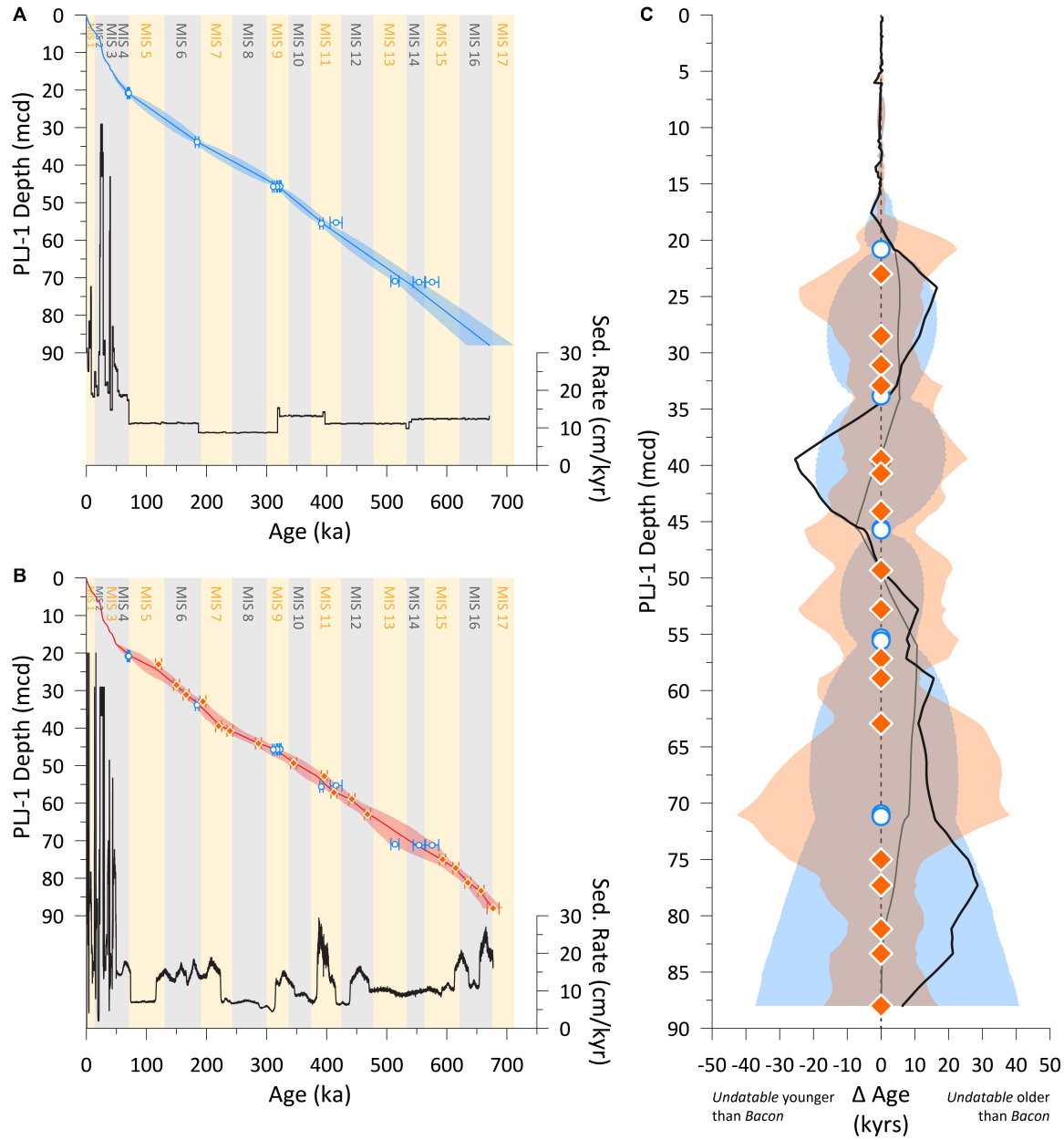

FIGURE 9 | (A) The existing *Bacon* age model (blue line) of Chen et al. (2020) reproduced from **Figure 1** for comparison. **(B)** The new *Undatable* derived age-depth model (red line) using 79 radiocarbon dates (not shown for clarity) from Woods et al. (2019), 18 U-Th age constraints for the Lake Junín splice [blue symbols as in **A**; (Chen et al., 2020)], and 17 paleomagnetic tie points (orange symbols) identified in **Figure 8**. The 2-sigma uncertainty (red shading) and calculated mean sedimentation rate (black line) is also shown. Marine Isotope Stages (MIS) are denoted by gray shading for glaciations and yellow shading interglaciations as defined in LR04 (Lisiecki and Raymo, 2005). **(C)** The *Bacon* age-depth mean-age model is subtracted from the *Undatable* age-depth mean-age model (black line) and the radiometric only *Undatable* age-depth mean-age model (thinner gray line, see text for details). Positive [negative] values imply an older [younger] age of the *Undatable* age-depth models compared to the *Bacon* age-depth model. The depth of U-Th age constraints (open blue circles) and paleomagnetic tie-points (orange diamonds) are shown alongside the uncertainty envelope of the existing *Bacon* age-depth model (blue) and new *Undatable* age-depth model (orange). Note that the offset of the two age models mostly falls within the uncertainty envelope of both age models.

model which remained entirely within the 1-sigma error of the results of the xfactor = 0.1, bootpc = 30 derived age-depth model.

The resulting age-depth plot is shown in **Figure 9B** alongside the existing radiometric-only *Bacon* (Blaauw and Christen, 2011) derived age model of Chen et al. (2020) that was parameterized using; *thickness = 50 cm, acc.mean = 80 yr/cm, acc.shape = 2.0, mem.strength = 15, and mem.mean = 0.8* (**Figure 9A**). In general terms the two age models possess a similar basal age, occurring during MIS 16, similar average sedimentation rates around 11 cm/kyr, and similar average uncertainties at the 95%

confidence interval for sediments older then ∼120 ka; ∼39 ka for the U-Th based age model, ∼37 ka for the new integrated age model. However, the greater density of age-depth constraints prior to ∼120 ka in the new age model results in clear variations in sedimentation rate, age model structure, and age model uncertainty in **Figure 9C**.

In order to examine whether these differences result from the inclusion of the paleomagnetic data, or the use of different age-depth modeling software, we reran *Undatable* using only the radiometric-based ^{14}C and U-Th ages. We adopted the same xfactor and bootpc parameters as before and constrained the basal age at 670.7 ka as projected by the mean *Bacon* age model. The differences between the *Undatable* and the *Bacon* radiometric-only results are shown as the thinner gray line in **Figure 9C**. In the interval 0–50 mcd, the average difference between the *Bacon* and *Undatable* mean results is 2.8 kyrs (maximum = 7.6 kyrs) (**Figure 9C**). These differences are an order of magnitude lower than the uncertainty structures of both age-models and imply relatively little difference between the two age-depth modeling approaches through these intervals. Between ∼50 and ∼88 mcd the radiometric-only *Undatable* age-model is generally older than the *Bacon* derived radiometric-only age-model with a maximum age-difference averaging around 10 kyrs between 55 and 71 mcd (**Figure 9C**). These differences likely arise from the way that the closely grouped data are input into *Bacon* and *Undatable*, respectively. While the *Undatable* age model is effectively sampling a cumulative and multi-modal PDF of the combined ages within a grouped interval, *Bacon* treats the individual ages as a spread of separate data points. For the U-Th age constraints clustered around 55 and 71 mcd the youngest age in each case has a lower uncertainty than the older ages from the same grouping (**Figure 8**). As the *Bacon* algorithm rewards samples with lower uncertainty (Blaauw and Christen, 2011), these younger ages are favored over the older and more uncertain ages in the close grouping. Indeed, the U-Th age constraints at 415.6 and 575.5 ka are effectively ignored by the *Bacon* algorithm, falling entirely outside the 2-sigma uncertainty structure of the resulting age model (**Figure 9A**). As a result the *Bacon* derived age-model is 9.7 and 8.2 kyrs younger than the *Undatable* age model at ∼55.5 and ∼71 mcd (the depths of the U-Th constraints) respectively (**Figure 9C**).

While the age-depth modeling approach used can account for a large part of the age-model difference between 55 and 71 mcd, significant deviations of the black and gray lines in **Figure 9C** reveals that the inclusion of paleomagnetic tie points also drives age-model variations. These deviations are greatest at ∼24.5, ∼40, and ∼77.5 mcd (**Figure 9C**). Between ∼34 and ∼50 mcd the *Undatable* age model is younger than the *Bacon* derived U-Th age model, while between ∼21 and ∼34 mcd and ∼50 and ∼88 mcd the *Undatable* age model is older than the *Bacon* age model. In general the uncertainty of the *Undatable* age model is greater than that of the *Bacon* age model, particularly around the deeper U-Th dated horizons (**Figure 9C**). We argue that this greater uncertainty and conservative approach is likely more appropriate as Chen et al. (2020) found no reason to reject the 415.6 and 575.5 ka U-Th ages that appear largely ignored by the *Bacon* age model. However, while the greater variability in age, sedimentation rate, and uncertainty structure in the *Undatable* age-model results from the inclusion of the paleomagnetic tie points, almost all of this age-model variability falls within the 2-sigma uncertainty of the original *Bacon* age model (**Figure 9C**).

Within the resolution of the *Undatable* age model (∼10^4 yrs; **Figure 9B**), sedimentation rate changes appear to mostly coincide with glacial-interglacial cycles. For example, sedimentation rates appear to be higher during the four periods of largest Pleistocene global ice volume associated with MIS 16, MIS 12, MIS 6, and MIS 2. These intervals are also characterized by higher magnetic concentration and MDF_{ARM} values suggesting that increases in clastic flux that occurred during the last local glacial maximum (Woods et al., 2019) may be a consistent and reproducible feature of the Lake Junín record over multiple glacial cycles. In addition to increases in glacial sediment fluxes, increased sedimentation rates also appear associated with the MIS 11 and MIS 9 interglaciations and the peak interglacial substages of MIS 5e and MIS 7c-a **Figure 9B**. These increases suggest that in addition to increases in glacial-clastic flux, variations in the efficiency of the in-lake carbonate pump affects sediment accumulation rate within the lake Junín basin as observed in the Holocene (Woods et al., 2019). These variations were not able to be resolved by the radiometric-based *Bacon* age model. Thus, the addition of the paleomagnetic chronological constraints to the existing radiometric derived age-model improves the chronological framework for Lake Junín, and establishes an age model capable of addressing the larger goals of the Lake Junín project.

CONCLUSION

The time interval covered and varying lithology of the Lake Junín sediments dictate that no single chronometer is able to develop a chronology required to address the larger goals of the Lake Junín project. Only the upper ∼17 mcd are within the radiocarbon window and the older U-Th dated intervals are limited to authigenic carbonate-rich horizons that are largely deposited during interglaciations. As a result, beyond MIS 3, glacial-interglacial variations in sedimentation rate remained unconstrained. Paleomagnetic data acquired from the Lake Junín splice record are of variable quality. Higher lithogenic content associated with glacial advances results in higher quality paleomagnetic records capable of constraining sedimentation rates, whereas carbonate facies are generally poorer paleomagnetic recorders. Filtering of the paleomagnetic record based upon magnetic concentration effectively separated these components, while still preserving almost 80% of the normalized remanence record that pass criteria for relative paleointensity estimates. Comparison to global intensity estimate reference curves show significant similarities on independent timescales with correlations greatly improved through minor age adjustments within the uncertainties of U-Th chronology. These age adjustments during glacial periods that were previously unconstrained by U-Th dating provide a series of new tie-points that were integrated with the radiometric data in the age-depth modeling program *Undatable*

to generate a new age-depth model for the Lake Junín splice and provide an estimate of uncertainty. The new age-depth model remains within the 2-sigma uncertainty structure of the existing radiometric-based age-model, but now produces glacial-interglacial variation in sedimentation rate that are similar to those found in the radiocarbon dated interval. By integrating the different chronometers, each with optimal temporal windows and/or lithologies of operation an improved orbital scale age model could be developed with realistic and transparent uncertainties that can facilitate the larger goals of the Lake Junín project.

DATA AVAILABILITY STATEMENT

All datasets generated for this study are included in the article/**Supplementary Material**.

AUTHOR CONTRIBUTIONS

JS, MA, DR, and DM conceived the Lake Junín project and acquired funding. RH and JS designed the paleomagnetic study of which this manuscript is the focus. RH, KS, and AM measured samples. RH and JS interpreted the data. All authors contributed to the writing, revision, and/or editing of the manuscript.

FUNDING

This research was carried out with support from the United States National Science Foundation awards EAR-1400903 (Stoner), EAR-1404113 (Abbott), EAR-1404414 (McGee), and EAR-1402076 (Rodbell) and from support by the ICDP, which in the United States is operated out of the Continental Scientific Drilling Coordination Office (CSDCO) at the University of Minnesota.

ACKNOWLEDGMENTS

The Lake Junín Project would not have been possible without the team of drillers from DOSECC Exploration Services (United States), GEOTEC (Peru), and the expertise of Doug Schnurrenberger, Kristina Brady Shannon, and Mark Shapley of CSDCO. Logistical assistance in the field was provided by Bryan Valencia, Angela Rozas-Davila, James Bartle, and Cecilia Oballe. RH would like to thank Cristina García-Lasanta and Bernie Housen at WWU for help measuring samples and Stephen Obrochta at Akita University for comments on using *Undatable*. We thank the three reviewers whose detailed and thoughtful comments improved this manuscript.

SUPPLEMENTARY MATERIAL

The Supplementary Material for this article can be found online at: https://www.frontiersin.org/articles/10.3389/feart.2020.00147/full#supplementary-material

DATA SHEET S1 | U-channel and color profile data on depth and age. Hysteresis and ARM ratio parameters on depth and age. HTMS data on heating (red) from 25-700 degrees Celsius and cooling (blue) from 700–50 degrees Celsius interpolated to the nearest degree.

REFERENCES

Banerjee, S. K., King, J., and Marvin, J. (1981). A rapid method for magnetic granulometry with applications to environmental studies. *Geophys. Res. Lett.* 8, 333–336. doi: 10.1029/GL008i004p00333

Blaauw, M., and Christen, J. A. (2011). Flexible paleoclimate age-depth models using an autoregressive gamma process. *Bayesian Anal.* 6, 457–474. doi: 10.1214/11-BA618

Blake-Mizen, K., Hatfield, R. G., Stoner, J. S., Carlson, A. E., Xuan, C., Walczak, M., et al. (2019). Southern Greenland glaciation and Western Boundary Undercurrent evolution recorded on Eirik Drift during the late Pliocene intensification of Northern Hemisphere glaciation. *Quat. Sci. Rev.* 209, 40–51. doi: 10.1016/j.quascirev.2019.01.015

Burns, S. J., Welsh, L. K., Scroxton, N., Cheng, H., and Edwards, R. L. (2019). Millennial and orbital scale variability of the South American Monsoon during the penultimate glacial period. *Sci. Rep.* 9, 1–5. doi: 10.1038/s41598-018-37854-3

Chang, L., Roberts, A. P., Tang, Y., Rainford, B. D., Muxworthy, A. R., and Chen, Q. (2008). Fundamental magnetic parameters from pure synthetic greigite (Fe3S4). *J. Geophys. Res. Solid Earth* 113:B06104. doi: 10.1029/2007JB005502

Chang, L., Vasiliev, I., Van Baak, C., Krijgsman, W., Dekkers, M. J., Roberts, A. P., et al. (2014). Identification and environmental interpretation of diagenetic and biogenic greigite in sediments: a lesson from the Messinian Black Sea. *Geochem. Geophys. Geosyst.* 15, 3612–3627. doi: 10.1002/2014GC005411

Channell, J. E. T. (2017). Mid-Brunhes magnetic excursions in marine isotope stages 9, 13, 14, and 15 (286, 495, 540, and 590 ka) at North Atlantic IODP Sites U1302/3, U1305, and U1306. *Geochem. Geophys. Geosyst.* 18, 473–487. doi: 10.1002/2016GC006626

Channell, J. E. T., Hodell, D. A., Singer, B. S., and Xuan, C. (2010). Reconciling astrochronological and 40Ar/39Ar ages for the Matuyama-Brunhes boundary and late Matuyama Chron. *Geochem. Geophys. Geosyst.* 11:Q0AA12. doi: 10.1029/2010GC003203

Channell, J. E. T., Hodell, D. A., Xuan, C., Mazaud, A., and Stoner, J. S. (2008). Age calibrated relative paleointensity for the last 1.5 Myr at IODP Site U1308 (North Atlantic). *Earth Planet. Sci. Lett.* 274, 59–71. doi: 10.1016/j.epsl.2008.07.005

Channell, J. E. T., Mazaud, A., Sullivan, P., Turner, S., and Raymo, M. E. (2002). Geomagnetic excursions and paleointensities in the Matuyama Chron at Ocean Drilling Program Sites 983 and 984 (Iceland Basin). *J. Geophys. Res* 107, EM1–EM14. doi: 10.1029/2001jb000491

Channell, J. E. T., Wright, J. D., Mazaud, A., and Stoner, J. S. (2014). Age through tandem correlation of Quaternary relative paleointensity (RPI) and oxygen isotope data at IODP Site U1306 (Eirik Drift. SW Greenland). *Quat. Sci. Rev.* 88, 135–146. doi: 10.1016/j.quascirev.2014.01.022

Channell, J. E. T., Xuan, C., and Hodell, D. A. (2009). Stacking paleointensity and oxygen isotope data for the last 1.5 Myr (PISO-1500). *Earth Planet. Sci. Lett.* 283, 14–23. doi: 10.1016/j.epsl.2009.03.012

Channell, J. E. T., Xuan, C., Hodell, D. A., Crowhurst, S. J., and Larter, R. D. (2019). Relative paleointensity (RPI) and age control in Quaternary sediment drifts off the Antarctic Peninsula. *Quat. Sci. Rev.* 211, 17–33. doi: 10.1016/j.quascirev.2019.03.006

Chen, C. Y., McGee, D., Woods, A., Pérez, L., Hatfield, R. G., Edwards, R. L., et al. (2020). *U-Th Dating of Lake Sediments: Lessons From the 700 kyr Sediment Record of Lake Junín, Peru*. Available online at: https://doi.org/10.31223/osf.io/c765k (accessed May 4, 2020).

Dankers, P. (1981). Relationship between median destructive field and remanent coercive forces for dispersed natural magnetite, titanomagnetite and hematite. *Geophys. J. R. Astron. Soc.* 64, 447–461. doi: 10.1111/j.1365-246X.1981.tb02676.x

Day, R., Fuller, M., and Schmidt, V. A. (1977). Hysteresis properties of titanomagnetites: grain-size and compositional dependence. *Phys. Earth Planet. Inter.* 13, 260–267. doi: 10.1016/0031-9201(77)90108-X

Dekkers, M. J. (1989). Magnetic properties of natural pyrrhotite. II. High- and low-temperature behaviour of Jrs and TRM as function of grain size. *Phys. Earth Planet. Inter.* 57, 266–283. doi: 10.1016/0031-9201(89)90116-7

Dekkers, M. J., Passier, H. F., and Schoonen, M. A. A. (2000). Magnetic properties of hydrothermally synthesized greigite (Fe3S4)-II. High- and low-temperature characteristics. *Geophys. J. Int.* 141, 809–819. doi: 10.1046/j.1365-246X.2000.00129.x

Edwards, R. L., Gallup, C. D., and Cheng, H. (2003). Uranium-series dating of marine and lacustrine carbonates. *Rev. Mineral. Geochem.* 52, 363–405. doi: 10.2113/0520363

Evans, H. F., Channell, J. E. T., Stoner, J. S., Hillaire-Marcel, C., Wright, J. D., Neitzke, L. C., et al. (2007). Paleointensity-assisted chronostratigraphy of detrital layers on the Eirik Drift (North Atlantic) since marine isotope stage 11. *Geochem. Geophys. Geosyst.* 8, 1–23. doi: 10.1029/2007GC001720

Fritz, S. C., Baker, P. A., Seltzer, G. O., Ballantyne, A., Tapia, P., Cheng, H., et al. (2007). Quaternary glaciation and hydrologic variation in the South American tropics as reconstructed from the Lake Titicaca drilling project. *Quat. Res.* 68, 410–420. doi: 10.1016/j.yqres.2007.07.008

Fujiwara, O., Aoshima, A., Irizuki, T., Ono, E., Obrochta, S. P., Sampei, Y., et al. (2019). Tsunami deposits refine great earthquake rupture extent and recurrence over the past 1300 years along the Nankai and Tokai fault segments of the Nankai Trough, Japan. *Quat. Sci. Rev* 227:105999. doi: 10.1016/J.QUASCIREV.2019.105999

Hatfield, R. G., Reyes, A. V., Stoner, J. S., Carlson, A. E., Beard, B. L., Winsor, K., et al. (2016). Interglacial responses of the southern Greenland ice sheet over the last 430,000 years determined using particle-size specific magnetic and isotopic tracers. *Earth Planet. Sci. Lett.* 454, 225–236. doi: 10.1016/j.epsl.2016.09.014

Hatfield, R. G., Woods, A., Lehmann, S. B., Weidhaas, N. IV, Chen, C. Y., Abbott, M. B., et al. (2020). Stratigraphic correlation and splice generation for sediments recovered from a large lake drilling project: an example from Lake Junín, Peru. *J. Paleolimnol.* 63, 83–100. doi: 10.1007/s10933-019-00098-w

Johnson, H. P., Lowrie, W., and Kent, D. V. (1975). Stability of anhysteretic remanent magnetization in fine and coarse magnetite and maghemite particles. *Geophys. J. R. Astron. Soc.* 41, 1–10. doi: 10.1111/j.1365-246X.1975.tb05480.x

Kanner, L. C., Burns, S. J., Cheng, H., and Edwards, R. L. (2012). High-latitude forcing of the South American summer monsoon during the last glacial. *Science* 335, 570–573. doi: 10.1126/science.1213397

Khokhlov, A., and Hulot, G. (2016). Principal component analysis of palaeomagnetic directions: converting a maximum angular deviation (MAD) into an α95angle. *Geophys. J. Int.* 204, 274–291. doi: 10.1093/gji/ggv451

King, J., Banerjee, S. K., Marvin, J., and Özdemir, Ö (1982). A comparison of different magnetic methods for determining the relative grain size of magnetite in natural materials: some results from lake sediments. *Earth Planet. Sci. Lett.* 59, 404–419. doi: 10.1016/0012-821X(82)90142-X

King, J. W., Banerjee, S. K., and Marvin, J. (1983). A new rock-magnetic approach to selecting sediments for geomagnetic paleointensity studies: application to paleointensity for the last 4000 years. *J. Geophys. Res.* 88, 5911–5921. doi: 10.1029/JB088iB07p05911

Kirschvink, J. L. (1980). The least−squares line and plane and the analysis of palaeomagnetic data. *Geophys. J. R. Astron. Soc.* 62, 699–718. doi: 10.1111/j.1365-246X.1980.tb02601.x

Lisiecki, L. E., and Raymo, M. E. (2005). A pliocene-pleistocene stack of 57 globally distributed benthic δ 18O records. *Paleoceanography* 20, 1–17. doi: 10.1029/2004PA001071

Liu, J. (2004). High-resolution analysis of early diagenetic effects on magnetic minerals in post-middle-Holocene continental shelf sediments from the Korea Strait. *J. Geophys. Res.* 109:15. doi: 10.1029/2003JB002813

Lougheed, B. C., and Obrochta, S. P. (2016). MatCal: open source bayesian 14C age calibration in Matlab. *J. Open Res. Softw.* 4:e42. doi: 10.5334/jors.130

Lougheed, B. C., and Obrochta, S. P. (2019). A rapid, deterministic age-depth modeling routine for geological sequences with inherent depth uncertainty. *Paleoceanogr. Paleoclimatol.* 34, 122–133. doi: 10.1029/2018PA003457

Lougheed, B. C., Snowball, I., Moros, M., Kabel, K., Muscheler, R., Virtasalo, J. J., et al. (2012). Using an independent geochronology based on palaeomagnetic secular variation (PSV) and atmospheric Pb deposition to date Baltic Sea sediments and infer 14C reservoir age. *Quat. Sci. Rev.* 42, 43–58. doi: 10.1016/j.quascirev.2012.03.013

Lund, S. P. (1996). A comparison of Holocene paleomagnetic secular variation records from North America. *J. Geophys. Res. Solid Earth* 101, 8007–8024. doi: 10.1029/95jb00039

Maher, B. A. (1988). Magnetic properties of some synthetic sub−micron magnetites. *Geophys. J.* 94, 83–96. doi: 10.1111/j.1365-246X.1988.tb03429.x

Melles, M., Brigham-Grette, J., Minyuk, P., Koeberl, C., Andreev, A., Cook, T., et al. (2011). The lake El'gygytgyn scientific drilling project – conquering Arctic challenges through continental drilling. *Sci. Drill.* 11, 29–40. doi: 10.2204/iodp.sd.11.03.2011

Ólafsdóttir, S., Geirsdóttir, Á, Miller, G. H., Stoner, J. S., and Channell, J. E. T. (2013). Synchronizing holocene lacustrine and marine sediment records using paleomagnetic secular variation. *Geology* 41, 535–538. doi: 10.1130/G33946.1

Peck, J. A., King, J. W., Colman, S. M., and Kravchinsky, V. A. (1996). An 84-kyr paleomagnetic record from the sediments of Lake Baikal, Siberia. *J. Geophys. Res. Solid Earth* 101, 11365–11385. doi: 10.1029/96jb00328

Peng, L., and King, J. W. (1992). A late Quaternary geomagnetic secular variation record from Lake Waiau, Hawaii, and the question of the Pacific nondipole low. *J. Geophys. Res.* 97, 4407–4424. doi: 10.1029/91jb03074

Peters, C., and Thompson, R. (1998). Magnetic identification of selected natural iron oxides and sulphides. *J. Magn. Magn. Mater.* 183, 365–374. doi: 10.1016/s0304-8853(97)01097-4

Reilly, B. T., Stoner, J. S., Hatfield, R. G., Abbott, M. B., Marchetti, D. W., Larsen, D. J., et al. (2018). Regionally consistent Western North America paleomagnetic directions from 15 to 35 ka: assessing chronology and uncertainty with paleosecular variation (PSV) stratigraphy. *Quat. Sci. Rev.* 201, 186–205. doi: 10.1016/j.quascirev.2018.10.016

Reimer, P. J., Bard, E., Bayliss, A., Beck, J. W., Blackwell, P. G., Ramsey, C. B., et al. (2013). IntCal13 and Marine13 radiocarbon age calibration curves 0–50,000 years cal BP. *Radiocarbon* 55, 1869–1887. doi: 10.2458/azu_js_rc.55.16947

Roberts, A. P., Chang, L., Rowan, C. J., Horng, C. S., and Florindo, F. (2011). Magnetic properties of sedimentary greigite (Fe3S4): an update. *Rev. Geophys* 49:RG1002. doi: 10.1029/2010RG000336

Roberts, A. P., and Turner, G. M. (1993). Diagenetic formation of ferrimagnetic iron sulphide minerals in rapidly deposited marine sediments, South Island, New Zealand. *Earth Planet. Sci. Lett.* 115, 257–273. doi: 10.1016/0012-821x(93)90226-y

Roberts, A. P., and Weaver, R. (2005). Multiple mechanisms of remagnetization involving sedimentary greigite (Fe3S4). *Earth Planet. Sci. Lett.* 231, 263–277. doi: 10.1016/j.epsl.2004.11.024

Roberts, A. P., and Winklhofer, M. (2004). Why are geomagnetic excursions not always recorded in sediments? Constraints from post-depositional remanent magnetization lock-in modelling. *Earth Planet. Sci. Lett.* 227, 345–359. doi: 10.1016/j.epsl.2004.07.040

Rodbell, D. T., Delman, E. M., Abbott, M. B., Besonen, M. T., and Tapia, P. M. (2014). The heavy metal contamination of Lake Junín National Reserve, Peru: an unintended consequence of the juxtaposition of hydroelectricity and mining. *GSA Today* 24, 4–10. doi: 10.1130/GSATG200A.1

Rowan, C. J., Roberts, A. P., and Broadbent, T. (2009). Reductive diagenesis, magnetite dissolution, greigite growth and paleomagnetic smoothing in marine sediments: a new view. *Earth Planet. Sci. Lett.* 277, 223–235. doi: 10.1016/j.epsl.2008.10.016

Scholz, C. A., Cohen, A. S., Johnson, T. C., King, J., Talbot, M. R., and Brown, E. T. (2011). Scientific drilling in the Great Rift Valley: the 2005 Lake Malawi scientific drilling project – an overview of the past 145,000 years of climate variability in Southern Hemisphere East Africa. *Palaeogeogr. Palaeoclimatol. Palaeoecol.* 303, 3–19. doi: 10.1016/j.palaeo.2010.10.030

Schwarz, E. J. (1975). *Magnetic Properties of Pyrrhotite and Their Use in Applied Geology and Geophysics*. Ottawa, ON: Geological Survey of Canada.

Seltzer, G., Rodbell, D., and Burns, S. (2000). Isotopic evidence for late Quaternary climatic change in tropical South America. *Geology* 28, 35–38. doi: 10.1130/0091-7613200028<35:IEFLQC<2.0.CO;2

Shanahan, T. M., Peck, J. A., McKay, N., Heil, C. W., King, J., Forman, S. L., et al. (2013). Age models for long lacustrine sediment records using multiple dating approaches – an example from Lake Bosumtwi, Ghana. *Quat. Geochronol.* 15, 47–60. doi: 10.1016/j.quageo.2012.12.001

Simon, Q., Suganuma, Y., Okada, M., and Haneda, Y. (2019). High-resolution 10Be and paleomagnetic recording of the last polarity reversal in the Chiba composite section: age and dynamics of the Matuyama–Brunhes transition. *Earth Planet. Sci. Lett.* 519, 92–100. doi: 10.1016/j.epsl.2019.05.004

Singer, B. S., Jicha, B. R., Mochizuki, N., and Coe, R. S. (2019). Synchronizing volcanic, sedimentary, and ice core records of Earth's last magnetic polarity reversal. *Sci. Adv.* 5:eaaw4621. doi: 10.1126/sciadv.aaw4621

Smith, J. A., Finkel, R. C., Farber, D. L., Rodbell, D. T., and Seltzer, G. O. (2005a). Moraine preservation and boulder erosion in the tropical Andes: interpreting old surface exposure ages in glaciated valleys. *J. Quat. Sci.* 20, 735–758. doi: 10.1002/jqs.981

Smith, J. A., Seltzer, G. O., Farber, D. L., Rodbell, D. T., and Finkel, R. C. (2005b). Climate change: early local last glacial maximum in the tropical Andes. *Science* 308, 678–681. doi: 10.1126/science.1107075

Stoner, J. S., Channell, J. E. T., and Hillaire-Marcel, C. (1998). A 200 ka geomagnetic chronostratigraphy for the Labrador Sea: indirect correlation of the sediment record to SPECMAP. *Earth Planet. Sci. Lett.* 159, 165–181. doi: 10.1016/S0012-821X(98)00069-7

Stoner, J. S., Channell, J. E. T., Hillaire-Marcel, C., and Kissel, C. (2000). Geomagnetic paleointensity and environmental record from Labrador Sea core MD95-2024: global marine sediment and ice core chronostratigraphy for the last 110 kyr. *Earth Planet. Sci. Lett.* 183, 161–177. doi: 10.1016/S0012-821X(00)00272-7

Stoner, J. S., Channell, J. E. T., Hodell, D. A., and Charles, C. D. (2003). A ∼580 kyr paleomagnetic record from the sub-Antarctic South Atlantic (Ocean Drilling Program Site 1089). *J. Geophys. Res. Solid Earth* 108: 2244. doi: 10.1029/2001JB001390

Stoner, J. S., Channell, J. E. T., Mazaud, A., Strano, S. E., and Xuan, C. (2013). The influence of high-latitude flux lobes on the Holocene paleomagnetic record of IODP Site U1305 and the northern North Atlantic. *Geochem. Geophys. Geosyst.* 14, 4623–4646. doi: 10.1002/ggge.20272

Stoner, J. S., Laj, C., Channell, J. E. T., and Kissel, C. (2002). South Atlantic and North Atlantic geomagnetic paleointensity stacks (0 –80 ka): implications for inter-hemispheric correlation. *Quat. Sci. Rev.* 21, 1141–1151. doi: 10.1016/s0277-3791(01)00136-6

Stoner, J. S., and St-Onge, G. (2007). Chapter three magnetic stratigraphy in paleoceanography: reversals, excursions, paleointensity, and secular variation. *Dev. Mar. Geol.* 1, 99–138. doi: 10.1016/S1572-5480(07)01008-1

Stott, L., Poulsen, C., Lund, S., and Thunell, R. (2002). Super ENSO and global climate oscillations at millennial time scales. *Science* 297, 222–226. doi: 10.1126/science.1071627

Suganuma, Y., Okuno, J., Heslop, D., Roberts, A. P., Yamazaki, T., and Yokoyama, Y. (2011). Post-depositional remanent magnetization lock-in for marine sediments deduced from 10Be and paleomagnetic records through the Matuyama-Brunhes boundary. *Earth Planet. Sci. Lett.* 311, 39–52. doi: 10.1016/j.epsl.2011.08.038

Tauxe, L. (1993). Sedimentary records of relative paleointensity of the geomagnetic field: theory and practice. *Rev. Geophys.* 31, 319–354. doi: 10.1029/93RG01771

Tauxe, L., Pick, T., and Kok, Y. S. (1995). Relative paleointensity in sediments: a pseudo−thellier approach. *Geophys. Res. Lett.* 22, 2885–2888. doi: 10.1029/95GL03166

Thompson, L. G., Mosley-Thompson, E., Bolzan, J. F., and Koci, B. R. (1985). A 1500-year record of tropical precipitation in ice cores from the Quelccaya Ice Cap, Peru. *Science* 229, 971–973. doi: 10.1126/science.229.4717.971

Thompson, L. G., Mosley-Thompson, E., and Henderson, K. A. (2000). Ice-core palaeoclimate records in tropical South America since the last glacial maximum. *J. Quat. Sci* 15, 377–394. doi: 10.1002/1099-1417(200005)15:4<377::AID-JQS542<3.0.CO;2-L

Thouveny, N., Creer, K. M., and Blunk, I. (1990). Extension of the Lac du Bouchet palaeomagnetic record over the last 120,000 years. *Earth Planet. Sci. Lett.* 97, 140–161. doi: 10.1016/0012-821X(90)90105-7

Turner, G. M., and Thompson, R. (1981). Lake sediment record of the geomagnetic secular variation in Britain during Holocene times. *Geophys. J. R. Astron. Soc.* 65, 703–725. doi: 10.1111/j.1365-246X.1981.tb04879.x

Valet, J. P., Meynadier, L., and Guyodo, Y. (2005). Geomagnetic dipole strength and reversal rate over the past two million years. *Nature* 435, 802–805. doi: 10.1038/nature03674

Vasiliev, I., Dekkers, M. J., Krijgsman, W., Franke, C., Langereis, C. G., and Mullender, T. A. T. (2007). Early diagenetic greigite as a recorder of the palaeomagnetic signal in Miocene-Pliocene sedimentary rocks of the Carpathian foredeep (Romania). *Geophys. J. Int.* 171, 613–629. doi: 10.1111/j.1365-246X.2007.03560.x

Williams, T., Thouveny, N., and Creer, K. M. (1998). A normalised intensity record from Lac du Bouchet: geomagnetic palaeointensity for the last 300 kyr? *Earth Planet. Sci. Lett.* 156, 33–46. doi: 10.1016/s0012-821x(98)00015-6

Woods, A., Rodbell, D., Abbott, M., Hatfield, R. G., Chen, C. Y., Lehmann, S., et al. (2019). *Abrupt Arctic Warming Repeatedly Led to Prolonged Drought and Glacial Retreat in the Tropical Andes During the Last Glacial Cycle*. Available online at: https://doi.org/10.31223/osf.io/7hd3a (accessed May 4, 2020).

Wright, H. E. (1983). Late-Pleistocene glaciation and climate around the Junin Plain, central Peruvian highlands. *Geogr. Ann. Ser. A* 65, 35–43. doi: 10.1080/04353676.1983.11880072

Xuan, C., and Channell, J. E. T. (2009). UPmag: MATLAB software for viewing and processing u channel or other pass-through paleomagnetic data. *Geochem. Geophys. Geosyst.* 10:Q10Y07. doi: 10.1029/2009GC002584

Xuan, C., Channell, J. E. T., and Hodell, D. A. (2016). Quaternary magnetic and oxygen isotope stratigraphy in diatom-rich sediments of the southern Gardar Drift (IODP Site U1304, North Atlantic). *Quat. Sci. Rev.* 142, 74–89. doi: 10.1016/j.quascirev.2016.04.010

Ziegler, L. B., Constable, C. G., Johnson, C. L., and Tauxe, L. (2011). PADM2M: a penalized maximum likelihood model of the 0-2 Ma palaeomagnetic axial dipole moment. *Geophys. J. Int.* 184, 1069–1089. doi: 10.1111/j.1365-246X.2010.04905.x

Conflict of Interest: The authors declare that the research was conducted in the absence of any commercial or financial relationships that could be construed as a potential conflict of interest.

frontiers in Earth Science

ORIGINAL RESEARCH
published: 05 June 2020
doi: 10.3389/feart.2020.00173

Magnetostratigraphy and Paleoenvironments of the Kuntila Lake Sediments, Southern Israel: Implications for Late Cenozoic Climate Variability at the Northern Fringe of the Saharo-Arabian Desert Belt

Juan Cruz Larrasoaña[1], Nicolas Waldmann[2], Steffen Mischke[3], Yoav Avni[4] and Hanan Ginat[5]*

[1] Instituto Geológico y Minero de España, Unidad de Zaragoza, Zaragoza, Spain, [2] Department of Marine Geosciences, University of Haifa, Haifa, Israel, [3] Institute of Earth Sciences, University of Iceland, Reykjavík, Iceland, [4] Geological Survey of Israel, Jerusalem, Israel, [5] The Dead Sea and Arava Science Center, Tamar Regional Council, Mount Masada, Israel

OPEN ACCESS

Edited by:
Kenneth Philip Kodama, Lehigh University, United States

Reviewed by:
Josep M. Pares, National Research Center on Human Evolution, Spain
James G. Ogg, Chengdu University of Technology, China

***Correspondence:**
Juan Cruz Larrasoaña
jc.larra@igme.es

Specialty section:
This article was submitted to Geomagnetism and Paleomagnetism, a section of the journal Frontiers in Earth Science

Received: *31 March 2020*
Accepted: *05 May 2020*
Published: *05 June 2020*

Citation:
Larrasoaña JC, Waldmann N, Mischke S, Avni Y and Ginat H (2020) Magnetostratigraphy and Paleoenvironments of the Kuntila Lake Sediments, Southern Israel: Implications for Late Cenozoic Climate Variability at the Northern Fringe of the Saharo-Arabian Desert Belt. Front. Earth Sci. 8:173. doi: 10.3389/feart.2020.00173

The Negev Desert in southern Israel hosts a number of late Cenozoic lacustrine and palustrine sedimentary sequences that attest for past wetter conditions in what today constitutes one of the driest deserts on Earth. These sequences are of special importance because the Negev Desert forms part of the Levantine Corridor, which was probably the only continental bridge that enabled initial out-of-Africa expansion of our genus *Homo*. Yet, the paleoclimatic significance of these sequences still remains unknown, mainly due to their uncertain (late Pliocene to early Pleistocene) age. Here we present a combined sedimentologic, paleontologic and magnetostratigraphic study of one of these sedimentary sequences, the so-called Kuntila Lake sediments, which was carried out at the 30 m-thick Kuntila Gate section in the Nahal Paran basin, southern Israel. Sedimentological evidence and ostracod faunas indicate that these sediments accumulated in a long-lasting lacustrine basin that underwent periodic lake-level variations. Magnetostratigraphic measurements enable the recognition of a normal (N1) and a reverse (R1) polarity zone in the lower and upper halves, respectively, of the Kuntila Gate section. Correlation of N1 to the Olduvai Subchron (1.778–1.945 Ma) appears as the most likely option in view of previously published ^{10}Be ages derived for the uppermost part of the Kuntila Member in nearby sections. The large errors associated with these ages, however, suggest that correlation of N1 to Subchron C2An.1n (2.582–3.032 Ma) is also possible. Although our results do not resolve the age of the Arava Formation, they unequivocally relate the Kuntila Lake sediments with a long period of enhanced climatic variability because the tops of both subchrons are associated with 400 kyr eccentricity maxima. The inferred wetter conditions in the Negev

Desert concurred, regardless of the age correlation, with periods of lake expansion in East Africa and clusters of short-lived expansions of the savannah throughout much of the Sahara. This would have facilitated the biogeographic connection between Africa and Eurasia, greening the path for the initial out-of-Africa dispersal of *Homo*. Further research on the Kuntila Lake sediments will be necessary to better determine the timing, extent and significance of such biogeographic connection.

Keywords: magnetochronology, Arava Formation, Pleistocene, Pliocene, *Homo* dispersal, Near East

INTRODUCTION

Magnetostratigraphy is a powerful tool to date sedimentary sequences that is based on the recognition of polarity intervals in the target sequence and their correlation to the Geomagnetic Polarity Timescale (GPTS, Gradstein et al., 2012). This is, in turn, mostly constructed through radiometric ages of sea-floor magnetic anomalies (Ogg, 2012) or astronomically-tuned reversals derived from cyclically-accumulated sedimentary successions (Hilgen et al., 2012). Magnetic stratigraphy has proven to be especially well-suited for dating continental sedimentary successions, where the general scarcity of fossil remains or intercalations of volcanic material (e.g., tephra) usually makes obtaining well-resolved age models by biostratigraphic and radiometric methods difficult. Thus, magnetostratigraphic data have been paramount for providing the basic chronostratigraphic framework for continental sediments worldwide [e.g., East and North Africa (Lepre et al., 2011; Sahnouni et al., 2018), Chinese Loess Plateau (Zhu et al., 2018), and the Nihewan Basin (Deng et al., 2008)]. Independent magnetostratigraphic dating can be achieved if a single correlation of the local polarity sequence to the GPTS can be proposed, a situation that is more likely to occur as the length of the sedimentary succession increases the distinctiveness of the polarity pattern (provided that sedimentation rates are rather constant). For short sections with a limited number of reversals, magnetostratigraphy can still provide very valuable chronological data provided some independent age constraint is available to anchor the local polarity sequence (e.g., Lepre et al., 2011; Sahnouni et al., 2018).

This latter situation might be the case of the Arava Formation in the Negev Desert of southern Israel, which is typified by interbedded lacustrine and alluvial sediments accumulated within the so-called Kuntila Lake basin (Avni et al., 2001; Ginat et al., 2018; **Figure 1**). These sediments are cropping out over an area of circa 300 km^2 exposed in the transition between the eastern Sinai Peninsula and the southern Negev, and their age is still unknown despite its relevance for understanding the environmental setting in the only land bridge that made the initial African dispersal of our genus *Homo* possible without involving seafaring (Anton et al., 2014). Attempts to date these sediments by cosmogenic burial methods rendered unreliable results (Guralnik, 2009), and at present only numerical ages derived from ^{10}Be data are available for the desert pavement developed on the conglomerate beds that resumed sedimentation in Kuntila Lake (Matmon et al., 2009; Guralnik et al., 2010; Amit et al., 2011). These data give a minimum age of 1.83 $\pm$ 0.2 Ma for the Kuntila Lake sediments, yet the large errors associated with cosmogenic exposure ages, coupled with uncertainties and assumptions behind their calculation (Matmon et al., 2009), result in a still somewhat uncertain age for these sediments.

Here we present a magnetostratigraphic study of the Kuntila Lake sediments at the Kuntila Gate (KG) section. Despite the relatively small thickness of the section (30 m), our results provide some important constraints for the age of these sediments. These constraints, combined with new sedimentological and paleontological evidence, enable an improved discussion on the paleoenvironmental significance of the Kuntila Lake sediments.

GEOLOGICAL SETTING

The Negev Desert in southern Israel is located between the Sinai Peninsula and the Dead Sea Basin, at the northernmost fringe of the Saharo-Arabian desert, and belongs to the only continental bridge that joins Africa to Eurasia (**Figure 1**). It is characterized by an arid to hyper-arid climate with a mean annual rainfall ranging from 200 mm in its northern part to less than 25 mm in its southern sector (Enzel et al., 2008). This situation results from a decreased southward penetration of the westerly winter rains brought to the region by eastern Mediterranean low-pressure systems (Enzel et al., 2008). Changes in the intensification of the Cyprus Low associated to North Atlantic climate shifts are considered as the main mechanism driving climate variability in the Negev during the Quaternary (Ziv et al., 2006; Enzel et al., 2008), although some studies contest this hypothesis and suggest that northward intrusion of tropical rains during boreal summers might also have played a role in contributing to wetter conditions during past interglacial periods (Vaks et al., 2007; Waldmann et al., 2010; Orland et al., 2019).

The geology of the region is dictated by the Miocene establishment of the Dead Sea Transform system, a fault system with a half-graben topography and a left-lateral motion that represents the boundary between the African and Eurasian plates (Garfunkel, 1981; Avni et al., 2012). This system led to formation of a central depression, represented by the Arava Valley, that was bounded by an uplifted eastern rift margin (the Trans-Jordan mountain belt) and by an arched and subsided western counterpart (the Negev Desert). Development of this transform system and the uplift of its shoulders led to the disruption of an initial regular topography developed during the Oligocene-Early Miocene (Avni et al., 2012), so that a new fluvial system was established draining the eastern part of the northern Sinai

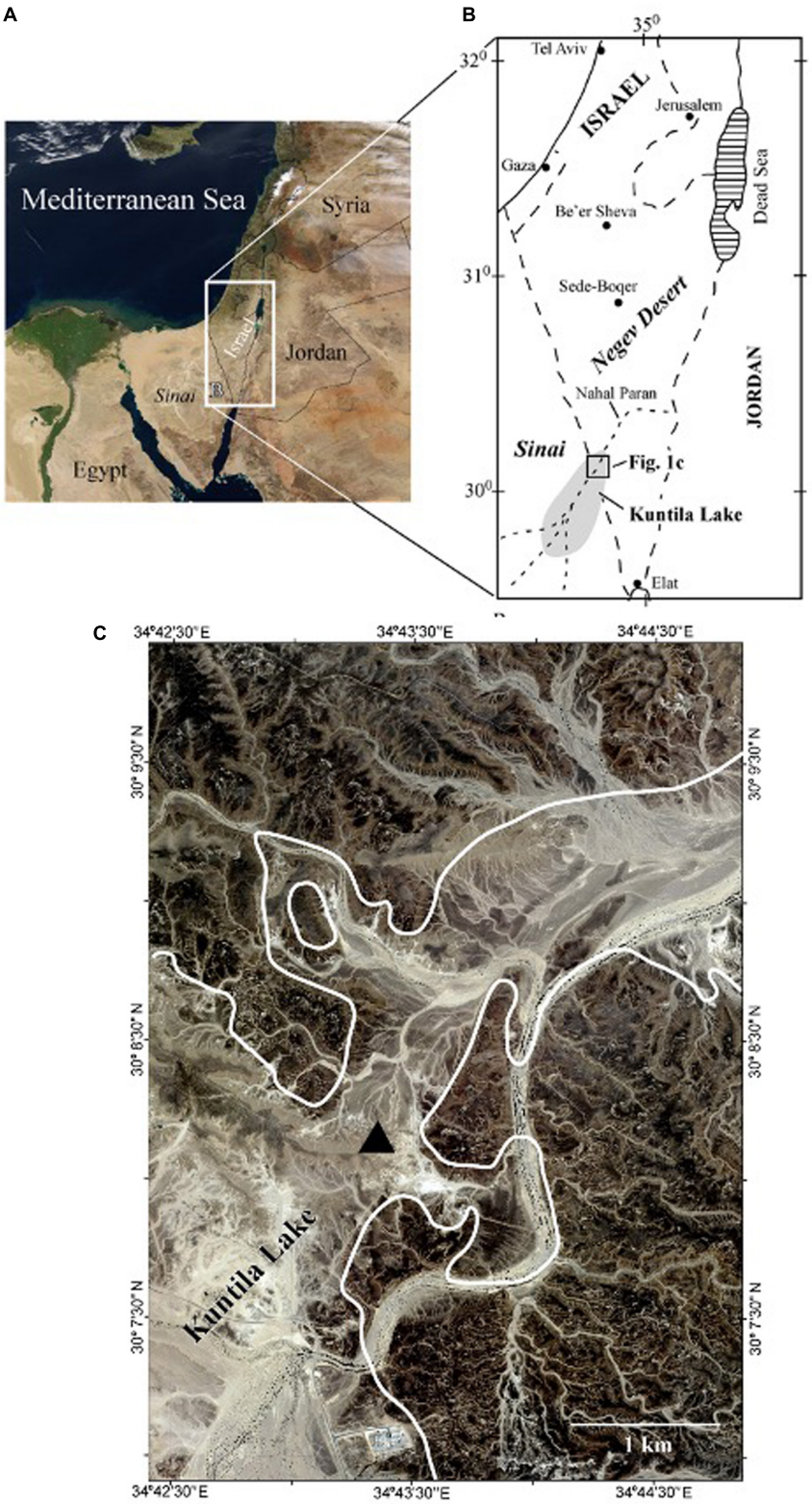

FIGURE 1 | (A) Satellite image showing the location of the Sinai Peninsula at the biogeographic bridge between Africa and Eurasia. The white rectangle is enlarged in **(B)** and depicts a sketch map of southern Israel with the inferred extension of the Kuntila Lake. **(C)** Satellite image of the Nahal Paran basin in the southern Negev Desert, with location of the Kuntila Gate section (black triangle). The thick white line delineates the outcrops of the Kuntila lacustrine sediments within the Arava Formation in the area.

Peninsula and much of the Negev northward into the young Dead Sea Basin (Avni et al., 2000). Evidence of this drainage system is provided by sediments of the Arava Formation, which accumulated after a period of extensive erosion associated with the initial rearrangement of the drainage network (Avni et al., 2000, 2001; **Figure 2**). Tectonic activity during the early Pleistocene faulted and tilted the Negev margin toward the east, hence terminating sedimentation of the Arava Formation and leading to the erosion of its uppermost strata at some locations (Avni et al., 2001). Deposition of the overlying Zehiha Formation took place broadly simultaneously with this period. Later incision of the newly formed drainage network led to deposition of Middle to Late Pleistocene alluvial terraces that also truncate previous deposits (Avni et al., 2001; Guralnik et al., 2010).

The Arava Formation has been formally described by Avni et al. (2001) to account for the sedimentary sequences deposited in the Negev and the Arava Valley after the Late Miocene birth of the Dead Sea Basin, and is composed of two members. The first one (Saggi Member) is made up of 5–20 m of poorly cemented conglomerate beds that include boulders of up to 2 m in diameter and were deposited along fluvial channels with a flash-flood hydrological regime. The second member (named Kuntila) was deposited after a short period of tectonic deformation and incision at a lower morphostratigraphic position (**Figure 2**). The Kuntila Member ranges in thickness between 30 and 80 m, and is made up of conglomerates, sandstones, mudstones, marls, and limestones. Mudstones, marls and limestones constitute a sequence of up to 35 m that attest to a lacustrine/palustrine setting along the course of the reconstructed paleo Paran-Neqarot drainage basin (Avni et al., 2000, 2001). Mapping of these sediments revealed that the largest lake, termed the Kuntila Lake, which had an elongated North-South direction and extended from the present-day Paran River well into the Egyptian side of the Sinai Peninsula, covered an area of more than 300 km^2 (Avni et al., 2001; Ginat et al., 2018; **Figure 1B**). Lacustrine sediments grade toward the periphery of the former lake basin into conglomerates, sandstones and mudstones of alluvial origin (Avni et al., 2001). Two main climatic scenarios have been proposed to explain the past occurrence of this and other water bodies scattered in the present-day hyper-arid Negev Desert (Ginat et al., 2018). The first scenario involves the alternating hyper- to semi-arid conditions, whereas the second implies fluctuations between hyper-arid and sub-humid conditions (Ginat et al., 2018). Although regional considerations suggest that the first scenario is more likely, the debate is still ongoing and new data are necessary to furnish our knowledge on the underlying mechanisms for this climatic variability (Ginat et al., 2018).

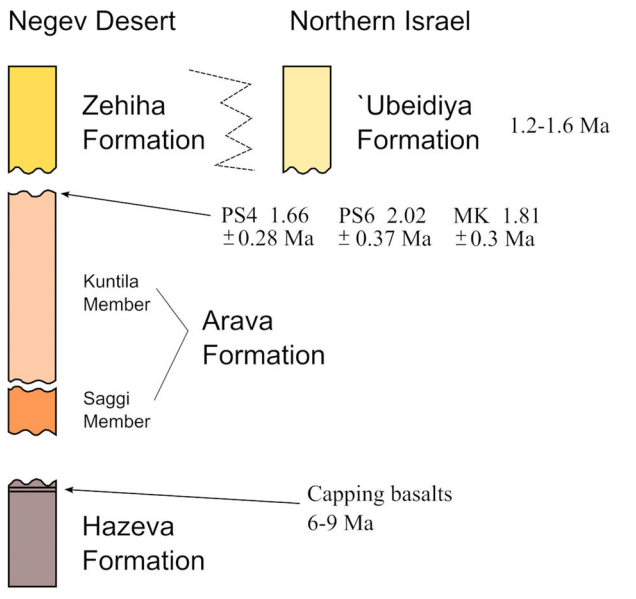

FIGURE 2 | Sketch showing the arrangement and lateral equivalences of the different formations discussed in the text. PS4, PS6 and MK indicate exposure ages (Matmon et al., 2009; Amit et al., 2011; Guralnik et al., 2010).

The age of the Arava Formation has been classically assigned from its geologic and geomorphological context. Thus, this formation post-dates the Hazeva Formation and its capping basalt flows, which have been dated to 9–6 Ma (Avni et al., 2001; **Figure 2**). It is, in turn, overlain by the Zehiha Formation, for which a similar age to the 'Ubeidiya Formation (which ranges between 1.2 and 1.6 Ma; Belmaker, 2010; Parés et al., 2013) has been proposed on the basis of its faunal assemblage (Ginat et al., 2003). All in all, the geological and geomorphological context points to a late Pliocene-early Pleistocene age for the Arava Formation (Avni et al., 2000). It has not been until the last decade that absolute chronological methods have been applied to determine the age of the upper member of the formation, the Kuntila Member. Efforts in providing numerical ages based on cosmogenic burial analyses have yielded unreasonable ages due to problems in extracting and measuring ^{26}Al in the studied sediments (Guralnik, 2009). Successful results have been provided, in contrast, by ^{10}Be exposure ages of a desert pavement developed on the reg soils that were formed, in turn, over the gravels that represent the last stages of sedimentation of the Kuntila Lake sediments (Matmon et al., 2009). Initial ages for sites PS4 and PS6 (Matmon et al., 2009) have been recalculated by Amit et al. (2011) to 1.66 ± 0.28 and 2.02 ± 0.37 Ma, respectively. Guralnik et al. (2010) added a third site (KM) from a similar position at the top of a Kuntila Member conglomerate sequence, located 28 km north-east of our KG section, with an age of 1.81 ± 0.3 Ma. These ages, therefore, provide a minimum age estimate that points to accumulation of the Kuntila Lake sediments sometime in the very early Pleistocene, yet this chronology should be considered with caution for three main reasons. First, these ages differ by up to 0.36 Myr despite the fact they were obtained almost at the same stratigraphic position. Second, the uncertainty associated to each individual age are rather wide (up to 0.74 Myr). And third, uncertainties and assumptions behind exposure-age calculations are noticeable, so that the initial age for site PS4 given by Matmon et al. (2009), which ranged between 1.75 and 2.35 ± 0.2 Ma depending on model input parameters, was later recalculated to 1.61 ± 0.26 and 1.66 ± 0.28 Ma by Guralnik et al. (2010) and Amit et al. (2011), respectively. It is clear that further dating techniques need to be

applied to better constrain the age of the Kuntila Lake sediments, with magnetochronology appearing as an obvious one.

MATERIALS AND METHODS

We have logged and described the lithology of the Kuntila Member sediments that crop out horizontally at the KG section in the Paran-Neqarot Basin, including description of color, grain size, bed thickness, and sedimentary structures and textures (Avni, 1998; Avni et al., 2001; **Figure 3**). We have selected this section because it includes some of the thickest and better exposed fine-grained lacustrine sediments within the sequence (Avni et al., 2001), and hence render optimal conditions for retrieving a local magnetozone succession. This information has been used to complement the observations made by Avni (1998) and Avni et al. (2001), and provide a revised view on the paleoenvironments of the Kuntila Lake sediments as inferred from basic sedimentological evidence.

Standard paleomagnetic samples were collected in the field using a battery-powered electric-drill equipped with a diamond drill-bit that was lubricated and cooled with water during sampling. A total of 19 samples were collected at 17 sites distributed throughout the section, giving an average stratigraphic resolution of ca. 1.7 m. We focused our sampling on mudstones and marls although some limestones and sandstones were also sampled. The samples were oriented in the field using a magnetic compass mounted on a paleomagnetic orienting fixture. After cutting the samples into standard paleomagnetic specimens and labeling, we conducted paleomagnetic analyses at the Paleomagnetic Laboratory of the Institute of Earth Sciences Jaume Almera (CCiTUB-CSIC) in Barcelona, Spain. A 2G superconducting rock magnetometer with a noise level of $< 7 \times 10^{-6}$ A/m was used to measure the Natural Remanent Magnetization (NRM) of the studied samples upon thermal demagnetization, which was conducted with a MMTD–80 furnace at intervals of 100, 50, 30, and 20°C, to a maximum temperature of 620°C. Stable Characteristic Remanent Magnetization (ChRM) directions were calculated by means of Principal Component Analysis (Kirschvink, 1980) after they were identified through visual inspection using the VPD software (Ramón et al., 2017).

In order to provide new paleoenvironmental information, we have also studied calcareous microfossils, mainly ostracod valves, at 23 stratigraphic levels distributed throughout the KG section. From each level, sediment sub-samples of 75–320 g (average 130 g) were treated with 3% H_2O_2 for 48 h and washed through 100, 250, and 1000 μm sieves. All ostracod remains including partly fragmented valves larger than half of a specimen were picked from the sieve residues. Valves and carapaces were recorded separately. Their preservation state was assessed as recrystallized or relatively well-preserved specimens. The portions of carapaces to all recorded valves (articulated and separated), and adult to all recorded valves were determined as proxies of post-mortem transport and preservation. Identification was conducted according to Meisch (2000), Fuhrmann (2012) and Meisch et al. (2019). Identification of *Ilyocypris* cf. *bradyi* Sars, 1890 followed van Harten (1979) by examining marginal ripplets on the inner lamella of left valves with a Zeiss Supra 40 VP Scanning Electron Microscope (SEM) at Freie Universität Berlin, Germany. In addition to ostracod remains, gastropod and bivalve shells, and charophyte remains were counted. Foraminifera tests were regarded as allochthonous, originating from locally exposed marine limestones of Maastrichtian to Paleocene age, and were qualitatively recorded.

RESULTS

Stratigraphy and Sedimentology

The Kuntila Member at the KG section (**Figure 3**) begins with a 2 m-thick package of massive, gray mudstones that is overlain by 5 m of also massive, gray-brownish silty mudstones. The following 2 m are composed of reddish sandy mudstones that include two tabular sandstone beds displaying low-angle cross bedding lamination (**Figure 4A**). Above them, about 4 m of massive, silty sands with thin reddish mudstone intercalations appear, with sands in the uppermost meter being indurated by carbonate cement. The next 5 m of the section are made up by three packages constituted by marls and a limestone bed each. Marls are gray in color, have an overall massive appearance, and include frequent organic debris at some darker gray horizons. Limestone beds range between 30 and 100 cm in thickness, display a tabular geometry with some occasional wavy morphology, and often have bioturbated tops (**Figure 4B**). These limestones are typically massive and contain remains of gastropods and charophytes. The uppermost limestone bed is overlain by 7 m of ochre sandy mudstones with occasional carbonate nodules in their upper part (**Figure 4C**). These sandy mudstones include two tabular, fining-upward conglomerate beds of around 50 and 100 cm in thickness. Clasts are well rounded, have a maximum size of 25 cm, and are mainly composed of carbonates, although chert and magmatic compositions are also found. The next 4.5 m of the section are characterized by sandy mudstones and sandstones with a silty matrix that show distinctive features such as color mottling, carbonated rhizoliths, and some gypsum gastropod steinkerns. The Kuntila Member is here erosively truncated by the Zehiha Formation, which is composed by a 1.7 m-thick conglomerate at the studied section (**Figure 4D**).

Fossil Remains

In total, 411 ostracod carapaces and 329 valves were identified in the sediments of the KG section. Ostracod remains are dominated by carapaces and valves of *Cyprideis torosa* (Jones, 1850; 56%). Carapaces and valves of *Neglecandona angulata* (Müller, 1900) occurred as the second most abundant ostracod remains (24%), followed by those of *Ilyocypris* cf. *bradyi* (8%) and *Neglecandona neglecta* (Sars, 1887; 7%; **Supplementary Plate S1**). Remains of seven additional ostracod taxa were recorded with very low abundances (**Supplementary Plate S2**). Relatively abundant ostracod remains in addition to those of *C. torosa* were only recorded in two samples from the basal and middle part of the KG section, respectively (**Figure 5**). Shells of four gastropod taxa were

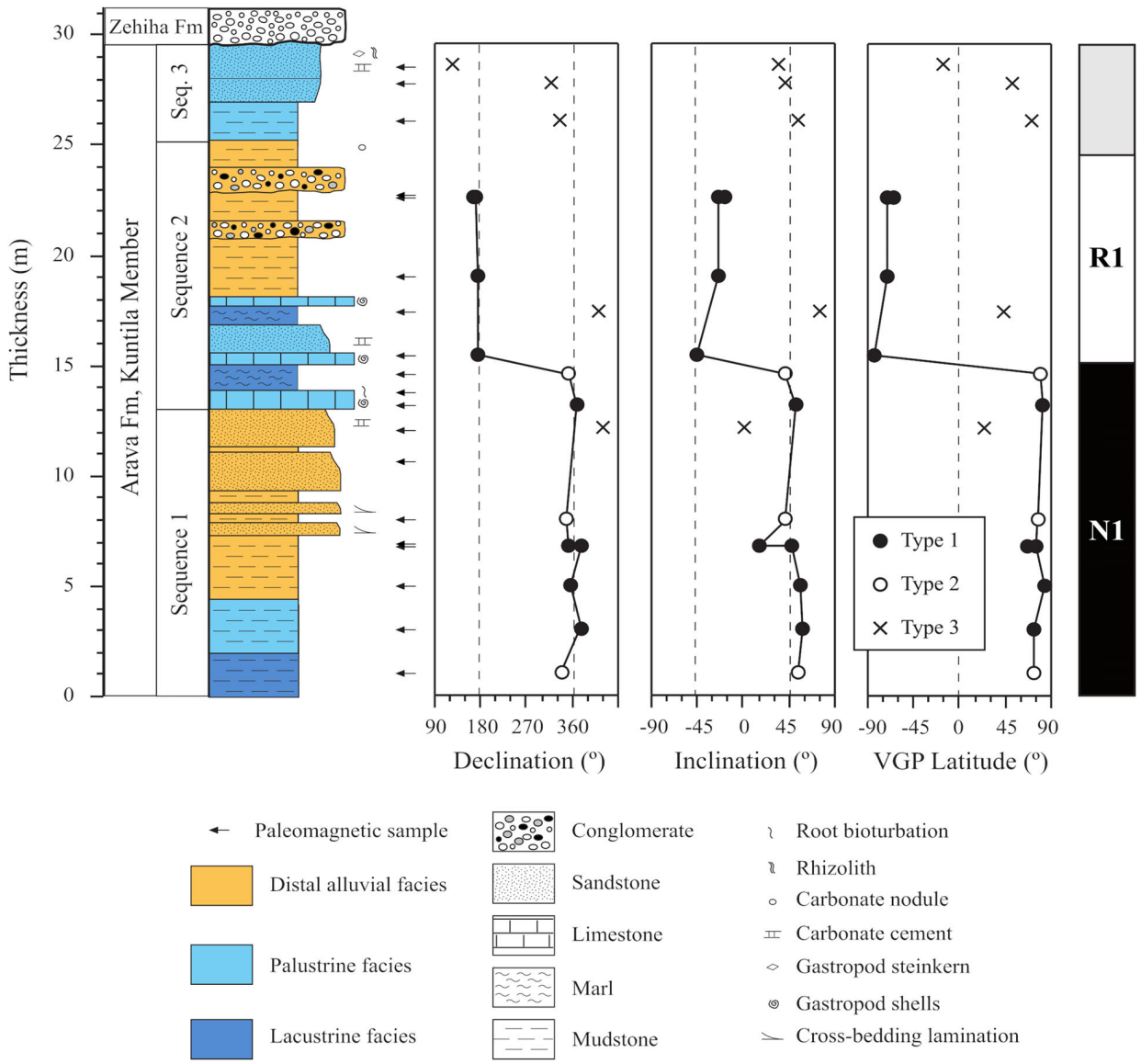

FIGURE 3 | Stratigraphic log of the Kuntila section, magnetostratigraphic results and the sequence of polarity zones identified in the section. The gray bar marks the position of the part of the sequence with uncertain polarity.

recorded in three samples, a shell of a bivalve in one sample, and gyrogonites of two *Chara* species in five samples (**Figure 5** and **Supplementary Plate S2**). All apart from two samples contain foraminifera tests, which attest to the contribution of eroded Maastrichtian-Paleocene chalk and marl sediments.

Magnetic Stratigraphy

The paleomagnetic quality of the samples is, overall, relatively good (see **Supplementary Tables S1, S2**). A low temperature component is typically identified between 100 and 225°C after removal of a viscous overprint. This low-temperature component shows northerly directions and positive, steep inclinations that are consistent with the present-day field overprint (**Figure 6**). Above 225–300°C, an additional stable component that unblocks below 590°C (occasionally up to 620°C) has been identified at most of the samples. This component is interpreted as the ChRM and can be divided into three types on the basis of quality. Type 1 ChRM directions are those that define strikingly linear trends directed toward the origin of the demagnetization plot, enable optimum polarity determination, and are associated with low mean angular deviation (MAD) angles (typically $< 8°$; **Figures 6A,D,E**). Type 2 ChRMs are characterized by either less linear trends or incomplete demagnetization due to the growth of new magnetic minerals in the oven. Despite this, they enable accurate calculation of ChRM directions with low to moderate MAD angles (typically between 10 and 20°) and reliable polarity determinations (**Figure 6C**). Type 3 ChRMs are characterized by lower intensities and scattered directions that provide ambiguous

FIGURE 4 | Field pictures of the studied sediments from the Kuntila Member of the Arava Formation. **(A)** Overall view of the lower part of the KG section, which encompasses sediments from S1 capped by the first limestone bed of S2. **(B)** Detail of the lacustrine limestone. **(C)** View of the ochre sandstones from the middle part of S2. **(D)** Conglomerate of the Zehiha Formation, erosively truncating the uppermost part of S3.

polarity determinations (**Figure 6B**); they were, therefore, not considered for establishing the local magnetozone succession. A total of nine, three and five ChRM directions display quality types 1, 2, and 3, respectively.

About half of the ChRM type 1 and 2 directions show northerly declinations with positive inclinations that appear well clustered in a stereographic projection around the expected direction for the studied site (**Figures 3**, **6F**). The rest of the ChRM type 1 and 2 directions show southerly declinations with negative inclinations of ca. −28° (**Figures 3**, **6F**). In the absence of a statistically significant reversal test, these circumstances suggest that the ChRM is a dual polarity, primary magnetization in which the reverse directions are overlapped to a small degree with the present-day field component. This is further supported by the depth variations of the latitude of the virtual paleomagnetic poles calculated from the ChRM directions, which are unrelated to lithological variations and enable a straightforward delineation of a normal polarity interval (N1) spanning the lower part of the section and a reverse polarity interval (R1) spanning most of its upper part (**Figure 3**). Above meter 25, the presence of only type 3 directions renders determination of the polarity uncertain (marked with a gray bar in **Figure 3**).

DISCUSSION

Sedimentological and Paleoenvironmental Inferences

The Kuntila Member sediments at the KG section are arranged in three sequences (**Figure 3**). The lowermost sequence (S1, 0–13 m) begins with gray mudstones interpreted to represent sedimentation in a lacustrine area, that grade upward into ochre and reddish silty mudstones typical for distal alluvial facies, and finally to reddish silty mudstones with tabular sandstone intercalations that attest to deposition by unconfined flows over a muddy flood plain. The second sequence (S2, 13–25 m) begins with the return to lacustrine sedimentation, which involved development of a carbonate cement within the uppermost distal alluvial sandstones of the underlying sequence. The three marl-limestone packages are interpreted as three periods of lacustrine sedimentation (represented by the marls) that evolved gradually to shallower palustrine conditions (represented by limestones with frequent bioturbated tops). Sedimentation then shifted to a distal alluvial plain (as indicated by ochre sandy mudstones) over which progradation of more proximal alluvial facies (as indicated by the conglomerates) occurred. The third sequence (S3, 25.0–29.5 m) begins with the return to palustrine sedimentation under the influence of detrital supply, as evidenced by gray and ochre sandy mudstones and sands with carbonate nodules. Shallower palustrine conditions prevailed later, as inferred from development of carbonate rhizoliths within silty sands. The occurrence of mottling and gypsic gastropod steinkerns within these sediments attest to the cessation of palustrine conditions and its pedogenic alteration.

Before detailed paleoenvironmental information can be derived from the recorded ostracod remains, two considerations are taken into account. First, the relatively low number of adult valves in comparison to those of juvenile specimens (**Figure 5**) indicate that the valves were likely formed autochthonous and not brought to the site as detrital particles. Second, the high proportion of carapaces in comparison to disarticulated valves (**Figure 5**) might indicate rapid burial and preservation of articulated valves or, alternatively, might result from poor preservation conditions for the more fragile isolated valves in comparison to carapaces. The frequent appearance of only *Cyprideis torosa*, whose valves are thicker than those of most non-marine species, in several samples is supporting evidence for the second alternative and suggests that the recorded ostracod specimens represent only a part of the original ostracod assemblage. Highest proportions of carapaces in comparison to all valves, and of recrystallized valves in comparison to all valves, occur in the lower half of the section suggesting that poor preservation is more significant in the lower part (**Figure 5**).

The dominance of *Cyprideis torosa* forma *torosa* between meters 1 and 6 suggests the past presence of brackish water conditions and a permanent water body that agree with the lacustrine sedimentation inferred for the lower part of S1. The combined occurrence of *Cyprideis torosa* forma *torosa* and *Cypridopsis vidua* (Müller, 1776) between meters 13 and 15 points to slightly brackish conditions associated with deposition of the lacustrine gray marls and limestones found in the lower half of S2. The occurrence of charophyte gyrogonites together with relatively abundant ostracod remains in addition to those of *C. torosa* in the same stratigraphic positions confirm that the lower parts of S1 and S2 represent deposition in permanent fresh to slightly brackish and predominantly clear waters. However, at least slightly brackish or even more saline conditions existed in more or less stagnant waters when the fine-grained and

carbonate-rich deposits of the KG section were accumulated. This inference is indicated by the dominance of *C. torosa*, and in addition for S1 by the presence of valves of *N. angulata*, *N. neglecta,* and *Heterocypris salina* (Brady, 1868), and a shell of *?Melanopsis* (**Figure 5**). The occurrence of *Paralimnocythere* sp., *Cypris*, *Herpetocypris*, *Vestalenula cylindrica* (Straub, 1952), and *Gyraulus* sp. in a sample of S2 points to the existence of small, spring-fed water bodies, possibly representing a wetland rather than a lake environment. With respect to S3, only few valves of *C. torosa*, *H. salina* and *Ilyocypris* cf. *bradyi*, and gyrogonites of *Chara* sp. 2 were recorded in its lower part (**Figure 5**). The brackish water conditions inferred from these remains and the occurrence of pedogenic features (rhizoliths, carbonate concretions) support the reconstruction of mainly palustrine conditions during the formation of S3, and its cessation likely in association with enhanced evaporation as indicated by gypsum casts. The rest of the studied samples, collected from distal alluvial sediments, are barren in ostracod valves or other organism remains with the exception of that around meter 11, where a few recovered *C. torosa* remains resulted probably from brackish stagnant or slowly flowing conditions on an alluvial plain (**Figure 5**). A shallow oxbow-lake or in-stream wetland scenario is reconstructed here.

In summary, our results indicate that the Kuntila Member at the KG section is composed by two sequences (S1 and S2) that witnessed a gradual shallowing from lacustrine to palustrine and distal alluvial conditions, plus a third sequence (S3) devoid of the initial lacustrine part (**Figure 3**). Previous studies have reported the presence, in addition to the ostracod assemblage similar to those presented here, of fish remains of *Tilapia* and *Haplochromis* and gastropod remains of *Bulimis* and *Melanoides operculata* (Avni, 1998; Ginat et al., 2018). Although we are unaware of the exact stratigraphic position of fish remains within the succession, they further demonstrate the past presence of permanent, stagnant waters, and thus, most likely fully lacustrine conditions at least for the lower parts of S1 and S2. Such sediments accumulated under fully lacustrine conditions account for about a third of the stratigraphic thickness exposed at the KG section. Palustrine, likely brackish water conditions prevailed through another third of the section, and distal alluvial conditions account for the remaining third of the succession. The alternation of alluvial sedimentation with lacustrine and palustrine conditions at the KG section location does not necessarily imply disruption of a lacustrine setting in the region. The KG section is located near the former depocenter of the Kuntila Lake but close to its northern outlet toward the paleo-Paran-Neqarot River, where the lake was narrowest (Avni et al., 2001; **Figure 1**). Thus, retraction of the Kuntila Lake led to progradation of distal alluvial sediments over the former lake at the location of the KG section, whereas lacustrine sedimentation likely prevailed in the central sector of its wider, southernmost part. The tabular geometry of the sandstone and conglomerate beds observed in the KG section attest to deposition by unconfined flows in a low-gradient alluvial plain, which suggests continued aggradation throughout the basin in response to a stable base level likely represented by a terminal lake. Any subsequent expansion of the lake would have resulted in the return to lacustrine sedimentation throughout most of the basin and the concomitant retreat of alluvial facies. The succession of three expanding/retracting lacustrine/palustrine sequences suggests, under the relatively quiet tectonic scenario inferred for deposition of the Arava Formation (Avni et al.,

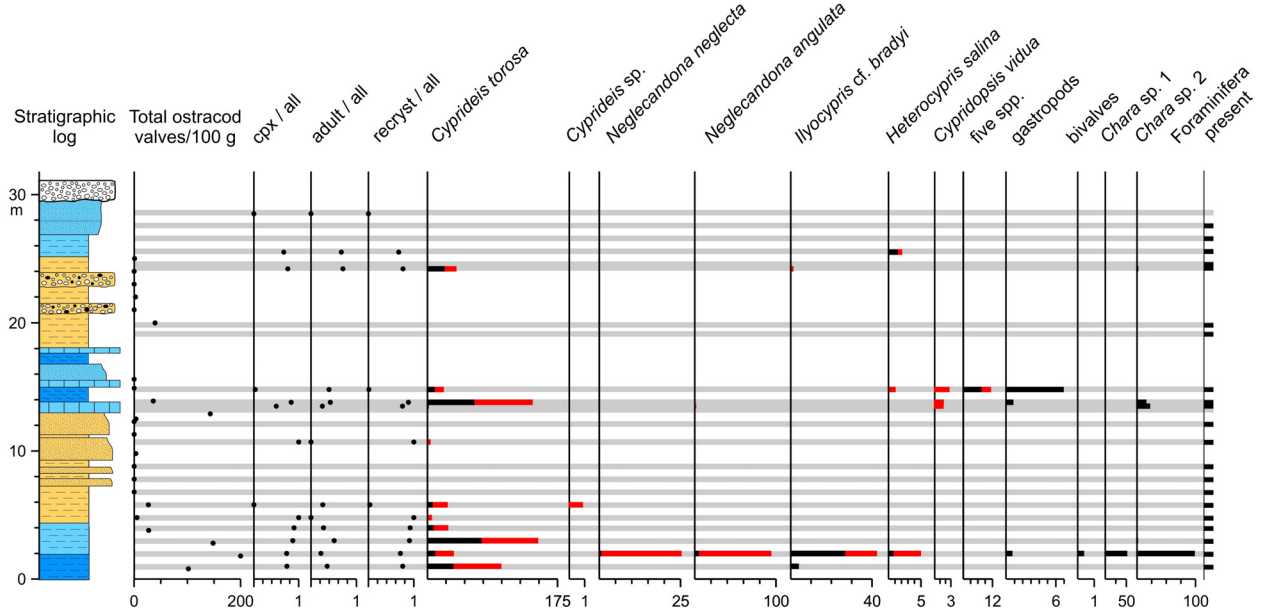

FIGURE 5 | Depth variations of relevant fossil remains from the Kuntila Lake sediments. The pooled five spp. are valves and larger fragments of the ostracods *Potamocypris* sp., *Vestalenula cylindrica*, *Paralimnocythere* sp., *Cypris* sp., and *Herpetocypris* sp. The gastropods are shells of *Gyraulus* sp., Lymnaeidae, *?Melanopsis* and *?Valvata*. Gray horizontal bars indicate the positions of samples.

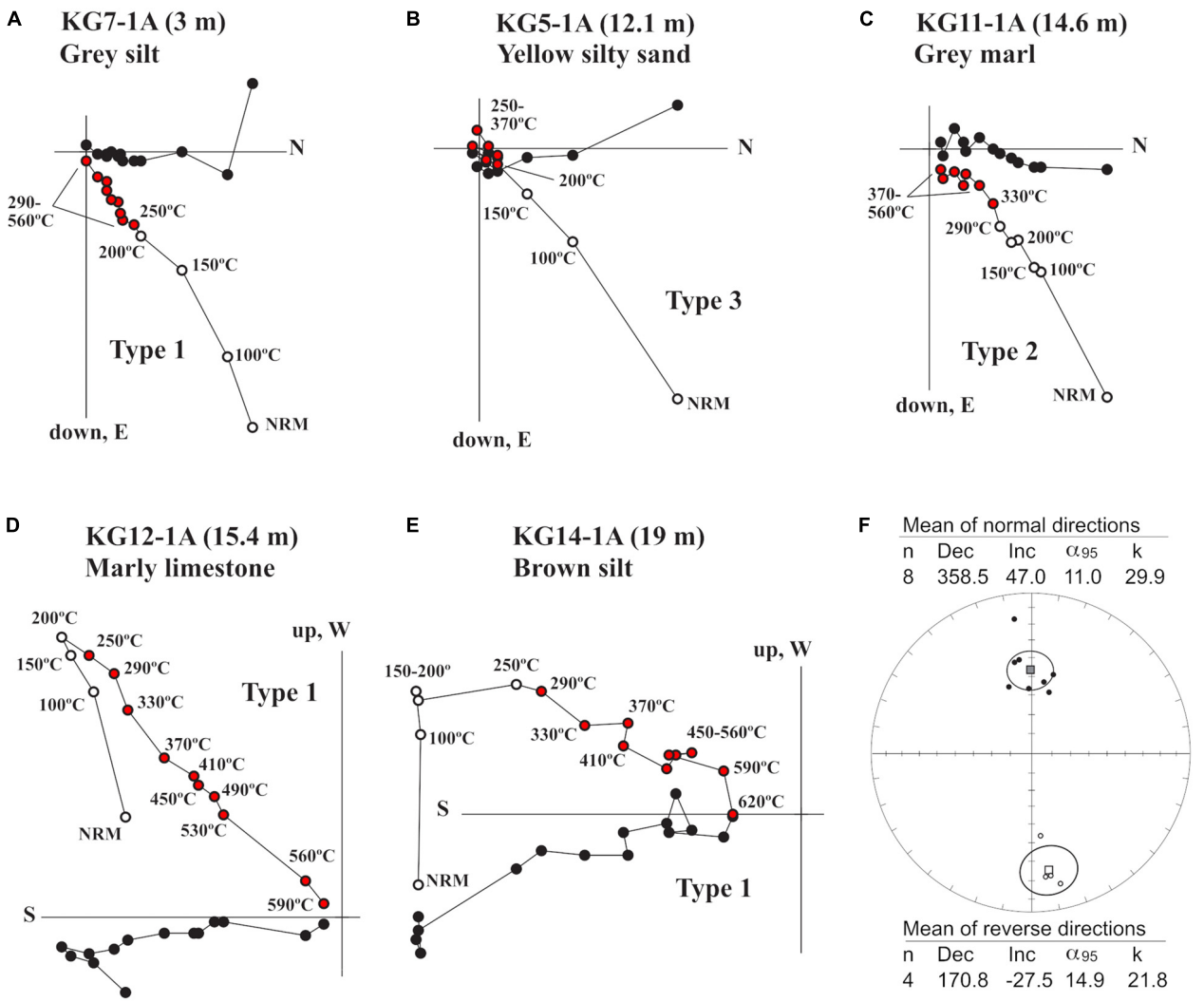

FIGURE 6 | Orthogonal demagnetization plots of samples representative for Type 1 **(A,D,E)**, Type 2 **(C)** and Type 3 **(B)** behaviors. Black and white dots represent projections in the horizontal and vertical planes, respectively. Red dots in the vertical projections indicate the temperature steps included in the calculation of the ChRM directions. **(F)** Equal-area stereonet projection of individual samples (circles), along with the mean directions and associated statistics of the normal and reverse polarity samples (squares). Bold (open) symbols represents projection in the lower (upper) hemisphere. Only types 1 and 2 samples have been considered for the calculations.

2001), that climatic variations were responsible for altering the hydrological budget of the drainage system to the point of enabling the formation of a long-lasting open-water surface in the present hyper-arid southern Negev Desert.

Age of the Kuntila Lake Sediments and Paleoclimatic Implications

Correlation of the KG section magnetostratigraphy to the astronomically-tuned Neogene time scale (ATNTS2012, Hilgen et al., 2012) is not straightforward. Of the three ^{10}Be exposure ages obtained atop of the Kuntila Member, which provide minimum age estimates for the sequence, one of them (MK, 1.81 ± 0.3 Ma; Guralnik et al., 2010) gives an age within the Olduvai Subchron (1.778–1.945 Ma, Hilgen et al., 2012), whereas the others give an age either younger (PS4, 1.66 ± 0.28 Ma; Amit et al., 2011) or older (PS6, 2.02 ± 0.37 Ma; Amit et al., 2011) than this subchron (**Figure 7**). Moreover, the errors of all three exposure ages encompass the entire Olduvai Subchron. Therefore, although the most straightforward solution is to correlate our magnetozone N1 to Olduvai (Option 1, **Figure 7**), other possibilities cannot be excluded. An alternative assessment is the correlation of magnetozone N1 with the uppermost part of the Gauss Chron, named C2An.1n (2.582–3.032 Ma; Hilgen et al., 2012; Option 2, **Figure 7**). The fact that an undetermined part of the uppermost Kuntila Member has been eroded at the KG section before deposition of the Zehiha Formation obliges us to consider this correlation, since an age still older than that indicated by the exposure ages should be attributed to the top of the Kuntila Member in this section. A third alternative,

correlating N1 to the Reunion Subchron within C2r (2.129–2.149 Ma; Hilgen et al., 2012) is discarded due to the high sediment accumulation rates implied (e.g., >75 cm/kyr). In order to provide a definitive age for the Kuntila Member, new sections exposing a thicker sequence need to be sampled for magnetostratigraphic analyses. Drilling a core at the base of the KG section might also resolve the chronology of the Kuntila Member provided a sufficiently long section can be recovered and magnetostratigraphically dated. A final option would be to apply other dating methods (e.g., electron spin resonance) to quartz grains of detrital sediments of the Kuntila Member.

The tops of both subchrons Olduvai and C2An.1n are associated with two 400 kyr eccentricity maxima (Laskar et al., 2004; **Figure 7**). This is significant because it relates sedimentation of the Kuntila Lake sediments with a period of enhanced climatic variability regardless of the correlation of our N1 magnetozone to either of these two subchrons. Thus, eccentricity variations influence climate by modulating precession, so that maxima in eccentricity drive maxima in precession that result, in turn, in enhanced northern-hemisphere insolation values (Laskar et al., 2004). Such periods of highest northern-hemisphere insolation values have been demonstrated to intensify eastern Mediterranean low-pressure systems and their associated winter rains (Toucanne et al., 2015), and might be responsible for the overall shift to wetter conditions that led to development of the Kuntila Lake. Simultaneous intensification of southerly low- and mid-latitude rains during northern-hemisphere insolation maxima (Waldmann et al., 2010) likely contributed to enhance the hydrological balance of the southern Negev. Considering typical accumulation rates of lacustrine-distal alluvial sequences formed in arid and semi-arid zones (typically 7–15 cm/kyr; Ginat et al., 2003; Larrasoaña et al., 2006; Pérez-Rivarés et al., 2018), a total span of about 200–400 kyr might be estimated for the Kuntila Member, which would be entirely consistent with its accumulation around the high eccentricity half of a 400 kyr maximum, regardless of the proposed correlation. These inferences, along with sedimentological and paleontological evidence, reinforce the notion of a long-lasting open-water surface in the context of a climatic shift to, at least, semi-arid conditions in the present-day hyper-arid Negev Desert and surrounding areas (Ginat et al., 2018). In addition to permanent fresh-water bodies, it is very likely that the enhanced hydrological balance would have also led to the retraction of arid dryland at the expense of more vegetated ecotones, and to the at least partial reactivation of the fluvial network. These circumstances resulted, coupled with a tectonically-driven heterogeneous topography, in a dynamic landscape favorable for human occupation and migration (Bailey et al., 2011).

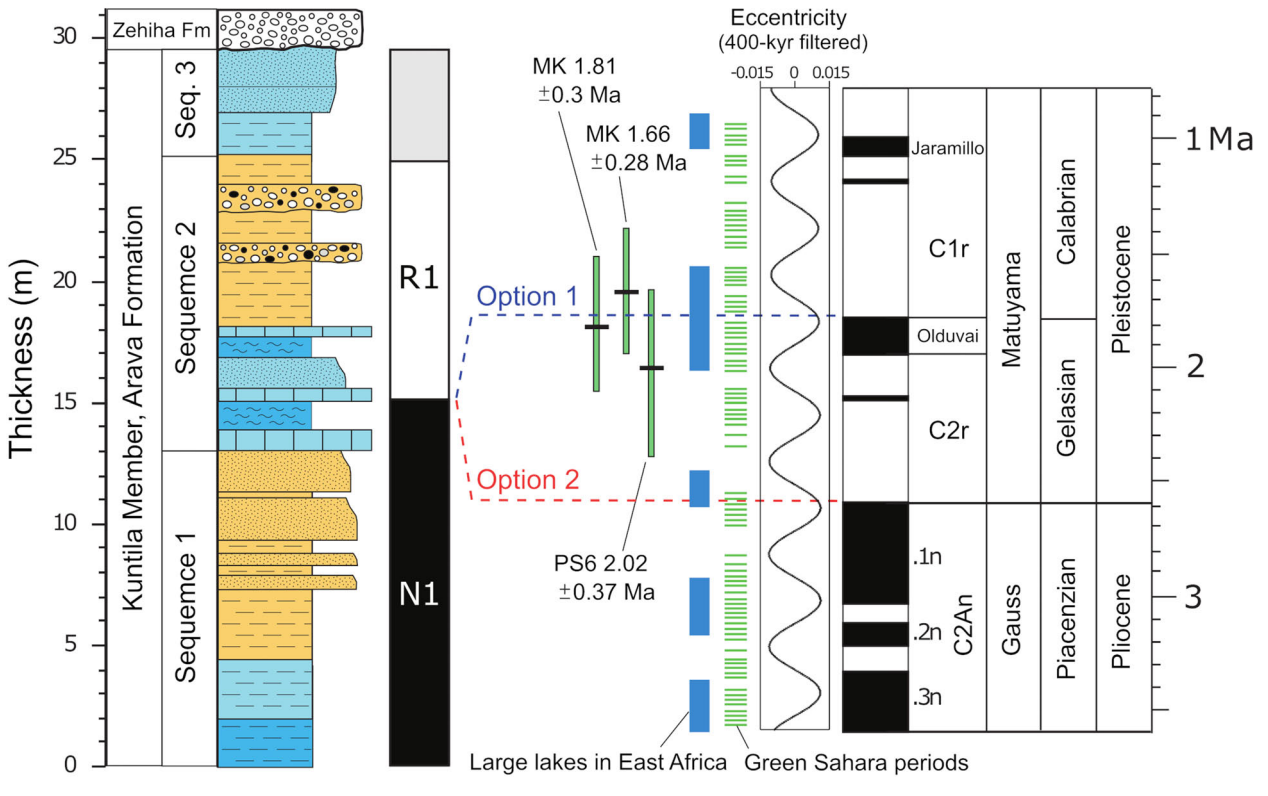

FIGURE 7 | Possible correlations of the Kuntila Lake sediments magnetostratigraphy with the astronomically-tuned Neogene times scale (ATNTS2012, Hilgen et al., 2012) taking into account the ^{10}Be exposure ages available for the top of the Arava Formation (after Guralnik et al., 2010; Amit et al., 2011). The 400-kyr band-pass filter of eccentricity (Laskar et al., 2004) is shown along with the inferred periods of large lake expansion in East Africa (Trauth et al., 2009) and clusters of Green Sahara periods (Larrasoaña et al., 2013).

It should be also noted that the 400 kyr eccentricity maxima associated with the tops of both the Olduvai and the C2An.1n Subchron are associated with protracted periods of lake expansion in East Africa (Trauth et al., 2009) and also with clusters of short-lived periods of savannah expansion throughout much of the Sahara (Larrasoaña et al., 2013; **Figure 7**). Simultaneous wetter conditions in East Africa, the Sahara and the Negev are a prerequisite for the establishment of the biogeographic connection between Africa and Eurasia that enabled the initial out-of-Africa dispersal of our genus *Homo*, whether it occurred around 1.85 Ma, as it is typically considered (Anton et al., 2014), or well before 2.12 Ma as pointed out by new evidence (Zhu et al., 2018) appears to indicate. Further research on Late Pliocene-Early Pleistocene sequences in the Levantine Corridor and surrounding areas is necessary to determine the timing and extent of African-Eurasia biogeographic connections.

CONCLUSION

Sedimentological evidence and ostracod faunas indicate that sediments of the Kuntila Member of the Arava Formation accumulated in a long-lasting lacustrine environment that underwent periodic changes in lake levels. The two lowermost sequences (S1 and S2) identified witnessed a gradual shallowing from fully lacustrine to palustrine conditions and, finally, to distal alluvial sedimentation. The third sequence identified (S3) shows a similar trend although it is devoid of the initial lacustrine part.

Magnetostratigraphic results enable recognition of a normal polarity (N1) zone in the lower half of the KG section and of a reverse polarity zone (R1) in its upper half. Correlation of the normal polarity zone to the Olduvai Subchron (1.778–1.945 Ma, Hilgen et al., 2012) appears as the most likely option in view of ^{10}Be ages derived for the uppermost part of the Kuntila Member in nearby sections (average of 1.83 Ma; Matmon et al., 2009; Guralnik et al., 2010; Amit et al., 2011). Nevertheless, the large errors associated with these cosmogenic exposure ages (typically spanning 0.6 Myr) make correlation of N1 with Subcrhon C2An.1n (2.582–3.032 Ma; Hilgen et al., 2012) also likely. Since the tops of both subchrons Olduvai and C2An.1n are associated with two 400 kyr eccentricity maxima (Laskar et al., 2004), our data unequivocally relate sedimentation of the Kuntila Lake sediments with a long period of enhanced climatic variability, driven by maxima in the Earth's eccentricity, regardless of the preferred correlation. Such enhanced climate variability drove the regional hydrological budget of the present-day hyper-arid Negev Desert to the point of enabling the formation of a long-lasting open-water surface. The 400 kyr eccentricity maxima associated with the tops of both the Olduvai and the C2An.1n Subchron also drove periods of lake expansion in East Africa (Trauth et al., 2009) and short-lived expansions of the savannah throughout much of the Sahara (Larrasoaña et al., 2013). Simultaneous wetter conditions in East Africa, the Sahara and the Negev would have generated optimal conditions for a biogeographic connection between Africa and Eurasia, facilitating initial out-of-Africa dispersal of our genus *Homo* possible. Further research on the Kuntila Lake sediments, as well as other Late Pliocene-Early Pleistocene sequences in the region, will be necessary to determine the timing and extent of such biogeographic connection between Africa and Eurasia.

DATA AVAILABILITY STATEMENT

All datasets generated for this study are included in the article/**Supplementary Material**.

AUTHOR CONTRIBUTIONS

JL performed the magnetostratigraphy and designed the research along with NW, who also led the sedimentological description of the studied sediments. SM studied the fossils. YA and HG provided the team with knowledge on the regional geological and geomorphological context. All coauthors contributed equally to fieldwork tasks and to the writing of the manuscript.

FUNDING

This study was funded by project CGL2012-30875 of the Ministerio de Economía y Competitividad of Spain and by Internal Funds of the University of Haifa.

ACKNOWLEDGMENTS

We thank Ari Matmon for assistance with cosmogenic exposure ages, Mina Weinstein-Evron for helping with the logistics for the field trip, and Bet Beamud for assistance with paleomagnetic measurements. We thank JP and JO for constructive reviews on the original manuscript.

SUPPLEMENTARY MATERIAL

The Supplementary Material for this article can be found online at: https://www.frontiersin.org/articles/10.3389/feart.2020.00173/full#supplementary-material.

TABLE S1 | Thermal demagnetization data for the studied samples.

TABLE S2 | Details on the calculation of the ChRM for the studied samples.

PLATE S1 | 1–4 *Ilyocypris* cf. *bradyi*, 1 right valve (RV) external view (ev), 2 left valve (LV) internal view (iv), 3–4 marginal ripplets on posteroventral part of inner lamella; 5 *Neglecandona angulata* ♀ carapace (cpx) slightly deformed at posterior margin; 6 *Potamocypris* sp. juvenile RV iv; 7–9 *Cyprideis torosa*, 7 ♀ cpx smooth form (*C. torosa* f. *littoralis*), 8 ♀ cpx with small nodes (arrow shows most prominent node, *C. torosa* f. *torosa*), 9 ♂ cpx smooth form. Scale bars are 50 and 250 μm. Specimens housed at Institute of Geological Sciences of Freie Universität Berlin (Germany).

PLATE S2 | 1–2 *Vestalenula cylindrica* RVs iv, 3 *Cypridopsis vidua* juvenile RV iv; 4–5 *Paralimnocythere* sp., 4 ♀ LV ev, 5 ♂ RV ev; 6–8 gyrogonites of *Chara* sp. 1, 6 apical view, 7 basal view, 8 lateral view; 9–11 gyrogonites of *Chara* sp. 2, 9 apical view, 10 basal view, 11 lateral view. Scale bar is 250 μm. Specimens housed at Institute of Geological Sciences of Freie Universität Berlin (Germany).

REFERENCES

Amit, R., Enzel, Y., Crouvi, O., Simhai, O., Matmon, A., Porat, N., et al. (2011). The role of the Nile in initiating a massive dust influx to the Negev late in the middle Pleistocene. *Geol. Soc. Am. Bull.* 123, 873–889. doi: 10.1130/b30241.1

Anton, S. C., Potts, R., and Aiello, L. C. (2014). Evolution of early Homo: an integrated biological perspective. *Science* 345:1236828. doi: 10.1126/science.1236828

Avni, Y. (1998). *Geological Evolution of the Central and Southern Negev as an Indicator of the Evolution of the Dead Sea Transform Western Margin in the Late Neogene and Quaternary*. Ph. D. Thesis, Hebrew University. Jerusalem.

Avni, Y., Bartov, Y., Garfunkel, Z., and Ginat, H. (2000). Evolution of the Paran drainage basin and its relations to the Plio-Pleistocene history of the Arava Rift western margin, Israel. *Isr. J. Earth Sci.* 49, 215–238. doi: 10.1560/w8wl-ju3y-km7w-8lx4

Avni, Y., Bartov, Y., Garfunkel, Z., and Ginat, H. (2001). The Arava formation – A pliocene sequence in the Arava Valley and its western margin, southern Israel. *Isr. J. Earth Sci.* 50, 101–120. doi: 10.1092/5u6a-rm5e-m8e3-qxm7

Avni, Y., Segev, A., and Ginat, H. (2012). Oligocene regional denudation of the northern Afar dome: pre and syn breakup stages of the Afro-Arabian plate. *Geol. Soc. Am. Bull.* 124, 1871–1897. doi: 10.1130/b30634.1

Bailey, G. N., Reynolds, S. C., and King, G. C. P. (2011). Landscapes of human evolution: models and methods of tectonic geomorphology and the reconstruction of hominin landscapes. *J. Hum. Evol.* 60, 257–280. doi: 10.1016/j.jhevol.2010.01.004

Belmaker, M. (2010). The presence of a large cercopithecine (cf. *Theropihecus* sp.) in the 'Ubeidiya formation (Early Pleistocene, Israel). *J. Hum. Evol.* 58, 79–89. doi: 10.1016/j.jhevol.2009.08.004

Deng, C., Zhu, R., Zhang, R., Ao, H., and Pan, Y. (2008). Timing of the Nihewan formation and faunas. *Quat. Res.* 69, 77–90. doi: 10.1016/j.yqres.2007.10.006

Enzel, Y., Amit, R., Dayan, U., Crouvi, O., Kahana, R., Ziv, B., et al. (2008). The climatic and physiographic controls of eatern Mediterranean over the late Pleistocene climates in the southern Levant and its neighboring deserts. *Glob. Planet. Change* 60, 165–192. doi: 10.1016/j.gloplacha.2007.02.003

Fuhrmann, R. (2012). Atlas quartärer und rezenter Ostrakoden Mitteldeutschlands. *Altenburger Naturwissenschaftliche Forschungen* 15, 1–320.

Garfunkel, Z. (1981). Internal structure of the Dead Sea leaky transform (rift) in relation to plate kinematics. *Tectonophysics* 80, 81–108. doi: 10.1016/0040-1951(81)90143-8

Ginat, H., Opitz, S., Ababneh, L., Faershtein, G., Lazar, M., Porat, N., et al. (2018). Pliocene-Pleistocene waterbodies and associated deposits in southern Israel and southern Jordan. *J. Arid Environ.* 148, 14–33. doi: 10.1016/j.jaridenv.2017.09.007

Ginat, H., Zilberman, E., and Saragusti, I. (2003). Early pleistocene lake deposits and Lower Paleolithic finds in Nahal (wadi) Zihor, Southern Negev desert, Israel. *Quaternary Res.* 59, 445–458. doi: 10.1016/s0033-5894(03)00029-2

Gradstein, F. M., Ogg, J. G., Schmitz, M. D., and Ogg, G. M. (2012). *The Geologic Time Scale*. Boston: Elsevier.

Guralnik, B. (2009). *Landscape and Tectonic Evolution of the Central Negev in Response to Dead Sea Rifting*. Ph. D. Thesis, The Hebrew University, Jerusalem.

Guralnik, B., Matmon, A., Avni, Y., and Fink, D. (2010). ^{10}Be exposure ages of ancient desert pavements reveal Quaternary evolution of the Dead Sea drainage basin and rift margin tilt. *Earth Planet. Sci. Lett.* 290, 132–141. doi: 10.1016/j.epsl.2009.12.012

Hilgen, F. J., Lourens, J. A., Van Dam, L. J., Beu, A. G., Boyles, A. F., Cooper, R. A., et al. (2012). "The Neogene period," in *The Geologic Time Scale*, eds F. M. Gradstein, J. G. Ogg, M. D. Schmitz, and G. M. Ogg (Boston: Elsevier), 923–978.

Kirschvink, J. L. (1980). The least-squares line and plane and the analysis of paleomagnetic data. *Geophys. J. R. Astron. Soc.* 62, 699–718. doi: 10.1111/j.1365-246x.1980.tb02601.x

Larrasoaña, J. C., Murelaga, X., and Garcés, M. (2006). Magnetobiocheonology of Lower Miocene (Ramblian) continental sediments from the Tudela Formation (western Ebro basin, Spain). *Earth Planet. Sci. Lett.* 243, 409–423. doi: 10.1016/j.epsl.2006.01.034

Larrasoaña, J. C., Roberts, A. P., and Rohling, E. J. (2013). Dynamics of Green Sahara periods and their role in hominin evolution. *PLoS One* 8:e76514. doi: 10.1371/journal.pone.0076514

Laskar, J., Robutel, P., Joutel, F., Gastineau, M., Correia, A. C. M., and Levrard, B. (2004). A long-term numerical solution for the insolation quantities of the Earth. *Astron. Astrophys.* 428, 261–285. doi: 10.1051/0004-6361:20041335

Lepre, C. J., Roche, H., Kent, D. K., Harmand, S., Quinn, R. L., Brugal, J. P., et al. (2011). An earlier origin for the Acheulian. *Nature* 477, 82–85. doi: 10.1038/nature10372

Matmon, A., Simhai, O., Amit, R., Haviv, I., Porat, N., McDonald, E., et al. (2009). Desert pavement-coated surfaces in extreme deserts present the longest-lived landforms on Earth. *Geol. Soc. Am. Bull.* 121, 688–697. doi: 10.1130/b26422.1

Meisch, C. (2000). *Freshwater Ostracoda of Western and Central Europe*. Heidelberg: Spektrum.

Meisch, C., Scharf, B., Fuhrmann, R., and Thiéry, A. (2019). *Neglecandona altoides* (Petkovski, 1961) nov. comb. and the genus *Neglecandona* Krstiæ, 2006 (Crustacea, Ostracoda, Candonidae). *Bull. Soc. Nat. Luxembourgeois* 121, 237–264.

Ogg, J. G. (2012). "Geomagnetic polarity timescale," in *The Geologic Time Scale*, eds F. M. Gradstein, J. G. Ogg, M. D. Schmitz, and G. M. Ogg (Boston: Elsevier), 85–113.

Orland, I. J., He, F., Bar-Matthews, M., Chen, G., Ayalon, A., and Kutzbach, J. E. (2019). Resolving seasonal rainfall changes in the middle East during the last interglacial period. *Proc. Natl. Acad. Sci. U.S.A.* 116:201903139. doi: 10.1073/pnas.1903139116

Parés, J. M., Duval, M., and Arnold, L. J. (2013). New views on an old move: hominin migration into Eurasia. *Quat. Int.* 295, 5–12. doi: 10.1016/j.quaint.2011.12.015

Pérez-Rivarés, F. J., Arenas, C., Pardo, G., and Garcés, M. (2018). Temporal aspects of genetic stratigraphic units in continental sedimentary basins: examples from the Ebro basin, Spain. *Earth Sci. Rev.* 178, 136–153. doi: 10.1016/j.earscirev.2018.01.019

Ramón, M. J., Pueyo, E. L., Oliva-Urcia, B., and Larrasoaña, J. C. (2017). Virtual directions in paleomagnetism: a global and rapid approach to evaluate the NRM components. *Front. Earth Sci.* 5:8. doi: 10.3389/feart.2017.00008

Sahnouni, M., Parés, J. M., Duval, M., Cáceres, I., Hariachane, Z., van der Made, J., et al. (2018). 1.9-million- and 2.4-million-year-old artifacts and sronetool-cutmarked bones from Ain Bucherit, Algeria. *Science* 362, 1297–1301. doi: 10.1126/science.aau0008

Toucanne, S., Minto'o, C. M. A., Fontanier, C., Bassetti, M. A., Jorry, S. J., and Jouet, G. (2015). Tracking rainfall in the northern Mediterranean borderlands during sapropel deposition. *Quat. Sci. Rev.* 129, 178–195. doi: 10.1016/j.quascirev.2015.10.016

Trauth, M. H., Larrasoaña, J. C., and Mudelsee, M. (2009). Trends, rhythms and events in Plio-Pleistocene African climate. *Quat. Sci. Rev.* 28, 399–411. doi: 10.1016/j.quascirev.2008.11.003

Vaks, A., Bar-Matthews, M., Ayalon, A., Matthews, A., Halicz, L., and Frumkin, A. (2007). Desert speleothems reveal climatic window for African exodus of early modern humans. *Geology* 35, 831–834.

van Harten, D. (1979). "Some new shell characters to diagnose the species of the *Ilyocypris gibba-biplicata-bradyi* group and their ecological significance," in *Taxonomy, Biostratigraphy and Distribution of Ostracodes*, *Proceedings of the 7th International Symposium on Ostracodes*, ed. Serbian Geological Society (Belgrade: Serbian Geological Society), 71–76.

Waldmann, N., Torfstein, A., and Stein, M. (2010). Northward intrusions of low- and mid-latitude storms across the Saharo-Arabian belt during past interglacials. *Geology* 38, 567–570. doi: 10.1130/g30654.1

Zhu, Z., Dennell, R., Huang, W., Wu, Y., Qiu, S., Yang, S., et al. (2018). Hominin occupation of the Chinese Loess Plateau since about 2.1 million years ago. *Nature* 559, 608–612. doi: 10.1038/s41586-018-0299-4

Ziv, B., Dayan, U., Kushnir, Y., Roth, C., and Enzel, Y. (2006). Regional and global atmospheric patterns governing rainfall in the southern Levant. *Int. J. Climatol.* 26, 55–73. doi: 10.1002/joc.1238

Conflict of Interest: The authors declare that the research was conducted in the absence of any commercial or financial relationships that could be construed as a potential conflict of interest.

frontiers in Earth Science

ORIGINAL RESEARCH
published: 26 June 2020
doi: 10.3389/feart.2020.00241

Rock Magnetic Cyclostratigraphy of Permian Loess in Eastern Equatorial Pangea (Salagou Formation, South-Central France)

Lily S. Pfeifer[1], Linda Hinnov[2], Christian Zeeden[3], Christian Rolf[3], Christian Laag[3,4] and Gerilyn S. Soreghan[1]*

[1] School of Geosciences, The University of Oklahoma, Norman, OK, United States, [2] Department of Atmospheric, Oceanic, and Earth Sciences, George Mason University, Fairfax, VA, United States, [3] Leibniz Institute for Applied Geophysics, Hanover, Germany, [4] Institut de Physique du Globe de Paris (IPGP), CNRS, Université de Paris, Paris, France

We present the findings from analysis and modeling of a stratigraphic series of magnetic susceptibility (MS) data measured with a portable MS meter from the Permian Salagou Formation loessite (south-central France). The results reveal discernible Milankovitch-scale paleoclimatic variability throughout the Salagou Formation, recording astronomically forced climate change in deep-time loessite of eastern equatorial Pangea. Optimal sedimentation rates are estimated to have ranged between 9.4 cm/kyr (lower Salagou Formation) and 13 cm/kyr (mid-upper Salagou Formation). A persistent 10-m-thick cyclicity is present that likely represents orbital eccentricity-scale (∼100 kyr) variability through the middle to late Cisuralian (ca. 285—275 Ma). Subordinate, higher frequency cycles with thicknesses of ∼3.3–3.5 and ∼1.8 m appear to represent obliquity and precession-scale variability. If the driver of magnetic enhancement is pedogenic, then the ∼10 m thick cyclicity that is consistent over ∼1000 m of section may represent the thickness of loessite–paleosol couplets in the Salagou Formation. Laboratory rock magnetic data show generally low magnetic enhancement compared to analogous Eurasian Quaternary loess deposits. This is related to the predominance of hematite (substantially weaker signal than magnetite or maghemite) in the Salagou Formation which may be explained by different conditions of formation (e.g., syn depositional processes, more arid, and/or oxidizing climate conditions) than in present Eurasia and/or post depositional oxidation of magnetite and maghemite.

Keywords: loess, cyclostratigraphy, magnetic susceptibility, Permian, rock magnetic

OPEN ACCESS

Edited by:
Hagay Amit,
Université de Nantes, France

Reviewed by:
Rui Zhang,
Northwest University, China
Diana Jordanova,
National Institute of Geophysics, Geodesy and Geography (BAS), Bulgaria

****Correspondence:***
Lily S. Pfeifer
Lspfeifer@ou.edu

Specialty section:
This article was submitted to Geomagnetism and Paleomagnetism, a section of the journal Frontiers in Earth Science

Received: *01 April 2020*
Accepted: *03 June 2020*
Published: *26 June 2020*

Citation:
Pfeifer LS, Hinnov L, Zeeden C, Rolf C, Laag C and Soreghan GS (2020) Rock Magnetic Cyclostratigraphy of Permian Loess in Eastern Equatorial Pangea (Salagou Formation, South-Central France). Front. Earth Sci. 8:241. doi: 10.3389/feart.2020.00241

INTRODUCTION

Loess-paleosol sequences of the Chinese Loess Plateau (CLP; thickness of ∼200 m) and other regions (e.g., Li et al., 2019) are widely regarded as high-resolution and continuous continental records of global Pleistocene climate change (e.g., Liu, 1985; Heller and Liu, 1986; Kukla, 1987; Kukla et al., 1988; Kukla and An, 1989; Maher and Thompson, 1991, 1992; Evans and Heller, 2001; Yang and Ding, 2004; Muhs, 2007; Maher and Possolo, 2013; Maher, 2016). These quasi-cyclic

loess-paleosol deposits commonly record a combination of glacial-interglacial oscillations and changes in monsoonal precipitation, and trends in their magnetic susceptibility (MS) correlate with marine-based oxygen isotope records of continental ice volume (Heller and Liu, 1982; Kukla et al., 1988; Shackleton et al., 1990; Parrish, 1993; Porter, 2001; Porter et al., 2001; Basarin et al., 2014; Ahmed and Maher, 2017; Zeeden et al., 2018).

Thick loessite deposits have also been associated with the Late Paleozoic Ice Age (e.g., Murphy, 1987; Johnson, 1989; Kessler et al., 2001; Mack and Dinterman, 2002; Soreghan et al., 2002; Tramp et al., 2004; Soreghan and Soreghan, 2007; Soreghan et al., 2008a,b; Soreghan G. S. et al., 2014; Soreghan M. J. et al., 2014; Giles et al., 2013; Sweet et al., 2013; Foster et al., 2014; Pfeifer et al., 2020). Voluminous paleo-loess accumulated in low latitudes of western and eastern Pangea and are exposed today in the western United States (exceeding 700 m thick) and western Europe (up to ∼1500 m thick in southern France). Loessite–paleosol intercalations in the deep-time record of western equatorial Pangea have been posited to represent icehouse glacial-interglacial oscillations on a 100 kyr-scale (Soreghan et al., 1997, 2002; Soreghan M. J. et al., 2014; Tramp et al., 2004), as well as higher frequency climatic signals occurring on obliquity and possibly precession scales (Soreghan M. J. et al., 2014). Recently, a radioisotopically-dated lower Guadalupian cyclic lacustrine record from the Junggar Basin of eastern Pangea (30—32°N paleolatitude) was discovered to exhibit astronomical frequencies (Huang et al., 2020). Importantly, this new evidence supports the hypothesis explored in this work for presumably analogous Milankovitch cycles recorded in the thick (∼1000 m) record of upper Paleozoic loess in eastern equatorial Pangea.

The objectives of this work are to (1) document Permian climatic variability and assess Milankovitch characteristics using MS data from the Salagou Formation loessite obtained with a portable MS meter, (2) leverage laboratory rock magnetic measurements to better understand the origin of the magnetic signal, and (3) compare this upper Paleozoic record with analogous successions from the Eurasian Quaternary record.

GEOLOGICAL SETTING

The Permian Salagou Formation is an exclusively fine-grained and internally massive deposit of red mudstone with local pedogenic overprinting and water-reworked interbeds that accumulated in the Lodève continental rift basin at equatorial latitudes (0–3°N; Domeier and Torsvik, 2014; Muttoni and Kent, 2019). Its characteristics are most consistent with eolian transport and deposition either as loess, or as dust deposited in a seasonal, shallow lacustrine environment (Pfeifer et al., 2020). The provenance of the Salagou Formation is the Montage Noire Dome, a local uplift of Variscan basement composed of gneiss, schist, and granite (**Figure 1**; Pfeifer et al., 2016). The recognition of great volumes of loess-sized silt, together with known coarse-grained granitic protoliths and deposition during global icehouse conditions, are all most consistent with a hypothesis of upland glaciation in this region (Pfeifer et al., 2020).

The late Artinskian to mid-Kungurian (upper Rotliegend I; Kiersnowski, 2013) age of the lower Salagou Formation (Octon Member) is well constrained by U-Pb ID-TIMS dates from ash layers (Michel et al., 2015; **Figure 2**). Chronostratigraphic constraints for the top of the formation (Merifons Member) are lacking, so the extent of Guadalupian deposition (cf. Schneider et al., 2006; Pochat and Van Den Driessche, 2011) is unclear. The Octon Member (basal to mid-upper Salagou) makes up the majority of the Salagou Formation and consists primarily of massive red mudstone with loessitic characteristics (Pfeifer et al., 2020). The MS data for this study were collected from the Octon Member to lower Merifons Member (**Figures 1**, **2**; red bar), which represents deposition through the mid-late Cisuralian (ca. 285–275 Ma).

Magnetic susceptibility has been used as a proxy for climatic signals in both Plio-Pleistocene loess, the Chinese "red clay," and Permian loessite recording climate-dependent pedogenesis and dust influx (e.g., Heller and Liu, 1984; Maher and Taylor, 1988; Soreghan et al., 1997, 2002; Soreghan M. J. et al., 2014; Tramp et al., 2004). MS measures the concentration and grain size of ferrimagnetic minerals which consist primarily of magnetite, secondarily of maghemite, and supplemented by hematite (e.g., Maher, 1986; Kukla and An, 1989; Porter et al., 2001; Muhs, 2007; Ahmed and Maher, 2017). In saturated, gleyed (reduced) and thus Fe-leached soils, MS values in parent loess can exceed those in pedogenic intervals (e.g., see Muhs, 2007 and the references within; Beget et al., 1990; Hayward and Lowell, 1993; Chlachula, 2003). But otherwise, *in situ* precipitation of ultra-fine-grained ferrimagnetic material [e.g., super-paramagnetic (SP) magnetite or maghemite] during warmer and wetter interglacial conditions has been widely recognized as a driver of elevated MS in pedogenically altered intervals compared to unaltered parent loess (deposited during arid and dusty glacial periods, and/or phases of monsoonal interference). This is true for both the CLP (cf. Heller and Liu, 1984; Maher and Taylor, 1988; Zhou et al., 1990; Maher and Thompson, 1991, 1992; Zheng et al., 1991; Maher et al., 1994; Porter et al., 2001; Ahmed and Maher, 2017), where bulk MS of paleosols is ∼4–10x higher than in loess (Heller and Liu, 1984, 1986; Liu et al., 1993) and in lower Permian loessite of western equatorial Pangea where bulk MS is commonly ∼1.5–2x (and up to 9x) higher in paleosols relative to loess (Soreghan et al., 1997, 2002; Cogoini et al., 2001; Tramp et al., 2004; Soreghan G. S. et al., 2014). The origin of the magnetic signal in Permian loessite of western equatorial Pangea (e.g., Maroon Formation, CO) is dominantly hematite, but is also driven locally by the inferred presence of submicron SP magnetite (Soreghan et al., 1997; Cogoini et al., 2001; Jia, 2020).

Rock magnetism of Quaternary loess (and loess-based paleosols) has been used as a proxy (directly proportional) for mean annual precipitation (MAP) of ∼300–1500 mm/year (e.g., Porter, 2001; Maher and Possolo, 2013; Maher, 2016; Gao et al., 2019). Depending on the parent material, amount of biological mixing, carbonate leaching, and clay illuviation, soils less penetrable by precipitation in areas with MAP > ∼600 mm may result in water-logged conditions. Together with the presence of organic matter, this promotes anoxia and post-depositional dissolution of (fine) magnetic minerals.

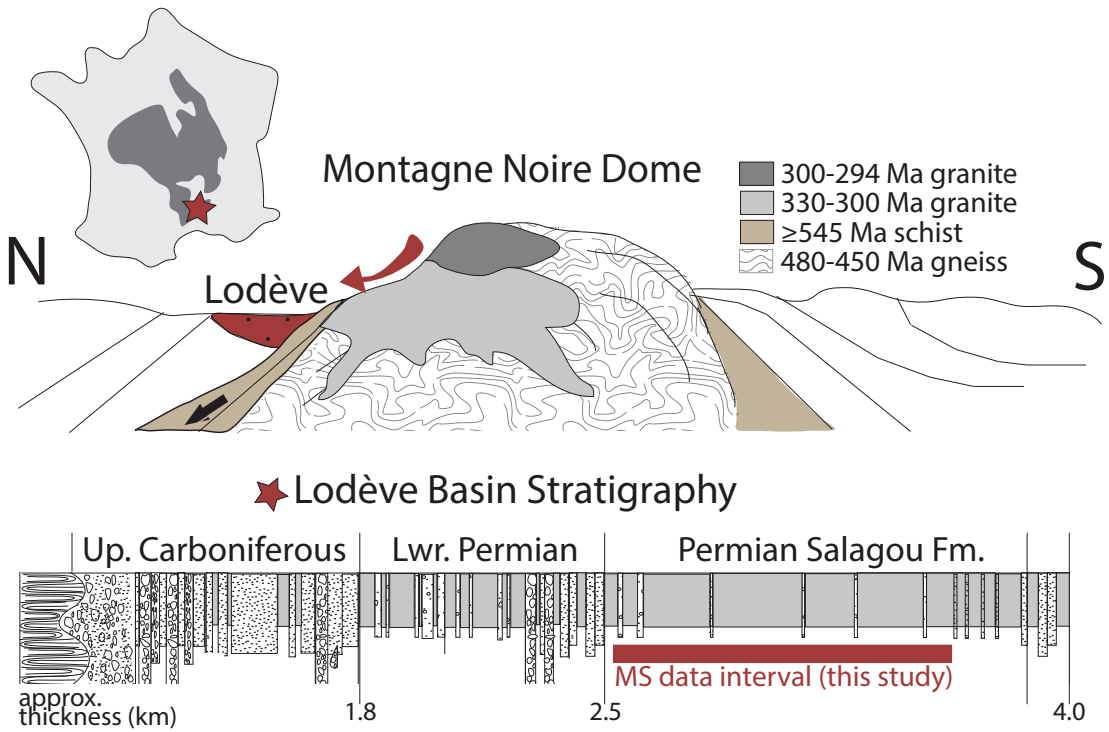

FIGURE 1 | Geological setting of the Lodève Basin in south-central France (southern Massif Central). The N-S cross section depicts the generalized position of the Lodève basin in relation to several source lithologies in the Montagne Noire Dome (interpreted source of sediment in the Lodève Basin; Pfeifer et al., 2016). The generalized stratigraphic column (adapted from Pochat and Van Den Driessche, 2011) of the upper Carboniferous – Permian strata in the Lodève Basin, depicting the stratigraphic interval of focus in this study with a red bar.

DATA AND METHODS

Magnetic Susceptibility Sampling

Sampling Magnetic Susceptibility in the Field (KT-10)

A detailed sedimentological investigation of the Salagou Formation (Pfeifer et al., 2020) included measurement and description (at a decimeter scale) of ∼1000 total meters of stratigraphic section exposed at the surface (**Figure 3**). One MS reading (each flanked by free air measurements) was taken every 0.5 m through the entire formation with the Terraplus KT-10 Plus v2 handheld MS meter that includes a pin and circular coil for uneven surfaces. In mathematical terms, MS (k) is the ratio of the intensity of magnetization (I) to the magnetic field (H) responsible for the magnetization. It is calculated with the KT-10 Plus handheld meter based on the difference in frequency between the rock and free air with a sensitivity of 1×10^{-6} SI units (Kt-10 manual, 2017). Results (k) in dimensionless units of 10^{-3} are reported as a curve constructed from the individual MS values at 0.5 m increments through each section.

The Salagou Formation was measured and described over nine stratigraphic sections (**Figure 3A**). Most sections are continuous (from the top of one to the base of the next) and can be concatenated for analysis. However, there is ∼500 m of missing section (inaccessible in outcrop) between the lowermost section (Section 1; **Figure 3A**) and the remainder of the formation (Sections 2–9; **Figure 3A**), necessitating the need to analyze Section 1 separately. Thus, time series analysis was done in two large segments (as noted in **Figure 3A**, lower horizontal bar): the lower (165 m of continuous Section 1; results in **Figure 5**) and the mid-upper (775 m of eight concatenated Sections 2–9; results in **Figure 6**).

Sampling for Laboratory Magnetic Measurements

Two sets of samples were collected from the middle Salagou Formation (**Figure 3A**) for laboratory rock magnetic analysis (section "Laboratory Magnetic Measurements") at two different increments. In the first set (**Figure 3B**), a 10 g sample was collected at a 5 m resolution for ∼80 m of section. The second set (**Figure 3C**) is higher resolution (a 10 g sample collected every 30 cm) but covers a shorter interval (∼10.2 m total).

Time Series Analysis and Modeling

Time series analysis of the MS stratigraphic series was carried out in MATLAB and Astrochron for R (Meyers, 2014) (see **Supplementary Appendix S1** for commands). MATLAB functions were used to display the stratigraphic series, and for spectral analysis and evolutionary spectrograms to assess the distribution of variability as a function of frequency (cycles/meter) and along stratigraphic position to assess potential changes in sedimentation rate. A low-pass Taner filter was applied

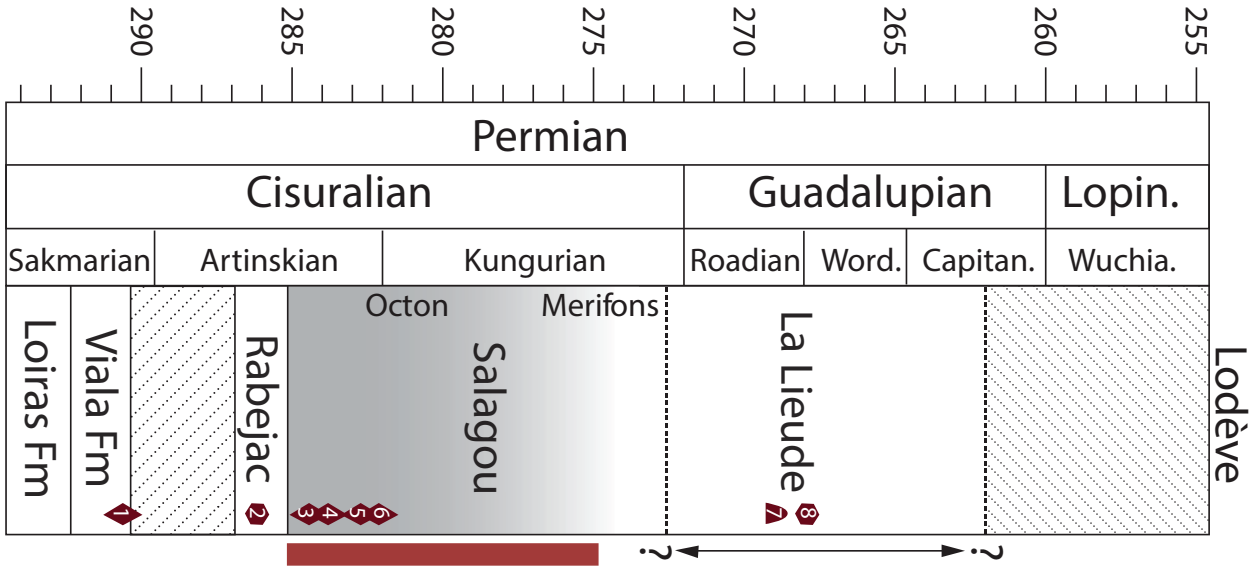

FIGURE 2 | A summary of the current Permian chronostratigraphic constraints of the Salagou Formation (Lodève Basin). The section where MS data were measured in this study is highlighted in gray and also indicated with the red bar. Note that the upper age of the Salagou Formation is very poorly constrained. Icon shapes indicate different types of age data, numbered 1–8 according to the sources from which they are derived; Specifically: (1) U/Pb ID-TIMS on ash 291.0 ± 0.2 from the upper Viala Formation (Michel et al., 2015), (2) tetrapod tracks, Dromopus–Erpetopus biochron boundary, ~290–284 Ma (Schneider, *pers. commun. 2020*); (3–6) U/Pb ID-TIMS on ash (in stratigraphic order: 284.4 ± 0.1, 284.5 ± 0.1, 283.5 ± 0.1, 282.9 ± 0.1) from the Octon Member of the Salagou Formation (Michel et al., 2015), (7) magnetostratigraphic data from the La Lieude Formation that suggests proximity to the end of the "Kiaman" or Permo-Carboniferous Reversed Superchron (PCRS), ca. 262 Ma (Evans, 2012), and (8) tetrapod track ichnofauna from the La Lieude Formation consistent with a Guadalupian age (Schneider et al., 2010, 2019).

to pre-whiten the stratigraphic series, for clarity in evaluating stratigraphic cyclicity potentially related to orbital eccentricity.

The absence of an adequately precise time scale (**Figure 2**) motivated the application of objective modeling with the average spectral misfit (ASM) method provided in Astrochron (Meyers and Sageman, 2007). The ASM method searches for astronomical frequencies in well-sampled stratigraphic series across a range of plausible sedimentation rates. For each test sedimentation rate, the stratigraphic series is converted to a time series and compared against an astronomical target (in kyr). Here the astronomical target is a collection of astronomical frequencies based on a precession frequency of $k = 56.6$ arcsec/year estimated for 298 Ma (Berger and Loutre, 1994) and assuming Solar System fundamental frequencies s_i, g_i from Laskar et al. (2004; **Table 1**). The sedimentation rate yielding time frequencies in the data that most closely match those of the astronomical target (with Monte Carlo testing for assessing significance) is taken as the "optimal sedimentation rate."

Laboratory Magnetic Measurements

More elaborate rock magnetic analysis was carried out for representative sections from the middle Salagou Formation (**Figures 3B,C**) to determine the origin of the magnetic signal and strengthen the validity of MS as a proxy for the ancient paleoclimate record. The analyses were done at the rock and paleomagnetic laboratory of the Leibniz Institute for Applied Geophysics (LIAG) in Grubenhagen, Germany. The samples were dried, homogenized, weighed, and filled into non-magnetic plastic boxes of 6.4 cm^3. The MS for all samples was measured using a frequency- and field-variable Magnon VSM susceptibility bridge at 505 Hz (low frequency susceptibility; χlf) and at 5050 Hz (high frequency susceptibility; χhf), both at a field of 400 A/m. These measurements were also used to detect the frequency dependence of the MS, which can be expressed as simple difference ($\Delta\chi$ or $\%\chi$fd). The temperature-dependent MS was determined using an AGICO MFK1-FA Kappabridge and the CS4 furnace, covering a temperature range of 20–700°C (**Figure 4**). Additionally, the system was rinsed by Argon provided in a constant flux and pressure. Thermally stable furnace holders were measured in an empty state and subtracted, based on their MS rusting of the full-range heating. The applied field strength was set to 400 A/m.

RESULTS

Sedimentology

Pfeifer et al. (2020) conducted detailed sedimentological analysis of the Salagou Formation. The dominant facies consist of thick and internally structureless mudstone beds (**Figure 3A**, gray; interpreted as loess deposits) with local pedogenic overprinting. There is a general up-section increase in interbedded units (calcareous mudstone, commonly with desiccation features and laminated mudstone, commonly with ripples) that reflect intermittent subaqueous deposition (**Figure 3A**, navy). Interpreted pedogenic intervals are nested within the loessite, defined in outcrop primarily by large

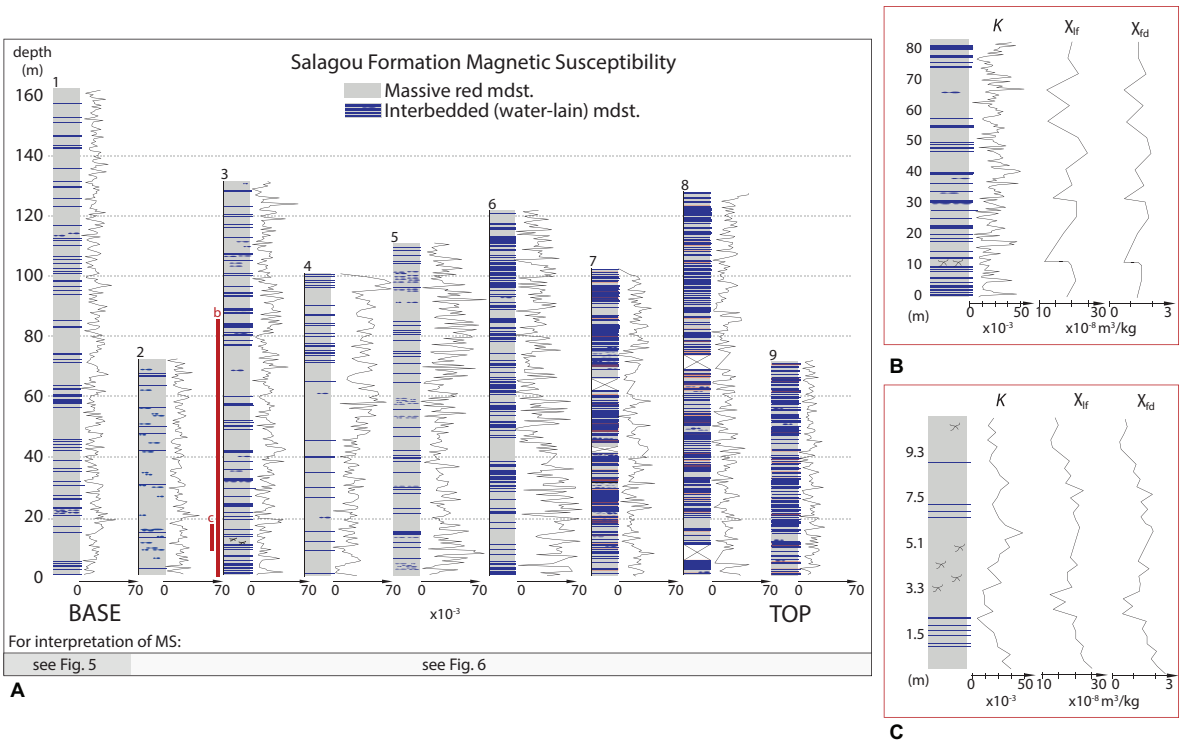

FIGURE 3 | Rock magnetic data from the Salagou Formation. **(A)** Stratigraphy with handheld (outcrop) MS data (in units of 10^{-3}). Section are numbered for reference and correspondence to **Table 2**. The dotted lines indicate depth intervals (see meter marks at left). The red bars on Section #3 represent the locations of detailed profiles sampled at two different intervals for detailed rock magnetic data (**B,C**; see insets). Bar at bottom of page indicates which stratigraphic section correspond with each interpreted MS series in **Figure 5** (#1 only) and **Figure 6** (#2–9). **(B,C)** Focused view showing the stratigraphy and outcrop MS again, but also displaying rock magnetic data obtained for these intervals. Specifically, mass normalized low-field MS (χlf) at 505 Hz in 10^{-8} m^3/kg and delta χ (χfd). **(B)** An 80-m section sampled at 5-m intervals. Note the pedogenic interval ∼11 m. The correlation between MS measured in the field to χlf is negligible (r^2 = 0.0059), but the relationship between the two datasets is highly significant (*P*-value < 0.05). **(C)** A 10-m section sampled at 30-cm intervals. Note the pedogenic interval ∼3–5 m. The correlation between MS measured in the field to χlf is weak (r^2 = 0.1758), but the relationship between the two datasets is highly significant (*P*-value < 0.05).

TABLE 1 | Periodicities (in kyr) of orbital eccentricity (from Laskar et al., 2004); precession index, and obliquity are from Earth's precession frequency (*k*) = 56.6 arcsec/year modeled at 298 Ma (Berger and Loutre, 1994).

Astronomical parameter	Frequency (arcsec/year)	Period (kyr)
Eccentricity		
g_2–g_5	3.194548	405.091
g_3–g_2	9.916	131.0
g_4–g_2	10.464	123.4
g_3–g_5	13.110548	98.9
g_4–g_5	13.658548	94.5
Precession index		
k+ g_5	60.857452	21.296
k+ g_2	64.052	20.234
k+ g_3	73.968	17.521
k+ g_4	74.516	17.392
Obliquity		
k+ s_6	30.252145	44.840
k+ s_3	37.750	34.331
k+ s_4	38.755	33.441
k+ s_2	49.55	26.155

g and s are Solar System fundamental frequencies from Laskar et al. (2004), and subscripts refer to the planets in order (2–6): Venus, Earth, Mars, Jupiter, Saturn.

(∼10+ cm), randomly oriented, semi-radial slickensides (**Figures 3B,C**). Micromorphologic attributes of samples from these localities include higher proportions of clay, wedge-shaped peds, clay coatings on grains, and porphyroskelic fabrics. Geochemical analyses reveal elevated chemical index of alteration (CIA) values from these intervals (compared to neighboring loessite). These features, together with a lack of horizonation, are most analogous to modern Vertisols which are typically indicative of environments with seasonal precipitation (e.g., Mack et al., 1993).

Magnetic Susceptibility Measurements by KT-10

Table 2 summarizes the statistics of MS data obtained by portable MS meter, reporting the mean and standard deviation of susceptibility readings overall and by section (#1–9; **Figure 3A**). Overall, the mean measurement of *k* (MS) for the Salagou formation is 0.253 ± 0.100 ($\times 10^{-3}$). The section with the lowest readings (uppermost Salagou; Section 9) averages 0.179 ± 0.034 ($\times 10^{-3}$) and the section with the highest readings (middle Salagou; Section 5) averages 0.366 ± 0.092 ($\times 10^{-3}$).

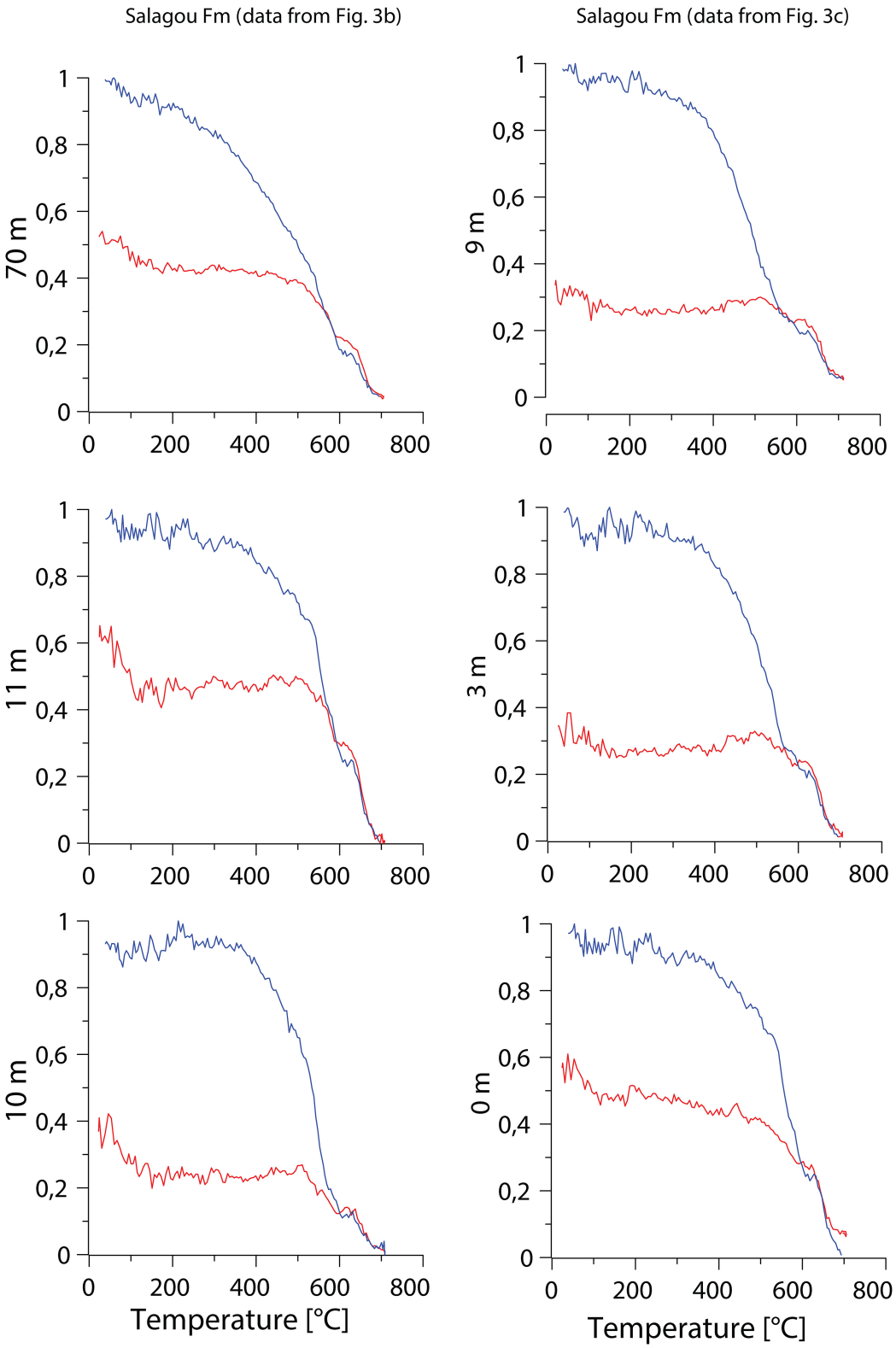

FIGURE 4 | Temperature-dependent susceptibilities of datasets for selected samples from discussed sections in **Figures 3B,C**. Heating (red) and cooling curves (blue) are plotted against χlf, scaled to a maximum of 1 for comparison. Note that an χlf decrease at the Curie temperature of magnetite (580°C) tends to be less expressed than the clear χlf decrease at the Curie temperature of hematite (675°C).

TABLE 2 | Basic statistics of MS measurements by KT-10 (field data) depicted in **Figure 3A** as curves constructed from individual MS values.

Section no.	Mean (10^{-3})	St. dev (10^{-3})	# Readings	Total m	Interval (m)
9	0.179	0.034	138	70	0.51
8	0.222	0.064	226	125	0.55
7	0.234	0.062	179	100	0.56
6	0.345	0.135	227	121.5	0.54
5	0.366	0.092	220	111	0.50
4	0.303	0.097	159	100	0.63
3	0.220	0.057	259	131.5	0.51
2	0.205	0.038	137	70	0.51
1	0.198	0.046	314	160	0.51
ALL	0.253	0.100	1859	989	0.53

*This table reports the mean and standard deviation of MS measurements overall, and also by section (#1–9; corresponding with the stratigraphic columns in **Figure 3A**). The number of readings (measurements) for each section is also reported, as well as the sampling interval. Note: the aim was to take a measurement every 0.5 m, but sampling intervals are slightly wider than 0.5 m because of unexposed parts of the section.*

Lower Salagou Formation

A repeating pattern appears in the MS series (**Figure 5A**), defined by a predominant peak at 0.1 cycles/m (10 m wavelength) in the power spectrum (**Figure 5B**) and warm colors in the spectrogram (**Figure 5C**). Prominent, shorter frequencies of 0.29 cycles/cm (3.45 m) and 0.57 cycles/m (1.75 m) are also consistent through the section. ASM analysis estimates an optimal sedimentation rate of ∼9.4 cm/kyr and indicates that astronomical forcing is statistically significant (P = 0.002; **Figure 5D**).

Mid-Upper Salagou Formation

Analysis of the mid-upper Salagou Formation (**Figure 6**) reveals a strong, very low-frequency signal—especially in the middle part of the section—coincident with observed ∼100–130 m (large-amplitude variations) in the MS series (**Figure 6A**). The most significant cyclicity is ∼0.1 cycles/m (0.13–0.08 cycles/m), i.e., 10 m thick cycles. Subordinate, higher frequency peaks at 0.28–0.31 and 0.55 cycles/m appear intermittently throughout the series. ASM analysis estimates an optimal sedimentation rate of 13 cm/kyr and indicates that astronomical forcing is statistically significant (P = 0.002; **Figure 6D**).

Laboratory Magnetic Measurements

Temperature (**Figure 4**) and frequency-dependent susceptibility measurements from the representative section (**Figures 3B,C**) indicate that the origin of the magnetic signal is primarily driven by hematite, as evinced by the decrease of the MS at its Curie temperature at 675°C, with a varying but generally minor contribution of magnetite at a Curie temperature of 580°C (**Figure 4**).

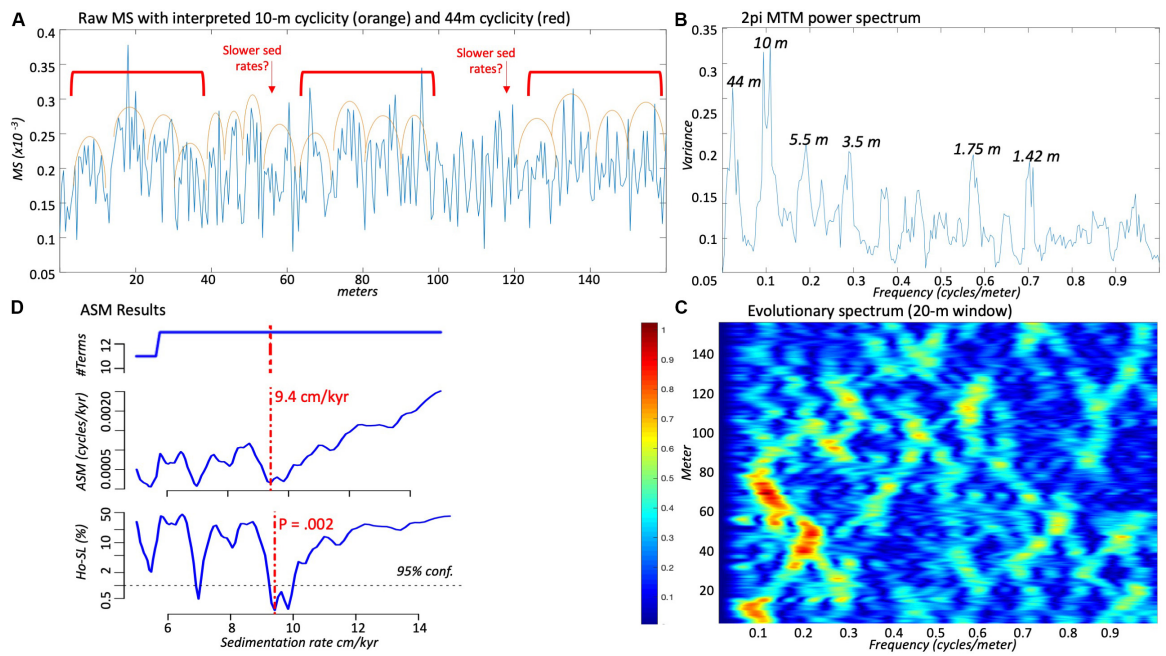

FIGURE 5 | Results of time series analysis and modeling for MS data collected in outcrop from the lower Salagou Formation (see stratigraphic context in **Figure 3**; lower bar). The section is measured in meters (from low to high is moving up-section). **(A)** Magnetic susceptibility data with interpretations shown by orange arcs [10 m cycles—short (∼100 kyr) orbital eccentricity] and red brackets [44 m cycles—long (∼405 kyr) orbital eccentricity]. **(B)** The power spectrum shows the proportion of power (or variance) as a function of frequency (in cycles/m). **(C)** The FFT spectrogram, computed with a 20 m running window. Warmer (red) colors represent high power and cooler (blue) colors low power. **(D)** Results of ASM analysis with the optimal sedimentation rate identified by the vertical red dashed curve. *Top*: number of astronomical frequencies used in the fit; *middle*: ASM statistic; *bottom*: statistical significance of Monte Carlo modeling with the critical level shown by the horizontal black dashed line.

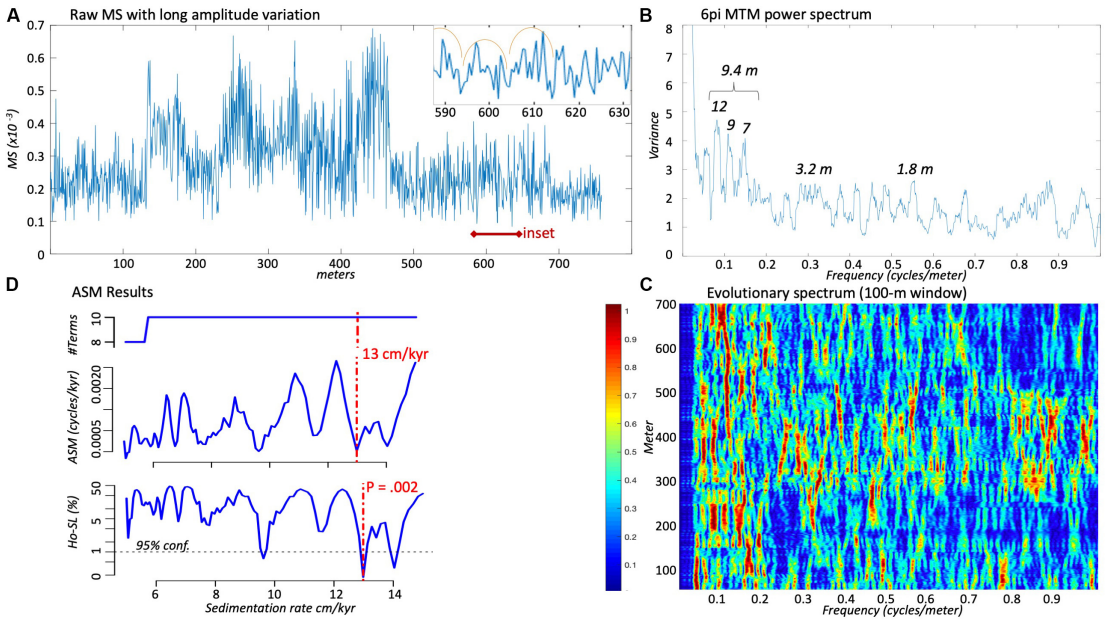

FIGURE 6 | Results from time series analysis and modeling for MS data collected in outcrop from the mid-upper Salagou Formation (see stratigraphic context in **Figure 3**; lower bar). The section is measured in meters (from low to high is moving up-section). **(A)** Magnetic susceptibility data with long-term amplitude variation (~100–130 m cycles). Higher frequency signals are not notable at this scale, but the inset zooms into an interval (590–630 m) to provide an example of the 10 m cycles (interpreted with orange arcs) that are also present in this section. **(B)** The power spectrum shows the proportion of power (or variance) as a function of frequency (in cycles/m). **(C)** The FFT spectrogram, computed with a 100 m running window and subtraction of low pass Taner filter with a cutoff frequency of 0.035 cycles/m (see **Supplementary Appendix S1** for script). Warmer (red) colors represent high power and cooler (blue) colors low power. **(D)** Results of ASM analysis with the optimal sedimentation rate identified by the vertical red dashed curve. *Top*: number of astronomical frequencies used in the fit; *middle:* ASM statistic; *bottom*: statistical significance of Monte Carlo modeling with the critical level shown by the horizontal black dashed line.

DISCUSSION

Calibration of Magnetic Susceptibility Measurements by KT-10

The data acquired by portable MS meter (see Section "Cyclicity in the Salagou Formation") demonstrate the tool's ability to recognize cyclic trends through extended stratigraphic successions of loessite. This methodology is relatively rapid, convenient, and inexpensive, but it is important to calibrate *in situ* outcrop MS data with rock magnetic analysis from the laboratory. The correlation between MS acquired by the portable MS meter in the field and detailed rock magnetic data acquired in the laboratory (χlf and $\Delta\chi$) is weak (r^2 = 0.1758; **Figure 3C**), but a simple *t*-test indicates with 95% confidence that the relationships between χlf and field MS, and $\Delta\chi$ and field MS, are both highly significant (*P*-values < 0.05). The standard deviations in most sections (**Table 2**; Sections 1–3 and 7–9) for MS readings obtained with the portable meter (0.179×10^{-3}–0.234×10^{-3}) are between 0.034×10^{-3}–0.064×10^{-3}, which further supports reproducibility. Prior to taking measurements through a section, several readings were recorded on the same sample to understand variability in the magnetic signal by lithology, and the tool always measured within 0.05×10^{-3}. For example, in Section 3 (**Figure 3A**), six measurements were taken on calcareous interbeds for a mean reading of $0.158 \pm 0.037 \times 10^{-3}$ and 11 measurements were taken on pedogenic slickensides for a mean reading of $0.232 \pm 0.055 \times 10^{-3}$. In comparison to the average loess reading for this same section ($0.220 \pm 0.056 \times 10^{-3}$), this demonstrates the reliability of the tool to capture magnetic signal variations in different lithologies as well as reproducibility of readings on the same sample.

However, there are limitations with *in situ* MS measurements. The poor correlation between field and laboratory data may be caused by inhomogeneous volumes measured in the field (e.g., uneven surfaces or fractures/cavities in outcrop). Elevated mean MS readings from the portable meter (0.303×10^{-3}–0.366×10^{-3}) in the middle Salagou formation (**Table 2**; Sections 4–6) have especially high standard deviations (0.092×10^{-3}–0.135×10^{-3}) compared to other sections. It is possible that elevated values in the middle Salagou Formation relate to a decline in calcareous cement observable in this interval.

Origin of the Magnetic Signal and Comparison to Quaternary Eurasian Loess

The direct relationship between χlf and $\Delta\chi$ (**Figure 7**; frequency dependence) demonstrates that magnetic enhancement (increased χ) is triggered by ultrafine SP particles close to the domain transition boundary. The production of SP magnetic grains can occur either *in situ* via pedogenic processes (Singer et al., 1996; Maher, 1998), by incorporation of detrital particles (e.g., Reynolds et al., 2001), and/or through conversion of

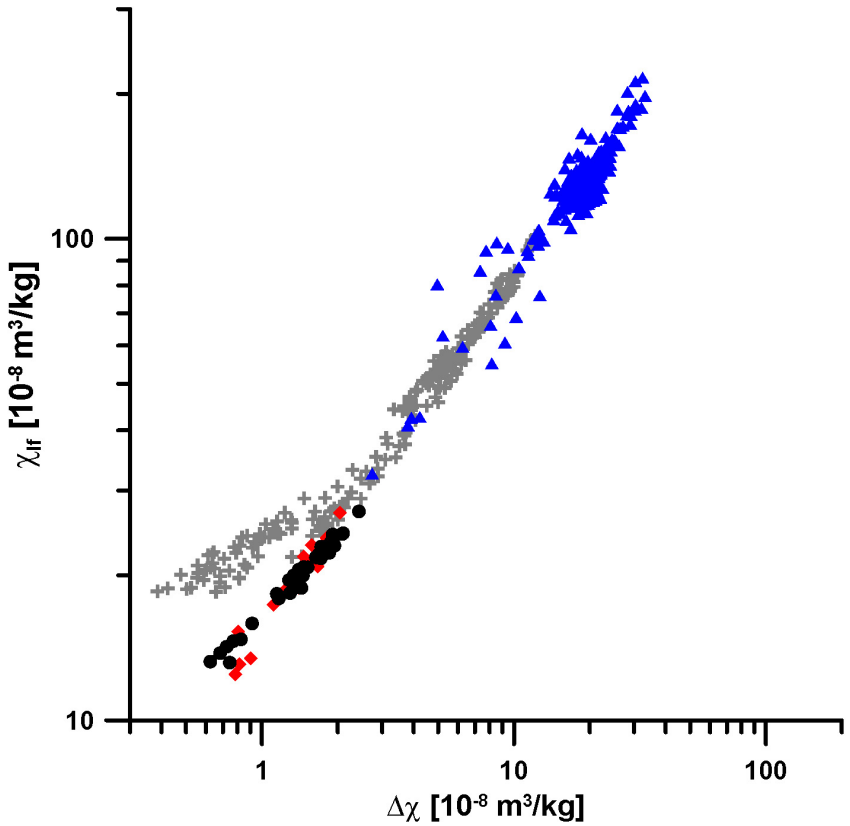

FIGURE 7 | Frequency-dependent susceptibility (χlf vs. Δχ) of the Salagou Formation loess samples (red spades from **Figure 3B**; black circles from **Figure 3C**) compared to data from the Quaternary CLP red clay (blue triangles; Song et al., 2007) and a loess-paleosol section from Romania (gray crosses; Zeeden et al., 2016).

magnetic mineral species during fluid or burial diagenesis (Katz et al., 1998; Woods et al., 2002). Given the burial history of the basin (T_{max} up to 500–600°C; Copard et al., 2000), we cannot dismiss the possibility that some SP particles may have formed as a result of diagenesis, but minimal evidence occurs for fluid flow or veining in the Salagou Formation exposures. We prefer the interpretation of primarily pedogenically formed magnetic particles for the following reasons: (1) Association with evidence for pedogenesis, namely Vertic features (section "Sedimentology"), and elevated clay mineral content and CIA (compared to parent loessite). Lindquist et al. (2011) show that the seasonal wetting and drying typical of Vertisols facilitate the formation of ferrimagnetic SP minerals. (2) There is no evidence for gleying: The Vertic characteristics of Salagou Formation paleosols are inconsistent with ever-wet conditions (Tabor and Myers, 2015). Numerous studies on recent and modern soils show consistently that non-water-logged (gleyed) soils have higher MS and greater abundances of pedogenically produced ultra-fine-grained ferrimagnetic material than in surrounding loess (cf. Heller and Liu, 1984; Maher and Taylor, 1988; and other references in section "Geological Setting"). Furthermore, (3) the alignment of χlf and Δχ with other Eurasian loess (**Figure 7**) suggests pedogenic control on the magnetic signal (see also discussion below) as opposed to trends typical of diagenesis.

Rock magnetic data from the Salagou Formation shows magnetic enhancement, but distinctly lower χlf and lower Δχ compared to reference data (**Figure 7**) from the Pliocene red clay on the CLP (Song et al., 2007) and a loess-paleosol sequence in Romania (Zeeden et al., 2016). A systematically lower χlf and Δχ relates to the predominance of hematite, which generally exhibits a weaker magnetic signal than magnetite and maghemite. The dominance of hematite and lower contribution of magnetite and maghemite in the Salagou Formation is similar to that found in Permian loessite from *western* equatorial Pangea (Soreghan et al., 1997; Cogoini et al., 2001; Jia, 2020), but unusual relative to Quaternary loess deposits. This difference may be attributable to syn-depositional processes (e.g., eolian sorting or dilution from rapid deposition of quartz and other non-iron-bearing minerals), more arid and/or oxidizing climate conditions preferring hematite formation over magnetite genesis or preservation (Maher, 1998), weak or stifled pedogenesis (documented sedimentologically; section "Sedimentology"), and/or post-depositional oxidation (of magnetite and maghemite). Eolian sorting is unlikely, because instead of the direct relationship between χlf and Δχ in the Salagou Formation (**Figure 7**), sorting tends to generate an inverse pattern (high χlf with low Δχ; e.g., Matasova and Kazansky, 2004). Similarly, hematite precipitates formed

during post-depositional processes tend to generate a magnetic signal with an inconsistent pattern between χlf and Δχ. The well-defined alignment of χlf and Δχ between these datasets (**Figure 7**) strongly suggests that the magnetic signal in the Salagou Formation is driven by pedogenesis. If there is no post-depositional (diagenetic) conversion of magnetite/maghemite to hematite, then the low contribution of magnetite in the Salagou Formation loess compared to Eurasian Quaternary loess might reflect substantially different paleoclimatic settings in the Permian of France.

If changes in the magnetic signal are pedogenically driven, then samples in this dataset represent a range of pedogenic alteration, where samples with more magnetic enhancement are more enriched in ultrafine particles of hematite. However, the average bulk χ from interpreted paleosol ($1.3 \pm 0.3 \times 10^{-3}$) and loess ($1.5 \pm 0.4 \times 10^{-3}$) units in the Salagou Formation overlap within error. This is atypical of Quaternary Eurasian loess, and even compared to ancient loessite from western equatorial Pangea wherein the magnetic signal of paleosols—also driven primarily by hematite—is 1.5–2× higher than in the parent loess. But the rock magnetic measurements in the Salagou Formation ($1–1.5 \times 10^{-3}$) are overall much lower compared to the Permian loessitic paleosols of western equatorial Pangea ($\sim 2–6 \times 10^{-3}$; Soreghan et al., 1997, 2002; Cogoini et al., 2001; Tramp et al., 2004; Soreghan G. S. et al., 2014), so it seems that the Salagou Formation preserves distinctively low concentrations of magnetite or maghemite in comparison even to time-equivalent loessite on the other (western) side of Pangea.

Cyclicity in the Salagou Formation

In the lower Salagou MS series (**Figure 5**), the persistent frequency at 0.1 cycles/m indicates a 10 m thick cyclicity. Higher frequencies at 0.29 and 0.57 cycles/m indicate 3.5 and 1.75 m thick cycles, respectively. This nested cyclicity, i.e., five to six shorter cycles within each 10 m "bundle," also appears in the MS series (**Figure 5A**). If the predominant (10 m thick) cyclicity represents the orbital eccentricity, then this section (160 m) represents a duration of ∼1.6 Myr, and the well-defined 3.5 and 1.75 m cycling represents the obliquity and precession index, respectively. There is also a very low frequency corresponding to a 44-m cycle, i.e., a candidate for 405 kyr orbital eccentricity.

In the mid-upper Salagou MS series (**Figure 6**), there is long-term amplitude variation that is potentially associated with the decreased presence of calcareous cement in the middle part of the section (resulting in elevated MS values) and/or missing or repeated strata in the concatenation of successive sections (**Figure 3A**). Regardless, the predominant cyclicity is ∼9.4 m thick, which appears to be broadened by variable sedimentation rates along the series, with multiple closely spaced spectral peaks from 0.13 to 0.08 cycles/m (7–12 m thick cycles). Higher frequencies at 0.28–0.31 and 0.55 cycles/m translate to ∼3.3 and 1.8 m thick cycles, respectively. If the predominant 9.4 m cycles represent short orbital eccentricity, then this section (775 m) represents ∼7.8 Myr of sedimentation. It is possible that ∼3.3 and 1.8 m thick cycles represent obliquity and precession (respectively) but are inconsistent through the section and locally poorly defined.

The ASM analysis confirms that astronomical frequencies are present and statistically significant (P-values < 0.05 for both MS series), rejecting the null hypothesis of no astronomical forcing for specific sedimentation rates of 9.4 cm/kyr (lower Salagou) and 13 cm/kyr (mid-upper Salagou). The up-section increase of optimal (ASM-based) sedimentation rates from 9.4 to 13 cm/kyr suggests that the Salagou Formation represents a duration of 9–10 Myr. This result is similar to estimates for the Salagou Formation from previous work (11–17 cm/kyr; Pochat and Van Den Driessche, 2011) as well as average sedimentation rates for the middle Permian Lucaogou Formation of northwest China (8.9–10.3 cm/kyr; Huang et al., 2020). It is slightly faster than lower Permian loess deposition in western equatorial Pangea (>700 m over ∼9 Myr so ≥7.8 cm/kyr; Johnson, 1989; Tramp et al., 2004; Soreghan M. J. et al., 2014), and on the lower end of sedimentation rates proposed for the Plio-Pleistocene CLP (Stevens and Lu, 2009).

If the driver of magnetic enhancement is pedogenesis (see section "Origin of the Magnetic Signal and Comparison to Quaternary Eurasian Loess"), then these data demonstrate fluctuation between loess accumulation and soil formation with loessite–paleosol couplets around 10 m thick in the Salagou Formation, which is similar to the lower Permian loessite of western equatorial Pangaea (Soreghan M. J. et al., 2014). Irregular cyclicity (e.g., 100–130 m; **Figure 5A**) may reflect long-term variability in atmospheric circulation, hydroclimate, and/or changes in sedimentation rates.

CONCLUSION

This study documents statistically significant astronomically forced climate change recorded in deep-time loessite of low-latitude Pangea. The results are as follows:

- Spectral analysis of handheld MS stratigraphic data shows a persistent 10 m thick cyclicity through the Permian Salagou Formation that denotes orbital eccentricity-scale (∼100 kyr) variability. Accordingly, subordinate, higher frequency cycles, at ∼3.3–3.5 and ∼1.8 m thick (most prominent in the lower Salagou Formation) likely represent 35 kyr obliquity and 17–21 kyr precession index-scale variations.
- Average spectral misfit analysis supports the interpretation of the presence of astronomical forcing frequencies, which are statistically significant in the MS series for optimal sedimentation rates of 9.4 cm/kyr (lower Salagou Formation) and 13 cm/kyr (mid-upper Salagou Formation): similar to the Permian of northwest China (∼9–10 cm/kyr) and the western United States (∼8 cm/kyr).
- Rock magnetic data from the Salagou Formation indicates magnetic enhancement wherein we interpret that magnetic particles (hematite) likely formed by pedogenesis, possibly with a diagenetic overprint.
- The uniquely low magnetic signal in the Salagou Formation compared to analogous Eurasian Quaternary loess deposits

relates to the predominance of hematite, which generally has a much weaker magnetic signal than magnetite and maghemite, and may be explained by differing conditions of formation (e.g., syn depositional processes, more arid and/or oxidizing climate conditions) than in present Eurasia (not unexpected), and/or post depositional oxidation of magnetite and maghemite.
- The portable MS meter allows for rapid and convenient *in situ* data acquisition. This study demonstrates the ability to recognize cyclic trends through extended stratigraphic successions of loessite using this method when calibrated with detailed rock magnetic analysis from the laboratory.

The evidence demonstrates that the Salagou Formation records climatic variability over a time interval of ∼9–10 Myr during the early Permian (middle to late Cisuralian). If the driver of magnetic enhancement is pedogenic, then the ∼10 m thick cyclicity that is consistent over ∼1000 m of section may represent the thickness of loessite–paleosol couplets in the Salagou Formation.

DATA AVAILABILITY STATEMENT

The raw data supporting the conclusions of this article will be made available by the authors, without undue reservation.

AUTHOR CONTRIBUTIONS

LP and GS (advisor) collected MS data and samples for rock magnetic analysis. LH mentored LP in MS interpretation (including MATLAB and R scripts). CZ conducted advanced rock magnetic analysis and interpreted this data (with close advice from CZ and CR). LP synthesized all data and conversations into manuscript format. All authors have made significant contributions to the editing and revision of this work, and approved the submitted version.

FUNDING

This work was supported by the National Science Foundation under International Research Experiences for Students (IRES) grant OISE-1658614 (PIs GS, M. J. Soreghan) and also EAR-1338331 (Sedimentary Geology and Paleobiology Program to GS).

ACKNOWLEDGMENTS

We thank M. J. Soreghan for suggesting collection of handheld MS data and our 2018 NSF IRES student participants for assistance with data collection (L. Alaniz, E. Simpson, V. Smith, and K. Yeager). We thank Stephane Pochat and Jean Van Den Driessche for field assistance and collaboration. We thank Kathrin Worm for support in the magnetic laboratory. This is IPGP contribution number 4143. Thank you to reviewers RZ and DJ, and editor HA.

SUPPLEMENTARY MATERIAL

The Supplementary Material for this article can be found online at: https://www.frontiersin.org/articles/10.3389/feart.2020.00241/full#supplementary-material

APPENDIX S1 | Coding procedures (MATLAB and R scripts).

REFERENCES

Ahmed, I. A. M., and Maher, B. A. (2017). Identification and paleoclimatic significance of magnetite nanoparticles in soils. *PNAS* 115:201719186. doi: 10.1073/pnas.1719186115

Basarin, B., Buggle, B., Hambach, U., Markoviæ, S. B., Dhand, K. O., Kovaèeviæ, A., et al. (2014). Time-scale and astronomical forcing of Serbian loess-palaeosol sequences. *Glob. Planet. Change* 122, 89–106. doi: 10.1016/j.gloplacha.2014.08.007

Beget, J. E., Stone, D. B., and Hawkins, D. B. (1990). Paleoclimatic forcing of magnetic susceptibility variations in Alaskan loess during the Quaternary. *Geology* 18, 40–43.

Berger, A., and Loutre, M. F. (1994). Astronomical forcing through geological time. *Spec. Publs Int. Ass. Sediment.* 19, 15–24. doi: 10.1002/9781444304039.ch2

Chlachula, J. (2003). The Siberian loess record and its significance for reconstruction of Pleistocene climate change in north- central Asia. *Q. Sci. Rev.* 22, 1879–1906. doi: 10.1016/s0277-3791(03)00182-3

Cogoini, M., Elmore, R. D., Soreghan, G. S., and Lewchuk, M. T. (2001). Contrasting rock-magnetic characteristics of two upper Paleozoic loessite-paleosol profiles. *Phys. Chem. Earth* 26, 905–910. doi: 10.1016/s1464-1895(01)00140-5

Copard, Y., Disnar, J. R., Becq-Giraudon, J.-F., and Boussafir, M. (2000). Evidence and effects of fluid circulation on organic matter in intramontane coalfields (Massif Central, France). *Int. J. Coal Geol.* 44, 49–68. doi: 10.1016/s0166-5162(99)00049-x

Domeier, M., and Torsvik, T. H. (2014). Plate tectonics in the late Paleozoic. *Geosci. Front.* 5, 303–350. doi: 10.1016/j.gsf.2014.01.002

Evans, M. E. (2012). Magnetostratigraphy of the Lodève Basin, France: Implications for the Permo-Carboniferous reversed superchron and the geocentric axial dipole. *Stud. Geophys. Geodaetica* 56, 725–734. doi: 10.1007/s11200-010-0082-y

Evans, M. E., and Heller, F. (2001). Magnetism of loess/paleosol sequences: Recent developments. *Earth Sci. Rev.* 54, 129–144. doi: 10.1016/s0012-8252(01)00044-7

Foster, T. M., Soreghan, G. S., Soreghan, M. J., Benison, K. C., and Elmore, R. D. (2014). Climatic and paleogeographic significance of eolian sediment in the Middle Permian Dog Creek Shale (Midcontinent U.S.). *Palaeogeogr. Palaeoclimatol. Palaeoecol.* 402, 12–29. doi: 10.1016/j.palaeo.2014.02.031

Gao, X., Hao, Q., Oldfield, F., Bloemendal, J., Deng, C., Wang, L., et al. (2019). New high-temperature dependence of magnetic susceptibility-based climofunction for quantifying paleoprecipitation from Chinese loess. *Geochem. Geophys. Geosyst.* 20, 4273–4291. doi: 10.1029/2019GC008401

Giles, J. M., Soreghan, M. J., Benison, K. C., Soreghan, G. S., and Hasiotis, S. T. (2013). Lakes, loess, and paleosols in the Permian Wellington Formation of Oklahoma, USA: implications for paleoclimate and paleogeography of the midcontinent. *J. Sediment. Res.* 83, 825–846. doi: 10.2110/jsr.2013.59

Hayward, R. K., and Lowell, T. V. (1993). Variations in loess accumulation rates in the mid-continent, United States, as reflected by magnetic susceptibility. *Geology* 21, 821–824.

Heller, F., and Liu, T.-S. (1982). Magnetostratigraphical dating of loess deposits in China. *Nature* 300, 431–433. doi: 10.1038/300431a0

Heller, F., and Liu, T.-S. (1984). Magnetism of Chinese loess deposits. *Geophys. J. R. Astron. Soc.* 77:125. doi: 10.1111/j.1365-246x.1984.tb01928.x

Heller, F., and Liu, T.-S. (1986). Palaeoclimatic and sedimentary history from magnetic susceptibility of loess in China. *Geophys. Res. Lett.* 13, 1169–1172. doi: 10.1029/gl013i011p01169

Huang, H., Gao, Y., Jones, M. M., Tao, H., Alan, R., Ibarra, D. E., et al. (2020). Astronomical forcing of Middle Permian terrestrial climate recorded in a large paleolake in northwestern China. *Palaeogeogr. Palaeoclimatol. Palaeoecol.* 2020:109735. doi: 10.1016/j.palaeo.2020.109735

Jia, J. (2020). Magnetic properties of upper Paleozoic loessite-paleosol couplets in the Western USA: The role of pedogenic hematite in magnetic enhancement. *Q. Int.* 544, 57–64. doi: 10.1016/j.quaint.2020.02.014

Johnson, S. Y. (1989). Significance of loessite in the Maroon Formation (Middle Pennsylvanian to lower Permian), Eagle Basin, Northwest Colorado. *J. Sediment. Petrol.* 59, 782–791.

Katz, B., Elmore, R. D., Cogoini, M., and Ferry, S. (1998). Widespread chemical remagnetization: Orogenic fluids or burial diagenesis of clays. *Geology* 26, 603–606.

Kessler, J. L. P., Soreghan, G. S., and Wacker, H. J. (2001). Equatorial aridity in western Pangea: Lower Permian loessite and dolomitic paleosols in northeastern New Mexico. *J. Sediment. Res.* 71, 818–833.

Kiersnowski, H. (2013). "Late Permian Aeolian sand seas from the Polish Upper Rotliegend Basin in the context of palaeoclimatic periodicity," in *Palaeozoic Climate Cycles: Their Evolutionary and Sedimentological Impact*, Vol. 376, eds A. Gasiewicz and M. Słowakiewicz (London: Geological Society Special Publication), 431–456. doi: 10.1144/SP376.20

Kt-10 manual (2017). KT-10 v2 Magnetic Susceptibility, Conductivity and Combined Magnetic Susceptibility-Conductivity Meter with GeoView: User's Guide. Version 2.2. Terraplus Geophysical Equipment Supplier. Available online at: http://www.terraplus.ca (accessed May, 2018).

Kukla, G. (1987). Loess stratigraphy in central China. *Q. Sci. Rev.* 6, 191–219. doi: 10.1016/0277-3791(87)90004-7

Kukla, G., and An, Z. S. (1989). Loess stratigraphy in central China. *Palaeogeogr. Palaeoclimatol. Palaeoecol.* 72, 203–225. doi: 10.1016/0031-0182(89)90143-0

Kukla, G., Heller, F., Liu, X. M., Xu, T. C., Liu, T. S., and An, Z. S. (1988). Pleistocene climates in China dated by magnetic susceptibility. *Geology* 16, 811–814.

Laskar, J., Robutel, P., Joutel, F., Gastineau, M., Correia, A. C. M., and Levrard, B. (2004). A long-term numerical solution for the insolation quantities of the Earth. *Astron. Astrophys.* 428, 261–285. doi: 10.1051/0004-6361

Li, Y., Shi, W., Aydin, A., Beroya-Eitner, M. A., and Gao, G. (2019). Loess genesis and worldwide distribution. *Earth-Sci. Rev.* 2019:102947. doi: 10.1016/j.earscirev.2019.102947

Lindquist, A. K., Feinberg, J. M., and Waters, M. R. (2011). Rock magnetic properties of a soil developed on an alluvial deposit at Buttermilk Creek, Texas, USA. *Geochem. Geophys. Geosyst.* 12, 1–12. doi: 10.1029/2011GC003848

Liu, T. (1985). *Loess and the Environment*. Beijing: China Ocean Press.

Liu, X. M., Shaw, J., Liu, T. S., and Heller, F. (1993). Magnetic susceptibility of the Chinese loess- paleosol sequence: Environmental change and pedogenesis. *Geol. Soc. Lond.* 150, 583–588. doi: 10.1144/gsjgs.150.3.0583

Mack, G. H., and Dinterman, P. A. (2002). Depositional environments and paleogeography of the Lower Permian (Leonardian) Yeso and correlative formations in New Mexico. *Mountain Geol.* 39, 75–88.

Mack, G. H., James, W. C., and Monger, H. C. (1993). Classification of paleosols. *GSA Bull.* 105, 129–136. doi: 10.1130/0016-7606(1993)105<0129:cop>2.3.co;2

Maher, B. (1986). Characterisation of soils by mineral magnetic measurements. *Phys. Earth Planet. Inter.* 42, 76–92. doi: 10.1016/s0031-9201(86)80010-3

Maher, B. A. (1998). Magnetic properties of modern soils and Quaternary loessic palaeosols: Palaeoclimatic implications. *Palaeogeogr. Palaeoclimatol. Palaeoecol.* 137, 2554. doi: 10.1016/S0031-0182(97)00103-X

Maher, B. A. (2016). Palaeoclimatic records of the loess/palaeosol sequences of the Chinese Loess Plateau. *Q. Sci. Rev.* 154, 23–84. doi: 10.1016/j.quascirev.2016.08.004

Maher, B. A., and Possolo, A. (2013). Statistical models for use of palaeosol magnetic properties as proxies of palaeorainfall. *Glob. Planet. Change* 111, 280–287. doi: 10.1016/j.gloplacha.2013.09.017

Maher, B. A., and Taylor, R. M. (1988). Formation of ultrafine-grained magnetite in soils. *Nature* 336, 368–370. doi: 10.1038/336368a0

Maher, B. A., and Thompson, R. (1991). Mineral magnetic record of the Chinese loess and paleosols. *Geology* 19, 3–6.

Maher, B. A., and Thompson, R. (1992). Paleoclimatic significance of the mineral magnetic record of the Chinese loess and paleosols. *Q. Res.* 37, 155–170. doi: 10.1016/0033-5894(92)90079-x

Maher, B. A., Thompson, R., and Zhou, L. P. (1994). Spatial and temporal reconstructions of changes in the Asian palaeomonsoon: A new mineral magnetic approach. *Earth Planet. Sci. Lett.* 125, 462–471.

Matasova, G. G., and Kazansky, A. Y. (2004). Magnetic properties and magnetic fabrics of Pleistocene loess/palaeosol deposits along west-central Siberian transect and their palaeoclimatic implications. *Geol. Soc. Lond. Spec. Publ.* 238, 145–173. doi: 10.1144/GSL.SP.2004.238.01.11

Meyers, S. R. (2014). *Astrochron: An R Package for Astrochronology*. Available online at: https://cran.r-project.org/package=astrochron (accessed March, 2019).

Meyers, S. R., and Sageman, B. B. (2007). Quantification of deep-time orbital forcing by average spectral misfit. *Am. J. Sci.* 307, 773–792. doi: 10.2475/05.2007.01

Michel, L. A., Tabor, N. J., Montanez, I. P., Schmitz, M. D., and Davydov, V. I. (2015). Chronostratigraphy and Paleoclimatology of the Lodève Basin, France: Evidence for a pan-tropical aridification event across the Carboniferous–Permian boundary. *Palaeogeogr. Palaeoclimatol. Palaeoecol.* 430, 118–131. doi: 10.1016/j.palaeo.2015.03.020

Muhs, D. R. (2007). "Loess deposits, origins, and properties," in *Encyclopedia of Quaternary Science*, eds C. J. Mock, and S. Elias (Amsterdam: Elsevier), 1405. doi: 10.1016/b0-444-52747-8/00158-7

Murphy, K. (1987). *Eolian origin of upper Paleozoic red siltstones at Mexican Hat and Dark Canyon*. 127. Utah M.S. Thesis, University of Nebraska-Lincoln, Lincoln.

Muttoni, G., and Kent, D. V. (2019). Adria as promontory of Africa and its conceptual role in the Tethys twist and Pangea B to Pangea A transformation in the Permian. *Res. Paleontol. Stratigr.* 12, 249–269.

Parrish, J. T. (1993). Climate of the Supercontinent Pangea. *J. Geol.* 101, 215–233. doi: 10.1086/648217

Pfeifer, L. S., Soreghan, G. S., Pochat, S., and Van Den Driessche, J. (2020). Loess in eastern equatorial Pangea archives a dusty atmosphere and possible upland glaciation. *GSA Bull.* doi: 10.1130/B35590.1

Pfeifer, L. S., Soreghan, G. S., Pochat, S., Van Den Driessche, J., and Thomson, S. N. (2016). Permian exhumation of the Montagne Noire core complex recorded in the Graissessac- Lodève Basin. *Basin Res.* 30, 1–14. doi: 10.1111/bre.12197

Pochat, S., and Van Den Driessche, J. (2011). Filling sequence in Late Paleozoic continental basins: A chimera of climate change? A new light shed given by the Graissessac – Lodève basin (SE France). *Palaeogeogr. Palaeoclimatol. Palaeoecol.* 302, 170–186. doi: 10.1016/j.palaeo.2011.01.006

Porter, S. C. (2001). Chinese loess record of monsoon climate during the last glacial–interglacial cycle. *Earth Sci. Rev.* 54, 115–128. doi: 10.1016/s0012-8252(01)00043-5

Porter, S. C., Hallet, B., Wu, X., and An, Z. (2001). Dependence of near-surface magnetic susceptibility on dust accumulation rate and precipitation on the Chinese Loess Plateau. *Q. Res.* 55, 271–283. doi: 10.1006/qres.2001.2224

Reynolds, R., Belnap, J., Reheis, M., Lamothe, P., and Luiszer, F. (2001). Aeolian dust in Colorado Plateau soils: Nutrient inputs and recent change in source. *Proc. Natl. Acad. Sci.* 98, 7123–7127. doi: 10.1073/pnas.121094298

Schneider, J. W., Körner, F., Roscher, M., and Kroner, U. (2006). Permian climate development in the northern peri-Tethys area —The Lodève basin, French Massif Central, compared in a European and global context. *Palaeogeogr. Palaeoclimatol. Palaeoecol.* 240, 161–183. doi: 10.1016/j.palaeo.2006.03.057

Schneider, J. W., Lucas, S. G., Scholze, F., Voigt, S., Marchetti, L., Werneburg, R., et al. (2019). Late paleozoic-early mesozoic continental biostratigraphy - links to the standard global chronostratigraphic scale. *Palaeoworld*. 531, 1–53.

Schneider, J. W., Lucas, S. G., Werneburg, R., and Rößler, R. (2010). Euramerican Late Pennsylvanian / Early Permian arthropleurid/tetrapod associations – implications for the habitat and paleobiology of the largest terrestrial arthropod

in Lucas, S. G., Schneider, J. W. and Spielmann, J. A., eds, Carboniferous-Permian transition in Canõn del Cobre, northern New Mexico. *New Mexico Museum Nat. History Sci. Bull.* 49, 49–70.

Shackleton, N. J., Berger, A., and Peltier, W. R. (1990). An alternative astronomical calibration of the lower Pleistocene timescale based on ODP Site 677. *Trans. R. Soc. Edinb. Earth Sci.* 81, 251–261. doi: 10.1017/s0263593300020782

Singer, M. J., Verosub, K. L., Fine, P., and TenPas, J. D. (1996). A conceptual model for the enhancement of magnetic susceptibility in soils. *Quat. Int.* 3436:243248. doi: 10.1016/1040-6182(95)00089-85

Song, Y., Fang, X., Torii, M., Ishikawa, N., Li, J., and An, Z. (2007). Late Neogene rock magnetic record of climatic variation from Chinese eolian sediments related to uplift of the Tibetan Plateau. *J. Asian Earth Sci.* 30, 324–332. doi: 10.1016/j.jseaes.2006.10.004

Soreghan, G. S., Elmore, R. D., Katz, B., Cogoini, M., and Banerjee, S. (1997). Pedogenically enhanced magnetic susceptibility variations preserved in Paleozoic loessite. *Geology* 25, 1003–1006.

Soreghan, G. S., Elmore, R. D., and Lewchuk, M. T. (2002). Sedimentologic–magnetic record of western Pangean climate in Upper Paleozoic loessite (Lower Cutler Beds, Utah). *Geol. Soc. Am. Bull.* 114, 1019–1035. doi: 10.1130/0016-7606(2002)114<1019:smrowp>2.0.co;2

Soreghan, G. S., Soreghan, M. J., and Hamilton, M. A. (2008a). Origin and significance of loess in late Paleozoic western Pangaea: a record of tropical cold. *Palaeogeogr. Palaeoclimatol. Palaeoecol.* 268, 234–259. doi: 10.1016/j.palaeo.2008.03.050

Soreghan, G. S., Soreghan, M. J., Poulsen, C. J., Young, R. A., Sweet, D. E., and Davogustto, O. C. (2008b). Anomalous cold in Pangaean tropics. *Geology* 36, 659–662.

Soreghan, G. S., Sweet, D. E., and Heavens, N. G. (2014). Upland Glaciation in tropical pangaea: geologic evidence and implications for late paleozoic climate modeling. *J. Geol.* 122, 1–30.

Soreghan, M. J., Heavens, N., Soreghan, G. S., Link, P. K., and Hamilton, M. A. (2014). Abrupt and high-magnitude changes in atmospheric circulation recorded in the Permian Maroon Formation, tropical Pangaea. *Geol. Soc. Am. Bull.* 126, 569–584. doi: 10.1130/B30840.1

Soreghan, M. J., and Soreghan, G. S. (2007). Whole-rock geochemistry of Upper Paleozoic loessite, Western Pangea: implications for paleo-atmospheric circulation. *Earth Planet. Sci. Lett.* 255, 117–132. doi: 10.1016/j.epsl.2006.12.010

Stevens, T., and Lu, H. (2009). Optically stimulated luminescence dating as a tool for calculating sedimentation rates in Chinese loess: comparisons with grain-size records. *Sedimentology* 56, 911–934. doi: 10.1111/j.1365-3091.2008.01004.x

Sweet, A. C., Soreghan, L. S., Sweet, D. E., Soreghan, M. J., and Madden, A. S. (2013). Permian dust in Oklahoma: source and origin for middle Permian (Flowerpot-Blaine) redbeds in Western Tropical Pangaea. *Sediment. Geol.* 28, 181–196. doi: 10.1016/j.sedgeo.2012.12.006

Tabor, N. J., and Myers, T. S. (2015). Paleosols as Indicators of Paleoenvironment and Paleoclimate. *Annu. Rev. Earth Planet. Sci.* 43, 333–363. doi: 10.1146/annurev-earth-060614-105355

Tramp, K. L., Soreghan, G. S., and Elmore, R. D. (2004). Paleoclimatic inferences from paleopedology and magnetism of the Permian Maroon Formation. *GSA Bull.* 116, 671–686. doi: 10.1130/B25354.1

Woods, S., Elmore, R. D., and Engel, M. (2002). Paleomagnetic dating of the smectite-to-illite conversion: Testing the hypothesis in Jurassic sedimentary rocks, Skye, Scotland. *J. Geophys. Res.* 107, 2–9. doi: 10.1029/2000JB000053

Yang, S. L., and Ding, Z. L. (2004). Comparison of particle size characteristics of the Tertiary "red clay" and Pleistocene loess in the Chinese Loess Plateau: Implications for origin and sources of the "red clay.". *Sedimentology* 51, 77–93. doi: 10.1046/j.1365-3091.2003.00612.x

Zeeden, C., Hambach, U., Obreht, I., Hao, Q., Abels, H. A., Veres, D., et al. (2018). Patterns and timing of loess-paleosol transitions in Eurasia: Constraints for paleoclimate studies. *Glob. Planet. Change* 162, 1–7. doi: 10.1016/j.gloplacha.2017.12.021

Zeeden, C., Kels, H., Hambach, U., Schulte, P., Protze, J., Eckmeier, E., et al. (2016). Three climatic cycles recorded in a loess-palaeosol sequence at Semlac (Romania) – Implications for dust accumulation in south-eastern Europe. *Quat. Sci. Rev.* 154, 130–142. doi: 10.1016/j.quascirev.2016.11.002

Zheng, H., Oldfield, F., Yu, L., Shaw, J., and An, Z. (1991). The magnetic properties of particle-sized samples from the Luo Chuan loess section: evidence for pedogenesis. *Phy. Earth Planet. Inter.* 68, 250–258. doi: 10.1016/0031-9201(91)90044-i

Zhou, L. P., Oldfield, F., Wintle, A. G., Robinson, S. G., and Wang, J. T. (1990). Partly pedogenic origin of magnetic variations in Chinese Loess. *Nature* 346, 737–739. doi: 10.1038/346737a0

Conflict of Interest: The authors declare that the research was conducted in the absence of any commercial or financial relationships that could be construed as a potential conflict of interest.

frontiers in Earth Science

ORIGINAL RESEARCH
published: 18 September 2020
doi: 10.3389/feart.2020.00375

The Birth of a Connected South Atlantic Ocean: A Magnetostratigraphic Perspective

Dan V. Palcu[1], Joy R. Muraszko[1,2]*, Plinio F. Jaqueto[3] and Luigi Jovane[1]*

[1] Instituto Oceanografico, Universidade de São Paulo, São Paulo, Brazil, [2] Laboratory of Orogenic Belts and Crustal Evolution, School of Earth and Space Sciences, Peking University, Beijing, China, [3] Instituto de Astronomia, Geofisica e Ciencias Atmosfericas, Universidade de São Paulo, São Paulo, Brazil

The early Paleogene sedimentary record of the Sao Paulo Plateau holds the key to understanding the timing and mechanisms of the onset of Atlantic oceanic circulation, with implications for ocean – climate feedback systems. The timing and evolution of South Atlantic Ocean connectivity remain poorly understood, hindering a full understanding of modern circulation mechanisms. In this work, we develop an improved magnetostratigraphic age model for the late- Cretaceous to Eocene sedimentary record of Deep-Sea Drilling Project (DSDP) Site 356, located on the São Paulo Plateau at the edge of the Rio Grande Rise. The model constrains the timing of the beginning of Atlantic Ocean circulation, as the last obstacle to a connected Atlantic was removed. We use the age model to quantify sedimentary rates, and correlate with rock magnetic and published geochemical data to explore links between ocean current rearrangement and climatic anomalies. We find that periods characterized by variations in the magnetic properties of sediments and sedimentation anomalies in the Sao Paulo Plateau are reflected in carbon isotope events, supporting a possible link between ocean circulation and hyperthermal events.

Keywords: São Paulo Plateau, paleocirculation, Danian, Selandian, Rio Grande Rise, Walvis Ridge, Paleogene, hyperthermals

OPEN ACCESS

Edited by:
Eric Font,
University of Coimbra, Portugal

Reviewed by:
Sara Satolli,
G. d'Annunzio University of Chieti and Pescara, Italy
Qingsong Liu,
Institute of Geology and Geophysics, China

****Correspondence:***
Dan V. Palcu
d.v.palcu@usp.br;
dan.palcu@gmail.com
Joy R. Muraszko
jrm220@pku.edu.cn

Specialty section:
This article was submitted to Geomagnetism and Paleomagnetism, a section of the journal Frontiers in Earth Science

Received: *07 April 2020*
Accepted: *11 August 2020*
Published: *18 September 2020*

Citation:
Palcu DV, Muraszko JR, Jaqueto PF and Jovane L (2020) The Birth of a Connected South Atlantic Ocean: A Magnetostratigraphic Perspective. Front. Earth Sci. 8:375. doi: 10.3389/feart.2020.00375

INTRODUCTION

Ocean circulation is one of the crucial factors driving the change of the climate in our modern world. Differences in temperature and salinity of seawater masses drive the thermohaline circulation, facilitating heat transport across the globe. One of the key components of the thermohaline circulation system is the Atlantic meridional overturning circulation (AMOC), which plays a fundamental role in Earth's climate system. The AMOC is one of the largest heat pumps and high-latitude heat sinks (Grassl, 2001; Buckley and Marshall, 2016), unique in the global oceans. The heat transport by AMOC is responsible for the relatively warm climate of the Northern Hemisphere, accounting for up to 25% of the total northward heat transport (Bryden and Imawaki, 2001; Buckley and Marshall, 2016; Chen and Tung, 2018). It is also one of the most important carbon sinks (Battle et al., 2000; Gruber et al., 2002), thus its strength is one of the regulators of climate change, with implications for understanding the consequences of anthropogenic global warming. To better understand the interplay between oceans and climate, we need to focus on the evolution of thermohaline circulation and in particular the onset of the Atlantic Ocean Circulation

(AOC), reaching back in the geological records to the birth of the Atlantic Ocean. In this study, we aim to contribute to the understanding of how the AOC developed by focusing on the Paleogene of the South Atlantic when the last submarine obstacles began to give way to a fully connected ocean, and the heat pump was initiated.

A Brief History of the South Atlantic

The South Atlantic Ocean resulted from the breakup of Gondwanaland. In its Central sector, situated between the Rio Grande – Walvis Ridge and the Ascension Fault Zone, the complex rifting can be simplified to several key episodes that occurred in the region during the Cretaceous time. According to Chaboureau et al. (2013), between Berriasian and Barremian times (141–129 Ma), rifting occurred in the northern half of the central South Atlantic. At that time, this region was a series of deep lakes, bordered by lateral highs (Pérez-Díaz and Eagles, 2017). From the upper Barremian to middle Aptian (128–116 Ma), the rifting extended southward, and so did the lake that reached the Rio Grande Rise – Walvis Ridge (RGR-WR) in the south. From the early Aptian, the realm was affected by brief marine influxes coming from the north, but by middle-upper Aptian, the whole region switched to an evaporitic regime (Chaboureau et al., 2013). The evaporitic phase of the South Atlantic ended after connectivity improved due to the development of a South-Central Atlantic passageway in the Albian-Cenomanian times (100 Ma).

While it is speculated that connections between the Brazilian Basin and Argentine Basin in the South Atlantic have existed in the form of shallow gateway(s), the south-north connectivity greatly improved by ∼80 Ma when it is estimated that the Vema Channel (marked A in **Figure 1**) was around 2000 m deep (Pérez-Díaz and Eagles, 2017). According to the same authors, connections over the Rio Grande Rise (black arrows in **Figure 1**) continued deepening during the Campanian-Maastrichtian (83–66 Ma) when in addition to the existing Vema Gap (marked A and B) the Hunter Gap (marked C) started opening. This may have initiated Southern Component Water formation in the oceans of the southern hemisphere and its northward circulation toward the North Atlantic across the Central Atlantic Seaway (Donnadieu et al., 2016). Ocean-climate changes starting at the end of the Cretaceous eventually lead to the establishment of thermohaline circulation as we know it today (Murphy and Thomas, 2013; Donnadieu et al., 2016). The breaching of the Rio Grande Rise – Walvis Ridge alignment continued to intensify, and by mid-Miocene (14.5 Ma) (Woodruff and Savin, 1989), it is thought that the connection would have expanded sufficiently to allow deep-water circulation between the Brazil and Argentine basins. The Walvis Ridge remains a partial barrier up to this day, partially blocking deep water circulation between the Cape and Angola Basins.

The RGR-WR alignment is the last obstacle to be overcome for a fully connected South Atlantic. Its subsidence allowed deep-water circulation north toward the North Atlantic. Nonetheless, the exact age and progression of this major current rearrangement remains an open question, as various models suggest widely varying dates for this shift, from the Campanian (80 Ma) (Robinson et al., 2010; Robinson and Vance, 2012), Maastrichtian (71–66 Ma) (Frank and Arthur, 1999; Murphy and Thomas, 2013; Donnadieu et al., 2016) and mid-Paleocene (60 Ma) (Voigt et al., 2013). To help improve our understanding of the evolution of ocean circulation in the South Atlantic there is a pressing need to investigate sedimentary records with robust chronology and wide geographic coverage. The Paleogene succession from the Deep-Sea Drilling Project (DSDP) Site 356 Leg 39 in the São Paulo Plateau represents such a record.

The São Paulo Plateau – A Record of Early Atlantic Circulation

The sedimentary records of the São Paulo Plateau (SPP) are key to understanding the RGR-WR region and its evolution from a sill significantly restricting water mass exchange, to a submerged elevation as it is today. The plateau is located in the proximity of the former sill zone. The bordering topographic highs have ensured nearly uninterrupted sedimentation during the late Cretaceous – early Paleogene times, recording changes in the water mass circulation between the Central and South Atlantic. The SPP itself forms a triangular-shaped elevation above the seafloor, extending up to 950 km off the Brazilian coastline (Perch-Nielsen et al., 1977). The southern boundary is marked by an east-west trending ridge arising due to the presence of an extensional fault. Spreading of the South Atlantic initiated to the south of the plateau, with the Rio Grande Rise – Walvis Ridge (RGR-WR) system forming an elevated barrier restricting ocean circulation. Early stages of rifting began in the Aptian-Albian, which created a narrow, restricted basin favorable for the formation of evaporites. As a result, the majority of the SPP is underlain by salt deposits and diapirs. São Paulo Plateau (Site 356) was drilled during DSDP Leg 39, an Expedition developed to accommodate research along the path of the *Glomar Challenger* from the Norwegian Sea drilling season to an Antarctic and Southern Ocean drilling season in 1974 (Supko et al., 1977). Among other drilling objectives, an important scientific goal was to improve the understanding of paleocirculation and geological history of the South Atlantic through the analysis of sedimentary sections of the Ceará Rise, Brazil and Argentine Basins, Rio Grande Rise (RGR) and São Paulo Plateau (Site 356). The coring site is located at a water depth of 3175 m, on a relatively stable section of the SPP escarpment, with a rough topology attributed to either diapiric structures or underlying igneous basement (Kumar and Gamboa, 1979). The location of the site in an area of restricted circulation above the abyssal plain creates favorable conditions for preserving a record of environmental fluctuations, sensitive to even minor changes in sea level and changes in ocean circulation.

We develop a magneto-bio-stratigraphic study, bridging our paleomagnetic research with biostratigraphic and geochemical studies from published records. Despite Site 356 having been drilled in the 70 s, it remains a source of valuable geological and paleoenvironmental information. There has been extensive research conducted using the core, such as the studies of Kochhann et al. (2014), who developed an age-model for the upper Cretaceous and estimated sedimentation rates in

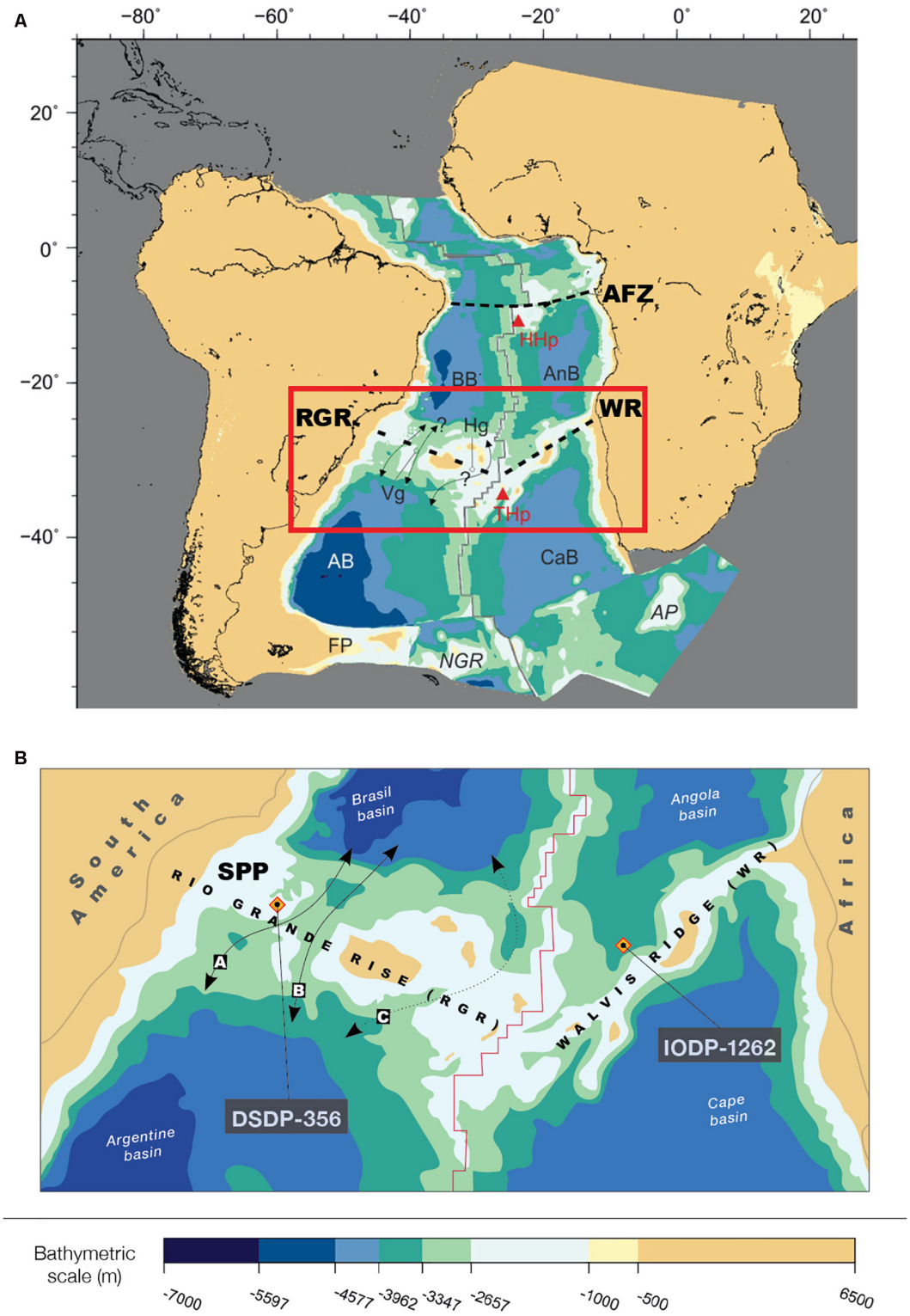

FIGURE 1 | Location of the Sao Paulo Plateau drill core [Deep-Sea Drilling Project (DSDP) Site 356] in the general paleogeographic context of the South Atlantic **(A)**, after Pérez-Díaz and Eagles (2017). Brazil Basin (BB) and Angola Basin (AnB) are bordered North by the Ascension Fracture Zone (AFZ) and South by the Rio Grande (RGR) – Walvis Ridge (WR) zone. South of this obstacle lay the Argentine Basin (AB), Cape Basin (CaB) and further toward the south the Falkland Plateau (FP), North Georgia Rise (NGR) and the Agulhas Plateau (AP) Red triangles represent hotspots: St Helena (HHp) and Tristan da Cunha (THp). **(B)** detail view of the drill core's location, in the proximity of the Vema Gap (a,b) and Hunter Gap (c), the main oceanic passages across the Rio Grande Rise – Walvis Ridge system. Marked is also the International Ocean Discovery Program (IODP) Site 1262, discussed in the text.

the Turonian-Maastrichtian interval; Wanderley and Pedrosa (2017), who improved the nannoplankton zonations in the Paleocene of the core; or Krahl et al. (2017) who refined planktic foraminifera zonation in the Paleocene. The research listed above provides the biostratigraphic controls for our magneto-bio-stratigraphic age model. Other studies include work on Paleocene coccolithophores by Mai et al. (1998); the study on ostracodes from Sites 356 and 357 by Supko and Perch-Nielsen (1977), and geochemical investigations concerning the Oceanic Anoxic Event 3 (OAE3) levels of upper Cretaceous age (Herbin et al., 1987; Arai, 1988; Wagreich, 2012). These contain valuable paleoenvironmental information and are taken into account in the reconstruction of the evolution of the São Paulo Plateau. Our results from Site 356 contribute to a broader picture which is of interest across many different fields of research, such as the breakup of Gondwanaland (Avilla et al., 2002; Cogne et al., 2012), the formation of Cretaceous evaporites (Koutsoukos, 1992; Tedeschi et al., 2017; Silva et al., 2020), pre-salt oil reservoirs and source rocks (Buckley et al., 2015; Pietzsch et al., 2018; de Oliveira et al., 2019) and post-salt deformation processes (Guardado et al., 1989; Mohriak, 2003; Mohriak et al., 2008; Davison et al., 2012).

LITHOLOGICAL DESCRIPTION

The sedimentary record drilled in Site 356 has been divided into seven individual Units (Perch-Nielsen et al., 1977), starting with Albian pelagic sediments (unit 7) with significant contributions from nanoplankton and fine-grained terrigenous input (Thiede, 1977), followed by coarse clastic Coniacian – Mid Turonian mudstones and clay-pebble conglomerates (unit 6). The clastic unit is characterized by breccias and conglomerates with calcareous mudstone, zeolitic siltstone, ferruginous mudstone, and basalt pebbles and cobbles. The coarse unit is overlain by fine-grained sediments that range from marly calcareous chalks (unit 5), nanno and nanno-foram chalks (unit 4); silicified calcareous chalks (unit 3); calcareous- siliceous and siliceous-calcareous oozes (unit 2) and calcareous oozes (unit 1). The post-Coniacian (Late Cretaceous sediments) were deposited under oxic conditions in shallow waters and are expressed as relatively pure nannofossil and foraminiferal chalk, which continue into the upper Paleocene.

We focus on the 420–220 m bsf interval (Cores 30–11), corresponding to units 4 and 3 (uppermost Maastrichtian – Lutetian) (Perch-Nielsen et al., 1977; **Figure 2**). Unit 4 corresponds to the upper Cretaceous – Paleogene interval and contains well bedded and moderately burrowed alternation of chalks (10–100 cm thick) and oozes (max. 100 cm thick). The lowermost part of the sequence is represented by monotonous gray chalks of upper Maastrichtian age, that grade into white mottled chalks just before the K/Pg boundary. Following in the succession, the Danian is expressed by a 50-meter-thick section of calcareous ooze (**Figure 2**). While the sequence is fairly homogeneous, environmental changes are reflected in the color of the sediment (brown, red and green levels) and associated minor compositional changes (Thiede, 1977). However, this work does not rely on these changes in coloration, in the investigation of environmental changes during the Danian. Selandian sediments consist of gray-dark gray chalks and contain two slump levels. A large slump is found at the base of the Selandian (364 m), comprising several large olistostromes (0.8 4 m) of middle-early Maastrichtian age. A smaller slump is found in the upper Selandian, at 319.5 m, containing olistostromes of early Maastrichtian – Campanian age and suggesting that a nearby part of the plateau was undergoing erosion and experienced periods of significant slope instability in the Selandian. Unit 3 corresponds to the Eocene part of the section and consists of alternating chalks (bands of 10 cm to 1 m thickness) and oozes (up to 1 m thick sections) of light greenish-gray color (Perch-Nielsen et al., 1977).

Biostratigraphic studies have confirmed the existence of sedimentation gaps in the uppermost Maastrichtian – Lutetian interval, either very short, such as a missing (P0) foram zone (∼100 kyr) at the Cretaceous- Paleogene boundary (Krahl et al., 2017), or large gaps (up to ∼7 Myr) from the Selandian/Thanetian boundary to mid-Ypresian (Perch-Nielsen et al., 1977). This study carefully considers the limitations posed by existing slump deposits. The main focus of this paper is the Danian-Selandian interval and the sedimentation rate changes during that period, with the uppermost Maastrichtian and the Ypresian-Lutetian serving as references for pre- and post- early Paleogene sedimentary environments.

MATERIALS AND METHODS

Natural remanent magnetization (NRM) was measured to compute the characteristic remanent magnetization (ChRM) and build a polarity sequence to correlate with the Geomagnetic Polarity Time Scale (GPTS). This was used to build an age model and calculate sedimentation rates. Later, a set of detailed environmental magnetism experiments (magnetic susceptibility, anhysteretic and isothermal remanent magnetizations, first-order reversal curve diagrams, Curie balance tests) were performed to characterize the sedimentary succession. Using our novel age model, we were able to correlate our obtained results with adjacent sites and discuss the implications.

Demagnetization Protocol and Construction of Magnetostratigraphic Age Model

Natural remanent magnetization is the remanent magnetization of a rock or sediment. It consists of a primary component – the ChRM, acquired during the formation of the rock or sediment, and often additional overlapping secondary components of later acquired magnetizations. Alternating field demagnetization (AF) technique is employed to isolate the primary component. It involves exposing the sample to a well-symmetrical alternating field that linearly decreases to zero in a magnetically shielded, null-field, environment. Multiple alternating field steps are used to completely demagnetize the specimen. This way, the secondary components may be removed, allowing us to identify the ChRM and reconstruct the magnetic field at the time of the formation of the sample. The stack of remanent magnetization results is

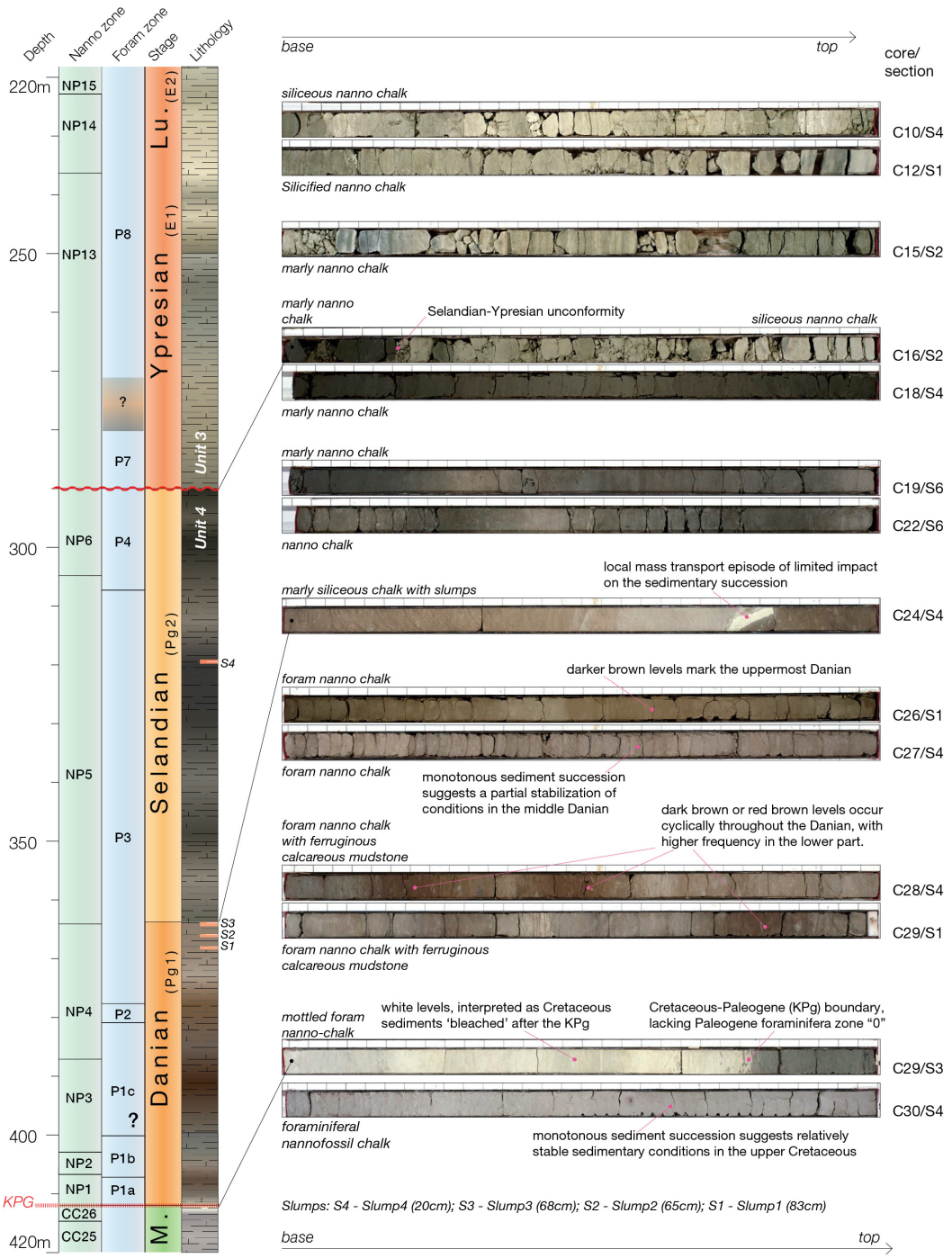

FIGURE 2 | Biostratigraphic zonation and lithological characteristics of the Paleogene succession at the Deep-Sea Drilling Project (DSDP) Site 356, with a selection of images representative for the sedimentary succession, taken during DSDP Leg 39 and their corresponding initial descriptions (in italics) (Perch-Nielsen et al., 1977), with added observations. Pink markers in Unit 4 (S1–S4) indicate intervals where slumps have been described.

plotted for each specimen and interpreted to extract the ChRM and corresponding paleomagnetic inclination value.

From Site 356 of DSDP Leg 39, a total of 297 oriented half core samples were requested from IODP (sample requests: 037143-IODP and 071140-IODP). They were collected at MARUM (Bremen, Germany) and transported to the University of São Paulo, where they were subsequently cut into 7-cm^3-cubes to be used for magneto-chronology, rock, and environmental magnetism experiments. The specimens were split into two sets and measured in São Paulo (Brazil) (n = 220) and in

Utrecht (Netherlands) (n = 77). Paleomagnetic measurements were performed at Instituto de Astronomia, Geofísica e Ciências Atmosféricas of the University of São Paulo (USPMAG) in a magnetically shielded room with an ambient field of <200 nT. Stepwise alternating field demagnetization (AF) procedure was performed in a RAPID system 2G Enterprises DC SQUID cryogenic magnetometer (noise level 5 × 10-12Am^2) in vertical position, with a built-in coil system (Kirschvink et al., 2008). AF demagnetization was achieved by applying increasing alternating field steps up to 100 mT, with increments of 2.5 mT for the 0–15 mT interval and increments of 5 mT for the 15–100 mT interval.

Another set of samples was demagnetized and measured for cross-comparison at Fort Hoofddijk Paleomagnetic Laboratory, Utrecht University. Alternating field demagnetization was performed up to a maximum of 250 mT, with field increments of 5 mT for the 0 50 mT interval, 10 mT for the 50 100 mT interval, 20 mT for the 100 160 mT interval and two supplementary steps of 200 and 250 mT on a robotized horizontal 2G Enterprises DC SQUID cryogenic magnetometer (noise level of 3 × 10^{-12}Am2) (Mullender et al., 2016). Results from the demagnetization experiments were processed using principal component analysis (Kirschvink, 1980) implemented in Remasoft 3.1 paleomagnetic data analyzer software (Chadima and Hrouda, 2006).

Rock Magnetic Measurements

To characterize the magnetic properties of the sediments, a series of rock magnetic experiments were carried out. Anhysteretic remanent magnetization (ARM) and isothermal remanent magnetization (IRM) were measured at USPMAG after the demagnetization procedure. An axial ARM was imparted using a peak alternating field of 100 mT with a bias DC field of 0.05 mT. For the IRM measurements, a pulsed field of 1 T was applied to the samples to obtain the saturation isothermal remanent magnetization (SIRM). Subsequently, a backfield of 0.3 T was applied and measured. The data were then used to calculate the S-ratio (Bloemendal et al., 1992) and K_{ARM}, representing ARM intensity divided by the bias field value to become a field-independent parameter, referred to as anhysteretic ARM susceptibility (due to its analogy with the low-field susceptibility) (Moskowitz, 2007).

Magnetic susceptibility was measured at the Centro Oceanográfico de Registros Estratigráficos (CORE) at the Oceanographic Institute of the University of São Paulo (IO USP) using an AGICO MFK1-KA Kappabridge (sensitivity 1 × 10-8 SI) at the operating frequency of 976 Hz and applied field of 200 A/m. A subset of samples (n = 17) were selected for detailed rock magnetic characterization using a Vibrating Sample Magnetometer (VSM) Micromag 3900 Princeton-Lakeshore Cryotronics at IO USP. First Order Reversal Curves (FORC) were acquired for each of the samples and processed in the FORCinel software package (Harrison and Feinberg, 2008) using VARIFORC smoothing (Egli, 2013).

Thermomagnetic measurements of the induced magnetization (J-T curves) were conducted with a modified horizontal translation-type Curie balance with a drift of ∼5 × 10-9Am2 at Fort Hoofddijk (Mullender et al., 1993). A field cycled between 100 and 300 mT was applied to powdered sediments (∼70 mg). Multiple heating runs (at a heating rate of 6°C/min) and cooling runs (at a cooling rate of 10°C/min) were performed between room temperature and steps of 150°, 250°, 350°, 450°, 525°, and 700°C.

RESULTS

Demagnetization Results

We obtained ChRM directions for 297 samples of both reversed and normal polarities. The demagnetization diagrams (**Figure 3**) reveal different types of magnetic behavior. In some samples, a weak, viscous overprint, without coherent directions, is present, generally removed by 15 mT. A second component that we consider the ChRM is demagnetized at fields between 15 and 45 mT, accounting for 30–70% of the sample intensity. A limited subset of 17 discrete samples develop a third type of behavior at fields above 45 mT, described as an unusual "NRM curling-up" (Fu et al., 2008) during AF demagnetization, associated with an increase of magnetization. Such behavior has been generally associated with a laboratory-induced gyroremanent magnetization (GRM) effect, which is characteristic of greigite (Snowball, 1997). The ChRM component was calculated from four or more consecutive field steps between 15 and 45 mT, using principal component analysis (Kirschvink, 1980). In order to provide a better understanding of the ChRM obtained, the data were grouped into two qualitative categories:

(1) Q1; high-quality directions, representing samples with a maximum angular deviation (MAD) up to 7° (**Figure 4**, black dots), and
(2) Q2; low-quality directions, comprising samples with abnormal orientations that do not demagnetize, deflect from a direction toward the origin, or have a MAD higher than 7° (**Figure 4**, white dots). We adopted the high-quality results from samples in the first group (n = 182, representing 60.67% of total samples) in the development of the polarity pattern for the section. Samples in the latter category (n = 118, representing the remaining 39.33% of the samples) were discarded and not used in the determination of polarity, but have been calculated and plotted to highlight areas where the ChRM is poorly preserved. Results obtained from the late Cretaceous-Eocene record from the São Paulo Plateau comprises 15 polarity intervals, seven normal and eight reversed (**Figure 4**).

The average magnetic inclination for the samples in group Q1 is 23.1°. We use the E-I method (Tauxe et al., 2008) on the online platform Paleomagnetism.org to detect and correct for inclination shallowing on directions of the São Paulo samples. After unflattening (**Supplementary Figure S1**), the average inclination changes from to 29.94° (after unflattening).

Magnetic Properties of Sediments at Site 356

The variation in low-field magnetic susceptibility is reflected in the magnetic mineralogy of the sample. **Figure 5E** shows

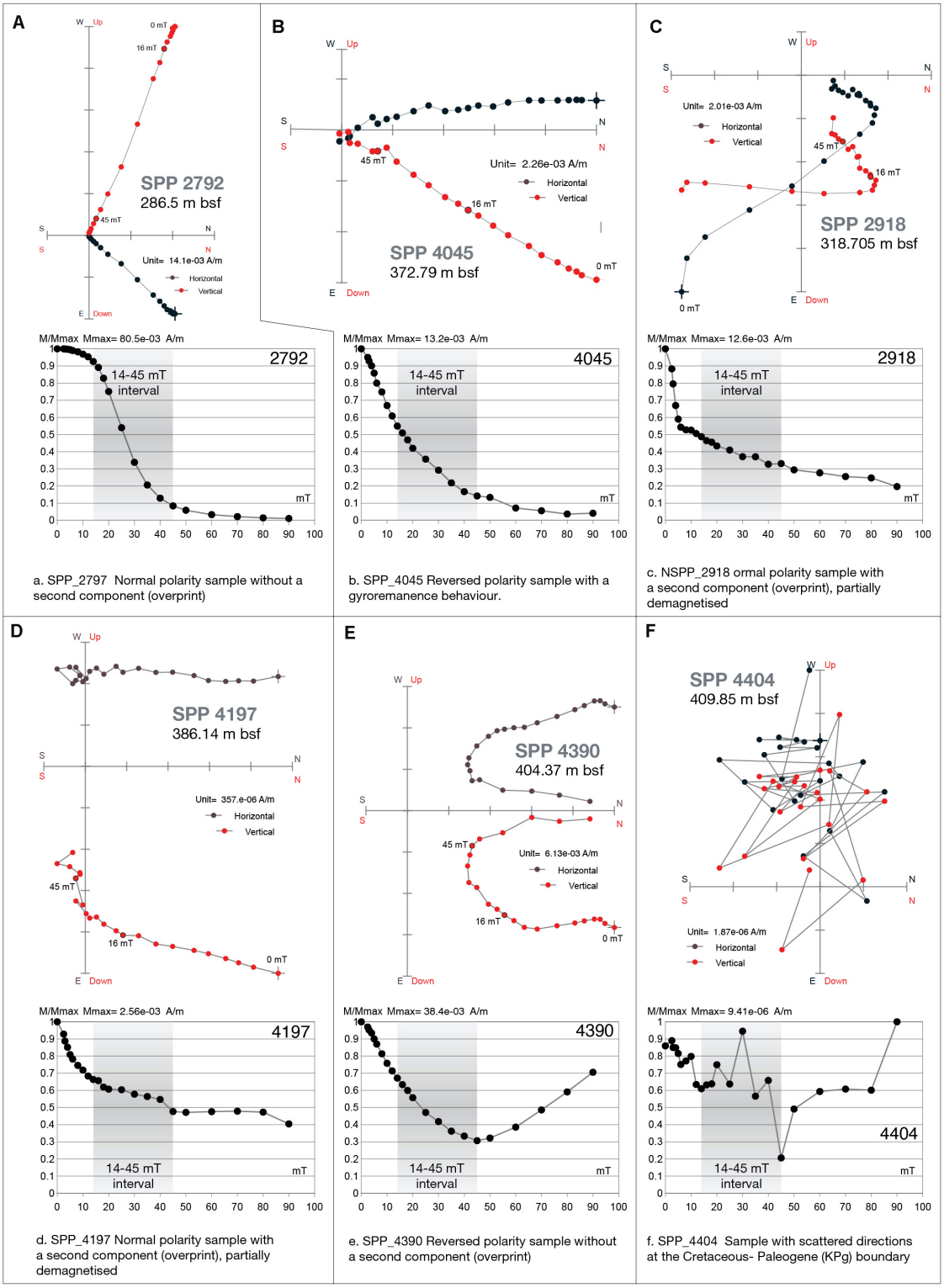

FIGURE 3 | Key types of magnetic behavior illustrated with Zijderveld diagrams and magnetic intensity plots. Samples **(A–C)** are considered reliable NRM carriers due to their stable directions during the demagnetization process, while samples **(D–F)**. are examples of problematic demagnetization: sample **(D)** does not demagnetize, sample **(E)** acquires a magnetic field in the course of demagnetization and sample **(F)** exhibits an erratic behavior during demagnetization.

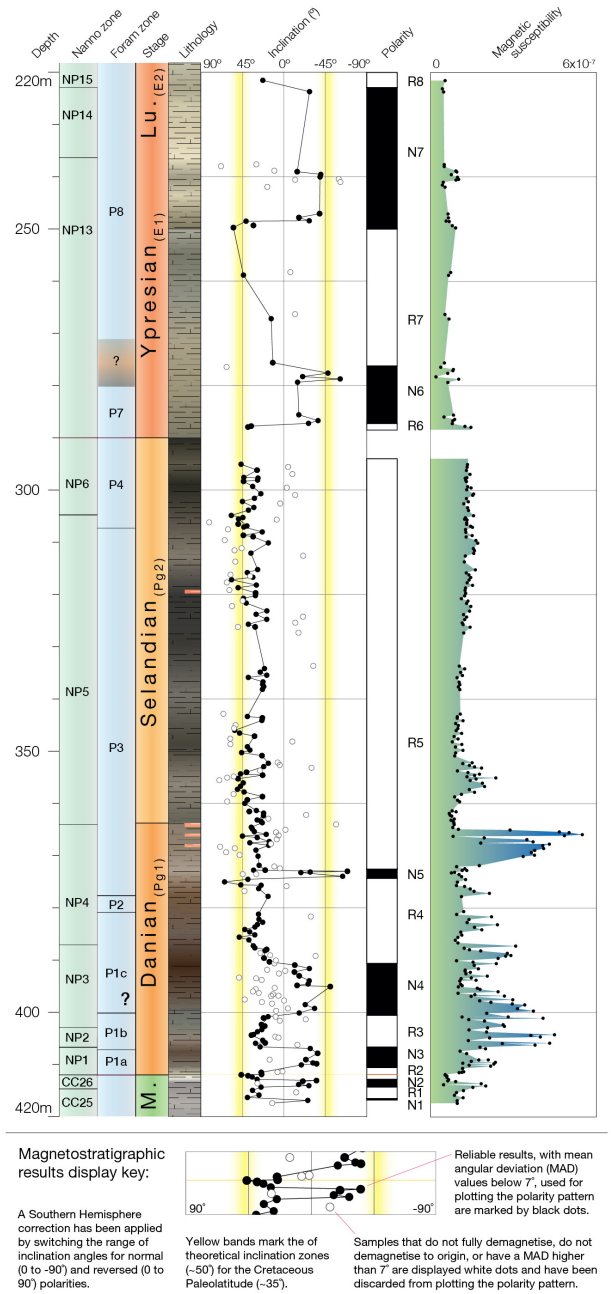

FIGURE 4 | Magnetostratigraphy and magnetic susceptibility results from DSDP Site 356.

a plot of volumetric susceptibility (κ) vs. the susceptibility of ARM (κARM), often used as a magnetic grain size proxy. While κ is a measure of the concentration of magnetic material within a sample, most sensitive to superparamagnetic (SP) grains (<0.03 μm) and large grains (<10 μm), κARM is strongly grain-size dependent, exhibiting highest values for the finest particles (Opdyke and Channell, 1996; Hillaire-Marcel and De Vernal, 2007). The properties are quite varied within the core, with Danian samples having the highest concentration of particles within the single-domain (SD) grain size range, considered ideal magnetic recorders. This is supported by FORC diagram signatures. Sample 4017 has a central ridge with a moderate degree of vertical spread indicative of slightly interacting SD grains, with peak coercivities at ∼40 mT (Egli, 2013). On the other hand, the lowest concentration and largest grain sizes are shown by Eocene samples. The FORCs show low coercivities below 20 mT. Samples 4197 and 3946 have intermediate values in the scatter plot, their FORC signatures showing overlapping features of a low coercivity central ridge suggesting an SD component, and a high coercivity lobe extending up to 200 mT. These kinds of high coercivity features can be indicative of hematite (Carvallo et al., 2006; Roberts et al., 2006). The downcore variations of the measured rock magnetic proxies are shown in **Figure 6** alongside stable isotope measurements from the nearby Walvis Ridge (Kochhann et al., 2014). In the Danian and partially the Selandian stages, the S-Ratio shows high variability, indicating a changing composition of low and high coercivity minerals. The high coercivity is most likely due to the presence of hematite, as indicated by the FORCs.

The thermal runs on the Curie balance indicate the presence of at least two different magnetic minerals. Samples such as 3866 are characterized by thermally stable magnetic carriers, indicated by the reversible behavior during the intermediate heating-cooling cycles (150°, 250°, 350°, 450°, 525°C). The Curie temperature of ∼580°C (853 K) is indicative of stoichiometric magnetite (Gehring et al., 2009), but the curved nature of the heating curve (**Figure 5**), indicates a contribution from a paramagnetic clay minerals component (Opdyke and Channell, 1996). Sample 4404 is representative of samples with stronger magnetic intensity. It has a thermally unstable component, indicated by irreversible behavior with a loss of magnetic intensity at each of the intermediate heating-cooling steps, indicated by the gray dotted lines (**Figure 5**), and a thermally stable component (marked with orange dotted lines) characterized by slightly higher unblocking temperature at ∼630°C. This is close to the thermal ranges attributed to maghemite (890 K) (Gehring et al., 2009). In our case, the behavior fits type C maghemite as described by Liu et al. (2010) – a partially thermally reversible carrier with a measurable Curie temperature of 640°C (Ozdemir and Banerjee, 1984).

As maghemite is formed by weathering or low-temperature oxidation of spinels containing ferrous iron, commonly magnetite (Gehring et al., 2009), it is possible specimens exhibiting this behavior correspond to levels of magnetite oxidation (Chang et al., 2013). The magnetic mineralogy of the core comprises multiple magnetic minerals present in different grain sizes. Nonetheless, all of them have the potential to preserve a stable magnetic signal through geologic time and do not show signs of pervasive remagnetization or alteration.

Magneto-Bio-Stratigraphy

We use an integrated magneto-bio-stratigraphic approach to correlate the Sao Paulo Plateau record with the geomagnetic polarity time scale (GPTS). A selected set of foraminifera and nannoplankton zones and sub-zone boundaries derived from previous studies on Site 356 were used as tie-points in the age-depth correlation (**Table 1**). As a global reference, we

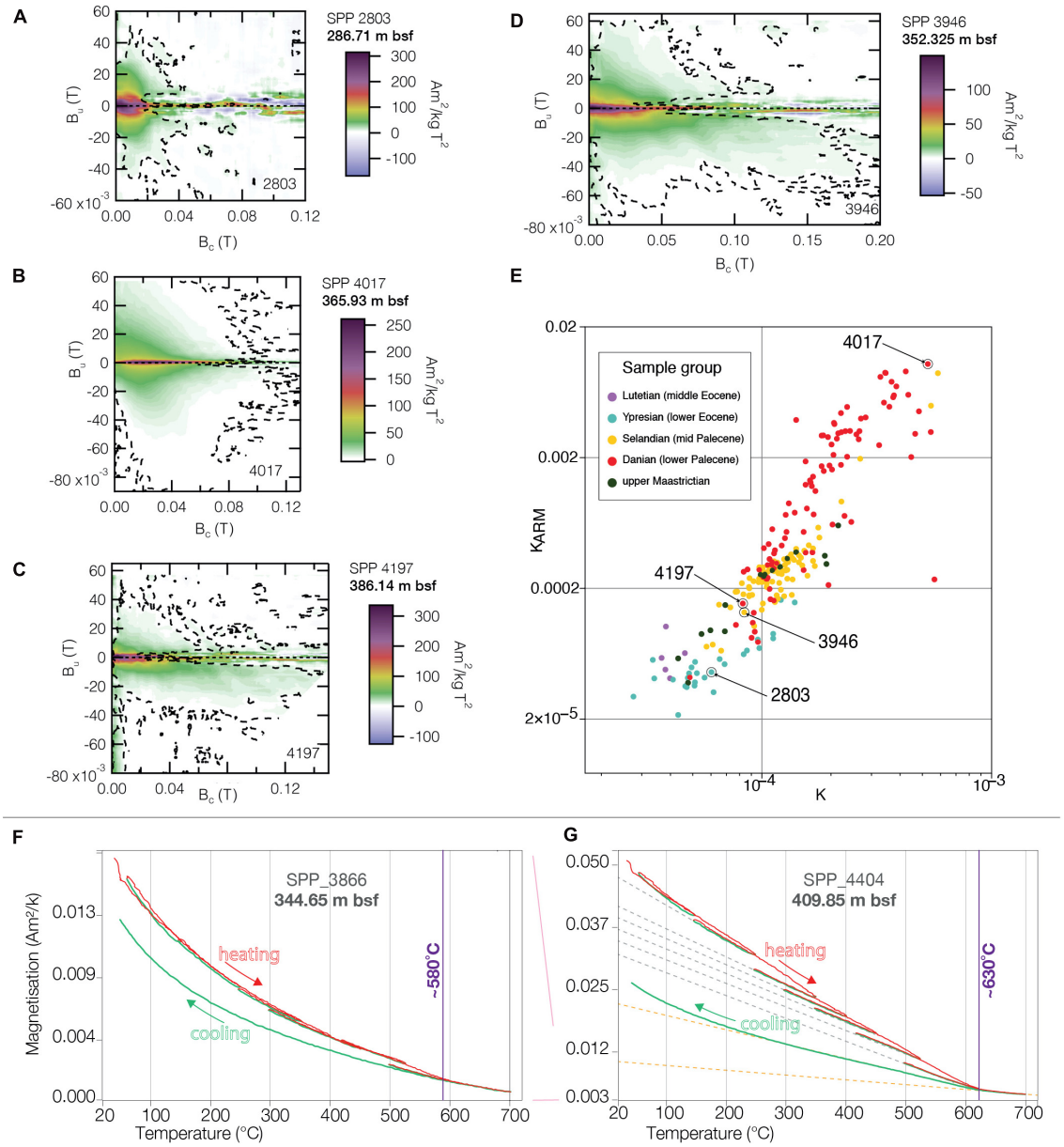

FIGURE 5 | Rock magnetic characterization of Site 356. **(A–D)** Selected First order reversal curve (FORC) diagrams from different stages: **(A)** Ypresian (2803), **(B,C)** Danian (4017, 4197) **(D)** Selandian (3946); **(E)** KARM/K plot (Banerjee et al., 1981; King et al., 1982) with marked locations of FORC diagrams; **(F–G)** Results of thermal experiments using a Curie Balance, for samples 3866 (Selandian) and 4404 (Danian). Purple lines indicate unblocking temperatures. Gray dotted lines represent the projected cooling curves at a given step. See text for interpretation.

use the TSCreator visualization of enhanced Geologic Time Scale 2016 database (Version 7.4; 2020) (Gradstein and Ogg, 2006), calibrated with the concise Geologic Time Scale 2016 (Ogg et al., 2016).

By cross-plotting the Paleogene nannozone boundaries from our section and the GPTS (**Figure 7**), we identify several reference chron's that can be attributed to polarity zones of the GPTS (**Table 2**). Several polarity zones in the record lack sufficient data points for a robust correlation with the GPTS. In the case of zone N1, the obtained dataset has too few points to confidently be attributed to a normal polarity zone, and we refrain from doing so at this stage. The normal polarity zone N7 corresponds to nannoplankton zones NP13 and NP14, in contradiction with the GPTS, where a reverse polarity zone would be expected at the NP13/NP14 boundary. We consider that the interval corresponding to the reverse polarity zone is missing. Based on nannoplankton data, we subsequently split N7 in two zones, N7a corresponding to upper Ypresian, and N7b that corresponds to Lutetian, but lacking more data points, we refrain from further correlations. The following interval (R8) would

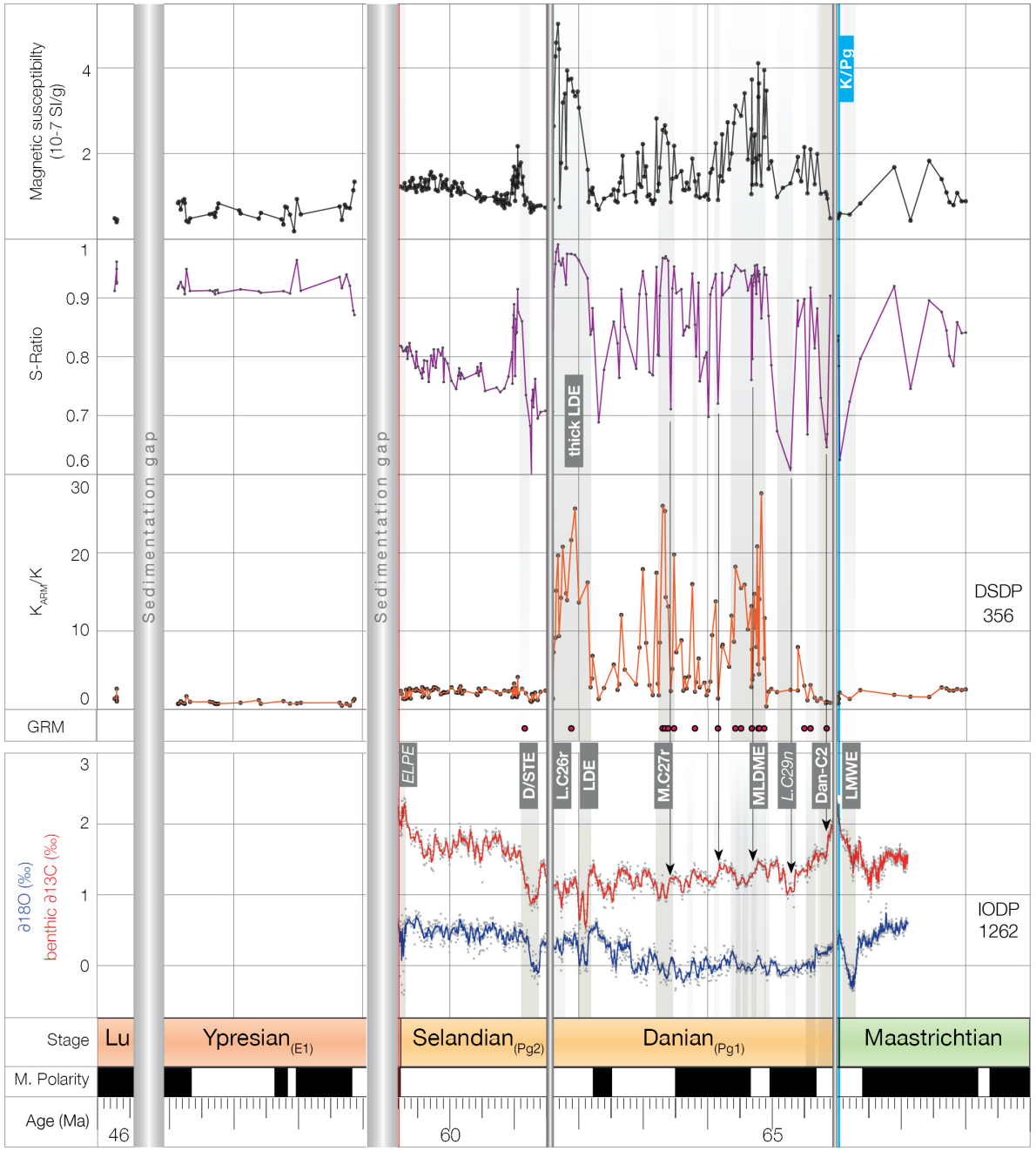

FIGURE 6 | Stratigraphic correlations of Site 356 with global events. From the top: magnetic susceptibility and S-ratio for Deep Sea Drilling Program (DSDP) Site 356 obtained in this study, stage and magnetic polarity, and benthic $\delta^{13}C$ from Barnet et al. (2019). Marked are the major recognized events reported in the literature discussed in the text: the Cretaceous-Paleogene boundary (blue) and suspected hyperthermal-like events (red): the Cretaceous-Paleogene boundary (K/Pg), the Dan-C2 event (Dinarès-Turell et al., 2014; Jehle et al., 2015), L.C29n (Barnet et al., 2019), M.27Cr (Barnet et al., 2019), Late Danian Events (LDEs) LDE1 and LDE2 (Sprong et al., 2012; Jehle et al., 2015; Deprez et al., 2017), L.C26r (Barnet et al., 2019), Danian/Selandian Transition Event (D/STE) (Arenillas et al., 2008), Early-Late Paleocene Event (ELPE) (Coccioni et al., 2019).

belong to Lutetian as well, but given limited data points remains difficult to correlate. These intervals have been excluded from further interpretation, such as sedimentation rates calculations or age model development. We obtain 11 tie-points based on the magneto-stratigraphic correlation that can be used for developing an age model for the section (**Table 2**).

Using the newly obtained magnetostratigraphic tie-points and biostratigraphic zone boundaries (nannoplankton tie points) we

TABLE 1 | Tie-points from previous studies used for the development of the age model for Site 356 in this study.

Nr	Site 356 Polarity zone	Event	CODE	Depth (mbsf)	Age (Ma)	Biblographic refference
1	NP15/NP14	boundary	Nanno	222.345	46.29	Perch-Nielsen et al., 1977
2	NP14/NP13	boundary	Nanno	238.4275	49.11	Perch-Nielsen et al., 1977
3	*ELPE*	*event*	*CIE*	*295*	*59.24*	*Barnet et al., 2019*
4	NP6/NP5	boundary	Nanno	304.365	59.54	Perch-Nielsen et al., 1977
5	P4/P3	boundary	Foraminifera	314.35	60.73	Gradstein and Ogg, 2006
6	P3a/b	boundary	Foraminifera	363.24	61.3	Krahl et al., 2017
7	NP5/NP4	boundary	Nanno	364.735	61.51	Perch-Nielsen et al., 1977
8	P3/P2	boundary	Foraminifera	377.24	62.297	Gradstein and Ogg, 2006
9	P2/P1	boundary	Foraminifera	385.24	62.597	Gradstein and Ogg, 2006
10	NP4/NP3	boundary	Nanno	388.08	63.25	Perch-Nielsen et al., 1977
11	P1 c/b	boundary	Foraminifera	391.77	x	Krahl et al., 2017
12	P1 b/a	boundary	Foraminifera	402.77	x	Krahl et al., 2017
13	NP3/NP2	boundary	Nanno	405.1	64.81	Perch-Nielsen et al., 1977
14	P1/Pα	boundary	Foraminifera	409.25	65.719	Krahl et al., 2017
15	NP2/NP1	boundary	Nanno	409.43	65.47	Perch-Nielsen et al., 1977
16	*KPG*	*boundary*	*event*	*411.75*	*66.063*	*Gradstein and Ogg, 2006*
17	CC25/CC26	boundary	Nanno	416.0725	67.84	Perch-Nielsen et al., 1977
18	*Racemiguembelina fructicosa*	LO	Foraminifera	412.25	66.4	Kochhann et al., 2014
19	*Abathomphalus mayaroensis*	LO	Foraminifera	415.25	66.35	Kochhann et al., 2014
20	*Gasserina gansseri*	LO	Foraminifera	415.25	66.49	Kochhann et al., 2014
21	*Pseudoguembelina hariaensis*	FO	Foraminifera	440.67	67.3	Kochhann et al., 2014
22	*Globotruncana linneiana*	LO	Foraminifera	445.16	68.37	Kochhann et al., 2014
23	*Abathomphalus mayaroensis*	FO	Foraminifera	443.51	69.18	Kochhann et al., 2014
24	*Racemiguembelina fructicosa*	FO	Foraminifera	443.51	70.14	Kochhann et al., 2014
25	*Pseudoguembelina palpebra*	FO	Foraminifera	462.83	71.75	Kochhann et al., 2014
26	*Gasserina gansseri*	FO	Foraminifera	459.78	72.97	Kochhann et al., 2014
27	*Globotruncana aegyptiaca*	FO	Foraminifera	462.83	74	Kochhann et al., 2014
28	*Radotruncana calcarata*	LO	Foraminifera	485.27	75.71	Kochhann et al., 2014
29	*Globotruncanella havanensis*	FO	Foraminifera	464.32	75.94	Kochhann et al., 2014
30	*Radotruncana calcarata*	FO	Foraminifera	489.77	76.18	Kochhann et al., 2014
31	*Contusotruncana plummerae*	FO	Foraminifera	518.27	79.2	Kochhann et al., 2014
32	*Globotruncanita elevata*	FO	Foraminifera	545.27	83.64	Kochhann et al., 2014
33	*Dicarinella asymetrica*	LO	Foraminifera	542.27	83.64	Kochhann et al., 2014
34	*Dicarinella concavata*	LO	Foraminifera	542.27	83.64	Kochhann et al., 2014
35	*Dicarinella asymetrica*	FO	Foraminifera	649.77	86.66	Kochhann et al., 2014
36	*Dicarinella concavata*	FO	Foraminifera	681.27	91.08	Kochhann et al., 2014

FO indicates first occurrences, LO last occurrences.

calculated the linear sedimentation rates (LSRs) and developed an age model which allows the attribution of an age to the depth levels of our samples, enabling correlations between Site 356 and other records on the planet.

DISCUSSION

Magnetic Mineralogy and the Reliability of the Magnetostratigraphic Record

The magnetic mineralogy of the core is complex, as highlighted by the scatter and variability of different magnetic behaviors apparent in the FORC diagrams, heating experiments, and modified Zijderveld plots (Zijderveld, 2013). This is perhaps not unexpected considering the varied lithology throughout the early Paleogene in the São Paulo Plateau. The conditions at the end of the Maastrichtian change drastically from a carbonate dominated regime into a ferruginous mudstone characterized by alternating shades of brown and red, prevalent throughout the Danian, as shown by S-ratio variability (**Figure 6**). The late Danian is marked by slumps and localized mass transport deposits. In the Selandian conditions begin to stabilize, which is reflected in a shift in the lithology, which becomes dominated by dark deposits of marly nannoplankton chalk with few disturbances of the sedimentary sequence. The change in sedimentation regime is reflected in the magnetic mineral composition, with the S-ratio settling at higher values (∼0.75). Moving into the Eocene, the environment settles into calmer settings with less terrigenous input present in the light-colored silicious chalk. The shift between the different sedimentary regimes is reflected in the magnetic susceptibility curve (**Figure 4**). With the changing environmental conditions,

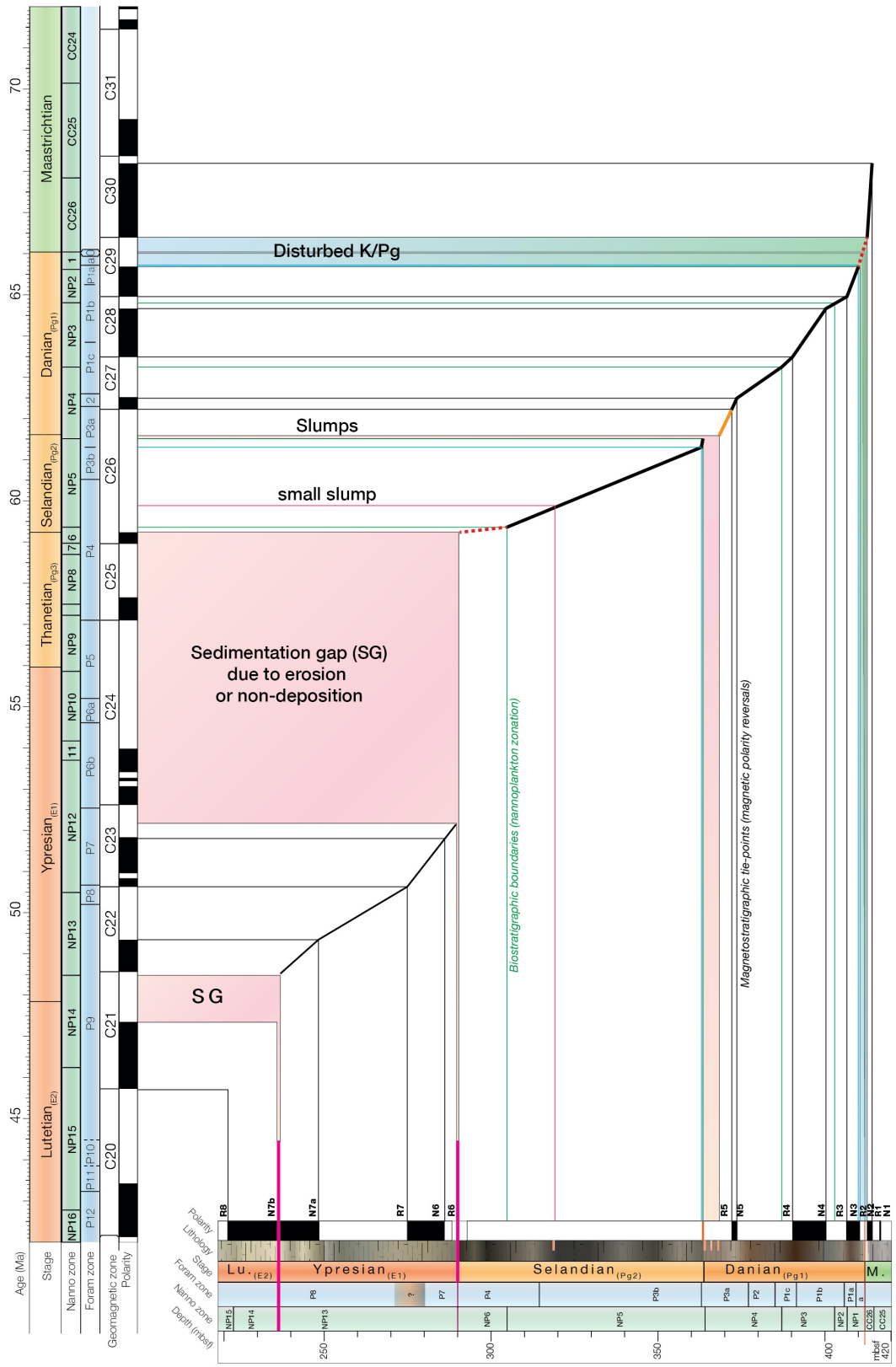

FIGURE 7 | Age model for Site 356 obtained by correlating the reversal pattern and biostratigraphic zonation from site 356 with the Geomagnetic Polarity Time Scale (GPTS 2012). Black lines magnetostratigraphic tie-points, while blue and green lines indicate biostratigraphic tie-points (based on foraminifera zones - blue, and nannoplankton zones – green).

TABLE 2 | Magnetostratigraphic tie-points used in the age model for Site 356.

Nr	Site 356 Polarity zone	Polaity	CODE	GPTS Correlation	Depth (mbsf)	Age of base (Ma)
1	R8	Reversed		C20r	223.13	x
2	N7B	Normal		C21	238	x
3	N7A	Normal		C22n	248.49	49.714
4	R7	Reversed		C22.r	276.65	50.778
5	N6	Normal		C23.n	286.975	51.774
6	R6	Reversed		C23.r	287.94	x
7	*ELPE*	*GAP*		*ELPE*	*295*	*59.24*
8	R5	Reversed		C26r	372.895	62.221
9	N5	Normal		C27n	373.4	62.517
10	R4	Reversed		C27r	390.795	63.494
11	N4	Normal		C28n	400.4825	64.667
12	R3	Reversed		C28r	406.775	64.958
13	N3	Normal		C29n	410.165	65.688
14	*K/Pg*	*GAP*		*K/Pg*	*411.75*	*66.063*
15	R2	Reversed		C29r	412.95	66.052
16	N2	Normal		C30n	414.19	67.61
17	R1	Reversed		C31r	416.305	x
18	N1	Normal		x		x

Reference chron's have been attributed to polarity chron's of the GPTS.

the magnetic mineral composition changes. Iron oxides are highly sensitive to fluctuating bottom water oxygenation, and the changes in ocean circulation are reflected in magnetic mineral composition. The rapid rate of change is reflected in the sawtooth pattern, which characterizes the early Paleogene, suggestive of unstable bottom water conditions. In the early Paleogene, the alternating red-brown layers are dominated by hematite and biogenic magnetite, respectively (**Figure 5**). The Selandian seems to be somewhat transitional, with a contribution of both components. Hematite input diminishes by the Eocene, where the magnetic mineral assemblage seems to be dominated by weak low coercivity magnetite, highly dispersed in the carbonate matrix. Surprisingly, the hematite – biogenic magnetite levels exhibit maghemite-like signatures during thermal runs (Sample 4404 in **Figure 5**), suggesting a complex iron oxide mix that is not present in the samples where the thermal runs picks up magnetite and paramagnetic clay minerals signals (Sample 3866).

It is challenging to resolve the origin of the magnetic minerals identified in this study, and it is not the primary focus of this study to discuss the environmental implications. The main concern for the reliability of the magnetostratigraphy and constructed age model is the lack of significant overprinting of the ChRM through secondary alteration processes. The presence of hematite, in particular in tectonically active regions such as the SPP, is often indicative of hydrothermal activity and magnetic overprinting (e.g., Ohmoto, 2003). In the case of Site 356, this seems not to be the case. In the context of the magnetostratigraphy and polarity patterns, samples with different magnetic mineral composition (hematite vs. magnetite dominated samples) do not plot outside the general trend. This indicates that the alternating mineralogy does not affect the ability of the samples to carry ChRM, and there is no evidence for a delayed, secondary acquisition of magnetization. This implies that the maghemite and hematite components are most likely primary in origin, rather than diagenetic or hydrothermal.

Nonetheless, some samples have clear magnetic overprints, evident in the Zijderveld diagrams. In particular, some exhibit gyroremanent-like behavior (Sample 4390 in **Figure 3**). Although most commonly associated with greigite-bearing sediments (e.g., Snowball, 1997). It is interesting to note that all the samples which show GRM like properties during the demagnetization plot within the anomalous Danian interval (red dots in **Figure 6**). Coinciding with peaks in κARM, they cluster in intervals of high magnetic susceptibility and S-ratios approaching 1. This indicates the predominance of SD magnetite in these intervals, in agreement with magnetite-maghemite Curie temperatures. Oxic conditions are at odds with the presence of greigite. Specimens which show gyroremanent behavior have polarities consistent with adjacent samples. The selected range of fields used for calculating the polarity pattern (low-medium fields) are not affected by gyroremanence. Despite the potential challenges in demagnetizing all samples completely, they carry significant information which is consistent with near-ideal samples. We therefore consider the magnetostratigraphy highly reliable. An exception are samples at the Cretaceous-Paleogene boundary, which do not carry any significant paleomagnetic information (Sample 4404 in **Figure 3**). Low intensities and spiderweb type Zijderveld diagrams point toward the possible dissolution of magnetic minerals due to acidification of oceans, commonly reported at the K/Pg (Hull et al., 2020). Another potential mechanism of loss of ChRM could be the physical disturbance of sediments as an immediate consequence of the impact. Evidence of such has not been reported at such southern latitudes to date to the best of our knowledge. To shed further light into the K/Pg interval, a high resolution geochemical and rock magnetic study would be required.

Sedimentary Anomalies and Trends Across the Paleogene

Sedimentation rates and sedimentation anomalies can point to key changes in ocean circulations and sea-straits dynamics and have been observed in other regions of the planet such as near the Gibraltar straits, in the North Atlantic (e.g., Hernández-Molina et al., 2014) or, on a larger scale, throughout the Southern Ocean (e.g., Dutkiewicz et al., 2016). -1562449187-1562449187We plot sedimentation anomalies, such as gaps or mass transport deposits extracted from direct core observations or seismics, that are more straightforward and provide an insight about moments of instability or change in the depositional regime of the basin together with the sedimentation-rates estimation, that can contribute with qualitative supplementary information.

Several sedimentation anomalies (**Figure 8**) have been reported from 356 (Perch-Nielsen et al., 1977). After the K/Pg, the section contains a small sedimentation gap (∼100 kyr) evidenced by the missing P(0) nannoplankton zone. Another sedimentation anomaly, characterized by slumps and sedimentary gaps, occurred before the Danian-Selandian boundary and, according to the nanno- and foram sub-zones P3a and P3b boundaries (Kochhann et al., 2014), corresponds to a time window between the top of the LDE and the base of the Selandian stage. Smaller slumps have also been reported in the middle of the Selandian interval, while the largest sedimentation gap begins at 59 Ma, roughly corresponding with the onset of the Early Late Paleocene Event (ELPE), and lasts until 51 Ma (**Figure 8**).

In addition to these anomalies, the sedimentation rates for the Paleogene, coupled with previous biostratigraphy based sedimentation rates for the Cretaceous of Kochhann et al. (2014) shows a big picture of sedimentation trends in this region of the Atlantic Ocean in the 50–90 Ma interval (**Figure 8**). During the Cretaceous, sedimentation rates in the São Paulo Plateau were relatively low and largely constant with two exceptions: (1) the Santonian, when sedimentation rates more than quadrupled, broadly coinciding with the Oceanic Anoxic Event 3 (OAE3) (Herbin et al., 1987; Wagreich, 2012); and (2) the latest Maastrichtian, when sedimentation rates increased again. The Danian appears to be characterized by an increase in sedimentation, interrupted by discrete short-lived anomalies, while the Selandian seems to be increased by higher sedimentation rates but the reduced chronological tie-points limits the interpretations for this interval.

The Danian contains a set of discrete intervals of either extremely high or extremely low sedimentation rates. We find that these are tied to the occurrence of well-known periods of rapid climate shifts, often reported as proposed hyperthermal events (Coccioni et al., 2012; Sprong et al., 2012; Dinarès-Turell et al., 2014; Jehle et al., 2015; Deprez et al., 2017; Barnet et al., 2019).

Evidence for a Changing Climate

Although the study of early Paleogene Carbon Isotope Excursions (CIE) and hyperthermals are somewhat overshadowed by the more spectacular End-Cretaceous Chicxulub cataclysm and the subsequent Cretaceous-Paleogene Extinction event, robust work has been conducted to determine the amplitude and duration of these climatic anomalies in the early Paleogene time. Our understanding of early Paleogene climate anomalies is based on key reference sites such as Walvis ridge (Leg 208, in particular, Hole 1262) in the South Atlantic (Barnet et al., 2019), Shatsky Rise (in particular Hole 1209) in the Central Pacific (Westerhold et al., 2011), Zumaia (Spain) in the North Atlantic (Dinarès-Turell et al., 2014), Gubbio-Contessa (Italy) in the western Tethys (Coccioni et al., 2012, 2019; Sinnesael et al., 2016; **Figure 9**), North-Eastern Desert and Sinai region (Egypt) in the south Tethys (Schulte et al., 2013), Boltysh crater lake (Ukraine) continental Eurasia in north Tethys (Gilmour et al., 2014) and Wombat plateau (IODP Leg 122, Hole 761) in the Indian Ocean (Quillevere et al., 2002). A particular feature of the early Paleogene climate anomalies (CIEs and hyperthermal events) is that unlike their Eocene counterparts, the Paleogene climate anomalies are much more complex and often consist of multiple minor events, creating a sawtooth-like appearance in climatic and rock magnetic proxies, similar to behavior also described in the Early Paleogene in the Tethyan region (Coccioni et al., 2012). In some instances, these anomalies have been interpreted as "multiple events anomalies," for example, Middle-Lower Danian Multiple Event (MLDME) in the Gubbio-Contessa sections (Sinnesael et al., 2016). In other settings, the same anomalies have been interpreted as discrete individual events (Barnet et al., 2019). This lead to the existence of different terminologies for synchronous anomalies, also due to the fact that the geographical distribution is not uniform, and some events are restricted to a certain region, such as it appears to be the case of the Dan-C2 event (Westerhold et al., 2011).

In this study, we correlate DSDP Site 356 with a proximal sedimentary record from the South Atlantic Walvis Ridge site (IODP Hole 1262) (see **Figure 1**). Both sites lie in the same region of the South Atlantic and belong to the RGR-WR system in the Cretaceous-Paleogene; however, they were separated by submarine obstacles of the Atlantic rift zone. The deep channels connecting the Brazil and Argentine Basins influenced the two sites in different ways. While Site 356 is more proximal to the deepest passage at the time, the Vema Gap (A and B in **Figure 1**), Site 1262 is distal, ∼2000 km away from the nearest channel. We thus expect small differences between the WR and SPP, nonetheless reflecting the same history of the evolution of the South Atlantic Ocean. Lacking stable isotope data ($\delta^{13}C$ and $\delta^{18}O$) for Site 356, we opt to compare the magnetic susceptibility and environmental magnetic parameters from Site 356 with the geochemical record of Site 1262.

Magnetic susceptibility is sensitive to the concentration of magnetic grains, their size, and mineralogy (Hatfield and Stoner, 2013). Though often controlled by the sum of various processes (detrital input, ocean current transport, diagenesis, etc.), they are often driven by changes in climate. S-ratio provides some insight into the magnetic mineralogy, quantifying the relative concentration of antiferromagnetic minerals in mineral mixtures (Bloemendal et al., 1988; Liu et al., 2007). The lower the S-ratio, the higher the contribution of hematite and goethite; when S-ratio approaches maximum values, the

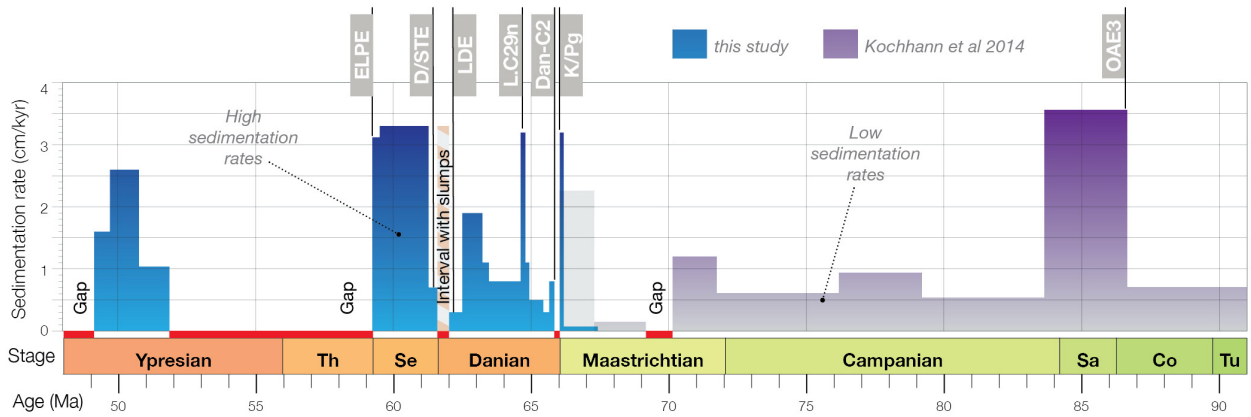

FIGURE 8 | Sedimentary rates for the Sao Paulo Plateau from the late Cretaceous to early Eocene. Blue color indicates values obtained in this study; purple is from Kochhann et al. (2014). Key anomalous intervals are marked and labeled. Sedimentary gaps marked in red.

magnetic mineralogy is interpreted to be dominated by low coercivity minerals (magnetite or maghemite). κARM/κ is a magnetic grain size proxy. A closer look at the correlation between ODP Site 1262 Walvis Ridge (Barnet et al., 2019) and DSDP Site 356 reveals that anomalous magnetic susceptibility and S-ratio levels match CIEs and hyperthermals reported in the Walvis Ridge: Dan-C2 (Jehle et al., 2015), L.C29n (Barnet et al., 2019), M.C27r (Coccioni et al., 2012), LDE (Westerhold et al., 2011; Deprez et al., 2017) and D/STE (Arenillas et al., 2008). The aforementioned climate anomalies correspond to peaks in magnetic susceptibility, recovery trends in the S-ratios that follow extreme low values and high values of κARM/κ. The L.C26r (Barnet et al., 2019) is difficult to identify and might be missing form 356 due to local slumping (Perch-Nielsen et al., 1977). The slumps likely induced an offset in our age model, visible as slight delays of LDE, when compared with the Walvis Ridge data. No similar anomalies can be correlated with ELPE (Coccioni et al., 2019) due to the presence of a large sedimentation gap, the onset which can be confidently correlated with ELPE, indicating a change in sedimentation occurred at the time.

We identify a series of intervals, characterized by anomalous values of the magnetic properties, that all consistently correlate with significant high- and low- sedimentation rates, or occur in the vicinity of sedimentary anomalies (**Figure 8**) and seem to correspond to the Dan-C2, L.C29n, M.C27r, LDE and D/STE carbon isotopic events. This seems to suggest that the anomalies may be linked to changes in deep-water circulation and/or water column instability near the Vema gap. Most anomalies occur during the Danian stage, fitting the model proposed by Voigt et al. (2013) for the onset deep-water circulation into the North Atlantic, and the model of a transition to a more connected Atlantic Ocean proposed by Batenburg et al. (2018). Deep-water circulation would be affected by the opening and enlargement of the deeper sectors of the Vema and Hunter passageways in the Rio Grande Rise region, outlined in **Figure 1**.

An expanded comparison of stable isotope ratios and magnetic properties throughout the Danian interval (**Figure 9**), reveals that the magnetic anomalies are not completely reflected in the magnetic susceptibility, showing that secondary indicators (e.g., S-Ratio) are necessary to depict a fuller picture of the anomalous magnetic properties of sediments during the CIE. That is due to the occurrence, during the CIEs, of diverse magnetic minerals that are not entirely revealed by magnetic susceptibility properties. It also appears that the early Danian CIE and magnetic anomalies are less coherent compared with the late Danian expressions, probably due to a phase of instability the water column in the South Atlantic region, either driven by the incipient deep-water circulation through the new passage (e.g., upwelling, stratification) or due to external factors such as climate anomalies (e.g., CIE and hyperthermals) disrupting the emerging ocean circulation pathways.

Dan-C2 – A Marker for Paleocirculation Change?

High-resolution studies on key sites form the Atlantic Walvis Ridge (Barnet et al., 2019) and the Pacific Shatsky Rise (Westerhold et al., 2011) show that the Early Paleocene Dan-C2 event is not a typical global hyperthermal, but rather a regional expression whilst the remaining Paleogene CIE are global and appear to be orbitally paced, occurring during maxima in the 405-kyr cycle (Barnet et al., 2019). From an ocean circulation perspective, our results indicate that during the Early Paleogene, the Rio Grande Rise – Walvis Ridge alignment was overcome, and deep-water currents from South Atlantic toward the North Atlantic were established. The geographical distribution of the Dan-C2 anomalies (Kroon et al., 2007; Quillevere et al., 2008; Westerhold et al., 2011; Coccioni et al., 2019) matches the areas that would be affected by the northward flow of South Atlantic deep waters. This raises the question of whether Dan-C2 may actually be an expression of this connectivity change in the South Atlantic. Throughout the Danian and Selandian time, the São Paulo Plateau records instability of magnetic properties and magnetic carriers in the sediments and sedimentation anomalies that match the chronology of CIEs and hyperthermals.

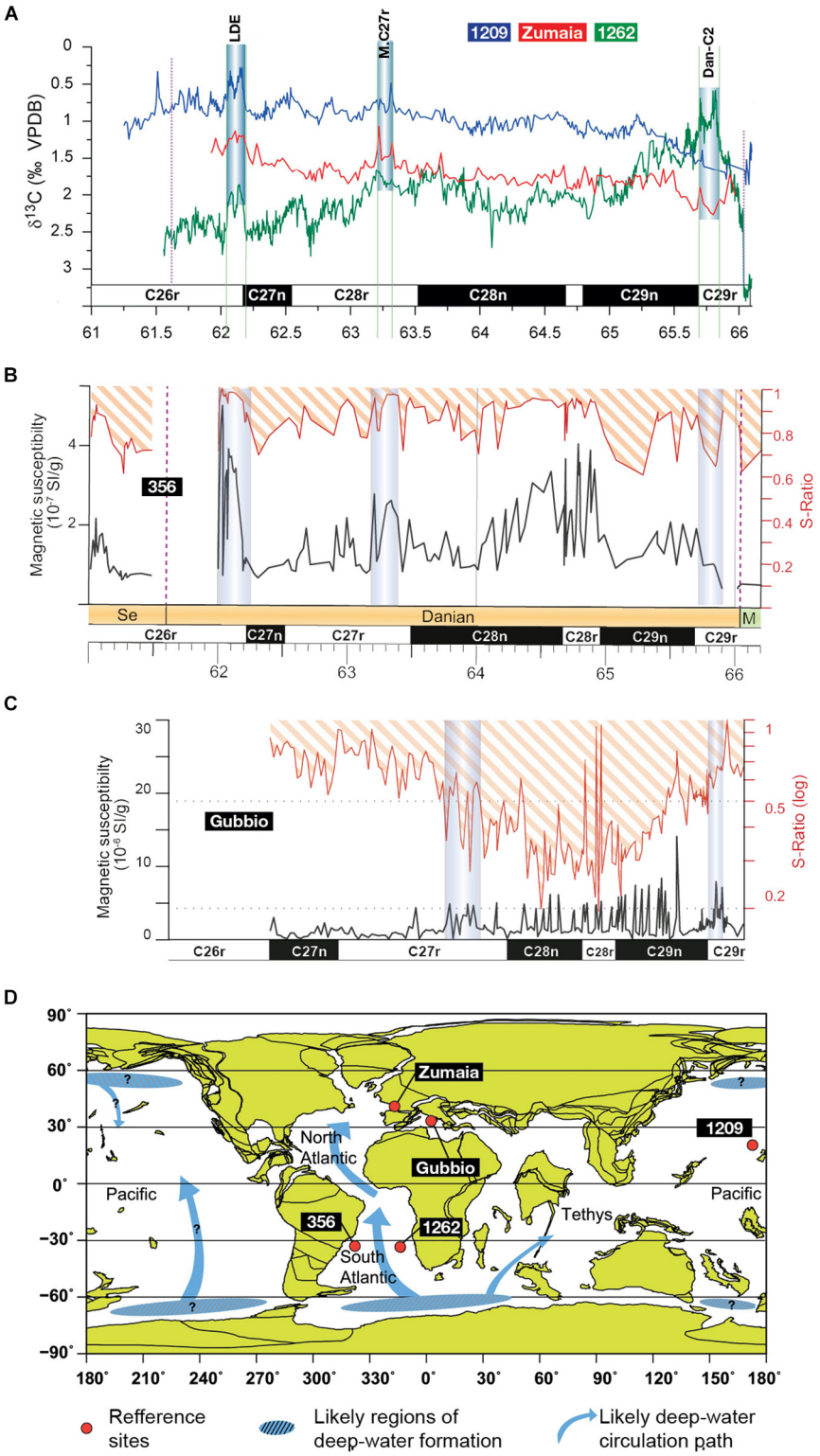

FIGURE 9 | Danian anomalies in the sedimentary record. Please note the discordant trends that correspond to the Dan-C2 event in carbon isotopes curves from Atlantic, Pacific and Tethys regions [**(A)** from Dinarès-Turell et al. (2014)] and the environmental magnetism results from South Atlantic [**(B)** site 356, this study] and Tethys region [**(C)** Gubbio, after Coccioni et al., 2012] and the geographic location of the compared sites [**(D)** after Littler et al., 2014].

CONCLUSION

We studied the sediments of DSDP Site 356 Leg 39, set on the São Paulo Plateau on the edge of the Rio Grande Rise in the South Atlantic. The position of the site next to the last obstacles to unrestricted ocean circulation meant that it preserves a sedimentary record of the onset and development of the Atlantic Ocean Circulation. We developed a new, improved age model with magnetostratigraphy for the Latest Maastrichtian – Early Lutetian interval (68–46 Ma) to shed light on the time interval where the RGR-WR was progressively breached, constraining the sedimentary rates as an indicator of bottom current activity. We find sharp anomalies in the early Paleogene, coinciding with rapid fluctuations in the magnetic properties of the sediment. Correlations with known hyperthermal events documented in the nearby Walvis Ridge indicate a potential link between climatic anomalies and paleocirculation. Drastic changes in the general sedimentation trends begin after the Dan-C2 anomaly, which we interpret as an indirect result of the change in connectivity following the breach of southern deep waters across the RGR-WR. We hypothesize that Dan-C2, given that it does not represent a true hyperthermal event, it rather marks a drastic change in bottom water conditions following the initiation of a deepwater connection in the South Atlantic Ocean, as the Atlantic Ocean Circulation gradually replaces the Tethys circum-equatorial oceanic circulation and ultimately leads to the onset of the modern Atlantic Meridional Overturning Circulation.

DATA AVAILABILITY STATEMENT

The raw data supporting the conclusions of this article will be made available by the authors, without undue reservation.

AUTHOR CONTRIBUTIONS

LJ requested samples, conceived and funded the study. DP and JM designed and conducted the research and wrote the manuscript. PJ helped in acquiring and processing the paleomagnetic data, and contributed to the drafting of the manuscript. All authors contributed to the article and approved the submitted version.

FUNDING

This work is part of the Coordenação de Aperfeiçoamento de Pessoal de Nível Superior (CAPES) – Finance Code 001, Ciência do Mar II. DP acknowledges the Fundação de Amparo a Pesquisa do Estado de São Paulo (FAPESP) for financial support through grant 2018/20733-6. LJ acknowledges FAPESP projects 2016/24946-9 and 2018/17061-6. This work has been (partially) performed at USPMag lab at Instituto de Astronomia, Geofísica e Ciências Atmosféricas (IAG) at Universidade de São Paulo (USP) funded by CAPES/FAPESP/CNPQ.

ACKNOWLEDGMENTS

The authors wish to sincerely thank the staff of USPMAG for access to the facilities and help with the acquisition and processing of the data. The authors thank the staff of Fort Hoofddijk Paleomagnetic Lab – Utrecht University and Mark Dekkers, in particular for helping with the preparation and acquisition of the data. The authors thank the staff of MARUM – University of Bremen and Holger Kuhlmann, in particular for facilitating sampling of the DSDP core.

SUPPLEMENTARY MATERIAL

The Supplementary Material for this article can be found online at: https://www.frontiersin.org/articles/10.3389/feart.2020.00375/full#supplementary-material

FIGURE S1 | Supplementary paleomagnetic results. Inclination unflattening for samples from the first quality group (q1).

REFERENCES

Arai, M. (1988). Geochemical reconnaissance of the mid-cretaceous anoxic event in the Santos Basin, Brazil. *Rev. Bras. Geociencias* 18, 273–282. doi: 10.25249/0375-7536.1988273282

Arenillas, I., Molina, E., Ortiz, S., and Schmitz, B. (2008). Foraminiferal and δ13C isotopic event- stratigraphy across the Danian-Selandian transition at Zumaya (northern Spain): chronostratigraphic implications. *Terra Nova* 20, 38–44. doi: 10.1111/j.1365-3121.2007.00784.x

Avilla, L. S., Candeiro, C. R., Buckup, P., and Bergqvist, L. P. (2002). Gondwana biogeography: a phylogenetic approach. *An. Acad. Bras. Cienc.* 74, 365–365. doi: 10.1590/s0001-37652002000200018

Banerjee, S. K., King, J., and Marvin, J. (1981). A rapid method for magnetic granulometry with applications to environmental studies. *Geophys. Res. Lett.* 8, 333–336. doi: 10.1029/gl008i004p00333

Barnet, J. S., Littler, K., Westerhold, T., Kroon, D., Leng, M. J., Bailey, I., et al. (2019). A high-fidelity benthic stable isotope record of late cretaceous–early eocene climate change and carbon-cycling. *Paleoceanogr. Paleoclimatol.* 34, 672–691. doi: 10.1029/2019PA003556

Batenburg, S. J., Voigt, S., Friedrich, O., Osborne, A. H., Bornemann, A., Klein, T., et al. (2018). Major intensification of Atlantic overturning circulation at the onset of Paleogene greenhouse warmth. *Nat. Commun.* 9:4954.

Battle, M., Bender, M. L., Tans, P. P., White, J. W., Ellis, J. T., Conway, T., et al. (2000). Global carbon sinks and their variability inferred from atmospheric O2 and δ13C. *Science* 287, 2467–2470. doi: 10.1126/science.287.5462.2467

Bloemendal, J., King, J. W., Hall, F. R., and Doh, S.-J. (1992). Rock magnetism of late neogene and pleistocene deep-sea sediments: relationship to sediment source, diagenetic processes, and sediment lithology. *J. Geophys. Res.* 97, 4361–4375. doi: 10.1029/91JB03068

Bloemendal, J., Lamb, B., and King, J. (1988). Paleoenvironmental implications of rock-magnetic properties of late quaternary sediment cores from the eastern equatorial Atlantic. *Paleoceanography* 3, 61–87. doi: 10.1029/PA003i001p00061

Bryden, H. L., and Imawaki, S. (2001). Chapter 6.1 Ocean heat transport. *Int. Geophys.* 77, 455–474. doi: 10.1016/S0074-6142(01)80134-0

Buckley, J. P., Bosence, D., and Elders, C. (2015). Tectonic setting and stratigraphic architecture of an early Cretaceous lacustrine carbonate platform, Sugar Loaf High, Santos Basin, Brazil. *Geol. Soc. Spec. Publ.* 418, 175–191. doi: 10.1144/SP418.13

Buckley, M. W., and Marshall, J. (2016). Observations, inferences, and mechanisms of the Atlantic Meridional Overturning Circulation: a review. *Rev. Geophys.* 54, 5–63. doi: 10.1002/2015rg000493

Carvallo, C., Muxworthy, A. R., and Dunlop, D. J. (2006). First-order reversal curve (FORC) diagrams of magnetic mixtures: micromagnetic models and

measurements. *Phys. Earth Planet. Inter.* 154, 308–322. doi: 10.1016/j.pepi.2005.06.017

Chaboureau, A. C., Guillocheau, F., Robin, C., Rohais, S., Moulin, M., and Aslanian, D. (2013). Paleogeographic evolution of the central segment of the South Atlantic during Early Cretaceous times: paleotopographic and geodynamic implications. *Tectonophysics* 604, 191–223. doi: 10.1016/j.tecto.2012.08.025

Chadima, M., and Hrouda, F. (2006). Remasoft 3.0 a user-friendly paleomagnetic data browser and analyzer. *Trav. Géophys.* 27, 20–21.

Chang, L., Winklhofer, M., Roberts, A. P., Heslop, D., Florindo, F., Dekkers, M. J., et al. (2013). Low-temperature magnetic properties of pelagic carbonates: oxidation of biogenic magnetite and identification of magnetosome chains. *J. Geophys. Res. Solid Earth* 118, 6049–6065. doi: 10.1002/2013jb010381

Chen, X., and Tung, K. K. (2018). Global surface warming enhanced by weak Atlantic overturning circulation. *Nature* 559, 387–391. doi: 10.1038/s41586-018-0320-y

Coccioni, R., Bancalà, G., Catanzarit, R., Fornaciari, E., Frontalini, F., Giusberti, L., et al. (2012). An integrated stratigraphic record of the Palaeocene-lower Eocene at Gubbio (Italy): new insights into the early Palaeogene hyperthermals and carbon isotope excursions. *Terra Nova* 24, 380–386. doi: 10.1111/j.1365-3121.2012.01076.x

Coccioni, R., Frontalini, F., Catanzariti, R., Jovane, L., Rodelli, D., Rodrigues, I. M., et al. (2019). Paleoenvironmental signature of the selandian-thanetian transition event (STTE) and early late paleocene event (ELPE) in the Contessa Road section (western Neo-Tethys). *Palaeogeogr. Palaeoclimatol. Palaeoecol.* 523, 62–77. doi: 10.1016/J.PALAEO.2019.03.023

Cogne, N., Gallagher, K., Cobbold, P. R., Riccomini, C., and Gautheron, C. (2012). Post-breakup tectonics in southeast Brazil from thermochronological data and combined inverse-forward thermal history modeling. *J. Geophys. Res. B Solid Earth* 117:B11413. doi: 10.1029/2012JB009340

Davison, I., Anderson, L., and Nuttall, P. (2012). Salt deposition, loading and gravity drainage in the Campos and Santos salt basins. *Geol. Soc. Spec. Publ.* 363, 159–174. doi: 10.1144/sp363.8

de Oliveira, V. C. B., Silva, C. M. D. A., Borghi, L. F., and Carvalho, I. D. S. (2019). Lacustrine coquinas and hybrid deposits from rift phase: pre-Salt, lower Cretaceous, Campos Basin, Brazil. *J. South Am. Earth Sci.* 95:102254. doi: 10.1016/j.jsames.2019.102254

Deprez, A., Jehle, S., Bornemann, A., and Speijer, R. P. (2017). Differential response at the seafloor during Palaeocene and Eocene ocean warming events at Walvis Ridge, Atlantic Ocean (ODP Site 1262). *Terra Nova* 29, 71–76. doi: 10.1111/ter.12250

Dinarès-Turell, J., Westerhold, T., Pujalte, V., Rohl, U., and Kroon, D. (2014). Astronomical calibration of the Danian stage (Early Paleocene) revisited: settling chronologies of sedimentary records across the Atlantic and Pacific Oceans. *Earth Planet. Sci. Lett.* 405, 119–131. doi: 10.1016/j.epsl.2014.08.027

Donnadieu, Y., Puceat, E., Moiroud, M., Guillocheau, F., and Deconinck, J. F. (2016). A better-ventilated ocean triggered by Late Cretaceous changes in continental configuration. *Nat. Commun.* 7:10316. doi: 10.1038/ncomms10316

Dutkiewicz, A., Dietmar Müller, R., Hogg, A. M. C., and Spence, P. (2016). Vigorous deep-sea currents cause global anomaly in sediment accumulation in the Southern Ocean. *Geology* 44, 663–666. doi: 10.1130/g38143.1

Egli, R. (2013). VARIFORC: an optimized protocol for calculating non-regular first-order reversal curve (FORC) diagrams. *Glob. Planet. Change* 110, 302–320. doi: 10.1016/j.gloplacha.2013.08.003

Frank, T. D., and Arthur, M. A. (1999). Tectonic forcings of Maastrichtian ocean-climate evolution. *Paleoceanography* 14, 103–117. doi: 10.1029/1998PA900017

Fu, Y., Von Dobeneck, T., Franke, C., Heslop, D., and Kasten, S. (2008). Rock magnetic identification and geochemical process models of greigite formation in quaternary marine sediments from the gulf of Mexico (iodp hole u1319a). *Earth Planet. Sci. Lett.* 275, 233–245. doi: 10.1016/j.epsl.2008.07.034

Gehring, A. U., Fischer, H., Louvel, M., Kunze, K., and Weidler, P. G. (2009). High temperature stability of natural maghemite: a magnetic and spectroscopic study. *Geophys. J. Int.* 179, 1361–1371. doi: 10.1111/j.1365-246X.2009.04348.x

Gilmour, I., Jolley, D., Kemp, D., Kelley, S., Gilmour, M., Daly, R., et al. (2014). "The early Danian hyperthermal event at Boltysh (Ukraine): relation to Cretaceous-Paleogene boundary events," in *Volcanism, Impacts, and Mass Extinctions: Causes and Effects*, eds G. Keller and A. C. Kerr (Boulder, CO: Geological Society of America), 133–146. doi: 10.1130/2014.2505(06

Gradstein, F., and Ogg, J. (2006). Ts-creator© - chronostratigraphic data base and visualisation: cenozoic- mesozoic-paleozoic integrated stratigraphy and user-generated time scale graphics and charts. *Geoarabia* 11, 181–184.

Grassl, H. (2001). Climate and oceans. *Int. Geophys.* 77, 3–9.

Gruber, N., Keeling, C. D., and Bates, N. R. (2002). Interannual variability in the North Atlantic ocean carbon sink. *Science* 298, 2374–2378. doi: 10.1126/science.1077077

Guardado, L. R., Gamboa, L. A. P., and Lucchesi, C. F. (1989). "Petroleum geology of the Campos Basin, Brazil, a model for a producing Atlantic type basin: PART 1," in *Divergent/Passive Margin Basins*, Vol. 48, eds J. D. Edwards and P. A. Santogrossi (Tulsa: AAPG), 3–36.

Harrison, R. J., and Feinberg, J. M. (2008). FORCinel: an improved algorithm for calculating first-order reversal curve distributions using locally weighted regression smoothing. *Geochem. Geophys. Geosyst.* 9:Q05016. doi: 10.1029/2008GC001987

Hatfield, R. G., and Stoner, J. S. (2013). "Magnetic proxies and susceptibility," in *Encyclopedia of Quaternary Science*, 2nd Edn, ed. S. Elias (Amsterdam: Elsevier), 884–898. doi: 10.1016/B978-0-444-53643-3.00307-1

Herbin, J. P., Muller, C., Graciansky, P. C. D., Jacquin, T., Magniez-Jannin, F., and Unternehr, P. (1987). Cretaceous anoxic events in the South Atlantic. *Rev. Bras. Geociencias* 17, 92–99. doi: 10.25249/0375-7536.19879299

Hernández-Molina, F. J., Stow, D. A. V., Alvarez-Zarikian, C. A., Acton, G., Bahr, A., Balestra, B., et al. (2014). Onset of Mediterranean outflow into the North Atlantic. *Science* 344, 1244–1250. doi: 10.1126/science.1251306

Hillaire-Marcel, C., and De Vernal, A. (2007). *Proxies in Late Cenozoic Paleoceanography*. Amsterdam: Elsevier.

Hull, P. M., Bornemann, A., Penman, D. E., Henehan, M. J., Norris, R. D., Wilson, P. A., et al. (2020). On impact and volcanism across the Cretaceous-Paleogene boundary. *Science* 367, 266–272.

Jehle, S., Bornemann, A., Deprez, A., and Speijer, R. P. (2015). The impact of the latest danian event on planktic foraminiferal faunas at ODP Site 1210 (Shatsky Rise, Pacific Ocean). *PLoS One* 10:e0141644. doi: 10.1371/journal.pone.0141644

King, J., Banerjee, S. K., Marvin, J., and Ozdemir, O. (1982). A comparison of different magnetic methods for determining the relative grain size of magnetite in natural materials: some results from lake sediments. *Earth Planet. Sci. Lett.* 59, 404–419. doi: 10.1016/0012-821X(82)90142-X

Kirschvink, J. L. (1980). The least-squares line and plane and the analysis of palaeomagnetic data. *Geophys. J. Int.* 62, 699–718. doi: 10.1111/j.1365-246X.1980.tb02601.x

Kirschvink, J. L., Kopp, R. E., Raub, T. D., Baumgartner, C. T., and Holt, J. W. (2008). Rapid, precise, and high-sensitivity acquisition of paleomagnetic and rock-magnetic data: development of a low-noise automatic sample changing system for superconducting rock magnetometers. *Geochem. Geophys. Geosyst.* 9:Q05Y01. doi: 10.1029/2007GC001856

Kochhann, K. G. D., Lopes, F. M., Krahl, G., Aguiar, E., and Fauth, G. (2014). Late cretaceous-early paleogene (Turonian? to early Danian) planktic foraminifera from DSDP site 356: a biostratigraphic reappraisal. *Rev. Bras. Paleontol.* 17, 157–168. doi: 10.4072/rbp.2014.2.04

Koutsoukos, E. A. (1992). Late aptian to maastrichtian foraminiferal biogeography and palaeoceanography of the Sergipe basin, Brazil. *Palaeogeogr. Palaeoclimatol. Palaeoecol.* 92, 295–324. doi: 10.1016/0031-0182(92)90089-n

Krahl, G., Koutsoukos, E. A., and Fauth, G. (2017). Paleocene planktonic foraminifera from DSDP Site 356, South Atlantic: paleoceanographic inferences. *Mar. Micropaleontol.* 135, 1–14. doi: 10.1016/j.marmicro.2017.07.001

Kroon, D., Zachos, J., Blum, P., Bowles, J., Gaillot, P., Hasegawa, T., et al. (2007). *Leg 208 Synthesis: Cenozoic Climate Cycles and Excursions*. College Station, TX: Ocean Drilling Program.

Kumar, N., and Gamboa, L. A. P. (1979). Evolution of the Sao Paulo Plateau (southeastern Brazilian margin) and implications for the early history of the South Atlantic. *GSA Bull.* 90, 281–293.

Littler, K., Röhl, U., Westerhold, T., and Zachos, J. C. (2014). A high-resolution benthic stable-isotope record for the South Atlantic: implications for orbital-scale changes in Late Paleocene–Early Eocene climate and carbon cycling. *Earth Planet. Sci. Lett.* 401, 18–30. doi: 10.1016/j.epsl.2014.05.054

Liu, Q., Roberts, A. P., Torrent, J., Horng, C.-S., and Larrasoaña, J. C. (2007). What do the HIRM and S-ratio really measure in environmental magnetism? *Geochem. Geophys. Geosyst.* 8:Q09011. doi: 10.1029/2007GC001717

Liu, X. M., Shaw, J., Jiang, J. Z., Bloemendal, J., Hesse, P., Rolph, T., et al. (2010). Analysis on variety and characteristics of maghemite. *Sci. China Earth Sci.* 53, 1153–1162. doi: 10.1007/s11430-010-0030-2

Mai, H., Hildebrand-Habel, T., Perch-Nielsen, K. V. S., and Willems, H. (1998). Paleocene coccospheres from DSDP Leg 39, Site 356, Sao Paulo Plateau, S Atlantic Ocean. *J. Nannoplankton Res.* 20, 21–29.

Mohriak, W., Nemcok, M., and Enciso, G. (2008). South Atlantic divergent margin evolution: rift-border uplift and salt tectonics in the basins of SE Brazil. *Geol. Soc. Spec. Publ.* 294, 365–398. doi: 10.1144/SP294.19

Mohriak, W. U. (2003). "Bacias sedimentares da margem continental Brasileira," in *Geologia, Tectonica e Recursos Minerais do Brasil*, eds L. Bizzi, C. Schobbenhaus, R. Vidotti, and J. Goncalves (Brasil: CPRM), 87–165.

Moskowitz, B. M. (2007). "Magnetization, anhysteretic remanent," in *Encyclopedia of Geomagnetism and Paleomagnetism*, eds D. Gubbins and E. Herrero-Bervera (Dordrecht: Springer).

Mullender, T. A. T., Frederichs, T., Hilgenfeldt, C., de Groot, L. V., Fabian, K., and Dekkers, M. J. (2016). Automated paleomagnetic and rock magnetic data acquisition with an in-line horizontal "2G" system. *Geochem. Geophys. Geosyst.* 17, 3546–3559. doi: 10.1002/2016GC006436

Mullender, T. A. T., Velzen, A. J., and Dekkers, M. J. (1993). Continuous drift correction and separate identification of ferrimagnetic and paramagnetic contributions in thermomagnetic runs. *Geophys. J. Int.* 114, 663–672. doi: 10.1111/j.1365-246X.1993.tb06995.x

Murphy, D. P., and Thomas, D. J. (2013). The evolution of Late Cretaceous deep-ocean circulation in the Atlantic basins: neodymium isotope evidence from South Atlantic drill sites for tectonic controls. *Geochem. Geophys. Geosyst.* 14, 5323–5340. doi: 10.1002/2013GC004889

Ogg, J. G., Ogg, G. M., and Gradstein, F. M. (2016). *A Concise Geologic Time Scale: 2016*. Amsterdam: Elsevier.

Ohmoto, H. (2003). Nonredox transformations of magnetite-hematite in hydrothermal systems. *Econ. Geol.* 98, 157–161. doi: 10.2113/gsecongeo.98.1.157

Opdyke, N. D., and Channell, J. E. (1996). "Magnetic stratigraphy," in *International Geophysics*, Vol. 64, eds N. D. Opdyke and J. E. Channell (London: Academic Press), 49–73. doi: 10.1016/S0074-6142(06)80006-9

Ozdemir, O., and Banerjee, S. K. (1984). High temperature stability of maghemite (γ-Fe2O3). *Geophys. Res. Lett.* 11, 161–164. doi: 10.1029/GL011i003p00161

Perch-Nielsen, K., Supko, P., Boersma, A., Carlson, R., Dinkelman, M., Fodor, R., et al. (1977). Site 356: Sao Paulo Plateau. *Initial Rep. Deep Sea Drill. Proj.* 39, 141–230.

Pérez-Díaz, L., and Eagles, G. (2017). South Atlantic paleobathymetry since early Cretaceous. *Sci. Rep.* 7:11819. doi: 10.1038/s41598-017-11959-7

Pietzsch, R., Oliveira, D. M., Tedeschi, L. R., Queiroz Neto, J. V., Figueiredo, M. F., Vazquez, J. C., et al. (2018). Palaeohydrology of the Lower Cretaceous pre-salt lacustrine system, from rift to post- rift phase, Santos Basin, Brazil. *Palaeogeogr. Palaeoclimatol. Palaeoecol.* 507, 60–80. doi: 10.1016/j.palaeo.2018.06.043

Quillevere, F., Aubry, M. P., Norris, R. D., and Berggren, W. A. (2002). Paleocene oceanography of the eastern subtropical Indian Ocean: an integrated magnetobiostratigraphic and stable isotope study of ODP Hole 761B (Wombat Plateau). *Palaeogeogr. Palaeoclimatol. Palaeoecol.* 184, 371–405. doi: 10.1016/S0031-0182(02)00275-4

Quillevere, F., Norris, R. D., Kroon, D., and Wilson, P. A. (2008). Transient ocean warming and shifts in carbon reservoirs during the early danian. *Earth Planet. Sci. Lett.* 265, 600–615. doi: 10.1016/j.epsl.2007.10.040

Roberts, A. P., Liu, Q., Rowan, C. J., Chang, L., Carvallo, C., Torrent, J., et al. (2006). Characterization of hematite (α-fe2o3), goethite (α-feooh), greigite (fe3s4), and pyrrhotite (fe7s8) using first-order reversal curve diagrams. *J. Geophys. Res. Solid Earth* 111:B12S35.

Robinson, S. A., Murphy, D. P., Vance, D., and Thomas, D. J. (2010). Formation of "Southern Component Water" in the Late Cretaceous: evidence from Nd-isotopes. *Geology* 38, 871–874. doi: 10.1130/g31165.1

Robinson, S. A., and Vance, D. (2012). Widespread and synchronous change in deep-ocean circulation in the North and South Atlantic during the Late Cretaceous. *Paleoceanography* 27:1102.

Schulte, P., Schwark, L., Stassen, P., Kouwenhoven, T. J., Bornemann, A., and Speijer, R. P. (2013). Black shale formation during the Latest Danian Event and the Paleocene-Eocene Thermal Maximum in central Egypt: two of a kind? *Palaeogeogr. Palaeoclimatol. Palaeoecol.* 371, 9–25. doi: 10.1016/j.palaeo.2012.11.027

Silva, R., de Moraes Rios-Netto, A., Silva, S. C., Valle, B., Borghi, L., and Abbots-Queiroz, F. (2020). Middle Cretaceous calcareous nannofossils from the cored well UFRJ-2-LRJ-01-SE, Sergipe-Alagoas Basin, Brazil: new biostratigraphy and paleobiogeographic inferences. *Cretac. Res.* 106:104245. doi: 10.1016/j.cretres.2019.104245

Sinnesael, M., De Vleeschouwer, D., Coccioni, R., Claeys, P., Frontalini, F., Jovane, L., et al. (2016). High-resolution multiproxy cyclostratigraphic analysis of environmental and climatic events across the Cretaceous-Paleogene boundary in the classic pelagic succession of Gubbio (Italy). *Spec. Pap. Geol. Soc. Am.* 524, 115–137. doi: 10.1130/2016.2524(09)

Snowball, I. F. (1997). Gyroremanent magnetization and the magnetic properties of greigite-bearing clays in southern Sweden. *Geophys. J. Int.* 129, 624–636. doi: 10.1111/j.1365-246x.1997.tb04498.x

Sprong, J., Kouwenhoven, T. J., Bornemann, A., Schulte, P., Stassen, P., Steurbaut, E., et al. (2012). Characterization of the Latest Danian Event by means of benthic foraminiferal assemblages along a depth transect at the southern Tethyan margin (Nile Basin, Egypt). *Mar. Micropaleontol.* 86–87, 15–31. doi: 10.1016/j.marmicro.2012.01.001

Supko, P., and Perch-Nielsen, K. (1977). "General synthesis of central and South Atlantic drilling results, Leg 39, Deep Sea Drilling Project," in *Initial Reports of the Deep-Sea Drilling Project*, Vol. 39, eds C. C. von der Borch and J. G. Sclater (Washington, DC: US Government Printing Office), 1099–1131.

Supko, P., Perch-Nielsen, K., and Carlson, R. (1977). Introduction and explanatory notes, Leg 39, Deep Sea Drilling Project, Initial Report. *Deep Sea Drill. Proj.* 39, 1–2.

Tauxe, L., Kodama, K. P., and Kent, D. V. (2008). Testing corrections for paleomagnetic inclination error in sedimentary rocks: a comparative approach. *Phys. Earth Planet. Inter.* 169, 152–165. doi: 10.1016/j.pepi.2008.05.006

Tedeschi, L. R., Jenkyns, H. C., Robinson, S. A., Sanjinés, A. E., Viviers, M. C., Quintaes, C. M., et al. (2017). New age constraints on Aptian evaporites and carbonates from the South Atlantic: implications for oceanic anoxic event 1a. *Geology* 45, 543–546. doi: 10.1130/G38886.1

Thiede, J. (1977). Sedimentary structures in pelagic and hemipelagic sediments from the central and southern Atlantic Ocean (Deep-Sea Drilling Project Leg 39). *Initial Rep. Deep Sea Drill. Proj.* 39, 407–415.

Voigt, S., Jung, C., Friedrich, O., Frank, M., Teschner, C., and Hoffmann, J. (2013). Tectonically restricted deep-ocean circulation at the end of the Cretaceous greenhouse. *Earth Planet. Sci. Lett.* 369–370, 169–177. doi: 10.1016/j.epsl.2013.03.019

Wagreich, M. (2012). "OAE 3" - Regional Atlantic organic carbon burial during the Coniacian-Santonian. *Clim. Past* 8, 1447–1455. doi: 10.5194/cp-8-1447-2012

Wanderley , M. D., and Pedrosa, F. (2017). Calcareous nannoplankton from the continuous K-Pg Boundary of the São Paulo Plateau: a biostratigraphic and paleoecological approach to the mass extinction. *Palaeogeogr. Palaeoclimatol. Palaeoecol.*

Westerhold, T., Rhl, U., Donner, B., McCarren, H. K., and Zachos, J. C. (2011). A complete high-resolution Paleocene benthic stable isotope record for the central Pacific (ODP Site 1209). *Paleoceanography* 26, 1–13. doi: 10.1029/2010PA002092

Woodruff, F., and Savin, S. M. (1989). Miocene deepwater oceanography. *Paleoceanography* 4, 87–140. doi: 10.1029/pa004i001p00087

Zijderveld, J. D. A. (2013). AC demagnetization of rocks: analysis of results. *Dev. Solid Earth Geophys.* 3, 254–286. doi: 10.1016/b978-1-4832-2894-5.50049-5

Conflict of Interest: The authors declare that the research was conducted in the absence of any commercial or financial relationships that could be construed as a potential conflict of interest.

frontiers in Earth Science

ORIGINAL RESEARCH
published: 06 November 2020
doi: 10.3389/feart.2020.544496

Southward Drift of Eastern Australian Hotspots in the Paleomagnetic Reference Frame Is Consistent With Global True Polar Wander Estimates

Jeroen Hansma[1]* *and Eric Tohver*[2]

[1]School of Earth Sciences, University of Western Australia, Perth, WA, Australia, [2]Institute of Astronomy, Geophysics and Atmospheric Sciences, University of Sao Paulo, Brazil

Eastern Australian hotspots produce the longest continental tracks on Earth (> 2, 000 km). These hotspots are generally assumed to be stationary with respect to one another, an observation reinforced by our analysis. If any motion between them occurred, it is within our 95% uncertainties of 370 km of accumulated motion between hotspots. In contrast, motion between eastern Australian hotspots and the spin axis is indicated by changing paleolatitudes of hotspots through time. Reconstructing Australian hotspot paleolatitudes makes use of the global reference frame established by the geocentric axial dipole hypothesis. The classic paleomagnetic approach to establishing paleolatitude typically uses studies of discrete formations of known age, but the nearly continuous record of volcanism over 34 Ma permit using paleomagnetic data from multiple, different studies that overlap in magnetization age in conjunction. This improves the robustness and precision of our paleolatitude estimates for Eastern Australian hotspot volcanoes. A northward shift of hotspot paleolatitudes between 15–24 Ma of ~300–1,010 km (95% confidence limits) is observed for volcanoes along the Comboyne, Canobolas and Tasmantid tracks, and for interpolated positions along the Cosgrove and Lord Howe tracks but is significantly resolved only for volcanoes along Comboyne and Canobolas tracks, as well as for two ages from the Stradbroke and Britannia seamounts on the Tasmantid track. Before 24 Ma most data plot to the North of a fixed present day hotspot location in the paleomagnetic reference but 95% confidence limits overlap with it. Notable exceptions are an age from Hillsborough Volcano (Cosgrove Hotspot), and an age from Horse Head (Lord Howe Hotspot) that lie a small distance to the North km, and kmNorth, respectively. Importantly, paleolatitude changes observed along eastern Australian tracks are all explainable by the net rotation of the solid Earth, or true polar wander, with hotspots embedded in the global moving hotspot reference frame.

Keywords: paleomagnetism, hotspots, true polar wander, combined poles, Australia, Cenozoic

OPEN ACCESS

Edited by:
Anita Di Chiara, Istituto Nazionale di Geofisica e Vulcanologia (INGV), Italy

Reviewed by:
Augusto Ernesto Rapalini, University of Buenos Aires, Argentina
Gary Dean Acton, Texas A&M University, United States

***Correspondence:**
Jeroen Hansma
jeroen.hansma@exxonmobil.com

Specialty section:
This article was submitted to Geomagnetism and Paleomagnetism, a section of the journal Frontiers in Earth Science

Received: *21 March 2020*
Accepted: *29 September 2020*
Published: *06 November 2020*

Citation:
Hansma J and Tohver E (2020) Southward Drift of Eastern Australian Hotspots in the Paleomagnetic Reference Frame Is Consistent With Global True Polar Wander Estimates. Front. Earth Sci. 8:544496. doi: 10.3389/feart.2020.544496

1. INTRODUCTION

Hotspot tracks are linear arrays of age-progressive volcanoes that mark the surface terminations of upwelling, hot mantle plumes (Wilson, 1963; Morgan, 1971). At their oldest end, hotspots are sometimes associated with a large igneous province, or flood basalt, presumed to denote the arrival of a plume head (Courtillot et al., 2003). The age progressive track that follows is associated with a plume tail, a structure that anchors the hotspot, the plume tail's surface termination, to lower mantle convection (Steinberger, 2000).

Presently active hotspots (e.g., Hawaii, Iceland) have an active volcano and a topographic high (related to the buoyancy flux of material flow from the mantle) above them, as well as a low shear wave velocity (V_s) region beneath them (Courtillot et al., 2003). Plumes have a finite lifespan, and so these features can be expected to disappear as activity wanes.

Hotspot track geometry reflects the relative motion between the tectonic plate and the hotspot, modified to a lesser degree by lateral magma transport along the lithosphere-asthenosphere boundary (Sleep, 1996; Sleep, 1997). Plate motions can be described by rotations about an Euler pole relative to a reference frame (Cox and Hart, 1986). Euler rotations can be defined by fitting the geometry and age progressions of a pair (or more) of hotspot tracks underlying a given plate (e.g., Hawaii and Louisville on the Pacific Plate), defining plate motion relative to the mantle (absolute plate motion), anchoring relative rotation models to a common reference. Commonly Euler rotations are defined relative to a neighboring plate (this is the case when reconstructing seafloor isochrons) and, by combining rotations for multiple plate pairs, a hierarchy can be constructed to define a relative plate rotation model. The observation that hotspot tracks get older in the direction of plate motion led to the early hypothesis that hotspots were stationary in the mantle (Morgan, 1971), and as such, might provide a means for defining a mantle reference frame, so linking surface tectonic processes to the deep Earth. But fixed Pacific hotspot reference frames failed to predict the age progression and geometry of those in the Indo-Atlantic realms (and vice versa) (Molnar and Atwater, 1973; Duncan, 1981; Molnar and Stock, 1987; Müller et al., 1993; Wessel and Kroenke, 2008). Uncertainties in the relative rotations between plates (forming plate circuits), used to translate hotspot geometries from one plate to another were originally hypothesized to account for these misfits, with possible Eocene extension between East and West Antarctica being the supposed cause of misfit between Pacific and Indo-Atlantic fixed hotspot reference frames. Failing to account for all the degrees of freedom when fitting rotations to hotspot tracks also contributed (Andrews et al., 2006) Sharp changes in hotspot track geometry, such as the Hawaiian-Emperor bend have been reproduced by Indo-Atlantic fixed hotspot reference frames by taking this circuit (Torsvik et al., 2017), but relative motion between hotspots is still indicated (the predicted length of the Emperor bend being ~800 km shorter than observed) (Torsvik et al., 2019).

Relative motion between hotspots, inferred from the misfit between different, fixed hotspot reference frames, indicates that a combination of hotspot motion, non-rigid plate behavior, and errors in plate motions is required to explain them (Wang et al., 2017). Although the rate of relative motion between hotspots is estimated to be quite slow (4.5±3.8 mm a^{-1}) (Wang et al., 2017), a new generation of hotspot reference frames emerged, based upon plume conduits embedded within whole-mantle convection cells (Steinberger and O'Connell, 1998; Steinberger, 2000; Torsvik et al., 2008; Doubrovine et al., 2012). Using a plate model for surface boundary conditions, this innovation allowed for hotspot motion, accommodating the motion inferred between earlier, fixed reference frames, while also defining a mantle reference of global extent. Such models predicted that hotspots are anchored by their plume tails to lower mantle return flow, moving away from subduction zones, and toward mid-ocean ridges (Steinberger, 2000).

Paleomagnetism has also proven to be a useful tool for examining hotspot motion, yielding paleolatitude estimates for extinct volcanoes along hotspot tracks. Paleomagnetic data provide latitude constraints with respect to Earth's geocentric axial dipole (symmetry prevents reconstruction of paleolongitude). If hotspots are fixed in the mantle, and true polar wander (TPW), that is, the rotation of the entire solid Earth (both lithosphere and mantle) with respect to Earth's axis of rotation were negligible, then paleolatitudes for extinct hotspot volcanoes should be invariant, and coincide with the hotspot's present day position. On the other hand, if hotspots were moving in latitude, then the paleolatitudes along their tracks should reflect this history. Paleolatitudes for both Hawaii and Kerguelen indicate past motion of these hotspots with respect to the spin axis (Grommé and Vine, 1972; Kono, 1980; Gordon and Cape, 1981; Cox and Gordon, 1984; Tarduno and Cottrell, 1997; Antretter et al., 2002; Tarduno et al., 2003; Doubrovine and Tarduno, 2004; Tarduno, 2007; Tarduno et al., 2009). As such, paleolatitude estimates reflect the combination of any hotspot motion together with TPW. Correcting for TPW involves subtracting absolute plate motion (in the mantle reference frame) from a continent's apparent polar wander path (APWP), that describes its motion with respect to the rotation axis. Conventionally this is done by rotating paleomagnetic data from the continents to a common reference frame, constructing a global apparent polar wander path (e.g., Torsvik et al., 2012), and then subtracting absolute plate motion away. That said, TPW corrected paleolatitudes for Hawaii and Kerguelen are incompatible with being caused entirely by TPW (Antretter et al., 2002; Torsvik et al., 2017). As such, a component of hotspot drift (with respect to the mantle) has been inferred from these results. Ridge-plume interactions have also been suggested to account for latitude changes at the time these hotspots were passing over or nearby ridges (Site 1140 for Kerguelen and Detroit Seamount for Hawaii, Antretter et al., 2002; Tarduno et al., 2009), suggesting that lithosphere-asthenosphere topography might play some role in augmenting hotspot volcano distribution.

Paleolatitudes for both of these oceanic hotspots were calculated from inclination-only drillcore of seamounts, by determining a virtual geomagnetic latitude (λ_{VGL}) for each flow mean inclination (I_m) (Doubrovine and Tarduno, 2004), and then solving for the maximum-likelihood estimate of virtual geomagnetic latitudes (McFadden and Reid, 1982; Arason and Levi, 2010). The precision of such an approach is limited by the number of flows sampled, and, as samples are all derived from the same location, also might be influenced by local, non-dipole contributions (Torsvik et al., 2017). In contrast, continental hotspot tracks offer several advantages over their oceanic counterparts. They are relatively easier to obtain samples from, while full orientation information affords complete treatment of magnetization vectors, in contrast to inclination only data. This last factor is a major advantage, as contemporaneous results from

other rocks can be used in reconstruction, affording both greater precision, as well as being less prone to any local, non-dipole effects. Any position on a continent can be reconstructed to its ancient paleolatitude given a corresponding paleomagnetic pole, by computing the paleocolatitude (p), the angle between pole and site positions (Butler, 1992). In this case the uncertainty on the pole (A_{95}) can be used to compute the uncertainty on the paleolatitude. Given coordinates of an extinct hotspot volcano and a paleomagnetic pole corresponding to the age the volcano was active, its paleolatitude at that time can be found.

Intraplate volcanism is widespread in Eastern Australia during the Cenozoic (**Figure 1**) and provides an ideal natural laboratory to study hotspot motion. Three types of magmatic provinces are classified onshore: 1) central volcanoes are complexes with differentiated magmatic products dominated by early basaltic flows and late-stage, felsic plugs intruding central vents; 2) leucitite suite edifices are low-volume features formed by distinctive potassium-rich, silica-poor lavas; and 3) lava fields are characterized by thin, effusive flows, scoria cones and maars (Wellman and McDougall, 1974). The location and age of lava fields follow no obvious trends (Vasconcelos et al., 2008), and are thought to result from edge-driven convection and shear-induced decompression melting over localized regions of thinner lithosphere (Conrad et al., 2011; Davies and Rawlinson, 2014; Aivazpourporgou et al., 2015; Rawlinson et al., 2017). In contrast, the central volcanoes and leucitite magmatic provinces define clear age-progressive tracks that reflect the Cenozoic motion of Australia over several hotspot anomalies. These tracks provide an important link between hotspots in the Pacific and Indo-Atlantic, and, together with the fact that they have not been used to determine hotspot reference frames, mean that their paleolatitudes provide a useful test case for evaluating the global moving hotspot reference frame (GMHRF), global apparent polar wander pathl (APWP) and their associated TPW estimates (Doubrovine et al., 2012; Torsvik et al., 2012).

From the roughly North to South trajectory of eastern Australian hotspot tracks, it is generally suggested that the underlying hotspots moved little with respect to one another,

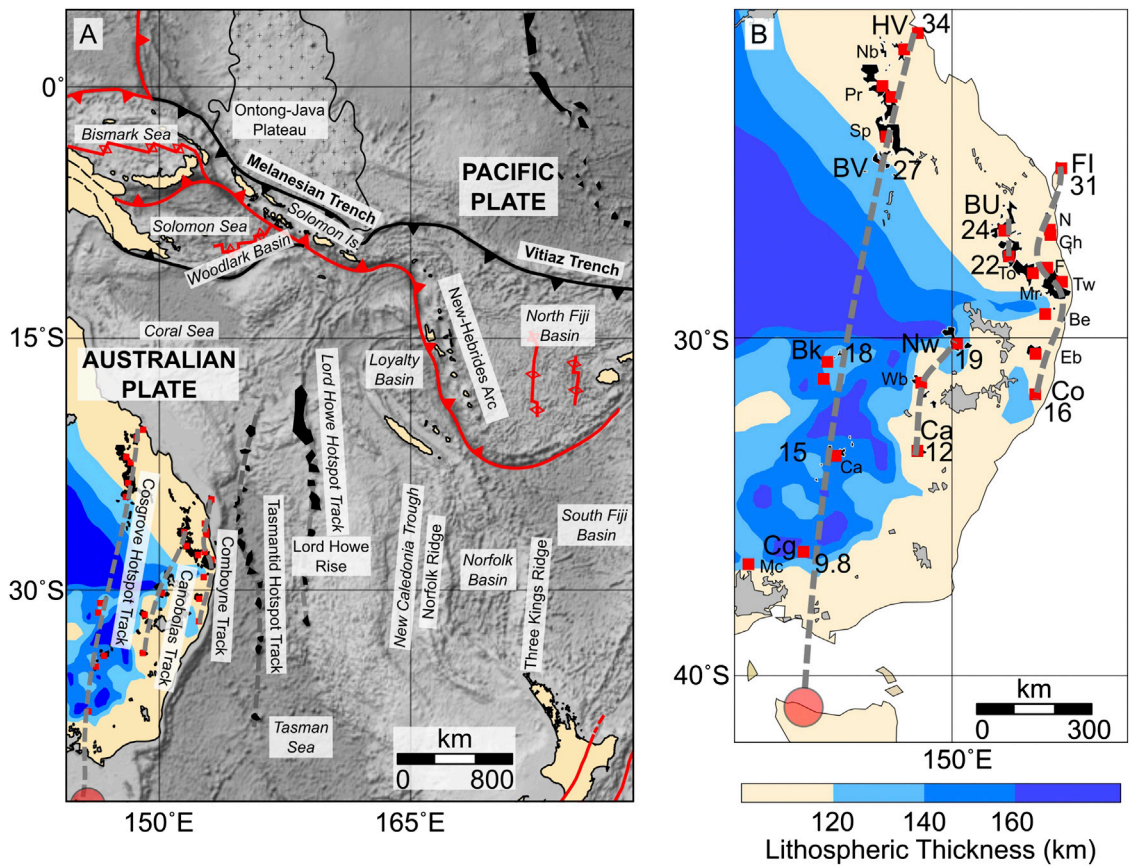

FIGURE 1 | Distribution of eastern Australian Cenozoic Volcanism, hotspot tracks and lithospheric thickness. Central volcanic fields are indicated in black, lava field provinces in gray (Wellman and McDougall, 1974). Hotspot tracks are indicated by dashed gray lines, with ages (in Ma) indicated (Cohen et al., 2007; Cohen et al., 2008; Knesel et al., 2008; Sutherland et al., 2012; Cohen et al., 2013). The red circle indicates a 100 km diameter melt region for the Cosgrove hotspot above its present day position as inferred from tomography (Montelli et al., 2006). HV, Hillsborough Volcano; Nb, Nebo Volcano; Pr, Peak Ranges (North and South); Sp, Springsure Volcano; BV, Buckland Volcano; Bk, Byrock Leucitite; Ca, Cargelligo; Cg, Cosgrove Leucitite; Mc, Macedon; FI, Fraser Island; N, Noosa; Gh, Glasshouses; F, Flinders Volcano; Tw, Tweed Volcano; BU, Bunya Volcano; To, Toowoomba Volcano; Mr, Main Range; Be, Belmore Volcano; Eb, Ebor Volcano; Nw, Nandewar Volcano; Wb, Warrumbungle Volcano; Ca, Canobolas Volcano; Co, Comboyne Volcano.

and that volcano termination accurately reflects the location of the underlying mantle plume (McDougall and Duncan, 1988; Knesel et al., 2008; Cohen et al., 2013; Crossingham et al., 2017; Mortimer et al., 2018). By applying linear, or segmented linear regression to fit volcano latitude with age along individual tracks, these authors derived rates for Australian plate motion from the slope, although strictly speaking, these estimates represent the relative motion between each hotspot and the Australian plate. Longitude is ignored in these analyses, and although multiple hotspots on the same plate occur, tests for relative motion between these hotspots have not been performed. If the fixed hotspot assumptions are valid, then hotspot tracks will be concentric small circles of one another, as would be expected for plate motion alone over a set of stationary hotspots (Cox and Hart, 1986). As such, the angular distance between pairs of hotspots should remain constant with time (Harada and Hamano, 2000; Wessel et al., 2006). Mantle modeling (dataset S1, Doubrovine et al., 2012) suggests eastern Australian hotspots moved relatively little with respect to one another and the GMHRF ($\leq 2^{\circ}$). Over the ~35 Ma of eastern Australian hotspot activity, this might manifest as much as ~ 350 km of relative motion between hotspot pairs, but actual tests of relative motion between these hotspots have not heretofore been carried out.

The Cosgrove track comprises the longest (~2,250 km) and westernmost of Australia's hotspot tracks, beginning with the formation of Hillsborough Volcano (34-33 Ma) in central Queensland, followed by Nebo, Peak Range, Springsure and Buckland Volcanoes along a ~ 450 km SSW trend (Cohen et al., 2013; Crossingham et al., 2018b). Volcanism along this track resumes south of a ~ 650 km magmatic gap with the eruption of leucitite magmas (18-10 Ma) along a younger, ~ 650 km segment (Cohen et al., 2008; Davies et al., 2015). The magmatic gap is attributed to suppression of partial melting below thick lithosphere, while reduced volumes of magma production, and a shift in lava composition that characterize the southern segment are attributed to diminished melt fractions produced under intermediate thickness lithosphere (Davies et al., 2015). Volcanoes of the Newer Volcanic Province (~2.5 Ma) lie to the South of the Cosgrove leucitite along the predicted path of the hotspot, although the nature of their source is less clear. The relatively large E-W extent of this region has conventionally been used to argue against a plume related source, although Rawlinson et al. (2017) suggest that entrainment of plume material in an existing edge/shear driven upwelling region might explain its extent, and temporal coincidence with the Cosgrove hotspot. The present day position of this hotspot is estimated at 41°S, 146°E with tomographic methods (Montelli et al., 2006) although a clear, deep plume tail is not observed (French and Romanowicz, 2015).

Along the coast of eastern Australia the Comboyne hotspot track defines a SSW trend bookended by Fraser Island (~ 31 Ma) and Comboyne volcanoes (~ 16 Ma) (Ashley et al., 1995; Cohen et al., 2007; Knesel et al., 2008). A peculiarity of this track is the relatively long-lived, and higher volume locus of volcanism at the Main Range-Tweed provinces, which is associated with eastward offset from the otherwise linear trend of volcanoes (Knesel et al., 2008). It, as well as deflections in the Tasmantid and Lord Howe seamount tracks has (under the assumption of hotspot fixity) been used to suggest a transient slowdown of the Australian plate between 26–23 Ma. Linking of these hotspot track distributions with unequivocal collision on Australia's margin has proved difficult to reconcile with geologic evidence. Originally the slowdown was used to infer the timing of collision between the Ontong-Java Plateau and the Melanesian arc, halting Pacific Plate subduction under the Australian Plate, and leading to Australian Plate subduction along SW Solomon Island trench (subduction polarity reversal) (Knesel et al., 2008). Such a model implies Oligocene shutdown of Melanesian Arc volcanism, together with arc deformation and terrane exchange of the Solomon Islands, from the Australian Plate, to the Pacific. Although reduced in volume, volcanism continued in the Solomon Islands through Oligocene to Miocene times (Hackman, 1980; Chivas, 1982), seismicity and swath mapping indicate that subduction along the Melanesian Arc continued through this interval (Petterson et al., 1999), paleomagnetic poles do not indicate terrane exchange of the Solomon Block from Australia to Pacific during the Oligo-Miocene (Musgrave, 1990; Musgrave, 2013), and deformation of the arc began in Pliocene times (Petterson et al., 1997; Petterson et al., 1999). Alternatively, slowdown may have been associated with collision in Papua New Guinea (Jones et al., 2017), although the collisional history of this region is complex, and making an unambiguous link therefore is challenging.

Two remaining segments of volcanoes also occur onshore, from Bunya-Toowoomba (24–22 Ma), and Nandewar-Canobolas (19–12 Ma), that have been grouped together as the Canobolas hotspot track (Davies et al., 2015), although a track joining these volcanoes would have a large westward offset between Toowoomba and Nandewar volcanos, not observed in either tracks onshore, or the two tracks offshore. The close temporal and spatial association between Bunya-Toowoomba and Main Range-Tweed volcanoes suggest these Bunya-Toowoomba volcanoes might be associated with the Comboyne hotspot, rather than a separate hotspot. The lack of younger volcanoes South of Comboyne and Canobolas volcanoes, together with decreasing estimated volumes of magma at progressively younger volcanoes (Jones and Verdel, 2015) is good evidence that these hotspots are now extinct, their plume tails presumably shearing away once their flux decreased below a critical value (Steinberger and O'Connell, 1998).

In the Tasman Sea are the Tasmantid (~33.5–6.5 Ma) (Crossingham et al., 2017), and Lord Howe (~ 28 – 4 Ma) (McDougall et al., 1981; Mortimer et al., 2018) seamount chains. Courtillot et al. (2003) estimate the present day position of Tasmantid hotspot to be (39°S, 150°E) and Lord Howe to be (33°S, 159°E) although these are not included in the Montelli et al. (2006) hotspot catalog. The youngest dated volcanoes along these chains are both ~ 6.5 Ma, at Gascoyne Seamount (Tasmantid) and Lord Howe Island (Lord Howe), and lie to the North of the predicted present day positions, although several smaller seamounts exist to the South of each of these estimates, that might be younger, related volcanoes. An unnamed seamount, possibly part of the Tasmantid hotspot track occurs at 40.1°S, 157.1°E, and the Flinders and Heemskerk/Zeehaen seamounts at 34.6°S, 159.8°E and 36.3°S,

159.8° E, respectively, might be part of the Lord Howe hotspot track. Without dating of rocks at these locations it is unclear if these hotspots remain active today, or went extinct in the Pliocene.

2. MATERIALS AND METHODS

2.1. Hotspot Geometries

We performed geometric analyses on hotspot tracks in eastern Australia to evaluate predicted present day positions for them, and to explore the possibility of relative motion between eastern Australian hotspots. To estimate present day positions of hotspots we determined motion paths based upon Doubrovine et al. (2012) plate model, anchored to well dated volcanoes along each track.

Available age data along each track are influenced by geological preservation, and so are not uniformly sampled with time. As such, it is required to approximate track geometry and for this we use spherical splines (Thompson and Clark, 1981). The smoothing parameter controls the trade-off between smoothness of the spline curve, and accuracy of the approximation. Smaller values will more accurately fit the data, but the spline will have greater curvature (smoothing of one will interpolate between points), while greater values will reduce the curvature, by allowing departure of the curve from data. We follow the criteria of Doubrovine et al. (2012) in evaluating appropriate smoothing parameter 1) track geometry should be accurately reproduced, 2) ages along curves should increase monotonically, and 3) the distance between predicted and observed track locations should not exceed 150 km. Angular distances of less than this could conceivably be the result of lateral magma transport between the hotspot melt region and its surface termination (Sleep, 1996; Sleep, 1997). The lack of ages for many of the seamounts along the Lord Howe track is problematic, and we interpolate ages for undated seamounts along this track using our linear latitude model for this track. To test for relative motion between hotspots, we compared angular distance between pairs of tracks using spline fits. If angular distances remain constant with time, we can be confident that particular pair of hotspots have remained stationary with respect to one another. Conversely, changes in this distance over time indicate relative motion between the two hotspots compared.

2.2. Paleomagnetic Poles From VGP Level Data

Reconstruction of paleolatitudes using the pole approach requires a robust set of poles over the time interval concerned. For reference, we compare paleomagnetic poles presented in Hansma and Tohver (2019), as this work presents a significant number of new Australian paleomagnetic results, together with a comprehensive review of existing Cenozoic paleomagnetic data. While these poles do justice in reconciling paleomagnetic data with the speading history between Antarctica and Australia, we take advantage of the commonplace overlapping magnetization ages between Australian paleomagnetic studies to systematically determine combined paleomagnetic poles for the Cenozoic interval, accounting for positional uncertainty (A_{95}) as well as uncertainties in the age of paleomagnetic data by randomizing VGP ages within their bounds and sampling VGPs with replacement to generate bootstrap pole samples (Tauxe et al., 1991). This allows for a more robust characterization of Australia's APWP during the Cenozoic.

Our reasoning for this approach is justified because although PSV timesacles range from 10^4 to 10^5 years (approaching 5 Ma at extremes), limited geological preservation routinely makes adequate sampling impractical, if not impossible at this temporal resolution, with $\sim$100 sites required for confident sampling (Tauxe et al., 2003). APWPs are commonly fit to study-based paleomagnetic poles, so two averaging steps are applied, firstly VGPs within each study are averaged to their study based pole position, then these poles are averaged again. Multiple averaging is known to introduce bias, and unlike averaging VGPs, where PSV is being sampled, there is not a clear phenomonological basis for averaging between poles. The averaging intervals commonly applied during this stage are 10 Ma or larger in duration, larger than PSV timescales and, usually, also larger than the intervals of time represented by VGPs from each study. A slightly better approach often used is to weight each pole by the number of sites, but transitional VGPs are often dealt with inconsistently between studies. Others have grouped VGPs from multiple studies into combined poles (a concept dating to at least as early as McElhinny et al., 1974), and the notion that grouping of VGPs based on geology is arbitrary, is not new. This approach becomes problematic for the case of three studies (A, B, and C) each a collection of VGPs: pole A overlaps (in time) with B, and B with C, but A and C do not overlap. How should VGPs from these three studies be combined? A possible reason why, in spite of the growing number of temporal overlaps between paleomagnetic studies, that the issue of double averaging in paleomagnetism has received less attention, is that the identification of suspect data (Van der Voo, 1990), and improvement in sampling and laboratory methods (e.g., Kirschvink, 1980) was of larger concern in the effort to define reliable APWPs deeper in Paleozoic time.

We provide a synthesis of the extant body of site-level paleomagnetic data for Cenozoic Australia (557 sites total, excluding undated sites from laterites) from studies where basic demagnetization techniques have been performed. Magnetization ages have been updated using modern geochronoloic and biostratigraphic constraints (**Figure 2**; **Supplementary Table S1**). Multiple studies of coeval rocks from different formations allow us to both validate the consistency of results between studies, and also develop a more robust technique for the determination of paleomagnetic poles, compared to traditional grouping of data by individual geologic formation, and subsequent averaging of these formation-based poles. Our new approach returns the calculation of a paleomagnetic pole to site-level statistics, using VGPs of equivalent age, incorporated from potentially multiple coeval geologic formations. We argue that this approach is superior to existing methods because it provides 1) poles for specific age intervals based on the largest possible dataset, 2) a more robust averaging of PSV during intervals constrained by multiple

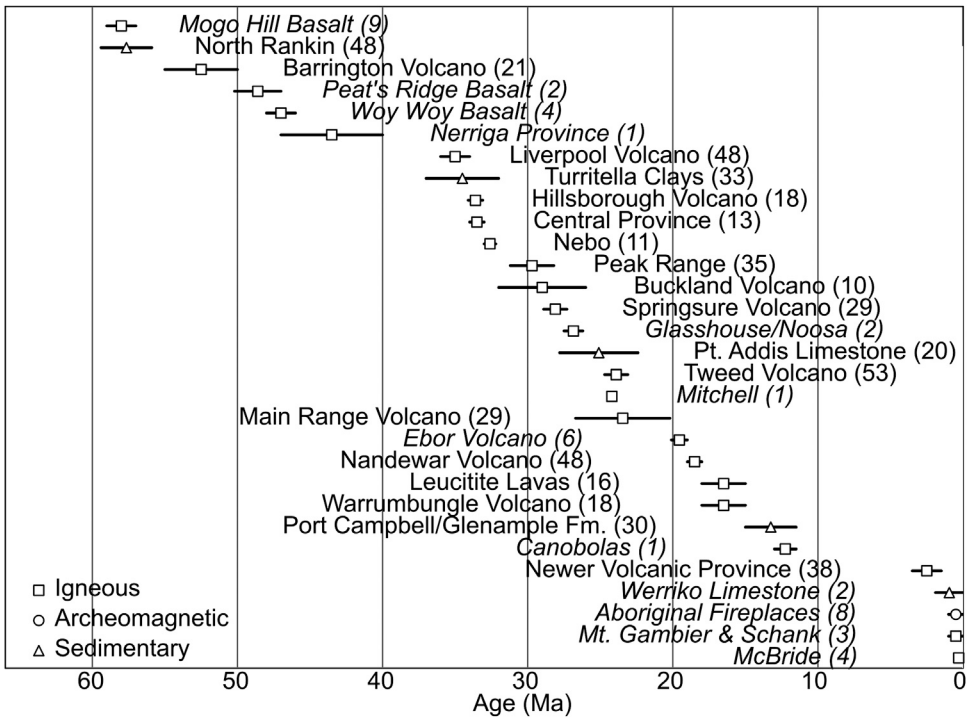

FIGURE 2 | Magnetization age bounds for Australian Cenozoic paleomagnetic data. Number of sites indicated in parenthesis. Studies are italicized where limited sampling indicate that secular variation has not been averaged within the region itself.

studies, 3) consistent identification of transitional VGPs, and 4) systematic treatment of VGP age uncertainties. A further advantage is that this method reduces to a traditional, study based average in the case of paleomagnetic data that do not overlap in time.

We compile the directional vector of individual VGPs for each site, together with upper and lower age bounds for the magnetization. Where multiple, comprehensive studies of a province have been conducted, e.g., replication studies of Barrington Volcano (Wellman et al., 1969; Hill et al., 2002), and the Newer Volcanic Province (Rahman, 1971; Opdyke and Musgrave, 2004), we exclude the legacy study to maintain VGP independence, and prevent duplication. We then perform common mean tests between contemporaneous VGPs from different studies formations to ascertain whether the results across coeval intervals are self-consistent. This validation process is described in detail in Hansma and Tohver (2018), Hansma and Tohver (2019), but we note here that blanket demagnetized sites from the Older Volcanics (Mumme, 1963) reject common mean tests with multiple coeval studies, and are for this reason excluded. In some cases common mean testing is rejected marginally [e.g., Oligocene results described in Section 3.5.5 of Hansma and Tohver (2019)], but these all fall within one circular standard deviation of each other. It is plausible that VGPs from these studies, taken individually, each represent a slightly biased sampling of PSV, manifesting itself as slight differences between the means of each study. Rather than selecting a subset here, it is more robust to include all of these results in analysis. Of the 557 VPGs that pass selection, 220 are blanket demagnetized ($Q \geq 4$ for these studies), although most of these magnetization directions are supported by more modern sites that sampled rock from the same region and employed stepwise demagnetization. Only 90 VGPs, specifically from Main Range, Liverpool Volcano and the Glasshouse Mountains are not directly corroborated by more modern demagnetization on the same rocks. Coeval studies employing stepwise demagnetization for all these time intervals exist, and as described above, common mean tests do not identify these results as suspect.

By first performing a common means test for contemporaneous VGP populations, we provide a better a priori test for suspect results, giving context to "quality filters" that are generally applied to individual formation-based poles (Van der Voo, 1990; Besse and Courtillot, 2002). Filtering based on a fixed quality score threshold is known to result in false positives and negatives, a caution that was both originally stressed (Van der Voo, 1990) and later reiterated (Van der Voo, 1993). Contextualization of results in the manner described above, followed by examination of their quality scores where differences are identified, does better justice to existing data. It can help minimize the false exclusion of lower score, but otherwise apparently reliable data, while also preventing the inclusion of any suspect data that quality schema fail to recognize.

To calculate poles, we apply a sliding-window approach after determining an optimum window size for the dataset. Two processes contribute to the observed distribution of VGP data with time: 1) short term variation as a consequence of PSV, and 2)

long term variation caused by APW. There is a natural trade-off between averaging PSV, which is more reliably achieved with larger intervals, and minimizing the averaging of APW, where the smaller intervals are desirable. To identify the optimum interval we systematically vary the window size from a narrow interval, to progressively larger and larger ones (here from 1 to 20 Ma). At narrow intervals PSV is unlikely to be adequately sampled; as such the variance in VGP scatter across the dataset is expected to be large. As window size is increased, this variance will stabilize as PSV is sampled. Similarly, the median VGP scatter across all intervals is examined for different window sizes and is expected to be unstable when these are narrow, stabilize as PSV is sampled, and then gradually increase as the interval size grows beyond the ideal interval, due to the averaging of increasing amounts of APW together with PSV.

For our dataset, window sizes below 10 Ma produce poles with large ranges of S, indicating that for some intervals of the Cenozoic Australian VGP dataset, such narrow window sizes do not adequately sample PSV (**Figure 3**). Window sizes ~ 10 Ma and greater have less variation in VGP scatter, but the median VGP scatter gradually increases, a consequence of averaging significant amounts of APW due to plate motion, together with PSV. As such, we applied a 10 Ma sliding window, with 1 Ma steps over the data. Our results here suggest that it is likely that the nature of paleomagnetic sampling through time, dictated in large part by incomplete geological preservation, plays a larger role in limiting paleomagnetic resolution than shorter timescale PSV.

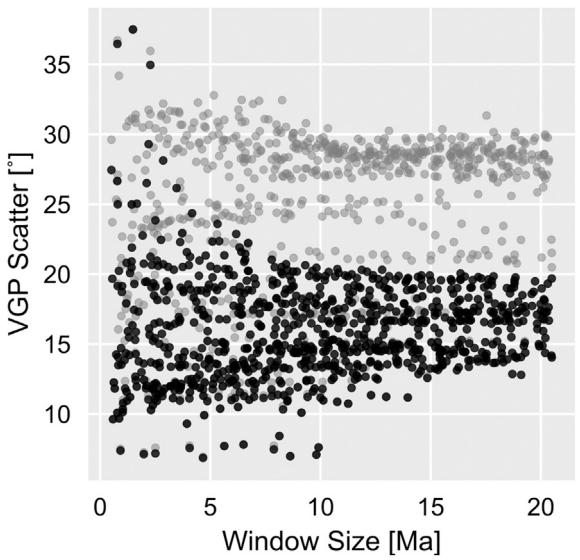

FIGURE 3 | Variation in VGP scatter across intervals of increasing window size for Australian VGPs during the Cenozoic. Black points are filtered with a variable VGP cutoff, gray points are unfiltered (each point is randomly jittered about their window size to prevent overplotting by Ma). The wide range of values at interval sizes (< 10 Ma) indicates that for some intervals, PSV is not adequately sampled, while the gradually increasing median values for S above 10 Ma is indicative of APW being averaged, together with PSV when intervals this large are used.

For reference, the procedure for determining poles is depicted in **Figure 4**, which we will describe in detail here. We calculate a Fisher mean pole where ≥ 50 sites are present, and where VGPs within the interval have an age range of > 3.5 Ma, and less than the window size (10 Ma). We identify transitional sites systematically with a variable VGP cut-off angle (Vandamme, 1994). VGP ages within each window are not usually normally distributed, so we assign the median age, rather than the center of the interval, or the mean VGP age to the pole calculated. We identify age outliers where VGP age is greater than 1.5 times the inter-quartile range, but this only excludes one datum, the 9.8 Ma Cosgrove leucitite (Hansma and Tohver, 2018), that occurs isolated in time from other Australian VGPs. Without any thresholding, for either minimum number of sites or minimum intervals of time, edge-effects associated with gaps and sparse intervals in the VGP record adversely affect the result near their boundaries. In our implementation, minimum time and site thresholding can be applied to the result after the fact (by setting these values to zero) but will increase runtime as the VGP-cutoff angle (Vandamme, 1994) is determined iteratively and is called more often. The effect of gaps in the VGP record are managed in three ways: 1) if a window is incremented in time, but no new VGP data are found, then this pole is suppressed, because it is equivalent to narrowing the window size, 2) a minimum number of sites prevents pole calculation in sparsely sampled intervals, and 3) a minimum range for VGPs within each interval prevents pole calculation in intervals where, although enough sites are present, they are concentrated into a narrow time range (i.e., the effective PSV sampling interval is not met). Where the sliding window transitions over well represented, to poorly represented data almost completely, this last threshold is triggered.

For the Australian Cenozoic dataset, the early Eocene represents a sparsely sampled interval, with a few sites distributed within it. The minimum sites threshold prevents poles from being calculated here. The minimum time interval threshold was chosen to prevent the calculation of poles where the ages of VGPs are concentrated into a narrow range, far below than the 10 Ma suggested by VGP scatter analysis described earlier. In our dataset, this affects one search interval, between 34 and 44 Ma, where VGPs are concentrated in the 2 Ma between 34 and 36 Ma, and there are few VGPs in the remaining 8 Ma (36–44 Ma). Such narrow intervals of VGP averaging are unsatisfactory given VGP scatter analysis (**Figure 3**) indicating these poles are not robust. Interquartile ranges for sites within this interval were all below 1.5 Ma, with ranges of < 3.5 Ma. The pole longitudes for this interval lie at ~100°E, 20° away from poles in the previous interval and the implied rotation for Australia is implausibly rapid. Examining VGP scatter for the poles found in this interval reveals they have significantly lower scatter S = 13.5° than poles in the interval before (33–43 Ma), as well as for older poles (although the older poles are Paleocene in age). This magnitude of VGP scatter is also lower than expected values based on geomagnetic field models (Tauxe and Kent, 2004), given that Australia during the early Oligocene was at middle to high latitudes >35°S.

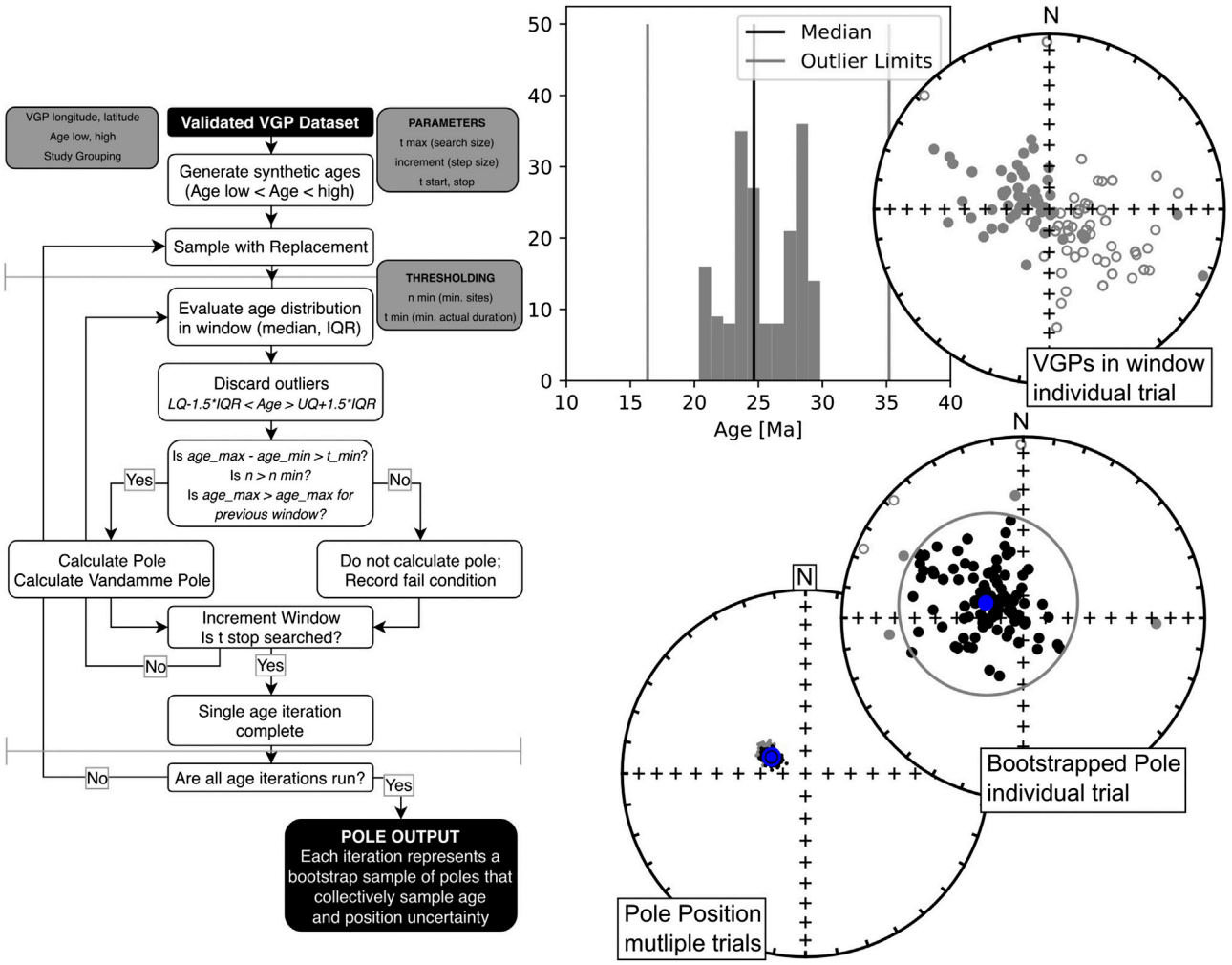

FIGURE 4 | Control flow diagram (**left**) describing method used to generate bootstrapped poles and an accompanying example (**right**) for the 20–30 Ma search window. t start and t stop represent the age range desired for the entire search (the Cenozoic in this case), t max being the window size. Thresholding rules n min (minimum number of sites) and t min (minimum age range for VGPs in a given interval) can be specified. Thresholding can, of course, be applied to pole results after the fact (by setting n min and t min to zero), but results in longer runtime for reasons described in text. Age distributions within each interval are evaluated first, and thresholding rules applied (in the example histogram these fall beyond the search domain as VGPs are well represented over the interval). A bootstrap paleomagnetic pole is calculated, both including and excluding transitional sites (the example showing the variable VGP cutoff-angle in gray) (Vandamme, 1994). The window is then incremented, and the process repeated for multiple trials until the search is complete, leading to a collection of bootrapped poles from which the pole position and uncertainty can be estimated.

There is uncertainty associated with the individual age of every VGP, regardless of accuracy and precision of the geochronological assay of the rock unit. This introduces a source of uncertainty in the set of poles that lie within a given interval, as VGPs with magnetization ages that straddle its boundary may, or may not fall within it. Although this is conventionally ignored in paleomagnetic analysis, we account for this by randomizing the set of VGP ages within their age bounds, and sampling with replacement (1,000 iterations, **Supplementary Table S2**). When reconstructing a feature over a given interval of time, the 95% confidence region surrounding bootstrapped poles with median ages within the interval is used.

2.3. Paleolatitude Reconstruction

Paleolatitudes were calculated using distance between corresponding paleomagnetic poles and sites for both for hotspot volcanoes (where hotspot magmas terminated at the surface and have been dated with geochronologic methods), as well as for the estimated position of each hotspot over time, using aforementioned spline fits (Section 2.1). This was done to quantify hotspot position with respect to the spin axis through time for each hotspot. Individual volcano estimates are based upon available geochronologic data presented in existing literature, following preferred ages of original authors (McDougall et al., 1981; McDougall and Duncan, 1988; Ashley et al., 1995; Cohen et al., 2007; McQueen et al., 2007; Cohen et al.,

2008; Mortimer et al., 2010; Sutherland et al., 2012; Cohen et al., 2013; Crossingham et al., 2017; Mortimer et al., 2018; Crossingham et al., 2018a; Crossingham et al., 2018b). $^{40}Ar/^{39}Ar$ results, where available, were preferred, but K-Ar ages for Lord Howe Island (McDougall et al., 1981) were included following Mortimer et al. (2018). Several (20 total) age analyses were present in figures, but absent in tabulated data, and were digitized from figures: Cohen et al. (2008, **Figure 7**) includes ages for Nandewar, Warrumbungle, Canobolas, and Macedon volcanoes, while Mortimer et al. (2018, Figure 7) shows an age for Gifford's Guyot. The 2σ values in these cases were estimated from data point size, this value generally being larger than quoted errors for tabulated age data within these papers, and is 0.6 Ma for those from Cohen et al. (2008) and 1.0 Ma for Gifford's Guyot. For each sample, paleomagnetic poles with median ages within the 2σ uncertainties of age analyses were used for reconstruction. Hotspot locations that might not precisely coincide with volcano terminations were estimated using aforementioned spline fitting.

There are two processes that can affect observed paleolatitudes for hotspots, either their independent motion in the mantle, or the changing moment of inertia of the solid Earth (relative rotation between the solid Earth and the spin axis). Paleolatitudes for the present day position of hotspots were corrected for TPW using the preferred synthetic global apparent polar wander path (and its uncertainties) presented in Torsvik et al. (2012) together with the plate rotations relative to the GMHRF presented in Doubrovine et al. (2012), following the procedure described in Torsvik et al. (2017).

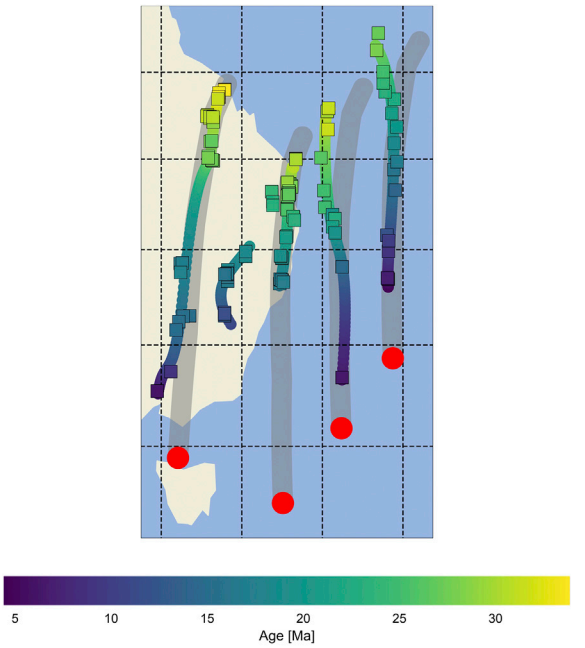

FIGURE 5 | Spline fits to eastern Australian hotspots based on geochronologic data (squares, Ashley et al., 1995; McDougall et al., 1981; McDougall and Duncan, 1988; Cohen et al., 2007; McQueen et al., 2007; Cohen et al., 2008; Knesel et al., 2008; Mortimer et al., 2010; Cohen et al., 2013; Crossingham et al., 2017; Mortimer et al., 2018; Crossingham et al., 2018a; Crossingham et al., 2018b; Sutherland et al., 2012). Present day positions are shown in red, based upon motion paths (in gray) derived from Doubrovine et al. (2012) (**Table 1**).

3. RESULTS

3.1. Geometric Analysis

The present day position for each hotspot was predicted by defining a motion path anchored to a well dated volcano at the age of activity along each track (**Table 1**) using the plate model of Doubrovine et al. (2012). The motion paths for each hotspot are depicted in (**Figure 5**). The estimate for Cosgrove lies close to the position inferred by Montelli et al. (2006), being half a degree farther North in latitude and the same longitude. The estimate for Tasmantid hotspot is remarkably close to that estimated by Courtillot et al. (2003), but the position given by these authors for the latitude of Lord Howe hotspot corresponds to Lord Howe Island, where volcanic rocks are dated at ~6 Ma (McDougall et al., 1981). Our estimate is farther South with a comparable longitude (35.7°S, 159.4°E), and lies close to the undated Heemskerk/Zeehaen seamounts.

Spline fits (**Figure 5**) were used to interpolate along hotspot tracks without invoking parametric assumptions inherent to linear models. The spline fit provides the best estimate for the position of the hotspot at any given time because individual volcanoes may not terminate precisely above their hotspot, and volcanism along each track is not always continuous. With one exception, misfits between spline fits and volcanoes are less than our cut-off distance. Only one datum from Comboyne volcano (sample Q83 from Cohen et al., 2007) has a larger misfit (178 km), but other analyses from this same area are suitably fit. The paucity of ages along the Lord Howe hotspot track meant that several seamount ages were interpolated using a linear age-latitude model and the spline fit using these seamounts. The angular distance between predicted hotspot location at any given time and their volcano termination is normally distributed away from the predicted hotspot center, with $2\sigma = 90$ km (**Figure 6**).

The angular distance between spline fits was used to test for relative motion between hotspot pairs during time intervals where both are active (**Figure 7**). Cosgrove and Comboyne hotspots appear most constant, but most hotspot pairs accumulate changes in angular distance over time. The cumulative effect of this is generally small, and within the

TABLE 1 | Estimated present day positions of eastern Australian hotspots derived from motion paths (Doubrovine et al., 2012), and from hotspot catalogs (Courtillot et al., 2003; Montelli et al., 2006) (in degrees N and E). λ indicates latitude, ϕ indicates longitude.

Hotspot Model	Anchor			Catalog	
	λ	ϕ		λ	ϕ
Cosgrove	−40.5	146.4	Hillsborough	−41	146
Comboyne	−42.6	152.5	Fraser Island	—	—
Tasmantid	−39.1	156.2	Derwent-Hunter	−39	156
Lord Howe	−35.7	159.3	Lord Howe Island	−33	159

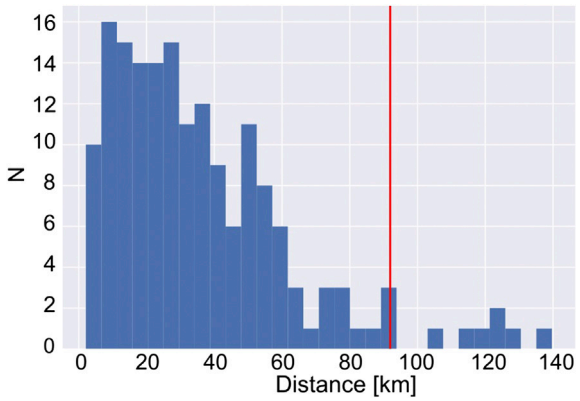

FIGURE 6 | Angular misfit, in kms, between hotspot locations and spline fits. Red line indicates 2σ = 92 km.

uncertainty of spline misfits for both hotspots (±368 km). The largest angular distance change was between Tasmantid and Lord Howe hotspot tracks (382 km), but ages were interpolated along the track and little significance is placed on this result. The second largest was between Cosgrove and Tasmantid tracks (361 km), but this was still within the uncertainties of the spline fit. While consistent with estimates of the relative motion of eastern Australian hotspots based upon mantle flow modeling (Doubrovine et al., 2012, auxiliary dataset 1) it is not necessary to invoke movement between Australia hotspots to explain the distribution of volcanoes along each of their tracks.

Age vs. latitude trends of Eastern Australian hotspot volcanoes have been used to infer changes in Australian plate speeds during the Oligo-Miocene (Knesel et al., 2008; Cohen et al., 2013), but this interpretation is complicated by misfits between eastern Australian hotspot track geometries (**Figure 7**). Plate rate changes implied in these studies occur over narrow time intervals and in our analysis equate to only small misfits between volcano termination and predicted position (**Figure 6**). While they may possibly represent changes in plate speed, they could also reasonably be explained by small amounts (~ 90 km) of lateral magma transport away from the hotspot center.

3.2. Cenozoic Poles for Australia

Our combined paleomagnetic poles are in general agreement with APWPs inferred from sea-floor spreading between Australia and Antarctica during the Cenozoic, as well as conventional APWP analysis (Hansma and Tohver, 2019) (**Figure 8**). Our new approach provides a more continuous record of Australian paleomagnetic poles for intervals that are well-represented by VGPs from penecontemporaneous rock formations. Confidence limits on our poles are more conservative, due to the inclusion of VGP age uncertainties. Pole latitudes change with time at a faster rate after Eocene times, consistent with an increase in Australia-Antarctica spreading rate, from slower NE-SW spreading to faster N-S directed spreading during the Eocene (there is a paucity of Eocene VGP data and more detailed comparison is not possible) (Whittaker et al., 2007; Whittaker et al., 2013). The change in spreading direction, from NE-SW to N-S, cannot currently be

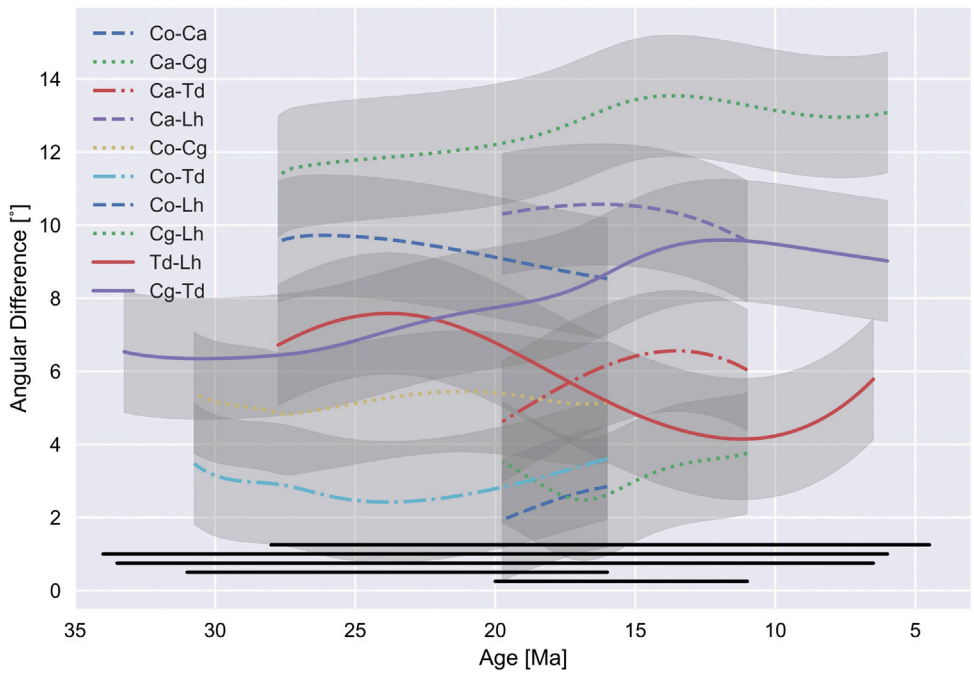

FIGURE 7 | Angular difference between hotspot track pairs with respect to time, showing relative motion between eastern Australian hotspots. Gray regions indicate 95% confidence limits. Black horizontal lines indicate range of ages over which each hotspot is active (from bottom to top: Ca, Canobolas; Co, Comboyne; Td, Tasmantid; Cg, Cosgrove; Lh, Lord Howe).

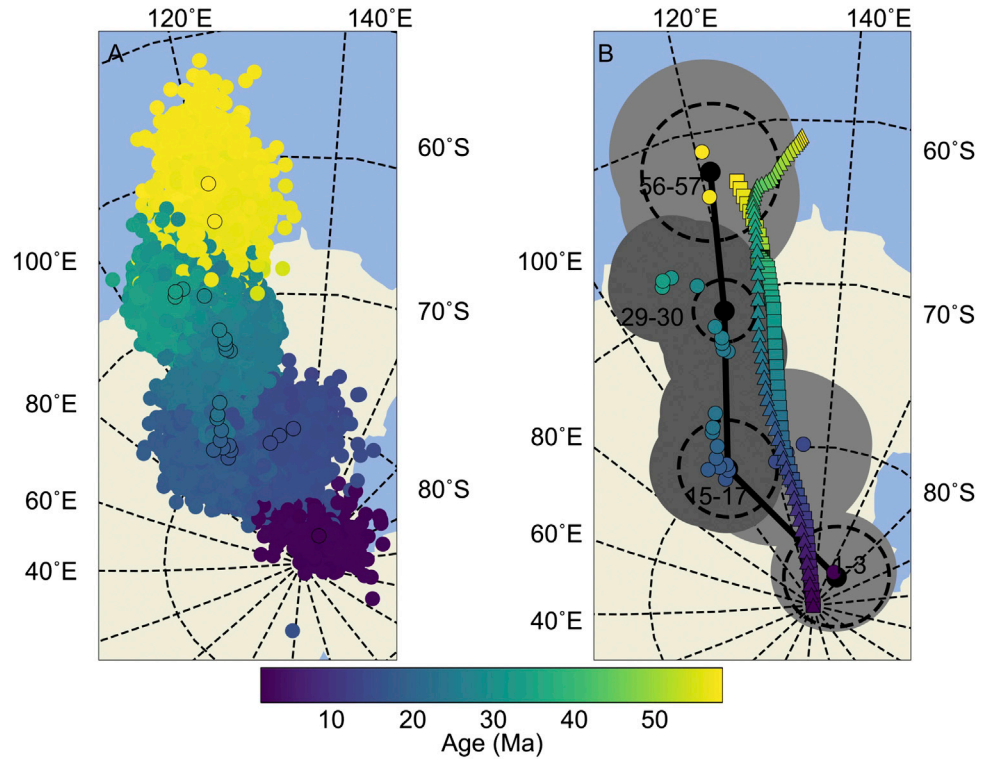

FIGURE 8 | Combined Paleomagnetic Poles for Cenozoic Australia. **(A)** Clusters of similar colored circles without outlines are bootstrap poles, while outlined are markers indicate the poles found in each 10 Ma search window (**Table 2**). Discontinuities in poles through time occur over intervals where VGP data are insufficient for pole calculation (e.g., between 2–12 Ma). **(B)** Poles from A. plotted with their A_{95} ellipses (in gray, darker gray where hotspot volcanoes are active) plotted together with synthetic APWP paths, indicated by squares (Seton et al., 2012) and triangles (Matthews et al., 2016) as well as conventional APWP construction (ages labeled in Ma) (Hansma and Tohver, 2019).

resolved from Australian Paleocene paleomagnetic data. For convenience, **Table 2** gives a summary of poles within each search window, while **Supplementary Table S2** gives results for all bootstrap samples.

In the 0–10 Ma interval, paleomagnetic data mostly come from the Newer Volcanic Province (Opdyke and Musgrave, 2004), and here our pole calculation reduces to the pole position for these VGPs. This demonstrates that where VGPs from different studies do not overlap continuously in time our method reduces to a conventional pole calculation.

VGP scatter for bootstrapped poles show a decrease from Paleocene times to present day (**Figure 9**). Australia has moved from high latitudes to lower ones throughout the Cenozoic, and a decrease in VGP scatter is consistent with geomagnetic field models and recent lavas (Tauxe and Kent, 2004). Including transitional VGPs increases the scatter because scatter is sensitive to the presence of outliers. Recent lavas from low latitudes have VGPs that are less scattered than those from higher latitudes, and it is remarkable that such an observation can be observed in aggregate through time for Australia.

The proportion of transitional sites identified by variable VGP cut-off is possibly, but not clearly related to reversal frequency (Ogg, 2012) (**Figure 10**). Such a correlation would be expected if transitional sites are chance recordings of magnetic field reversals. Correlation of their normalized values between 15 and 28 Ma, as well as between 55 and 60 Ma is encouraging, but transitional directions are recovered less often than would be expected before 5 Ma, and more often between 28 and 34 Ma. There are numerous reasons for imperfect correlation between these quantities. Transitional VGPs could be over- or under-represented by sampling. Transitional VGPs could reflect magnetic excursions. Other factors that might produce sites with VGPs apparently distant from their means may also play a role (e.g., unrecognized local rotation, local lightning remagnetization, or for the case of blanket demagnetized data, incompletely removed overprints). The interval compared does not contain superchrons, and does not sample intervals of low reversal rate, and as such does not sample the entire range observed for the polarity history of Earth. In spite of this, the correlations between reversal rate and proportion of transitional sites recovered are exciting and warrant further study.

3.3. Paleolatitudes for Australian Hotspots

Despite the relatively large uncertainties inherent in paleomagnetic data and the small effect size expected given TPW manifest since 35 Ma, paleolatitude estimates for eastern Australian hotspots are incompatible with hotspots that are fixed with respect to Earth's spin axis, but within uncertainty are all compatible with

TABLE 2 | Summary Poles (Vandamme (1994) filtered) for 10 Ma search intervals (in degrees N and E). Median age assigned to pole (in Ma), λ indicates pole latitude, ϕ indicates pole longitude, with in degrees, *k*: precision parameter, *n*: number of valid bootstrap samples (out of 1,000), *r*: resultant, and indicates low age bound of search window. For bootstrap samples, unfiltered poles and hotspot paleolatitudes interpolated with spline fits see **Supplementary Material**.

Age	ϕ	λ	α_{95}	*k*	*n*	*r*	$bound_{low}$
2.0	345.5	87.5	3.8	1,346.8	343	342.7	0
14.3	311.6	79.9	4.2	1,130.6	214	213.8	6
14.7	305.5	80.3	5.1	748.4	459	458.4	7
14.9	300.9	80.7	5.3	708.1	734	733.0	8
16.9	280.9	80.5	3.3	1,746.5	1,000	999.4	9
17.1	283.6	80.1	3.4	1,730.4	982	981.4	10
17.6	284.0	79.7	3.3	1,836.6	982	981.5	11
18.0	281.4	79.6	3.4	1,687.6	945	944.4	12
18.2	277.8	79.4	3.6	1,519.0	949	948.4	13
18.7	282.1	79.1	3.5	1,591.9	1,000	999.4	14
20.4	284.4	78.5	3.3	1,829.4	1,000	999.5	15
22.7	285.2	77.6	3.3	1,794.6	998	997.4	16
23.2	286.0	77.4	3.2	1,886.6	1,000	999.5	17
23.5	288.3	76.6	3.4	1,714.1	1,000	999.4	18
24.4	296.6	73.4	3.6	1,517.4	999	998.3	19
24.6	295.7	73.2	3.7	1,459.6	999	998.3	20
25.4	295.9	72.8	3.6	1,494.5	1,000	999.3	21
25.9	296.2	72.5	3.7	1,449.4	971	970.3	22
27.0	295.6	71.8	3.6	1,535.2	1,000	999.3	23
28.7	294.9	69.1	4.0	1,252.2	1,000	999.2	24
31.1	291.3	68.0	3.8	1,371.1	1,000	999.3	25
33.1	289.3	68.3	3.3	1,759.2	1,000	999.4	26
33.3	289.8	68.0	3.2	1,905.1	993	992.5	27
56.4	300.4	64.1	5.5	654.5	651	650.0	48
57.1	300.8	61.3	5.7	603.8	947	945.4	49

hotspots that are embedded in the convecting deep mantle (**Figure 11**). Estimates plotted in **Figure 11** are tabulated in **Supplementary Material**. Contemporary estimates of TPW presented here (Doubrovine et al., 2012; Torsvik et al., 2012) have a resolution of 10 Ma, and even at our finer resolution, our results agree remarkably well with these estimates. Within uncertainties, differentiating between TPW models is not possible. Eastern Australian hotspots lie between the Pacific (Hawaii and Louisville) and Atlantic (New England, Reunion and Tristan) hotspots that constitute the basis for the GMHRF. Paleolatitude estimates from eastern Australian hotspots provide important validation of this reference frame for Oligocene and younger times.

A northward shift of hotspot paleolatitudes between 15 and 24 Ma is observed for both volcanoes and spline interpolated positions along the Comboyne, Canobolas, and Tasmantid tracks, and for interpolated positions along the Cosgrove and Lord Howe tracks where volcano or seamount age data are absent (**Table 2**). To illustrate the magnitude of this, at 23.2 Ma the Comboyne hotspot paleolatitude is $-36.7^{\circ} \pm 3.2^{\circ}$ (300–1,010 km North of the present day position, were it fixed to the spin axis). While this trend is significant for all interpolated positions along hotspot tracks, it is only significantly resolved for age data from volcanoes along Comboyne and Canobolas tracks (where there are numerous ages), as well as for two ages from the Stradbroke and Britannia seamounts on the Tasmantid track.

Before 24 Ma most data plot to the North of a fixed present day hotspot location in the paleomagnetic reference but 95% confidence limits overlap with it. Exceptions are found for an age from Hillsborough Volcano (Sample BC-98; Cohen et al.,

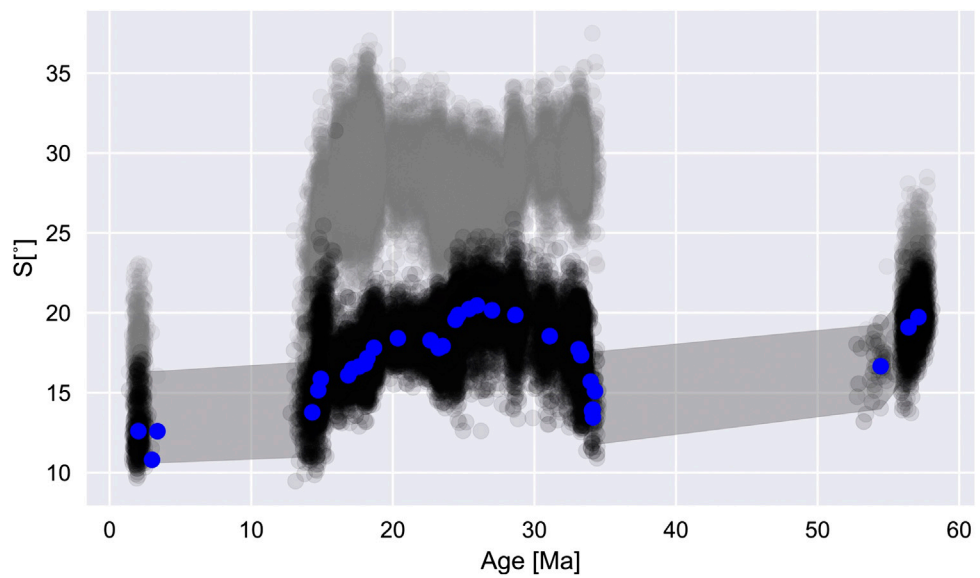

FIGURE 9 | VGP scatter and 95% confidence limits with time for Australian Cenozoic paleomagnetic data (1,000 iterations). Black data with indicate filtered values (Vandamme, 1994), with medians given by blue markers. Gray (unfiltered values) are also shown. Marker transparency of 1% per iteration was used. A trend of decreasing VGP scatter with time is consistent with northward motion for Australia, and falls within expected values based on field models (Tauxe and Kent, 2004) over this time interval.

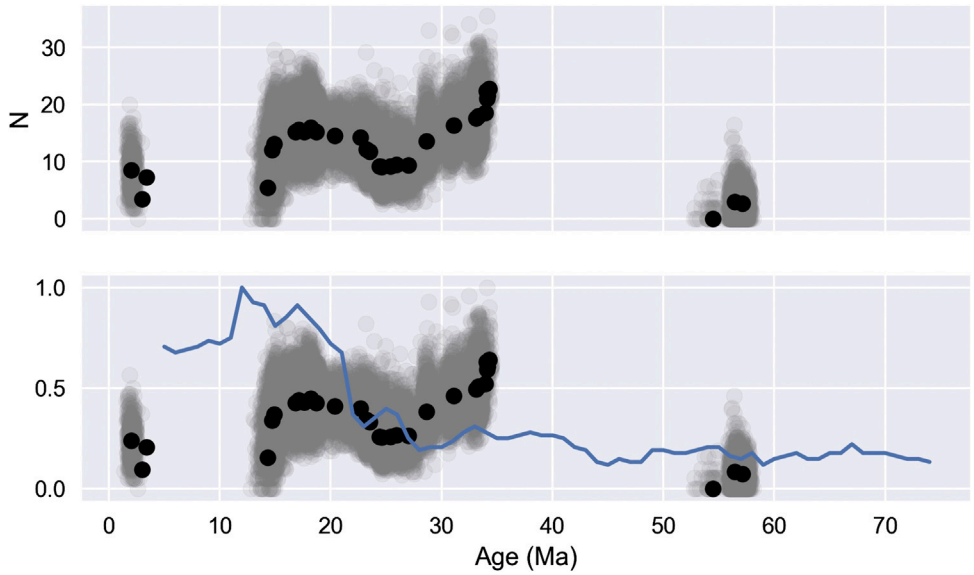

FIGURE 10 | Number of transitional sites identified from Australian continental paleomagnetic data **(top)**, and these values normalized, plotted with normalized reversal rate per Ma for 10 Ma intervals **(below)** (Ogg, 2012).

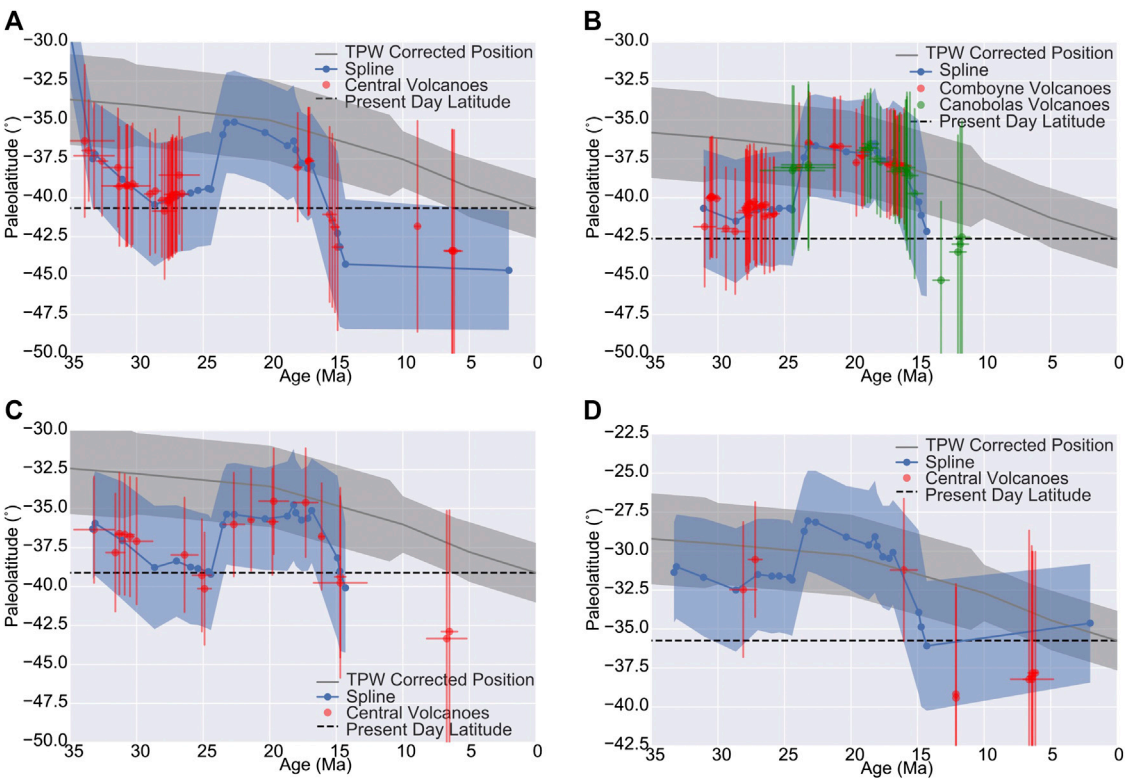

FIGURE 11 | Paleolatitudes for the **(A)** Cosgrove, **(B)** Comboyne, Canobolas, **(C)** Tasmantid, and **(D)** Lord Howe hotspots. Red (and green) data indicate paleolatitude of volcanic rock localities with geochronologic constraint (with 2σ age errors, and 95% confidence on paleolatitudes) along each hotspot track. The blue line represents paleolatitudes for spline fits with shaded 95% confidence region. Tabulated values are given in **Supplementary Material**. The black dashed line is a fixed point, in the paleomagnetic reference frame, at the present day position of each hotspot. The gray line is the TPW corrected position of this point through time (that is, fixed in the mantle reference frame) with associated shaded 95% confidence limits (Doubrovine et al., 2012; Torsvik et al., 2012).

2013) along the Cosgrove track. It has a paleolatitude estimate of −37.0° ± 3.2°, 22–743 km North of the present day estimated position. If the (Montelli et al., 2006) hotspot estimate is used, this distance is 33 km greater. Paleolatitudes for the northern Peak Range (29–30 Ma) also lie North of these positions when using conventional paleomagnetic poles for Australia (Hansma and Tohver, 2019), but overlap in our analysis as pole uncertainties are more conservative, and so larger. Although there is a paucity of age data along the Lord Howe hotspot track (**Figure 11D**), analytical ages as well as our interpolated ages follow a similar trend to the other hotspots. While most analytical ages along the Lord Howe hotspot overlap at 95% confidence with both paleomagnetic fixed, and TPW corrected values, an age from Horse Head (Mortimer et al., 2018; Sample DR15) along the Lord Howe track gives a paleolatitude of −30.5° ± 3.7°, 167 − 988 km North of the present day estimated position were it fixed with respect to the spin axis. As with other eastern Australian hotspots, within uncertainty, this motion is compatible with a hotspot fixed in the GMHRF.

4. CONCLUSION

The distribution of hotspot volcanoes along tracks in eastern Australia, combined with Australia's Cenozoic paleomagnetic data indicate that hotspots moved little with respect to one another and were not fixed to the geocentric axial dipole. That the changes in hotspot paleolatitude with respect to the paleomagnetic reference frame are consistent across all of the eastern Australian hotspots is remarkable, especially so as the motion observed corresponds with the predicted amount of true polar wander over the interval for which these hotspots are active (Doubrovine et al., 2012). The results from eastern Australian hotspots, lie between the Pacific and Indo-Atlantic hotspots used to define this prediction, and so provide important validation for the GMHRF and TPW estimate for Oligocene and younger times.

DATA AVAILABILITY STATEMENT

The datasets analyzed for this study are included in the manuscript/**Supplementary Material**.

AUTHOR CONTRIBUTIONS

ET and JH both worked on the original idea of reconstructing eastern Australian hotspot paleolatitudes. JH developed the combined pole approach and wrote the Python implementation. ET and JH both wrote and edited the manuscript. We wish to thank both reviewers for their insightful comments that significantly improved the final version of this manuscript.

FUNDING

The University of Western Australia supported JH with a Robert and Maude Gledden Scholarship and was supported by an Australian Government Research Training Program (RTP) Scholarship. ET acknowledges Visiting Professor Fellowship from the Fundação CAPES.

SUPPLEMENTARY MATERIAL

The Supplementary Material for this article can be found online at: https://www.frontiersin.org/articles/10.3389/feart.2020.544496/full#supplementary-material

REFERENCES

Aivazpourporgou, S., Thiel, S., Hayman, P. C., Moresi, L. N., and Heinson, G. (2015). Decompression melting driving intraplate volcanism in Australia: evidence from magnetotelluric sounding. *Geophys. Res. Lett.* 42, 346–354. doi:10.1002/2014gl060088

Andrews, D. L., Gordon, R. G., and Horner-Johnson, B. C. (2006). Uncertainties in plate reconstructions relative to the hotspots; Pacific-hotspot rotations and uncertainties for the past 68 million years. *Geophys. J. Int.* 166, 939–951. doi:10.1111/j.1365-246x.2006.03029.x

Antretter, M., Steinberger, B., Heider, F., and Soffel, H. (2002). Paleolatitudes of the Kerguelen hotspot: new paleomagnetic results and dynamic modeling. *Earth Planet Sci. Lett.* 203, 635–650. doi:10.1016/s0012-821x(02)00841-5

Arason, P., and Levi, S. (2010). Maximum likelihood solution for inclination-only data in paleomagnetism. *Geophys. J. Int.* 182, 753–771. doi:10.1111/j.1365-246X.2010.04671.x

Ashley, P. M., Duncan, R. A., and Feebrey, C. A. (1995). Ebor Volcano and crescent complex, northeastern new south wales: age and geological development. *Aust. J. Earth Sci.* 42, 471–480. doi:10.1080/08120099508728217

Besse, J., and Courtillot, V. (2002). Apparent and true polar wander and the geometry of the geomagnetic field over the last 200 Myr. *J. Geophys. Res.* 107, 6. doi:10.1029/2000JB000050

Butler, R. F. (1992). *Paleomagnetism: magnetic domains to geologic terranes*. Palo Alto, CA: Blackwell Science.

Chivas, A. R. (1982). Geochemical evidence for magmatic fluids in porphyry copper mineralization. *Contrib. Mineral. Petrol.* 78, 389–403. doi:10.1007/bf00375201

Cohen, B. E., Knesel, K. M., Vasconcelos, P. M., Thiede, D. S., and Hergt, J. M. (2008). $^{40}Ar/^{39}Ar$ constraints on the timing and origin of Miocene leucitite volcanism in southeastern Australia ^{39}Ar constraints on the timing and origin of Miocene leucitite volcanism in southeastern Australia. *Aust. J. Earth Sci.* 55, 407–418. doi:10.1080/08120090701769514

Cohen, B. E., Knesel, K. M., Vasconcelos, P. M., and Schellart, W. P. (2013). Tracking the Australian plate motion through the Cenozoic: constraints from $^{40}Ar/^{39}Ar$ geochronology $^{40}Ar/^{39}Ar$ geochronology. *Tectonics* 32, 1371–1383. doi:10.1002/tect.20084

Cohen, B. E., Vasconcelos, P. M., and Knesel, K. M. (2007). $^{40}Ar/^{39}Ar$ constraints on the timing of Oligocene intraplate volcanism in southeast Queensland. *Aust. J. Earth Sci.* 54, 105–125. doi:10.1080/08120090600981483

Conrad, C. P., Bianco, T. A., Smith, E. I., and Wessel, P. (2011). Patterns of intraplate volcanism controlled by asthenospheric shear. *Nat. Geosci.* 4, 317–321. doi:10.1038/ngeo1111

Courtillot, V., Davaille, A., Besse, J., and Stock, J. (2003). Three distinct types of hotspots in the Earth's mantle. *Earth Planet Sci. Lett.* 205, 295–308. doi:10.1016/s0012-821x(02)01048-8

Cox, A., and Gordon, R. G. (1984). Paleolatitudes determined from paleomagnetic data from vertical cores. *Rev. Geophys.* 22, 47–72. doi:10.1029/rg022i001p00047

Cox, A., and Hart, R. (1986). *Plate tectonics: how its works*. Palo Alto, CA: Blackwell Science Publications.

Crossingham, T. J., Ubide, T., Vasconcelos, P. M., and Mallmann, G. (2018a). Parallel plumbing systems feeding a pair of coeval volcanoes in eastern Australia. *J. Petrol.* 59, 1035–1066. doi:10.1093/petrology/egy054

Crossingham, T. J., Ubide, T., Vasconcelos, P. M., Knesel, K. M., and Mallmann, G. (2018b). Temporal constraints on magma generation and differentiation in a continental volcano: Buckland, eastern Australia. *Lithos* 302-303, 341–358. doi:10.1016/j.lithos.2018.01.009

Crossingham, T. J., Vasconcelos, P. M., Cunningham, T., and Knesel, K. M. (2017). $^{40}Ar/^{39}Ar$ geochronology and volume estimates of the Tasmantid Seamounts: support for a change in the motion of the Australian plate ^{39}Ar geochronology and volume estimates of the Tasmantid Seamounts: support for a change in the motion of the Australian plate. *J. Volcanol. Geoth. Res.* 343, 95–108. doi:10.1016/j.jvolgeores.2017.06.014

Davies, D. R., Rawlinson, N., Iaffaldano, G., and Campbell, I. H. (2015). Lithospheric controls on magma composition along Earth's longest continental hotspot track. *Nature* 525, 511–514. doi:10.1038/nature14903

Davies, D. R., and Rawlinson, N. (2014). On the origin of recent intraplate volcanism in Australia. *Geology* 42, 1031–1034. doi:10.1130/g36093.1

Doubrovine, P., and Tarduno, J. (2004). Late Cretaceous paleolatitude of the Hawaiian hot spot: new paleomagnetic data from Detroit Seamount (ODP Site 883). *Geochem. Geophys. Geosyst.* 5, Q11L04. doi:10.1029/2004gc000745

Doubrovine, P. V., Steinberger, B., and Torsvik, T. H. (2012). Absolute plate motions in a reference frame defined by moving hot spots in the Pacific, Atlantic, and Indian oceans. *J. Geophys. Res.* 117, 30. doi:10.1029/2011jb009072

Duncan, R. A. (1981). Hotspots in the Southern Oceans—an absolute frame of reference for motion of the Gondwana continents. *Tectonophysics* 74, 29–42. doi:10.1016/0040-1951(81)90126-8

French, S. W., and Romanowicz, B. (2015). Broad plumes rooted at the base of the Earth's mantle beneath major hotspots. *Nature* 525, 95–99. doi:10.1038/nature14876

Gordon, R. G., and Cape, C. D. (1981). Cenozoic latitudinal shift of the Hawaiian hotspot and its implications for true polar wander. *Earth Planet Sci. Lett.* 55, 37–47. doi:10.1016/0012-821x(81)90084-4

Grommé, S., and Vine, F. J. (1972). Paleomagnetism of Midway Atoll lavas and northward movement of the Pacific plate. *Earth Planet Sci. Lett.* 17, 159–168. doi:10.1016/0012-821x(72)90271-3

Hackman, B. (1980). *The geology of Guadalcanal*. Solomon Islands: Overseas memoir of the Institute of Geological Sciences, Vol. 6, 115.

Hansma, J., and Tohver, E. (2018). Palaeomagnetism of mid-Miocene leucitite volcanics in eastern Australia. *Geophys. J. Int.* 215, 303–313. doi:10.1093/gji/ggy281

Hansma, J., and Tohver, E. (2019). Paleomagnetism of Oligocene hot spot volcanics in central Queensland, Australia. *J. Geophys. Res. Solid Earth* 124, 6280–6296. doi:10.1029/2019JB017639

Harada, Y., and Hamano, Y. (2000). "Recent progress on the plate motion relative to hotspots," in *The history and dynamics of global plate motions*. Editors M. A. Richards, R. G. Gordon, and R. D. van der Hilst (Washington, DC: American Geophysical Union), 121. 327–338.

Hill, M. J., Gratton, M. N., and Shaw, J. (2002). Palaeomagnetic investigation of Tertiary lava from Barrington Tops, NSW, Australia, using thermal and microwave techniques. *Earth Planet Sci. Lett.* 198, 245–256. doi:10.1016/s0012-821x(02)00534-4

Jones, I., and Verdel, C. (2015). Basalt distribution and volume estimates of Cenozoic volcanism in the Bowen Basin region of eastern Australia: implications for a waning mantle plume. *Aust. J. Earth Sci.* 62, 255–263. doi:10.1080/08120099.2015.997796

Jones, I., Verdel, C., Crossingham, T., and Vasconcelos, P. (2017). Animated reconstructions of the Late Cretaceous to Cenozoic northward migration of Australia, and implications for the generation of east Australian mafic magmatism. *Geosphere* 13, 460–481. doi:10.1130/ges01405.1

Kirschvink, J. L. (1980). The least-squares line and plane and the analysis of palaeomagnetic data. *Geophys. J. Int.* 62, 699–718. doi:10.1111/j.1365-246x.1980.tb02601.x

Knesel, K. M., Cohen, B. E., Vasconcelos, P. M., and Thiede, D. S. (2008). Rapid change in drift of the Australian plate records collision with Ontong Java plateau. *Nature* 454, 754. doi:10.1038/nature07138

Kono, M. (1980). *Initial reports of the deep sea drilling project*. Washington, DC: U.S. Government Printing Office, Vol. 55.

Matthews, K. J., Maloney, K. T., Zahirovic, S., Williams, S. E., Seton, M., and Müller, R. D. (2016). Global plate boundary evolution and kinematics since the late Paleozoic. *Glob. Planet. Change* 146, 226–250. doi:10.1016/j.gloplacha.2016.10.002

McDougall, I., and Duncan, R. A. (1988). Age progressive volcanism in the Tasmantid seamounts. *Earth Planet Sci. Lett.* 89, 207–220. doi:10.1016/0012-821x(88)90173-2

McDougall, I., Embleton, B. J. J., and Stone, D. B. (1981). Origin and evolution of Lord Howe Island, southwest pacific ocean. *Aust. J. Earth Sci.* 28, 155–176. doi:10.1080/00167618108729154

McElhinny, M. W., Embleton, B. J. J., and Wellman, P. (1974). A synthesis of Australian Cenozoic palaeomagnetic results. *Geophys. J. Int.* 36, 141–151. doi:10.1111/j.1365-246x.1974.tb03629.x

McFadden, P. L., and Reid, A. B. (1982). Analysis of palaeomagnetic inclination data. *Geophys. J. Int.* 69, 307–319. doi:10.1111/j.1365-246x.1982.tb04950.x

McQueen, K. G., Gonzalez, O. R., Roach, I. C., Pillans, B. J., Dunlap, W. J., and Smith, M. L. (2007). Landscape and regolith features related to Miocene leucitite lava flows, el capitan northeast of cobar, new south wales. *Aust. J. Earth Sci.* 54, 1–17. doi:10.1080/08120090600923311

Molnar, P., and Atwater, T. (1973). Relative motion of hot spots in the mantle. *Nature* 246, 288–291. doi:10.1038/246288a0

Molnar, P., and Stock, J. (1987). Relative motions of hotspots in the pacific, atlantic and Indian oceans since late cretaceous time. *Nature* 327, 587–591. doi:10.1038/327587a0

Montelli, R., Nolet, G., Dahlen, F. A., and Masters, G. (2006). A catalogue of deep mantle plumes: new results from finite-frequency tomography. *Geochem. Geophys. Geosyst.* 7, Q11007. doi:10.1029/2006gc001248

Morgan, W. J. (1971). Convection plumes in the lower mantle. *Nature* 230, 42–43. doi:10.1038/230042a0

Mortimer, N., Gans, P. B., Meffre, S., Martin, C. E., Seton, M., Williams, S., et al. (2018). Regional volcanism of northern Zealandia: post-Gondwana break-up magmatism on an extended, submerged continent. *Geol. Soc. Spec. Pub.* 463, 199–226. doi:10.1144/sp463.9

Mortimer, N., Gans, P. B., Palin, J. M., Meffre, S., Herzer, R. H., and Skinner, D. N. B. (2010). Location and migration of Miocene-Quaternary volcanic arcs in the SW Pacific region. *J. Volcanol. Geotherm. Res.* 190, 1–10. doi:10.1016/j.jvolgeores.2009.02.017

Mumme, W. G. (1963). Thermal and alternating magnetic field demagnetization experiments on Cainozoic basalts from Victoria, Australia. *Geophys. J. Int.* 7, 314–327. doi:10.1111/j.1365-246x.1963.tb05553.x

Müller, R. D., Royer, J.-Y., and Lawver, L. A. (1993). Revised plate motions relative to the hotspots from combined Atlantic and Indian Ocean hotspot tracks. *Geology* 21, 275–278. doi:10.1130/0091-7613(1993)021<0275:rpmrtt>2.3.co;2

Musgrave, R. J. (1990). Paleomagnetism and tectonics of malaita, Solomon Islands. *Tectonics* 9, 735–759. doi:10.1029/tc009i004p00735

Musgrave, R. J. (2013). Evidence for late Eocene emplacement of the malaita terrane, Solomon Islands: implications for an even larger Ontong java nui oceanic plateau. *J. Geophys. Res. Solid Earth* 118, 2670–2686. doi:10.1002/jgrb.50153

Ogg, J. (2012). "Geomagnetic polarity time scale," in *The geologic time scale*. New York, NY: Elsevier. 85–113.

Opdyke, N. D., and Musgrave, R. (2004). Paleomagnetic results from the Newer Volcanics of Victoria: contribution to the time averaged field initiative. *Geochem. Geophys. Gepsyst.* 5, Q03H09. doi:10.1029/2003gc000632

Petterson, M. G., Babbs, T., Neal, C. R., Mahoney, J. J., Saunders, A. D., Duncan, R. A., et al. (1999). Geological-tectonic framework of Solomon Islands, SW Pacific: crustal accretion and growth within an intra-oceanic setting. *Tectonophysics* 301, 35–60. doi:10.1016/s0040-1951(98)00214-5

Petterson, M. G., Neal, C. R., Mahoney, J. J., Kroenke, L. W., Saunders, A. D., Babbs, T. L., et al. (1997). Structure and deformation of north and central Malaita, Solomon Islands: tectonic implications for the Ontong Java Plateau-Solomon arc collision, and for the fate of oceanic plateaus. *Tectonophysics* 283, 1–33. doi:10.1016/s0040-1951(97)00206-0

Rahman, A.-u. (1971). Palaeomagnetic secular variation for recent normal and reversed epochs, from the newer volcanics of victoria, Australia. *Geophys. J. Int.* 24, 255–269. doi:10.1111/j.1365-246x.1971.tb02177.x

Rawlinson, N., Davies, D. R., and Pilia, S. (2017). The mechanisms underpinning Cenozoic intraplate volcanism in eastern Australia: insights from seismic tomography and geodynamic modeling. *Geophys. Res. Lett.* 44, 9681–9690. doi:10.1002/2017gl074911

Seton, M., Müller, R. D., Zahirovic, S., Gaina, C., Torsvik, T., Shephard, G., et al. (2012). Global continental and ocean basin reconstructions since 200Ma. *Earth Sci. Rev.* 113, 212–270. doi:10.1016/j.earscirev.2012.03.002

Sleep, N. H. (1996). Lateral flow of hot plume material ponded at sublithospheric depths. *J. Geophys. Res.* 101, 28065–28083. doi:10.1029/96jb02463

Sleep, N. H. (1997). Lateral flow and ponding of starting plume material. *J. Geophys. Res.* 102, 10001–10012. doi:10.1029/97jb00551

Steinberger, B. (2000). Plumes in a convecting mantle: models and observations for individual hotspots. *J. Geophys. Res.* 105, 11127–11152. doi:10.1029/1999jb900398

Steinberger, B., and O'Connell, R. J. (1998). Advection of plumes in mantle flow: implications for hotspot motion, mantle viscosity and plume distribution. *Geophys. J. Int.* 132, 412–434. doi:10.1046/j.1365-246x.1998.00447.x

Sutherland, F. L., Graham, I. T., Meffre, S., Zwingmann, H., and Pogson, R. E. (2012). Passive-margin prolonged volcanism, East Australian Plate: outbursts, progressions, plate controls and suggested causes. *Aust. J. Earth Sci.* 59, 983–1005. doi:10.1080/08120099.2012.688293

Tarduno, J. A. (2007). On the motion of Hawaii and other mantle plumes. *Chem. Geol.* 241, 234–247. doi:10.1016/j.chemgeo.2007.01.021

Tarduno, J. A., and Cottrell, R. D. (1997). Paleomagnetic evidence for motion of the Hawaiian hotspot during formation of the Emperor seamounts. *Earth Planet Sci. Lett.* 153, 171–180. doi:10.1016/s0012-821x(97)00169-6

Tarduno, J. A., Duncan, R. A., Scholl, D. W., Cottrell, R. D., Steinberger, B., Thordarson, T., et al. (2003). The emperor seamounts: southward motion of the Hawaiian hotspot plume in Earth's mantle. *Science* 301, 1064–1069. doi:10.1126/science.1086442

Tarduno, J., Bunge, H.-P., Sleep, N., and Hansen, U. (2009). The bent Hawaiian-Emperor hotspot track: inheriting the mantle wind. *Science* 324, 50–53. doi:10.1126/science.1161256

Tauxe, L., Constable, C., Johnson, C. L., Koppers, A. A., Miller, W. R., and Staudigel, H. (2003). Paleomagnetism of the southwestern USA recorded by 0–5 Ma igneous rocks. *Geochem. Geophys. Geosyst.* 4, 8802. doi:10.1029/2002gc000343

Tauxe, L., and Kent, D. (2004). "A simplified statistical model for the geomagnetic field and the detection of shallow bias in paleomagnetic inclinations: was the ancient magnetic field dipolar?," in *Timescales of the paleomagnetic field*. Editors J. E. T. Channell, D. V. Kent, W. Lowrie, and J. G. Meert (Washington, DC: American Geophysical Union), 145, 101–116.

Tauxe, L., Kylstra, N., and Constable, C. (1991). Bootstrap statistics for paleomagnetic data. *J. Geophys. Res.* 96, 11723–11740. doi:10.1029/91jb00572

Thompson, R., and Clark, R. M. (1981). Fitting polar wander paths. *Phys. Earth Planet. In.* 27, 1–7. doi:10.1016/0031-9201(81)90082-0

Torsvik, T. H., Doubrovine, P. V., Steinberger, B., Gaina, C., Spakman, W., and Domeier, M. (2017). Pacific plate motion change caused the Hawaiian-emperor bend. *Nat. Commun.* 8, 1–12. doi:10.1038/ncomms15660

Torsvik, T. H., Müller, R. D., Van der Voo, R., Steinberger, B., and Gaina, C. (2008). Global plate motion frames: toward a unified model. *Rev. Geophys.* 46, RG3004. doi:10.1029/2007rg000227

Torsvik, T. H., Steinberger, B., Shephard, G. E., Doubrovine, P. V., Gaina, C., Domeier, M., et al. (2019). Pacific-panthalassic reconstructions: overview, errata and the way forward. *Geochem. Geophys. Geosyst.* 20, 3659–3689. doi:10.1029/2019gc008402

Torsvik, T. H., Van der Voo, R., Preeden, U., Mac Niocaill, C., Steinberger, B., Doubrovine, P. V., et al. (2012). Phanerozoic polar wander, palaeogeography and dynamics. *Earth Sci. Rev.* 114, 325–368. doi:10.1016/j.earscirev.2012.06.007

Van der Voo, R. (1990). The reliability of paleomagnetic data. *Tectonophysics* 184, 1–9. doi:10.1016/0040-1951(90)90116-p

Van der Voo, R. (1993). *Paleomagnetism of the atlantic, tethys, and iapetus oceans*. Cambridge, United Kingdom: Cambridge University Press.

Vandamme, D. (1994). A new method to determine paleosecular variation. *Phys. Earth Planet. In.* 85, 131–142. doi:10.1016/0031-9201(94)90012-4

Vasconcelos, P. M., Knesel, K. M., Cohen, B. E., and Heim, J. A. (2008). Geochronology of the Australian Cenozoic: a history of tectonic and igneous activity, weathering, erosion, and sedimentation. *Aust. J. Earth Sci.* 55, 865–914. doi:10.1080/08120090802120120

Wang, C., Gordon, R. G., and Zhang, T. (2017). Bounds on geologically current rates of motion of groups of hot spots. *Geophys. Res. Lett.* 44, 6048–6056. doi:10.1002/2017gl073430

Wellman, P., and McDougall, I. (1974). Cainozoic igneous activity in eastern Australia. *Tectonophysics* 23, 49–65. doi:10.1016/0040-1951(74)90110-3

Wellman, P., McElhinny, M. W., and McDougall, I. (1969). On the polar-wander path for Australia during the Cenozoic. *Geophys. J. Int.* 18, 371–395. doi:10.1111/j.1365-246x.1969.tb03575.x

Wessel, P., Harada, Y., and Kroenke, L. W. (2006). Toward a self-consistent, high-resolution absolute plate motion model for the Pacific. *Geochem. Geophys. Geosyst.* 7, Q03L12. doi:10.1029/2005GC001000

Wessel, P., and Kroenke, L. (2008). Pacific absolute plate motion since 145 Ma: an assessment of the fixed hotspot hypothesis. *J. Geophys. Res.* 113, 21. doi:10.1029/2007jb005499

Whittaker, J. M., Müller, R. D., Leitchenkov, G., Stagg, H., Sdrolias, M., Gaina, C., et al. (2007). Major Australian-Antarctic plate reorganization at Hawaiian-Emperor Bend time. *Science* 318, 83–86. doi:10.1126/science.1143769

Whittaker, J. M., Williams, S. E., and Müller, R. D. (2013). Revised tectonic evolution of the eastern Indian Ocean. *Geochem. Geophys. Geosyst.* 14, 1891–1909. doi:10.1002/ggge.20120

Wilson, J. T. (1963). Hypothesis of Earth's behaviour. *Nature* 189, 925–929. 10.1038/198925a0

Conflict of Interest: The authors declare that the research was conducted in the absence of any commercial or financial relationships that could be construed as a potential conflict of interest.

frontiers in Earth Science

ORIGINAL RESEARCH
published: 14 December 2020
doi: 10.3389/feart.2020.563453

Magnetostratigraphic Chronology of a Cenozoic Sequence From DSDP Site 274, Ross Sea, Antarctica

Luigi Jovane[1], Fabio Florindo[1,2,3], Gary Wilson[4,5], Stephanie de Almeida Pecchiai Saldanha Leone[1], Muhammad Bin Hassan[1], Daniel Rodelli[1] and Giuseppe Cortese[4]*

[1]Instituto Oceanográfico, Universidade de São Paulo, São Paulo, Brazil, [2]Istituto Nazionale di Geofisica e Vulcanologia, Rome, Italy, [3]Institute for Climate Change Solutions, Pesaro e Urbino, Italy, [4]GNS Science, Lower Hutt, New Zealand, [5]Department of Geology and Marine Science, University of Otago, Dunedin, New Zealand

New paleomagnetic results from the late Eocene-Middle Miocene samples from Deep Sea Drilling Project Site 274, cored during Leg 28 on the continental rise off Victoria Land, Ross Sea, provide a chronostratigraphic framework for an existing paleoclimate archive during a key period of Antarctic climate and ice sheet evolution. Based on this new age model, the cored late Eocene-Middle Miocene sequence covers an interval of almost 20 Myr (from ~35 to ~15 Ma). Biostratigraphic constraints allow a number of possible correlations with the Geomagnetic Polarity Time Scale. Regardless of correlation, average interval sediment accumulation rates above 260 mbsf are ~6 cm/kyr with the record punctuated by a number of unconformities. Below 260 mbsf (across the Eocene/Oligocene boundary) interval, sedimentation accumulation rates are closer to ~1 cm/kyr. A major unconformity identified at ~180 mbsf represents at least 9 Myr accounting for the late Oligocene and Early Miocene and represent non-deposition and/or erosion due to intensification of Antarctic Circumpolar Current activity. Significant fluctuations in grain size and magnetic properties observed above the unconformity at 180 mbsf, in the Early Miocene portion of this sedimentary record, reflect cyclical behavior in glacial advance and retreat from the continent. Similar glacial cyclicity has already been identified in other Miocene sequences recovered in drill cores from the Antarctic margin.

Keywords: magnetostratigraphy, grain size, Ross Sea Antarctica, circumpolar current, Oligocene-Early Miocene

OPEN ACCESS

Edited by:
Hagay Amit,
Université de Nantes, France

Reviewed by:
Belén Oliva-Urcia,
Autonomous University of Madrid, Spain
Chenglong Deng,
Chinese Academy of Sciences (CAS), China

****Correspondence:***
Luigi Jovane
jovane@usp.br

Specialty section:
This article was submitted to Geomagnetism and Paleomagnetism, a section of the journal Frontiers in Earth Science

Received: *18 May 2020*
Accepted: *13 November 2020*
Published: *14 December 2020*

Citation:
Jovane L, Florindo F, Wilson G, de Almeida Pecchiai Saldanha Leone S, Hassan MB, Rodelli D and Cortese G (2020) Magnetostratigraphic Chronology of a Cenozoic Sequence From DSDP Site 274, Ross Sea, Antarctica. Front. Earth Sci. 8:563453. doi: 10.3389/feart.2020.563453

INTRODUCTION

Deep Sea Drilling Program (DSDP) Leg 28 (**Figure 1**) was designed to explore the long-term climatic, biostratigraphic and geological history of Antarctica and its environments (Hayes and Frakes, 1975). Such geological records provide insights into modern and future climate sensitivity estimates, particularly for time periods characterized by the presence of continental ice sheets and a paleogeography similar to modern (e.g., Markwick, 2007; Farnsworth et al., 2019).

Earth's climate underwent a stepwise shift from greenhouse to icehouse conditions during the Cenozoic. Major ice sheets first appeared on Antarctica across the Eocene/Oligocene boundary coincident with the earliest Oligocene Oi-1 oxygen isotope event (1.0‰ $\delta^{18}O$ increase at ca. 33.55 Ma; e.g., Miller et al., 1991; Zachos et al., 1996; Zachos et al., 2001; Miller, 2005a; Miller et al., 2005b; Francis et al., 2009; Lurcock and Florindo, 2017, Westerhold et al., 2020). While long thought to be associated with the early glaciation of Antarctica (Kennett, 1977), the Antarctic Circumpolar Current

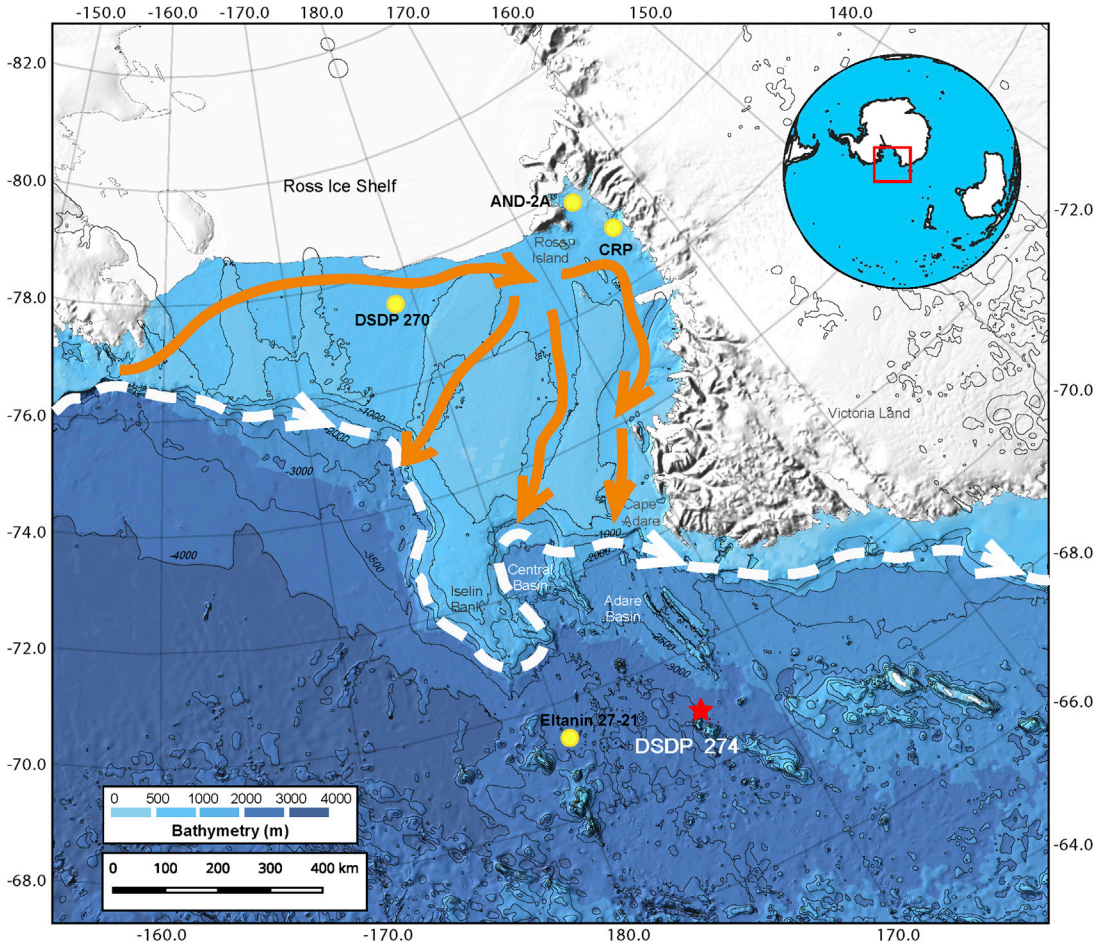

FIGURE 1 | Map of Ross Sea with schematic representation of present-day Antarctic Slope Current (dashed white line) and the continental shelf current flow (orange lines) (Ainley and Jacobs, 1981; Whitworth et al., 1995; Orsi and Wiederwohl, 2009). Location of DSDP Site 274 is indicated by a red star. DSDP 270, AND-2A, Eltanin 27–21 and CRP are also shown because they are reference cores in the area (respectively, Kulhanek et al., 2019, Jovane et al., 2019; Jovane et al., 2008; Roberts et al., 2013).

did not appear until the Late Oligocene (Lyle, et al., 2007). Throughout the Oligocene, Antarctic ice sheets experienced repeated cycles of advance and retreat, as indicated by large and rapid changes in global sea level (Kominz and Pekar, 2001) and $\delta^{18}O$ variations in deep-ocean sediment (Pälike et al., 2006). Following the inception of the Antarctic Circumpolar Current, the Oligocene terminated with another transient global cooling event (Mi-1, at ca. 23 Ma), characterized by a ~1‰ positive excursion in marine benthic foraminiferal $\delta^{18}O$ records (e.g., Wilson et al., 2009; Beddow et al., 2016) and associated with a large-scale Antarctic ice sheet expansion at the Oligocene-Miocene transition. This event was dramatic in scale, with the East Antarctic Ice Sheet (EAIS) estimated to have grown from 50 to 125% of its present-day size (e.g., Pekar et al., 2006). It was the first of a series of similar "Mi-" oxygen isotope events that, while less extreme than Mi-1, were responsible for the progressive cooling and glaciation experienced by Antarctica during the Miocene. As in the Oligocene, however, the cooling during the Miocene was not monotonic, but characterized by swings between cooler and warmer climate (e.g., Miller et al., 1991; Zachos et al., 1997; Zachos et al., 2001; Lear et al., 2004; Holbourn et al., 2005; Shevenell et al., 2008; Holbourn et al., 2013; Holbourn et al., 2014; Holbourn et al., 2015; Lear et al., 2015; Holbourn et al., 2018; Liebrand et al., 2017; Westerhold et al., 2020).

After the initial onset of and recovery from Mi-1, the Early Miocene experienced relatively warm intervals. The warming cycles of the Early Miocene culminated in the Mid-Miocene Climatic Optimum (MMCO) at around 17–14 Ma, immediately followed by the Middle Miocene Climate Transition (MMCT) at 14.2–13.8 Ma (Shevenell et al., 2004). The transition, as recorded in deep-ocean $\delta^{18}O$ variations, was a significant one: the MMCO was the warmest interval since the Eocene, while the MMCT, and the subsequent cooling during the rest of the Miocene, produced temperatures colder than any previously observed in the Cenozoic. During this time, there

was a sizable EAIS, as inferred from $\delta^{18}O$, sea level curves and direct sedimentological evidence from the Antarctic continent itself (e.g., Lewis et al., 2007).

In this paper, we present the first magnetostratigraphic chronology of a late Eocene-Early Miocene record from a sediment core (DSDP Leg 28, Site 274) obtained from offshore Cape Adare in the Ross Sea Sector of the Antarctic continent in 1973. The new age model will allow further studies of this unique core to produce future paleoenvironmental reconstructions focusing on the discharge of sediments from the catchment areas in this region of the Ross Sea (e.g., Sagnotti, et al., 1998; Jovane et al., 2004; Jovane et al., 2019; Roberts et al., 2013).

SITE LOCATION AND LITHOLOGY

DSDP Site 274 was drilled during Expedition Leg 28 in February 1973, on the continental rise off Victoria Land, Ross Sea, about 250 km north-northeast of Cape Adare (**Figure 1**) (68°59.81S, 173°25.64′E; water depth of 3,326 m). A 421-m thick, largely terrigenous, sedimentary section was drilled with an average core recovery of 66%.

A graben-like structure, with relief of several hundred meters (Houtz and Meijer, 1970), lies to the southwest of the site and probably served as an effective barrier to the downslope transport of terrigenous material. Seafloor magnetic lineations in the area and detailed biostratigraphic studies suggested a late Eocene/Early Oligocene age for the base of the sedimentary cover (Hayes et al., 1975; Hayes and Frakes, 1975). However, paleomagnetic analysis has not been carried out on those cores until this study.

For this study, half-core samples were obtained from the International Ocean Discovery Program (IODP) Gulf Coast Repository from 320 m below sea floor (mbsf) (close to the contact with basement) to 123 mbsf. This interval comprises silty claystone, diatom-detrital silty clay ooze and diatom-rich silty clay (Hayes et al., 1975; Hayes and Frakes, 1975). An unconformity was identified at 180.5 mbsf by Frakes (1975) and interpreted to represent a time interval between late Oligocene (Core 20) and Early-Middle Miocene (Core 19).

MATERIAL AND METHODS

For the present study, DSDP Site 274 working half core samples were provided by the IODP Gulf Coast Repository from which we collected 8 cm^3 cubic samples, using a non-magnetic double blade saw. The core was dry but preservation was excellent.

Two hundred and sixty samples were taken from the center of the working halves between 316 mbsf (Core 34) and 123 mbsf (Core 14), with a sample collected at least every meter (depending on the core recovery, drilling-induced disturbance and where sufficient material was available). Sediment samples from the interval between 320 and 180 mbsf are stiffer and more consolidated, while those from the interval between 180 and 123 mbsf are softer and less consolidated. Samples were oriented only with respect to vertical direction, therefore absolute paleomagnetic declinations could not be determined. Paleomagnetic analyses were performed at Instituto de Astronomia, Geofísica e Ciências Atmosféricas da Universidade de São Paulo (IAG USP) in a magnetically shielded room using a 2 G Enterprises magnetometer (Model 755–4K). Grain size, magnetic susceptibility and rock magnetic analyses were conducted at the Centro Oceanográfico de Registros Estratigráficos (CORE) at the Instituto Oceanográfico da Universidade de São Paulo (IO USP) using a Microtrac Bluewave-SIA, an AGICO MFK1-FA Kappabridge, and a Vibrating Sample Magnetometer (VSM) MicroMag 3,900 Princeton-Lake Shore Cryotronics, respectively.

Grain Size

Samples were prepared by crushing ~0.2 g of bulk sediment in an agate mortar. The crushed samples were further disaggregated using 10% hydrogen peroxide to remove organic matter. After 48 h of reaction, the samples were passed through 2 mm sieves and dried in an oven. After drying, sodium pyrophosphate was added to prevent the particles from flocculating. The Microtrac Bluewave equipment was used to measure the particles by laser diffraction in water, with their size being calculated according to the modified Mie theory for non-spherical particles (Chýlek et al., 1976). To establish the basic statistical parameters of particle size, as well as particle size distribution, the GRADISTAT v. 4.0 program, developed by Blott and Pye (2001), was used to establish the basic statistical parameters of particle size, as well as particle size distribution.

Mineral Magnetic Properties

Rock magnetic analyses were conducted on 21 selected samples distributed along the studied interval to estimate downcore variations in the composition, concentration, and grain size of magnetic minerals. These analyses included volume normalized low-field magnetic susceptibility (κ), hysteresis loops, with maximum fields of 0.5 T, isothermal remanent magnetization (IRM) imparted in progressively (100 acquisition steps) to saturation (SIRM), or to the maximum attainable direct field of 1.8 T. IRM curves were subdivided into discrete coercivity components, as in Robertson and France (1994), with cumulative log-Gaussian (CLG) functions, using the spreadsheet developed by Kruiver et al. (2001) and Heslop et al. (2002).

In addition, we investigated the temperature dependence of magnetic susceptibility using a MFK1-FA equipped with CS4 furnace (AGICO) Kappabridge, to discriminate ferromagnetic mineralogy. Samples were measured up to a maximum temperature of 700°C in an argon atmosphere, in order to minimize thermochemical alteration.

Demagnetization

In order to remove secondary NRM components, an Alternating Field (AF) demagnetization technique was employed, with stepwise demagnetization at peak AF fields of 2.5, 5, 10, 15, 20, 30, 40, 50, 60, 70, 80, 90 and 100 mT. Vector component diagrams (Zijderveld, 1967) were used to display stepwise demagnetization data. Characteristic remanent magnetization (ChRM) directions were determined using principal component analysis (PCA) with linear best fits calculated from three or more demagnetization steps using the PuffinPlot

paleomagnetic analysis application (Lurcock and Wilson, 2012; Lurcock and Florindo, 2019).

RESULTS

Grain Size

The lithology of the studied interval is predominantly clay. The average grain size is 11.16 phi (0.435 μm), while the mode is 11.17 phi (0.432 μm), with a standard deviation of 0.33. The coarsest average grain size (9.87 phi; 1.065 μm) is found at 158.09 mbsf. The finest average grain size (12.41 phi; 0.181 μm) was observed at 162.11 mbsf. Several samples have multiple peaks in the grain size distribution (**Figure 2**).

A drop-stone, 2 cm in diameter, was found at 319.74 mbsf, and additional ice rafted debris (IRD) particles greater than 5 mm in diameter were identified at 258.5 and 247.5 mbsf. Frakes (1975) also reported the presence of a coarse fraction in Cores 19 and 18 (180.5 and 161.5 mbsf, respectively) interpreted to reflect ice rafting events.

We observed a lower proportion of clay and a higher proportion of sand in the interval between 180 and 130 mbsf (Cores 19–14, respectively), where the variability of the average grain size is greater and ranges between 10 and 12 phi (0.98–0.24 μm). Between 180 and 160 mbsf (Cores 19–18, respectively) the average grain size is finer between 11 and 12 phi (0.48–0.24 μm) and coarsens between 160 and 130 mbsf (Cores 17–14) to values ranging between 9.7 and 11.7 phi (1.20–0.30 μm). The average grain size is finer in the lower interval of the core (between ~300 and ~180 mbsf; Cores 34–20) with values ranging between 11 and 11.5 phi (0.48–0.34 μm), with a slight coarsening in average grain size in the interval ~320–~304 mbsf (Cores 34–33). Abrupt changes in grain size at ~262, ~240 and ~224 mbsf suggest the possibility of minor unconformities in the sedimentary succession.

Magnetic Properties

Magnetic susceptibility (κ) values range widely between 1.8×10^{-6} and 92.9×10^{-6} SI with a mean value of 10.9×10^{-6} SI (**Figure 2**). Below the unconformity at ~180 mbsf, the highest κ values occur in samples between 280 and 210 mbsf and are associated with IRD intervals with coarser sediments and larger clasts. Above 180 mbsf, κ gradually increases reaching peak values at 140 mbsf.

IRM acquisition curves obtained for the samples were separated into four coercivity components (**Figure 3**). Both samples (at 218.92 and 285.41 mbsf) show a component with

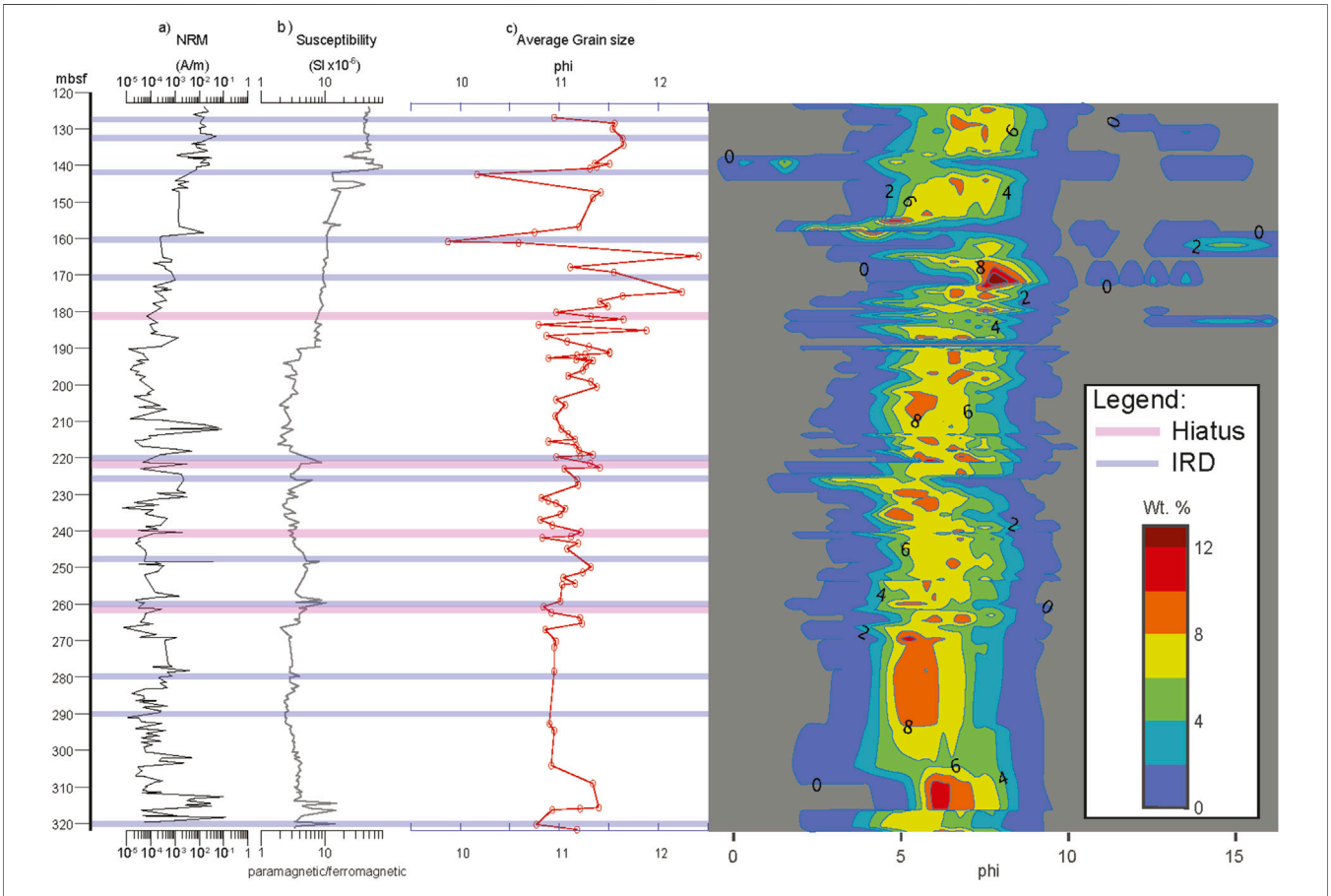

FIGURE 2 | Downcore variations of **(A)** NRM intensity, **(B)** low-field magnetic susceptibility (κ), **(C)** average grain size and **(D)** sediment grain size distribution in a contour. Hiatuses and IRD horizons are highlighted as pink and light blue, respectively.

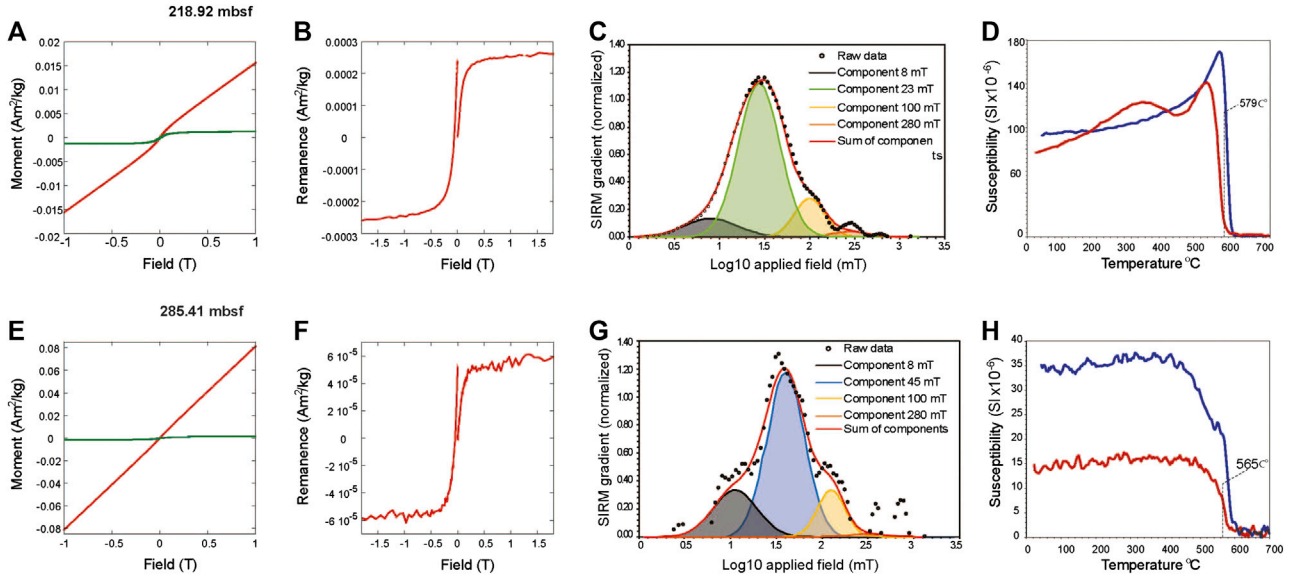

FIGURE 3 | Rock magnetic properties of two selected samples at. **(A)**, **(E)** hysteresis loops before (red) and after (green) subtracting the paramagnetic contribution, by applying an automatic linear slope correction. **(B)**, **(F)** backfield and IRM saturaton acquisitions. **(C)**, **(G)** IRM acquisition curves gradient with the separated components. Black component: low coercivity detrital magnetite, blue and green components: SD magnetite; orange components: hematite. **(C)**, **(F)** thermomagnetic curves, the red curve represents the heating portion and the blue line the cooling portion of the cycle.

very low coercivity (mean 8 mT) and dispersion parameter of 0.30, which corresponds to coarse detrital magnetite with different coercivity or activation of superparamagnetic (SP) particles dispersed in the material (Heslop et al., 2004; Abrajevitch and Kodama, 2011; Savian et al., 2014; Savian et al., 2016). The two middle-coercivity components show values consistent with single domain (SD) magnetite (mean coercivity of 23 mT, dispersion parameter 0.23 in samples 218.92 mbsf and 45 mT, dispersion parameter 0.19 in sample 285.41 mbsf, respectively). Those components are assumed to represent low-coercivity SD magnetite and high-coercivity SD magnetite, probably of biogenic origin (Egli, 2004; Jovane et al., 2012; Yamazaki , 2012; Heslop et al., 2004; Rodelli et al., 2019). The component characterized by mean coercivities of 100 and 280 mT (dispersion parameter = 0.15 and 20, respectively), are interpreted as hematite (Kruiver et al., 2001; Abrajevitch et al., 2009; Rodelli et al., 2019). The overall contribution to the IRM in sample 218.92 mbsf from the SD magnetite is 72, and 9% is linked instead to detrital magnetite. Hematite only represents 19% of the total contribution. IRM acquisition curves for a sample at 285.41 mbsf, typical of samples with lower κ, was fitted with only four components (**Figure 3E**): the low coercivity SD magnetite component is missing, and the hard SD magnetite is less abundant, corresponding to only 64% of the magnetic signal, and the detrital magnetite is more abundant (18%). Hematite is slightly less abundant (18%).

A κ-T curve for sample at 218.92 mbsf (**Figure 3C**) shows increasing values up to about 330°C, which can be interpreted as maghemite (Rodelli et al., 2018; Rodelli et al., 2019), possibly related to partial oxidation of magnetite. This is followed by a peak at about 520°C and a major inflection at 579°C, calculated with the two-tangent method of Grommé et al. (1969), and consistent with chemically pure magnetite (Thompson and Oldfield, 1986). A κ-T curve for sample at 285.41 mbsf (**Figure 3F**) has a sharp drop at 565°C consistent with magnetite probably mixed with titano-magnetite (Ozima and Larson, 1970). The cooling curve for sample at 285.41 mbsf has higher overall κ than the heating curve, which indicates production of new magnetic phases during heating while sample at 218.92 mbsf maintain similar values.

Demagnetization Behavior

NRM intensities (**Figure 2A**) for the DSDP 274 succession range widely between 9.36×10^{-2} and 6.58×10^{-5} A/m about a mean of 4.72×10^{-3} A/m. At the base of the sequence (320–310 mbsf), values are higher than for the rest of the sequence below the unconformity, then increase again above 180 mbsf. Glaciomarine sediments at the base are coarser and contain larger clasts that can increase intensities and lead to non-reliable paleomagnetic behavior (e.g., unstable remanence, low inclination or multi-component magnetizations). For these reasons, samples at the base were excluded from magnetostratigraphic interpretations.

Some samples exhibit a low coercivity horizontal component of remanence (**Figure 4**) interpreted to be a drilling induced radial overprint related to strong magnetic fields in the cutting-shoe and/or core barrel (e.g., Acton et al., 2002; Florindo et al., 2003). In most cases, this is removed by AF demagnetization in a peak field of 20 mT, but in some cases the horizontal overprint is harder and persists to higher coercivities (>80 mT; **Figure 4D**)

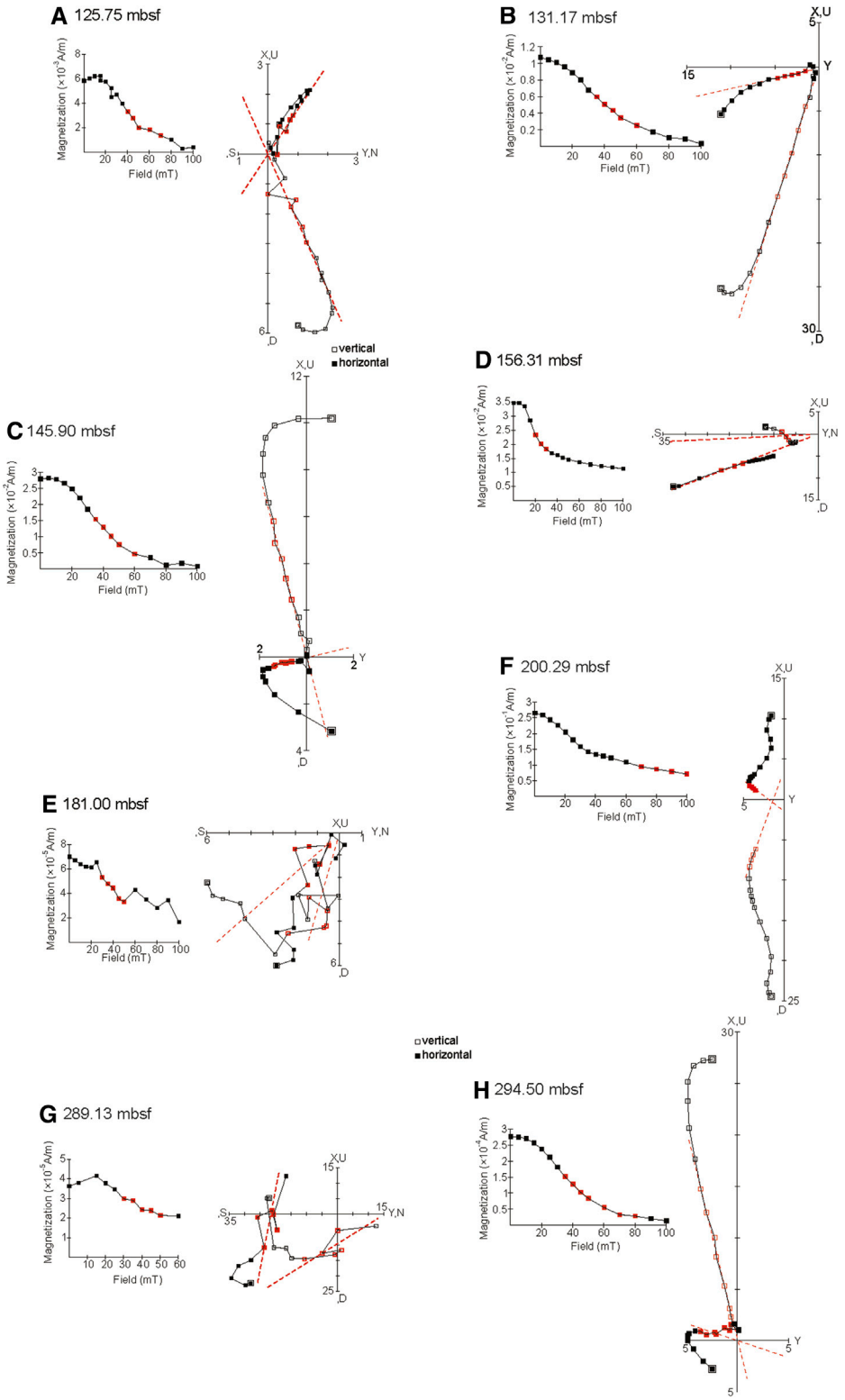

FIGURE 4 | AF (alternating field) demagnetization behavior for eight representative samples. For the vector component diagrams, open (closed) symbols represent projections onto the vertical (horizontal) plane. The red dashed lines represent PCA fits that indicate the ChRM direction for each sample. **A)**, **F)**, **B)** examples of reverse polarity. **C)**, **H)**, **E)**, **G)** examples of normal polarity; Samples **A)**, **E) G)** are noisy but it is possible to identify a ChRM. Sample **D)** has a radial overprint that resists AF demagnetization. The cores were not azimuthally oriented and declinations are, therefore, arbitrary. See text for discussion.

and prevents the isolation of a ChRM. In a few samples, characterized by the lowest NRM intensities, this overprint could not be removed by AF demagnetization. We cannot rule out that drying may have further hardened the radial overprint.

The ChRM is identified in most samples, regardless of polarity, between AFs of 20 and 70 mT (**Figure 4**). Approximately half of the ChRMs are directed to the origin of vector component plots (**Figures 4A,C**) and half follow a trajectory toward a high coercivity component not removed by peak AFs of 100 mT (**Figures 4F,G**). The high coercivity component of samples containing a small amount of hematite is assumed to be a secondary chemical remanent magnetism and unanchored ChRM components are reported.

Magnetozones

Of the total of 287 samples, 65.51% (188) were used to determine the magnetic polarity zonation, with discrete magnetozones defined as an interval where at least two consecutive samples show polarities different from adjacent intervals. The other 99 samples were discarded according to the following criteria. Samples were discarded from the final analysis if they met the following conditions: 1) samples with a radial overprint (**Figure 4D**); 2) single samples showing a ChRM with an inclination of opposite polarity to that of the previous and following samples; 3) samples with anomalous low inclination (shallower than ±25°) were also not considered (**Figure 4G**); 4) samples containing IRD which do not demagnetize due to the presence of high-coercivity minerals and 5) samples with overprints (drilling overprint (Fuller et al., 1998) or core-splitting overprint (Wilson et al., 2000; Florindo et al., 2001) that could not be removed by low field AF demagnetization.

Mean ChRM inclinations were computed separately for normal and reverse polarity populations using a maximum likelihood method (Arason and Levi, 2010) as implemented in the PuffinPlot application (Lurcock and Florindo, 2019). The normal polarity intervals have a mean inclination of −55.01° (N = 56, α_{95} = 6.67°, θ_{63} = 27.03°), the reverse polarity intervals have a mean of 68.3° (N = 132, α95 = 4.45°, θ_{63} = 27.8°) (**Figure 5**). Some samples have lower inclination than the expected Geocentric Axial Dipole (GAD) inclination (±64.5° at 20 Ma and ±63.9° at 40 Ma; Torsvik et al., 2012) for this period and for this site latitude. A post depositional tilt of ~5° the strata is

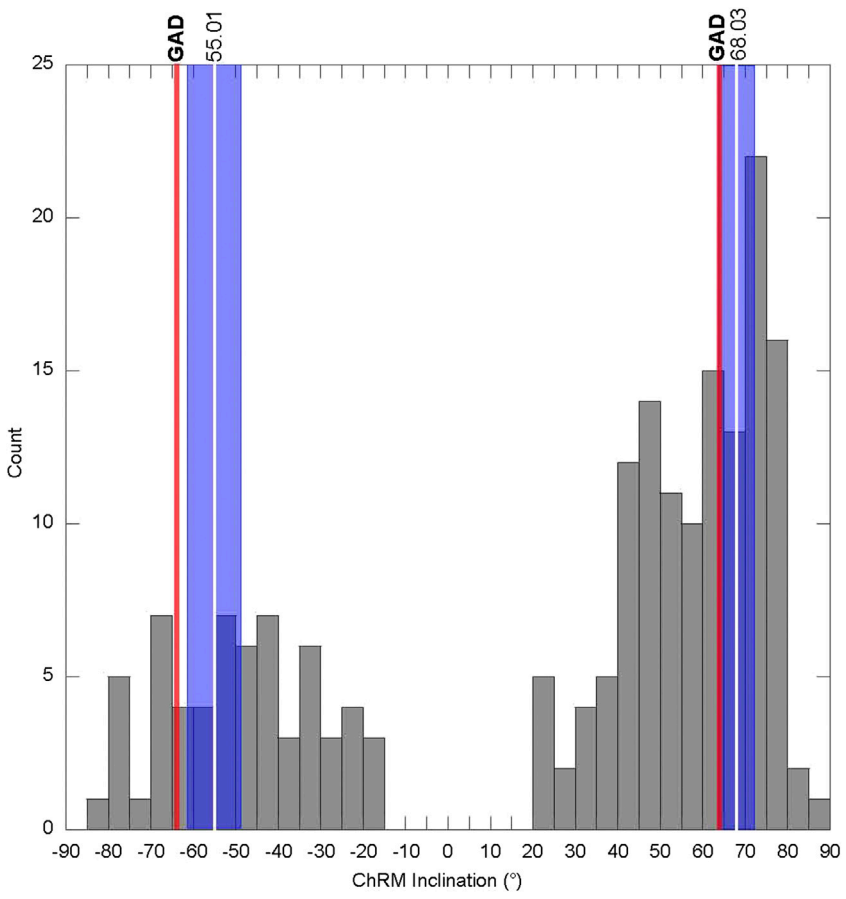

FIGURE 5 | Histograms of paleomagnetic inclinations from discrete samples for DSDP Site 274 after AF demagnetization. Mean ChRM inclinations (shown in blue), and associated α_{95}, were computed separately for normal and reverse polarity populations using a maximum likelihood method (Arason and Levi, 2010). The expected inclinations for the GAD are shown in red for this period and for the site latitude (Torsvik et al., 2012).

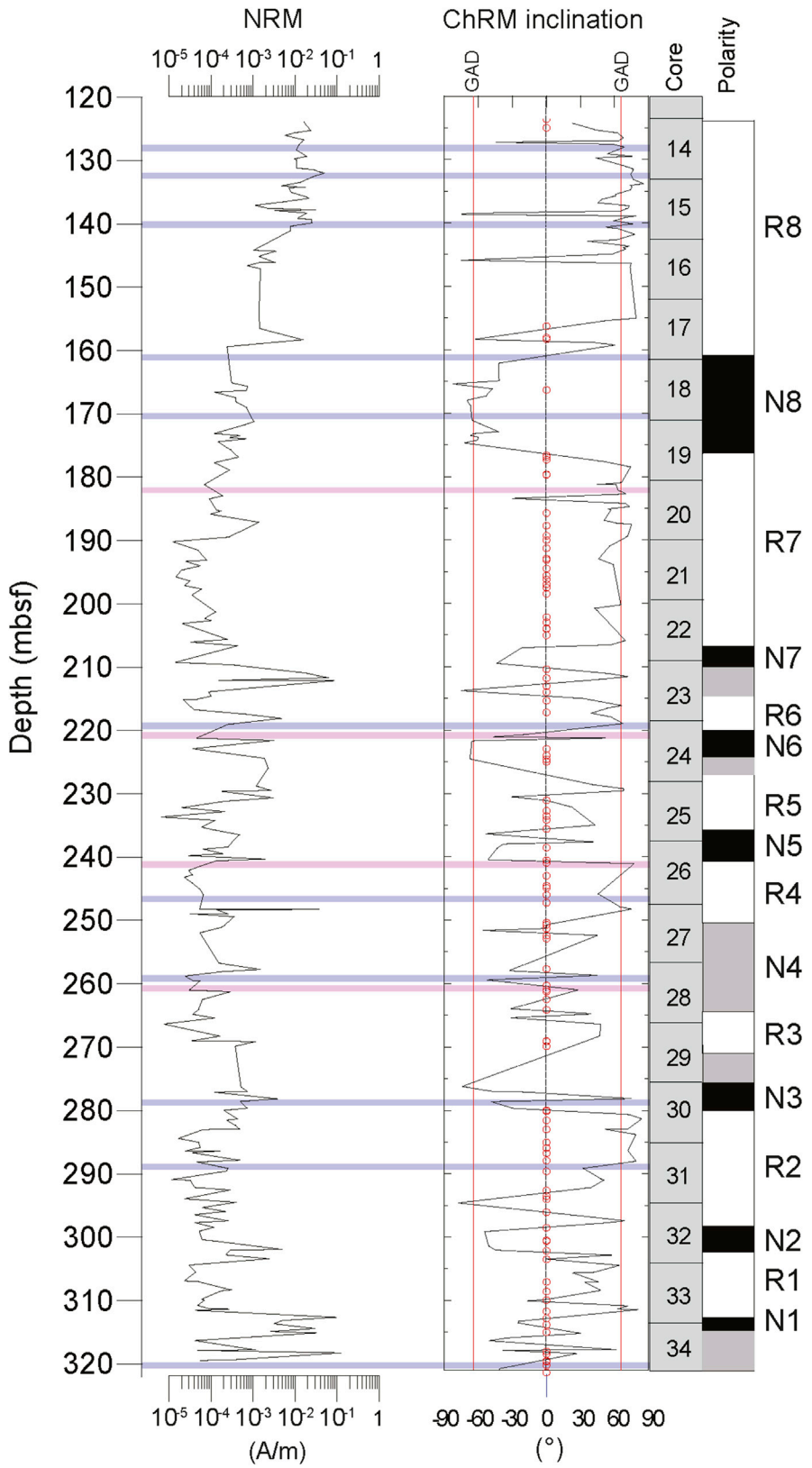

FIGURE 6 | Downcore variations of NRM intensity, ChRM inclination, and magnetic polarity zonation (black denotes normal polarity and white denotes reversed polarity).

implied by the difference in normal and reversed polarity inclinations.

We recognize eight normal and eight reversed magnetozones (**Figure 6**). The base of magnetozone N1 is not identified due to an interval of undefined polarity at the base of the core with most samples characterized by radial overprints. The upper part of magnetozone N1 is well defined by four normal polarity samples. Samples 313.21 (normal polarity) and 311.4 (reversed polarity) mbsf define the boundary of magnetozone N1 with R1. Between 312.3 and 302.38 mbsf magnetozone R1 is clearly identified, although it includes several samples with noisy data and others that do not demagnetize. Magnetozone N2 is well defined by three normal polarity samples between 302.82 (top of magnetozone R1) and 297.72 mbsf, which is the base of magnetozone R2. Between 298.4 and 280.09 mbsf, magnetozone R2 includes a long series of samples with reversed polarity with only occasional samples that do not demagnetize. The boundary between magnetozones N3 and R3 lies within an 8-m-interval where polarity could not be determined due to samples in which the radial overprints do not demagnetize. The interval between ca. 270 and 241.08 mbsf includes two intervals of well-defined reversed polarity: magnetozones R3 and R4, with a long interval magnetozone N4 where polarity is unclear with several samples not demagnetizing and others with persistent overprints. Magnetozone N5 is defined at its base between 241.08 and 240.49 mbsf and at its top between samples 236.37 and 235 mbsf. Magnetozones R5, N5 and N4 contain several samples that do not fully demagnetize. The boundary between magnetozones R5 and N6 is not well defined due to an interval including some samples that do not demagnetize and are noisy and have radial overprints. Magnetozone N6 is represented by four samples but also contains some samples that do not demagnetize. The boundary between magnetozones N6 and R6 is at 219.83 mbsf; at the midpoint between samples of opposite polarity at 220.74 and 218.92 mbsf. Magnetozone N7 includes only two samples and is separated from magnetozone R6 by an interval of questionable polarity conditions containing several noisy samples that do not demagnetize and have radial overprints. The interval of the core above 210 mbsf includes a well-defined N-R-N-R pattern of polarity, with the boundary between magnetozones N7 and R7 at 206.70 mbsf between samples 206.94 and 206.47 mbsf. Magnetozone R7 includes several noisy samples that do not demagnetize and have radial overprints. The boundary between magnetozones R7 and N8 is at 175.87 mbsf midway between a reversed sample at 177.53 mbsf and a normal sample at 174.22 mbsf. The boundary between magnetozone N8 and R8 is identified at 160.65 mbsf between samples at 162.11 and 159.20 mbsf.

Although most of the magnetozone boundaries were identified, some of the boundaries, particularly in the lower interval of the core, could not be located precisely because of intervals with uncertain polarity due to strong radial overprints, samples that do not demagnetize and others which were truncated by sedimentary unconformities identified by abrupt grain size changes. The boundaries between magnetozones N6 and R6, R4 and N5, and within N4 occur within sedimentary unconformities.

AGE MODEL

Biostratigraphic Data

No further biostratigraphic information has been reported for the 316–123 mbsf interval (Cores 34–14) since the original biostratigraphic first and last occurrence information provided by the Shipboard Report (**Table 1**; Hayes et al., 1975). Here, we update those occurrences accounting for more recent age and occurrence data from other Southern Ocean drill holes in order to correlate our magnetic polarity stratigraphy with the Geomagnetic Polarity Time Scale (GPTS) (**Figure 7**).

Planktonic foraminifera occur exclusively within Core 21 (190–199.5 mbsf) *Introduction* (92–88 cm) and *Material and Methods* (73–69 cm), including *Globigerina (Subbotina) angiporoides* (LO 29.18–30.28 Ma, FO 40.40–41.89 Ma; Olsson et al., 2006; Wade et al., 2018) and *Globoturborotalita labiacrassata* Jenkins (LO 21.12–22.44 Ma, FO 30.28–32.10 Ma; Spezzaferri et al., 2018). There is some indication that the assemblage may be reworked, but a penecontemporaneous redeposition was suggested by Kaneps (1975, **Table 1**).

Calcareous nannofossils are present only in isolated horizons and burrows in the interval covered by Cores 28–21 (266–190 mbsf), but only in Core 21 (199.5–190 mbsf), *Introduction*, 93 cm and *Material and Methods*, 70 cm, was the assemblage sufficient for an age determination (*Chiasmolithus altus* assemblage) (Burns, 1975; Bukry, 1975, **Table 1**). Fioroni et al. (2012), in a Southern Ocean calibration, attributed the *Chiasmolithus altus* biozone to the time interval from chrons C12r to C8n, which was later confirmed by Kulhanek et al. (2019). *Dictyococcites scrippsae* (middle Eocene to Upper Oligocene; Bukry and Percival, 1971), *Coccolithus pelagicus* (Danian to present; Wallich, 1877) and *Reticulofenestra* species (Ypresian to present, Fioroni et al., 2015) were also found in the same samples.

Diatoms are generally abundant with preservation ranging from fair/poor (Cores 19–1) to excellent (Cores 34–20). Down through Core 19 (180.5–171 mbsf), diatoms are of Miocene age (*Denticula antarctica* Zone) and below this, through Core 34 (323–313.5 mbsf), of Oligocene age (*Pyxilla prolongata*; See Figures 8A,B of McCollum, 1975, **Table 1**).

Ciesielski (1975) identified silicoflagellates in the interval between Cores 19–13, from 179 to 114 mbsf, with this interval containing an assemblage of low diversity and abundance, poor preservation, and broken specimens. *Distephanus speculum* and *D. boliviensis* are identified throughout this interval providing poor age-diagnostic forms (Guiry and Guiry, 2011). However, the interval comprising Cores 34 to 20 (321.5–181 mbsf) displays a uniform assemblage of silicoflagellates with excellent preservation and high abundance. *Mesocena apiculata, Dictyocha deflandrei s.l, Distephanus* cf. *D. boliviensis, Distephanus crux, Corbisema apiculata,* and *Naviculopsis trispinosa* (See Tables 6C, D of Ciesielski, 1975) define this interval as belonging to the *Dictyocha deflandrei* Zone, which is subdivided into two subzones: 1) *Dictyocha deflandrei* Subzone (Cores 30–20) characterized by the presence of *Dictyocha frenguellii* and 2) *Mesocena apiculata* subzone (Cores 34–30) (Guiry and Guiry, 2011, **Table 1**).

TABLE 1 | Biostratigraphic data from previous studies in the DSDP Initial Reports -Hayes et al. (1975), Radiolaria (Chen, 1975), Diatoms (McCollum, 1975), Silicoflagellates (Ciesielski, 1975), Planktonic Foraminifera (Kaneps, 1975), Calcareous nannoplankton (Bukry, 1975; Burns, 1975) - used to correlate of the DSDP Site 274 magnetic polarity zonation with the Geomagnetic Polarity Time Scale. Ages for radiolarian datum levels were assigned, where available, by the composite ordering of events and hybrid age model output from constrained optimization (CONOP) analyses of Southern Hemisphere data sets and Ocean Drilling Program (ODP) Site 744 (Florindo et al., 2013). Ages for all other events are as reported in the biozonation by Takemura and Ling (1997), or from other reports, such as Weaver (1983). The age calibrations of the events reported in Funakawa and Nishi (2005) and Takemura and Ling (1997) were converted to the Gradstein et al. (2012) timescale from the original Berggren et al. (1995) age calibration, using the converter at: http://www.odsn.de/cgi-bin/conv_ts.pl; **(A)** 27.1–27.5, **(B)** 28.2–28.3, **(C)** ?28.28–29.40, **(D)** 28.9–29.1, **(E)** 30.48-?33.06, **(F)** 36.2–36.4.

Event and source References	Base Depth (mbsf)	Top Depth (mbsf)	Datum (Ma) or period of occurrence (Myr)	References of Datum or occurrence
FORAMINIFERA	—	—	—	—
(Kaneps, 1975)	—	—	—	—
Globigerina (Subbotina) angiporoides **(F1)**	190.90	193.71	LO 29.18–30.28	Olsson et al., 2006; Wade et al., 2018
Globoturborotalita labiacrassata Jenkins **(F2)**	190.90	193.71	LO 21.12–22.44	Spezzaferri et al., 2018
—	—	—	—	—
Calcareous NANNOFOSSILS	—	—	—	—
(Bukry, 1975; Burns, 1975)	—	—	—	—
Chiasmolitus altus **(N1)**	190.93	197.00	HO 25 ma (C12r to C8n)	Fioroni et al., 2012; Kulhanek et al., 2019
Dictyococcites scrippsae	190.93	197.00	Mid Eocene/Late Oligocene	Bukry and Percival, 1971
Coccolithus pelagicus	190.93	197.00	Danian/present	Wallich, 1877
Reticulofenestra sp.	190.93	197.00	Ypesian/present	Fioroni et al., 2015
RADIOLARIA	—	—	—	—
(Chen, 1975)	—	—	—	—
Antarctissa deflandrei (= *A. conradae*)	128.62	—	FO 13.25	Florindo et al., 2013
Cyrtocapsella isopera **(R1)**	128.62	—	LO Early/Middle Miocene	Weaver, 1983
Eucyrtidium cienkowskii	128.62	—	LO 8.40	Florindo et al., 2013
Eucyrtidium cienkowskii **(R2)**	161.50	—	FO 19.47	Florindo et al., 2013
Cycladophora bicornis (=*Theocalyptra bicornis*	165.10	—	FO 12.19	Florindo et al., 2013
Cyrtocapsella isopera	177.95	—	FO Early/Middle Miocene	Weaver, 1983
Larcopyle frakesi (=*Prunopyle frakesi*) **(R3)**	183.95	—	LO 22.08	Florindo et al., 2013
Lithomelissa robusta **(R4)**	183.95	—	LO 26.499–26.93	Funakawa and Nishi, 2005 (A)
Lithomelissa sphaerocephalis **(R5)**	183.95	—	LO 27.747–27.876	Funakawa and Nishi, 2005 (B)
Lithomelissa challengerae **(R6)**	183.95	—	LO ?27.855–29.182	Takemura and Ling, 1997 (C)
Cyclampterium milowi (= *C. longiventer*) **(R7)**	183.95	—	LO 28.492–28.768	Funakawa and Nishi, 2005 (D)
Calocyclas semipolita (?) **(R8)**	183.95	—	LO 30.592-?33.159	Takemura and Ling, 1997 (E)
Dendrospyris stabilis (**R9**)	333.63	—	FO 36.561–36.757	Funakawa and Nishi, 2005 (F)
POLLEN	—	—	—	—
(Ciesielski, 1975)	—	—	—	—
Leiofusa	133.00	171.00	Devonian	Couper, 1960
Classopollis torosus	133.00	171.00	Jurassic-Early Cretaceous	Couper, 1960
Areosphaeridium diktyoplokus	199.50	218.50	Late Eocene	Wilson et al., 1998
Spinidinium aperturum	199.50	218.50	Oligocene-Paleocene	Fensome et al., 1993
Deflandrea asymmetrica	199.50	218.50	Oligocene-Paleocene	Levy and Harwood, 2000
Thalassiphora cf. *pelagica*	199.50	218.50	Oligocene-Late Cretaceous	Hall, 1977
Aiora fenestrata	199.50	218.50	Early Oligocene-late Eocene	Hall, 1977
Nothofagus	199.50	218.50	Oligocene-Eocene	Couper, 1960
DIATOMS	—	—	—	—
(McCollum, 1975)	—	—	—	—
Hemialus sp. 1	180.80	313.80	LO 22–30 Ma	Olney et al., 2007
Pseudopyxilla americana	180.80	313.80	LO 13.8 Ma	—
Pyxilla sp.	180.80	313.80	LO 24.22 Ma	Scherer et al., 2000
Rhizosolenia barboi	146.80	313.80	LO 20 - FO 22 Ma	Olney et al., 2007
Rhizosolenia hebetata f. hiemalus	190.30	294.80	HO 21 Ma	Scherer et al., 2000
Stephanopyxis (sp.)	153.40	—	LO 22 Ma	Olney et al., 2007
Trinacria excavata	123.90	313.80	FO 24.1 Ma	Olney et al., 2007
SILICOFLAGELLATES	—	—	—	—
(Bukry, 1975; Ciesielski, 1975)	—	—	—	—
Dictyocha sp.	180.50	322.00	Eocene	Mandra and Mandra, 1970
Mesocena apiculata	180.50	322.00	Late Oligocene-Miocene	Bukry, 1974
Corbisema apiculata	180.50	322.00	Maastrichtian	Cornell, 1974
Corbisema hastata	180.50	322.00	Cretaceous/Paleocene	Bukry, 1974
Corbisema triacantha	180.50	322.00	Eocene-Miocene	Bukry, 1974
Mesocena oamaruensis	180.50	322.00	Late Eocene	Mandra and Mandra, 1971
Distephanus sp.	180.50	322.00	Eocene	Mandra and Mandra, 1970

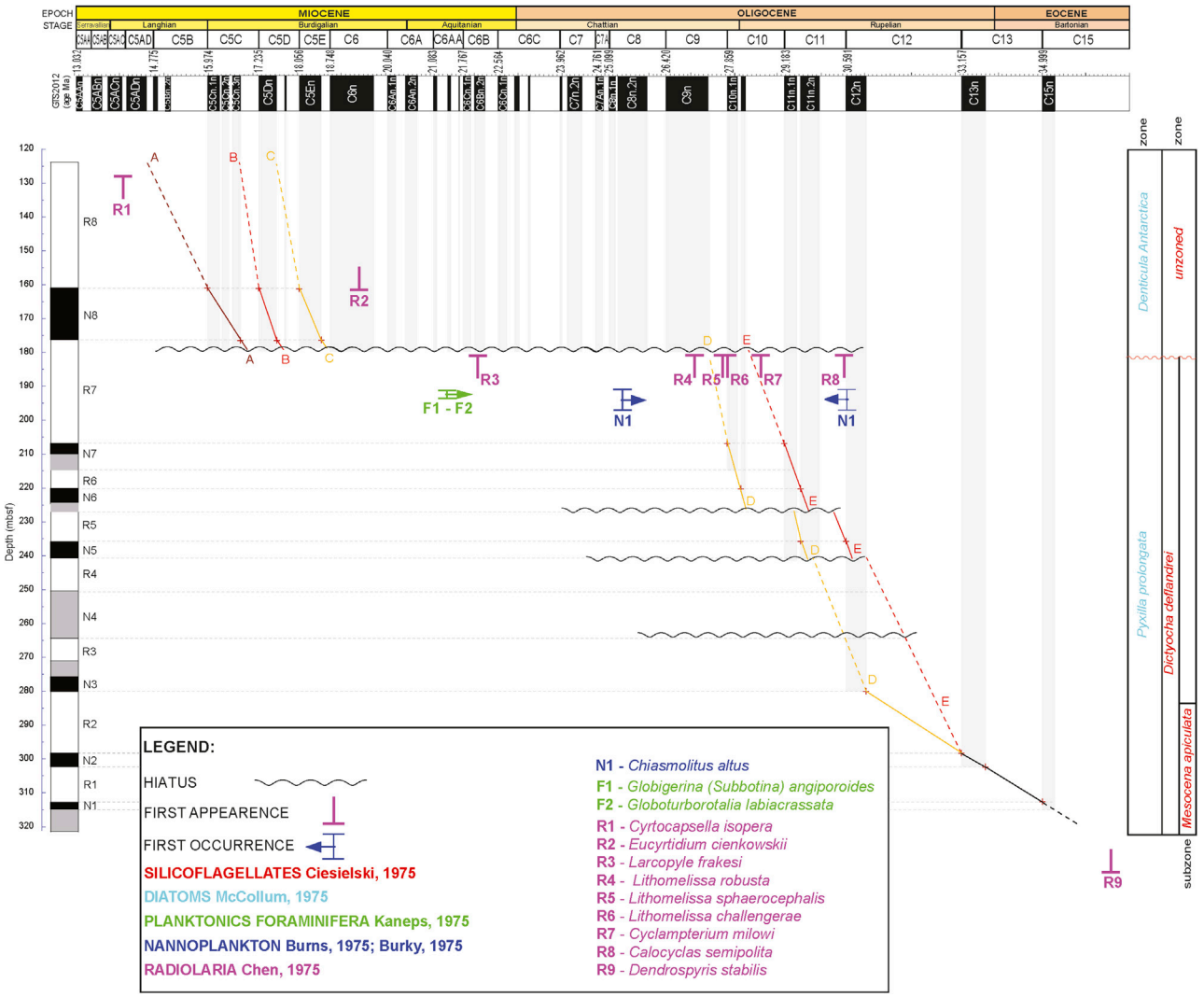

FIGURE 7 | Age vs. depth plot with correlation of DSDP Site 274 polarity zonation to the GPTS of Gradstein et al. (2012). Hiatuses defined from the sedimentological data and biostratigraphical datum are represented following the legend. Magnetostratigraphic model A is in dark red; models B and E are in red; models C and D are in orange.

Chen (1975) originally reported radiolarian occurrences at Site 274. Many of the species he found or described are however junior synonyms (see **Table 1** for their correct names, along with a reinterpretation of his reported occurrences of bioevents at Site 274). A very typical modern to Pliocene sequence of radiolarian events is observed in cores 11–1, followed by several late to middle Miocene LADs occurring in Core 12 (*Antarctissa deflandrei*, 5.87 Ma, *Cycladophora spongothorax*, 8.62 Ma, *Actinomma golownini*, 10.87 Ma, *Cycladophora golli*, 14.92 Ma). In the interval between Cores 19–15 (180.5–133 mbsf), radiolarian associations are dominated by *Cyrtocapsella isopera* indicating a middle to early Miocene age (see Table 9A, Chen 1975; Weaver, 1983). Associations are completely different in the interval between cores 34 and 20, where abundant radiolarians are present, such as *Amphisphaera* sp., *Calocyclas* sp., *Cenosphaera* sp., *Eucyrtidium* sp. This interval is assigned an age of Chattian or older, based on *Lithomelissa challengerae*, *Lithomelissa robusta*, *Lithomelissa sphaerocephalis*, *Lithomelissa tricornis*, *Prunopyle frakesi* and *Prunopyle hayesi* (see Table 9B, Chen, 1975; **Table 1**).

On the basis of radiolarian assemblages and their comparison with foraminiferal and calcareous nannofossil assemblages, Chen (1975) hypothesized a hiatus between cores 20 (190.0–180.5 mbsf) and 19 (180.5–171.0 mbsf). This interpretation seems to be supported by his data, with the Miocene and younger portion of the sequence being well constrained based on radiolarian marker species which are well calibrated, and an older section starting with Core 20 (sample 20R-3, 40–50 cm) which is substantially different, older and much more uniform in its radiolarian assemblage (**Table 1**). The LADs recorded in Core 20 include *Larcopyle*

frakesi (22.08 Ma), *Lithomelissa sphaerocephalis* (23.35–24.73 Ma), *Lithomelissa challengerae* (?28.28–29.40 Ma), and *Calocyclas* (?) *semipolita* (30.48-?33.06 Ma) which, while clearly identifying this core as substantially older than Core 19, make it difficult to assign it a well-constrained age.

Correlation to the Geomagnetic Polarity Time Scale

Correlation of the paleomagnetic polarity zonation with the GPTS (Gradstein et al., 2012) provides an age interpretation between the upper Eocene and the Middle Miocene (from Chron C15n to C5Br) (**Figure 7**).

Biostratigraphic data identify a major unconformity at ~180 mbsf (Hayes et al., 1975) separating Early/Late Oligocene strata below from Early/Middle Miocene strata above. More recent constraints on age data (**Table 1**) restrict the interval of core beneath the unconformity to the late Eocene–Early Oligocene and above the unconformity to the late Early–Middle Miocene (**Figure 7**).

Beneath the unconformity, magnetozones N1 to R7 are correlated to chrons C15–C9 as follows (**Figure 7**): Between 315 and 281 mbsf the normal magnetozones N1 and N2 are correlated with chrons C15n and C13n, respectively, and reversed magnetozones R2 and R2 with chrons C13r and C12r, respectively. This correlation implies a sedimentation rate of ~1 cm/kyr for the late Eocene/Early Oligocene interval of the core with the Eocene/Oligocene boundary at ~304 mbsf between Core 33 and Core 32. Two correlations are considered between 280 and 180 mbsf (magnetozones N3–R7; **Figure 7**). The younger correlates magnetozones N3. N5, R5, N6, R6, N7 and R7 with chrons C12n, C11n.2n, C11n.1r, C10n.2n, C10n.1r, C10n.1n and C9r (model D), respectively and implies that the last appearances of radiolarians *Cyclampterium milowi* and *Calocyclas semipolita* are almost one million year younger than their currently identified last occurrences. The older correlation links magnetozones N5, R5, N6, R6, N7 and R7 with chrons C12n, C11r, C11n.2n, C11n.1r, C11n.1n and C10r (model E) and has a smaller lag and consequently more consistent with the radiolarian late occurrence data but leaves magnetozone N3 with no corresponding chron in the GPTS. While we expect to see magnetozones truncated and potentially missing from the DSDP Site 274 record, magnetozone N3 is represented by several samples and multiple normal polarity chrons, and we would not expect to see an additional magnetic polarity interval not identified in the GPTS. Regardless, we observe that the sediment accumulation rate in the mid Oligocene interval of the core (280–180 mbsf) is more than four times that of the lower Eocene-Oligocene boundary interval, with 25% of the time interval accounted for by distributed unconformities as identified by marked grain size changes (**Figures 2, 7**).

Above the unconformity at 180 mbsf, the interval between 180 and 123 mbsf (cores 19–14), has few biostratigraphical constraints (Hayes et al., 1975, **Table 1**), and we identify three possible magnetostratigraphic age model reconstructions: where R8 N8 and upper part of R7 correspond to (A) chrons C5Br, C5Cn and C5Cr (B) chrons C5Cr, C5Dn and C5Dr. and (C) chrons C5Dr., C5En and C5Er, respectively (**Figure 7**). However, sediment accumulation rates are quite high for all reconstructions (between 2 and 5 cm/kyr), similar to the sediment accumulation rates observed beneath the unconformity.

Our new age model implies that the unconformity at 180 mbsf accounts for between 9 Myr at its shortest and 11 Myr at its longest, which is significantly shorter than the >15 Myr identified from biostratigraphy only in the original age depth model of Hayes et al. (1975).

According to our correlation and calculation of the sedimentary accumulation rate, the studied section encompasses ~20 Myr. For the interval 180–123 mbsf (cores 19–14), we produced the following estimates of mean sedimentation rates for the two most likely age reconstructions: (model A) 2.0 cm/kyr (C5B-C5C), (model B) 5.1 cm/kyr (C5C-C5D) and (model C) 3.3 cm/kyr (C5D-C5E). The interval between 320 and 180 mbsf (cores 34–20) has a mean sediment accumulation rate of 1.5 cm/kyr (model D) and 1.4 cm/kyr (model E) with a mean of 0.8 cm/kyr between chrons C12n and C15n. The highest sedimentation rate is observed during C5Cn (following model B) with 5.1 cm/kyr and lowest sediment accumulation rate is observed during Chron C12n 0.7 cm/kyr.

DISCUSSION

We present a new magnetostratigraphic chronology for an upper Eocene to Middle Miocene sedimentary section cored during DSDP Leg 28 (Site 274) on the continental rise off Victoria Land, Ross Sea. We confirm a significant hiatus between chrons C9r and C5Cr/C5Dr/C5Er, i.e., from the earliest Chattian to the mid Burdigalian (**Figure 7**), and its duration is significantly shorter than previous estimates.

Our new age model also identifies a four-fold increase in sedimentation rate on the Antarctic margin after the Eocene/Oligocene boundary (**Figure 7**). Previous drilling in McMurdo Sound (southern Victoria Land) also identified a significant early Oligocene unconformity (Wilson et al., 1998) and a significant increase in sediment accumulation rates across the Eocene/Oligocene boundary (Wilson et al., 1998; Wilson et al., 2000; Hannah et al., 2001). The increase in sedimentation rate has been linked to the onset of Antarctic ice sheet growth across the Eocene/Oligocene boundary (Salamy and Zachos, 1999; Galeotti et al., 2016). We confirm those findings across the wider Antarctic shelf and slope. The unconformity at 180 mbsf, is coincident with other significant Late Oligocene unconformities reported from the Ross Embayment (Florindo et al., 2005) but extends into the mid Miocene. We relate the long unconformity to be linked to the early evolution of the Antarctic Circumpolar Current which was established in the Late Oligocene and intensified into the Miocene after the growth of Antarctic ice sheets at the Eocene-Oligocene Boundary (Barker et al., 2007; Lyle et al., 2007; Jovane and Verosub, 2011). Sedimentation did not begin again at DSDP Site 274 until the Antarctic Polar Front

migrated northward coincident with Mid Miocene Glacial intensification (Nelson and Cook, 2001).

The unconformity at ca. 180 mbsf could also be partially related to the formation of the Adare Basin, which accommodates the sediments from the West Antarctica Rift System and forms a barrier for the arrival of sediments to the site (Granot et al., 2010, 2013).

Regardless of the exact explanation of the unconformity, these insights are invaluable because they demonstrate that the Early Miocene is characterized by long-term fluctuations of the Antarctic Ice Sheets (Levy et al., 2016; Levy et al., 2019; Jovane et al., 2019; Evangelinos et al., 2020) and that, prior to the Middle Miocene Climatic Optimum (~15 Ma), there was a period of climatic instability modulated by long-term variations with phases of bottom current intensification which either eroded or did not allow the deposition of sediments in the deep parts of the basin.

CONCLUSION

We provided new paleomagnetic results from the late Eocene-Middle Miocene samples from DSDP Site 274, cored during Leg 28 on the continental rise off Victoria Land, Ross Sea.

- Based on our new age model, the cored late Eocene-Middle Miocene sequence covers an interval of almost 20 Myr, from ~35 to ~15 Ma.
- We confirm and better define a major unconformity identified at ~180 mbsf which represents at least 9 Myr from the earliest Chattian to the mid Burdigalian. It may represent non-deposition and/or erosion due to intensification of Antarctic Circumpolar Current activity.
- Significant fluctuations in grain size and magnetic properties are observed above the unconformity (above 180 mbsf) interpreted as cyclical behavior in glacial advance and retreat from the continent.

This new age model will allow further studies of this unique core to reconstruct paleoenvironmental studies focusing on the discharge of sediments from the catchment areas in this region of the Ross Sea.

DATA AVAILABILITY STATEMENT

The raw data supporting the conclusions of this article will be made available by the authors, without undue reservation.

AUTHOR CONTRIBUTIONS

LJ: paleomagnetic measurements, data analysis, discussion and writing; FF: discussion and writing; DR: paleomagnetic measurements, data analysis, and writing; SL: grain size measurements, data analysis, and writing; MH: paleomagnetic measurements, data analysis, and writing; GC: radiolaria and writing; GW: data analysis, discussion and writing.

ACKNOWLEDGMENTS

We thank the editor Hagay Amit and the reviewers for useful comments and corrections which greatly improved the manuscript. The Deep Sea Drilling Project samples and data were provided by the International Ocean Discovery Program (sample requests: 043328-IODP and 069232-IODP). The samples were collected at the UC Davis Paleomagnetism Laboratory as part of NSF grant OPP 06-17194 to K. L. Verosub. LJ, MBH and DR acknowledge funding from Fundação de Amparo á Pesquisa do Estado de São Paulo (FAPESP) grant 2016/24946-9 and 2018/17061-6. LJ is also financed by the Coordenação de Aperfeiçoamento de Pessoal de Nível Superior - Brasil (CAPES)—Finance Code 001. The data are available from the authors upon request.

REFERENCES

Abrajevitch, A., and Kodama, K. (2011). Diagenetic sensitivity of paleoenvironmental proxies: a rock magnetic study of Australian continental margin sediments. *Geochem. Geophys. Geosyst.* 12, Q05Z24. doi:10.1029/2010GC003481

Abrajevitch, A., Van der Voo, R., and Rea, D. K. (2009). Variations in relative abundances of goethite and hematite in Bengal Fan sediments: climatic vs. diagenetic signals. *Mar. Geol.* 267, 191–206. 10.1016/j.margeo.2009.10.010

Acton, G. D., Okada, M., Clement, B. M., Lund, S. P., and Williams, T. (2002). Paleomagnetic overprints in ocean sediment cores and their relationship to shear deformation caused by piston coring. *J. Geophys. Res.* 107 (B4), 2067. doi:10.1029/2001JB000518

Ainley, D. G., and Jacobs, S. S. (1981). Sea-bird affinities for ocean and ice boundaries in the Antarctic. *Deep Sea Res. Part A Oceanogr. Res. Pap.* 28 (10), 1173–1185. doi:10.1016/0198-0149(81)90054-6

Arason, P., and Levi, S. (2010). Maximum likelihood soultion for inclination-only data in paleomagnetism. *Geophys. J. Int.* 182, 753–771. doi:10.1111/j.1365-246X.2010.04671.x

Barker, P. F., Filippelli, G. M., Florindo, F., Martin, E. E., and Scher, H. D. (2007). Onset and role of the antarctic circumpolar current. *Deep Sea Res. Part II Top. Stud. Oceanogr.* 54 (21–22), 2388–2398. doi:10.1016/j.dsr2.2007.07.028

Beddow, H. M., Liebrand, D., Sluijs, A., Wade, B. S., and Lourens, L. J. (2016). Global change across the oligocene-miocene transition: high-resolution stable isotope records from IODP site U1334 (equatorial pacific ocean): the OMT at site U1334. *Paleoceanography* 31, 81–97. doi:10.1002/2015PA002820

Berggren, W. A., Kent, D. V., Swisher, C. C., III., and Aubry, M.-P. (1995). "A revised Cenozoic geochronology and chronostratigraphy," in *Geochronology, time scales and global stratigraphic correlation*. Editors W.A. Berggren, D.V. Kent, M.P. Aubry, and J. Hardenbol (Society for Sedimentary Geology).

Blott, S. J., and Pye, K. (2001). GRADISTAT: a grain size distribution and statistics package for the analysis of unconsolidated sediments. *Earth Surf. Process. Landforms* 26, 1237–1248. doi:10.1002/esp.261

Bukry, D. (1975). "Coccolith and silicoflagellate stratigraphy near Antarctica, Deep Sea drilling Project, Leg 28," in *Initial reports of the deep sea drilling project*. Editor A. G. Kaneps (Washington, DC: U.S. Government Printing Office), Vol. 28.

Bukry, D., and Percival, S. F., Jr. (1971). New Tertiary calcareous nannofossils. *Tulane Studies in Geology and Paleontology* 8 (3).

Bukry, D. (1974). Stratigraphic value of silicoflagellates in nontropical regions. *Geol. Soc. Am. Bull.* 85 (12), 1905–1906. doi:10.1130/0016-7606(1974)85<1905:SVOSIN>2.0.CO;2

Burns, D. A. (1975). "Nannofossil biostratigraphy for antarctic sediments, Leg 28, Deep Sea drilling Project," in *Initial reports of the Deep Sea drilling Project*.

Editor A. G. Kaneps (Washington, DC: U.S. Government Printing Office), Vol. 28.

Chen, P. H. (1975). *Antarctic radiolaria. Initial Reports of the Deep Sea drilling Project*. Washington, DC: U.S. Government Printing Office). Vol. 28.

Chýlek, P., Grams, G. W., and Pinnick, R. G. (1976). Light Scattering by Irregular Randomly Oriented Particles. *Science* 193 (4252), 480–482. doi:10.1126/science.193.4252.480

Ciesielski, P. F. (1975). "Biostratigraphy and paleoecology of neogene and Oligocene silicoflagellates from cores recovered during antarctic Leg 28, Deep Sea drilling Project," in *Initial reports of the Deep Sea drilling Project*. Editor A. G. Kaneps (Washington, DC:U.S. Government Printing Office), Vol. 28.

Cornell, W. C. (1974). Maastrichtian silicoflagellates of the great valley, California. *Geosci. Man* 9 (1), 37–43. doi:10.1080/00721395.1974.9989747

Couper, R. A. (1960). Southern Hemisphere mesozoic and tertiary *podocarpaceae* and *fagaceae* and their palaeogeographic significance. *Proc. Roy. Soc. Lond. B Biol. Sci.* 152 (949), 491–500. doi:10.1098/rspb.1960.0056

Egli, R. (2004). Characterization of individual rock magnetic components by analysis of remanence curves: 3. Bacterial magnetite and natural processes in lakes. *Phys. Chem. Earth* 29, 867–884. 10.1016/j.pce.2004.03.010

Evangelinos, D., Escutia, C., Etourneau, J., Hoem, F., Bijl, P., Boterblom, W., et al. (2020). Late oligocene-miocene proto-antarctic circumpolar current dynamics off the wilkes Land margin, East Antarctica. *Global Planet. Change* 191, 103221. doi:10.1016/j.gloplacha.2020.103221

Farnsworth, A., Lunt, D. J., O'Brien, C. L., Foster, G. L., Inglis, G. N., Markwick, P., et al. (2019). Climate sensitivity on geological timescales controlled by nonlinear feedbacks and Ocean circulation. *Geophys. Res. Lett.* 46, 9880–9889. doi:10.1029/2019GL083574

Fensome, R. A., Gocht, H., Stover, L. E., and Williams, G. L. (1993). *The Eisenack catalog of fossil Dinoflagellates*. Stuttgar: Schweizerbart Science Publishers, Vol. 2.

Fioroni, C., Villa, G., Persico, D., and Jovane, L. (2015). Middle Eocene-Lower Oligocene calcareous nannofossil biostratigraphy and paleoceanographic implications from Site 711 (equatorial Indian Ocean). *Mar. Micropaleontol.* 118, 50–62. doi:10.1016/j.marmicro.2015.06.001

Fioroni, C., Villa, G., Persico, D., Wise, S. W., and Pea, L. (2012). Revised middle eocene-upper Oligocene calcareous nannofossil biozonation for the Southern Ocean. *Rev. Micropaleontol.* 55, 53–70. doi:10.1016/j.revmic.2012.03.001

Florindo, F., Bohaty, S. M., Erwin, P. S., Richter, C., Roberts, A. P., Whalen, P. A., et al. (2003). Magnetobiostratigraphic chronology and palaeoenvironmental history of cenozoic sequences from ODP sites 1165 and 1166, prydz bay, Antarctica. *Palaeogeogr. Palaeoclimatol. Palaeoecol.* 198, 69–100. doi:10.1016/S0031-0182(03)00395-X

Florindo, F., Farmer, R. K., Harwood, D. M., Cody, R. D., Levy, R. H., Bohaty, S. M., et al. (2013). Paleomagnetism of sediments from ODP Site 744, southern Kerguelen Plateau: implications for early to-middle Miocene climate in Antarctica. *Global Planet. Change* 110 (C), 434–454. doi:10.1016/j.gloplacha.2013.05.004

Florindo, F., Wilson, G. S., Roberts, A. P., Sagnotti, L., and Verosub, K. L. (2005). Magnetostratigraphic chronology of a late Eocene to early Miocene glacimarine succession from the Victoria Land basin, Ross Sea, Antarctica. *Global Planet. Change* 45, 207–236. doi:10.1016/j.gloplacha.2004.09.009

Florindo, F., Wilson, G. S., Roberts, A. P., Sagnotti, L., and Verosub, K. L. (2001). Magnetostratigraphy of late eocene-early Oligocene strata from the CRP-3 core, Victoria Land basin, Antarctica. *Terra Antartica* 8 (4), 599–614.

Frakes, L. A. (1975). "Paleoclimatic significance of some sedimentary components at site 27," in *Initial reports of the Deep Sea drilling Project*. Editor A. G. Kaneps (Washington, D. C:U.S. Government Printing Office), Vol. 28.

Francis, J. E., Marenssi, S., Levy, R., Hambrey, M., Thorn, V. C., Mohr, B., et al. (2009). "From greenhouse to icehouse—the eocene/oligocene in Antarctica," in *Developments in Earth and environmental Sciences*. Amsterdam, Netherlands: Elsevier, 309–368.

Fuller, M., Hastedt, M., and Herr, B. (1998). Coring-induced magnetization of recovered sediments. *Proc. Ocean Drill. Progr. Sci. Results* 157, 47–56.

Funakawa, S., and Nishi, H. (2005). Late middle Eocene to late Oligocene radiolarian biostratigraphy in the Southern Ocean (maud rise, ODP Leg 113, site 689). *Mar. Micropaleontol.* 54, 213–247. doi:10.1016/j.marmicro.2004.12.002

Galeotti, S., DeConto, R., Naish, T., Stocchi, P., Florindo, F., Pagani, M., et al. (2016). Antarctic ice sheet variability across the Eocene-Oligocene boundary climate transition. *Science* 352, 76–80. doi:10.1126/science.aab0669

Gradstein, F. M., Ogg, J. G., Schmitz, M. D., and Ogg, G. M. (2012). *The geological time scale 2012*. Amsterdam, Netherlands: Elsevier, 1142.

Granot, R., Cande, S. C., Stock, J. M., and Damaske, D. (2013). Revised eocene-oligocene kinematics for the west antarctic rift system. *Geophys. Res. Lett.* 40, 279–284. doi:10.1029/2012GL054181

Granot, R., Cande, S. C., Stock, J. M., Davey, F. J., and Clayton, R. W. (2010). Postspreading rifting in the Adare Basin, Antarctica: regional tectonic consequences. *Geochem. Geophys. Geosyst.* 11, Q08005. doi:10.1029/2010GC003105

Grommé, C. S., Wright, T., and Peck, D. (1969). Magnetic properties and oxidation of irontitanium oxide minerals in Alae Makaupuki lava lakes, Hawaii. *J. Geophys. Res.* 74, 5277–5293. 10.1029/JB074i022p05277

Guiry, M. D., and Guiry, G. M. (2011). AlgaeBase. World-wide electronic publication. Galway: National University of Ireland. . Avialable at: https://www.algaebase.org (Accessed April 04, 2020).

Hall, S. A. (1977). Cretaceous and tertiary dinoflagellates from seymour Island, Antarctica. *Nature* 267 (5608), 239–241. doi:10.1038/267239a0

Hannah, M. J., Wrenn, J. H., and Wilson, G. J. (2001). Preliminary report on early Oligocene and latest Eocene marine palynomorphs from CRP-3 drillhole, Victoria Land basin, Antarctica. *Terra Antartica* 8, 383–388.

Hayes, D. E., Frakes, L. A., Barrett, P. J., Burns, D. A., Chen, P.-H., Ford, A. B., et al. (1975). "Shipboard site report - site 274," in *Initial reports of the Deep Sea drilling Project*. Editor A. G. Kaneps (Washington, DC:U.S. Government Printing Office), Vol. 28.

Hayes, D. E., and Frakes, L. A. (1975). "General synthesis, Deep Sea drilling Project Leg 28," in *Initial reports of the Deep Sea drilling Project*. Editor A. G. Kaneps (Washington, DC:U.S. Government Printing Office), Vol. 28.

Heslop, D., Dekkers, M. J., Kruiver, P. P., and van Oorschot, I. H. M. (2002). Analysis of isothermal remanent magnetization acquisition curves using the expectation-maximization algorithm. *Geophys. J. Int.* 148, 58–64. 10.1046/j.0956-540x.2001.01558.x

Heslop, D., McIntosh, G., and Dekkers, M. J. (2004). Using time- and temperature-dependent Preisach models to investigate the limitations of modelling isothermal remanent magnetization acquisition curves with cumulative log Gaussian functions. *Geophys. J. Int.* 157, 55–63. doi:10.1111/j.1365-246X.2004.02155.x

Holbourn, A. E., Kuhnt, W., Clemens, S. C., Kochhann, K. G. D., Jöhnck, J., Lübbers, J., et al. (2018). Late Miocene climate cooling and intensification of southeast Asian winter monsoon. *Nat. Commun.* 9, 1584. doi:10.1038/s41467-018-03950-1

Holbourn, A., Kuhnt, W., Frank, M., and Haley, B. A. (2013). Changes in Pacific Ocean circulation following the Miocene onset of permanent Antarctic ice cover. *Earth Planet Sci. Lett.* 365, 38–50. doi:10.1016/j.epsl.2013.01.020

Holbourn, A., Kuhnt, W., Kochhann, K. G. D., Andersen, N., and Sebastian Meier, K. J. (2015). Global perturbation of the carbon cycle at the onset of the miocene climatic optimum. *Geology* 43, 123–126. doi:10.1130/G36317.1

Holbourn, A., Kuhnt, W., Lyle, M., Schneider, L., Romero, O., and Andersen, N. (2014). Middle Miocene climate cooling linked to intensification of eastern equatorial Pacific upwelling. *Geology* 42, 19–22. doi:10.1130/G34890.1

Holbourn, A., Kuhnt, W., Schulz, M., and Erlenkeuser, H. (2005). Impacts of orbital forcing and atmospheric carbon dioxide on Miocene ice-sheet expansion. *Nature* 438, 483–487. doi:10.1038/nature04123

Houtz, R., and Meijer, R. (1970). Structure of the Ross Sea shelf from profiler data. *J. Geophys. Res. Solid Earth* 75, 6592–6597. doi:10.1029/JB075i032p06592

Jovane, L., Acton, G., Florindo, F., and Verosub, K. L. (2008). Geomagnetic field behavior at high latitudes from a paleomagnetic record from Eltanin core 27–21 in the Ross Sea sector, Antarctica. *Earth Planet Sci. Lett.* 267, 435–443. 10.1016/j.epsl.2007.12.006

Jovane, L., Florindo, F., Acton, G., Ohneiser, C., Sagnotti, L., Strada, E., et al. (2019). Miocene glacial dynamics recorded by variations in magnetic properties in the ANDRILL-2A drill core. J. Geophys. Res. *Solid Earth* 124, 2297–2312. doi:10.1029/2018JB016865

Jovane, L., Florindo, F., Bazylinski, D. A., and Lins, U. (2012). Prismatic magnetite magnetosomes from cultivated Magnetovibrio blakemorei strain MV-1: a

magnetic fingerprint in magnetic sediments?. *Environ Microbiol Rep* 4, 664–668. doi:10.1111/1758-2229.12000

Jovane, L., Florindo, F., and Dinarès-Turell, J. (2004). Environmental magnetic record of paleoclimate change from the Eocene-Oligocene stratotype section, Massignano, Italy. *Geophys. Res. Lett.* 31, L15601. doi:10.1029/2004GL020554

Jovane, L., and Verosub, K. L. (2011). "Magnetic properties of oligocene-eocene cores from SHALDRIL II, Antarctica," in *Tectonic, climatic, and cryospheric Evolution of the antarctic peninsula*. Editors J. B. Anderson and J. S. Wellner (Washington, DC: American Geophysical Union), Vol. 63, 115–130.

Kaneps, A. G. (1975). "Cenozoic planktonic foraminifera from antarctic deep-sea sediments, Leg 28, DSDP," in *Initial reports of the Deep Sea drilling Project*. Editor A. G. Kaneps (Washington, D. C: U.S. Government Printing Office), Vol. 28.

Kennett, J. P. (1977). Cenozoic evolution of Antarctic glaciation, the circum-Antarctic Ocean, and their impact on global paleoclimate. *J. Geophys. Res.* 82, 3843–3860. 10.1029/JC082i027p03843

Kominz, M. A., and Pekar, S. F. (2001). Oligocene eustasy from two-dimensional sequence stratigraphic backstripping. *Geol. Soc. Am. Bull.* 113 (3), 291–304. doi:10.1130/0016-7606(2001)113<0291:OEFTDS>2.0.CO;2

Kruiver, P. P., Dekkers, M. J., and Heslop, D. (2001). Quantification of magnetic coercivity components by the analysis of acquisition curves of isothermal remanent magnetization. *Earth Planet Sci. Lett.* 189, 269–276. 10.1016/S0012-821X(01)00367-3

Kulhanek, D. K., Levy, R. H., Clowes, C. D., Prebble, J. G., Rodelli, D., Jovane, L., et al. (2019). Revised chronostratigraphy of DSDP site 270 and late Oligocene to early Miocene paleoecology of the Ross Sea sector of Antarctica. *Global Planet. Change* 178, 46–64. doi:10.1016/j.gloplacha.2019.04.002

Lear, C. H., Coxall, H. K., Foster, G. L., Lunt, D. J., Mawbey, E. M., Rosenthal, Y., et al. (2015). Neogene ice volume and ocean temperatures: insights from infaunal foraminiferal Mg/Ca paleothermometry. *Paleoceanography* 30 (11), 437–1454. doi:10.1002/2015PA002833

Lear, C. H., Rosenthal, Y., Coxall, H. K., and Wilson, P. A. (2004). Late Eocene to early Miocene ice sheet dynamics and the global carbon cycle. *Paleoceanogr. Paleoclimatol.* 19, PA4015. doi:10.1029/2004PA001039

Levy, R., Harwood, D., Florindo, F., Sangiorgi, F., Tripati, R., von Eynatten, H., et al. (2016). Antarctic ice sheet sensitivity to atmospheric CO2 variations in the early to mid-Miocene. *Proc. Natl. Acad. Sci. Unit. States Am.* 113 (13), 3453–3458. doi:10.1073/pnas.1516030113

Levy, R. H., and Harwood, D. M. (2000). "Tertiary marine palynomorphs from the McMurdo Sound erratics, Antarctica," in *Paleobiology and Paleoenvironments of Eocene Rocks: McMurdo Sound, East Antarctica*. 76, 183–242.

Levy, R. H., Meyers, S. R., Naish, T. R., Golledge, N. R., McKay, R. M., Crampton, J. S., and Harwood, D. M. (2019). Antarctic ice-sheet sensitivity to obliquity forcing enhanced through ocean connections. *Nat. Geosci.* 12 (2), 132–137. doi:10.1073/pnas.1516030113

Lewis, A. R., Marchant, D. R., Ashworth, A. C., Hemming, S. R., and Machlus, M. L. (2007). Major middle Miocene global climate change: evidence from East Antarctica and the transantarctic mountains. *Geol. Soc. Am. Bull.* 119, 1449–1461. doi:10.1130/00167606(2007)119[1449:MMMGCC]2.0.CO;2

Liebrand, D., de Bakker, A. T. M., Beddow, H. M., Wilson, P. A., Bohaty, S. M., Ruessink, G., et al. (2017). Evolution of the early Antarctic ice ages. *Proc. Natl. Acad. Sci. Unit. States Am.* 114, 3867–3872. doi:10.1073/pnas.1615440114

Lurcock, P. C., and Florindo, F. (2017). *Antarctic climate history and global climate changes*. Cambridge: Oxford University Press.

Lurcock, P. C., and Florindo, F. (2019). New developments in the PuffinPlot paleomagnetic data analysis program. *Geochem. Geophys. Geosyst.* 20, 5578–5587. doi:10.1029/2019GC008537

Lurcock, P., and Wilson, G. (2012). PuffinPlot: a versatile, user-friendly programme for paleomagnetic analysis. *Geochem. Geophys. Geosyst.* 13, Q06Z45. doi:10.1029/2012GC004098

Lyle, M., Gibbs, S., Moore, T. C., and Rea, D. K. (2007). Late Oligocene initiation of the antarctic circumpolar current: evidence from the South Pacific. *Geology* 35, 691. doi:10.1130/G23806A.1

Mandra, Y. T., and Mandra, H. (1970). Antarctic Tertiary marine climate based on silicoflagellates. *Antarct. J. U. S.* 5 (5), 178–180.

Mandra, Y. T., and Mandra, H. (1971). Upper-eocene silicoflagellates from new-zealand. *Antarct. J. U. S.* 6 (5), 177–178.

Markwick, P. J. (2007). "The palaeogeographic and palaeoclimatic significance of climate proxies for data-model comparisons," in *Deep-time Perspectives on climate change: Marrying the Signal from computer Models and biological proxies*. Editors M. Williams, A. M. Haywood, F. J. Gregory, and D. N. Schmidt (London, United Kingdom: The Geological Society of London on behalf of The Micropalaeontological Society), 251–312.

McCollum, D. W. (1975). "Diatom stratigraphy of the Southern Ocean," in *Initial reports of the Deep Sea drilling Project*. Editor A. G. Kaneps (Washington, DC: U.S. Government Printing Office), Vol. 28.

Miller, K. G. (2005a). The phanerozoic record of global sea-level change. *Science* 310, 1293–1298. doi:10.1126/science.1116412

Miller, K. G., Wright, J. D., and Browning, J. V. (2005b). Visions of ice sheets in a greenhouse world. *Mar. Geol.* 217, 215–231. doi:10.1016/j.margeo.2005.02.007

Miller, K. G., Wright, J. D., and Fairbanks, R. G. (1991). Unlocking the Ice House: Oligocene-Miocene oxygen isotopes, eustasy, and margin erosion. *J. Geophys. Res.* 96, 6829–6848. doi:10.1029/90JB02015

Nelson, C. S., and Cook, P. J. (2001). History of oceanic front development in the New Zealand sector of the Southern Ocean during the Cenozoic—a synthesis. *N. Z. J. Geol. Geophys.* 44 (4), 535–553. doi:10.1080/00288306.2001.9514954

Olney, M. P., Scherer, R. P., Harwood, D. M., and Bohaty, S. M. (2007). Oligocene–early Miocene Antarctic nearshore diatom biostratigraphy. *Deep-Sea Research II* 54, 2325–2349. doi:10.1016/j.dsr2.2007.07.020

Olsson, R. K., Hemleben, C., Huber, B. T., and Berggren, W. A. (2006). "Taxonomy, biostratigraphy, and phylogeny of Eocene *Globigerina, Globoturborotalita, subbotina,* and *turborotalita*," in *Atlas of Eocene planktonic foraminifera*. Editors P. N. Pearson, R. K. Olsson, C. Hemleben, B. T. Huber, and W. A. Berggren (Cushman Foundation for Foraminiferal Research, Special Publication), Chap. 6, 41, 111–168.

Orsi, A. H., and Wiederwohl, C. L. (2009). A recount of Ross Sea waters. *Deep Sea Res. Part II Top. Stud. Oceanogr.* 56 (13–14), 778–795. doi:10.1016/j.dsr2.2008.10.033

Ozima, M., and Larson, E. E. (1970). Low- and high-temperature oxidation of titanomagnetite in relation to irreversible changes in the magnetic properties of submarine basalts. *J. Geophys. Res.* 75 (5), 103–101. 10.1029/JB075i005p01003

Pälike, H., Norris, R. D., Herrle, J. O., Wilson, P. A., Coxall, H. K., Lear, C. H., et al. (2006). The heartbeat of the Oligocene climate system. *Science* 314, 1894–1898. doi:10.1126/science.1133822

Pekar, S. F., DeConto, R. M., and Harwood, D. M. (2006). Resolving a late Oligocene conundrum: deep-sea warming and Antarctic glaciation. *Palaeogeogr. Palaeoclimatol. Palaeoecol.* 231, 29–40. doi:10.1016/j.palaeo.2005.07.024

Plantz, P. E. (2007). SL-AN-25 revision A. Blue laser technology applied to the microtrac unified scatter technique for full-range particle size Measurement. *Application note* 8. Available at: https://pdfs.semanticscholar.org/bba0/410e2cbffeb8f6f8f426e5a9fdcd22dbbf4f.pdf (Accessed 2007).

Roberts, A. P., Sagnotti, L., Florindo, F., Bohaty, S. M., Verosub, K. L., Wilson, G. S., et al. (2013). Environmental magnetic record of paleoclimate, unroofing of the transantarctic mountains, and volcanism in late Eocene to early Miocene glaci-marine sediments from the Victoria Land basin, Ross Sea, Antarctica. *J.* Geophys. Res. *Solid Earth* 118, 1845–1861. doi:10.1002/jgrb.50151

Robertson, D. J., and France, D. E. (1994). Discrimination of remanence-carrying minerals in mixtures, using isothermal remanent magnetisation acquisition curves. *Phys. Earth Planet. In.* 82, 223–234. doi:10.1016/0031-9201(94)90074-4

Rodelli, D., Jovane, L., Giorgioni, M., Rego, E. S., Cornaggia, F., Benites, M., et al. (2019). Diagenetic fate of biogenic soft and hard magnetite in chemically stratified sedimentary environments of mamanguá ría, Brazil. *J. Geophys. Res. Solid Earth* 124, 2313–2330. doi:10.1029/2018JB016576

Rodelli, D., Jovane, L., Roberts, A. P., Cypriano, J., Abreu, F., and Lins, U. (2018). Fingerprints of partial oxidation of biogenic magnetite from cultivated and natural marine magnetotactic bacteria using synchrotron radiation: fingerprints of partial oxidation of biogenic magnetite. *Environ. Microbiol. Rep.* 10, 337–343. doi:10.1111/1758-2229.12644

Sagnotti, L., Florindo, F., Verosub, K. L., Wilson, G. S., and Roberts, A. P. (1998). Environmental magnetic record of antarctic palaeoclimate from eocene/oligocene glaciomarine sediments, Victoria Land basin: magnetic record of antarctic palaeoclimate. *Geophys. J. Int.* 134, 653–662. doi:10.1046/j.1365-246x.1998.00559.x

Salamy, K. A., and Zachos, J. C. (1999). Latest Eocene—early Oligocene climate change and Southern Ocean fertility: inferences from sediment accumulation rates and stable isotope data. *Paleogeog. Paleoclim, Paleoecol.* 145, 61–77. doi:10.1016/S0031-0182(98)00093-5

Savian, J. F., Jovane, L., Frontalini, F., Trindade, R. I., Coccioni, R., Bohaty, S. M., et al. (2014). Enhanced primary productivity and magnetotactic bacterial production in response to middle Eocene warming in the Neo-Tethys Ocean. *Palaeogeogr. Palaeoclimatol. Palaeoecol.* 414, 32–45. doi:10.1016/j.palaeo.2014.08.009

Savian, J. F., Jovane, L., Giorgioni, M., Iacoviello, F., Rodelli, D., Roberts, A. P., et al. (2016). Environmental magnetic implications of magnetofossil occurrence during the Middle Eocene Climatic Optimum (MECO) in pelagic sediments from the equatorial Indian Ocean. *Palaeogeogr. Palaeoclimatol. Palaeoecol.* 441, 212–222. 10.1016/J.PALAEO.2015.06.029

Scherer, R., Bohaty, S. M., and Harwood, David. M. (2000). Oligocene and lower Miocene siliceous microfossil biostratigraphy of Cape Roberts Project core CRP-2/2A, Victoria Land basin, Antarctica. *Papers in the Earth and atmospheric Sciences*, 282.

Shevenell, A. E., Kennett, J. P., and Lea, D. W. (2008). Middle Miocene ice sheet dynamics, deep-sea temperatures, and carbon cycling: a Southern Ocean perspective. *Geochem. Geophys. Geosyst.* 9, Q02006. doi:10.1029/2007GC001736

Shevenell, A. E., Kennett, J. P., and Lea, D. W. (2004). Middle Miocene Southern Ocean cooling and antarctic cryosphere expansion. *Science* 305, 1766–1770. doi:10.1126/science.1100061

Spezzaferri, S., Olsson, R. K., Hemleben, C., Wade, B. S., and Coxall, H. K. (2018). "Taxonomy, biostratigraphy, and phylogeny of Oligocene and lower Miocene *Globoturborotalita*," in *Atlas of Oligocene planktonic foraminifera*. Editors B. S. Wade, R. K. Olsson, P. N. Pearson, B. T. Huber, and W. A. Berggren (Cushman Foundation for Foraminiferal Research), 46, 231–268.

Takemura, A., and Ling, H. Y. (1997). Eocene and Oligocene radiolarian biostratigraphy from the Southern Ocean: correlation of ODP legs 144 (atlantic ocean) and 120 (Indian ocean). *Mar. Micropaleontol.* 30, 97–116. doi:10.1016/S0377-8398(96)00017-5

Thompson, R., and Oldfield, F. (1986). *Environmental magnetism*. London: Allen & Unwin.

Torsvik, T. H., Van der Voo, R., Preeden, U., Mac Niocaill, C., Steinberger, B., Doubrovine, P. V., et al. (2012). Phanerozoic polar wander, palaeogeography and dynamics. *Earth Sci. Rev.* 114 (3–4), 325–368. doi:10.1016/j.earscirev.2012.06.007

Wade, B. S., Olsson, R. K., Pearson, P. N., Edgar, K. M., and Premoli Silva, I. (2018). "Taxonomy, biostratigraphy, and phylogeny of Oligocene *subbotina*," in *Atlas of Oligocene planktonic foraminifera*. Editors B. S. Wade, R. K. Olsson, P. N. Pearson, B. T. Huber, and W. A. Berggren (Cushman Foundation for Foraminiferal Research, Special Publication), Chap. 10, 46, 307–330.

Wallich, G. C. (1877). XXXIV—observations on the coccosphere. *J. Nat. Hist.* 19 (112), 342–350. doi:10.1080/00222937708682153

Weaver, F. M. (1983). "Cenozoic radiolarians from the southwest atlantic, falkland plateau region, Deep Sea drilling Project Leg 71," in *Init. Repts. DSDP, 71*. Editor J. W. Ludwig and V. A. Krasheninnikov (Washington, DC: U.S. Govt. Printing Office).

Westerhold, T., Marwan, N., Drury, A. J., Liebrand, D., Agnini, C., Anagnostou, E., et al. (2020). An astronomically dated record of Earth's climate and its predictability over the last 66 million years. *Science* 369, 1383–1387. doi:10.1126/science.aba6853

Whitworth, T., III., Orsi, A. H., Kim, S.-J., Nowlin, W. D., Jr., and Locarnini, R. A. (1995). "Water masses and mixing near the Antarctic slope front," in *Antarctic research series (volume 75): ocean, ice, and atmosphere: interactions at the antarctic continental margin*. Editors S.S. Jacobs and R.F. Weiss (Washington, DC: American Geophysical Union), 1–27.

Wilson, G. S., Florindo, F., Sagnotti, L., Verosub, K. L., and Roberts, A. P. (2000). Magnetostratigraphy of oligocene-miocene glaciomarine strata from CRP-2/2A, Victoria Land basin. *Antarct.* Terra Ant. 7, 631–646.

Wilson, G. S., Pekar, S. F., Naish, T. R., Passchier, S., and DeConto, R. (2009). "The Oligocene – Miocene boundary – antarctic climate response to orbital forcing," in Developments in Earth and environmental Sciences, *Vol 8, antarctic climate EvolutionFabio Florindo and martin siegert.* (Amsterdam, Netherlands: Elsevier), 369–400.

Wilson, G. S., Roberts, A. P., Verosub, K. L., Florindo, F., and Sagnotti, L. (1998). Magnetobiostratigraphic chronology of the eocene—oligocene transition in the CIROS-1 core, Victoria Land margin, Antarctica: implications for antarctic glacial history. *Geol. Soc. Am. Bull.* 110 (1), 35–47. doi:10.1130/0016-7606(1998)110<0035:MCOTEO>2.3.CO;2

Yamazaki, T. (2012). Paleoposition of the Intertropical Convergence Zone in the eastern Pacific inferred fromglacial–interglacial changes in terrigenous and biogenicmagnetic mineral fractions. *Geology* 40, 151–154. doi:10.1130/G32646.1

Zachos, J. C., Flower, B. P., and Paul, H. (1997). Orbitally paced climate oscillations across the Oligocene/Miocene boundary. *Nature* 388, 567–570. doi:10.1038/41528

Zachos, J. C., Quinn, T. M., and Salamy, K. A. (1996). High-resolution (10 4 years) deep-sea foraminiferal stable isotope records of the Eocene-Oligocene climate transition. *Paleoceanography* 11, 251–266. doi:10.1029/96PA00571

Zachos, J., Pagani, M., Sloan, L., Thomas, E., and Billups, K. (2001). Trends, rhythms, and aberrations in global climate 65 Ma to present. *Science* 292, 686–693. doi:10.1126/science.1059412

Zijderveld, J. D. A. (1967). "A.C. demagnetization of rocks," in *Methods in paleomagnetism*. Editors D. W. Collison, K. M. Creer, and S. K. Runcorn (Amsterdam, Netherlands: Elvesier), 256–286.

Conflict of Interest: The authors declare that the research was conducted in the absence of any commercial or financial relationships that could be construed as a potential conflict of interest.

Advantages of publishing in Frontiers

OPEN ACCESS
Articles are free to read for greatest visibility and readership

FAST PUBLICATION
Around 90 days from submission to decision

HIGH QUALITY PEER-REVIEW
Rigorous, collaborative, and constructive peer-review

TRANSPARENT PEER-REVIEW
Editors and reviewers acknowledged by name on published articles

Frontiers
Avenue du Tribunal-Fédéral 34
1005 Lausanne | Switzerland

Visit us: www.frontiersin.org
Contact us: frontiersin.org/about/contact

REPRODUCIBILITY OF RESEARCH
Support open data and methods to enhance research reproducibility

DIGITAL PUBLISHING
Articles designed for optimal readership across devices

FOLLOW US
@frontiersin

IMPACT METRICS
Advanced article metrics track visibility across digital media

EXTENSIVE PROMOTION
Marketing and promotion of impactful research

LOOP RESEARCH NETWORK
Our network increases your article's readership